



Journal of Engineering for Gas Turbines and Power

Published Quarterly by ASME

VOLUME 128 • NUMBER 1 • JANUARY 2006

Editor
LEE S. LANGSTON (2006)

Assistant to the Editor
LIZ LANGSTON

Associate Editors
Fuels and Combustion Technologies
K. M. BRYDEN (2008)

Internal Combustion Engines
J. C. COWART (2008)
M. S. WOOLDRIDGE (2008)

International Gas Turbine Institute
IGTI Review Chair
H. R. SIMMONS (2003)
A. J. STRAZISAR (2004)
K. C. HALL (2005)

Combustion and Fuels
P. MALTE (2006)

Structures and Dynamics
N. ARAKERÉ (2007)

PUBLICATIONS DIRECTORATE
Chair, **ARTHUR G. ERDMAN**

OFFICERS OF THE ASME
President, **RICHARD E. FEIGEL**

Executive Director,
VIRGIL R. CARTER

Treasurer,
T. PESTORIUS

PUBLISHING STAFF

Managing Director, Publishing
PHILIP DI VIETRO

Production Coordinator
JUDITH SIERANT

Production Assistant
MARISOL ANDINO

TECHNICAL PAPERS

Fuels & Combustion Technology

- 1 Shapes of Elliptic Methane Laminar Jet Diffusion Flames
Jorge R. Camacho and Ahsan R. Choudhuri
- 8 Visualization of Steam Addition Effect on OH Distribution in a Flame by Isotope Shift/Planar Laser-Induced Fluorescence (IS/PLIF) Spectroscopy
Atsushi Katoh, Masahisa Shinoda, Kuniyuki Kitagawa, and Ashwani K. Gupta

Gas Turbines: Aircraft Engine

- 13 A Generic Approach for Gas Turbine Adaptive Modeling
W. P. J. Visser, O. Kogenhop, and M. Oostveen
- 20 Experimental Operating Range Extension of a Twin-Spool Turbofan Engine by Active Stability Control Measures
Stephan G. Scheidler and Leonhard Fottner

Gas Turbines: Combustion and Fuels

- 29 Unsteady Aerodynamics of an Aeroengine Double Swirler Lean Premixing PrevapORIZING Burner
Edward Canepa, Pasquale Di Martino, Piergiorgio Formosa, Marina Ubaldi, and Pietro Zunino
- 40 Towards Modeling Lean Blow Out in Gas Turbine Flameholder Applications
Won-Wook Kim, Jeffrey J. Lienau, Paul R. Van Slooten, Meredith B. Colket, III, Robert E. Malecki, and Saadat Syed

Gas Turbines: Controls, Diagnostics & Instrumentation

- 49 An Integrated Fault Diagnostics Model Using Genetic Algorithm and Neural Networks
Suresh Sampath and Riti Singh
- 57 Assessment of the Effectiveness of Gas Path Diagnostic Schemes
K. Mathioudakis and Ph. Kamboukos
- 64 Bayesian Network Approach for Gas Path Fault Diagnosis
C. Romessis and K. Mathioudakis
- 73 Validation of CESI Blade Life Management System by Case Histories and in situ NDT
Claudia Rinaldi, Valerio Bicego, and Pier Paolo Colombo

Gas Turbines: Cycle Innovations

- 81 Proposal and Analysis of a Novel Zero CO₂ Emission Cycle With Liquid Natural Gas Cryogenic Exergy Utilization
Na Zhang and Noam Lior
- 92 Component Map Generation of a Gas Turbine Using Genetic Algorithms
Changduk Kong, Seonghee Kho, and Jayoung Ki

(Contents continued on inside back cover)

This journal is printed on acid-free paper, which exceeds the ANSI Z39.48-1992 specification for permanence of paper and library materials. ©™

♻️ 85% recycled content, including 10% post-consumer fibers.

Transactions of the ASME, Journal of Engineering for Gas Turbines and Power (ISSN 0742-4795) is published quarterly (Jan., April, July, Oct.) by The American Society of Mechanical Engineers, Three Park Avenue, New York, NY 10016. Periodicals postage paid at New York, NY and additional mailing offices.
POSTMASTER: Send address changes to Transactions of the ASME, Journal of Engineering for Gas Turbines and Power, c/o THE AMERICAN SOCIETY OF MECHANICAL ENGINEERS, 22 Law Drive, Box 2300, Fairfield, NJ 07007-2300.
CHANGES OF ADDRESS must be received at Society headquarters seven weeks before they are to be effective. Please send old label and new address.

STATEMENT from By-Laws. The Society shall not be responsible for statements or opinions advanced in papers or printed in its publications (B7.1, par. 3).

COPYRIGHT © 2006 by the American Society of Mechanical Engineers. For authorization to photocopy material for internal or personal use under circumstances not falling within the fair use provisions of the Copyright Act, contact the Copyright Clearance Center (CCC), 222 Rosewood Drive, Danvers, MA 01923. Tel: 978-750-8400, www.copyright.com. Canadian Goods & Services Tax Registration #126148048

- 97 The Effect of Water Injection on Multispool Gas Turbine Behavior
A. J. Meacock and A. J. White

Gas Turbines: Heat Transfer

- 103 Influence of Operating Condition and Geometry on the Oil Film Thickness in Aeroengine Bearing Chambers
P. Gorse, S. Busam, and K. Dullenkopf
- 111 A Numerical Model for Oil Film Flow in an Aeroengine Bearing Chamber and Comparison to Experimental Data
Mark Farrall, Kathy Simmons, Stephen Hibberd, and Philippe Gorse
- 118 Flow Characteristics and Stability Analysis of Variable-Density Rotating Flows in Compressor-Disk Cavities
Bruce V. Johnson, J. D. Lin, William A. Daniels, and Roger Paolillo
- 128 Buoyancy-Induced Flow in a Heated Rotating Cavity
J. Michael Owen and Jonathan Powell

Gas Turbines: Industrial and Cogeneration

- 135 Influence of High Fogging Systems on Gas Turbine Engine Operation and Performance
Giovanni Cataldi, Harald Güntner, Charles Matz, Tom McKay, Jürgen Hoffmann, Anton Nemet, Stefan Lecheler, and Jost Braun

Gas Turbines: Manufacturing, Materials, and Metallurgy

- 144 Hot Corrosion of Lanthanum Zirconate and Partially Stabilized Zirconia Thermal Barrier Coatings
Basil R. Marple, Joël Voyer, Michel Thibodeau, Douglas R. Nagy, and Robert Vassen

Gas Turbines: Marine

- 153 Understanding Royal Navy Gas Turbine Sea Water Lubricating Oil Cooler Failures When Caused by Microbial Induced Corrosion ("SRB")
Richard Bolwell

Gas Turbines: Structures and Dynamics

- 163 Modeling Oil Flows in Engine Sumps: Drop Dynamics and Wall Impact Simulation
Vladimir D. Weinstock and Stephen D. Heister
- 173 A Continuum Damage Mechanics Model on Creep Rupture Life Assessment of a Steam Turbine Rotor
Jing JianPing, Meng Guang, Sun Yi, and Xia SongBo
- 178 Reduction of Power Losses in Bearing Chambers Using Porous Screens Surrounding a Ball Bearing
Michael Flouros
- 183 Adjoint Harmonic Sensitivities for Forced Response Minimization
Mihai C. Duta, Michelle S. Campobasso, Michael B. Giles, and Leigh B. Lapworth

Microturbines & Small Turbomachinery

- 190 Performance Enhancement of Microturbine Engines Topped With Wave Rotors
Pezhman Akbari, Razi Nalim, and Norbert Müller

Internal Combustion Engines

- 203 The Development of a Dual-Injection Hydrogen-Fueled Engine With High Power and High Efficiency
Y. Y. Kim, Jong T. Lee, and J. A. Caton
- 213 The Advanced Injection Low Pilot Ignited Natural Gas Engine: A Combustion Analysis
K. K. Srinivasan, S. R. Krishnan, S. Singh, K. C. Midkiff, S. R. Bell, W. Gong, S. B. Fiveland, and M. Willi
- 219 Heat Transfer in Reciprocating Planar Curved Tube With Piston Cooling Application
Shyy Woei Chang and Yao Zheng

(Contents continued)

Journal of Engineering for Gas Turbines and Power

JANUARY 2006

Volume 128, Number 1

230 Hydrogen Fueled Spark-Ignition Engines Predictive and Experimental Performance
Hailin Li and Ghazi A. Karim

The ASME Journal of Engineering for Gas Turbines and Power is abstracted and indexed in the following:

AESIS (Australia's Geoscience, Minerals, & Petroleum Database), Applied Science & Technology Index, Aquatic Sciences and Fisheries Abstracts, Civil Engineering Abstracts, Compendex (The electronic equivalent of Engineering Index), Computer & Information Systems Abstracts, Corrosion Abstracts, Current Contents, Engineered Materials Abstracts, Engineering Index, Enviroline (The electronic equivalent of Environment Abstracts), Environment Abstracts, Environmental Science and Pollution Management, Fluidex, INSPEC, Mechanical & Transportation Engineering Abstracts, Mechanical Engineering Abstracts, METADEX (The electronic equivalent of Metals Abstracts and Alloys Index), Pollution Abstracts, Referativnyi Zhurnal, Science Citation Index, SciSearch (The electronic equivalent of Science Citation Index), Shock and Vibration Digest

Shapes of Elliptic Methane Laminar Jet Diffusion Flames

Jorge R. Camacho

Ahsan R. Choudhuri

e-mail: ahsan@utep.edu

Combustion and Propulsion Research
Laboratory,
Department of Mechanical and Industrial
Engineering,
The University of Texas at El Paso,
500 West University,
El Paso, TX 79968-0521

Buoyant and nonbuoyant shapes of methane flames issued from a 2:1 aspect ratio elliptic tube burner were measured. Nonbuoyant conditions were obtained in the KC-135 microgravity research aircraft operated by NASA's Johnson Space Center. A mathematical model based on the extended Burke-Schumann flame theory is developed to predict the flame length of an elliptic burner. The model utilizes Roper's theoretical method for circular burners and extends the analysis for elliptic burners. The predicted flame length using the theoretical model agrees well with experimental measurements. In general for the elliptic burner the nonbuoyant flames are longer than the buoyant flames. However, measured lengths of both buoyant and nonbuoyant flame lengths change proportionally with the volumetric fuel flow rate and support the L vs Q correlation. The maximum flame width measured at buoyant and nonbuoyant conditions also show a proportional relation with the volumetric fuel flow rate. Normalized buoyant and nonbuoyant flame lengths of the elliptic burner correlate ($L/d \propto Re$) with the jet exit Reynolds number and exhibit a higher slope compared to a circular burner. Normalized flame width data show a power correlation ($w/d = c Fr^n$) with the jet exit Froude number. [DOI: 10.1115/1.2032449]

Introduction

The CO and NO_x emissions from combustion systems can be reduced if fuel-air-mixing rates at different zones of the flame are controlled. This generally requires a more complicated combustion system design such as staged combustion. Another option is the post combustion removal of pollutants possible through catalytic conversion or exhaust gas-processing techniques requiring a high setup and maintenance cost. A more cost-effective way is to modify the burner geometry, for example nonaxisymmetric geometry, to enhance mixing through an alteration of the near burner flow-field characteristics [1–4]. Previous investigations have shown promising improvements of combustion systems with nonaxisymmetric burner configurations, especially elliptic, rectangular, and triangular shapes with a small aspect ratio of 2–5 [5,6]. Some researchers have stated that the elliptic jet entrainment rate is about three to eight times that of the circular jet of the same equivalent diameter. Elliptic jet combustion efficiency is 10% higher than that of circular jets because of better mixing [3]. Further, diffusion pilot flames have been used in lean premixed gas turbine combustors to avoid the possibility of blowout. In many cases the diffusion pilot flames are dominant source of NO_x, particularly when the mass fraction of the total combustor fuel flow to the pilot flame exceeds 0.3. Due to its superior NO_x emission performance elliptic burner pilot flames may be an attractive solution to this problem.

Elliptic jets are known for its unusual mixing characteristics, sometimes capable of switching its major and minor axis directions in different cross sections along the jet [6,7]. In these types of jets, the deformation of large-scale vortical structures is comparable to an isolated elliptic ring. An elliptical vortex ring in a plane will attempt to take on a circular shape as it propagates downstream [5–7]. This ring is naturally unstable due to the azimuthal variation of the nozzle curvature that causes a nonuniform self-induction mechanism. As a result, the two axes of the ring interchanges and promotes a large increase in mixing and entrainment of surrounding fluid into the jet flow compared to that in

circular jets [6]. The distance from the nozzle to the axis switching location is approximately linearly proportional to the aspect ratio [5,6].

Laminar diffusion flames are fundamental to combustion and their study provides better understanding of transport and kinetic processes associated with energy release mechanisms. Flame length and width are important flame characteristics and in past, have been modeled and measured numerous to delineate convective and kinetic time scales of jet flames [8]. Flame shape measurements can also be used to validate laminar flame theories which are a precursor to understanding more complex turbulent flames. The classical relation of laminar jet flame predicts a proportional relation between flame length and mass flow rate, which is independent of pressure and burner diameter. This is commonly expressed as $L \propto Q$ and can be obtained by equating convection time scale L/u and diffusion scale $d^2/8D$. Similarly most theoretical model predicts a proportional relation between flame width and burner diameter ($w \propto d$) regardless of pressure and mass flow rate. This relation is generally derived from the equity between axial convective (L/u) and radial diffusion time scales ($w^2/4D$). Most past experimental measurements have confirmed this relation in buoyant and nonbuoyant flames for circular burners [9,10].

Although there have been abundant past efforts of developing theoretical and empirical correlations for flame shape of circular burner flames, flame shape correlations for asymmetric burners (especially elliptic burners) are largely absent from the literature. In this context, the objectives of the present research were to obtain flame shape measurements of buoyant and nonbuoyant laminar jet flames issued from elliptic flames and to compare them with theoretical models. Theoretical models were developed based on Burke-Schumann and Spalding analysis of jet flames. Digital flame images were obtained for luminous and nonluminous methane flame at buoyant and nonbuoyant conditions. Nonbuoyant flame measurements were conducted onboard NASA's KC-135 Microgravity Research aircraft, which provided around 20 s of a low gravity condition by flying parabolic trajectories.

Experimental Methodology

The elliptic 2:1 stainless steel burner used in the study had a length/diameter ratio of 20 (to insure fully developed laminar flow) and a major and minor axis dimension of 1.9 mm and 1 mm, respectively. It was placed inside a closed optically accessible combustion chamber as shown in Fig. 1 (see Table 1). The alumi-

Contributed by the Fuels and Combustion Technologies Committee of the International Gas Turbine Institute of ASME for publication in the JOURNAL OF ENGINEERING FOR GAS TURBINES AND POWER. Manuscript received May 20, 2004; final manuscript received October 21, 2004. Editor: S. R. Gollahalli.

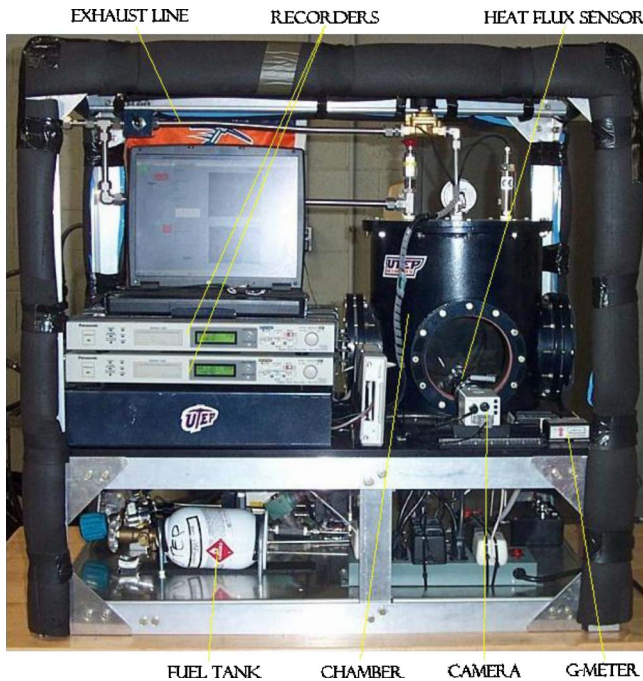


Fig. 1 Experimental setup

num walled combustion chamber had three windows to provide optical access for nonintrusive flow diagnostic methods. Experiments were supported by air and fuel intake systems, air exhaust systems, and safety systems and data acquisition instrumentation. Methane was stored at a pressure of $1.72 \times 10^6 \text{ N/m}^2$ in a $5 \times 10^{-4} \text{ m}^3$ cylinder and controlled by a digital mass flow meter, a precision flow control valve and a timing device. The flow rate was varied between $4.8 \times 10^{-7} \text{ m}^3/\text{s}$ to $1.4 \times 10^{-6} \text{ m}^3/\text{s}$. The air intake and air exhaust systems were designed to maintain a constant pressure level inside the combustion chamber. In present experiments, air pressure was maintained at 101 kPa. Prior to each measurement the combustion chamber was evacuated to 48.3 kPa using the pressure difference the air inside at an altitude of 6400 m (the low point of the flight parabola 42.7 kPa atmospheric pressure) and was refilled with dry calibrated air from a pressure bottle. During a typical run the flame inside the chamber burnt only 5% of the chamber air. Two remotely operated spark igniters initiated the combustion process. Nonbuoyant conditions were obtained onboard NASA's KC-135 microgravity research aircraft. A time-synchronized g meter records the g levels during the flight. Typical variations of the g level are shown in Fig. 2. Two high-resolution charge-coupled device cameras located 90° from each other record the flame images. The images were collected into two digital hard disk recorders.

One concern with extracting flame length data from digital images of hydrocarbon fueled flames is the luminosity due to visible radiation of soot particles. In luminous flames, length measurements obtained from direct photography generally yield luminous flame length data. The relation between luminous flame length

Table 1 Nominal experimental conditions

Minor axis length	1 mm
Major axis length	1.9 mm
Flow rates	$4.7833 \times 10^{-7} - 1.4352 \times 10^{-6} \text{ m}^3/\text{s}$
Jet exit Reynolds number	7.57–22.7
Jet exit Froude number range	4.27×10^{-5} to 1.28×10^{-4}
Chamber pressure	1.03 kg/cm^2
Chamber temperature	296 K

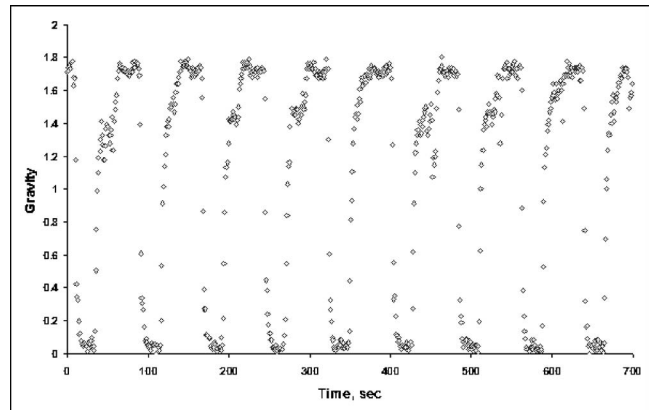


Fig. 2 Measured g -level variations during a flight parabola

and the stoichiometric flame is important since the latter can only be compared with the theoretical models. Previously investigators have indicated that the ratios of luminous and stoichiometric flame lengths are in the range of 0.9–1.8 and the ratios increases as the laminar smoke point flame length is reached. The volumetric fuel flow rates used in the present investigation covers both the nonsooting and sooting range of methane flames. To measure flame length direct digital photography was used to extract the data (the estimated measurement uncertainties at 95% confidence interval are $\pm 2.3\%$ of the mean value) of flame length measurements. However, for luminous flames images were filtered through a polarized CH line filter to measure the flame length.

Flame Length Model Development

The basic assumptions used by Roper [11,12] to estimate the length of diffusion flame issued from circular burner include (a) temperature and diffusivity are constant throughout the areas of the flame, (b) combustion does not change the number of molecules, and diffusion is only radial and not axial, (c) the unity Schmidt number and Lewis number, (d) gas velocity component parallel to the flame axis does not change across the area of the flame but varies with height. Although the above assumptions can be justified for circular burners, assumption (d) needs to be modified to account for the unique flow field encountered in elliptic burners. Hence for the elliptic burner it is assumed that the flame gases start with an axial velocity and continue with a mean upward acceleration due to buoyant forces [11].

For an ellipse, the aspect ratio (AR) is defined as the relationship between the characteristic width of flame in the major (x_f) and minor axis (y_f),

$$AR y_f = x_f \quad (1)$$

The vertical flame velocity varies with respect to x_f and y_f by the equation

$$x_f y_f = x_{1y_1} (v_1 T / v_2 T_1) \quad (2)$$

The dimensionless oxygen defect (see Ref. [12] for details) [11–13], C , is used to solve for the flame length and is given by

$$C = \frac{1}{4\pi\sqrt{\theta_x\theta_y}} \int \int \exp\left\{-\frac{\eta^2}{4\theta_x} - \frac{\xi^2}{4\theta_y}\right\} d\eta d\xi \quad (3)$$

where

$$\theta_\alpha = D \int_0^z \left(\frac{dz}{v_z \alpha_f^2}\right), \quad \alpha = x, y \quad (4)$$

The equation for θ_x is

$$\theta_x = D \int_0^z dz/v_z x_f^2 \quad (5)$$

and θ_x is related with θ_y by

$$\theta_y = AR^2 \theta_x. \quad (6)$$

The port boundaries correspond to

$$\frac{\eta^2}{1} + \frac{\xi^2}{4} = r^2 = 1 \quad (7)$$

thus Eq. (3) can be simplified to

$$C_m = (2\pi\theta_y)^{-1} \int \int \exp - \frac{r^2}{\theta_y} d\eta d\xi. \quad (8)$$

The parameter equations of an ellipse are

$$\eta = ar \sin \phi, \quad (9)$$

$$\xi = br \cos \phi. \quad (10)$$

Applying substitution and evaluating r from 0 to 1 and ϕ from 0 to 2π Eq. (8) becomes

$$C_m = \frac{ab}{2} \left[1 - \exp - \left(\frac{1}{\theta_y} \right) \right]. \quad (11)$$

The volume of air needed to complete the combustion of one unit volume of fuel gas S is related to C_m , thus,

$$C_m = (1 + S)^{-1} = \frac{ab}{2} \left[1 - \exp - \left(\frac{1}{\theta_y} \right) \right]. \quad (12)$$

Taking the natural logarithm gives

$$\ln \left[\frac{2}{ab} \left(1 + \frac{1}{S} \right) \right] = \frac{1}{\theta_y} \quad (13)$$

then substituting θ_y into Eq. (13) and solving for the flame length L gives

$$L = \frac{x_1 y_1 v_1 T_f}{D_0 (T_f/T_0)^{1.67} 2T_1 \ln \left[\frac{2}{ab} \left(1 + \frac{1}{S} \right) \right]}. \quad (14)$$

The primary mixture flow rate Q for the elliptic burner is given by

$$Q = \pi x_1 y_1 v_1 \frac{T_0}{T_1}. \quad (15)$$

Therefore the relationship between the flame length and flow rate is

$$\frac{L}{Q} = \frac{1}{D_0 \left(\frac{T_f}{T_0} \right)^{0.67} AR \pi \ln \left[\frac{2}{ab} \left(1 + \frac{1}{S} \right) \right]}. \quad (16)$$

Results and Discussion

Flame Appearance. Due to the relative shorter duration of the microgravity condition, the flame length measurements at nonbuoyant conditions are affected by ignition disturbances and unsteady flame developments. In the present investigation, flames were ignited at microgravity conditions and time-extrapolation methods were employed to minimize these effects. After ignition beginning of the flight parabola, nonbuoyant flames quickly reached their steady-state dimensions. The time extrapolation analysis showed that within the microgravity duration, flames' shapes reached within $\sim 4.3\%$ of their steady-state shapes. Figures 3(a)–3(d) show buoyant and nonbuoyant flame appearances at different volumetric fuel flow rates. At low fuel flow rates buoyant flames [Figs. 3(a) and 3(b)] have a prominent blue flame boundary with a faint blue interior. As the fuel flow rate increases a yellow soot wing form at the tip of the flame. With further increase in

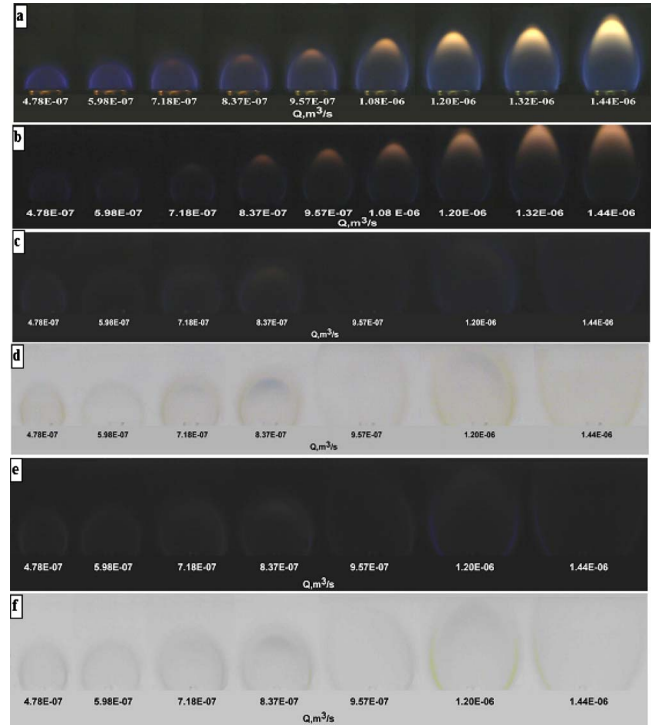


Fig. 3 Flame images: (a) buoyant major axis, (b) buoyant minor axis, (c) nonbuoyant major axis, (d) nonbuoyant major axis inverted CH filtered, (e) nonbuoyant minor axis, (f) nonbuoyant minor axis inverted CH filtered

flow rate the soot wing completely overlaps the flame tip. At buoyant conditions flames are wider along the major axis [Fig. 3(a)] in compared to the minor axis [Fig. 3(b)] locations. Due to increased diffusion and reduced advection nonbuoyant flames are spherical and extend below the burner leap [Figs. 3(c)–3(f)]. Nonbuoyant flames contain almost no soot and have an almost invisible interior (the lens and camera settings were kept identical for imaging buoyant and nonbuoyant flames). Thus for an accurate determination of flame shapes, nonbuoyant flame images were filtered for the CH line [Figs. 3(d) and 3(f)] and digitally inverted. It also appears that unlike their buoyant counterparts nonbuoyant flames have similar dimensions in both major and minor axes. This is most likely due to the dominance of diffusion over convection at nonbuoyant conditions. At the buoyant condition, flames issued from an elliptic burner grow faster along the major axis until axis switching occurs. This is due to a higher convective entrainment along the major axis. However, as the buoyancy level diminishes the entrainment is largely governed by axial and radial diffusions. Since the diffusion process is independent of the flame surface area and only depends on concentration gradients, the entrainment pattern in both axes becomes identical and the flame grows uniformly in both axes. Hence one can infer that the convective entrainment in nonbuoyant flames (large Reynolds number) may be independent of burner exit geometries. The authors believe that the present study is the first to report this behavior of asymmetric flames.

Flame Length. The measured flame lengths of the 2:1 elliptic burner at buoyant and nonbuoyant conditions for different volumetric fuel flow rates are shown in Fig. 4. The predicted [Eq. (16)] flame length values are also shown in the same figure. The least-square fit of measured buoyant and nonbuoyant flame lengths confirms the L vs Q correlation for the elliptic burner. Figure 5 shows the correlation between the normalized flame length and the jet exit Reynolds number at buoyant and nonbuoyant conditions. Flame length data are normalized by major and minor axis dimen-

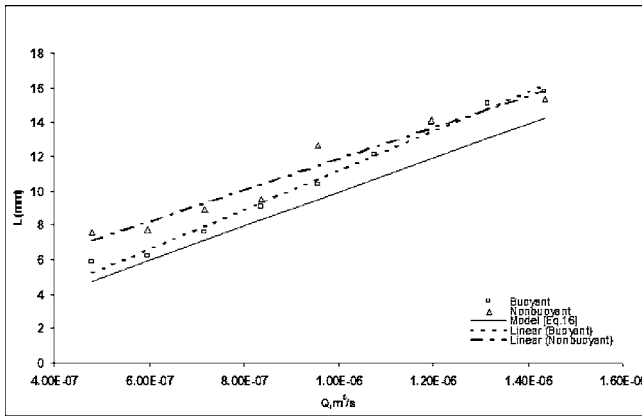


Fig. 4 Buoyant and nonbuoyant flame lengths

sions and plotted against corresponding Reynolds numbers. Within experimental uncertainties, the normalized elliptic flame length data support a $L/d \propto Re$ correlation.

At nonluminous conditions, nonbuoyant flames are longer than

buoyant flames. The difference in flame lengths of buoyant and nonbuoyant flames diminishes at higher fuel flow rates. The longer nonbuoyant flames are due to the higher axial diffusion and the lower radial convection at microgravity conditions. The data suggest that similar to circular burner flames, elliptic burner flames also experience the same order of magnitude increase in axial diffusion at microgravity conditions. However, with the increase in fuel mass flow rate increases, flame Froude number increases, and buoyant flames approaches nonbuoyant behavior. The flame length model developed in this work includes the radial convection and the effects of gravity on the flame length. However, the gravity term cancels from the final expression and the model predicts flame lengths independent of the gravitational level as shown in Fig. 4.

To understand the temporal behavior of the flame development, flame lengths measured at 1-g condition onboard the KC-135 aircraft and the laboratory are shown in Fig. 6. It appears that in most flow rates laboratory measurements were within 4% of KC-135 measurements. The data support the time-extrapolation analysis $L(\tau)/L(\infty) = e^{-\tau_{\text{chemical}}/\tau}$ and confirm that KC-135 flames attain steady-state value within the measurement time scale. It is interesting to note that compared to the sooting flame, the flame shapes of nonsooting flames are closer to the steady-state value. The on-

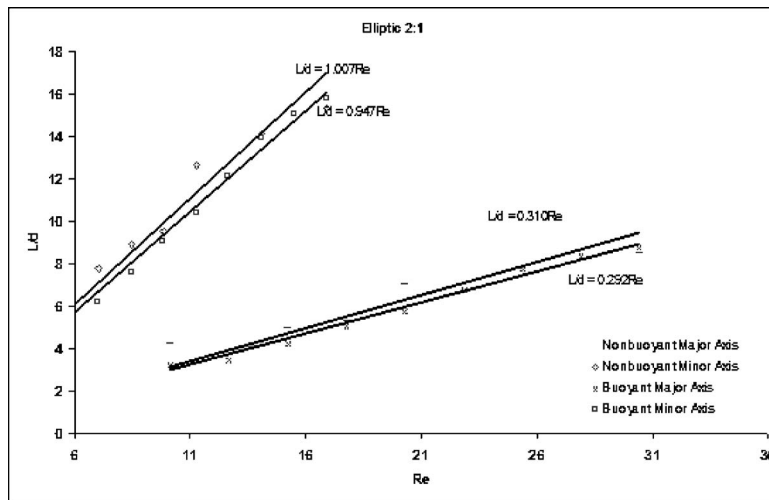


Fig. 5 Correlation between the normalized flame length and the jet exit Reynolds number at buoyant and nonbuoyant conditions

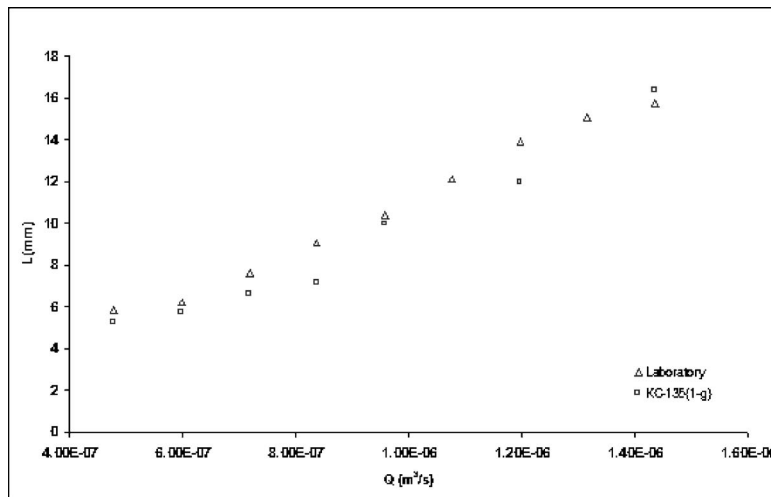


Fig. 6 Comparison of flame length at 1-g in the lab with the measurements at 1-g aboard the KC-135

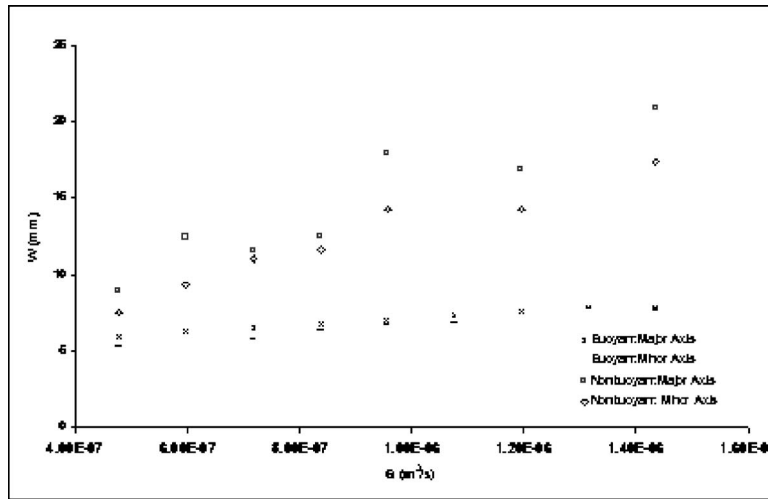


Fig. 7 Buoyant and nonbuoyant flame widths

set of soot formation may delay the temporal development of the flame and smaller nonsooting flames suffer less effects of g jitters induced by the structural vibrations.

Flame Width. Figure 7 shows the variation of maximum flame width with the volumetric fuel flow rate at both major and minor axes for buoyant and nonbuoyant conditions. For the buoyant condition, at low volumetric flow rate, the maximum flame width at the major axis is higher than the minor axis flame width. However, the difference disappears as the volumetric flow rate increases. This can be attributed to the strong radial convection at the low volumetric fuel flow rate (i.e., low jet exit Reynolds number). The merger of major and minor axes maximum flame widths at high flow rate results from the suppression of radial convection with the strong upward convection of hot gases. At high Reynolds number the convective current becomes significant and it diminishes the effect of radial convective processes. Furthermore, the axis switching phenomenon of elliptic jets is especially pronounced at high Reynolds number, which may also dictate the maximum width of the flame contour. However, unlike buoyant flames, the maximum flame width of nonbuoyant flames at the major axis remains larger than the minor axis flame width for the range of flow rate studied in the present investigation. Again, this is due to the relative strength of the radial and axial convection processes. Since the axial convection process is very weak at low gravity conditions, the location of flame contour is primarily dictated by radial convection processes. The minor axis has larger slope in concentration gradient and thus experiences a stronger radial convection and a smaller flame width.

Figures 8 and 9 show the correlation between the normalized maximum flame width and the jet exit Froude number at buoyant and nonbuoyant conditions. The maximum flame widths measured at each axis are normalized by the respective axis dimension. The characteristic dimension used to calculate the Froude number is also the dimension of the same axis. For buoyant conditions, the maximum flame width data at both axes suggest a $w/d=cFr^m$ correlation (correlation coefficient $R^2 > 0.98$) with the jet exit Froude number. The value of m for major and minor axes maximum flame width is 0.14 and 0.19, respectively. The nonbuoyant flames support a similar correlation between the normalized flame width and the jet exit Reynolds number. For nonbuoyant flames, m has a value of 0.36 for both major and minor axes flame widths.

Laminar Flame Shape Comparisons of Elliptic and Circular Burners. Part of the motivation of the present investigation is also to understand the differences of buoyant and nonbuoyant shapes of laminar flames issued from circular and elliptic burners. Present measurements of elliptic burner flames are examined against the

circular flame data available in the literature [9,10]. The slope of the normalized flame length vs Reynolds number correlation for circular and elliptic burners at buoyant and nonbuoyant conditions are listed in Table 2. It appears that compared to the circular burner the slope is considerably higher for the elliptic burner. Table 3 lists c and m values of the flame width correlation for elliptic and circular burners at buoyant and nonbuoyant conditions.

Conclusions

Although laminar diffusion flame is fundamental to combustion process, a complete analytical treatment of such a flow field requires many crucial assumptions to avoid the mathematical complexity. However, some of these assumptions are only valid for geometrically symmetric flow condition and need to be modified before applying to an asymmetric flow field. This paper presents a theoretical analysis of the flame length and width of 2:1 elliptic burners with the modified assumptions and mathematical procedures. Flame shape measurements at normal and microgravity environments were done to validate the model and to gain insight of buoyant and nonbuoyant flame processes of elliptic burners. The specific conclusions drawn from the present investigation are as follows:

- i. Similar to circular burners, flames issued from elliptic burner support the linear correlation between the laminar flame length and the volumetric fuel flow rate.

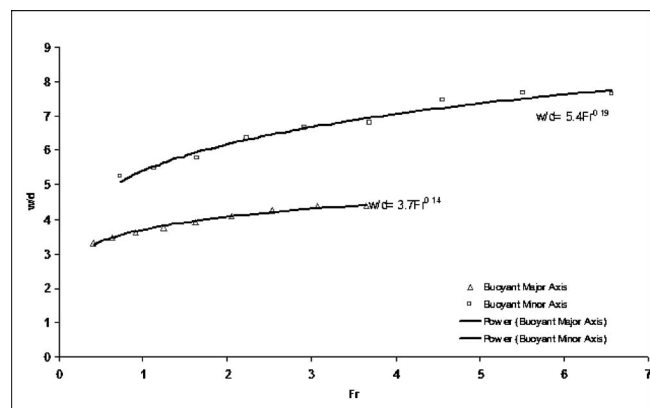


Fig. 8 Correlation between the normalized maximum flame width and the jet exit Froude number at buoyant conditions

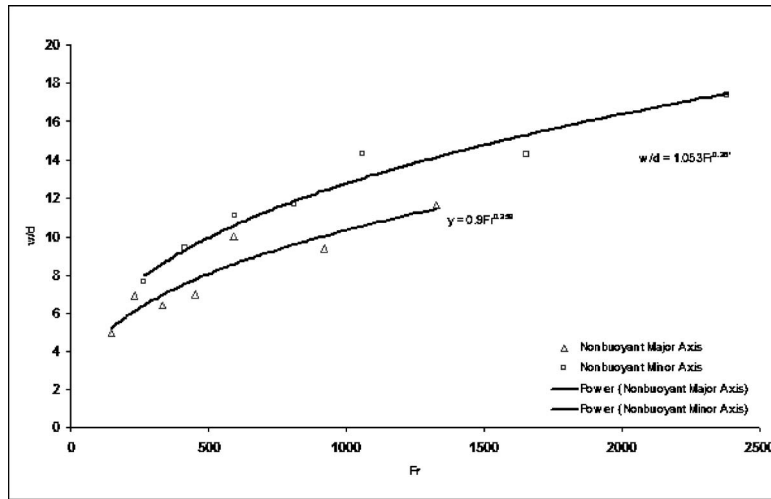


Fig. 9 Correlation between the normalized maximum flame width and the jet exit Froude number at nonbuoyant conditions

- ii. Theoretical predictions of flame length agree well with experimental measurements.
- iii. In general the nonbuoyant flames are longer than buoyant flames for the range of volumetric fuel flow rate used in the present investigation.
- iv. The normalized flame lengths scale with jet exit Reynolds number. However, elliptic burner flames show a higher slope compared to circular burner flames.
- v. Maximum flame widths of buoyant and nonbuoyant flames at major and minor axes are proportional to volumetric fuel flow rate.
- vi. Maximum flame widths of buoyant and nonbuoyant flames correlate with the jet exit Froude number.

Acknowledgment

The authors gratefully acknowledge the NASA Johnson Space Center KC-135 Reduced Gravity Program's support for their research. Jorge Camacho was supported by NASA Harriett G. Jenkins Predoctoral Student Fellowship Grant. The authors would also like to acknowledge Ivan Anchondo, Issac Estrada, and Ricardo Gallarzo of the Combustion and Propulsion Research Laboratory for their contributions in the design, development, and operations of the microgravity test hardware.

Table 2 Slope of the L/d vs Re correlation

Elliptic burner buoyant	major axis	0.292
	minor axis	0.947
Elliptic burner nonbuoyant	major axis	0.849
	minor axis	1.007
Circular burner buoyant (Refs. [9,10])		0.129
Circular burner nonbuoyant (Refs. [9,10])		0.192

Table 3 c and m value for w/d vs Fr correlation

		c	n
Elliptic burner buoyant	major axis	3.7	0.14
	minor axis	5.4	0.19
Elliptic burner nonbuoyant	major axis	0.9	0.359
	minor axis	1.053	0.361
Circular burner buoyant (Refs. [9,10])		2.17	0.154
Circular burner nonbuoyant (Refs. [9,10])			

Nomenclature

- α = x, y
 ϵ = emissivity
 ζ = normalized streamwise distance
 η = x/x_f
 θ = $D \int_0^t (dt/x_f^2)$
 ξ = y/y_f
 ρ = density
 σ = hard-sphere collision diameters
 σ_s, k_B = Stefan-Boltzmann constant
 ϕ = angle
 AR = aspect ratio
 a_u = mean upward acceleration
 C = dimensionless oxygen defect
 C_f = empirical flame length parameter
 C_m = value of C on the flame axis
 c = correlation coefficient
 d = jet exit diameter
 D, D_o = mass diffusivity
 f = mixture fraction
 g = gravity
 L = stoichiometric flame length
 n = correlation coefficient
 Q = volumetric flow rate
 r = radius
 Re = jet Reynolds number
 S = molar stoichiometric air-fuel ratio
 T_1 = fuel gas temperature
 T_∞, T_o = oxidizer stream temperature
 T_f = mean flame temperature
 V = volume
 v_1 = mean fuel gas velocity at burner mouth
 v_z = vertical flame velocity
 w = luminous flame diameter
 x_1, a = half of the major axis length
 x_f = flame width in major axis
 y_1, b = half of the minor axis length
 y_f = flame width in minor axis
 z = streamwise distance

References

- [1] Kolluri, P., Kamal, A., and Gollahalli, S. R., 1996, "Application of Elliptical Primary-Air Inlet Geometries in the Inshot Burners of Residential Gas Fur-

- naces," ASME J. Energy Resour. Technol., **118**, pp. 58–64.
- [2] Gollahalli, S. R., 1998, "Effect of Flame Lift-off on the Differences Between the Diffusion Flames from Circular and Elliptic Burners," J. Energy Resour. Technol., **120**, pp. 161–166.
- [3] Gollahalli, S. R., Khanna, T., and Prabhu, N., 1992, "Diffusion Flames of Gas Jets Issued from Circular and Elliptic Nozzles," Combust. Sci. Technol., **86**, pp. 267–288.
- [4] Gollahalli, S. R., and Subba, S., 1996, "Partially Premixed Laminar Gas Flames from Triangular Burner," AIAA Paper No. 96-0285, 34th Aerospace Sciences Meeting, Reno, NV, J. Propul. Power, **13**, pp. 226–232.
- [5] Ho, C.-M., and Gutmark, E., 1987, "Vortex Induction and Mass Entrainment in a Small-Aspect-Ratio Elliptical Jet," J. Fluid Mech., **179**, pp. 383–405.
- [6] Akin, J. E., and Bass, J., 2001, "Asymmetric Turbulent Jet Flows," Comput. Methods Appl. Mech. Eng., **191**, pp. 515–524.
- [7] Gutmark, E., and Ho, C.-M., 1983, "Near-Field Pressure Fluctuations of an Elliptical Jet," AIAA J., **23**, pp. 354–358.
- [8] Jost, W., 1946, *Explosion and Combustion Processes in Gases*, McGraw-Hill, New York, p. 212.
- [9] Lin, K.-C., Faeth, G. M., Sunderland, P. B., Urban, D. L., and Yuan, Z.-G., 1999, "Shapes of Nonbuoyant Round Luminous Hydrocarbon/Air Laminar Jet Diffusion Flames," Combust. Flame, **116**, pp. 415–431.
- [10] Sunderland, P. B., Mendelson, B. J., Yuan, Z.-G., and Urban, D. L., 1999, "Shapes of Buoyant and Nonbuoyant Laminar Jet Diffusion Flames," Combust. Flame, **116**, pp. 376–386.
- [11] Roper, F. G., 1977, "The Prediction of Laminar Jet Diffusion Flame Sizes: Part I. Theoretical Model," Combust. Flame, **29**, pp. 219–226.
- [12] Camacho, J., 2003, "Theoretical Analysis and Measurements of Elliptical Jet Flames," M.S. thesis, Combustion and Propulsion Research Laboratory, University of Texas at El Paso, El Paso, TX.
- [13] Roper, F. G., 1977, "The Prediction of Laminar Jet Diffusion Flame Sizes: Part II. Experimental Verification," Combust. Flame, **29**, pp. 227–234.

Visualization of Steam Addition Effect on OH Distribution in a Flame by Isotope Shift/Planar Laser-Induced Fluorescence (IS/PLIF) Spectroscopy

Atsushi Katoh

Masahisa Shinoda

Kuniyuki Kitagawa

Research Center for Advanced Energy Conversion,
Nagoya University,
Furo-cho, Chikusa-ku,
Nagoya 464-8603, Japan

Ashwani K. Gupta¹

Department of Mechanical Engineering,
University of Maryland,
College Park, MD 20742
e-mail: ak Gupta@eng.umd.edu

Addition of steam to a flame has important implications in the combustion process. The dissociation of the added steam (e.g., $\text{H}_2\text{O} \leftrightarrow \text{H} + \text{OH}$, etc.) is one of the effects that contribute to the production of radical species, such as OH, H, and O, in the flame. In order to distinctly visualize two types of OH radicals produced from the fuel-air combustion reaction and that from the dissociation reaction with the added steam, we have developed a new method for planar laser-induced fluorescence spectroscopy in combination with isotope shift (herein called IS/PLIF spectroscopy). This technique has been applied to examine a methane-oxygen-nitrogen premixed flame. Two-dimensional fluorescence intensity distributions of OH radicals in the flames were monitored under three different conditions. They include without steam addition, with H_2O steam addition, and with D_2O steam addition. From the experimental data obtained under the three conditions, the distinction between the two types of OH radicals could be obtained. The results showed that steam addition reduced the total concentration of OH produced from the combustion and dissociation reactions and that the dissociation reaction of the added steam contributed to the production of OH. Furthermore, the results indicated that the percentage decrease in OH from fuel-air combustion reactions due to the temperature decrease effect with steam addition was almost independent of the equivalence ratio during combustion. In contrast, the percentage increase in OH produced from dissociation reaction with the steam depended on the equivalence ratio.

[DOI: 10.1115/1.2056528]

Introduction

Combustion phenomenon in all types of combustion systems must be effective and efficient for clean conversion of chemical energy to thermal energy. Combustion generates not only the thermal energy but also several different environmental pollutants (e.g., NO_x , SO_x , CO_2 , soot, etc.), to cause (i) degradation of the air and human health and (ii) greenhouse effect. Therefore, investigation of combustion control is very important from both academic and industrial interests because this directly impacts global energy availability and use as well as the continuing environment problems.

Recently, several techniques have been developed for achieving effective control of the combustion process in combustors. One of such method is injection of water or steam into combustors [1,2]. Since water and steam have a lower temperature and large heat capacity, its addition into the combustion field brings about the decrease in flame temperature. This temperature decrease is very effective for the suppression of thermal NO_x formation. For this reason, water or steam addition into the combustor has been used as one of the effective techniques for the suppression of NO_x .

The decrease in flame temperature also lowers the concentration of several radical species (e.g., OH, CH, O, H, etc.), which are produced during combustion reactions between the fuel and air. However, even if the steam addition does not cause a signifi-

cant decrease in the flame temperature, it has another effect on the species concentrations. This is because the increase in H_2O concentration in the combustion field causes the shift of chemical equilibrium in some combustion reactions involving H_2O (e.g., $\text{CH}_4 + 2\text{O}_2 \leftrightarrow \text{CO}_2 + 2\text{H}_2\text{O}$, $\text{O} + \text{H}_2\text{O} \leftrightarrow \text{OH} + \text{OH}$, $\text{CH}_3 + \text{H}_2\text{O} \leftrightarrow \text{CH}_4 + \text{OH}$, etc.). Several studies have reported the effect of the steam addition on some chemical species [1,3–5]. For example, Zhao et al. [1,4] have conducted a one-dimensional (1D) numerical simulation to examine the chemical kinetic effect on species, such as NO, OH, CH, HCN, N, in a methane-air counterflow diffusion flame using detailed chemical kinetic mechanism. In order to eliminate the effect of decreased flame temperature from the steam addition, they controlled the initial gas temperature so that the maximum flame temperature with the steam addition was effectively the same as that without the steam addition.

The dissociation reactions of the added steam (e.g., $\text{H}_2\text{O} \leftrightarrow \text{H} + \text{OH}$, etc.) are also among the steam addition effects. Such reactions contribute to the production of radical species, such as OH, H, and O, which play an important role in combustion reactions. Therefore, such radical species in the steam-added flame can be classified into two types according to their origins; one comes from the combustion reactions of fuel and air, and the other from the dissociation reactions of the added steam. The separate measurement of these two types of radicals is useful for unraveling the respective contributions from the fuel-air combustion reactions and that from the dissociation reactions associated with the steam addition into the flame. For such purposes, we have developed a new diagnostics tool for planar laser-induced fluorescence (PLIF) spectroscopy using isotope shift (IS/PLIF spectroscopy). This technique has been applied to examine a methane-oxygen-

¹To whom correspondence should be addressed.

Contributed by Fuels and Combustion Technologies Committee of the International Gas Turbine Institute of ASME for publication in the JOURNAL OF ENGINEERING FOR GAS TURBINES AND POWER. Manuscript received January 23, 2004; final manuscript received October 7, 2004. Editor: S. R. Gollahalli.

Table 1 Equivalence ratio and gas flow rate

ϕ	CH ₄	O ₂	N ₂ +steam
0.9	0.79 l/min (16.6 mmol/min)	1.78 l/min (37.4 mmol/min)	6.24 l/min(131.0 mmol/min) (steam:0 or 14 mmol/min)
	0.89 l/min (18.7 mmol/min)	1.78 l/min (37.4 mmol/min)	6.14 l/min(129.0 mmol/min) (steam:0 or 14 mmol/min)
1.2	1.09 l/min (22.9 mmol/min)	1.78 l/min (37.4 mmol/min)	5.94 l/min(124.8 mmol/min) (steam:0 or 14 mmol/min)

effectively attenuate the interference from the undesirable emissions by controlling the pulsed Nd:YAG laser and the ICCD camera. The gate delay time of the Q-switch is set at 260 μ s. The gate delay time and the gate width of the ICCD camera are 260.126 μ s and 50 ns, respectively.

A 2D cylindrical coordinate system (r, z), in which the origin of r - and z -axes are set at the center of the burner outlet, is considered here as shown in Fig. 2. The region observed by the ICCD camera are from -10 to 10 mm in the r direction and from 5 to 45 mm in the z direction, which corresponds to the 165×327 pixels of the camera. The accumulation of 200 individual OH-PLIF images is conducted in order to reduce the influence of flame fluctuation on the OH image. Furthermore, the measured OH fluorescence intensity distributions are corrected so as to remove any nonuniformity in z -direction intensity distribution of the laser sheet.

The methane-oxygen-nitrogen premixed flame is formed using a cylindrical fused-silica burner. The inside diameter and wall thickness of the burner are 5.9 and 1.0 mm, respectively. The premixed flame is ~ 80 mm in height. The burner is connected to a heating chamber that is wound with a nichrome wire, where water aerosols are heated to produce steam. The nebulizer supplies water aerosols into the heating chamber. The preheat temperature of the premixed gas and steam is regulated at ~ 580 K at the burner outlet. The flow rate of each component in the premixed gas at the burner outlet is listed in Table 1. Three equivalence ratios, $\phi=0.9, 1.0,$ and $1.2,$ are employed here to examine the effect of steam addition on the combustion field under fuel-lean and fuel-rich conditions. The amount of steam added is $\sim 7\%$ of the total flow rate of premixed gas. The flow rate of nitrogen is controlled so that the total flow rate of premixed gases is the same under both cases of with and without steam addition to the flame.

The 2D temperature distributions have been measured with a 0.1 mm dia R-type thermocouple to examine the effect of H₂O and D₂O steam addition on thermal field distribution. The measurements were made at 11 points from 0 to 10 mm at 1 mm intervals in the r direction, and 17 points from 5 to 45 mm at 2.5 mm intervals in the z direction, respectively. An x - y stage is used to move the thermocouple relative to the fixed burner position.

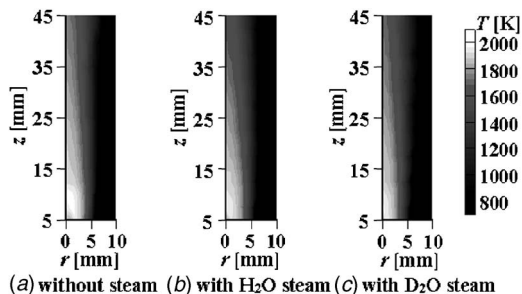


Fig. 3 2D distribution of flame temperature at $\phi=0.9$

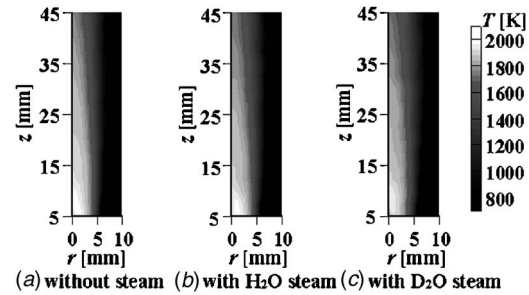


Fig. 4 2D distribution of flame temperature at $\phi=1.0$

Results and Discussion

Flame Temperature. Figures 3–5 show the 2D profiles of flame temperature measured with the R-type thermocouple at equivalence ratios of $\phi=0.9, 1.0,$ and $1.2,$ respectively. The profiles of flames without steam addition, with H₂O steam addition, and with D₂O steam addition, are shown in panels (a)–(c), respectively, Figs. 3–5. A comparison of panels (a) and (b) in Figs. 3–5 shows that H₂O steam addition lowers the flame temperature by about 20–30 K at inner regions of the flame where the temperature is ~ 1800 K. In contrast there is little difference in flame temperature distribution with H₂O and D₂O steam addition to the flame (compare panels (b) and (c) in Figs. 3–5). This is attributed to the fact that the amount of added steam is only a few percent of the total flow rate of premixed gas and that the difference in heat capacity between H₂O and D₂O steams at 600 K is also small. Therefore, it is expected that these differences have no significant influence on the high-temperature region of the flame and that the thermal effect of D₂O steam addition becomes almost equal to that of H₂O steam addition for the experimental conditions examined here.

IS/PLIF Intensity of OH Radical. Figures 6–8 show the 2D OH distributions measured by the PLIF system at equivalence ratio, $\phi=0.9, 1.0,$ and $1.2,$ respectively. Panels (a)–(c) in these figures represent the same conditions as those described for Figs. 3–5. As mentioned in the section on IS/PLIF Spectroscopy, the 2D distribution of OH radicals in the flame with D₂O steam addition, panel (c), corresponds to the distribution of OH radicals produced from the fuel-air combustion reaction in the flame with the H₂O steam addition. In all cases at $\phi=0.9, 1.0,$ and $1.2,$ it is pointed out that the OH fluorescence intensity in the flame without steam addition is stronger than that with H₂O and D₂O steam addition. This indicates lowering of the flame temperature and shift of chemical equilibrium caused by steam addition to cause a decrease of number density of OH radicals in the flame. In addition, the increase in equivalence ratio shifts the location of OH abundant zone from inner to outer regions of the flame. This shift is mainly attributed to the increase in equivalence ratio to cause a deficiency in oxygen concentration in the inner flame regions and

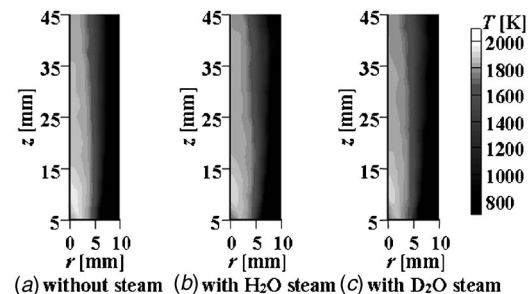


Fig. 5 2D distribution of flame temperature at $\phi=1.2$

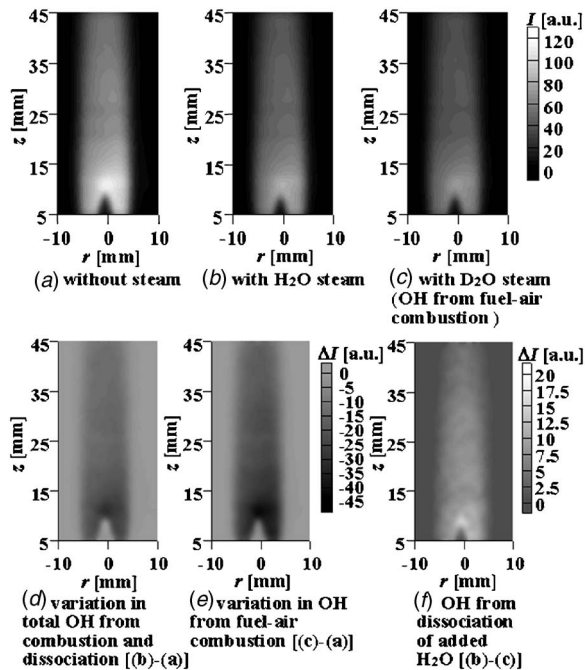


Fig. 6 2D distribution of OH fluorescence intensity at $\phi=0.9$

to make dominant reaction with ambient air in the outer flame regions.

Panels (d)–(f) in Figs. 6–8 are obtained by the image processing of panels (a)–(c) in Figs. 6–8, i.e., by subtracting panels (a) from (b), (a) from (c), and (c) from (b), respectively. Panels (d) and (e), respectively, in Figs. 6–8 directly indicate the effect of steam addition on fluorescence intensity profiles of total OH produced from combustion and dissociation reactions, and for only the OH from combustion reaction. Figures 6(f), 7(f), and 8(f) shows the

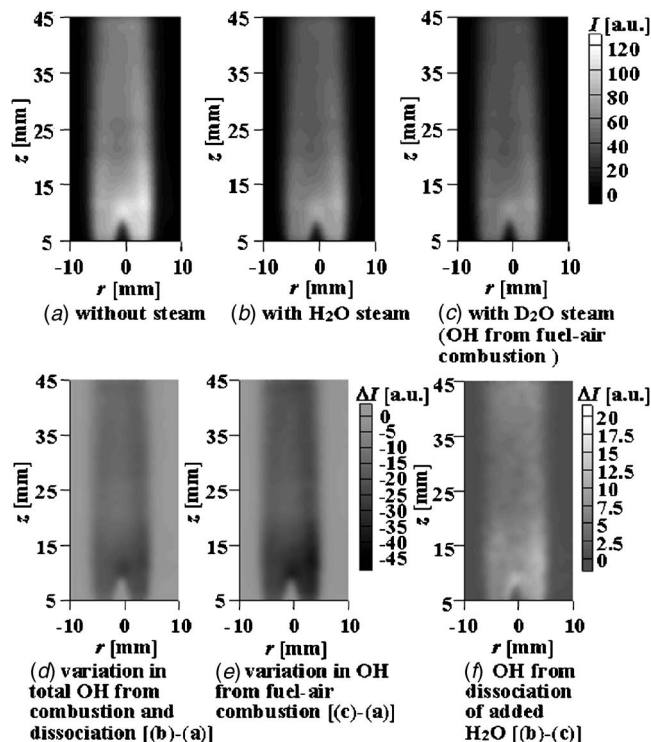


Fig. 7 2D distribution of OH fluorescence intensity at $\phi=1.0$

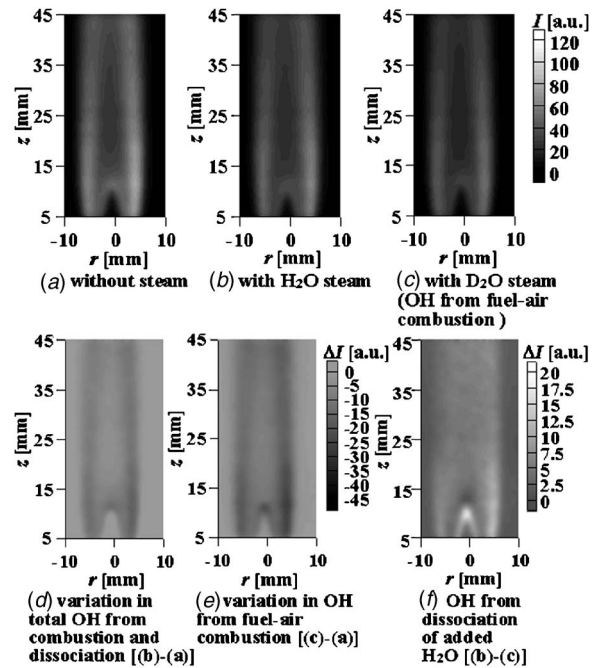


Fig. 8 2D distribution of OH fluorescence intensity at $\phi=1.2$

profile of OH produced with the dissociation reaction associated with added H₂O steam in the flame. The OH fluorescence intensity distributions in panels (d)–(f) of Figs. 6–8 are almost proportional to the respective OH number density distributions. Consequently, panel (d) of Figs. 6–8 indicates that steam addition reduces the total OH in flame under all equivalence ratio conditions of $\phi=0.9$, 1.0, and 1.2 examined here. However, it is confirmable from panel (f) of Figs. 6–8 that dissociation from the added H₂O steam leads to the production of OH.

For a quantitative comparison on the OH radicals produced from the fuel-air combustion reaction and from the dissociation reaction with the added H₂O steam, we calculate the integral value of 2D distribution of OH fluorescence intensity by summing the intensities at all pixels in the measurement region. The results for $\phi=0.9$ are given in Table 2. It is to be noted from panels (e) and (f) of Table 2 that H₂O steam addition decreases the integral value for OH produced from the fuel-air combustion reaction by 33% and increases that from the dissociation reaction of the added H₂O steam by 8%, as compared to the case without any steam addition. This means that the percentage decrease in the number density of OH produced from the fuel-air combustion reaction becomes larger than that from the dissociation reaction of the

Table 2 Integral values of 2D distributions of OH fluorescence intensity at $\phi=0.9$

Case	Integral value (a.u.)
(a) Without steam	1.91×10^5 (100%)
(b) With H ₂ O steam	1.44×10^5 (75%)
(c) With D ₂ O steam (OH from fuel-air combustion reaction)	1.28×10^5 (67%)
(d) Variation in total OH from combustion and dissociation reactions [(b)–(a)]	-0.48×10^5 (–25%)
(e) Variation in OH from fuel-air combustion reaction [(c)–(a)]	-0.63×10^5 (–33%)
(f) OH from dissociation reaction of added H ₂ O steam [(b)–(c)]	$+0.16 \times 10^5$ (+8%)

Table 3 Integral values of 2D distributions of OH fluorescence intensity at $\phi=1.0$

Case	Integral value (a.u.)
(a) Without steam	2.23×10^5 (100%)
(b) With H ₂ O steam	1.69×10^5 (76%)
(c) With D ₂ O steam (OH from fuel-air combustion reaction)	1.48×10^5 (66%)
(d) Variation in total OH from combustion and dissociation reactions [(b)-(a)]	-0.54×10^5 (-24%)
(e) Variation in OH from fuel-air combustion reaction [(c)-(a)]	-0.75×10^5 (-34%)
(f) OH from dissociation reaction of added H ₂ O steam [(b)-(c)]	$+0.21 \times 10^5$ (+9%)

added H₂O steam.

The results obtained at $\phi=1.0$ and 1.2 are listed in Tables 3 and 4, respectively. It is noted from panels (e) and (f) of Tables 3 and 4 that for $\phi=1.0$, the H₂O steam addition decreases the integral value for OH produced from the fuel-air combustion reaction by 34% and increases that from the dissociation reaction of the added H₂O steam by 9%, as compared to the case with no steam addition. These values are almost the same as those obtained for $\phi=0.9$. However, it should be pointed out that under for $\phi=1.2$, the H₂O steam addition decreases the integral value for OH produced from the fuel-air combustion reaction by 33% and increases that from the dissociation reaction of the added H₂O steam by 16%. The percentage decrease in OH produced from the fuel-air combustion reaction is nearly the same in all the cases at equivalence ratios of $\phi=0.9$, 1.0, and 1.2. This suggests that an OH decrease due to temperature reduction in flames from H₂O steam addition is almost independent of the equivalence ratio. In contrast, the percentage increase in OH produced from the dissociation reaction of steam at $\phi=1.2$ considerably differs from those at $\phi=0.9$ and 1.0. This may be attributed to the existence of more abundant radical species, such as CH₃, CH, etc., in the fuel-rich combustion field in comparison to the fuel-lean case. In fuel-rich conditions, the chemical reactions between these radical species and the added H₂O steam (e.g., CH₃+H₂O \leftrightarrow CH₄+OH, CH+H₂O \leftrightarrow CH₂+OH, etc.) can become more active to accelerate the dissociation of added H₂O steam in flames.

Table 4 Integral values of 2D distributions of OH fluorescence intensity at $\phi=1.2$

Case	Integral value (a.u.)
(a) Without steam	1.58×10^5 (100%)
(b) With H ₂ O steam	1.31×10^5 (83%)
(c) With D ₂ O steam (OH from fuel-air combustion reaction)	1.06×10^5 (67%)
(d) Variation in total OH from combustion and dissociation reactions [(b)-(a)]	-0.27×10^5 (-17%)
(e) Variation in OH from fuel-air combustion reaction [(c)-(a)]	-0.52×10^5 (-33%)
(f) OH from dissociation reaction of added H ₂ O steam [(b)-(c)]	$+0.26 \times 10^5$ (+16%)

Conclusions

The dissociation reaction associated with steam addition to flames (e.g., H₂O \leftrightarrow H+OH, etc.) has been demonstrated to provide an important role on the amount of OH radicals in flames. The effects of steam addition in flames provides an important contribution on the production of radical species, such as OH, H, and O, which play an important role in the combustion reactions. Such radical species in the steam-added flame can be classified into two types owing to their origin; one comes from the fuel-air combustion reactions, and the other from dissociation reactions of the added steam. In this paper, we have developed a new method for planar laser-induced fluorescence (PLIF) spectroscopy using isotope shift (IS/PLIF spectroscopy). Using this technique, 2D distributions of OH fluorescence intensity in methane-oxygen-nitrogen premixed flames have been observed under the three different conditions of without steam addition, with H₂O steam addition, and with D₂O steam addition. The experimental distinction of the two types of OH radicals from combustion and from steam addition was found feasible by obtaining the differential profiles.

The 2D distributions of OH fluorescence intensity measured with the PLIF system at equivalence ratios of $\phi=0.9$, 1.0, and 1.2 showed that steam addition reduces the total OH radicals in flames. The results have also indicated that dissociation reaction with the added H₂O steam leads to the production of OH radicals. An estimate on the integral value of 2D distributions of OH fluorescence intensity, calculated by summing the intensities at all pixels in the measurement region, revealed important information on the net OH produced from flames under different conditions. The percentage decrease in OH produced from fuel-air combustion reaction was nearly the same at the three equivalence ratios of $\phi=0.9$, 1.0, and 1.2 examined here. This suggests that an OH decrease due to the temperature decrease caused by the H₂O steam addition is almost independent of the equivalence ratio, i.e., negligible sensitivity to fuel-lean or fuel-rich combustion conditions. In contrast, the percentage increase in OH produced from the dissociation reaction of steam depends on the equivalence ratio. This can probably be attributed to the existence of more abundant radical species, such as CH₃, CH, etc., in fuel-rich condition than fuel-lean condition. In the fuel-rich field, these radical species could accelerate the dissociation of added H₂O steam through such chemical reactions as CH₃+H₂O \leftrightarrow CH₄+OH, CH+H₂O \leftrightarrow CH₂+OH, etc.

References

- [1] Zhao, D., Yamashita, H., Yamamoto, T., Furuhashi, T., and Arai, N., 1999, "Consideration of Chemical Kinetics on Mechanism of NO_x Reduction by Steam Addition," *Kagaku Kogaku Ronbunshu*, **25**, (6), pp. 955-960 (in Japanese).
- [2] Harano, A., and Sadakata, M., 2001, "Production of Air Pollutants," *Anatano Jitsuyo Nenshoro Sekkei oyobi Seigyo*, Arai, N. and Miura, T., eds., 2001, Techno-system, Tokyo, pp. 261-287 (in Japanese).
- [3] Miyauchi, T., and Mori, Y., 1980, "Effect of Steam Addition on NO Formation," *Nensho Kenkyu*, **55**, pp. 11-24 (in Japanese).
- [4] Zhao, D., Yamashita, H., Kitagawa, K., Arai, N., and Furuhashi, T., 2002, "Behavior and Effect on NO_x Formation of OH Radical in Methane-Air Diffusion Flame With Steam Addition," *Combust. Flame*, **130**, pp. 352-360.
- [5] Li, S. C., Ilincic, N., and Williams, F. A., 1997, "Reduction of NO_x Formation by Water Sprays in Strained Two-Stage Flames," *Trans. ASME: J. Eng. Gas Turbines Power*, **119**, pp. 836-843.
- [6] NIST, 2005, *NIST Web Book*, <http://webbook.nist.gov/> NIST, Gaithersburg, MD.
- [7] Dieke, G. H., and Crosswhite, H. M., 1961, "The Ultraviolet Bands of OH," *J. Quant. Spectrosc. Radiat. Transf.*, **2**, pp. 97-199.
- [8] Sastry, M. G., and Rao, K. R., 1941, "Structure of the Electronic Bands of The OD Molecule.-Part I," *Indian J. Phys.*, **15**, pp. 27-51.

A Generic Approach for Gas Turbine Adaptive Modeling

W. P. J. Visser

SKF/Delta Consult,
Kapelle, The Netherlands
e-mail: visser@delticonsult.nl

O. Kogenhop

National Aerospace Laboratory,
NLR,
Amsterdam, The Netherlands
e-mail: okogenho@nlr.nl

M. Oostveen

Delft University of Technology,
Delft, The Netherlands
e-mail: moostveen@orange.nl

For gas turbine engine performance analysis, a variety of simulation tools is available. In order to minimize model development and software maintenance costs, generic gas turbine system simulation tools are required for new modeling tasks. Many modeling aspects remain engine specific however and still require large implementation efforts. One of those aspects is adaptive modeling. Therefore, an adaptive modeling functionality has been developed that can be implemented in a generic component-based gas turbine environment. A single component in a system modeling environment is able to turn any new or existing model into an adaptive model without extra coding. The concept has been demonstrated in the GSP gas turbine modeling environment. An object-oriented architecture allows automatic addition of the necessary equations for the adaptation to measurement values. Using the adaptive modeling component, the user can preconfigure the adaptive model and quickly optimize gas path diagnostics capability using experimentation with field data. The resulting adaptive model can be used by maintenance engineers for diagnostics. In this paper the integration of the adaptive modeling function into a system modeling environment is described. Results of a case study on a large turbofan engine application are presented. [DOI: 10.1115/1.1995770]

Introduction

The last few decades have provided gas turbine performance engineers with increasingly powerful modeling tools. At an early stage, the opportunity was identified to use simulation models for diagnostics purposes, requiring modeling of deterioration and fault effects. Much focus was put on gas path analysis (GPA) methods, linking measured gas path parameter deviations to engine condition. A large number of publications show the development of different GPA approaches including linear GPA [1–3], nonlinear GPA including adaptive modeling [4,5], neural networks [6–10] and genetic algorithms [11–14]. Linear and nonlinear GPA often employ cycle models to calculate deterioration and fault effects. Adaptive models have an inherent capability to generate deterioration and fault data by adapting to measured engine data that are somehow deviating from the reference engine. Most efforts to apply adaptive modeling for diagnostics have resulted in engine-type specific tools [4,5,15,16]. This is because many cycle models used as a starting point already are engine specific. Moreover, the optimal configuration of an adaptive model in terms of measured parameters and unknown condition modifiers depends on engine type [15,16].

The Gas Turbine Simulation Program (GSP) was developed with flexibility as a primary objective and has successfully demonstrated the capability to model virtually any gas turbine configuration [17,18]. With the need for improved diagnostics capabilities in many gas turbine operational environments in The Netherlands, a research program was conducted to develop a powerful generic GPA capability inside GSP. The objectives of this research program funded by the Netherlands Agency for Aerospace Programmes (NIVR) were to be able to

1. Turn any existing GSP model into an adaptive model
2. Rapidly configure an effective diagnostics tool for any engine type

Although GSP was used as environment for implementation, the

concept presented can be used in any program with a flexible and generic structure.

Approach

Most gas turbine cycle models calculate steady-state or transient off-design operating points by solving sets of nonlinear differential equations. The equation set represents the conservation laws that apply for the specific engine. Truly generic modeling tools, such as GSP, must somehow automatically build up the equation set during model initialization [17]. The individual gas turbine component models then must be able to add any equation and free state variable to the set that is processed by a separate generic solver. An adaptive model can be represented numerically by just adding a number of equations equal to the number of measurements to adapt to. To obtain a “square” equation set with a single solution, then also an equal number of unknowns must be added representing various engine or component conditions, such as efficiency and mass flow deltas or “map modifiers.” Naturally, the condition parameter set must include realistic deterioration modes and/or faults with identifiable effects on performance via the gas path.

Object-Oriented Implementation

Object orientation provides an efficient means to implement functionality common to different modeling elements in a simulation environment. The inheritance principle of object orientation enables the introduction of additional gas turbine component model capabilities in a single “ancestor” component model class [17]. All child classes of that class inherit that capability, automatically, without requiring any additional coding. Existing GSP models for example can simply be opened and run with a newer implementation of a component model extended with new modeling capabilities. This convenient mechanism allows the implementation of capabilities required for adaptive modeling in a single component model class, common to all gas path components. The capabilities added are

1. a list of measurement values corresponding to component performance parameters
2. a list of condition factors to be multiplied with condition parameters, such as efficiencies and map flow rates
3. an interface to have the user select the measurements and

Contributed by the International Gas Turbine Institute (IGTI) of ASME for publication in the JOURNAL OF ENGINEERING FOR GAS TURBINES AND POWER. Manuscript received October 1, 2003; final manuscript received March 1, 2004. IGTI Review Chair: A. J. Strazisar. Paper presented at the International Gas Turbine and Aeroengine Congress and Exhibition, Vienna, Austria, June 13–17, 2004, Paper No. GT2004-53721.

condition factors that are active during “adaptive simulation” mode (the user must be able to quickly change parameter selections in order to evaluate and optimize the adaptive model configuration)

4. user interface elements to present results, such as bar charts, to visualize deltas on performance and component condition parameter values

Although not essential, object orientation clearly provides significant advantages over alternative approaches to implement generic adaptive modeling functions.

Numerical Methods

As explained in the previous sections, the numerical solution of the set of adapted condition factors is simply found by adding the corresponding equations to the equation set that represents the reference engine. In Eq. (1) the complete set of equations for an adaptive model is shown. The upper-left section represents the reference engine: f_1-f_n are the n error equations based on the conservation laws with the unknown states s_1-s_n . ε represents the relative equation tolerance (convergence criterion for the conservation equations) and should be very close to zero (typically 0.0001). $f_{m1}-f_{mm}$ represent the m additional equations added in adaptive modeling mode and simply require a model output parameter to be equal to a specified measurement value. $s_{c1}-s_{cm}$ are the scalars representing the unknown condition factors that need to be solved for. $\varepsilon_{m1}-\varepsilon_{mm}$ represent the separate tolerances for the adaptation to the measurement parameters.

$$\begin{aligned} f_1(s_1)+ \dots f_1(s_n)+ f_1(s_{c1})+ \dots f_1(s_{cm}) &= \varepsilon \\ \vdots & \\ f_n(s_1)+ \dots f_n(s_n)+ f_n(s_{c1})+ \dots f_n(s_{cm}) &= \varepsilon \\ f_{m1}(s_1)+ \dots f_{m1}(s_n)+ f_{m1}(s_{c1})+ \dots f_{m1}(s_{cm}) &= \varepsilon_{m1} \\ \vdots & \\ f_{mm}(s_1)+ \dots f_{mm}(s_n)+ f_{mm}(s_{c1})+ \dots f_{mm}(s_{cm}) &= \varepsilon_{mm} \end{aligned} \quad (1)$$

A more compact notation for Eq. (1) using vectors is

$$F(\bar{s}) \leq \bar{\varepsilon} \quad (2)$$

with \bar{s} including both the s and s_c elements and $\bar{\varepsilon}$ including elements equal to the conservation equation tolerance ε and measurement tolerances ε_m . The measurement equations representing the adaptation constrains for a measurement i are

$$f_{mi} = P_{i\ mdl} - P_{i\ meas} \leq \varepsilon_{mi} \quad (3)$$

with $P_{i\ mdl}$ and $P_{i\ meas}$ the adapted and measured values of parameter P_i , respectively.

A Newton-Raphson-based (or other) solver can be used to iterate toward the solution, and at this stage there are no further numerical additions required. The absence of outside iteration loops provides optimal stability and minimal complexity.

Reference Models

The objective is to extend an existing gas turbine model with an adaptive modeling capability, without having to interfere with the model itself. In GSP, this can be simply done by drag and drop of the adaptive model control component icon (top-left in Fig. 1). With the adaptive mode turned off, the model represents the reference or baseline engine.

The reference model must be tuned to performance data in order to obtain an accurate baseline. This means matching the model design point to a specific engine operating point data set, usually at high power levels at standard conditions, such as maximum takeoff thrust for a turbofan engine. If necessary, model parameters can be further fine tuned to improve the match with available off-design data. Even if component maps are not available and

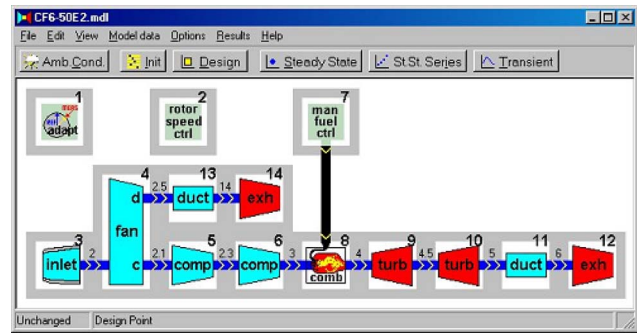


Fig. 1 GSP model with (top-left) adaptive model control icon

must be scaled from similar public domain maps, errors can be kept small as long as the operating point stays close to the design point. This is the case, for example, with gas path analysis diagnostics on maximum takeoff power engine pass-off tests at KLM engine overhaul facility Amsterdam (see Case Study section).

The accuracy of the reference model match affects the adaptive model simulation process. Reference engine model errors will interfere with the adaptive modeling numerical solution. Therefore, “calibration factors” f_c are introduced, compensating the adaptive model numerics for model errors. Equation (4) shows how a model parameter $P_{i\ mdl\ raw}$ is calibrated using the ratio of the design point measured and model parameter values

$$P_{i\ mdl} = P_{i\ mdl\ raw} \cdot f_{ci} \quad (4)$$

$$f_{ci} = \frac{P_{i\ meas\ des}}{P_{i\ mdl\ des}}$$

Normally, if an accurate design point match has been obtained, the f_c factors are very close to 1. The f_c factor calibration method was found to have a significant effect on adaptive model stability and results, even if the f_c factors only deviated 1% from unity.

Another important consideration is the source of the data for tuning the reference engine model design point. This source, optimally, is the same engine test bed under the same calibration settings. Data from a single engine test, well corresponding to the average (new or overhauled) engine performance, are usually sufficient to be used for an entire engine fleet, and this approach has been used for the case study at KLM. Even better results would be obtained if a range of engine tests would be used and averaged to eliminate measurement scatter effects. Ultimately, the best but also most laborious approach would be to match models to every new engine at the start of its service life (or time between overhauls) and keep the model for diagnostics for the particular engine. Then engine-to-engine variation is eliminated, and performance deviations will only be because of deterioration or faults. This approach may well be applied in the future in on-wing or remote-wireless continuous engine monitoring systems [19–23]. With the adaptive model continuously running on-board in the FADEC, more interesting opportunities emerge, such as adaptive control logic [24].

Selection of Parameters

The square equation set with an equal number of measurements and condition parameters is the most straightforward approach. However, the number of condition parameters and especially measurements may vary among engine types and applications. Ideally, a large number of accurate measurements is available, covering the gas path conditions at most engine stations and exceeding the number of condition parameters. In that case, the solution of the “overdetermined” equation set would be a minimization problem, for example, using a weighted least-squares method [1,25]. In most cases, however, the number of measurements is limited and

often smaller than the number of condition parameters required for a complete representation of engine health, including all deterioration and failure modes. Several solutions have been proposed to handle the case of fewer measurements than condition parameters, including multipoint [12,14,26], adding constraints or equations derived from knowledge of the (relations among) deterioration modes [27] or working with optimized selections of condition parameter “subsets,” equal to the number of measurements. With the latter approach, methods proposed by [12,15,28] can be used to define a measurement and condition parameter set that is best able to isolate specific problems. A method suggested by Ogaji [28] is used in the case study described later in this paper.

Different sets can be used to identify different fault or deterioration cases. With an adaptive modeling tool that can be rapidly configured, this approach is attractive and therefore has been used in the GSP diagnostics module at this stage. As will be explained in the following sections, the GSP diagnostics component includes a powerful generic GUI, allowing rapid configuration of adaptive models for any GSP modeled gas turbine engine. Results with different subselections of both the measurement and condition parameters can be quickly analyzed.

Measurement Uncertainty

The measurement tolerances $\varepsilon_{m1} - \varepsilon_{mm}$ are independent of conservation law inaccuracy ε and represent measurement specific tolerances for the adaptation equations. The ε_m values are separately user specified corresponding to measurement uncertainty data. Normally, the ε_m values will be larger than ε and can be tuned to obtain optimal results.

With large ε_m values, solutions may be found at the extremes of ε_m margins, which are unrealistic in a sense that the deviation from the reference engine parameter value is “ignored” by the solution. In the future, additional methods may be applied to account for statistical probability distribution of measurement error using weight factors, for example. This will allow better representation of measurement error and provide solutions with maximum probability with larger measurement uncertainty margins.

Standard and Adaptive Simulation Modes

The engine simulation tool only needs to solve the additional equations during adaptive modeling mode. The adaptation of the model can simply be deactivated by replacing the f_m equations (Eq. (3)) by

$$f_{mi} = s_{ci} - 1 \quad (5)$$

The result will be a solution with all condition scalars being equal to 1, representing the case of the healthy reference engine. Every adaptive simulation must be preceded by a standard (non-adaptive) simulation to determine the reference engine baseline performance and deltas at the particular operating point. In GSP this is done automatically.

Obviously, the ability to use the same model for both performance analysis with the reference engine model and adaptive simulations and diagnostics in the same session is very convenient. Following a diagnostics session, the performance of the adapted model can be analyzed and directly compared to the reference engine by plotting curves for varying power setting for both cases in simple X-Y graphs and compressor maps for example (see Figs. 2 and 3).

Figures 2 and 3 represent results of the case study discussed later in this paper.

Model Stability

Large measurement errors may well result in attempts to find engine operating points that are impossible, even with extreme component condition variations. In such cases the conservation equations for mass and energy can simply not be satisfied while simultaneously matching the measured performance parameters.

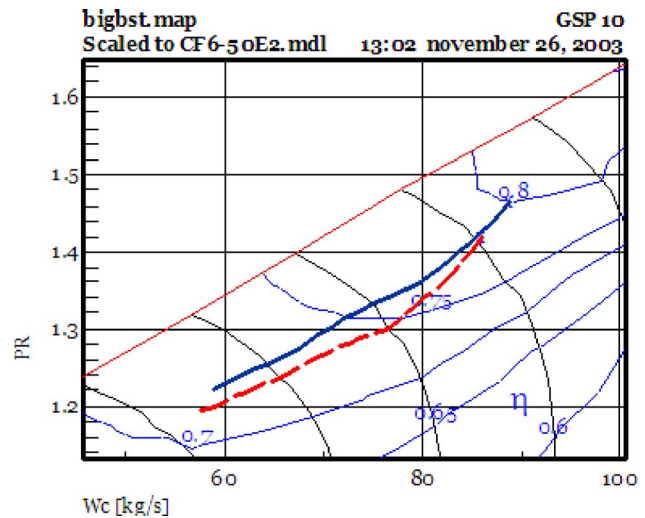


Fig. 2 Booster running lines for reference (solid) and deteriorated (dashed) engine (case 1)

In this case widening the ε_m tolerance margins may help to a certain extent, but with large measurement uncertainty (especially scatter) it often is better to omit the particular measurement from the measurement set.

Another problem is multiple solutions. Especially with a small measurement data set the model may adapt with unrealistic condition factors, such as very high efficiencies. A slightly different measurement then may have totally different results, indicating there are multiple solutions for the condition vector \bar{s}_c . In this case more measurements are required to “more tightly” capture engine performance.

In the case study with the twin spool turbofan described later in this paper, at least six parameters were required to obtain realistic results pointing in the right direction. As described in the Case Study section, the low-pressure section behaves more or less independently from the gas generator. If only a few parameters, such as fan duct pressure and fan duct side efficiency, are added, results become unstable. It appeared that either the low-pressure (fan and LPT exit) parameters must be fully omitted or sufficient measurement parameters must be added to unambiguously determine fan and LPT performance.

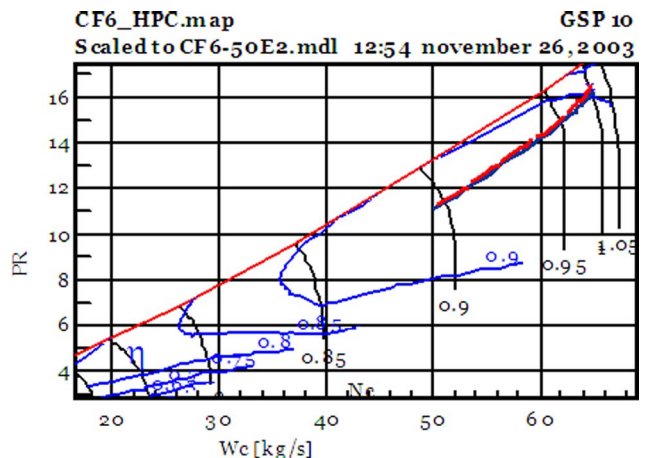


Fig. 3 HPC running lines for reference (solid) and deteriorated (dashed) engine (case 1)

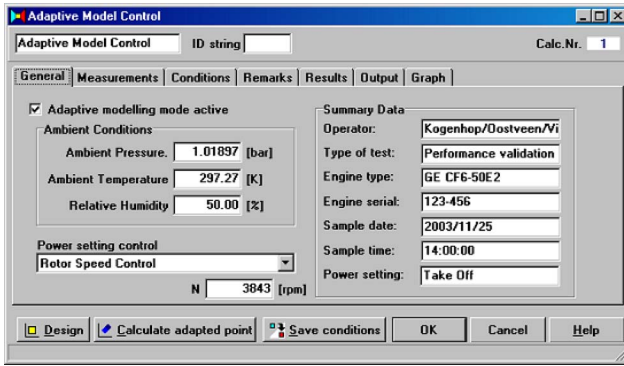


Fig. 4 GSP adaptive model control component window

User Interface

A major challenge is to develop a graphical user interface (GUI) capable of effectively controlling adaptive models based on any model configuration. For application to virtually any working cycle configuration, a highly flexible concept is required. Several examples of GUIs for GPA exist [16,22], but these usually are engine specific, so a new approach was required.

Generic component-based simulation environments usually have a GUI with separate data entry windows for individual component models. In GSP, for example, these are accessed by double clicking the component icons shown in Fig. 1. This approach can easily be used for the adaptive modeling capability. However, for adaptive modeling, the focus is on the engine as a system and therefore a separate single interface is required to control all adaptive modeling functions on the system model level. A concept using a tree view with multiple columns was chosen as the best solution for this.

In GSP, an interface component was inherited from a “model control component” object class that has access to all other component models. Tree views are used, including all component models as top level elements. The resulting adaptive model control window is accessed via the top-left adaptive model component icon in Fig. 1 and includes the tab sheets shown in Figs. 4–8 with screenshots.

Figure 4 shows the general configuration tab sheet for specification of engine and session reference data, ambient conditions, and engine power setting. Depending on the model configuration, rotor speeds, fuel flow, thrust, or other parameters can be specified

Parameter	Unit	Ref Model	Measur.	Tol.	Delta	Adapt.	Error	- [%]	+ [%]
<input checked="" type="checkbox"/> P _{sin}	[bar]	1.86745	1.81477	1	-2.821	1.815	0.012		
<input checked="" type="checkbox"/> T _{sout}	[K]	843.10	841.45	1	-0.196	841.45	0.000		
<input checked="" type="checkbox"/> P _{sout}	[bar]	30.49521	30.0374	1	-1.501	30.04136	0.013		
<input checked="" type="checkbox"/> N%	[%]	106.28	105.73	1	-0.518	105.73	0.000		
<input checked="" type="checkbox"/> T _{tout}	[K]	1118.46	1141.15	1	2.029	1141.07	-0.007		
<input checked="" type="checkbox"/> P _{tout}	[bar]	6.51986	6.493422	1	-0.405	6.4943	0.014		
<input checked="" type="checkbox"/> W _{total}	[kg/s]	2.4625	2.4786	1	0.654	2.4786	0.000		

Fig. 5 Measurements tab sheet

Tol. [%]	Delta [%]	Adapted	Error [%]	- [%]	+ [%]
1	-2.821	1.815	0.012		

Fig. 6 Detail of measurement tab sheet

for power setting. Two tree views are defined, one for measurements (Fig. 5) and one for the condition parameters (Fig. 7).

In the measurements tree (Fig. 5), each component in the tree has subelements representing the individual performance parameters that can be used for adaptive modeling. The parameters listed depend on the component type. For each parameter, measurement values can be entered and these are compared to reference model calculation results. The check boxes are used to select the set of parameters to adapt to (i.e., the parameters used in the f_m equations). Note that Fig. 5 shows the tree view with an option activated making the unchecked parameters invisible for user convenience. For each parameter, the reference model calculated value, the user-specified measured value, and tolerance for adaptation (ϵ_m), the calculated delta (reference measured), the calculated adapted value (should be within tolerance range of measured), and the error (adapted measured, should be close to zero) are shown. Not displayed are the columns for the design point calibration factors f_c of Eq. (5). By scrolling to the right three columns with model design and measured design values, and the calibration factors are shown.

The horizontal bars (see detail in Fig. 6) indicate measured performance delta (solid blue bar), tolerance for adaptation ϵ_m (red range indicator), and the calculated adapted value (black dot). The latter value must be in the red tolerance range for the modeling system to be accepted as a valid adapted operating point. In Fig. 6 a result was found exactly matching the measurement value so the black dot is in the middle of the tolerance range.

In the conditions tree (Fig. 7), each component has subelements representing the individual condition parameters (s_c) that are adapted to match measured performance. The parameters listed depend on component type. The check boxes are used to select the subset of parameters that are allowed to be adapted (i.e., represent the \bar{s}_c vector). Figure 7 shows the tree view with all possible condition parameters visible (the scroll bar must be used to scroll up and down to cover all components). The horizontal bars indicate the deviations of the condition parameters, thereby providing the gas path diagnostics information. Individual threshold values can be specified to indicate levels beyond which the condition

Parameter	Unit	Reference	Adapted	Delta	Threshold	- [%]	+ [%]
<input checked="" type="checkbox"/> Eta _{ie}	[H]	1.0000	0.9924	-0.762	1		
<input checked="" type="checkbox"/> W _c	[H]	1.0000	0.9379	-6.211	1		
<input type="checkbox"/> PR	[H]	1.0000					
<input checked="" type="checkbox"/> Eta _{is}	[H]	1.0000	1.0068	0.677	1		
<input type="checkbox"/> W _c	[H]	1.0000					
<input type="checkbox"/> PR	[H]	1.0000					
<input checked="" type="checkbox"/> Eta _{is}	[H]	1.0000	0.9939	-0.611	1		
<input checked="" type="checkbox"/> W _c	[H]	1.0000	0.9968	-0.320	1		
<input checked="" type="checkbox"/> Eta _{is}	[H]	1.0000	0.9920	-0.805	1		
<input checked="" type="checkbox"/> W _c	[H]	1.0000	0.9847	-1.534	1		

Fig. 7 Conditions tab sheet

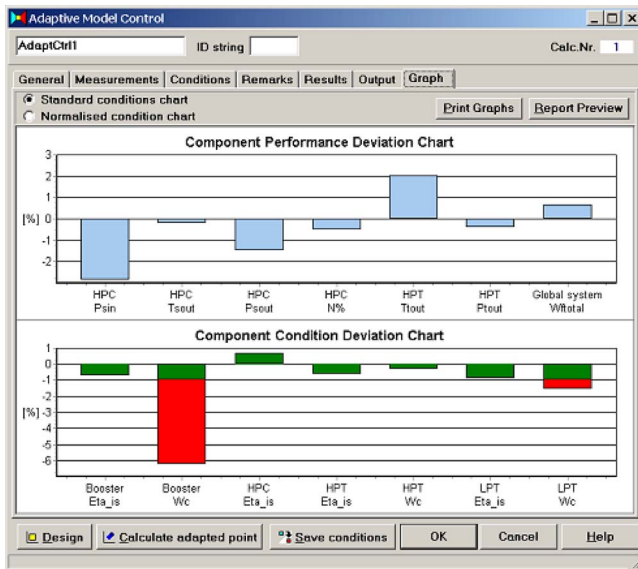


Fig. 8 Gas path analysis results chart window, case 1

parameter deviation is considered significant. Beyond the thresholds, the bars turn red. The chart can optionally be normalized to the threshold values. Figure 8 shows the graphical report output of the results with both the performance and condition parameter deltas.

The information described above can be assembled in a comprehensive diagnostics report to be printed or digitally stored for later reference. Also, event logs are kept to store settings, user comments, and results generated during the diagnostics session. The resulting GUI and reporting functions enable the deployment of GSP models as user-friendly diagnostics tools.

Results

During development, the adaptive modeling component has been tested and experimented with a variety of engine models for which measurement data were available. It was found that results (stability and realistic result data) are sensitive to both model and measurement inaccuracy. The model accuracy can be improved by better tuning to known data and the use of accurate component maps (rather than maps scaled from generic ones) if available. With the addition of the user measurement tolerance and the design point calibration factors, stability and results were significantly improved.

The user interface was evaluated by several engineers and, after an evolution via several designs, approved as a tool that can be preconfigured to an effective diagnostic aid. The ultimate test was an industrial application as described in the following section.

Case Study

A case study has been performed on an application that is very suitable for gas path analysis diagnostics. At the KLM Royal Dutch Airlines CF6 engine maintenance facility, CF6 family engines are overhauled and finally submitted to a “pass-off test” before being returned into service. GPA is one of the techniques used to diagnose problems indicated by deviating or unacceptable test-bed measurement results. Costs could be significantly reduced if more accurate GPA tools than those currently used were available. Therefore, the GSP tool was tested on a number of cases with CF6-50 engines to assess its potential. Two cases will be described in this section.

First a baseline model was developed and tuned to data measured on an average healthy turbofan engine. This data point corresponds to the GSP design point. In the adaptive model component, the residual design point deviations are stored in the design

Table 1 Measurement parameter sensitivity rankings

	Wf=control parameter	N1=control parameter
1	Ps2.5	Pt4.5
2	Pt4.5	Ps2.5
3	Ts3	Wf
4	N1	N2
5	N2	Tt4.5
6	Ps3	Ps3
7	Tt4.5	Ts3
8	FN	FN
9	Pt1.3	Pt1.3

point calibration factors, to be later used for the adaptive modeling mode. Note that the GSP design point is at arbitrary ambient conditions. Power setting in GSP (and on the test bed) is represented by a particular N1 fan rotor speed using the GSP rotor speed controller.

Next, the measurement data of the problem engine under consideration are entered in the particular measurement column in the data entry window shown in Fig. 5. In this case either fuel flow or N1 rotor speed can be used to specify power setting (i.e., represent an input parameter). If N1 is chosen, then fuel flow can be defined as a measurement parameter and vice versa.

To obtain an optimal measurement set, the parameter offset method as suggested by Ogaji [28] was applied. This method provides a ranking of measurement parameter sensitivities to (1%) component condition parameter offsets. A cycle simulation tool, such as GSP, can be used to determine the individual sensitivity values. The parameter set should be selected from the top of the sensitivity ranking order. In Table 1 the ordered lists of the nine measurement parameters available are shown for the two alternative power-setting parameters available.

Although the power-setting parameter has an effect on the ranking, the diagnostics end results are not significantly affected by the power-setting selection, as may be expected. For the case study, N1 was chosen as power-setting parameter since N1 is also the test-bed power-setting indicator.

Condition parameters were selected using engineering judgement and trial and error. With the powerful GUI, many combinations can be tested very rapidly.

Best results were obtained with the top seven measurement parameters from Table 1 including Ps2.5 (booster exit), Ps3, Ts3, N2, Tt4.5 (EGT), Pt4.5, and Wf. Extending the set with the remaining number of eight or nine parameters FN and Pt1.3 did not generate stable and realistic results with any combination of condition parameters. Using nine parameters, including both Pt1.3 and FN, prevented the model from finding a solution at all. This is because of the strong correlation between FN and Pt1.3. As a result, the set could not be extended to include fan conditions at this stage due to the limited data for the low-pressure system performance. It is expected that with additional measurements, such as hot exhaust (station 5) pressure and/or temperature, this could well be improved. This will be the subject of future research.

Case 1. With the seven parameters described above, a diagnostics session was performed on a CF6-50 engine with a low EGT margin. The engine test indicated an EGT of 23 K over the expected value for a healthy engine but still within acceptance limits. For GPA this means a more difficult case because of the relatively small performance deviation.

Condition factors chosen for this case were booster efficiency and mass flow, HPC efficiency, HPT efficiency and flow capacity, and LPT efficiency and flow capacity. As explained above, this set is mainly focused on booster and gas generator health and will not be able to identify fan problems.

Results are shown in Fig. 8, depicting a screenshot of the “graph” tab sheet of the adaptive model control window. The up-

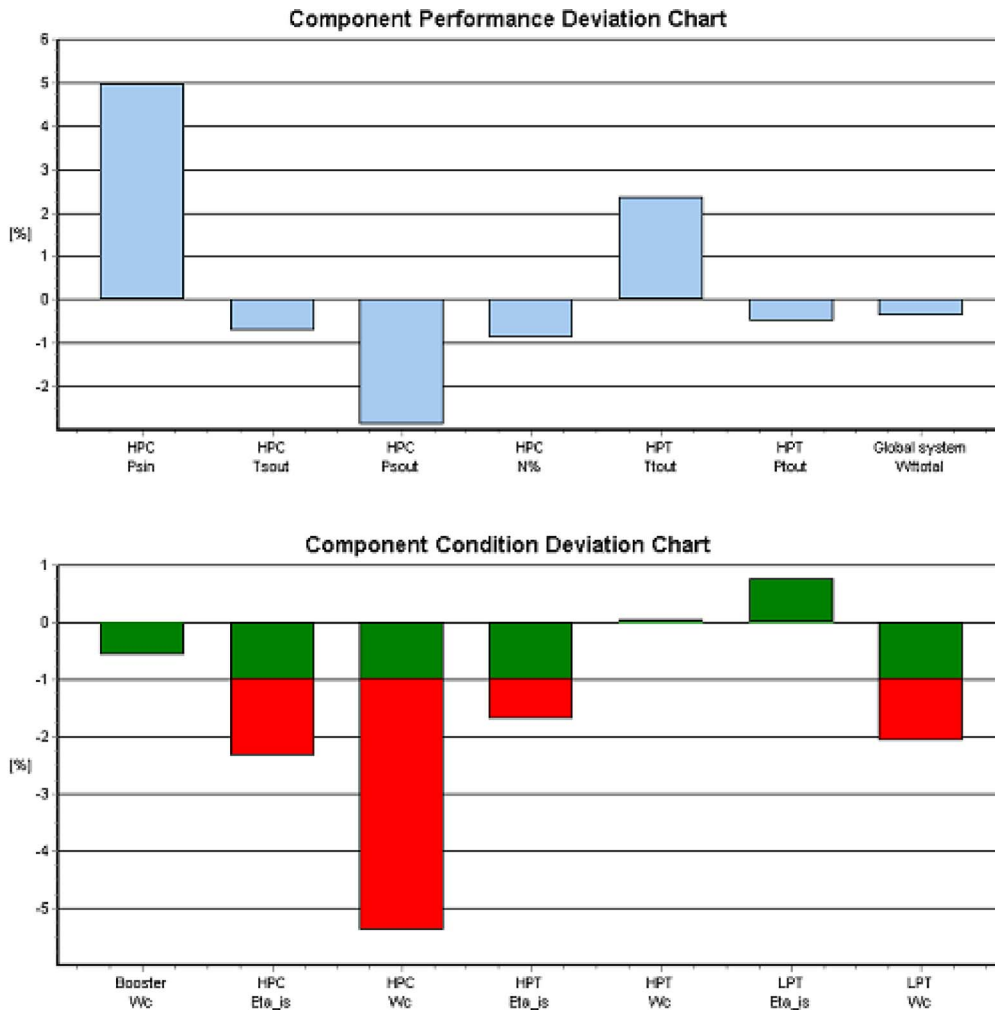


Fig. 9 Gas path analysis results case 2

per part of the figure depicts the performance deviation relative to the reference engine. The lower part shows the adaptations needed to fit the base model to the measurement set. As stated above, the performance delta is small, i.e., within 3% for all seven parameters (including the 23 K EGT delta). The adaptive model calculation indicates the booster to be responsible for the poor performance due to a flow capacity problem. Since the booster has no variable geometry, VSV misrigging is ruled out as a cause, leaving, at least, blow-off valve leakage or tip clearance as candidates for further investigation. This outcome was confirmed after further analysis at KLM, proving the accuracy of the GSP adaptive model to identify engine problems on component level.

After a valid diagnostics result has been found, the resulting adapted engine model performance can be analyzed. The deterioration deltas are stored in the model and adapted (deteriorated) versus reference engine performance can be compared at various other operating conditions and power settings.

Figure 2 shows the calculated booster running lines for the case 1 reference and deteriorated engine in the booster map. A significant shift away from the stall limit is shown as may be expected from the deteriorated booster flow capacity. Figure 3 shows the HPC running line is not significantly affected as may be expected if only the booster condition has changed.

Case 2. In a second case, an engine was analyzed that was rejected at the performance test after overhaul. The performance test was eventually passed after replacement of the HPC during a second shop visit, although this was not recommended by the

available conventional diagnostic methods. However, the GSP adaptive model indicated an HPC mass flow deficiency (Fig. 9), thereby clearly proving its capability to effectively isolate component faults.

Note that the condition set is different from case 1 and includes HPC mass flow instead of booster efficiency. The case 1 set was used first but did not generate realistic results, which were caused by the absence of the condition factor responsible for the engine problem. Case 2 demonstrates the benefit of the ability to rapidly evaluate results with different condition parameter sets.

Conclusions

Generic gas turbine simulation environments can be extended to generic adaptive modeling tools for diagnostics and gas path analysis of deteriorated engine performance. Critical elements for the extension are

- modeling structure
- flexibility with regard to the model equations and numerical methods
- graphical user interface (GUI)

With a flexible object-oriented architecture, an efficient implementation can be realized and has been demonstrated. New additions to the adaptive modeling system can be easily implemented because of object orientation.

With tree-view elements, a GUI can be developed that adapts to

any gas turbine model. Different combinations of measurement and condition parameter sets can be rapidly evaluated and optimized for specific engines and deterioration types. The different sets can be saved and later activated on request to verify different hypotheses and assumptions with regard to the engine problem.

The approach has been successfully demonstrated in the object-oriented gas turbine simulation environment (GSP). Component faults were successfully isolated in a number of test cases with a high bypass turbofan engine. The GSP adaptive model control component turns existing GSP models into adaptive models that can be rapidly configured to become powerful user-friendly GPA (gas path analysis) tools.

The adaptation function can be applied to new GSP component models derived from existing ones using object inheritance. Condition factors and measurement equations can be added for any component model. This means other system models, including additional systems such as load compressors and combined cycle components, can be included for GPA diagnostics.

The GSP adaptive modeling GUI enables deployment of GSP models as user-friendly diagnostics tools. A configuration for a specific engine type is currently being validated by maintenance engineers at KLM.

Although a flexible concept is working, not all options for powerful GPA with GSP have been explored yet and future work is planned to enhance GSP's adaptive modeling and diagnostic tool capabilities, including the following:

- application to cases with more measurement data (i.e., including exhaust gas pressure and/or temperature)
- adding a numerical minimization option for cases with more measurements than condition factors
- exploration of feasibility of multipoint GPA
- additional methods to compensate measurement uncertainty (constraints on and relations among condition parameter variations)
- separate GSP adaptive modeling versions with optional hiding of model configuration data entry items to provide a secure and user friendly diagnostics tool at flight line or test bed

Acknowledgment

This work was funded by the Netherlands Agency for Aerospace Programmes NIVR as a Basic Research Program (BRP) with Project No. 49212N. The authors wish to express their gratitude to KLM Royal Dutch Airlines CF6 engine maintenance facility Amsterdam for their cooperation.

Nomenclature

EGT	=	exhaust gas temperature
FADEC	=	full authority digital engine control
GPA	=	gas path analysis
GSP	=	Gas Turbine Simulation Program
GUI	=	graphical user interface
HPC	=	high-pressure compressor
HPT	=	high-pressure turbine
N1	=	low-pressure (fan) spool speed
N2	=	high-pressure spool speed
NIVR	=	Netherlands Agency for Aerospace Programmes
NLR	=	National Aerospace Laboratory
Ps2.5	=	static booster exit pressure
Ps3	=	static HPC exit pressure
Pt1.3	=	total fan bypass exit pressure
Pt4.5	=	total HPT exit pressure
Ts3	=	static HPC exit temperature

Tt4.5 = total HPT exit temperature (EGT)

Wf = fuel flow

References

- [1] Doel, D. L., 1992, "Temper—A Gas Path Analysis Tool for Commercial Jet Engines," ASME Paper No. 92-GT-315.
- [2] Urban, L. A., 1972, "Gas Path Analysis Applied to Turbine Engine Condition Monitoring," AIAA Paper No. 72-1082.
- [3] Kamboukos, Ph., and Mathioudakis, K., 2003, "Comparison of Linear and Non-Linear Gas Turbine Performance Diagnostics," ASME GT-2003-38518.
- [4] Stamatis, A., Mathioudakis, K., and Papailiou, K., 1989, "Adaptive Simulation of Gas Turbine Performance," ASME Paper No. 89-GT-205.
- [5] Lambiris, B., Mathioudakis, K., Stamatis, A., and Papailiou, K., 1994, "Adaptive Modeling of Jet Engine Performance With Application of Condition Monitoring," J. Propul. Power, **10**(6), pp. 890–896.
- [6] Kanelopoulos, K., Stamatis, A., and Mathioudakis, K., 1997, "Incorporating Neural Networks Into Gas Turbine Performance Diagnostics," ASME Paper No. 97-GT-035.
- [7] Romessis, C., and Mathioudakis, K., 2002, "Setting up of a Probabilistic Neural Network for Sensor Fault Detection Including Operation With Component Fault," ASME Paper No. GT-2002-30030.
- [8] Lu, P. J., Zhang, M. C., Hsu, T. C., and Zhang, J., 2000, "An Evaluation of Engine Faults Diagnostics Using Artificial Neural Networks," ASME Paper No. 2000-GT-0029.
- [9] Bin, S., Jin, Z., and Shaoji, Z., 2000, "An Investigation of Artificial Neural Networks (ANN) in Quantitative Fault Diagnosis for Turbofan Engine," ASME Paper No. 2000-GT-32.
- [10] Embrechts, M. J., Schweizerhof, A. L., Bushman, M., and Sabatella, M. H., 2000, "Neural Network Modeling of Turbofan Parameters," ASME Paper No. 2000-GT-0036.
- [11] Zedda, M., and Singh, R., 1999, "Gas Turbine Engine and Sensor Diagnostics," ISABE Paper No. 99-7238.
- [12] Grönstedt, T. U. J., 2002, "Identifiability in Multi-Point Gas Turbine Parameter Estimation Problems," ASME Paper No. GT-2002-30020.
- [13] Sampath, S., Gulati, A., and Singh, R., 2002, "Fault Diagnostics Using Genetic Algorithm for Advanced Cycle Gas Turbine," ASME Paper No. GT-2002-30021.
- [14] Sampath, S., Ogaji, S. O. T., Li, Y. G., and Singh, R., 2003, "Fault Diagnosis of a Two Spool Turbo-Fan Engine Using Transient Data: A Genetic Algorithm Approach," ASME Paper No. GT-2003-38300.
- [15] Kamboukos, Ph., Oikonomou, P., Stamatis, A., and Mathioudakis, K., 2001, "Optimizing Diagnostic Effectiveness of Mixed Turbofan by Means of Adaptive Modelling and Choice of Appropriate Monitoring Parameters," *RTO Symp. on Aging Mechanisms and Control*.
- [16] Mathioudakis, K., Stamatis, A., Tsalavoutas, A., and Aretakis, N., 2000, "Instructing the Principles of Gas Turbine Performance Monitoring and Diagnostics by Means of Interactive Computer Models," ASME Paper No. 2000-GT-584.
- [17] Visser, W. P. J., and Broomhead, M. J., 2000, "GSP, A Generic Object Oriented Gas Turbine Simulation Environment," ASME-2000-GT-0002.
- [18] GSP website: www.gspteam.com.
- [19] Roemer, M. J., and Kacprzyński, G. J., 2000, "Advance Diagnostics and Prognostic Technologies for Gas Turbine Engine Risk Assessment," ASME Paper No. 2000-GT-30.
- [20] Moreno Barragán, J. A., 2001, "Engine Vibration Monitoring and Diagnosis Based on On-Board Captured Data," *NATO/RTA AVT Symposium*, Manchester.
- [21] Stamatis, A., Mathioudakis, K., Ruiz, J., and Curnock, B., 2001, "Real Time Engine Model Implementation for Adaptive Control and Performance Monitoring of Large Civil Turbofans," ASME Paper No. 2001-GT-0362.
- [22] Tsalavoutas, A., Aretakis, N., Mathioudakis, K., and Stamatis, A., 2000, "Combining Advanced Data Analysis Methods for the Constitution of an Integrated Gas Turbine Condition Monitoring and Diagnostic System," ASME Paper No. 2000-GT-0034.
- [23] Zoller, T., 2000, "Advanced Engine Monitoring and Diagnosis Systems: Actual System for the EJ200 Engine of the Eurofighter 2000 Aircraft and Future Trends," MTU Aero Engines GmbH.
- [24] Dambrosio, L., Camporeale, S. M., and Fortunato, B., 2000, "Performance of Gas Turbine Power Plants Controlled by One Step Ahead Adaptive Technique," ASME Paper No. 2000-GT-0037.
- [25] Doel, D. L., 2002, "Interpretation of Weighted-Least-Squares Gas Path Analysis Results," ASME Paper No. GT-2002-30025.
- [26] Stamatis, A., Mathioudakis, K., Berios, G., and Papailiou, K., 1989, "Jet Engine Fault Detection With Discrete Operating Points Gas Path Analysis," *ISABE Meeting*, Paper No. 89-7133.
- [27] Aretakis, N., Mathioudakis, K., and Stamatis, A., 2002, "Non-Linear Engine Component Fault Diagnosis From a Limited Number of Measurements Using a Combinatorial Approach," ASME Paper No. GT-2002-30031.
- [28] Ogaji, S. O. T., and Singh, R., 2002, "Study of the Optimization of Measurement Sets for Gas Path Fault Diagnosis in Gas Turbines," ASME Paper No. GT-2002-30050.

Experimental Operating Range Extension of a Twin-Spool Turbofan Engine by Active Stability Control Measures

Stephan G. Scheidler

e-mail: stephan.scheidler@unibw-muenchende

Leonhard Fottner

Institut für Strahlantriebe,
Universität der Bundeswehr München,
D-85577 Neubiberg, Germany

Modern engine operation is guided by the aim to broaden the operating range and to increase the stage loading allowing the stage count to be reduced. This is possible by active stability control measures to extend the available stable operating range. Different strategies of an active control system, such as air injection and air recirculation have been applied. While in the past results have been published mainly regarding the stability enhancement of compressor rigs or single-spool engines, this experimental study focuses on both the stability as well as the operating range extension of a twin-spool turbofan engine as an example of a real engine application on an aircraft. The objective of this investigation is the analysis of the engine behavior with active stabilization compared to unsupported operation. For this purpose, high-frequency pressure signals are used and analyzed to investigate the effects of air injection with respect to the instability onset progress and the development of any instabilities, such as rotating stall and surge in the low-pressure compression (LPC) system. These Kulite signals are fed to a control system. Its amplified output signals control fast acting direct-drive valves circumferentially distributed ahead of the LPC. For the application of air injection described in the paper, the air is delivered by an external source. The control system responsible for air injection is a real-time system which directly reacts on marked instabilities and their precursors. It allows the LPC System to recover from fully developed rotating stall by asymmetric air injection based on the pressure signals. Additionally, a delayed appearance of instabilities can be provoked by the system. Air injection guided by this control system resulted in a reduction of the required amount of air compared to constant air injection. Also, disturbances travelling at rotor speed can be detected, damped, and eliminated by this control system with a modulation of the injected air in such a way that the injection maximum travels around the ten injection positions. [DOI: 10.1115/1.2031247]

Introduction

The efficiency in operation of gas turbine engines and its improvement is a mandatory task in the design process of an engine of the next generation. The highest efficiency can be expected close to the surge line, therefore it is useful to reduce the design surge margin. As a consequence, the compression system must have a higher loading. It can be reached by either increasing the pressure ratio while keeping the same number of stages or by reducing the stage count and leaving the pressure ratio unchanged. For any operational aspects, such as handling characteristics at engine dynamics or inlet distortions the capability of sufficient operational reliability has to be ensured. For this purpose, a system is required to handle all possible effects and tolerate all negative influences on the operation process. Such a system is presented in this paper. Based on the air injection system, a control program supervises the pressure signals in the compression system and gives an input signal to the air injection valves to open to the required position. This allows the system to react on instabilities such as rotating stall, surge, and also their precursors.

Air injection into the front stage of a compressor has been demonstrated as an effective method of stabilization. Thereby, the air is injected in the vicinity of the tip gap ahead of the first rotor

blades. While in the first attempts, research work has concentrated on simple applications, such as high-speed compressor rigs by Spakovszky et al. [1] and Weigl et al. [2], small gas turbines by Nelson et al. [3], and single-spool turbojet engines by Freeman et al. [4]. In recent years, the first investigations of constant air injection on a twin-spool turbofan engine by Leinhos et al. [5], also at inlet distortions by Scheidler et al. [6], have been published. These studies demonstrated two different ways to achieve the stabilizing effect of air injection. While a constant air injection at defined circumferential positions can eliminate spikes and precursors [4], a superposed modulated air injection is suited to eliminate modal waves in those turbomachinery applications where they occur [1,2]. The instability inception process of several high-speed compressors is not accompanied by modal waves and it varies with spool speed and inlet flow conditions, as published by Day et al. [7]. Also, some earlier investigations by Leinhos et al. [8] on the twin-spool turbofan engine presented here demonstrated that this test vehicle does not build modal waves on which a control system can react properly. The LARZAC 04 twin-spool turbofan engine contains a tip-critical first low-pressure compressor (LPC) rotor and exhibits different types of instability inception in different speed regimes. In the lower-speed range from idle speed up to about $n_{LPC}=76\%$, the compression system develops a rotating stall cell, caused by the LPC and travelling around with a fluctuating mode. The result of other previous examinations by Höss et al. [9] has been affirmed. The tested engine generates a disturbance rotating at LPC rotor frequency as a shaft order perturbation which causes the stall in the higher-speed range. Therefore, two different control strategies have to be applied to cover

Contributed by the International Gas Turbine Institute (IGTI) of ASME for publication in the JOURNAL OF ENGINEERING FOR GAS TURBINES AND POWER. Manuscript received October 1, 2003; final manuscript received March 1, 2004. IGTI Review Chair: A. J. Strazisar. Paper presented at the International Gas Turbine and Aeroengine Congress and Exhibition, Vienna, Austria, June 13–17, 2004, Paper No. GT2004-53077.

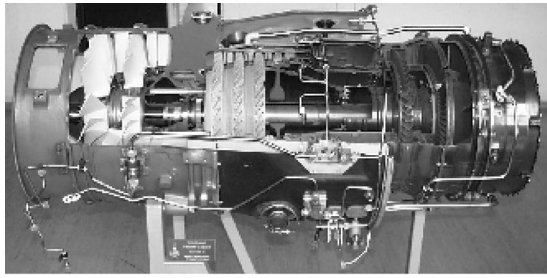


Fig. 1 Cutaway model of the LARZAC 04 C5 turbofan engine

the entire operating range of the engine to (re-)stabilize its compression system over the whole speed band. The control strategy for the lower-speed range to react on and avoid the rotating stall occurrence has been presented in another assay by Scheidler et al. [10]. The study presented here focuses on the upper speed range, commencing from $n_{\text{LPC}}=78\%$ up to maximum power setting, at which a distortion travelling at rotor speed around the circumference is responsible for triggering the instability onset process. Hence, a control system piloting the air injection system has been adopted to cover the described phenomenon and to extend the stable operating range in this speed area. For this purpose, an available commercial controller has been applied as a derivative of the so-called active instability control (AIC) system, which is in use for the active control of thermoacoustic instabilities in stationary gas turbines in Hermann et al. [11]. Here, it serves as a control device for attenuating rotor frequency shaft order perturbations and other rotating disturbances by modulated air injection ahead of the first LPC rotor in order to postpone or to avoid the instability onset process. The injected air is provided by an external source and is guided through an appropriate action of high-bandwidth direct-drive valves (DDVs).

The objective is to explore the capabilities of an active stability control measure taking into account the specific conditions and the practical imperfections of an operational twin-spool turbofan engine as a real application onboard an aircraft. Therewith, more can be learned about limitations of such a system and its potential benefits.

Experimental Setup

Test Engine. The tests were performed at the Jet Propulsion Institute's Ground Test Facility using the low-bypass turbofan engine LARZAC 04 C5. The engine is of modular twin-spool design and does not contain inlet guide vanes in front of the LPC. On this account it is well suited for the survey described herein, with air injection ahead of the first LPC rotor, since the injected air flow directly affects the critical stream in the tip region of the first LPC rotor blades. The engine consists of a two-stage highly transonic LPC, a four-stage high-pressure compressor (HPC), an annular combustion chamber and single-stage high- (HP) and low-pressure (LP) turbines (see Fig. 1).

Table 1 lists the main engine's performance data at ISA

Table 1 LARZAC 04 C5 design point performance data

F_s	13 kN
TET	1403 K
μ (BPR)	1.13
W (mass flow)	27.64 kg/s
Π_{LPC}	2.26
Π_{HPC}	4.60
n_{LPC}	17,500 rpm
n_{HPC}	22,561 rpm

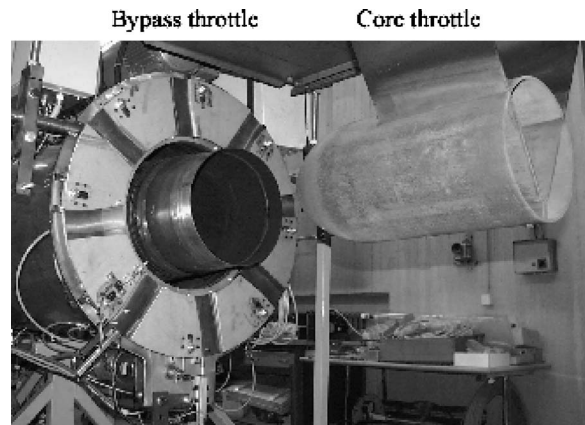


Fig. 2 Bypass and core throttle devices

conditions.

The core and bypass flow expand through separate nozzles without being mixed which allows an almost independent throttling of both compressors. In order to operate the compressors of the test engine above their steady-state running line, both nozzles are equipped with independently working throttling devices. Thereby it is possible to run the LPC close to its stability boundary by activating the so-called bypass throttle (see Fig. 2). It consists of circular arc segments which are driven by a motor via a chain and can be moved in radial direction (see Höss et al. [9]). Thus, it is possible to reduce the bypass nozzle exit area and to throttle the LPC independently from the HPC at a first glance. To throttle the HPC the rotational body of the core throttle can be moved in axial direction. This device has not been used in these investigations.

Air Injection System. The Air Injection System consists of a casing which accommodates ten injection channels. The three-dimensional computer-aided design designed casing was manufactured by wire-electric discharge machining to blank the injection channels. It is mounted as a part of the engine's inlet duct directly ahead of LPC casing. At the end of each injection channel, a pivoted nozzle is located to accelerate the injected airflow and to ensure a highly subsonic velocity. The pivoted arrangement allows the direction of the injected airstream to be varied between angles of -30 deg and $+30$ deg (Fig. 3). The injection nozzles are moved in circumferential direction simultaneously in a collective manner by an actuator ring they are connected with. A positive injection angle corresponds to the direction of rotation of the LPC spool. Some results of investigations of air injection at different angles are published in Leinhos et al. [5] and Scheidler et al. [6].

The distance between the injection nozzles and the first LPC

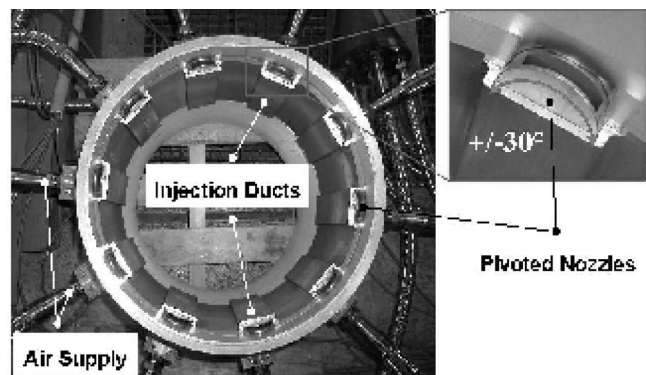


Fig. 3 Air injection system with pivoted nozzles

First nozzle design:
Exit Area 360 mm²
(9 mm x 40 mm)

Enhanced nozzle design:
Exit Area 180 mm²
(5 mm x 36 mm)

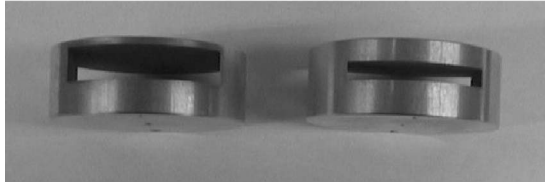


Fig. 4 Comparison of air injection nozzle exit area design

rotor blades corresponds to two mean chord lengths of the blades. This distance allows one to efficiently fight instabilities and their precursors and it also provides sufficient space with regard to mechanical safety aspects. Nevertheless, this arrangement permits the injected air stream to spread somewhat to hit a wider range of the blades' tip region. The results of former investigations by Leinhos et al. [8], also with air recirculation by Scheidler et al. [6], lead to the conclusion that an improved nozzle exit area would lead to better results. Therefore an enhanced air injection nozzle exit area was designed. Compared to the first design the nozzle exit area was reduced significantly. The new designed nozzles were applied for the first time for the investigations of which this paper partially reports about. Figure 4 gives an impression and a comparison of the first and the enhanced nozzle exit area design.

The reduced exit area of the enhanced nozzle design offers an increased injection velocity of the supplied air stream. A discussion about the influence of the injection velocity on the stabilization effects is given in Suder et al. [12]. The air is delivered by an external air supply system, illustrated in Fig. 5, consisting of a screw compressor, a compressed air dryer, storage vessels, a microfilter, and a pressure reducer to adjust the pressure magnitude of the fed air.

The screw compressor delivers pressurized air at a value of 15 bar. Together with the storage quantity of 7500 liters, this external air supply system enables to investigate the restabilizing effects at test conditions which could be kept stable and stationary for a sufficient time. The amount of maximum available injection air arises from the product of the available air volume in the vessels and the difference in pressure head between the stored air and the pressure magnitude adjusted at the pressure reducer. The maximum pressure of the injected air was set to 8 bar. After the pressure reducer the air flows through a flexible tube system, passing a mass flow measurement device. The flexible metal tubes are connected to DDVs. These DDVs ensure the proper amount of delivered air and are guided by the control system. They are a

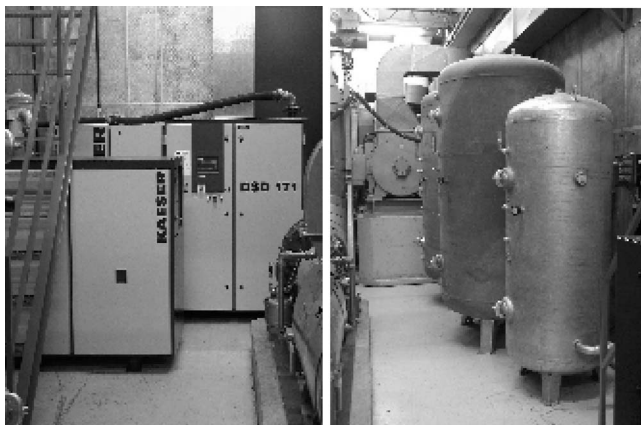


Fig. 5 Screw compressor, air dryer, and storage vessels

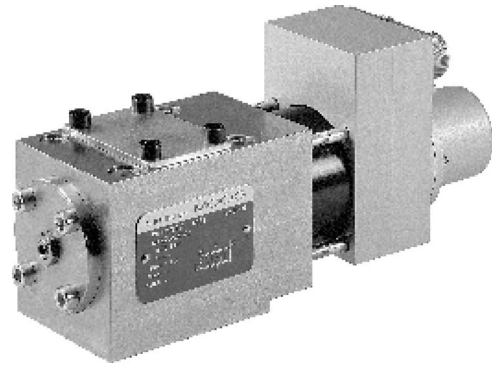


Fig. 6 Direct drive valve by the Moog Company, Germany

derivative of an earlier version by the Moog Company, Germany. Compared to their predecessor, the maximum possible mass flow has been increased by adding a second port and by scaling up the spool diameter. These valves (Fig. 6) dispose of a bandwidth of up to 280 Hz. They can be almost linearly positioned anywhere between fully closed (0%) and fully open (100%). With a supply pressure of 8 bar at ambient temperature, each valve can provide a mass flow maximum of about 130 g/s. Either the injected air flow is rated at a constant value with a predefined opening position of them or, in case the control system is active, the valves receive their input signal by the controller and therefore can react properly on any instabilities and precursors but also on an improvement due to the active stabilization effects obtained by the air injection just done.

The control system is a derivative from a commercial active control system for thermoacoustic instabilities in gas turbines by Hermann, et al. [11]. The system contains all electronics required for signal processing, data transmission for driving and controlling the DDVs.

The controller is fed with five sensor signals from high sample rate pressure transducers (Kulites) located at the LPC inlet plane. These sensor signals are processed within the controller. Details about the processing method can be found in Scheidler et al. [10]. The output signal is supplied to the valve(s) necessary to antagonize the instability phenomenon. This can be either only one valve or a few one on a selective basis or all ten of them, depending on the complexion of the instability. Additionally, the mode of the air injection, a constant air flow or a modulated air flow or a flexible combination of both is guided by the control system, too. While previous investigations in this facility by Scheidler et al. [6] and Leinhos et al. [8] also considered air recirculation, the analyses in this publication focus on controlled active stability measures by injection of air delivered by the external source only. The entire test setup is displayed in Fig. 7.

The test bed equipment also affords one the opportunity to investigate the effects of inlet distortions, as well during instability onset process as during active stability measures as during engine dynamics, for example. Results on these topics are published in Scheidler et al. [6,13] and Leinhos et al. [14].

On the basis of the experimental investigations and results, a numerical model was generated to reproduce the active stabilization effects of controlled air injection. This model predicts the time-dependent pressure level in each of the system modules during the throttling phase of the compression system. It is created to simulate the stable and unstable operation of the engine. For the modeling of unstable processes, the simulation starts always at stable operating conditions. The model consists of a straight duct ahead of the LPC, the two LPC stages and a flow splitter which divides the main flow into the core flow and the bypass flow. Behind the HPC, a volume is affixed to represent the combustion chamber. Since the main object of the model was focused on the compression system and its behavior, the simulation of the HP

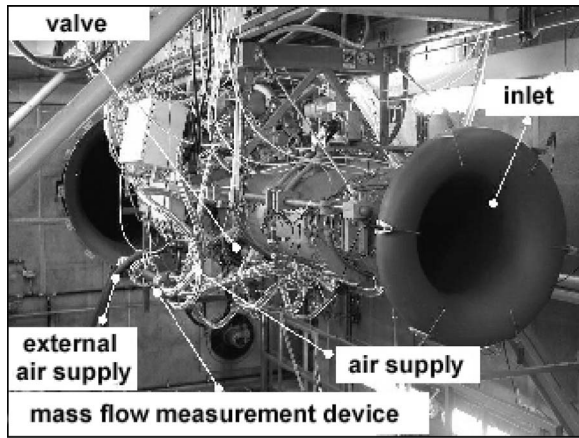


Fig. 7 Engine test setup in air injection configuration

turbine and LP turbine was abandoned to simplify the numerical calculation process. More details about the model, its configuration and setup, its adaptation, and some results gained with it, are discussed in Scheidler et al. [10].

Instrumentation and Data Acquisition. The LARZAC 04 is equipped with two different kinds of instrumentation. Both are assigned to different tasks and exceed the standard instrumentation of an aeroengine on board an aircraft by far. A number of thermocouples, wall static pressure probes, and total pressure probes, connected with standard pressure transducers are installed throughout the engine (Fig. 8). They represent the so-called conventional instrumentation, a low sample rate data collecting technique. In total, 96 channels are allocated to individual parameters. Each of the 96 channels is sampled at 1 kHz for 20 ms, providing

20 values. These were averaged during the next 80 ms. Altogether, this results in an average sampling rate of 10 Hz. The data is digitized with a 16-bit resolution.

Also, the rotor shaft speeds (n), the thrust (F_s), the fuel flow (V_F), the fuel temperature (T_F), and the bypass throttle position (y) are measured. All of the parameters recorded this way afford mass flow calculations and a detailed gas path analysis for steady and transient engine operations. By this means, it is possible to compute operating points, compressor maps, and some performance data. A detailed outline of this kind of instrumentation, its sensor types, and the position of the probes can be found in Höss et al. [9]. The data correction and the gas path analysis procedure applied to derive compressor maps, running lines, and performance data is detailed in Herpel et al. [15].

Besides the just illustrated conventional instrumentation, a special high-frequency instrumentation is applied to the compression system in order to detect relevant pressure fluctuations during instability onset and to identify different types of instabilities.

High-frequency response of the probes is assured by incorporating miniature piezo-resistive Kulite pressure transducers into the front end of the probes. This gives a minimum time lag and damping of the pressure signals during the process of recording. The parameters are sampled at 51.2 kHz, and they are digitized with a 16-bit resolution. For this purpose, a 16-channel VXI input module by Agilent is used. The signals are filtered with a 20 kHz analog low-pass filter before they are digitized and transferred to a storage device within the control computer. Therefore, in total, 14 wall static and freestream total pressure probes are installed at various positions throughout the LPC and the HPC (Fig. 9). A simultaneous instrumentation of both compressors, together with the five wall static pressure sensors circumferentially distributed at each of their inlet planes, enables to observe the interaction between the LPC and the HPC, also during instability onset.

With the five sensors in one plane, spatial disturbances up to the second harmonic can be resolved. For the measurements pre-

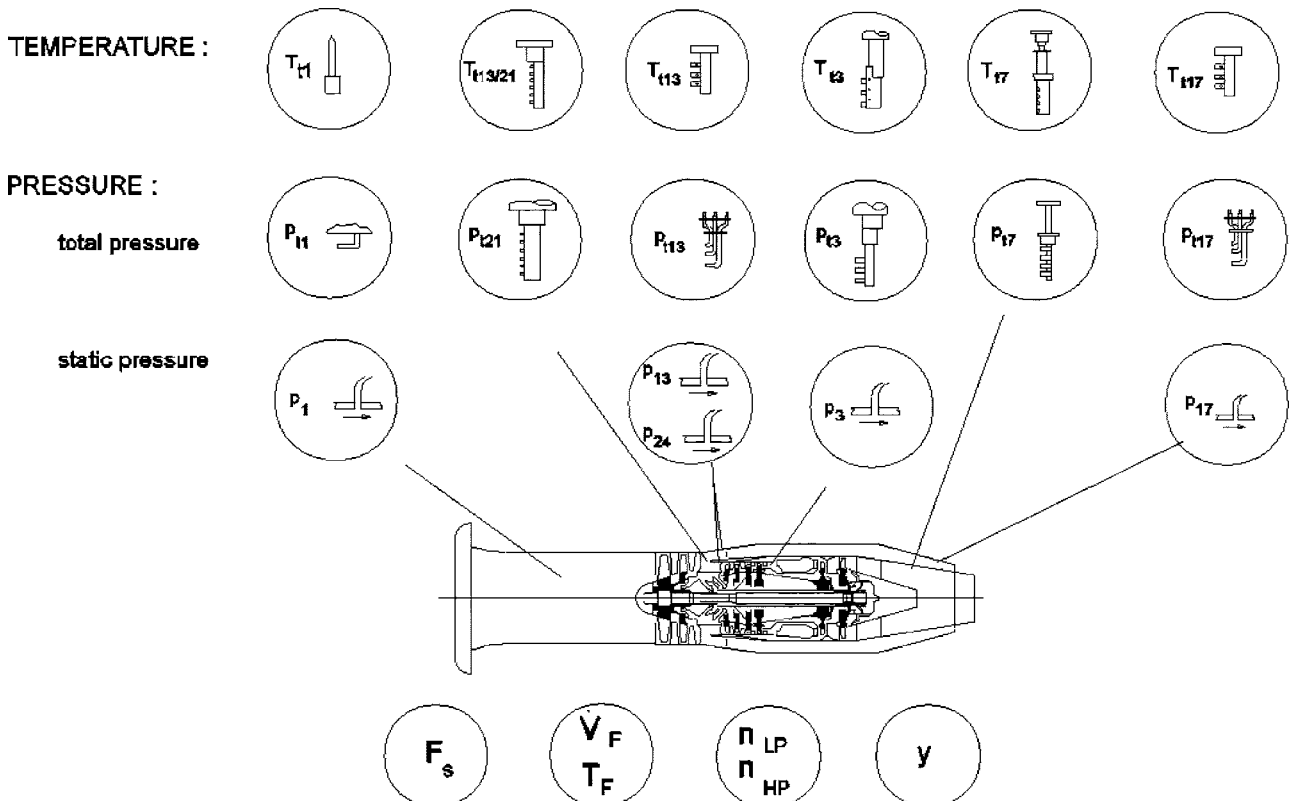


Fig. 8 Conventional low-frequency instrumentation

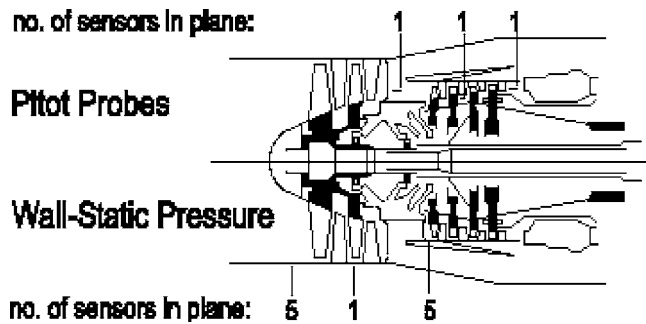


Fig. 9 Position of high-frequency instrumentation

sented in this paper, five wall static pressure probes are installed 7 mm upstream of the first LPC rotor in an equal circumferential distance, at 332 deg (sensor 1), 44 deg (sensor 2), 116 deg (sensor 3), 188 deg (sensor 4), and 260 deg (sensor 5), counting in the direction of rotation of the LPC spool. Due to mechanical constraints caused by accessory components in the entry plane of the HPC, the five wall static sensor probes cannot be positioned in an equal circumferential distance. Hence, they are located at 40 deg, 130 deg, 230 deg, 290 deg, and 339 deg (sensors 8–12), again counting in the direction of rotation of the spool. As displayed in Fig. 8, four more pressure probes are incorporated in different planes of the compression system to encounter the axial extension of pressure fluctuations and the position at which they start and to track their growth and behavior. Another wall static pressure probe is placed in the first LPC stator (sensor 6). The total pressure probes are located each at the LPC exit in front of the splitter casing (sensor 7), in the second-stage stator of the HPC (sensor 13) and at the HPC exit (sensor 14). This one is resistant against high temperatures and is designed to measure pressure values up to 10 bar. More details about this high sample rate instrumentation are described in Höss, et al. [9]. The two remaining channels of the input module of the VXI system were used to track the position signal of one of the high-bandwidth DDVs and to record the actual position of the bypass throttle. This enables one to exactly resolve the time lag between the valve input signal and the time after which the compressor flow is affected by the active stability control intervention. The signal of the bypass nozzle enables one to determine a direct relationship between the throttling rate of the LPC, its corresponding instability, and the effect resulting from the active stability control input.

Experimental Results

This paper is the publication of some new results of the investigations made with the enhanced air injection nozzle design (see details in the Experimental Setup section of this paper). It marks the continuation of the research work done under this topic at earlier studies by Leinhos et al. [5,8] and Scheidler et al. [6], which start as a feasibility study. While in Scheidler et al. [10] the newly designed air injection nozzles have also been used (for the first time) and that publication focuses on the results of an improved rotating stall control (only the speed range from idle up to max. $n_{\theta LPC}=76\%$ was investigated), this survey concentrates on the active stability control at the upper speed band, from $n_{\theta LPC}=78\%$ up to maximum power setting. Additionally, it constitutes the preliminary completion of the investigations quoted above. For comparison purposes, but also to demonstrate the different development of instabilities over the speed bands, the engine behavior and the possibilities of active stability control measures have been analyzed for $n_{\theta LPC}=78\%$, $n_{\theta LPC}=84\%$, and $n_{\theta LPC}=90\%$. In this speed band, from $n_{\theta LPC}=78\%$ up to maximum power setting, a disturbance travelling with rotor speed is respon-

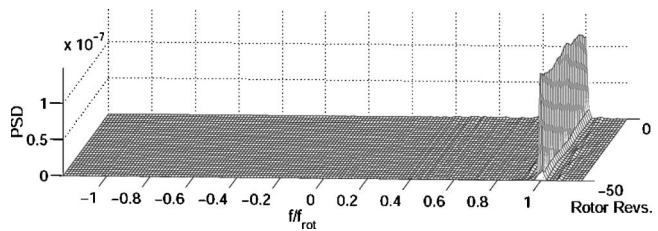


Fig. 10 Disturbance at rotor frequency f_{rot} , $n_{\theta LPC}=78\%$

sible for triggering the instability onset process. Therefore, this paper concentrates on the active stability control measures of this phenomenon.

Stabilization at $n_{\theta LPC}=78\%$. While up to a speed line of $n_{\theta LPC}=76\%$ the LPC creates a rotating stall which influences the HPC and the entire compression system (see Scheidler et al. [10]), caused by a distortion at lower-frequency rates ($\sim f/f_{rot}=0.66$), the spool speed of $n_{\theta LPC}=78\%$ is the first speed line at which the compression system generates a surge as a reaction on one individual or multiple pressure spikes. Investigations have shown that a disturbance rotating with the rotor frequency is responsible for triggering the instability onset process (see Fig. 10). The speed band between $n_{\theta LPC}=76\%$ and $n_{\theta LPC}=78\%$ is a region where the transition between the two different instability onset processes is fluent.

Once this distortion is antagonized and eliminated by a controlled air injection the system recovers to a stable operating condition. Figure 11 reveals the switch-on of the controller, its control input and action and the stabilized condition after about 130 rotor revolutions of successful intervention. A comparison between constant air injection and air injection guided by the control system at the same opening rate of the DDVs (30%) substantiates the advantage of the control system. While at constant air injection, the stable operating line breaks off earlier, the controlled air injection

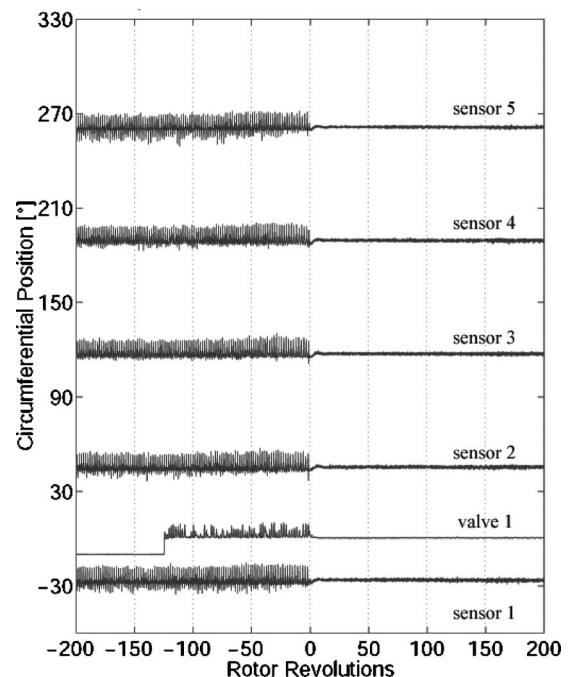


Fig. 11 Time series of sensor signals and valve No. 1 at $n_{\theta LPC}=78\%$

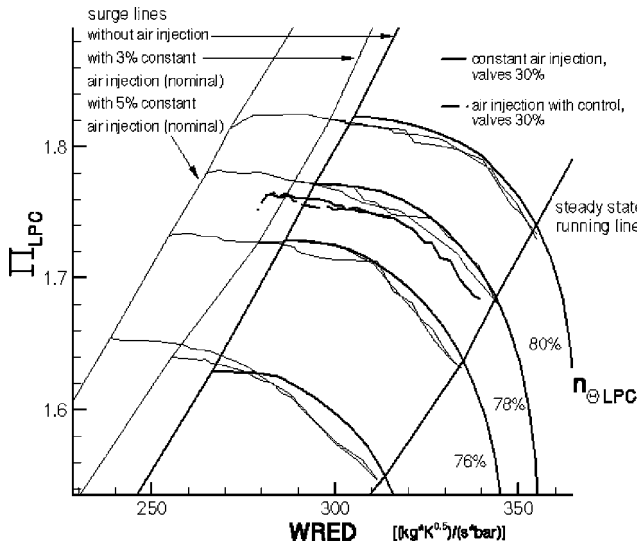


Fig. 12 Comparison of constant and controlled air injection, valves opened 30%, at $n_{\theta LPC}=78\%$

enables a further throttling of the LPC and therewith a wider operating range. At $n_{\theta LPC}=78\%$, this is still of slight appearance but it can be recognized in Fig. 12.

Stabilization at $n_{\theta LPC}=84\%$. The investigation of the stabilization effects for $n_{\theta LPC}=84\%$ was started with an assessment of several opening degrees of the valves at constant air injection conditions. As former examinations have already proved, an increased opening degree of the valves improves the stabilizing input. Additionally, in Fig. 13, the benefit of the enhanced air injection nozzle design is proved. While with the first air injection nozzle generation a valve opening to 50% allowed “only” an extraction of the stable speed line up to the red-colored surge barrier (surge and speed line with 3% constant air injection), the new modified air injection nozzles enable a much wider stable operation at that running line ($n_{\theta LPC}=84\%$, green color). Again, a comparison between constant air injection and air injection guided by the control system at the same opening rate of the DDVs (30%, Fig. 14) reveals a slight difference in the outcome of the stabili-

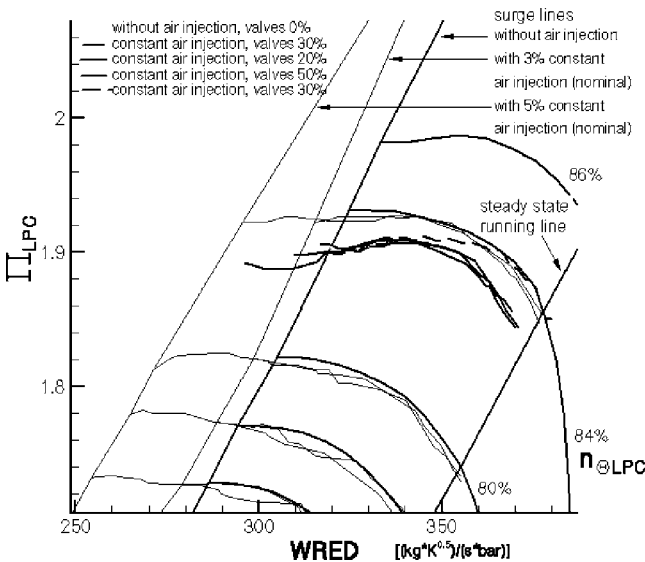


Fig. 13 Several opening degrees of the valves at constant air injection for $n_{\theta LPC}=84\%$

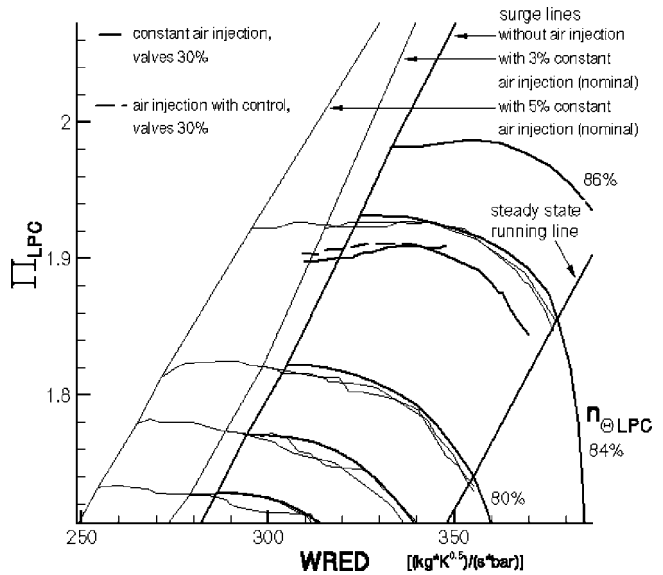


Fig. 14 Comparison of constant and controlled air injection, valves opened 30%, at $n_{\theta LPC}=84\%$

zation. The air injection with control results in light higher values of pressure ratio at the same values of corrected mass flow, also for $n_{\theta LPC}=84\%$, proving the efficiency of the controller.

An analysis of some performance parameters also highlights the positive effects of air injection. As well at unthrottled operation, the influence of air injection increases the total pressure level at the LPC exit significantly (Fig. 15). As a result of this, the performance of the entire turbofan engine arises. The success of the air injection, especially with the control system active, is depicted in Fig. 16. While within one test, the LPC is throttled two times and the pressure value of the LPC drops two times dramatically, connected with a surge occurrence each time, the controlled air injection is in the position to recover the compression system and to restabilize the air flow within it, respectively. This gives good confidence in the effectiveness and the reliability of the applied control system together with the impact of air injection.

Stabilization at $n_{\theta LPC}=90\%$. As for the two lower-speed lines ($n_{\theta LPC}=78\%$, $n_{\theta LPC}=84\%$) and for $n_{\theta LPC}=90\%$, a compressor map was analyzed. The effectiveness and mode of functioning of the air injection guided by the control system appear with a much bigger significance at $n_{\theta LPC}=90\%$, compared to the lower-speed lines, where this effect was less distinctive. A view of Fig. 17 highlights the greater stable operating range achieved when control is active compared to constant air injection, again for the same

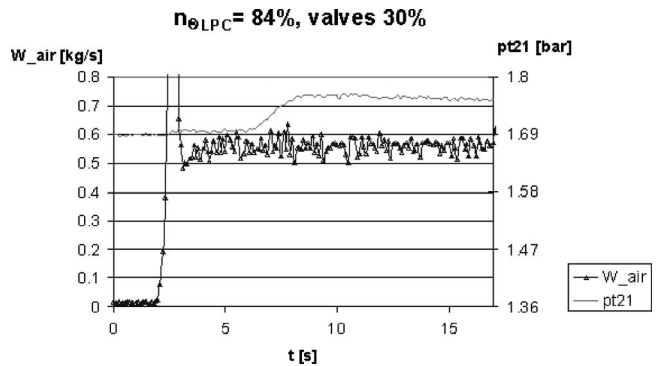


Fig. 15 Stabilizing effect of air injection, also at unthrottled operation at $n_{\theta LPC}=84\%$

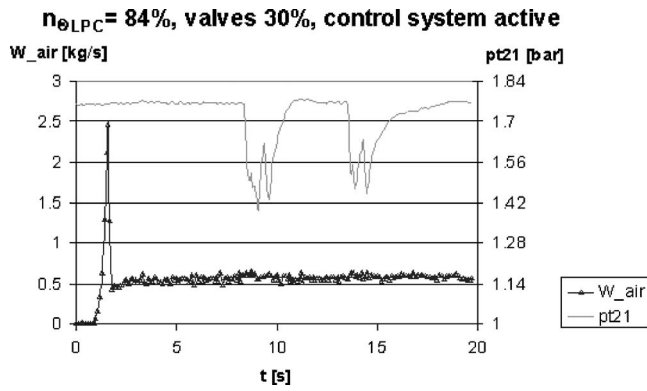


Fig. 16 Restabilization of the LPC after two instability occurrences, at $n_{\theta LPC}=84\%$

opening rate of the valves (30%). This dominant advantage allows one to reduce the amount of air necessary to recover from an unstable operating condition and to keep the system running stable, also at deep throttled conditions. Nevertheless, again the improvement with the enhanced air injection nozzles is also demonstrated, since a valve opening rate of 30% at constant air injection exceeds the speed and surge limit reached with the first air injection nozzle generation for 3% constant air injection, which for an eminent larger opening position of the injection valves was necessary.

As for the spool speed of 84% also for $n_{\theta LPC}=90\%$, a survey of some performance parameters was made. Again, the air injection control system was able to restore the stable operating conditions after a severe instability occurrence. Figure 18 demonstrates the recurrence of the pressure level at the LPC exit after the controlled input of the air injection system. Once stabilized, also at throttled and charged conditions, the system stays stable even if the controlled air injection is switched of (as happened after about 14 s in the displayed test).

To answer open questions and for a deeper understanding of the effects of the controlled air injection, some data from the high-frequency Kulite pressure signals in front of the LPC and of one DDV are analyzed with the spatial Fourier transformation (SFT) and the power spectral density (PSD) of the time series of spatial Fourier coefficients, as applied by Garnier et al. [16] and Tryfoni-

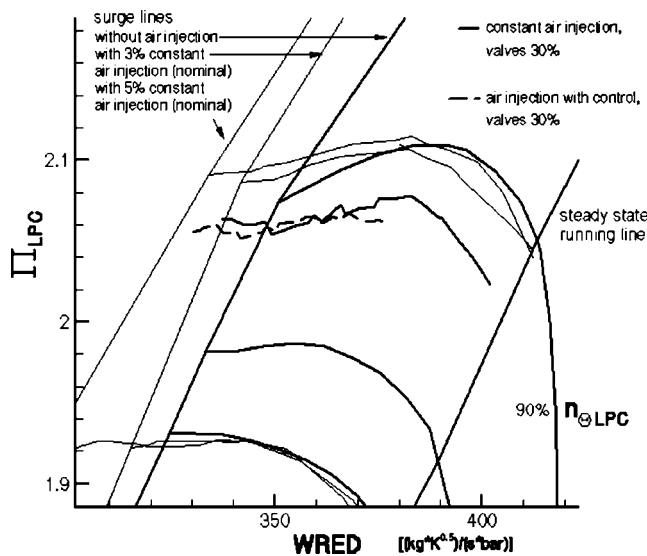


Fig. 17 Comparison of constant and controlled air injection, valves opened 30%, at $n_{\theta LPC}=90\%$

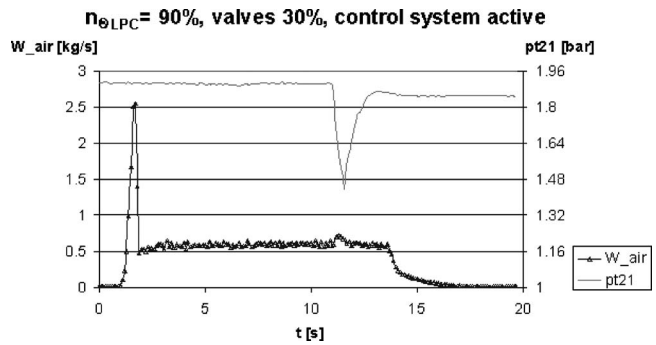


Fig. 18 Restabilization of the LPC after an instability occurrence, at $n_{\theta LPC}=90\%$

dis et al. [17]. Since the described frequency analysis has also been accomplished for the lower speeds $n_{\theta LPC}=78\%$ and $n_{\theta LPC}=84\%$ and the findings were the same or very similar to these of $n_{\theta LPC}=90\%$, respectively. In this publication, only some extracts of the entire fast Fourier transformation (FFT) analysis at $n_{\theta LPC}=90\%$ are presented on an exemplary basis.

Starting from the lapse of the time signals of the sensors in Fig. 19, a detailed analysis of the instability causing disturbances and their damping by the controlled air injection has been performed. In Fig. 19, the controlled action of DDV No. 1 can be tracked. Valve No. 1 is chosen as a representative actuator of all ten DDVs. The valves react directly on the signals coming from the pressure sensors. Starting at the zero point of rotor revolutions, an instability is detected by the control system and an adequate air injection input is generated. After about 190 rotor revolutions, the instability is eliminated and the disturbance is completely damped out, as can be seen in the diagram.

The instability onset process and its progression can be pursued easily in the curves of the circumferential FFT (Fig. 20). The amplitude of the first-harmonic order shows an increasing charac-

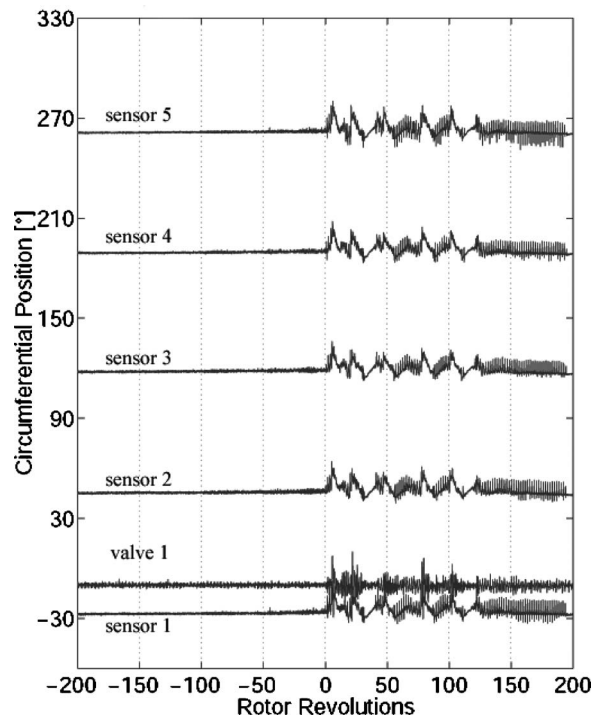


Fig. 19 Time series of sensor signals and valve No. 1 at $n_{\theta LPC}=90\%$

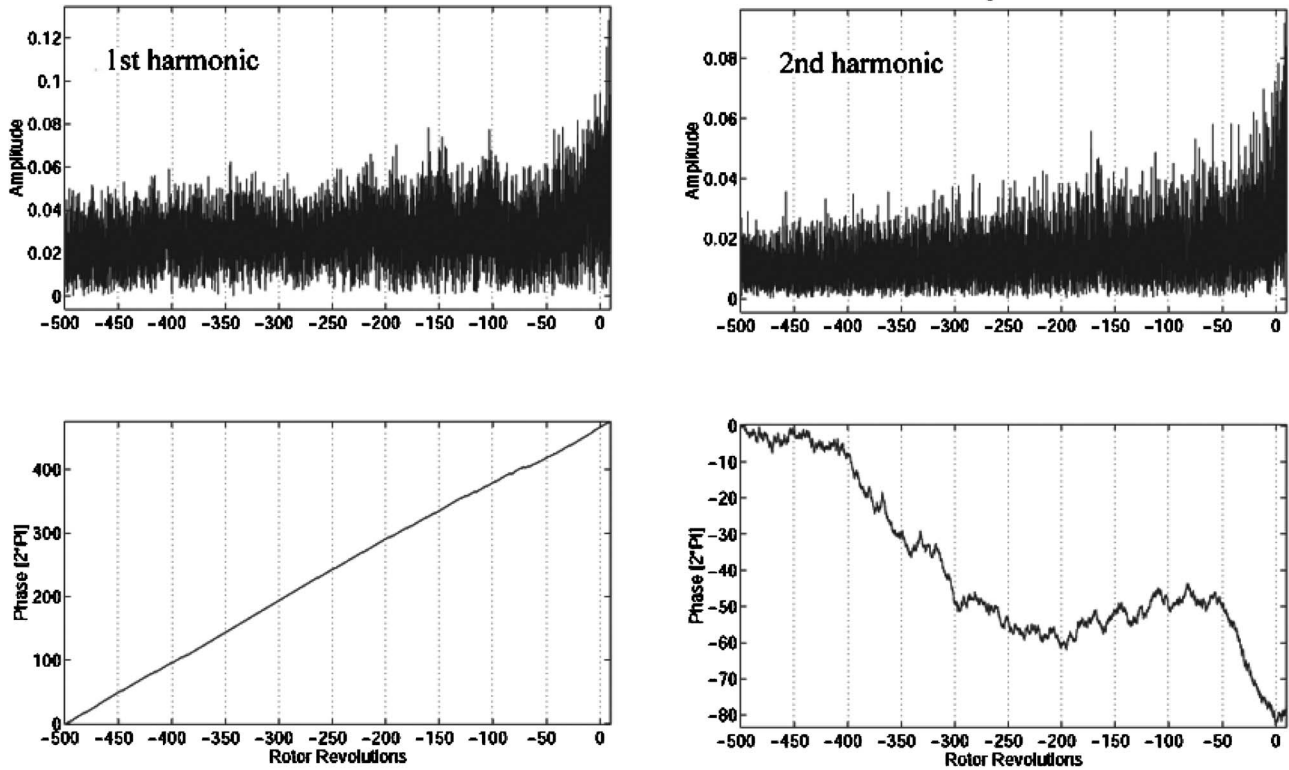


Fig. 20 SFT of the first-harmonic and second-harmonic order for $n_{\theta LPC}=90\%$

teristic with a rising gradient. The corresponding phase runs as an almost ideal linear line. The amplitude of the second-harmonic order shows nearly the same characteristic as the one for the first-harmonic. The phase is uncontinuously falling.

Based on this information, the PSD analysis was drawn. Figure 21 represents the PSD of an growing instability. In the frequency spectrum of the first-harmonic order, only one significant disturbance appears, which is situated exactly at the rotor frequency. In

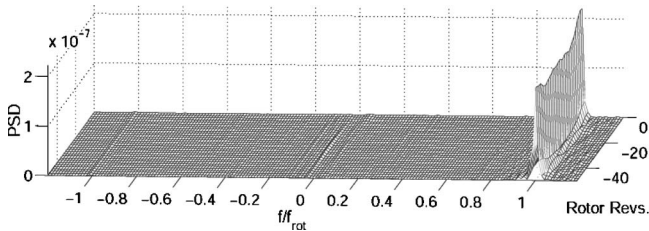


Fig. 21 PSD of the first-harmonic, disturbance at rotor frequency, (f_{rot}), at $n_{\theta LPC}=90\%$

Fig. 22, the successful damping of exactly this disturbance is demonstrated.

Summary and Conclusion

The present experimental study demonstrated the successful damping of the responsible instability onset disturbances by active stability control measures with steered air injection. Specifically, at the higher part-load operation range up to the maximum power setting, the perturbation moving at rotor frequency is successfully eliminated and the engine is restabilized.

While at lower engine speeds, the effectiveness of the controlled active stabilization measures is less distinctive, its profits appear at the higher engine speeds up to maximum power in a significant extent. Since the frequency spectra of the first-harmonic order deliver only one perturbation, which moves at rotor frequency and is responsible for instability onset, the control system can be fed with these signals and it is able to track this perturbation and eliminate it systematically by dedicated air injection. This air injection can happen in a constant manner, pulsed, or any other way, without any regularity.

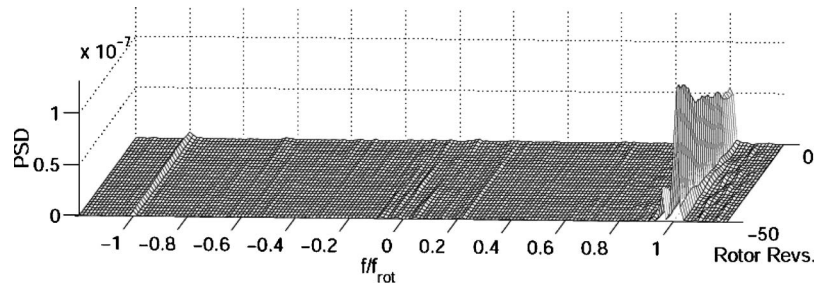


Fig. 22 PSD of the first-harmonic, disturbance at rotor frequency (f_{rot}) damped, at $n_{\theta LPC}=90\%$

Also, the analysis of some performance parameters proves the positive effects of the air injection supplied to the gas turbine engine. The compressor's pressure level can be increased. The controller also demonstrated its capability to recover the engine from a surge if the responsible perturbation is damped by an adequate active stabilization measure with air injection.

Acknowledgment

This study was supported by the Bavarian State Government (Bayerisches Luftfahrtforschungs- und Technologieprogramm), which is gratefully acknowledged. The authors are also indebted to The Moog Company, Germany, for the kind contribution of valve hardware. The cooperation of Dr. Mettenleiter and Dr. Hermann by the IFTA company and the contribution of Dr. Hiller by MTU Aero Engines company are also gratefully acknowledged. The published investigations have been performed at the engine test facility of the Jet Propulsion Institute of the Federal Armed Forces University of Munich, whose head was Professor Leonhard Fottner. He unforeseeably died in 2002. This publication is dedicated to him. His fatherly leadership of the Institute and his benevolent support of research work done under his responsibility will not be forgotten and are gratefully acknowledged.

Nomenclature

- F = thrust (kN)
 f, f_{rot} = frequency, rotor frequency (Hz)
 n = mechanical spool speed (rpm)
 p_s, p_t = static pressure, total pressure (Pa)
 Π, PI = pressure ratio
 $n_{\theta, \text{LPC}}$ = relative corrected spool speed,
 $(n_{\text{LPC}} / \sqrt{T_{t, \text{LPC, inlet}}})_{\text{rel}}$ (%)
 W = mass flow (kg/s)
 W_{RED} = corrected mass flow (kg/s · $\sqrt{\text{K}/\text{bar}}$)

References

- [1] Spakovszky, Z. S., Weigl, H. J., Paduano, J. D., van Schalkwyk, C. M., Suder, K. L., and Bright, M. M., 1999, "Rotating Stall Control In A High-Speed Stage With Inlet Distortion, Part I-Radial Distortion," *Pract. Period. Hazard., Toxic, Radioact. Waste Manage.* **121**, pp. 510–516, "Part II-Circumferential Distortion," *Pract. Period. Hazard., Toxic, Radioact. Waste Manage.*, pp. 517–524.
- [2] Weigl, H. J., Paduano, J. D., Fréchette, A. G., Epstein, A. H., Greitzer, E. M., Bright, M. M., and Strazisar, A. J., 1998, "Active Stabilization of Rotating Stall in a Transonic Single Stage Axial Compressor," *Pract. Period. Hazard., Toxic, Radioact. Waste Manage.* **120**, pp. 625–636.
- [3] Nelson, E. B., Paduano, J. D., and Epstein, A. H., 2000, "Active Stabilization of Surge in an Axi-Centrifugal Turboshaft Engine," *Pract. Period. Hazard., Toxic, Radioact. Waste Manage.* **122**, pp. 485–493.
- [4] Freeman, C., Wilson, A., Day, I. J., and Swinbanks, M. A., 1998, "Experiments in Active Control of Stall on an Aeroengine Gas Turbine," *Pract. Period. Hazard., Toxic, Radioact. Waste Manage.* **120**, pp. 637–647.
- [5] Leinhos, D. C., Scheidler, S., and Fottner, L., 2001, "Active Stabilization of a Low-Pressure Compressor in a Turbofan Engine With Constant Air Injection," *Proc., AIAA-2001-3312*.
- [6] Scheidler, S. G., and Fottner, L., 2003, "Active Stabilization of the Compression System in a Twin-Spool Turbofan Engine at Inlet Distortions," *Proc. XVI International Symposium on Air Breathing Engines (ISABE)*, ISABE-2003-1083.
- [7] Day, I. J., Breuer, T., Escuret, J., Cherrett, W., and Wilson, A., 1999, "Stall Inception and the Prospects for Active Control in Four High Speed Compressors," *Pract. Period. Hazard., Toxic, Radioact. Waste Manage.* **121**, pp. 18–27.
- [8] Leinhos, D. C., Scheidler, S., Fottner, L., Grauer, F., Hermann, J., Mettenleiter, M., and Orthmann, A., 2002, "Experiments in Active Stall Control of a Twin-Spool Turbofan Engine," *ASME Paper No. GT-2002-30002*.
- [9] Höss, B., Leinhos, D. C., and Fottner, L., 2000, "Stall Inception in the Compressor System of a Turbofan Engine," *Pract. Period. Hazard., Toxic, Radioact. Waste Manage.* **122**, pp. 32–44.
- [10] Scheidler, S. G., Mundt, Ch., Mettenleiter, M., Hermann, J., and Hiller, S.-J., 2004, "Active Stability Control of the Compression System in a Twin-Spool Turbofan Engine By Air Injection," *Proc. 10th International Symposium on Transport Phenomenon and Dynamics of Rotating Machinery*, ISROMAC10-2004-073.
- [11] Hermann, J., Orthmann, A., and Hoffmann, S., 1999, "Active Instability Control of Combustion Oscillations in Heavy Duty Gas Turbines," *Proc. 6th International Congress on Sound and Vibration*.
- [12] Suder, K. L., Hathaway, M. D., Thorp, S. A., Strazisar, A. J., and Bright, M. B., 2001, "Compressor Stability Enhancement Using Discrete Tip Injection," *Pract. Period. Hazard., Toxic, Radioact. Waste Manage.* **123**, pp. 14–23.
- [13] Scheidler, S. G., and Fottner, L., 2003, "Operational Characteristics of a Twin-Spool Turbofan Engine at Inlet Distortions With Reduced Surge Margin," *Proc. Symposium on Vehicle Propulsion Integration*, RTO-AVT-100-029, RTO-AVT-100.
- [14] Leinhos, D. C., Schmid, N. R., and Fottner, L., 2001, "The Influence of Transient Inlet Distortions on The Instability Inception of a Low Pressure Compressor in a Turbofan Engine," *Pract. Period. Hazard., Toxic, Radioact. Waste Manage.* **123**, pp. 1–8.
- [15] Herpel, Th., and Fottner, L., 1993, "A System for Monitoring, Measurement, and Analysis of Transient Performance and Stall Phenomena of Gas Turbine Engines," *Proc. ICIASF '93 Record*, IEEE, New York, IEEE Publication 93CH3199-7.
- [16] Garnier, V. H., Epstein, A. H., and Greitzer, E. M., 1992, "Rotating Waves as a Stall Inception Indication in Axial Compressors," *Pract. Period. Hazard., Toxic, Radioact. Waste Manage.* **113**, pp. 290–301.
- [17] Tryfonidis, M., Etchevers, O., Paduano, J. D., Epstein, A. H., and Hendricks, G. J., 1995, "Prestart Behavior of Several High-Speed Compressors," *Pract. Period. Hazard., Toxic, Radioact. Waste Manage.* **117**, pp. 62–80.

Unsteady Aerodynamics of an Aeroengine Double Swirler Lean Premixing Prevaporizing Burner

Edward Canepa
DIMSET—Università di Genova,
I-16145 Genova, Italy
e-mail: edward.canepa@unige.it

Pasquale Di Martino
Avio S.p.A.—R.&D.,
I-80038 Pomigliano d'Arco,
Napoli, Italy
e-mail: pasquale.dimartino@aviogroup.com

Piergiorgio Formosa
e-mail: formosap@libero.it

Marina Ubaldi
e-mail: zunmp@unige.it

Pietro Zunino
e-mail: Pietro.zunino@unige.it

DIMSET—Università di Genova,
I-16145 Genova, Italy

Lean premixing prevaporizing (LPP) burners represent a promising solution for low-emission combustion in aeroengines. Since lean premixed combustion suffers from pressure and heat release fluctuations that can be triggered by unsteady large-scale flow structures, a deep knowledge of flow structures formation mechanisms in complex swirling flows is a necessary step in suppressing combustion instabilities. The present paper describes a detailed investigation of the unsteady aerodynamics of a large-scale model of a double swirler aeroengine LPP burner at isothermal conditions. A three-dimensional (3D) laser Doppler velocimeter and an ensemble-averaging technique have been employed to obtain a detailed time-resolved description of the periodically perturbed flow field at the mixing duct exit and associated Reynolds stress and vorticity distributions. Results show a swirling annular jet with an extended region of reverse flow near to the axis. The flow is dominated by a strong periodic perturbation, which occurs in all the three components of velocity. Radial velocity fluctuations cause important periodic displacement of the jet and the inner separated region in the meridional plane. The flow, as expected, is highly turbulent. The periodic stress components have the same order of magnitude of the Reynolds stress components. As a consequence the flow-mixing process is highly enhanced. Turbulence acts on a large spectrum of fluctuation frequencies, whereas the large-scale motion influences the whole flow field in an ordered way that can be dangerous for stability in reactive conditions. [DOI: 10.1115/1.1924720]

Introduction

Because of the rapid increase of air traffic, which, according to projections, will be doubled by 2020, the reduction of pollutants associated with air traffic has become a primary objective in the design of modern aircraft gas turbine engines.

The trend of the advanced combustion chamber is to increase inlet pressure and temperature in order to increase the efficiency of the engine cycle and reduce fuel consumption. This is the only way to reduce CO₂ emissions, one of the most important causes of the greenhouse effect. Increasing of maximum temperature in the combustor has the drawback of high NO_x emissions that are produced at high temperature.

In conventional combustors the fuel is injected in the primary zone, provoking regions of stoichiometric mixture burning at very high temperature with high NO_x production. One of the most promising ways to reduce emissions is to inject the fuel into premixing ducts, at exit of which the fuel is prevaporized and the mixture is lean. In this case occurrence of stoichiometric zones is avoided and NO_x production is reduced.

Unfortunately lean premixed combustors suffer from serious problems related to combustion instabilities, flashback, and autoignition in the premixing ducts. Self-sustained large-amplitude pressure oscillations may cause severe mechanical damage to the combustion chambers and, in the case of flashback, injectors may even be destroyed.

Because of the technical relevance and scientific challenge of the problem, numerical and experimental efforts have been made in recent years by the industrial and scientific communities in order to identify and understand the physical mechanisms that

govern the instabilities of lean premixed combustors. An extensive research activity is currently being carried out on combustion instabilities in aeroengines in the framework of a European Commission (EC) funded project titled ICLEAC (Instability Control of Low Emission Aeroengine Combustors). The research approach of ICLEAC includes studies on aerothermodynamics of the air-fuel mixing process, thermoacoustics of the combustion chambers, heat release, and flame response to velocity and pressure fluctuations. The present investigation contributes to the research project with detailed experiments on the unsteady aerodynamics of lean premixing prevaporizing (LPP) systems in isothermal conditions. The investigation is focused on the detection of large-scale periodic flow structures that may drive low-frequency combustion instabilities in real LPP geometries.

A special feature of the present experiment is the large scale of the LPP model under investigation, which results in a very high spatial resolution of the measurements. The injector is a double corotating swirler premixing device representative of advanced aeroengine LPP technology.

The great details of the experiment and the simultaneous detection of the three velocity components allow a comprehensive description of the unsteady flow field, which includes Reynolds stress distributions and time-resolved vorticity vectors. The results help to clarify some still unresolved aspects of the unsteady aerodynamics of premixing swirler devices and provide a suitable database for advanced computational fluid dynamics (CFD) codes assessment.

Experimental Facility and Instrumentation

Experimental Setup. The experiments were carried out on a large-scale model (5:1) of an LPP injector for aeroengine applications. The LPP injector was designed by Avio S.p.A with the targets to have a limited length and fixed external and exit diameters in order to be mounted in a preexisting annular combustion chamber. The design was divided into two phases. In the first one,

Contributed by the International Gas Turbine Institute (IGTI) of ASME for publication in the JOURNAL OF ENGINEERING FOR GAS TURBINES AND POWER. Manuscript received October 1, 2003; final manuscript received March 1, 2004. IGTI Review Chair: A. J. Strazisar. Paper presented at the International Gas Turbine and Aeroengine Congress and Exhibition, Vienna, Austria, June 13–17, 2004, Paper No. 2004-GT-54212.



Fig. 1 LPP injector

simple one-dimensional (1D) methods were used to obtain a limited number of premix duct geometries with specified swirler angles and number of blades that assured the desired swirl number. In the second phase the chosen geometries were analyzed by CFD (single-phase and two-phase flow) to assess if the performance (including the vaporization rate) were acceptable. In the design phase also the configuration with contrarotating blades was considered. At the same swirl number the configuration with contrarotating vanes gave a better mixing and evaporation rate because the shear stress at the lip was higher, but the vane angles were too high and discharge coefficients of swirler were drastically reduced.

The LPP injector geometry is currently being utilized in the framework of the EC project ICLEAC for research purposes: assessment of numerical tools (RANS and URANS codes) versus experimental results and investigation of unsteady flow phenomena in swirling flow LPP combustion systems.

The device is a corotating double swirler centripetal injector. The injector is depicted in Fig. 1. The meridional section is shown in Fig. 2. The mixer is composed of two swirlers with radial blades. The internal swirler has 21 blades with an exit angle of 40 deg with respect to the radial direction, the external one has 25 blades with an exit angle of 53 deg. The duct downstream of the blades has been designed by means of circular arcs and constant section areas up to the lip where the flows mix together.

The injector has been designed with the objective to obtain a high degree of prevaporization and air-fuel mixing within the premixing tube. The large initial section of the mixing tube accompanied by a large degree of swirling flow determines a suitable residence time for fuel vaporization. The following strong contraction with flow acceleration maintains a thin boundary layer at the wall, helps preventing flame flashback, and keeps residence time moderate in order to not exceed autoignition limits. The design swirl number is 0.5 according to the definition

$$S = \left[\int_0^{D/2} C_a C_r r^2 dr \right] / \left[(D/2) \int_0^{D/2} C_a^2 r dr \right]$$

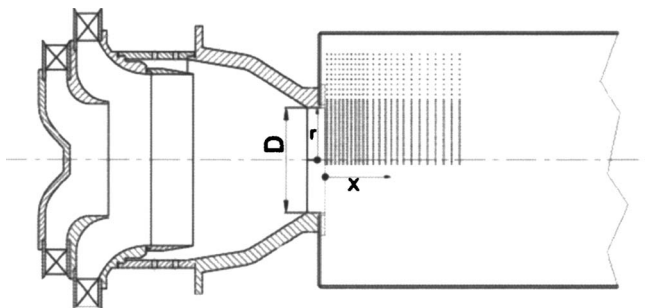


Fig. 2 Measuring-point locations

Table 1 Test conditions

Upstream total pressure	$p_{t1} = 103520$ Pa
Upstream temperature	$T_{t1} = 298$ K
Static pressure downstream	$p_2 = 101300$ Pa
Reynolds number	$Re = 2.6 \times 10^5$

The mass flow rate was split according the effective areas of the swirlers: it was 44% through the internal swirler, 46% through the external one, and 10% through the holes. The holes were not only for cooling. As the flow through them was not swirled, they allowed one to get a higher swirl number in the mixing zone (near the lip) and, therefore, a higher evaporation rate of droplets for a fixed swirl number value.

The experiments were carried out within an atmospheric test rig with isothermal flow. Because of the relevance of aerodynamic phenomena in the subsonic range, real operating conditions were scaled down to atmospheric conditions using the Reynolds similarity.

Different operating conditions have been tested. Extensive investigations have been performed at the maximum power operation. The corresponding Reynolds number based on the mixing tube exit diameter and the mean axial velocity at the exit is 260,000. The corresponding burner pressure drop is 2.2%. Test conditions are summarized in Table 1.

Air is fed to the LPP injector model through the settling chamber of a wind tunnel equipped with a honeycomb and screens to guarantee steady uniform flow at the inlet. The LPP mixing tube terminates in a rectangular single-sector combustor. The mixing tube exit diameter is 104 mm. The 750 mm long flame tube has a square cross section of 250×250 mm² with optical access from three sides.

A CFD analysis was carried out to investigate the effect of the square cross-sectional flame tube instead of the circular one. The shape of the cross section influences the corner recirculation, but no appreciable differences were noted in the central recirculation or in the other measuring points.

The large scale of the test article allows for a high degree of spatial resolution. This is an important prerequisite for a careful investigation of the flow organized structures, which may affect the flow field, and for the generation of databases of experimental results suitable for CFD code assessment.

The experimental domain is shown in Fig. 2. The experimental grid is made of 25 radial traverses from $x/D=0$ to $x/D=1.29$. Each traverse is defined by 40 measuring points ranging from $r/D=0$ to $r/D=1.00$. The total number of measuring points is 1000. Time-averaged axisymmetry was checked in some of the radial traverses and found acceptable.

The main instrumentation consists of a fiber-optic 3D laser-Doppler velocimetry (LDV) system. A hot-wire anemometer was employed for preliminary investigations, for frequency domain unsteady flow analysis, and for the generation of the reference signal for phase-locked LDV data acquisition and data processing. The measurement chain is shown in Fig. 3.

3D LDV System Characteristics. Time-resolved measurements of the three velocity components of the flow at the exit of the LPP burner have been performed by means of a six-beam three-color fiber-optic LDV system with back scatter collection optics (Dantec Fiber Flow). The light source is a 300 mW argon ion laser operating at 514.5 nm (green), 488 nm (blue), and 476.5 nm (dark blue). The LDV setup is obtained combining a 2D and 1D optical probe, both with 310 mm focal length. Typical probe volume dimensions were 90 μ m diam and 1.9 mm length.

In order to obtain coincidence of the two probe volumes, one of

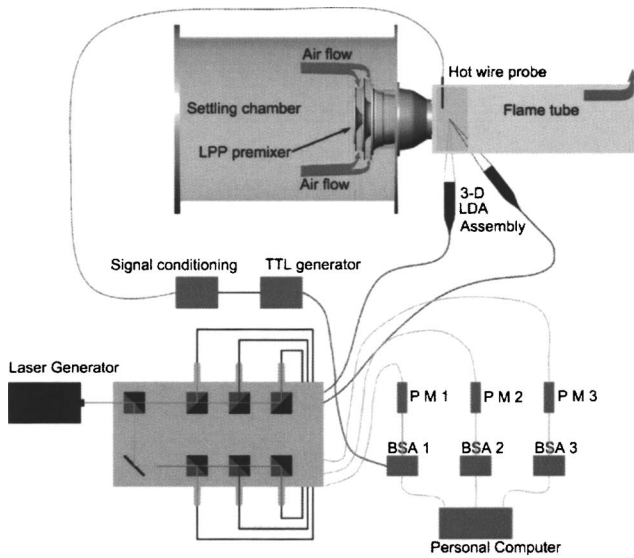


Fig. 3 LDV measurement chain

the optical probes is mounted on a manual micrometric three-axis plus rotation stage. A special viewfinder made of a $120\ \mu\text{m}$ pin-hole and two photodiodes is used to monitor the micrometric movements and verify the volumes coincidence.

The twin-probe assembly is stiffly mounted on a three-axis computer-controlled probe traversing mechanism. The motion is transmitted to the carriages by stepping motors through a pre-loaded ball-screw assembly with a minimum linear translation step of $8\ \mu\text{m}$. A Bragg cell is used to apply a frequency shift ($40\ \text{MHz}$) to one of each pair of beams, allowing one to solve directional ambiguity and reduce angle bias.

The flow is seeded with a $0.5\text{--}2\ \mu\text{m}$ atomized spray of mineral oil injected into the settling chamber. The signal from the photomultipliers were processed by three Burst Spectrum Analyzers (Dantec BSA). Measurements of the three velocity components were made in coincidence mode. Typical values of the data rate were in the range $1000\text{--}5000\ \text{Hz}$. In the recirculating flow regions, the data rate failed down to a few hundred Hertz.

LDV Data Processing. In the present experiment an ensemble-averaging technique suitable for LDV data processing has been applied. A single-sensor hot-wire probe located in the flow field provides a reference signal in phase with the relevant periodic phenomenon. To obtain statistically accurate ensemble averages, a total of 120,000 validated data for each velocity component has been sampled at each measuring position. Instantaneous velocities are sorted into 30 phase bins, each representing a particular phase of the cycle. The hot-wire reference signal was bandpass filtered, and a suitable electronic circuit was used to seek the maximum of the periodic function and generate a transistor-transistor logic (TTL) signal to be used as trigger. The uncertainty in evaluating the reference instant was estimated lower than $1/200$ of a period. Since the phase sampling is based on $1/30$ of period window, the added effect on rms is negligible.

According to the triple decomposition scheme proposed by Reynolds and Hussian [1] for the study of coherent structures in shear flows, a generic velocity component v in a generic position P can be represented as the sum of the time-averaged contribution \bar{v} , the fluctuating component due to the periodic motion $(\tilde{v}-\bar{v})$, and the random fluctuation v'

$$v = \bar{v} + (\tilde{v} - \bar{v}) + v' \quad (1)$$

The time-varying mean velocity component \tilde{v} can be obtained by ensemble averaging the samples

$$\tilde{v}(i) = \frac{1}{K_i} \sum_{k=1}^{K_i} v(i, k) \quad (2)$$

where $i=1, \dots, I$ is the index of the phases into which a perturbation period is subdivided and $k=1, \dots, K_i$ is the index of the samples for each window associated with a particular phase i .

The time-averaged velocity component \bar{v} can be simply determined as

$$\bar{v} = \frac{1}{I} \sum_{i=1}^I \tilde{v}(i) \quad (3)$$

Ensemble-averaged rms, which are proportional to the Reynolds stress normal components, are obtained as

$$\sqrt{\overline{v'^2}(i)} = \sqrt{\frac{1}{(K_i-1)} \sum_{k=1}^{K_i} [v(i, k) - \tilde{v}(i)]^2} \quad (4)$$

The results are collected in a database of three ensemble-averaged velocity components ($\bar{C}_a, \bar{C}_t, \bar{C}_r$) and six ensemble-averaged Reynolds stress components ($\overline{C_a'^2}, \overline{C_t'^2}, \overline{C_r'^2}, \overline{C_a' C_t'}, \overline{C_a' C_r'}, \overline{C_t' C_r'}$). Each component is defined as a function of the spatial coordinates (x, r) and time t (phase) for a total of $25 \times 40 \times 30$ values.

The ensemble-averaged velocity and Reynolds stress components have been further averaged in time to obtain a set of time-averaged components defined on the spatial measuring domain ($\bar{C}_a, \bar{C}_t, \bar{C}_r, \overline{C_a'^2}, \overline{C_t'^2}, \overline{C_r'^2}, \overline{C_a' C_t'}, \overline{C_a' C_r'}, \overline{C_t' C_r'}$).

According to the triple decomposition theory, the time-averaged momentum equation of a flow with relevant periodic fluctuations contains additional terms, analog to the Reynolds stress components, because of the time correlations of the large scale periodic fluctuations. The following six additional stress components have also been evaluated:

$$\overline{(\bar{C}_a - \bar{C}_a)^2}, \overline{(\bar{C}_t - \bar{C}_t)^2}, \overline{(\bar{C}_r - \bar{C}_r)^2}, \overline{(\bar{C}_a - \bar{C}_a)(\bar{C}_t - \bar{C}_t)}, \\ \overline{(\bar{C}_a - \bar{C}_a)(\bar{C}_r - \bar{C}_r)}, \overline{(\bar{C}_t - \bar{C}_t)(\bar{C}_r - \bar{C}_r)}$$

LDV Measurement Accuracy. A comprehensive review of errors in laser-Doppler velocimetry measurements and guidelines to evaluate them are given by Boutier [2] and Strazisar [3]. A specific evaluation of the errors for frequency domain processors is given by Modarress et al. [4].

The error on the instantaneous velocity due to random noise from the photomultiplier tube depends on the background scattered light and processing technique. The burst spectrum analyzer (BSA) can measure with a signal to noise ratio as low as $-5\ \text{dB}$, without apparent increase of the standard deviation [4]. The resolution of the BSA processor depends on the record length of the fast Fourier transform (FFT) and on the background noise. For the present experiment, even in the worst cases, it was below 1% of the mean velocity.

A statistical bias can occur because the arrival times of the measurable particles are not statistically independent on the flow velocity, which brings them into the probe volume. If the velocity is not constant in time, then the resulting nonuniform data sampling causes an error when simple arithmetic averages are performed. To obtain correct time averages, instantaneous data need to be weighted with the residence time of the particles in the measuring volume. However the ensemble-averaging procedure that has been widely adopted in the present experiment, where the samples in each bin are statistically independent because they were collected during different cycles, avoids statistical bias, as observed by Lyn et al. [5].

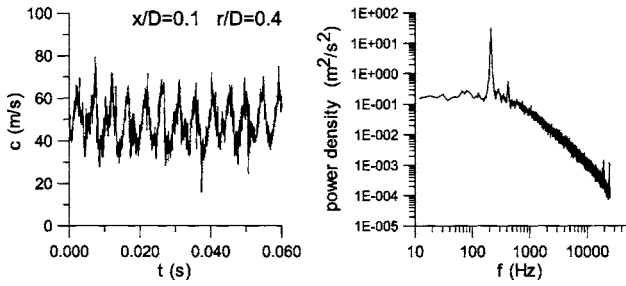


Fig. 4 Velocity time trace and power spectrum

Angle bias occurs when the particle trajectories are not normal to fringe orientation. Moving the fringe pattern in the probe volume by means of the Bragg cell allows one to minimize this error. For the present experiment the angle bias was kept lower than 1% of the mean velocity.

Statistical uncertainty in mean and rms velocities depends on the number of sampled data, turbulence intensity, and confidence level [2]. For the present experiment, considering a typical set of 1000 sampled data, a confidence level of 95% and a local turbulence intensity of 50%, uncertainties of $\pm 3\%$ and $\pm 5\%$ are expected for the mean and rms velocities, respectively.

Preliminary measurements with a two-sensor hot-wire probe were performed in regions of nonreverse flow. The agreement between LDV and hot-wire results was of the order of $\pm 10\%$ for both periodic and turbulent rms results.

Results and Discussion

Spectral Characteristics of the Flow. To evaluate the time-varying flow characteristics, a single-sensor hot-wire probe (DANTEC P11) was operated with a Constant Temperature Anemometer (DANTEC M10).

For each measuring point the CTA signal was low-pass filtered at 25 kHz and sampled at a frequency of 50 kHz. The total number of data taken for measuring point was 135,168. These data were used for evaluating power density spectra with 32 FFT of 8196 data, 50% overlapping.

The hot-wire probe was traversed at several locations within the experimental domain shown in Fig. 2. An example of velocity time traces ($x/D=0.1, r/D=0.4$) and associated power spectral density is shown in Fig. 4. At this point the flow is perturbed by large-amplitude oscillations. From the density spectra a distinct frequency containing energy at about 220 Hz is detectable. The corresponding Strouhal number $St_D=fD/U$ based on mixing tube exit diameter D and averaged exit axial velocity U is 0.58.

Similar frequencies were identified in swirling flows by Chao et al. [6] and Li and Gutmark [7]. They associated these velocity oscillations to the precessing vortex related to the vortex breakdown phenomenon. Similar features are reported also by other authors investigating swirling flow burners [8,9].

In the present investigation the same frequencies have been detected for all the axial traverses investigated and for most radial locations. However the energy peak attenuated toward the axis and was completely suppressed in the region outside the exhaust swirling jet.

To find typical perturbation propagation speeds, two hot-wire probes were displaced in space: in the axial direction (same radial and circumferential positions) and in the circumferential direction (same radial and axial positions). Signals from the two probes were sampled simultaneously and cross-correlated in time.

At $r/D=0.4$ the propagation speed in the axial direction was approximately 20 m/s, which is about one-half the mean axial velocity at the mixing tube exit. This value is fairly close to the axial phase speed evaluated in the experiments of Panda and

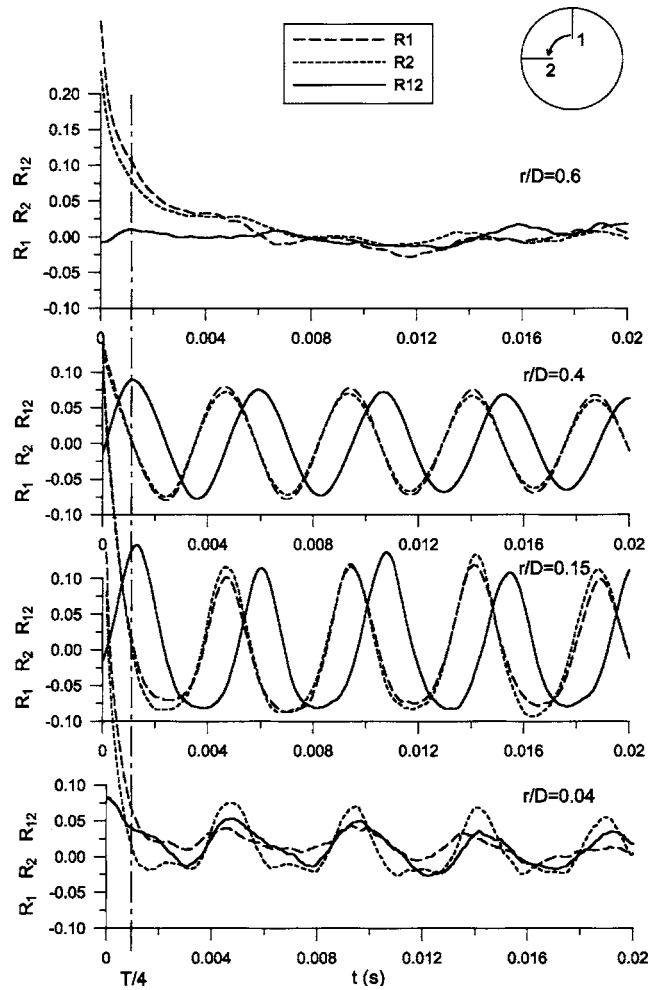


Fig. 5 Auto- and cross-correlations of signals of probes 1 and 2 at the premixer duct outlet ($x/D=0.1$)

McLaughlin [10] on the instabilities of excited swirling jets.

At $x/D=0.1$ the two probes were circumferentially displaced of 90 deg as shown in Fig. 5. Auto- and cross-correlations of the signals according to the following definitions were evaluated at different radial locations:

$$R_{uu} = \lim_{T \rightarrow \infty} \frac{1}{T} \int_0^T u'(t)u'(t + \tau)dt$$

$$R_{uv} = \lim_{T \rightarrow \infty} \frac{1}{T} \int_0^T u'(t)v'(t + \tau)dt$$

where u' and v' are the fluctuating signals from the two hot-wire probes.

Autocorrelation functions show that signal periodicity is conserved for a large radial extension. Periodicity is attenuated near the axis ($r/D=0.04$) and is completely lost outside the jet ($r/D=0.6$). At $r/D=0.4$ the autocorrelation peak for $t=0$ is only slightly larger than the amplitude of the periodic oscillation, indicating a very relevant periodic content compared to the stochastic part of the signal.

It is interesting to observe that from $r/D=0.4$ to $r/D=0.15$ the time lag between the signals of the two probes evaluated by the cross-correlation function peak positions was nearly constant and equal to one-quarter of the fluctuation period $\tau=0.0045$ s. That means the periodic phenomenon observed is a perturbation, which propagates in a circumferential direction at constant rotational

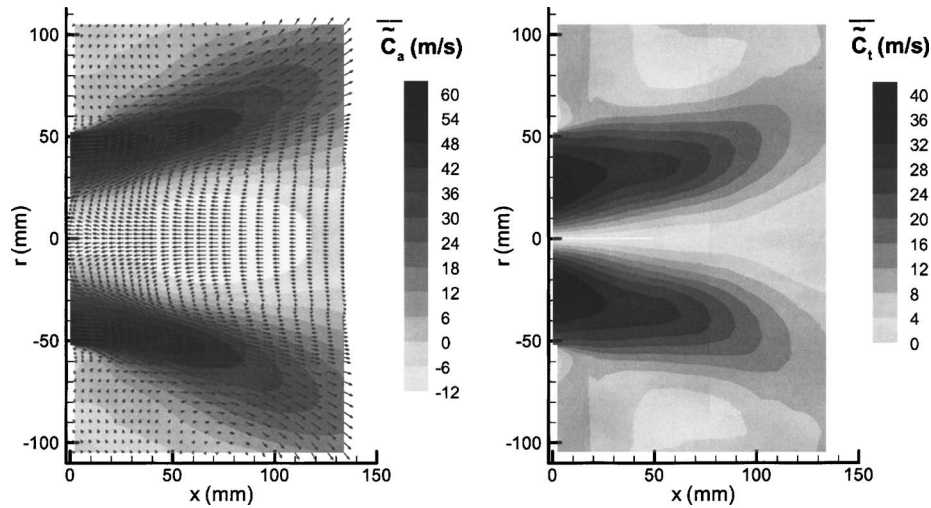


Fig. 6 Time-averaged velocity components distributions

speed, covering one revolution during one period of the velocity fluctuation for all the radial positions. The rotational speed of the perturbation resulted in $\omega = 2\pi/0.0045 = 1382$ rad/s.

This analysis confirms the precessing nature of the fluctuations. It establishes also the rationale for the spatial reconstruction of the periodic flow field from phase-locked velocity distributions detected with a common phase reference signal at different spatial positions.

Time-Averaged Velocity Distributions. A survey of the time-averaged distributions precedes the analysis of the time-varying periodic flow to provide an overall understanding of the flow field. The time-averaged flow field represents the base on which the motion of organized flow structures is superimposed.

Figure 6 (on the left) shows the time-averaged axial velocity distribution in the meridional plane downstream of the mixing tube exit. The vector plot of the meridional velocities is superimposed. The distribution of the axial velocity reveals that the flow is concentrated in an annular jet confined by two recirculation zones. Close to the mixing tube exit the jet has large positive values of axial velocity that gradually decrease with axial coordinate increase. Moving downstream, the jet diverges and the cross section becomes larger. At the same time, because of turbulent mixing, the distribution tends to attenuate nonuniformities.

A moderate corner recirculation zone is present between the external edge of the jet and the flame tube wall, but the most important feature is the existence of an extended recirculation zone near the centerline associated with the large tangential momentum and the sudden jet enlargement in the combustion chamber.

The superimposed vector plot provides an immediate representation of the meridional mean flow field. The sudden jet section enlargement and the two inner and outer separated flow regions are highlighted. Two couples of vortices can be well identified: the first one is located in the outer region of the jet in the initial part of the flame duct, which is typical of abrupt section enlargement; the second couple is situated at the interface between the jet and the inner recirculation bubble at $x=70$ mm. This second couple seems to separate the ringlike flow into two regions: an upstream one characterized by the reverse flow leaving the bubble and a downstream area where the flow enters the bubble moving from outer diameter toward the duct axis.

The distribution of the time-averaged tangential velocity component is shown in Fig. 6 (on the right). The tangential velocity component behaves like a Rankine vortex with free vortex distribution in the external region and solid body rotation near the jet centerline.

Moving downstream the tangential velocities undergo a rapid decay that can be explained by the divergence of the jet and the dissipation of the angular momentum because of the turbulent diffusion action against flow nonuniformities. The decay of the centrifugal force associated to the tangential velocity represents, in swirling flows, the main mechanism of flow separation at the centerline, as explained by Merkle et al. [11]. In the meridional plane the flow is in equilibrium in the radial direction under the centrifugal acceleration associated with the swirl (C_t^2/r) and the centripetal radial pressure gradient $[-(1/\rho)(\partial p/\partial r)]$. The radial equilibrium generates a minimum of pressure on the axis. If the centrifugal force decays in downstream direction, then the radial pressure gradient also decreases and, consequently, the minimum of pressure on the axis attenuates, generating a positive gradient along the axis. If the axial gradient of angular momentum is large (large swirl number and rapid tangential velocity decay), then the flow near the axis separates and a flow recirculation bubble forms.

It is a well-known fact that a recirculation core, obtained by a swirling ringlike jet, is a flow structure suitable for combustion chamber applications acting as a fluid-dynamic flame holder. The recirculation zone must not extend upstream of the premixing duct exit section to avoid flashback phenomena. The profile of mean axial velocity shows that the reverse flow zone interests, at the end of the converging nozzle, a round section with a radius of about 20 mm. That indicates that the recirculating bubble begins within the premixing duct. Once the bubble reaches the flame duct, it enlarges quickly up to a diameter of ~ 40 mm, which remains quite constant through the channel until the end of the investigated zone, where no trend of closure appears.

Time-Averaged rms of Turbulent and Periodic Fluctuations.

Figure 7 shows the distributions in the meridional plane of the time-averaged rms of turbulent and periodic fluctuations.

The $\overline{\text{rms}}(C'_a)$ distribution indicates that large turbulent fluctuations are placed at the border between the reverse flow zone and the swirling jet, and maximum values are located in later axial positions (from $x=40$ to $x=130$ mm). On the other hand, the $\overline{\text{rms}}(\tilde{C}_a - \bar{C}_a)$ distribution shows that the intensity of periodic fluctuations in the flow is strong in a region very close to the inlet section and decreases quickly in axial direction. Downstream $x=100$ mm the periodic feature is no longer significant. In this zone the turbulent fluctuations increase and reach the maximum. On the axis, within the reverse flow internal core, both $\overline{\text{rms}}(C'_a)$ and $\overline{\text{rms}}(\tilde{C}_a - \bar{C}_a)$ values are low.

The $\overline{\text{rms}}(C'_r)$ has the same order of magnitude as the mean

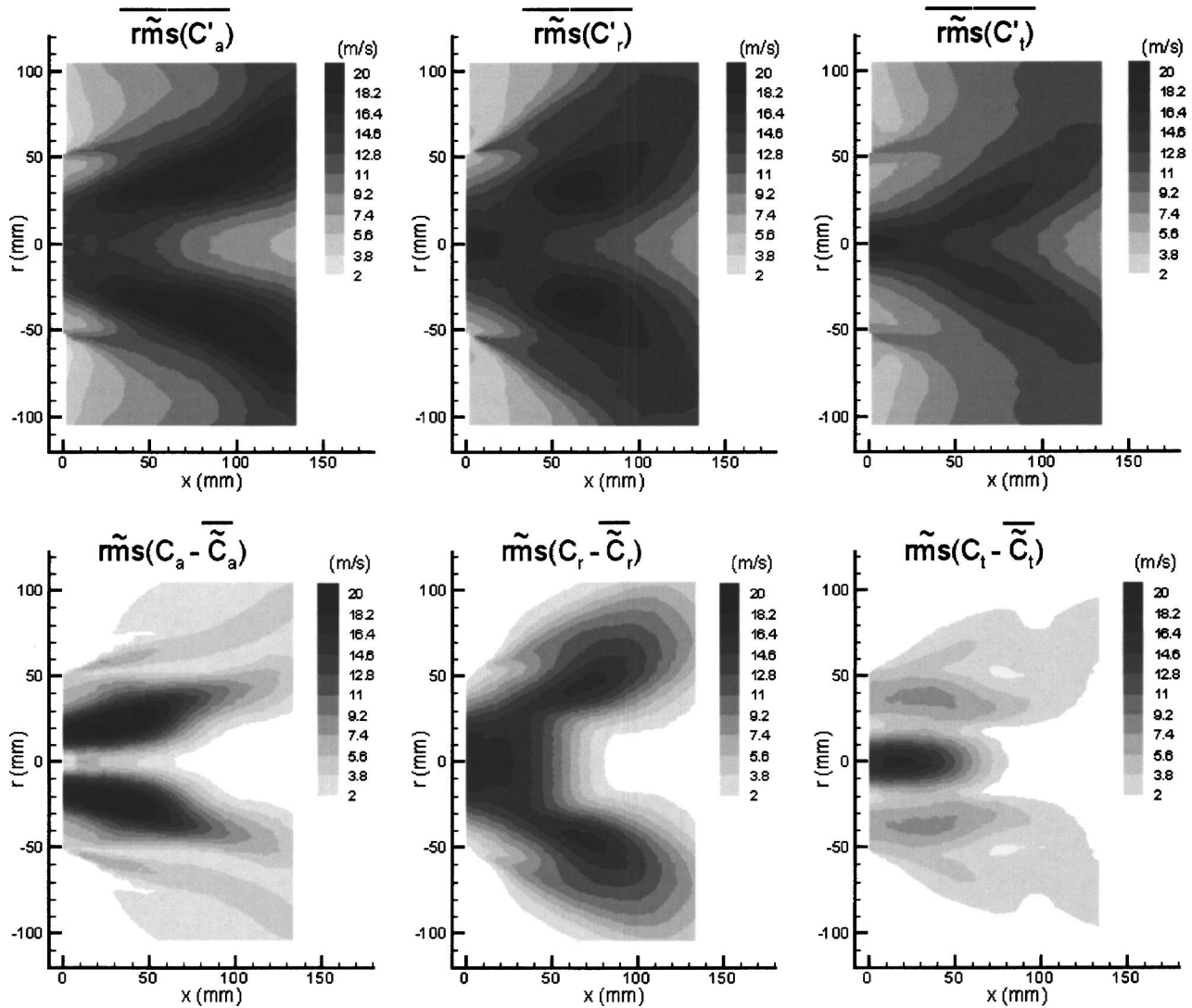


Fig. 7 Time-averaged rms of turbulent and periodic fluctuations

radial velocity component. Two symmetrical maxima for $x = 70$ mm and $r = 30$ mm are present. Also in the same region, $\widetilde{\text{rms}}(\bar{C}_r - \bar{C}_r)$ is large. The general behavior of $\widetilde{\text{rms}}(\bar{C}_r - \bar{C}_r)$ indicates that the strongest periodic fluctuations are localized near the axis at the premix duct exit. Moving downstream, this periodic unsteadiness remains high on a conical region extending up to $x = 100$ mm and $r = 70$ mm.

Both periodic and random fluctuations of C_t show high intensity near to the axis, especially in the sections near the mixing duct exit. The zone of solid body rotation distribution is located here, where the mean tangential velocity undergoes the maximum radial gradient, decreasing to zero on the centerline.

Concerning intensity of turbulent and periodic fluctuations, the axial components are by far the largest, whereas the tangential ones are the lowest.

Time-Averaged Turbulent and Periodic Shear Stresses.

Time-averaged turbulent and periodic shear stresses have been evaluated according to the definitions reported in the data-processing section. A qualitative analysis of the distributions can be attempted, making reference to the eddy viscosity concept. In the present paper only the $\widetilde{C'_a C'_r}$ component is considered (Fig. 8)

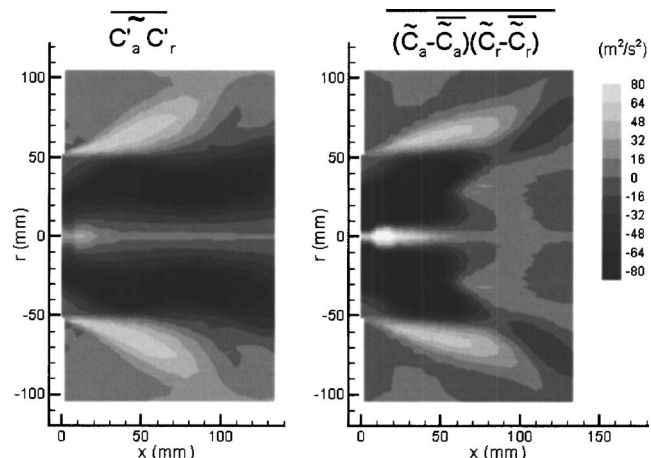


Fig. 8 Time-averaged turbulent and periodic shear stresses

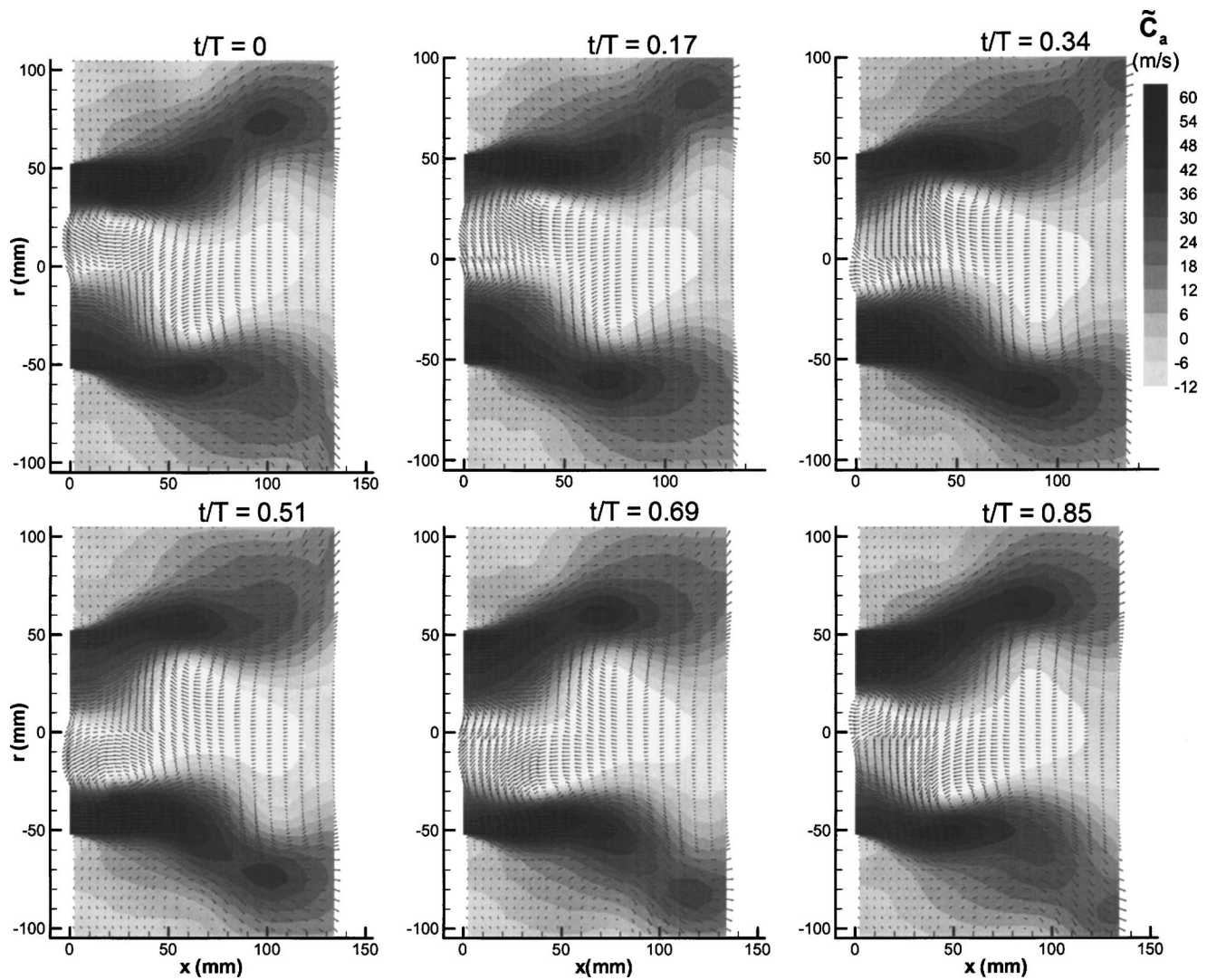


Fig. 9 Vector plots superimposed to ensemble-averaged axial velocity in the meridional plane

$$\tau_{ar} = \tau_{ra} = \overline{\rho C'_a C'_r} = -\mu_T \left[\frac{\partial \bar{C}_a}{\partial r} + \frac{\partial \bar{C}_r}{\partial x} \right]$$

Assuming that streamwise variations ($\partial/\partial x$) are smaller than radial variations ($\partial/\partial r$), a simplified relationship for τ_{ar} can be obtained $\tau_{ar} \cong -\mu_T [\partial \bar{C}_a / \partial r]$.

Looking at the radial variation of the axial velocity components (Fig. 6), one can observe an initial positive radial gradient of the velocity near the axis that is followed in the external part of the annular jet by a negative velocity gradient. This distribution explains the alternating of negative and positive variations of this shear stress component in radial direction.

The $\overline{C'_a C'_r}$ term represents the axial momentum transfer in radial direction. Its effect on the axial velocity distribution can be understood, making reference to the turbulent diffusion term in the axial momentum equation, the most significant contribution should, in fact, come from the term $-(1/r)[\partial(r\tau_{ra})/\partial r]$. The term can be evaluated taking the radial gradient of the $\overline{C'_a C'_r}$ distribution (Fig. 8). Beginning from the axis outward, initially negative gradients result in positive axial momentum transfer to the flow near the axis, then positive radial gradients result in negative axial momentum transfer in the region of the largest jet axial velocity. Finally, negative radial gradients correspond to a positive axial

momentum transfer to the peripheral region of the jet. Therefore $\overline{C'_a C'_r}$ acts to make uniform the axial flow distribution. The periodic stress component has the same order of magnitude of the Reynolds stress component, and the distributions are very similar. Therefore both terms act in a similar way, and the jet mixing is highly enhanced. However, while turbulence acts with a large spectrum of fluctuation frequencies, the large-scale motion influences the whole flow field in an ordered way, which can be dangerous for stability in reactive conditions.

Time Evolution of Ensemble-Averaged Quantities. Figure 9 shows the axial velocity component distribution in the meridional plane during six sequential phases within the period of the perturbation. Superimposed is the vector plot of meridional velocity.

Considering the axial velocity component at the nondimensional time $t/T=0$, an intense velocity spot (~ 60 m/s) is placed at the beginning of the investigated area in the upper part of the flow field, near the outer radius of the converging nozzle of the premixing duct. Increasing the t/T parameter, the spot moves toward larger diameters and, proceeding downstream, progressively reduces its intensity. For $t/T=0.51$ a new spot arises in the same initial section, but in the opposite part of the flow field, behaving in the same way of the first one, and therefore defining an evident periodic pattern with a spot release every half period. This veloc-

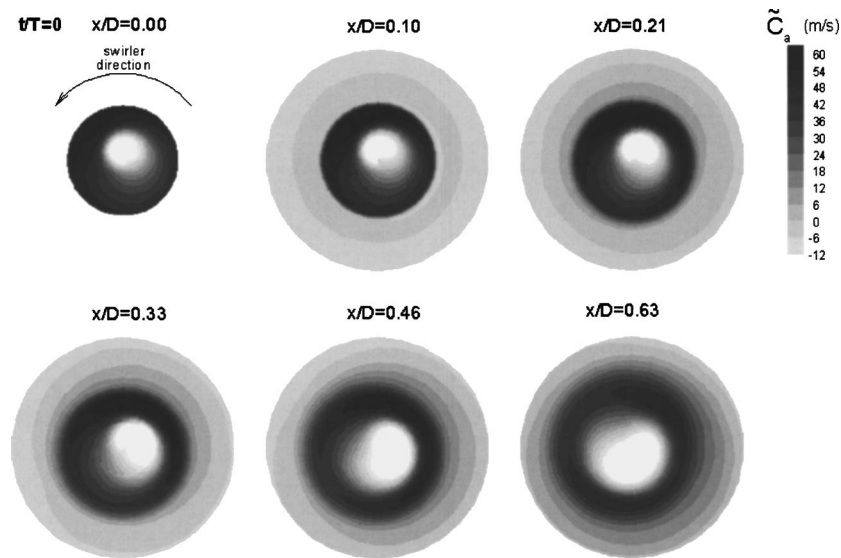


Fig. 10 Instantaneous distribution of ensemble-averaged axial velocity in cross-sectional planes

ity distribution is consistent with a rotating spiral flow structure, whose intersection with the meridional plane is a high axial velocity spot that appears alternatively in the upper and in the lower part of the duct and, proceeding downstream, moves to increasing diameters.

Another relevant feature is that the recirculation bubble loses the axisymmetric time-averaged configuration, and its deformation is strongly connected with high-velocity spots in the outer flow. The region nearby the axis is affected by large oscillations in velocity: during the period, for a radius between $r=20$ mm and $r=30$ mm, the axial velocity fluctuates from a maximum of around 30 m/s to a minimum of 12 m/s in the reverse direction.

The vector plots point out the presence of large eddies located at the border between the jet and the inner reverse flow zone. For instance, at the nondimensional time $t/T=0$, three major structures are clearly recognizable; they are located at about $x=30$ mm and $r=25$ mm, $x=65$ mm and $r=-30$ mm, and $x=105$ mm and $r=40$ mm. The two eddies in the upper region of the channel are rotating clockwise, the one in the lower half plane is rotating counterclockwise. This peculiar configuration can be explained by the presence of a spiral vortex core, whose winding cut by the meridional plane appears as a sequence of vortex cores. When t/T increases, the eddies move downstream. For $t/T=0.34$ one of the two upper eddies has already left the investigated area, at $t/T=0.51$ the general flow structure is similar to the one showed in the distribution at $t/T=0$, but simply 180 deg turned around the centerline and the same occurs for next phases.

Another important feature pointed out by the time sequence of vector plots of Fig. 9 is the close connection between the asymmetry of the inner separation bubble and the location of the spiral vortex cores. The presence of the vortex core determines a local outward radial displacement of the separated bubble contour, which gives rise to radial oscillations of the separated region and, consequently, also of the surrounding jet.

Ensemble-Averaged Axial Velocity Distributions in Cross-Sectional Planes. Figure 10 shows the ensemble-averaged axial velocity distributions at a fixed time instant for six different cross sections located in the first part of the investigated region, i.e., in nondimensional coordinates between $x/D=0$ and $x/D=0.63$. The distributions in cross-sectional planes have been derived from the time-resolved ensemble-averaged velocity components considering that the circumferential coordinate and time are directly correlated because of the rigid rotation of perturbation, as demon-

strated by the cross correlation analysis (Fig. 5).

Moving downstream, the inner recirculation bubble enlarges, whereas the annular jet moves toward increasing diameters and the external recirculation zone observable in the initial sections disappears.

Furthermore, the circumferential distribution of the axial component in the annular jet shows a high-velocity spot, which, moving through the six sections, spreads up and reduces its intensity. The spot's axial evolution allows one to determine what the spiral winding enveloping sense is. By following the circumferential displacement of the high-velocity core in the six sections, it is possible to find that the helix is formed by windings whose direction is clockwise and, therefore, opposite to the main flow rotation. Also the central recirculating bubble is not fixed with respect to the centerline of the exhaust duct, showing an oscillation strictly connected with the azimuthal motion of the helix.

Vorticity. Thanks to the fine spatial resolution of measurements, the time-varying vorticity was numerically evaluated directly from the curl of the ensemble-averaged velocity components

$$\tilde{\Omega}_t = \frac{\partial \tilde{C}_r}{\partial x} - \frac{\partial \tilde{C}_a}{\partial r}$$

$$\tilde{\Omega}_a = \frac{1}{r} \frac{\partial}{\partial r} (r \tilde{C}_t) - \frac{1}{r} \frac{\partial \tilde{C}_r}{\partial \vartheta}$$

$$\tilde{\Omega}_r = \frac{1}{r} \frac{\partial \tilde{C}_a}{\partial \vartheta} - \frac{\partial \tilde{C}_t}{\partial x}$$

Tangential Vorticity. The time evolution of the tangential component of the vorticity of the time-varying flow field, depicted on the meridional plane, is shown in Fig. 11. The meridional plane is approximately divided in two concentric regions of positive and negative vorticity. The dividing surface is not axisymmetric and changes with time. The negative vorticity in the inner region is associated with the shear layer existing between jet and separated flow zone. The positive vorticity in the external region is associated with the shear layer between jet and quiescent external flow.

Vorticity associated with the spiral vortex is organized in nuclei of large negative values. They are shed at the mixing tube exit, since the forward stagnation point of the inner recirculation zone

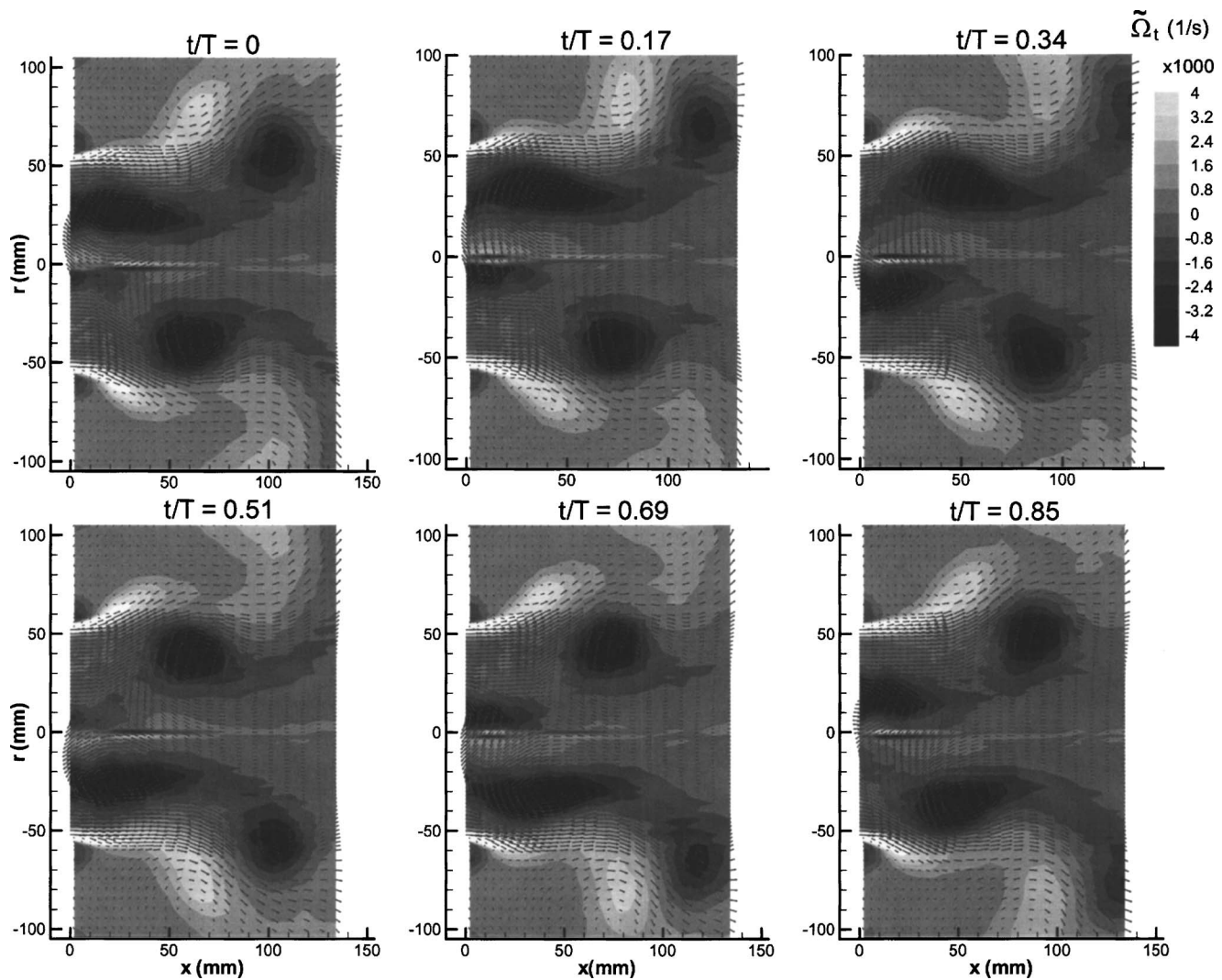


Fig. 11 Time evolution of ensemble-averaged tangential vorticity in the meridional plane

is internal to the duct and the spiral vortex is expected to originate (breakdown point) from the centerline near to the stagnation point, as demonstrated in the experiment of Brücker [12].

In practice the positive vorticity annulus seems to be more stable in time, whereas the negative vorticity starts near the axis (see, for instance, $t/T=0.69$), moves progressively outward ($t/T=0.85$, $t/T=0.0$, $t/T=0.17$), and at a certain position ($t/T=0.34$, $t/T=0.51$) it interacts and “cuts” the positive vorticity into organized loops.

The vorticity peak values are of the order of 4000 s^{-1} , a value that is one order of magnitude larger than the reference vorticity based on the maximum tangential velocity and the mixing tube radius. The vorticity nuclei move downstream with a velocity that can be calculated from the axial distance (90 mm) traveled in one period ($T=1/f=1/220 \text{ s}$). This propagation velocity results in 20 m/s, which is approximately half of the mean axial velocity of the jet and it is equal to the axial propagation speed previously evaluated from the cross-correlation of the hot-wire signals.

Axial Vorticity. The distributions of the axial vorticity in the cross-sectional planes, all represented at $t/T=0$, are shown in Fig. 12. The axial vorticity is structured in a positive nucleus near the center and an external annulus of negative values. The pattern is not axisymmetric, but displays a clear eccentricity, and rotates in clockwise direction when the axial distance of the plane from

the mixing tube exit is increased.

Basically, the axial vorticity distribution results from the swirling flow rotating counterclockwise with positive tangential velocity C_t . The inner positive vorticity is associated with the forced vortex distribution (C_t increasing with radius), while the external negative annulus is due to the external free vortex distribution (C_t decreasing with radius). The asymmetry is due to the periodic perturbation of the radial distribution of C_t that modifies the free-vortex and forced-vortex repartition. The radial displacement of zero tangential velocity determines the occurrence of sporadic conditions of negative swirling flow near the axis.

The clockwise rotation of eccentricity confirms that the sense of winding of the spiral is opposite to the mean swirling flow. Some experimental results for spiral breakdown reported by Lucca-Negro and O’Doherty [13] indicate that the sense of winding of spiral is the same as that of the mean flow, whereas other experiments indicate the sense of windings opposite to the mean flow. Different explanations for this discrepancy are discussed in [13], but the problem is still not understood.

Conclusions

The unsteady nonreacting aerodynamics of the large-scale model of a LPP injector has been investigated by means of constant temperature anemometry and 3D laser-Doppler velocimetry.

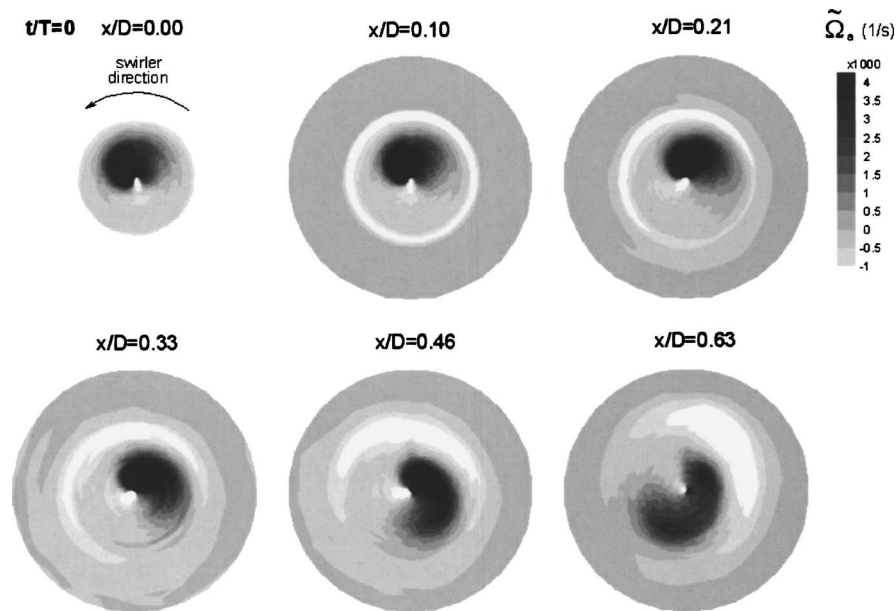


Fig. 12 Instantaneous distribution of ensemble-averaged axial vorticity in cross-sectional planes

Hot-wire probes provided the spectral characteristics of the unsteady flow. A well-defined high-energy periodic velocity perturbation was found to affect the swirling flow issued by the injector. Cross-correlation of the signals demonstrated that the perturbation rotates with constant angular speed and propagates in a downstream direction at half the flow mean axial velocity.

Phase-locked simultaneous 3D LDV velocity measurements provided the time evolution of the 3D flow field and time-dependent Reynolds stress distributions. High resolution in space of the measurements allowed direct evaluation of the time-dependent vorticity field.

Complementary analysis of ensemble-averaged velocity, turbulence, and vorticity fields provided the basis for the physical explanation of the time-dependent aerodynamics of the injector. The flow is dominated by a vortex breakdown phenomenon, which results in a complex flow configuration. An external annular jet and an extended reverse flow inner region oscillate because of the interaction with a precessing spiral vortex developing at the interface between jet and separated bubble.

The time-resolved vorticity field demonstrated that the spiral vortex originates at the centerline within the mixing tube and propagates downstream in axial and radial directions with a spiral winding in a sense opposite to the mean swirling flow.

Turbulence is extremely large, and the periodic stresses have the same magnitude of the turbulent stresses. As a consequence, the flow-mixing process is strongly enhanced and flow nonuniformities decay rapidly. Unfortunately, while turbulence acts through a large spectrum of fluctuation frequencies, the large-scale organized motion influences the whole flow in an ordered way, which may be dangerous for stability in reacting conditions.

Means for attenuation of aerodynamic instability through modifications of swirler radial distribution are presently under investigation. Future work will focus on the mutual interaction between the fuel spray and the unsteady air flow, since this mechanism is expected to have significant influence on burner aerodynamic instabilities.

Acknowledgment

The authors gratefully acknowledge the financial support of the European Commission as part of the GROWTH program, research project ICLEAC "Instability Control of Low Emission Aero-engine Combustors," Contract No. G4RD-CT2000-00215.

Nomenclature

C	= velocity
D	= mixing tube exit diameter
f	= frequency
p	= static pressure
r	= radial coordinate
R_1, R_2	= autocorrelation of signal 1 or 2
R_{12}	= crosscorrelation of signals 1 and 2
t	= time
T	= period
x	= axial coordinate at the mixing tube exit
ρ	= density
Ω	= vorticity

Subscripts

a	= in the axial direction
r	= in the radial direction
t	= in the tangential direction

Superscripts and Overbars

'	= fluctuating component
—	= time averaged
~	= ensemble averaged

References

- [1] Reynolds, W. C., and Hussain, A. K., 1972, "The Mechanics of an Organized Wave in Turbulent Shear Flow, Part 3: Theoretical Models and Comparisons with Experiments," *J. Fluid Mech.*, **54**(2), pp. 263–288.
- [2] Boutier, A., 1991, "Accuracy of Laser Velocimetry," Lecture Series 1991-05, VKI, Brussels.
- [3] Strazisar, T., 1986, "Laser Anemometry in Compressors and Turbines," ASME Lecture on Fluid Dynamics of Turbomachinery.
- [4] Modarress, D., Tan, H., and Nakayama, A., 1988, "Evaluation of Signal Processing Techniques in Laser Anemometry," *Proc. of Fourth Int. Symp. on Application of Laser Anemometry to Fluid Dynamics*, Instituto Superior Técnico, Lisbon, paper 1.20.
- [5] Lyn, D. A., Einav, S., Rodi, W., and Park, J.-H., 1995, "A Laser Doppler Velocimetry Study of Ensemble-Averaged Characteristics of the Turbulent Near Wake of a Square Cylinder," *J. Fluid Mech.*, **304**, pp. 285–319.
- [6] Chao, Y., Leu, J., and Hung, Y., 1991, "Downstream Boundary Effects on the Spectral Characteristics of a Swirling Flow Field," *Exp. Fluids*, **10**, pp. 341–348.
- [7] Li, G., and Gutmark, E., 2003, "Geometry Effects on the Flow Field and the Spectral Characteristics of a Triple Annular Swirler," ASME Paper No. GT2003-38799.
- [8] Schildmacher, K., Kock, R., Witting, S., Krebs, W., and Hoffman, S., 2000,

- "Experimental Investigation of the Temporal Air-Fuel Mixing Fluctuations and Cold Flow Instabilities of a Premixing Gas Turbine Burner," ASME Paper No. 2000-GT-0084.
- [9] Carrotte, J., and Batchelor-Wylam, C., 2003, "Characterization of the Instantaneous Velocity and Mixture Field Issuing from a Lean-Premixed Module (LPM)," ASME Paper No. GT2003-38663.
- [10] Panda, J., and McLaughlin, D. K., 1994, "Experiments on the Instabilities of a Swirling Jet," *Phys. Fluids*, **6**(1), pp. 263–276.
- [11] Merkle, K., Büchner, H., Zarzalis, N., and Sara, O. N., 2003, "Influence of Co and Counter Swirl on Lean Stability Limits of an Airblast Nozzle," ASME Paper No. GT-2003-38004.
- [12] Brücker, C., 1993, "Study of Vortex Breakdown by Particle Tracking Velocimetry (PTV), Part 2: Spiral-Type Vortex Breakdown," *Exp. Fluids*, **14**, pp. 133–139.
- [13] Lucca-Negro, O., and O'Doherty, T., 2001, "Vortex Breakdown: A Review," *Prog. Energy Combust. Sci.*, **27**, pp. 431–481.

Won-Wook Kim
Jeffrey J. Lienau

Pratt & Whitney,
East Hartford, CT 06108

Paul R. Van Slooten
Meredith B. Colket III

United Technologies Research Center,
East Hartford, CT 06108

Robert E. Malecki
Saadat Syed

Pratt & Whitney,
East Hartford, CT 06108

Towards Modeling Lean Blow Out in Gas Turbine Flameholder Applications

The objective of this study was to assess the accuracy of the large-eddy simulation (LES) methodology, with a simple combustion closure based on equilibrium chemistry, for simulating turbulent reacting flows behind a bluff body flameholder. Specifically, the variation in recirculation zone length with change in equivalence ratio was calculated and compared to experimental measurements. It was found that the present LES modeling approach can reproduce this variation accurately. However, it understated the recirculation zone length at the stoichiometric condition. The approach was assessed at the lean blow out condition to evaluate its behavior at the lean limit and to analyze the physics of combustion instability. [DOI: 10.1115/1.2032450]

Introduction

As modern combustion system designs evolved, they have pushed the envelope on operability, durability, and fuel efficiency. Additionally, pollutant emissions requirements are becoming increasingly stringent. Emissions and combustion dynamics are intimately related to each other due to the dynamic nature of fuel-air mixing and combustion. For example, low oxides of nitrogen (NO_x) emissions can be achieved by making the fuel-air mixture very lean. However, as the equivalence ratio approaches the lean flammability limit, undesirable dynamics begin to occur. Furthermore, as the equivalence ratio is decreased and approaches the lean flammability limit, the CO emissions first decrease, and then suddenly increase exponentially (see, for example, Ref. [1]). Local flame quenching and formation of unburnt hydrocarbons (UHC) can also occur in the very lean limit. These phenomena (observed in both liquid- and gaseous-fueled gas turbine combustors) can be followed by combustion instability during which the flame undergoes rapid oscillations and eventually blows out completely. This process is often called "lean blow out" (LBO). Understanding and predicting LBO is important for achieving fuel-efficient, stable, and low-emissions gas turbine combustion systems.

In gas turbine combustion systems, flame stabilization is often achieved through the use of recirculation zones created by flameholders to provide a continuous ignition source, facilitating the mixing of hot combustion products with the incoming fuel and air mixture. Bluff bodies, swirl vanes, rearward facing steps, and cavities are commonly employed to establish the recirculation zones for flameholding. Each method creates a low-velocity zone of sufficient residence time and turbulence levels such that the combustion process becomes self-sustaining. The present study is focused on the bluff-body flameholders. The aim of this ongoing study is to achieve a predictive capability in understanding the complex coupling between turbulence, chemistry, and heat release

in the bluff-body flameholder wake flows, and eventually in understanding the mechanisms through which LBO is created.

One approach to improve the accuracy of simulating the bluff body fluid dynamics is to employ large-eddy simulation (LES). LES lies between the extremes of direct numerical simulation (DNS) and Reynolds-averaged Navier-Stokes simulation (RANS), using modified Navier-stokes equations in which eddies smaller than grid spacing are eliminated by low-pass filtering while their effects on the resolved motions are provided by subgrid-scale (SGS) models. RANS also solves modified Navier-stokes equations in a similar form as used in LES. However, the physical significance of the flow variables involved in the governing equations is significantly different between two methodologies. The difference is typically parametrized by a modeled turbulence length scale which is related to the grid size for LES, and to the integral flow scale for RANS. Therefore, in LES the modeled portion of turbulence scales decrease with finer numerical meshes and, eventually, LES can be converted to DNS if the numerical mesh becomes fine enough to resolve the Kolmogorov length scale. On the other hand, in RANS the whole range of turbulence scales are modeled regardless of the numerical mesh resolution used. Therefore, the accuracy of RANS will remain limited even with increased mesh resolution. DNS simulations are impractical at the high Reynolds numbers characterizing gas turbine engine combustion environments. However, with today's computer processor speeds and modeling technology progress, LES simulations are becoming more feasible, with analysis resource and time requirements within the same order of magnitude as steady RANS simulations.

It will be shown in this paper that the steady RANS approach is not capable of accurately calculating the unsteady flow field generated by the bluff body flameholders, and the utilization of LES significantly improves the modeling accuracy. It will be also demonstrated that one of the most commonly used industrial turbulent combustion models can be extended to work with LES, and the resulting fluid and combustion dynamics agree well with experimental data.

In the following section, the present LES modeling approach will be described. This will be followed by the discussion on turbulent combustion models. First, turbulent combustion modeling will be briefly discussed in general. Then the specific models

Contributed by the International Gas Turbine Institute (IGTI) of ASME for publication in the JOURNAL OF ENGINEERING FOR GAS TURBINES AND POWER. Manuscript received October 1, 2003; final manuscript received March 1, 2004. IGTI Review Chair: A. J. Strazisar. Paper presented at the International Gas Turbine and Aeroengine Congress and Exhibition, Vienna, Austria, June 13–17, 2004, Paper No. GT2004-53967.

employed in this study will be presented. The test case description and results of nonreacting and reacting simulations will follow. This paper will conclude by discussing the physics observed in the simulations.

Aero Modeling Approach

LES Modeling. Since the fluid dynamics at the combustion lean limit is highly transient, it is clear that the numerical methodology utilized to simulate this phenomenon must be able to accurately capture the unsteady features in both space and time. At present, LES appears to be a viable approach to tackle this problem. Some noteworthy examples of the potential of LES in the gas turbine engine applications can be found in recent papers by Black and Smith [2], Cook et al. [3], Grinstein and Fureby [4], Kim and Syed [5], Mahesh et al. [6], Pitsch [7], Stone and Menon [8], and Wang et al. [9].

In the present study, the one-equation LES model of Kim and Menon [10] was adopted to achieve the required modeling accuracy for unsteady simulation. The one-equation model, based on the subgrid-scale kinetic energy, is well suited for high-Reynolds number flow simulations because it does not assume local equilibrium between energy production and dissipation in the subgrid. Fureby et al. [11] demonstrated that the grid resolution requirement of this model is lower relative to most algebraic models. Furthermore, this model provides local subgrid turbulence intensity information which is needed for most turbulent combustion models with higher fidelity by solving a transport equation instead of estimating with an algebraic relation. Therefore, it is considered a preferred model for reacting flow applications.

Solver Numerics. The aerodynamics was modeled by solving conservation equations for mass, momentum, and energy using Pratt & Whitney's proprietary CFD flow solver, Allstar. Allstar is a derivative of the National Combustion Code [12], utilizing its unstructured data-structure. Allstar supports unstructured meshes of various shapes including hexahedrals, tetrahedrals, prisms, pyramids, quadrilaterals, and triangles. A standard $k-\epsilon$ RANS version of Allstar has been described in detail by Malecki et al. [13] and application of this tool to combustor design has been demonstrated by Snyder et al. [14].

The flow solver is based on a pressure-based, finite-volume algorithm that discretizes the conservative form of the governing equations using second-order accurate cell-centered differencing. Temporal differencing is also second-order accurate. For the continuity equation, control-volume face mass fluxes are constructed using the momentum-weighted interpolation of Rhie and Chow [15]. Transport equations are solved individually using an algebraic multigrid (AMG) matrix inverter for pressure, energy, and species, and a conjugate-gradient matrix inverter for all other quantities. A two-step pressure-correction procedure couples the momentum and continuity equations. The solver is parallelized for optimal performance on distributed computing infrastructures.

The numerics in Allstar have been modified for LES to ensure that the numerical dissipation does not contaminate the physical dissipation calculated by the subgrid-scale turbulence model. The overall order of accuracy of the Allstar code was tested using the Taylor-Green vortex problem, which is an exact closed-form solution of two-dimensional, incompressible Navier-Stokes equations. The maximum errors between analytical solutions and numerical results are shown in Fig. 1 for three different grid resolutions. The error curve has a slope of 2.0, indicating that the improved Allstar numerics are second-order accurate. A contour plot of the horizontal velocity component, with velocity vectors superimposed, at the time the error was calculated is also shown in the figure.

The present LES code has been validated against experimental data for various applications. It was observed that LES consistently produced significant improvement over standard $k-\epsilon$ RANS for those applications. A detailed description of the validations is

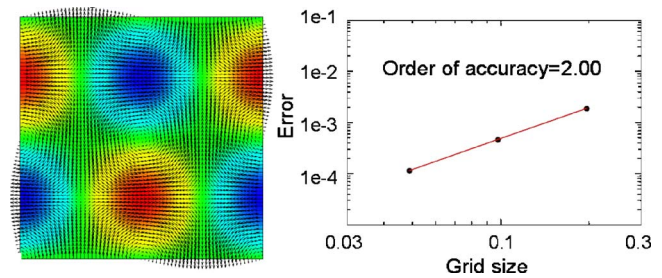


Fig. 1 Test using Taylor-Green vortex demonstrated that the Allstar code has second order of accuracy

omitted here for brevity. The LES code was further validated in the present study by comparing the results with both non-reacting and reacting experimental data of a bluff body flameholder flow.

Combustion Modeling Approach

In turbulent combustion systems, the details of flame structure can be substantially different depending upon the local turbulence level. The Borghi diagram is typically used to show that depending upon the turbulence intensity and characteristic length scale, the flame structure can change from the corrugated flamelet, to the thin reaction zone, to the broken reaction zone regimes [16]. All these regimes may co-exist in gas turbine engine combustion. Many gas turbine combustion systems operate in the thin-reaction zone regime when it is operating in the lean but stable condition. However, when the equivalence ratio is decreased for a given flow condition, the flame structure quickly shifts to the broken reaction zone regime, and the classical premixed flame structure is no longer present. From a turbulent combustion modeling perspective, the implication of this shift has been discussed by various authors (e.g., Kim and Menon [17], Duchamp de Lageneste and Pitsch [18], Menon [19]).

At the lean combustion limit, local flame quenching can occur since such flames have a very low tolerance for aerodynamic stretching caused by high intensity turbulence. Local extinction can lead to combustion instabilities, which in turn can lead to global extinction and LBO. Clearly, accurate modeling of very lean combustion requires that these dynamic features must be captured. Since these phenomena occur under conditions where classical flame structure is lost, it is clear that this type of combusting flow field cannot be easily addressed by an *ad hoc* extension of models that work reasonably in the other regimes of combustion. Therefore, a more comprehensive modeling approach is required to model LBO, and LES has high potential to contribute in this regard. In the following section, a general turbulent combustion modeling strategy for LES will be briefly discussed, and will be followed by the description of the model utilized in the present study.

Turbulent Combustion Modeling. A complete turbulent combustion model for LES of gas turbine engine combustion systems is made up of four component parts: a turbulent mixing model, a chemical reaction model, a turbulence-chemistry interaction model, and a time-accurate fuel spray dynamics model. Based on this categorization, Fig. 2 categorizes existing submodels spanning from the most commonly used models in industry to the state-of-the-art academic models. For brevity, detailed discussions on the individual models are omitted here. Instead, the reader is referred to the books by Poinot and Veynante [20] and Peters [21], or the review article by Candel et al. [22]. As illustrated in the figure, all the component parts interact with each other in a complicated manner. For accuracy, it is desirable to use the turbulent combustion model which integrates the most advanced model from each component part. However, this is not practical for the complicated flow fields of engineering interest due to lack of maturity of the more advanced models, and their higher computa-

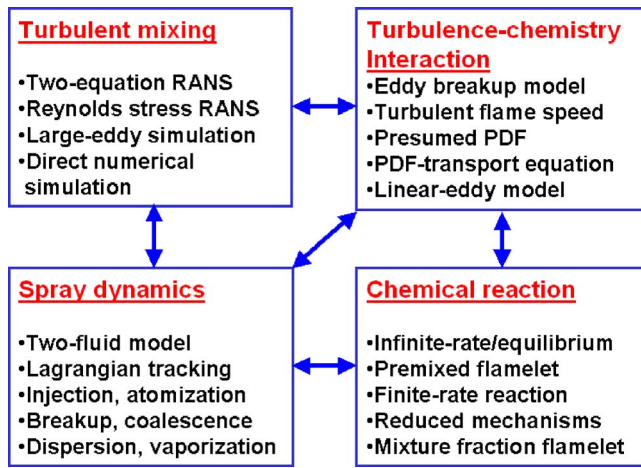
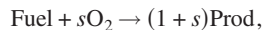


Fig. 2 Four component parts of turbulent combustion model

tional expense. Nevertheless, adaptation of LES methodology for reacting turbulent flow analysis may still be desirable since LES can provide significantly higher accuracy compared to RANS, even with a similar turbulent combustion model. A simple turbulent combustion model such as the eddy breakup (EBU) model by Magnussen-Hjertager [23] may provide reasonable accuracy within an LES framework under certain conditions (i.e., if turbulent mixing can be identified as the controlling process). The objective of this work was to evaluate such an engineering LES model for a gas turbine engine flameholder application.

In this effort, the modeling was further simplified by restricting the test case to pure gaseous premixed combustion in order to isolate the combustion and heat release issues from fuel-air mixing and spray issues. Therefore, the turbulent combustion model used in the present study was composed of three parts: LES turbulence model, EBU turbulence-chemistry interaction model, and an infinite-rate reaction and equilibrium temperature model. The latter two components were chosen to be widely used industrial models for RANS simulations. Therefore, any improvement achieved by the present modeling will be attributable to the LES turbulence model. Eventually, all the component models will be replaced with more advanced models. Therefore, the present study is the first step towards achieving high-fidelity prediction capability of the combustion instability. The details of the turbulent combustion models used in this study are discussed below.

EBU Model. The chemistry was simplified by assuming the instantaneous attainment of “equilibrium” conditions, based on the simplified irreversible reaction between fuel and oxidizer O_2 :



where s is the stoichiometric coefficient. In the EBU model, the reaction rate is based upon turbulent mixing, and the assumption of infinitely fast chemistry. The turbulent mean reaction rate is expressed as

$$\bar{\omega} = \bar{\rho} \alpha \frac{\varepsilon}{k} \text{Min} \left(\bar{Y}_{\text{Fuel}}, \frac{1}{s} \bar{Y}_{O_2}, \frac{\beta}{s+1} \bar{Y}_{\text{Prod}} \right),$$

where $\bar{\rho}$, \bar{Y}_{Fuel} , \bar{Y}_{O_2} , \bar{Y}_{Prod} are the mean density, the mean fuel, oxidizer, and product mass fractions, respectively. k and ε are the turbulent kinetic energy and its dissipation rate, and α and β are the EBU model constants. In the present LES model, k is solved from a transport equation and ε is algebraically estimated using k and the local grid size [10].

EDC Extinction Model. The baseline EBU model was refined by incorporating the extinction model based on the eddy dissipation concept (EDC) of Magnussen [24]. The extinction model

turns off reaction if there exist turbulent eddies whose scales are small enough to disturb the flame reaction zone structures, i.e., the characteristic turbulence time scale is smaller than the characteristic chemical time scale, as described by Gran et al. [25]. The characteristic turbulence time scale is related to the Kolmogorov time scale by

$$\tau_{\text{turb}} = C_K (\nu/\varepsilon)^{1/2},$$

where ν denotes the kinematic viscosity and C_K is the proportionality constant. The characteristic chemical time (τ_{chem}) is assigned to be the extinction time of a perfectly stirred reactor (PSR), as computed using a modified version of a reactor code [26] and an internally developed, detailed reaction mechanism for propane. This modification to the EBU model leads to a more realistic simulation of the flame front location because τ_{chem} includes detailed kinetic information.

The originally suggested value for C_K was 0.41 [24]. However, after close examination of the EBU and EDC models, it was found that the mixing time scale used in both models was defined inconsistently. If a consistent definition is applied, the constant should be $C_K=0.82$. This new constant results in less extinction than the original one. In our experience, the new constant provides a more realistic flame front location. Similarly, Kjaldman et al. [27] have reported an overestimation of extinction with $C_K=0.41$. The modified constant was used for the present study.

Equilibrium Temperature Model. Temperature was determined using a pregenerated table lookup method. The temperature was tabulated using the NASA enthalpy-temperature relationship [28]. Since thermal coefficients for fuel, O_2 and N_2 are readily available, the main issue in the preprocessing step is to determine the artificial product coefficients as a function of equivalence ratio. Thermal coefficients (in NASA format) were determined for the artificial product species at each fuel-air ratio. Then, the thermal coefficients were fitted as a function of the fuel-air ratio and stored in a data file for access by the Allstar solver for enthalpy and temperature computations. Absolute errors using this approach were previously demonstrated to be small [13].

Extension of EBU Model to Premixed Combustion. The EBU model was originally devised to solve mixing-limited combustion systems and, by its nature, allows chemical reaction even with an infinitesimal temperature rise (i.e., infinitesimal introduction of product). To elaborate, the integration of the product species equation with the EBU reaction rate source term shows that, in the case of a premixed flame in a one-dimensional duct, the Favre-averaged mean product mass fraction in the region of the flame front can be approximated as

$$\bar{Y}_{\text{Prod}} \approx \exp \left(\frac{\varepsilon L}{k \bar{U}} \right),$$

where \bar{U} is the Favre-averaged mean velocity. This exponential growth often leads to nonphysical flashback in premixed flame calculations, driven by numerical diffusion. The EDC extinction model cannot control this problem since it was not designed to extinguish flames in free streams.

The standard approach for implementing the EBU model in commercial CFD codes is to couple it with a laminar global combustion mechanism by selecting the minimum between EBU and laminar rate (e.g., Ref. [29]). However, the global combustion mechanism often requires tailoring, and has the potential to alter the turbulent combustion flame front in a nonphysical manner.

Utilizing the notion that specifying a minimum temperature for combustion is equivalent to specifying a maximum local chemical time for reaction to occur, the present study directly utilizes the characteristic chemical time scales to prevent nonphysical flashback behavior. The limiting maximum reaction time was set by

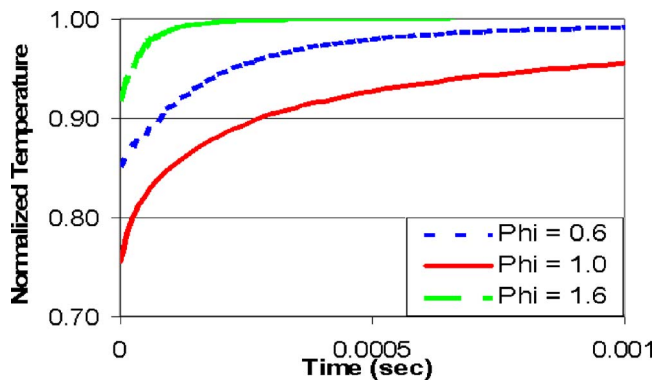


Fig. 3 Combined PSR-PFR test indicates that chemical reaction at the stoichiometric condition has the most nonequilibrium nature

$$(\tau_{\text{chem}})_{\text{burnt}}^{0.8}$$

where $(\tau_{\text{chem}})_{\text{burnt}}$ denotes the equivalent PSR chemical time scale at the fully burnt temperature. The effect of this correction is to limit combustion to regions of the flow where back mixing of combustion products is able to sufficiently raise the reactant temperatures (and subsequently lower the characteristic chemical time scale). Nonphysical flashback is thus eliminated. The exponent of 0.8 was chosen to ensure that the limiting reaction time scale lies between the characteristic chemical time scales of the unburned mixture and the burnt product throughout the range of lean and rich blow out equivalence ratios. Testing has shown that results are not very sensitive to the exponent selection. Nevertheless, the extension of this expression to broad range of inlet temperatures and pressures should be investigated.

Errors Involved With Equilibrium Chemistry. Combustion blowout is a highly transient phenomenon. Its unsteady nature is also very sensitive to aerodynamic and thermodynamic conditions. For instance, blowout is generally abrupt and represents a competition between fluid mixing and nonlinear chemistry. Therefore, in order to achieve an accurate simulation of blowout, finite-rate chemistry, utilizing detailed mechanisms, should be incorporated. In fact, most advanced turbulent combustion models require the calculation of detailed (or reduced) chemical mechanisms during the CFD calculations. Those advanced models include the unsteady flamelet model [7], the linear-eddy model (LEM) [19], and the probability density function (PDF) transport equation model [30].

As discussed earlier, the combustion model used in this study is based on simplified equilibrium chemistry. Therefore, a certain degree of error is unavoidable in the prediction. The simulation errors were qualitatively assessed by evaluating the nonequilibrium levels of chemical reactions near limiting lean and rich conditions as well as at the stoichiometric condition. Figure 3 shows the results of the plug flow reactor (PFR) calculations which are normalized to final temperatures. The PFR calculations could not be carried out with propane at 300 K because the ignition delay times are infinity at this temperature. Thus, the PSR code was first run using propane and air, with reactants initially at 300 K and for a residence time just exceeding the PSR extinction time. Using the PSR exit conditions as the starting conditions for a PFR, the PFR code was run with the time reset to be zero. The normalized temperatures in Fig. 3 illustrate that to get from the initial reaction condition to 95% of equilibrium, it takes the stoichiometric case more than ten times longer than for the rich case and about four times longer than the fuel lean case. For the particular combustor which was considered in this study, the time scale involved with the longitudinal acoustic mode of the combustor was about 3 ms. Therefore, the nonequilibrium time scale of chemical reactions at

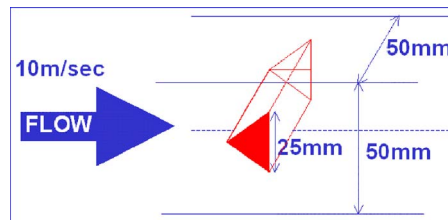


Fig. 4 Schematic of the bluff body flameholder

the stoichiometric condition is not small compared with this largest time scale associated with the chamber acoustic modes. (It will be shown later that this longitudinal mode has a significant impact on the reacting flows.) On the other hand, the nonequilibrium chemical time scales near limiting lean and rich conditions are at least one order of magnitude smaller than the time scale of the longitudinal acoustic mode. This result is contrary to intuition and requires explanation. For virtually all conditions, many radicals (e.g., OH, H, O, etc.) as well as CO and H₂ overshoot equilibrium and it takes time to relax them to equilibrium. The problem is accentuated for the stoichiometric case because superequilibrium levels are largest, and because the reverse reactions, e.g., CO₂ + H = CO + OH are the fastest and inhibit approach to equilibrium. The net result is that the equilibrium assumption overstates the “instantaneous” density rise across the flame front, and the error is greatest for the stoichiometric conditions.

Test Case Description

The triangular-shape bluff-body flameholder experiments carried out by Fujii et al. for cold flows [31] and reacting flows [32] were selected as the test case. This test case was chosen for the following four reasons:

- The test rig geometry and flow field conditions for the experiments were well defined. Simulating the proper geometry and flow conditions is very important for unsteady flows behind bluff bodies because these flows are associated with severe pressure gradients, separation and recirculation, all of which are extremely sensitive to those details.
- The test measurements were extensive. The flow configurations included both nonreacting and reacting cases, and the reacting case covered a complete range of equivalence ratio conditions from lean blowout to rich blowout.
- Various quantities which are useful in characterizing the fluid dynamics aspect of the flame blowout process were measured. Those quantities include mean velocities, turbulent fluctuations, static pressures, and mass exchange rates.
- Because of the complexity of the physics being addressed in this study, model flameholders with simplified geometry such as the present test case are extremely useful because the first-order physics which leads the combustion blowout can be isolated from other secondary effects.

Experiments were carried out in an open circuit, forced flow type wind tunnel. The model combustor had a test section consisting of a 50 × 50 mm straight duct in which a two-dimensional flameholder was installed. The flameholder had an equilateral triangular rod with base height, $B = 25$ mm. A schematic diagram of the bluff body flameholder is depicted in Fig. 4. The combustor had a length of 305 mm in the axial direction. Air or homogeneous propane-air mixture was blown through a nearly 100:1 contraction in a settling chamber before it entered the combustor. A two-dimensional velocity profile with magnitude of about 10 m/sec was maintained at the combustor inlet. The Reynolds number based on the hydraulic diameter of the combustor was 410,000. The turbulence intensity level was about 2% of the mean velocity magnitude.

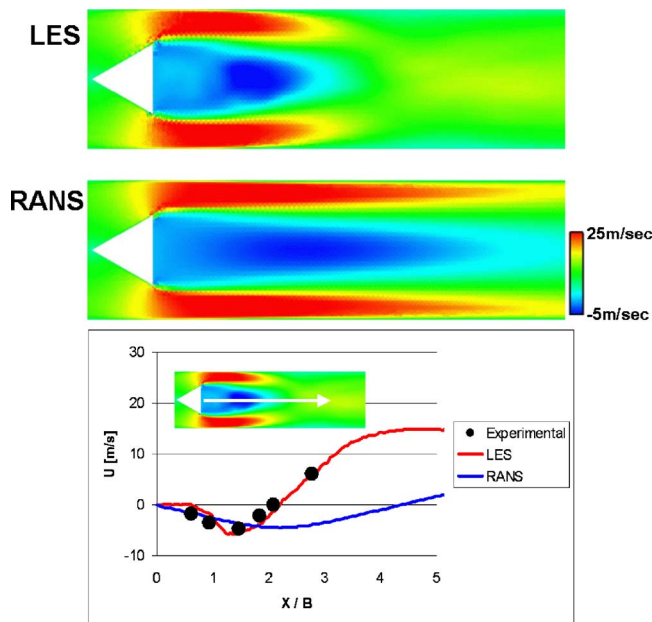


Fig. 5 Time-averaged axial velocity flow fields calculated by LES and RANS models; comparison of the mean axial velocity along the centerline of the combustor

An unstructured tetrahedral mesh with prism layers was used for the present study. The mesh contained 1.6 million elements. The same grid was used for the nonreacting and reacting simulations. Fine-resolution, uniform tetrahedral meshes were used in the near-field wake zone, which is the most critical location for capturing both the unsteady aerodynamics and the flame instabilities. This fine mesh region was extended from just before the flame holder point to six base heights (B) downstream. The rest of the domain used tetrahedrals, which had two times the edge length of that used in the fine region. The grid resolution and arrangement were determined based on our previous experience with similar configurations.

The measured velocity and turbulent fluctuations were imposed at the inlet of the computational domain. The mass flow rate at the inlet and the pressure at the exit were fixed, so that flow and flame unsteadiness should be created only by instabilities inside the combustor. Various equivalence ratio conditions (Φ) have been tested in the experiment and seven different equivalence ratios ($\Phi=0.0, 0.52, 0.6, 0.7, 1.0, 1.4, 1.62$) were chosen for the present study.

Results and Discussion

Nonreacting LES. Since the flame blowout characteristics of bluff bodies are largely determined by the aerodynamics of the flow around the body, it is worthwhile to investigate the aerodynamics under nonreacting conditions where data for the distributions of mean velocities, turbulent characteristics, static pressures, and mass exchange rates are available. Both the Allstar-LES code and the Allstar-RANS code based on $k-\epsilon$ model were applied to simulate the nonreacting flow using the same computational mesh. The LES simulation required additional time stepping with smaller time step to collect statistical samples for time averaging after initial transient states were washed out. Due to these additional procedures, the overall computational cost of the LES simulation was about five times higher than that of the RANS simulations. Typical comparisons between LES, RANS, and data are presented below.

Figure 5 shows the time-averaged axial velocity flow fields calculated by LES and RANS models. Note that only the near wake region is shown here. There is a significant difference between

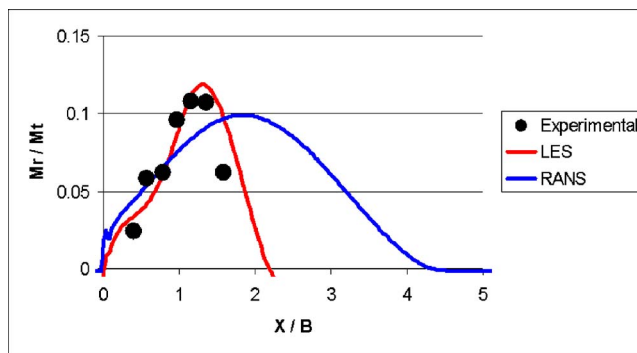


Fig. 6 Comparison of the axial distribution of the normalized reverse flow rate

two numerical solutions. The LES results show the recirculation length to be about half of what the RANS results show. The instantaneous velocity fields (not shown here) clearly demonstrated that the LES calculation captured the time-dependent asymmetric von Karman vortex shedding. As a result of the rapid mixing by the unsteady coherent vortices, the time mean length of the recirculation zone was reduced in the LES simulation. The resulting Strouhal number, based on the flow speed at the flameholder lip, was 0.2 which agrees with the experimental observation by Twigge-Molecey and Baines [33].

Figure 5 also shows a comparison of the mean axial velocity along the centerline of the combustor. The comparison confirms that the LES model provided superior agreement with data. This improvement is mostly attributable to the ability of the LES model to capture the inherently unsteady vortex shedding in this flow field. Large-scale vortex shedding is a highly flow-dependent phenomenon that cannot be captured through conventional steady RANS modeling approaches.

The improved accuracy of the LES model is also seen in the comparison of the axial distribution of the normalized reverse flow rate (M_r/M_t) as shown in Fig. 6. Here, M_r and M_t represent the integrated reverse and total flow rates, respectively. This parameter is indicative of the recirculation strength. Both the maximum reverse flow point and the maximum value of the reversed mass flow rate were accurately calculated in the LES model. On the other hand, the steady RANS model missed both.

Figure 7 shows the comparison of the axial distribution of turbulent kinetic energy at four different normal locations ($Y/B=0.0, 0.2, 0.5, 0.6$). It is observed that the LES model has better agreement with data than the steady RANS model. The LES results show slightly lower turbulence within the first base height of the bluff body. This suggests that the von Karman vortex shedding was a little delayed in the LES simulation.

Reacting LES. The reacting simulations were carried out using the same numerical methodology and mesh utilized for the nonreacting simulation. Therefore, any changes in fluid dynamics can be attributed to the heat release from the combustion model described earlier. The effects of combustion on the mean flow behind the flameholder are illustrated in Fig. 8, which shows the comparison of the time-averaged velocity field (depicted by the velocity vector arrows superimposed with the axial velocity contours) and the time-averaged temperature field. Three different combustion conditions are compared: nonreacting, and lean and stoichiometric combustion. The aerodynamics inside the recirculation zone is quite different between the nonreacting case and the reacting cases. In the nonreacting case, the flow recirculation is much more pronounced in the second half of the recirculation zone. In both reacting cases, the flows are strongly recirculating throughout the entire length of the recirculation zone, with the maximum reverse flow point located at $\sim 30\%$ of the recirculation zone length from the flameholder base. In the nonreacting case,

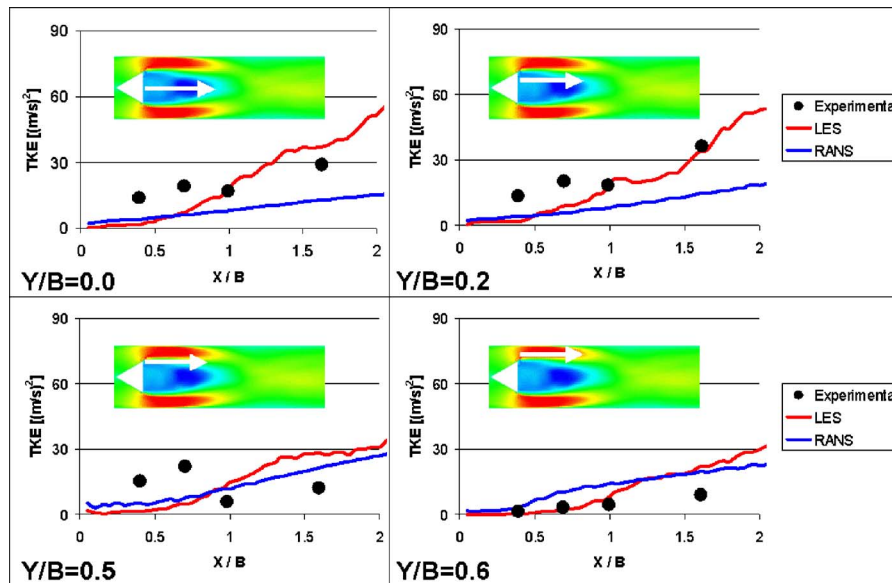


Fig. 7 Comparison of the axial profiles of turbulent kinetic energy at four different normal locations

this maximum reverse flow point is located at $\sim 60\%$ of the recirculation zone length from the flameholder base. Even though the flow reversal is stronger in the reacting cases, the maximum value of reverse mass flow rate is smaller compared to the nonreacting case since the density in the recirculation zone is significantly lower in the reacting cases.

Comparing the nonreacting case and the lean combustion case ($\Phi=0.7$), it is evident that combustion extended the recirculation region further downstream. It was observed that in the instantaneous flow fields (not shown here) the asymmetric von Karman shedding of coherent vortices no longer exists in the reacting case. Therefore, the reacting case does not possess any large-scale mixing mechanisms which typically reduce the recirculation zone

length. Mehta and Soteriou [34] attributed this absence of asymmetric von Karman shedding for reacting conditions to the dilatation effect of the heat release. They also found that baroclinic vorticity augments the impact of dilatation, but its effect is secondary.

The recirculation length difference between two reacting cases ($\Phi=0.7$ and 1.0) shown in Fig. 8 can be attributed to the different levels of the volumetric expansion due to heat release. The volume expansion increases the velocity along the flow direction, and thus shrinks the recirculation zone. Since heat release is the greatest near the stoichiometric condition, the recirculation length is correspondingly the smallest.

Analyzing the instantaneous flame response to the aerodynamics (results are not shown here), the current combustion modeling approach yielded a more gradual response to turbulent eddy motions compared to a flame tracking technique based on the G -equation model (e.g., Ref. [35]). In the G -equation model, the flame is viewed as an infinitely thin propagating surface defined by the isolevels of G where aerodynamic convection and flame burning are balanced. The G equation includes a source term based on turbulent flame speed. Therefore, the flame surface represented by an isolevel of G can respond more directly to local turbulent fluctuations.

Figure 9 shows the comparison of the mean axial velocity distribution at the combustor centerline for three different combustion conditions: $\Phi=0.6$, 1.0 , and 1.4 . The agreement is reasonably good between the LES calculation and experimental data, except at the stoichiometric condition. This shortcoming of the model will be discussed later. It is also notable that the LES model showed better agreement with measurements at the lean condition than it did at the rich condition.

Figure 10 summarizes the comparison between the simulated and experimental recirculation zone lengths. The mean recirculation zone is defined as the region where the mean axial velocity is negative. Physically, its length is related to the degree of unsteady asymmetric vortex shedding (nonreacting case), or gas expansion by combustion heat release (reacting case). One focus of the present study was to assess the accuracy of the LES model for calculating the recirculation zone length variation with respect to the change in equivalence ratio. The experiment observed a bucket shape curve of recirculation zone length, with the minimum near the stoichiometric condition. Either leaner or richer fuel

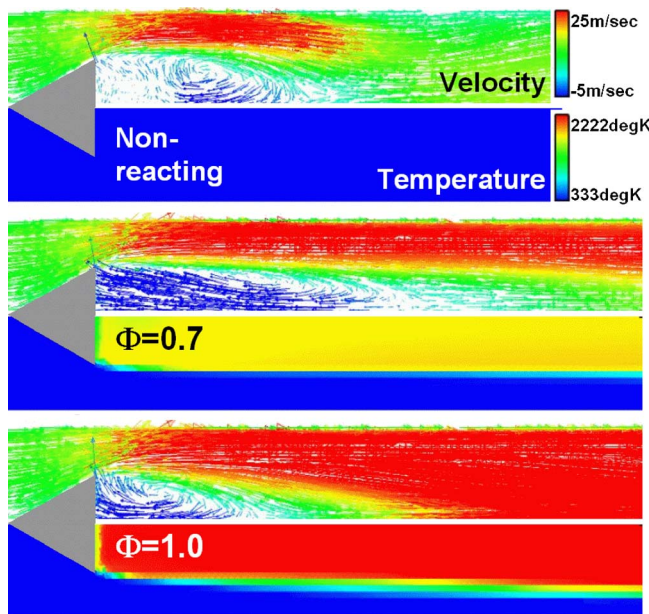


Fig. 8 Comparison of the time-averaged velocity field (depicted by the velocity vector arrows superimposed with the axial velocity contours) and the time-averaged temperature field at three different equivalence ratios ($\Phi=0.0$, 0.7 , and 1.4)

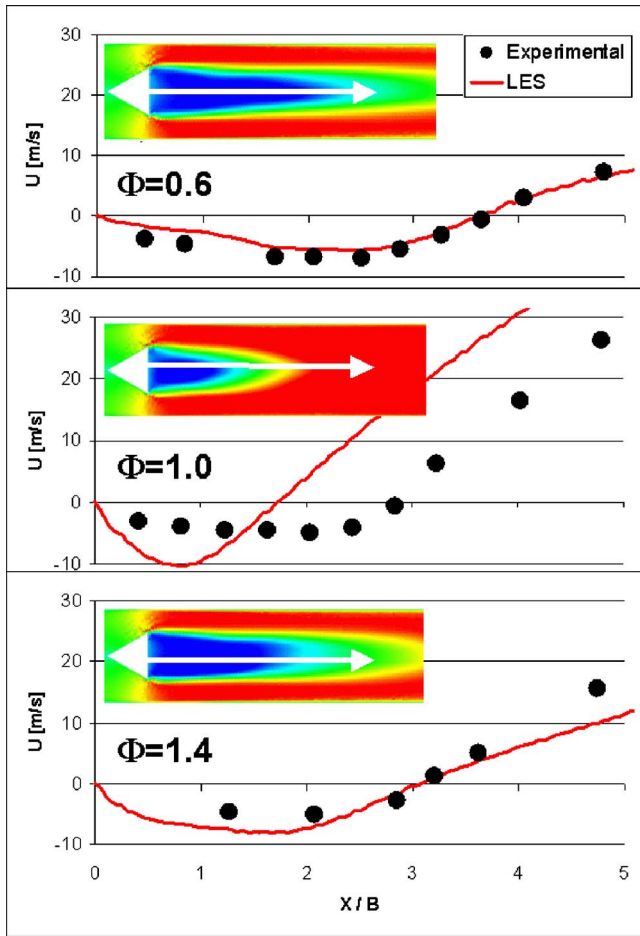


Fig. 9 Comparison of the mean axial velocity distribution at the combustor centerline with three different equivalence ratios ($\Phi=0.6, 1.0, \text{ and } 1.4$)

condition enlarges the recirculation zone almost linearly until blow out. Once the flame blows out, the recirculation zone length drops to the size of the nonreacting case, which is smaller than the minimum reacting recirculation zone length. The present LES results also show the same variation with the equivalence ratio

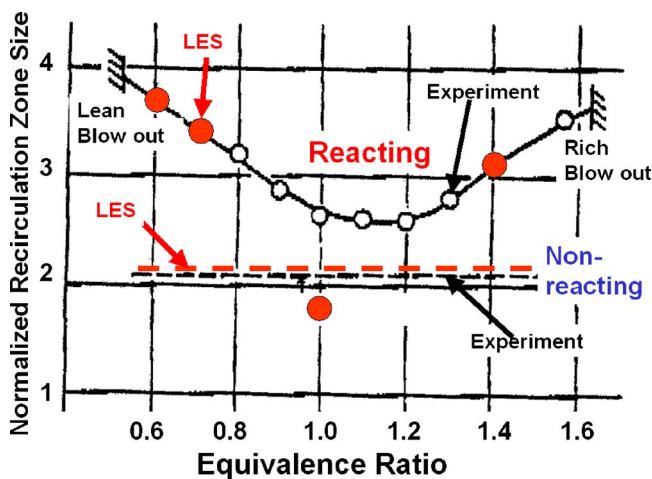


Fig. 10 Comparison between LES results and experimental data of the recirculation zone length as a function of equivalence ratio

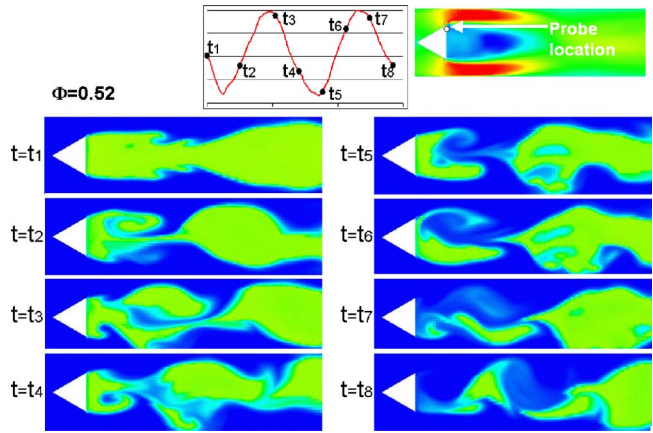


Fig. 11 Time sequence of instantaneous temperature fields at the lean blow out condition

change. The comparison is outstanding at both the lean and rich conditions. However, the current LES model understates the recirculation zone length at the stoichiometric condition. This miss can be partly attributed to the errors involved with the equilibrium chemistry assumption. As was discussed in the combustion modeling section, this test case exhibits the most nonequilibrium chemistry nature at the stoichiometric condition.

It is encouraging that the present numerical model predicted the lean blow out at the same equivalence ratio, $\Phi=0.52$, as observed in the experiment. The transient behavior of the flame detaching from the flameholder, and convecting downstream before completely blowing out is shown in Fig. 11. The figure depicts the temperature field behind the flameholder at a sequence of different times. The occurrence of lean blow out may be sensitive to initial conditions. However, it is observed that, in this particular case, the lean blow out occurred at the same equivalence ratio regardless of any initial conditions used. The figure shows the case where the combustion was first stabilized with a higher equivalence ratio, $\Phi=0.55$. At this higher equivalence ratio, a fairly uniform symmetric shedding was observed as shown at $t=t1$. Then, the equivalence ratio and the burnt product temperature were instantly lowered to the lean blow out condition. The time period shown in the figure includes about two cycles of pressure oscillations which are equivalent to a physical time of 5.7 ms. The pressure at the lip of the flameholder reaches a maximum just before $t3$. At this time, a pair of counter-rotating vortices is shed simultaneously from both corners of the flameholder. These vortices have different strength. Thus, the temperature field is not symmetric. As the vortices are convected downstream, the flame becomes stretched and strained, and eventually is broken up. Just before $t7$, the pressure peaks again triggering another vortex pair. By this time, the upper wake region immediately behind the flameholder is completely occu-

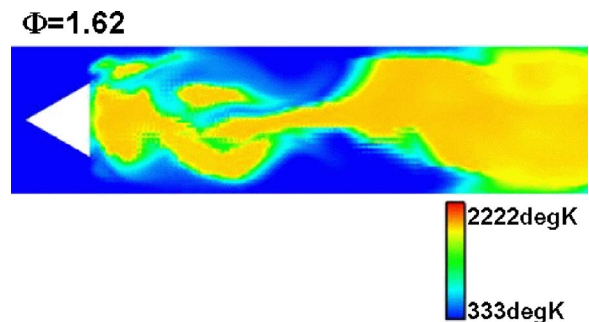


Fig. 12 Instantaneous temperature field at the rich blow out condition

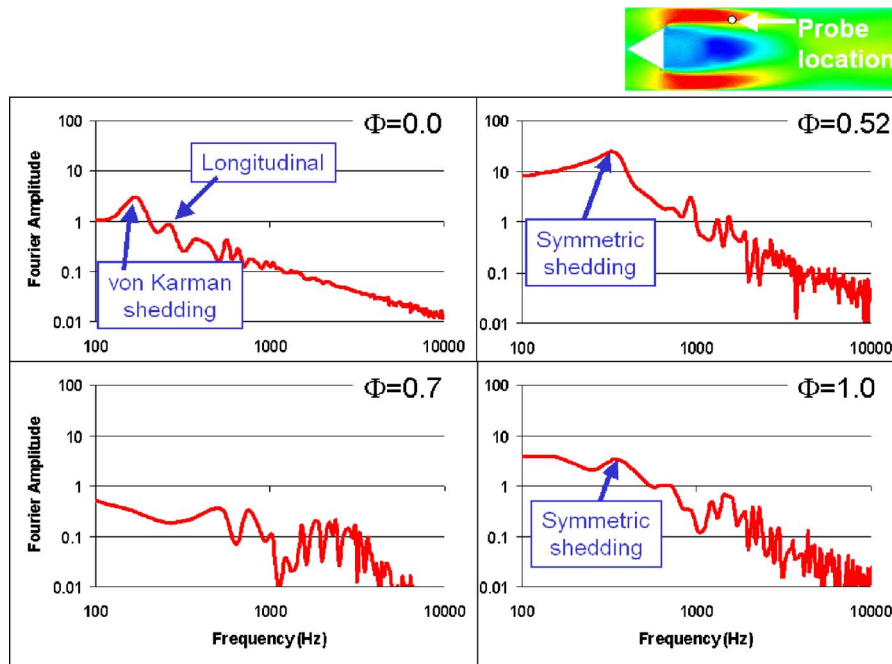


Fig. 13 Fourier transformation of the normalized pressure fluctuations for four different equivalence ratio cases

ped by cold unburnt mixture. The newly generated vortex pair accelerates the cold unburnt mixture into the entire recirculation zone, and finally, the flame is blown out.

Rich blow out also was calculated to be at the same equivalence ratio, $\Phi=1.62$, as observed in the experiment. Figure 12 shows the instantaneous temperature field just before the flame blows out. The flame structure is similar to the one observed at lean blow out, but with a higher product temperature.

Figure 13 shows Fourier transformation of the normalized combustor pressure. Four different equivalence ratio cases are shown, including the nonreacting case. The probe is located outside of the recirculation, two base heights downstream from the flameholder base, and 0.6 base heights above the combustor centerline.

In the nonreacting case, a pronounced frequency of 170 Hz is observed. The corresponding Strouhal number based on the flameholder lip flow velocity is 0.2, suggesting that this mode corresponds to von Karman shedding. The experiment also observed an excitation at almost the same frequency. The second excitation is observed at the frequency of 270 Hz. This mode corresponds to the most unstable longitudinal mode based on the computational domain used. Even though the computational domain was arbitrarily extended in the axial direction (approximately by a factor of 2), the shifted longitudinal mode is still separated from the vortex shedding mode. Some harmonic mode excitations can also be observed.

At the lean, stable combustion condition, $\Phi=0.7$, the amplitude of the excitation is almost negligible at all frequencies. At the stoichiometric condition, an amplitude peak is observed at 340 Hz. It is relatively broad, suggesting that the pressure oscillations are somewhat irregular. This mode corresponds to the longitudinal mode changed by the elevated temperature. Symmetric shedding is observed in this fuel condition with the frequency at 340 Hz. This result suggests that, in this particular case, the frequency of the symmetric shedding is synchronized by the longitudinal mode. At the lean blow out condition, the amplitude of the fluctuations was significantly increased compared to those at all other equivalence ratios. A peak is observed at the 340 Hz. Again this mode corresponds to the longitudinal pressure oscillation as well as the symmetric shedding.

Conclusions

Large-eddy simulation using a simple combustion closure based on the Magnussen model demonstrated promise in calculating a bluff body wake flow at both nonreacting and premixed, reacting conditions. It was shown that the recirculation zone length variation with varying equivalence ratio could be accurately calculated with the present LES model, although it showed some deviation from data at the stoichiometric condition. This deviation seemed to be due to the strong nonequilibrium nature of chemistry at that particular condition. The present LES model also demonstrated potential to predict lean blow out. LES represents a flexible modeling approach; it can provide continuously improving fidelity up to direct numerical simulation as available computational resources increase, and with different approximations representing various levels of scale resolution between RANS and DNS. This paper demonstrated the potential of this LES + simple combustion modeling approach for simulating of turbulent reacting flows behind a bluff body flameholder. While the results of this study are encouraging, and the benefits of LES are clear, it is also clear that more advanced turbulent combustion models are necessary to accurately capture the unsteady flame dynamics behind bluff body flameholders.

Acknowledgment

The authors would like to thank H.-M. Shang and C.-M. Rhie for their contributions to the improvement of the Allstar solver for LES; P. Colucci and T. Brogan for their contributions to the validation of the premixed combustion model; and M. C. Soteriou, C. A. Eckett, and D. J. Hautman for providing valuable suggestions for the modeling and validation of this study.

References

- [1] Bhargava, A., Kendrick, D. W., Colket, M. B., Sowa, W. A., Casleton, K. H., and Maloney, D. J., 2000, "Pressure Effects on NOx and CO Emission in Industrial Gas Turbines," ASME Paper 2000-GT-0008.
- [2] Black, D. L., and Smith, C. E., 2003, "Transient Lean Blowout Modeling of an Aero Low Emission Fuel Injector," AIAA Paper 2003-4520.
- [3] Cook, D. J., Pitsch, H., and Peters, N., 2003, "Numerical Simulation of Com-

- bustion Instabilities in a Lean Premixed Combustor with Finite Rate Chemistry," ASME Paper GT2003-38558.
- [4] Grinstein, F. F., and Fureby, C., 2003, "LES Studies of the Flow in a Swirl Gas Combustor," AIAA Paper 2003-0484.
 - [5] Kim, W.-W., and Syed, S., 2004, "Large-Eddy Simulation Needs for Gas Turbine Combustor Design," AIAA Paper 2004-0331.
 - [6] Mahesh, K., Constantinescu, G., Apte, S., Iaccarino, G., Ham, F., and Moin, P., 2002, "Progress Toward Large-Eddy Simulation of Turbulent Reacting and Non-reacting Flows in Complex Geometries," CTR Annual Research Briefs, pp. 115–142.
 - [7] Pitsch, H., 2002, "Improved Pollutant Predictions in Large-Eddy Simulations of Turbulent Non-Premixed Combustion by Considering Scalar Dissipation Rate Fluctuations," *Proceedings of the Combustion Institute*, Vol. 29.
 - [8] Stone, C., and Menon, S., 2002, "Adaptive Swirl Control of Combustion Dynamics in Gas Turbine Combustors," *Proceedings of the Combustion Institute*, Vol. 29, pp. 155–160.
 - [9] Wang, S., Hsieh, S. Y., and Yang, V., 2002, "Vortical Dynamics and Acoustic Response of Gas-Turbine Swirl-Stabilized Injectors," AIAA Paper 2002-1008.
 - [10] Kim, W.-W., and Menon, S., 1995, "A New Dynamic One-Equation Subgrid-Scale Model for Large-Eddy Simulations," AIAA Paper 95-0356.
 - [11] Fureby, C., Tabor, G., Weller, H. G., and Gosman, A. D., 1997, "A Comparative Study of Subgrid Scale Models in Homogeneous Isotropic Turbulence," *Phys. Fluids*, **9**, pp. 1416–1429.
 - [12] Liu, N. S., and Quealy, A., 1999, "NCC—A Multidisciplinary Design/Analysis Tool for Combustion Systems," NASA CP-1999-208757, pp. 183–188.
 - [13] Malecki, R. E., Rhie, J., McKinney, R., Colket, M., Madabhushi, R., Ouyang, H., and Syed, S., 2001, "Application of a CFD-Based Analysis System to the PW6000 Combustor to Optimize Exit Temperature Distribution, Part I: Description and Validation of the Analysis Tool," ASME Paper 2001-GT-0062.
 - [14] Snyder, T., Stewart, J., Stoner, M., and McKinney, R., 2001, "Application of an Advanced CFD-Based Analysis System to the PW6000 Combustor to Optimize Exit Temperature Distribution, Part II: Comparison of Calculations to Full Annular Rig Test Data," ASME Paper 2001-GT-0064.
 - [15] Rhie, C. M., and Chow, W. L., 1983, "Numerical Study of the Turbulent Flow Past an Airfoil with Trailing Edge Separation," *AIAA J.*, **21**, pp. 1525–1532.
 - [16] Peters, N., 1999, "The Turbulent Burning Velocity for Large-Scale and Small-Scale Turbulence," *J. Fluid Mech.*, **384**, p. 107.
 - [17] Kim, W.-W., and Menon, S., 2000, "Numerical Modeling of Turbulent Premixed Flames in the Thin-Reaction-Zones Regime," *Combust. Sci. Technol.*, **160**, pp. 119–150.
 - [18] Duchamp de Lageneste, L., and Pitsch, H., 2002, "Comparison of Turbulent Premixed Flames at Different Turbulence Levels," CTR Annual Research Briefs, pp. 91–101.
 - [19] Menon, S., 2003, "Modeling Pollutant Emission and Lean Blow Out in Gas Turbine Combustors," AIAA Paper 2003-4496.
 - [20] Poinsot, T., and Veynante, D., 2001, *Theoretical and Numerical Combustion*, Edwards, Flourentown, PA.
 - [21] Peters, N., 2000, *Turbulent Combustion*, Cambridge University Press, Cambridge, England.
 - [22] Candel, S., Thevenin, D., Darabiha, N., and Veynante, D., 1999, "Progress in Numerical Combustion," *Combust. Sci. Technol.*, **149**, pp. 297–337.
 - [23] Magnussen, B. F., and Hjertager, B. H., 1976, "On Mathematical Modeling of Turbulent Combustion With Special Emphasis on Soot Formation and Combustion," *Proceedings of the Combustion Institute*, Vol. 16, pp. 719–729.
 - [24] Magnussen, B. F., 1981, "On the Structure of Turbulence and a Generalized Eddy Dissipation Concept for Chemical Reactions in Turbulent Flow," *19th AIAA Aerospace Sciences Meeting*, St. Louis.
 - [25] Gran, R., Melaaen, M. C., and Magnussen, B. F., 1994, "Numerical Simulation of Local Extinction Effects in Turbulent Combustor Flows of Methane Air," *Proceedings of the Combustion Institute*, Vol. 25, pp. 1283–1291.
 - [26] Glarborg, P., Kee, R. J., Grcar, J. F., and Miller, J. A., 1986, "PSR: A Fortran Program for Modeling Well-Stirred Reactors," Sandia Report SAND86-8209.
 - [27] Kjaldman, L., Brink, A., and Hupa, M., 2000, "Micro Mixing Time in the Eddy Dissipation Concept," *Combust. Sci. Technol.*, **154**, pp. 207–227.
 - [28] Gordon S., and McBride, B. J., 1971, "Computer Program for Calculation of Complex Chemical Equilibrium Compositions, Rocket Performance, Incident and Reflected Shocks and Chapman-Jouget Detonations," NASA SP-273.
 - [29] Fureby, C., and Lofstrom, C., 1994, "Large-Eddy Simulations of Bluff Body Stabilized Flames," *Proceedings of the Combustion Institute*, Vol. 25, pp. 1257–1264.
 - [30] Pope, S. B., 1985, "PDF Methods for Turbulent Reactive Flows," *Prog. Energy Combust. Sci.*, **11**, p. 119.
 - [31] Fujii, S., Gomi, M., and Eguchi, K., 1978, "Cold Flow Tests of a Bluff-Body Flame Stabilizer," *J. Fluids Eng.*, **100**, pp. 323–332.
 - [32] Fujii, S., and Eguchi, K., 1981, "A Comparison of Cold and Reacting Flows Around a Bluff-Body Flame Stabilizer," *J. Fluids Eng.*, **103**, pp. 328–334.
 - [33] Twigg-Molecey, C. F. M., and Baines, W. D., 1973, "Aerodynamic Forces on a Triangular Cylinder," *J. Eng. Mech. Div.*, **99**, pp. 803–818.
 - [34] Mehta, P. G., and Soteriou, M. C., 2003, "Combustion Heat Release Effects on the Dynamics of Bluff Body Stabilized Premixed Reacting Flows," AIAA Paper 2003-0835.
 - [35] Kim, W.-W., Menon, S., and Mongia, H. C. 1999, "Large-Eddy Simulation of a Gas Turbine Combustor Flow," *Combust. Sci. Technol.*, **143**, pp. 25–62.

An Integrated Fault Diagnostics Model Using Genetic Algorithm and Neural Networks

Suresh Sampath

Riti Singh

Department of Power Propulsion and Aerospace,
School of Engineering,
Cranfield University,
Cranfield, Bedfordshire MK43 0AL, UK

This paper presents the development of an integrated fault diagnostics model for identifying shifts in component performance and sensor faults using the Genetic Algorithm and Artificial Neural Network. The diagnostics model operates in two distinct stages. The first stage uses response surfaces for computing objective functions to increase the exploration potential of the search space while easing the computational burden. The second stage uses the concept of a hybrid diagnostics model in which a nested neural network is used with genetic algorithm to form a hybrid diagnostics model. The nested neural network functions as a pre-processor or filter to reduce the number of fault classes to be explored by the genetic algorithm based diagnostics model. The hybrid model improves the accuracy, reliability, and consistency of the results obtained. In addition significant improvements in the total run time have also been observed. The advanced cycle Inter-cooled Recuperated WR21 engine has been used as the test engine for implementing the diagnostics model. [DOI: 10.1115/1.1995771]

Introduction

It is a commonly known fact that engine condition monitoring is an effective but complex way to improve safety and reduce operating and maintenance costs of gas turbines. Engine health monitoring systems have become increasingly important in recent years due to the development of engines with improved power to weight ratios. Additionally, the need to show enhanced reliability at reduced costs will require major advances in engine controls and engine fault diagnosis capability. In the fundamental sense, performance monitoring and fault diagnosis involves processing of engine measurements. In all the cases, a comparison of some parameter values of an engine under examination is performed with the corresponding values of an engine which is considered "healthy." The parameters used and the method of analyzing them characterizes each different diagnostic method. Broadly speaking, these techniques have not changed much from the 1970s and mainly rely on what is known as the Gas Path Analysis (GPA) [1,2]. The advantages and limitations of the GPA have been extensively debated and different ways to overcome the limitations were proposed [3]. In recent times the use of artificial intelligence techniques and optimization techniques like the genetic algorithm have been on the rise. Interesting research has been undertaken by several researchers [4,5] including work on Kalman filters [6]. Zedda and Singh [7] used the ANN technique for engine fault diagnosis and Sensor Fault Diagnosis and Isolation (SFDI) and reported high accuracy.

Engine Fault Diagnostics Using Ga

The use of a genetic algorithm for engine fault diagnostics has been investigated by several authors in the recent past and reported good accuracy. Zedda [8] used this technique for developing a diagnostics model for the EJ200 engine with test bed instrumentation. Gulati [9] extended the technique to a poorly instrumented engine using the concept of multiple objective point analysis. He validated the technique on the RB199 engine. Sam-

path et al. [10] have used the GA based technique for investigating faults in advanced cycle engines like the ICR WR21 and reported considerable success. All the methods used a similar objective function given by Eq. (1).

$$J(x) = \sum_{j=1}^M \frac{|z_j - h_j(x, w)|}{z_{odj}(w) \cdot \sigma_j} \quad (1)$$

Integrated Fault Diagnostics Model

The diagnostics system developed for the advanced cycle ICR WR21 was able to detect the component faults and instrumentation faults to reasonable accuracy. However, the model had its own limitations, particularly the long run times and, therefore, has necessitated further enhancement. It is clear that the center of gravity of the algorithm lies in the calculation of the objective function, which in turn is mapped to the fitness function. The fitness function is the parameter which dominates the search process.

The calculation of the objective function requires the performance model to be run twice (clean condition and faulty condition). Therefore, any reduction in the number of calls to the performance model can significantly reduce the overall run time of the algorithm. It has been estimated that the engine performance code run constitutes almost 75%–80% of the total runtime.

After carrying out a detailed study of the problem, several techniques have been worked out to overcome the limitations, while enhancing the accuracy, consistency, and reliability of the diagnostics system. The speed of convergence of the performance model is beyond the control of a diagnostics engineer, but one way to overcome this problem is to make fewer calls to the performance code. Perhaps, the use of a function or a response surface which is a suitable representation of the engine performance model for the initial generations to eliminate the weaker individual can reduce the total run time.

Response Surface Method

In many problems we have specific knowledge that allows us to construct approximate models of our problem. In turn, modeling capability allows us to create more or less accurate approximations to our objective function. With genetic algorithms, this knowledge can be put to good use by reducing the number of

Contributed by the International Gas Turbine Institute (IGTI) of ASME for publication in the JOURNAL OF ENGINEERING FOR GAS TURBINES AND POWER. Manuscript received October 1, 2003; final manuscript received March 1, 2004. IGTI Review Chair: A. J. Strazisar. Paper presented at the International Gas Turbine and Aeroengine Congress and Exhibition, Vienna, Austria, June 13–17, 2004, Paper No. GT2004-53914.

full-cost function evaluations. In many optimization and search problems, a single function evaluation is a fairly costly process, involving many layers of subroutines, numerical or symbolic computation, iterations and various coding and decoding functions. As a result, if savings in computation time are possible through approximate, perhaps a rough estimation, of the objective function, they are worth pursuing so that more evaluations can be performed in the same time. Interesting work in this regard have been carried out by Montgomery [11] and Myers [12]. This observation is particularly relevant to genetic algorithms, as we expect GAs to behave robustly under error and noise because of their population -sampling approach.

In this case a response surface is a complex nonlinear function representing the engine performance model. The aim of the response surface method is to obtain an objective function of a given string without having to run the performance code. This method, which completely avoids the performance model, is very useful in the earlier generations of the GA diagnostics model. A suitable representation of the performance code is essential in order to implement this technique, which can be beneficial in speeding up the overall process. The rationale behind this concept is to avoid spending time on evaluating strings which are to be discarded in the initial generations.

In order to implement the response surface method, the traditional objective function shown in Eq. (1) needs to be modified by splitting it into two objective functions. Since the response surface is created by implanting faults and comparing it with baseline values, the objective function obtained from the response surface will be with respect to the baseline and needs to be compared with the objective function obtained from the actual data and baseline. The modified objective function is given by:

$$\Delta J = \left| \sum_{j=1}^{NM} \frac{|z_j^b - h_j(x, w)|}{z_{odj}(w) \cdot \sigma_j} - \sum_{i=1}^{NM} \frac{|z_i^b - z_i^s|}{z_{odj}(w) \cdot \sigma_i} \right| \quad (2)$$

The parameters are the same except for the superscripts "b" and "s," which mean baseline and simulated, respectively. A set of measurements is obtained from the engine and is compared with the corresponding baseline (clean parameters) measurements. An objective function is calculated which is designated as J_1 . This is required to be calculated only once. The other objective function, J_2 , is directly obtained from the response surface. The optimization of ΔJ (difference between J_1 and J_2) tends to achieve the best solution or more appropriately, eliminates the bad solutions.

At this point it is pertinent to mention that the optimization of ΔJ shown in Eq. (2) may not produce the exact match, for the reason that faults with different signatures could also have similar values of objective function. The fault signatures producing J_1 and J_2 could be different and it is not the same as calculating J between the faulty data and the simulated parameter using Eq. (1). However, what is important at this stage is to identify the strong individuals and create a condition for the weak individuals to be eliminated early in the search process. The calculation of J_1 gives the sum of deviations from the baseline. This value indicates that, deviations producing J_2 , which are close to J_1 in magnitude are likely candidates for further examination. At this point, the signs of deviations are not considered as they will be eliminated when the objective function is calculated with measurements obtained from the performance model using Eq. (1).

Data for the response surface is generated using the engine performance model. It is very similar to generating the search space by varying the engine performance parameters (component flow capacities and efficiencies) in small steps from its baseline values and implanting it into the engine performance model. A set of measurements are obtained for these conditions and compared with corresponding engine baseline parameters. The sum of the deviations is the objective function. This data is used to generate a response surface. Some of the ways to develop a response surface which have been investigated are enumerated below.

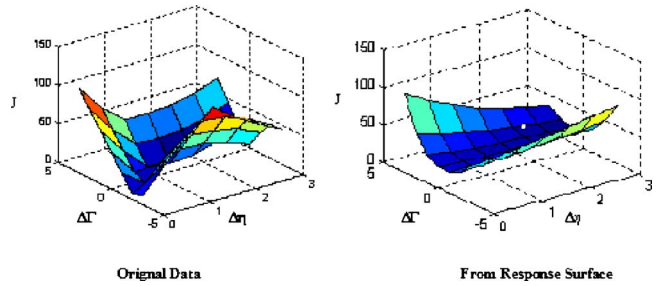


Fig. 1 Objective function using Gaussian function

The first method involved the development of a general regression function using the Gaussian functions and high-order polynomials. A sample is shown by Eq. (3) which represents a complex function like the search space. The aim is to evolve an equation which can readily return an objective function when given a set of deviation in the engine performance parameter. Once the regression coefficients have been obtained, the reanalysis and sensitivity analysis represented by Eqs. (3) and (4) require trivial computational effort. The constants and coefficients have been obtained using the MATLAB statistical toolbox.

$$f(x, y) = Ae^{(-b_1x-b_2y)} + Be^{(-b_3x-b_4y)} + \dots \quad (3)$$

in the case of engine fault analysis the equation can be re-written as

$$J_{RS} = Ae^{(-b_1\Delta\eta-b_2\Delta\Gamma)} + Be^{(-b_3\Delta\eta-b_4\Delta\Gamma)} + \dots \quad (4)$$

Figure 1 shows a comparison between the original data and the data generated from the response surface generated using the Gaussian function shown in Eq. (4). It is evident that the response surface is barely able to reproduce the original data and, therefore, would not be of much value considering the fact that it is expected to reproduce the surface details to reasonable accuracy.

The second option was to use the Radial Basis Functions (RBF). RBFs have attracted a great deal of interest due to their rapid training, generality, and simplicity. They have been widely used for the Generalized Regression Neural Networks (GRNN). They are several orders of magnitude faster in training when compared to the standard back propagation but have a major disadvantage: After training, they are generally slower to use, requiring more computation to perform a classification or function approximation. It can approximate any arbitrary function between input and output vectors, drawing the function estimate directly from the training data. Furthermore, it is consistent, that is, as the training set size becomes large, the estimation error approaches zero. The accuracy of the estimated function is very high as long as the input vector is close to the training vector. The RBFs are highly localized and, therefore, need large amounts of training data. The large amount of training data creates a large number of nodes. Though the training is very quick, the function approximation is a computationally intensive process.

Having investigated the possibility of representing the search space in the form of a response surface using the first two options and carefully considering the advantages and disadvantages of the process, it was decided to investigate the possibility of using a FFBPNN for the generation of a response surface. The FFBPNN is a standard neural network widely used for classification. The FFBPNN are known to represent complex functions very accurately when trained with appropriate and adequate samples. Figure 2 shows the response surface developed using the data from Fault class-2 (Fault in HPC) The network (8-20-20-1) was trained using data generated by implanting faults in the engine performance model and the objective function calculated with measurements obtained and baseline measurements.

From Fig. 2 it can be seen that the data represented using FFBPNN is accurate for the same data set. It is a trade-off between the

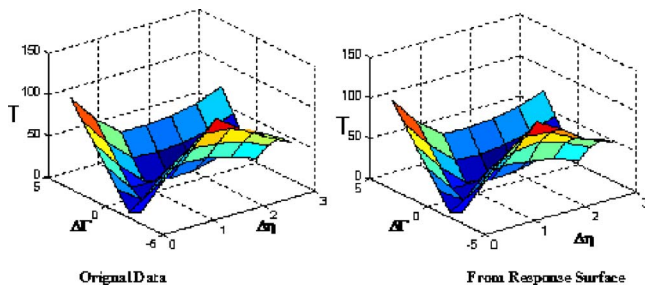


Fig. 2 Data representation using FFBPN

other two methods and can be used effectively in the initial stages of the search process. While the calculation of an objective using the engine performance model takes a significant portion of a second, several hundred objective functions can be obtained during the same time using the response surface.

The number of generations for which the RSM is not fixed and is a matter of choice. Experiments show that using the RSM for the initial 25% of the total number of generations is beneficial.

Though a considerable amount of time can be saved by using the RSM, However, the algorithm has to search all the fault classes in order to arrive at a solution. Figure 3 shows a typical optimization process consisting of 100 generations out of which 25 generations use the RSM to compute the fitness values of strings. The diagnosis of multiple component faults lead to a large number of fault classes to be explored, which in turn leads to large run times. The number of fault classes that need to be searched could be further reduced by developing a hybrid system in which a pre-processor algorithm can be used to classify the fault classes into the appropriate groups and suggest a single/group of fault classes to be explored by the GA optimizer.

There are several fault diagnostics techniques and optimization techniques which can be combined with the GAs to form a hybrid system for efficient fault diagnostics. Researchers like Gulati [6] have suggested the use of the GA for a broader search and the use of calculus-based methods for the local search. The approach adopted here is to identify a method which could be used to reduce the number of fault classes, so that the GA module can be used to search the fault classes for faulty components and quantify the fault. The rationale behind this is to avoid searching fault classes which are not likely to have faulty components.

Hybrid Diagnostics Model Using Ga and ANN

When problem specific knowledge exists, it may be advantageous to consider a GA hybrid. Genetic algorithms can be crossed with various problem specific search techniques to form a hybrid

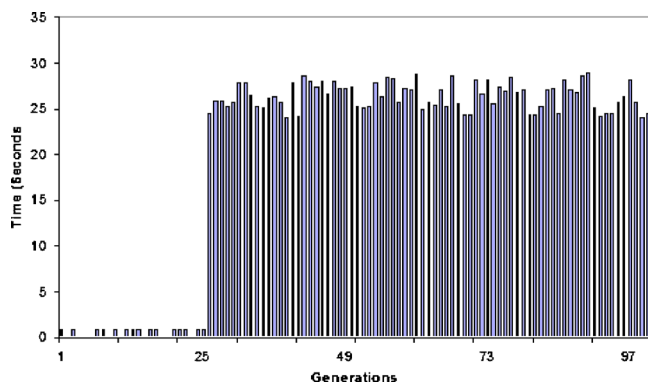


Fig. 3 Comparison of time taken for objective function

that exploits the global perspective of the GA and the convergence of the problem specific technique. A number of authors have suggested such hybridization (Bethke [13]; Bosworth et al. [14]; Goldberg [15]). However, there is not much published work describing the results of GA-hybrid studies. Nonetheless, the idea is simple, has merit and may be used to improve the ultimate genetic search performance.

For the problem in hand, an analogy can be drawn with the diagnostic engineers of yesteryear, when modern-day engine fault diagnosis techniques were in their infancy and when an analyst would make an intelligent assessment based on certain thumb rules. The method used was similar to the fault tree method in which the branches of the fault tree are traversed by eliminating certain criteria to arrive at the fault. The fault tree technique has the limitation that only single component faults can be identified. However, in the case of the proposed hybrid system, a Fault Class Classifier (FCC) is expected to identify the likely fault class(es) and the GA optimizer would subsequently explore the fault classes and quantify the faults associated with the components.

An extensive literature study showed that the feed forward back propagation network remains an effective paradigm and is by far the most commonly applied neural network for classification problems. Ogaji and Singh [16] have successfully used the concept of cascade neural networks for component and sensor fault identification. An informal count indicates that more than 85% of published applications have used the FFBPN. In difficult applications where the input-output relationships are nonlinear and/or involve high-order correlations among the input variables, back propagation has produced accurate results. The disadvantage of its slow training is partially offset by its rapid computation in the forward direction.

It was felt that the ability of the ANN to classify the given data with a relatively small network can be used to act as a preprocessor for the GA diagnostics. Even if the neural network is able to classify the given data as a single or multiple component fault, the search time is reduced to 25% of the original time in the case of single component faults (the GA module has to search only the first 7 fault classes) or 75% of the original time in case of multiple components fault (the GA module has to search 21 fault classes).

A schematic diagram of the concept of the hybrid model is shown in Fig. 4. The hybrid model consists of a Nested Neural Network (NNN) in which each network has a limited task of classifying the data into subgroups.

Perhaps, one way to classify is to train a network for all possible combinations of faults. But the training set required to fully represent all possible combinations of health parameters and sensor biases will be prohibitively large. It would take excessive time to train such a neural network and their performance might not reach satisfactory levels. In the light of the above, the problem domain has been partitioned into smaller and specific tasks. A node in the NNN is trained to classify the given input into any one of the subcategories, usually two or more subcategories or BRANCH nodes (described later).

This approach has been found to be more accurate when compared to training a single large network to identify the faulty components. The dark line shows the flow of the algorithm to arrive at the final stage, for an arbitrary set of measurements. The nodes are classified into "BRANCH" nodes and "TERMINAL" nodes. The bottom most level of each branch/path consists of the terminal nodes. The "TERMINAL" nodes have an important task of extracting and submitting the fault class(es) for optimization by the GA Module.

Input data from an engine is fed into the NNN pre-processor. The first step is to identify whether the input data was generated due to a faulty component or a faulty sensor. Once the classification has been made, the data is forwarded to the next level. If the input data is associated with a component fault, then it is forwarded to a node classifying the input data into Single or Multiple component faults. In the same way, the input data traverses

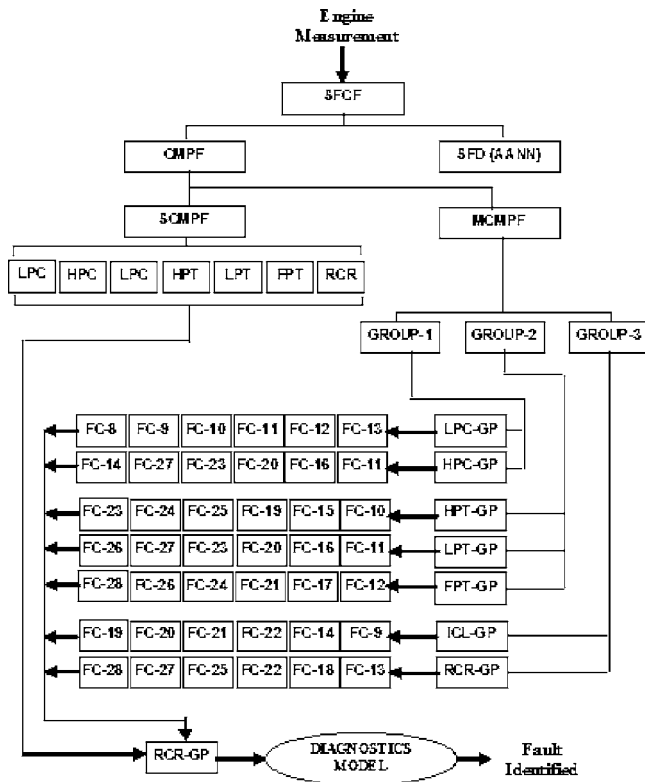


Fig. 4 Schematic of a hybrid diagnostics model

through the BRANCH nodes and arrives at the TERMINAL node. A terminal node will classify the input data into a single fault class or a group of fault classes to be explored by the GA optimizer.

Whether in classification or regression, it is necessary to employ appropriate training algorithms. For the feed forward back propagation network, various training algorithms such as resilient backpropagation, delta-bar-delta, conjugate gradient algorithms, Levenberg Marquardt, Bayesian regularization, etc. are available. The choice of algorithm is usually a trade-off between many factors such as minimum RMS error obtainable, length of training time or speed of convergence, memory requirements, nature of the problem. The choice of the algorithm is left to the user and the type of problem being solved.

In the present work, several algorithms were tested and the conjugate gradient method was found to be most suitable from the point of the speed of convergence and memory requirement. The algorithm gave good results by improving the generalization especially with respect to classification, which is the main require-

ment in the model. The radial basis functions were also experimented but they need a large amount of nodes and that gives a particularly good result if the input data is close to the training data.

The number of layers and number of processing elements per layer are important decisions to be made during the design of an ANN. The number of processing elements in the input and output layers are fixed by the number of input measurements and required output vectors, respectively, and, therefore, only the number of hidden layers and number of processing elements in the hidden layers are to be determined. There are no good solutions to this problem and is again dependent of the nature of the problem being addressed. In general, as the complexity in the relationship between the input data and the desired output increases, then the number of processing elements in the hidden layer should also increase. The number of processing elements may also depend on the amount and the quality of training data. It is noteworthy that a fewer number of processing elements would mean there are insufficient network parameters (weights and biases) to undertake the required tasks (which leads to under learning of the problem domain), while more than necessary processing elements in the hidden layers would lead to poor generalization as the features of the training patterns are memorized (making the network less capable to apply knowledge learned to patterns that were not included in the training process though within the problem domain). In other words, the network becomes useless on new data sets.

Table 1 shows the description of individual nodes. The letter "L" denotes the level and the number gives the level number. The letter "N" denotes the node and the number suffixed shows the position of the node in a particular level. Each node has a specific function to perform as part of the network. Table 2 shows the type of network and configuration of the individual nodes in the nested neural network.

Various configurations of the MLPs were tried and the configuration shown in Table 2 was found to give good classification. The fault classes used to train the nodes are shown in the last column of Table 2.

Confidence Rating of Networks

Once the individual networks have been trained to classify data into specific subgroups, they can be integrated to form a nested neural network for different levels of classification. Before entrusting the networks with the classification job, a Confidence Factor (CF) of each network has to be established to have confidence in the final output from the NNN. The CF of each network is obtained by simulating the network output with a large amount of randomly generated data set for that particular node. This is an important aspect of the HDM as the GA module depends on the classification ability of NNN. As it was described earlier, the nodes, particularly the TERMINAL nodes, are not constrained to give one fault class, but can suggest a set of fault classes to the

Table 1 Description of nodes

Node	Designation	Function
LIN1	SFCF	Classifies Sensor fault and Component Fault
L2N1	CMPF	Classifies between Single or Multiple Component Faults
L2N2	SFD	Identifies Sensor Fault
L3N1	SCMPF	Identifies fault classes in case of single component fault
L3N2	MCMFP	Classifies multiple fault component faults into subgroups
L4N1	GROUP-1	Classifies the faults with compressors into LP and HP groups
L4N2	GROUP-2	Classifies the faults with turbines into subgroups
L4N3	GROUP-3	Classifies the faults with ICL and RCR into subgroups
L5N1	LPC-GP	Identifies fault classes with LPC as a common component
L5N2	HPC-GP	Identifies fault classes with HPC as a common component
L5N3	HPT-GP	Identifies fault classes with HPT as a common component
L5N4	LPT-GP	Identifies fault classes with LPT as a common component
L5N5	FPT-GP	Identifies fault classes with FPT as a common component
L5N6	ICL-GP	Identifies fault classes with ICL as a common component
L5N7	RCR-GP	Identifies fault classes with RCR as a common component

Table 2 Configuration of nodes

Network	Type	Configuration	FCs-Involved in training
L1N1	MLP	10-30-30-2	FC-1: FC-28
L2N1	MLP	10-30-30-2	FC-1: FC-28
L2N2	AANN	10-30-4-30-10	MEASUREMENTS
L3N1	MLP	10-25-25-3	FC-1: FC-7
L3N2	MLP	10-30-30-2	FC-8: FC-28
L4N1	MLP	10-25-25-2	FC-8:FC-18
L4N2	MLP	10-25-25-2	FC-23:FC28
L4N3	MLP	10-25-25-2	FC-19:FC22
L5N1	MLP	10-25-25-3	FC-8:FC-13
L5N2	MLP	10-25-25-3	FC-14:FC-18,FC-8
L5N3	MLP	10-25-25-3	FC-23:FC-25,FC-19,FC-15,FC-10
L5N4	MLP	10-25-25-3	FC-26,FC-27,FC-23,FC-20,FC-16,FC-11
L5N5	MLP	10-25-25-3	FC-28,FC-26,FC-24,FC-21,FC-17,FC-12
L5N6	MLP	10-25-25-3	FC-19,FC-20,FC-21,FC-22,FC-14,FC-9
LFN7	MLP	10-25-25-3	FC-28,FC-27,FC-25,FC-22,FC-18,FC-13

GA module. This feature has been provided to reduce the probability of a wrong fault class being given to the GA module. While classifying the fault classes the CF of that node plays an important role in the number of fault classes being suggested. The higher the CF the lesser will be the number of fault classes suggested, and also more confidence in the fault classes suggested.

High CF is particularly necessary in the BRANCH nodes as the decision made at the branch level is crucial for the progress of the solution in the correct direction. It is also possible that under some extreme conditions the network makes an incorrect classification in the beginning, which can lead to input data being passed through the wrong branches.

To avoid such a situation, different network topologies can be used for classification. Different topologies would mean longer training time. However, once the networks are trained for a particular operating point, the classification is instantaneous. The confidence factors shown in Table 3 have been obtained by subjecting the nodes to a large amount of test data. The various decisions made at the BRANCH nodes and TERMINAL nodes are dependent on these CF values. The CFs for classification of individual nodes and the layer are obtained and is indicative of the confidence one can have in the classification ability of the nodes

Discussion of Results From HDM

The process starts with a node classifying the input data as having a component fault or a sensor fault. If it is identified as a sensor fault, the data is forwarded to an Auto-Associative Neural Network (AANN) for isolation of faulty sensor(s) as well as assessment of the fault magnitudes. On the other hand, if a pattern is identified as a component fault by the node, it is then passed to the next node which classifies it as a single component or multiple component faults. If it is identified as a single component fault then the input data is passed onto to a node which further classifies it into the appropriate category (fault class). If it is classified as a multiple components fault, then it is forwarded to nodes for classification to appropriate subgroups and finally classified into fault classes. A brief description of the constituent nodes is presented:

Node L1N1. The test measurements are introduced to this node which is trained to accomplish an important task of classifying the data into: Component fault or sensor. The node was subjected to a series of rigorous tests with randomly simulated test patterns as follows:

Table 3 Confidence ratings of nodes in the NNN

NODE	CLASSIFICATION OF CATEGORIES (%)						CF(%)	
L1N1	SF		CF				99.36	
	99.45		99.27					
L2N1	SCMPF		MCMPF				94.54	
	96.23		92.86					
L3N1	FC-1	FC-2	FC-3	FC-4	FC-5	FC-6	FC-7	99.74
	99.90	99.97	99.88	99.54	99.92	99.71	99.25	
L3N2	GROUP-1		GROUP-2		GROUP-3			98.87
	99.83		99.52		97.12			
L4N1	LPC-GP		HPC-GP					99.80
	100.00		99.60					
L4N2	HPT-GP		LPT-GP		FPT-GP			99.80
	98.44		98.87		99.26			
L4N3	ICL-GP		RCR-GP					98.95
	99.79		98.92					
L5N1	FC-8	FC-9	FC-10	FC-11	FC-12	FC-13		98.62
	98.50	99.17	97.88	98.54	98.92	98.71		
L5N2	FC-14	FC-15	FC-16	FC-17	FC-18	FC-8		98.47
	97.62	99.23	98.38	97.94	99.12	98.54		
L5N3	FC-23	FC-24	FC-25	FC-19	FC-15	FC-10		98.67
	98.49	99.56	98.67	98.89	97.84	98.59		
L5N4	FC-26	FC-27	FC-23	FC-20	FC-16	FC-11		98.34
	97.68	98.64	99.33	98.21	98.72	97.48		
L5N5	FC-28	FC-26	FC-24	FC-21	FC-17	FC-12		98.01
	97.29	99.09	97.78	98.67	97.37	97.88		
L5N6	FC-19	FC-20	FC-21	FC-22	FC-14	FC-9		98.43
	97.56	99.27	98.59	98.74	97.92	98.51		
L5N7	FC-28	FC-27	FC-25	FC-22	FC-18	FC-13		98.03
	97.34	99.21	96.73	98.67	97.45	98.78		

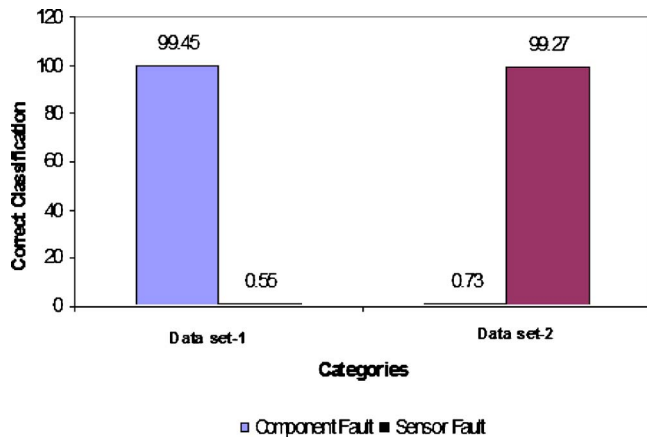


Fig. 5 Results from L1N1 classification

- data with only sensor faults
- data with only component faults
- data with component and sensor faults (not occurring simultaneously)

The break down of the classification by L1N1 is shown in Fig. 5. Data set-1 has patterns only from component faults and Data set-2 has patterns only from sensor faults.

The accuracy achieved by the network was over 99%. Investigation of the misclassified data revealed that some input data with low levels of sensor faults were classified as having component faults or input data with low levels of component faults were classified as having sensor faults. The levels of faults involved were very small and, therefore, the patterns were indistinguishable. For practical sense, such faults would not make a significant impact on the performance of the engine or endanger the safe operation of the engine. It should be noted that the data from 28 fault classes are involved and, therefore, the network is subjected to a large amount of data and needs good generalization capability.

Node-L2N1. This node is required to classify the input data as having a single component fault or multiple component faults (restricted to a maximum of two components simultaneously faulty). The node was subjected to a series of tests with randomly generated fault data. The classification accuracy or the overall confidence factor achieved was 94%. The individual break down of classification is shown in Fig. 6. Data set-1 consists of only single component faults and data set-2 consists of only multiple compo-

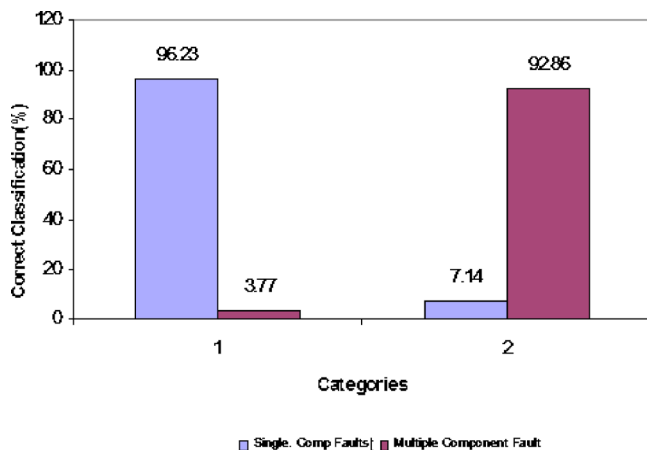


Fig. 6 Results from L2N1 classification

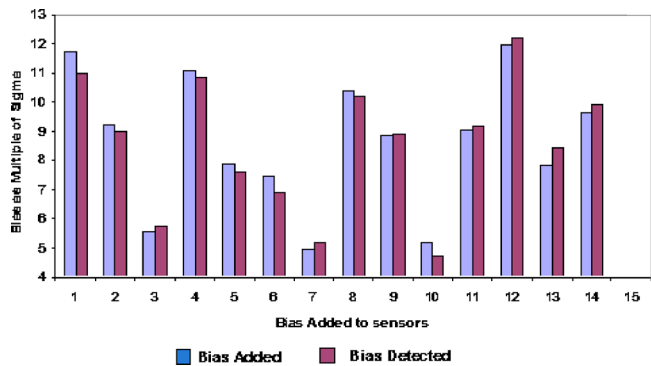


Fig. 7 Results from L2N2 node (Sensor bias detection)

nent faults.

The network achieved low accuracy due to the large variety of data involved in the training. The training data involved patterns from 28 fault classes, which implies various combinations of components and different fault levels. Therefore, the network generalization capability was poor. Many cases of overlaps in classification among the two categories were found. Further investigation revealed that single component fault with high fault levels were classified as multiple component faults and multiple component faults with very low fault levels were classified as single component faults. However, the misclassification does not seriously affect the diagnostics process, as closer examination showed that a single component fault misclassified as a multiple component fault normally detects the fault class which has the same component as the actual faulty component (single component fault) and “smears” as small amount of the fault to the other components. When multiple component faults are classified as single component faults, it is normally observed that one of the components has a low level fault and the other, which has a high level fault, can be identified by the nest level.

Node-L3N1. This is a TERMINAL node and is required to provide the fault classes for further examination by the GA module. This node exhibits a high level of classification accuracy as the patterns produced by the faults in the components are distinguishable by the network. The task of classification can be carried out by a network smaller than the ones used for the above two networks, i.e., L1N1 and L2N1. In general, if the confidence rating of the network is very high, it would identify only one fault class to be examined by the GA module. However, in order to make the NNN robust, a simple logic is incorporated, which considers the individual fault class classification levels before deciding the fault class(es) to be examined.

Node L2N2 (Sensor Fault Diagnosis). Once the L1N1 node identifies the data as having sensor fault, the input data is forwarded to the node identifying the sensor faults. The Auto-Associative Neural Network (AANN) is found to be most appropriate for the sensor fault diagnostics. The AANN basically consists of several layers of nodes which form a symmetrical structure with a bottleneck. The number and configuration of the nodes on either side of the bottleneck layer are identical. Several test were carried out to validate the performance of the node in isolating the faulty sensors. Bias ranging from 4σ to 15σ for respective instruments were used to generate the faulty sensor data. A sample of a bias implanted in the HPC (Exit) pressure sensor is shown in Fig. 7. The bias levels have been correctly identified by the network in all the cases. The small deviations in the identified values are mainly due to the measurement noise. It was observed that, small levels of bias which are close to noise levels are more difficult to isolate.

The hybrid model attempts to combine the strengths of two different techniques to create a more robust diagnostics model.

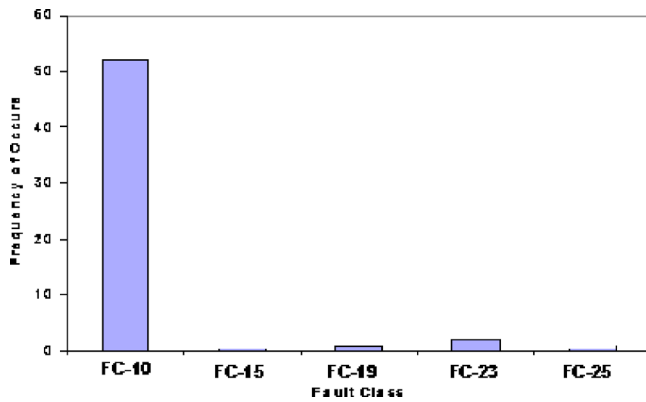


Fig. 8 Results from multiple runs of HDM

The ANNs are known to have good classification properties and also the ability to represent a complex function which is otherwise difficult to solve analytically. The hybrid system developed has reduced the total run time of the fault diagnostics model significantly. The reduction in the run time gives the opportunity for the diagnostics model to be run several times to ascertain the fault identified.

The long run times of the initial GA based diagnostics model was a discouraging factor in the implementation of the model. However, the HDM reduces the overall runtime which makes it possible to run the model several times to increase the confidence in the output. The FCC could suggest more than one fault class (depending on the CF of TERMINAL node) to be explored by the GA model. In a test case, the FCC suggested five fault classes to be explored (instead of 28). The GA diagnostics model uses probabilistic transition rules and, therefore, it is also possible that occasionally the model detects the faults in other fault classes erroneously, especially the competing fault classes, this is attributable mainly to the randomness in the application of the GA operators coupled with the measurement noise and model inaccuracies. The GA based diagnostics model was ran 60 times and it has identified the FC-10 to have the faulty components shown in Fig. 8.

A distribution of the faults quantified by the GA based diagnostics model is shown in Fig. 9. It can be seen that the average of the deviations are close to the implanted values and also the extreme values are within the acceptable limits. It is more important to identify the faulty component more accurately than the actual quantification of the fault as on most occasions the remedial action might be the same. E.g., if the actual fault had a 2% drop in compressor efficiency and the diagnostics model detected 2.5%, the corrective action remains unchanged.

Figure 10 shows a comparison of the overall runtimes for various schemes taken for the ICR WR21 engine. The MOPA based diagnostics model developed initially took ~22 h for convergence. The IFDM1 (with 25% RSM) took about 18 h and the IFDM2 (with 50% RSM) took close to 12 h. The HDM took

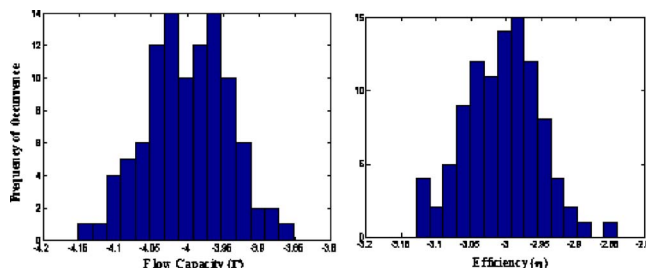


Fig. 9 Distribution of fault quantification

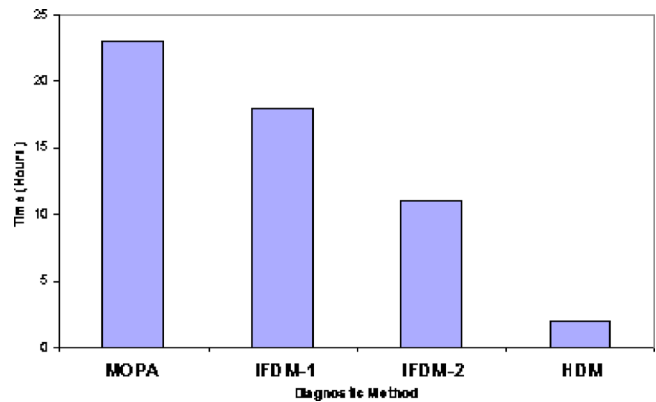


Fig. 10 Comparison of run times for different schemes

about 2 h to converge to a solution. It is ten times faster than the initial model developed. In fact this time can further be reduced if the terminal node can suggest only one fault class to be searched (in the present case it has suggested five Fault classes).

Comparison with Other Methods

In the present study and related studies in the past, the GA based engine diagnostics technique has been tested quite extensively for various combinations of component faults and instrumentation faults while varying the level of noise. It has been observed that the technique has certain advantages when compared with other techniques. One of the main advantages is that the technique is robust and consistent in the face of instrument noise and also the implementation of the Sensor Fault Detection and Accommodation is simple. The GA based method works with a group of solutions and once a reasonably close solution is identified, further refinement is possible. The GA based technique has the ability to detect very small deviations in component performance parameters due to its solution refinement capability. One major limitation in the implementation of the technique, is the long time taken for the algorithm to converge. While the initial GA based methods [9,10] took several hours to converge, the hybrid method developed by the authors has been successful in reducing the run times significantly (~10–12 times). However, the run time still remains large when compared with other techniques. A comparison of four different diagnostics method was conducted using the WR21 performance code and a sample result is presented in Table 4. It is evident that the GA based method scores over the other methods in identifying the fault levels which are very small.

A comparison of the overall fault identification capability was obtained by introducing the same set of one hundred faults to the four different diagnostics techniques. It can be observed from Fig. 11 that the GA based technique has been able to successfully identify the faults in almost 95% of the cases.

Table 4 Comparison of different diagnostics techniques

Method	Component-LPC		Component-HPT		RMS Error
	η	Γ	η	Γ	
Fuzzy Logic	-1.0	-2.6	-0.2	1.3	0.83
Gas Path Analysis	-0.82	-2.1	-1.1	1.2	1.29
Neural Network	-0.95	-2.87	-0.8	1.5	0.45
Genetic Algorithm	-1.12	-3.11	-0.56	1.88	0.16

*Fault Implanted. Percentage Deviation in: LPC: η : -1.2% Γ : -3.0% Percentage Deviation in: HPT: η : -0.6% Γ : 1.8%

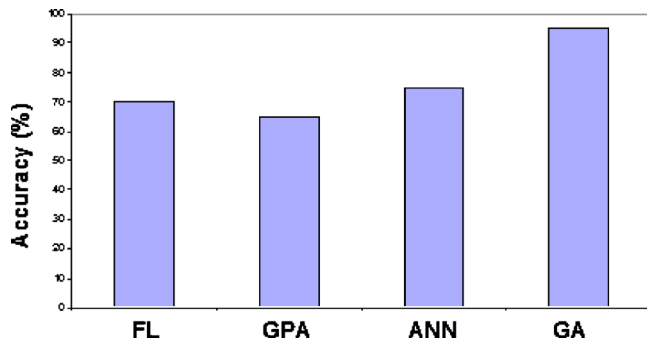


Fig. 11 Comparison of accuracy of fault detection

Large deviations in component performance parameters have been identified by all the techniques correctly with comparable RMS errors. However, the GA based technique has been able to identify more faults of small magnitudes and, therefore, has been shown to have identified a higher percentage of faults for the given sample data.

Conclusion

In this paper a novel method of combining the ANN and GAs have been examined. Though the diagnostic model based purely on the GA had merit but was reported to have long run times and, therefore, necessitated modification in order to be implemented for engine fault diagnostics. Despite research in the various methods for engine fault diagnostics, there is still no “magic formula” which can effectively address all issues. One way to approach the problem is to try and offset the limitations of one technique with the strength of the other. The hybrid model developed, to an extent, has attempted to bridge this gap. The results obtained were encouraging and further investigation is being carried out to make it more efficient.

Nomenclature

- Γ = flow capacity
- η = efficiency
- Δ = small change
- J = objective function
- σ = standard deviation for noise

Abbreviations

- RBF = radial basis function

- AANN = auto associative neural network
- ANN = artificial neural network
- CF = confidence factor
- FC = fault class
- FFBPNN = feed forward back propagation neural network
- GA = genetic algorithm
- GPA = gas path analysis
- HDM = hybrid diagnostics model
- HPC = high pressure compressor
- ICR = inter-cooled recuperated
- NNN = nested neural network
- FCC = fault class classifier
- RSM = response surface method
- MLP = multi-layer perceptron

References

- [1] Doel, D. L., 1994, “TEMPER: Gas-Path Analysis Tool for Commercial Jet Engines,” ASME J. Eng. Gas Turbines Power, **116**(1), pp. 82–89.
- [2] Doel, D., 2002, “Interpretation of Weighted-Least-Squares Gas Path Analysis Results,” ASME Turbo Expo 2002, June 3–5, Amsterdam.
- [3] Deol, D. L., 1993, “Gas Path Analysis—Problems and Solutions,” Symposium of Aircraft Integrated Monitoring Systems, Sept. 21–23, Bonn, Germany.
- [4] Mathioudakis, K., Kamboukos, P., Stamatis, S., 2002, “Turbofan Performance Deterioration Tracking Using Non-Linear Models and Optimization Techniques,” ASME TE-2002, June 3–5, Amsterdam, The Netherlands.
- [5] Kamboukos, P., and Mathioudakis, K., 2002, “Comparison of Linear and Non-Linear Gas Turbine Performance Diagnostics,” ASME TE-2003, June 16–19, Atlanta, GA.
- [6] Kobayashi, T., and Simon, D. L., 2003, “Application of a Bank of Kalman Filters for Aircraft Engine Fault Diagnostics,” ASME TE-2003, June 16–19, Atlanta, GA.
- [7] Zedda, M., and Singh, R., 1998, “Fault Diagnosis of a Turbopfan Engine Using Neural Networks: A Quantitative Approach,” Paper No. AIAA 98-3062.
- [8] Zedda, M., and Singh, R., 1999, “Gas Turbine Engine and Sensor Fault Diagnosis Using Optimisation Techniques,” Paper No. AIAA 99-2530.
- [9] Gulati, A., 2002, “An Optimization Tool for Gas Turbine Engine Diagnostics,” Ph.D. thesis, School of Engineering, Cranfield University, UK.
- [10] Sampath, S., Gulati, A., and Singh, R., 2002, “Fault Diagnostics Using Genetic Algorithm for Advanced Cycle Gas Turbine,” ASME TE-2002, June 3–5, Amsterdam, The Netherlands.
- [11] Montgomery, D. C., 1984, “Design and Analysis of Computer Experiments,” 2nd ed., Wiley, New York.
- [12] Myers, R. H., 1999, “Response Surface Methodology Current Status and Future Direction,” J. Quality Technol., **31**(1), pp. 30–74.
- [13] Bethke, A. D., 1981, “Genetic Algorithm as Function Optimizers,” Doctoral dissertation, University of Michigan.
- [14] Bosworth, J., Foo, N., and Zeigler, B. P., 1972, “Comparison of Genetic Algorithms With Conjugate Gradient Method,” National Aeronautics and Space Administration, Washington, DC, Report No. CR-2093.
- [15] Goldberg, D. E., 1989, *Genetic Algorithms in Search, Optimization and Machine Learning*, Addison-Wesley, Reading, MA.
- [16] Ogaji, S. O. T., and Singh, R., 2002, “Gas Path Fault Diagnosis Framework for a 3-Shaft Gas Turbine,” IMechE Journal of Power and Energy, **217**, A3.

Assessment of the Effectiveness of Gas Path Diagnostic Schemes

K. Mathioudakis
Associate Professor

Ph. Kamboukos
Research Assistant

Laboratory of Thermal Turbomachines,
National Technical University of Athens,
Iroon Polytechniou 9,
Athens 15773, Greece

A variety of methods can be used for the diagnosis of faults in gas path components of gas turbines. Problems that are common for diagnostic method implementation are the choice of measured quantities, choice of health parameters, and choice of operating conditions for data retrieval. The present paper introduces some general principles for evaluation of the effectiveness of different diagnostic schemes. They encompass criteria proposed in past publications, while they offer additional possibilities for assessment of diagnostic effectiveness in various situations. The method is based on the evaluation of the behavior of linear systems, which are a good approximation of the nonlinear ones for small deviations and employs the concept of system condition number to formulate criteria. The determination of limits for this number for establishing system condition criteria and quantification of observability is examined, on the basis of uncertainty propagation. Sample problems evaluated are: maximizing effectiveness of individual component identification from a multiplicity of available measurements, selection of individual operating points for multipoint applications. [DOI: 10.1115/1.1924535]

Introduction

A large variety of diagnostic methods for gas turbine faults based on gas path measurements exist today. Different types of approaches are employed, and a broad division can be into linear and nonlinear methods. An extensive review of methods that exist today has been provided by Li [1].

One of the main reasons for the development of many different methods is the fact that gas path measurements are difficult and costly to perform and are thus very limited in number, in contrast to the large number of parameters needed to be known for engine health assessment. On the other hand, measurement data are always contaminated by noise, and we are usually interested in minimizing the effect of its propagation into estimated health parameters.

It is for these reasons that an interest has risen in assessing the way of obtaining diagnostic information in an optimal way, in view of this type of restriction.

A systematic study for methods of choice of measurements and parameters in a way optimal as to diagnostic effectiveness was first presented by Stamatis et al. [2]. They introduced Criteria for optimal measurement or health parameter selection. In later years more works have appeared, approaching the problem from different angles, as for example the work of Provost [3], who employed correlation matrices to examine the existence of linear dependencies (see also a recent publication by Provost [4]). Kamboukos et al. [5] have also addressed this problem, but only as to the condition of the systems involved, while measurement and parameter selection was studied only for square problems.

Another aspect that has received more attention in recent years is the choice of operating points in multipoint techniques, since these techniques promise to provide the only solution for unbiased estimates in cases that measurements are fewer than parameters. Zedda and Singh [6], Gronstead [7], and Pinelli et al. [8] have proposed such methods.

In the present paper a unified approach is introduced, covering both the above groups of applications. It can be used to assess different types of problems, such as the measurement or parameter

optimal selection but also the operating points for a multi point method or the appropriate sets that are identifiable by a nonlinear method.

Diagnostic Algorithm Formulation

An engine is considered as a system observed through measured variables (denoted as Y), with operating point defined by set point variables (denoted as u), establishing a relation of the form

$$Y = F(u, f) \quad (1)$$

Engine components health condition is represented through appropriate "health parameters," denoted as f . Any mechanical or other alteration, which can be classified as engine fault, affects the performance of the damaged component and is expressed through deviations Δf_i of health parameters from the reference state. Overall performance of the engine is influenced, resulting to deviations ΔY_i on measured quantities.

A diagnostic method can determine the values of the condition parameters f from known values of measurements Y at given operating conditions u . This problem is usually expressed in a more effective way as the problem of deriving the deviations Δf from known deviations ΔY . A diagnostic algorithm that achieves this purpose can be represented through a general relation of the form

$$\Delta f = \mathcal{D}(\Delta Y) \quad (2)$$

The diagnostic operator \mathcal{D} represents the method employed. Examples of this operator are: For a square linear diagnostic problem this is the inverse of the Jacobian matrix of measurements with respect to variables. For measurements larger in number than parameters, this is the diagnostic matrix, formed with a design matrix Jacobian. For fewer measurements than unknowns this matrix is still called diagnostic matrix but the existence of a priori information is needed to derive a solution. For a nonlinear method it represents the inversion of the nonlinear relation (1).

The question that will be considered here is how to assess the behavior of a diagnostic operator for handling a particular diagnostic situation. The type of problems that can be studied are (a) the selection of the most appropriate measurements, (b) the selection of the appropriate health parameters, (c) the selection of operating points, for multipoint methods, (d) the selection of sets that can be handled by nonlinear methods.

Contributed by the International Gas Turbine Institute (IGTI) of ASME for publication in the JOURNAL OF ENGINEERING FOR GAS TURBINES AND POWER. Manuscript received October 1, 2003; final manuscript received March 1, 2004. IGTI Review Chair: A. J. Strazisar. Paper presented at the International Gas Turbine and Aeroengine Congress and Exhibition, Vienna, Austria, June 13–17, 2004, Paper No. GT2004-53862.

Criteria for Effective Estimation

The basic principle employed here is that study of the behavior of any diagnostic algorithm can be based on the linearized representation of Eq. (1):

$$\Delta Y = J \cdot \Delta f \quad (3)$$

where ΔY and Δf are column vectors of measurement and health parameter deltas, respectively, and J is the Jacobian matrix. This relation is a good approximation for most diagnostic situations, since the deviations of parameters or measurements is usually of small magnitude (for further discussion on linear versus nonlinear methods, see Kamboukos and Mathioudakis [9]).

When a linearized method is employed, this equation is the one actually forming the basis of the method. Even though, accuracy of estimates using this equation could be questionable for large deviation magnitudes, the fact is that the local behavior of an algorithm is well represented by this relation. The study of the linearized form of nonlinear control systems is a well-known practice for examining "local stability" in control theory (see for example Elgerd [10]).

When an algorithm is formulated, the fundamental question is whether the measurements available can lead to a unique set of values for the health parameters sought, namely if the materialization of Eq. (1) in a particular situation can produce an invertible system of equations. Inversion is not meant in the simple mathematical sense of existence of a unique solution, but rather in the sense of a system that can provide a numerically stable solution. A second question is how noise propagates through the solution of the system. The desire is to minimize the propagation of measurement noise into the estimates of health parameters.

The criterion we propose for studying the answer to the first question is the condition number of the equivalent linear relation for the diagnostic problem studied. The condition number of a square matrix A is defined as

$$\kappa = \|A\| \|A^{-1}\| \quad (4)$$

It is known that this number is indicative of the "magnification" of disturbances through a linear system of equations (see for example [11]) and represents the "condition" of the system. When the norm-2 for the matrix is used, the condition number is equal to the ratio of the maximum to minimum singular values of the matrix.

$$\kappa = \frac{\max\{w_j\}}{\min\{w_j\}} \quad (5)$$

This definition gives also a means of evaluation of the condition number, through use of the method of singular value decomposition. (Any $m \times n$ matrix A of rank r can be decomposed as a matrix product as follows: $A = U \cdot W \cdot V^T$ ($U_{m \times n}$, $V_{n \times n}$ are orthogonal matrices and W is a diagonal matrix with r nonzero elements, which are called the singular values of A . The columns of U and V are called left-hand and right-hand singular vectors of A , respectively. For more information see, for example, Meyer [11], while for implementation see Press et al. [12]), which is known to be the most robust method for this purpose. The way of using this number for assessing the different diagnostic situations examined will be discussed case by case in the different problems examined in the following.

The relation showing how the condition number of a matrix is related to amplification of disturbances is as follows: For a linear system $Ax = b$, a disturbance in the values of the components of the known vector b , is related to the disturbance of the obtained solution x , through the relation

$$\frac{1}{\kappa} \frac{\|b - \tilde{b}\|}{\|b\|} \leq \frac{\|x - \tilde{x}\|}{\|x\|} \leq \kappa \frac{\|b - \tilde{b}\|}{\|b\|} \quad (6)$$

where \tilde{x} is the estimated vector of unknowns and \tilde{b} the corresponding vector of knowns: $A \cdot \tilde{x} = \tilde{b}$.

This relation indicates that large condition numbers allow large amplification of disturbances. For the diagnostic problem expressed through Eq. (3), the implication is that noise in the measurements can be amplified in the estimated parameters. It is noted here that Eq.(6) does not indicate that disturbances *will* be magnified, but rather than they *may* be magnified. Therefore, noise may be kept small, but also may be much larger. Although a large condition number does not necessarily imply that amplification will be strong, a small one guarantees a weak amplification. From this perspective a requirement for a small condition number is a means of ensuring small noise amplification.

Concerning noise propagation, it is proposed that parameter noise is calculated by employing the well-known noise propagation formula:

$$\sigma_f^2 = \left(\frac{\partial f}{\partial Y_1} \sigma_{Y_1} \right)^2 + \left(\frac{\partial f}{\partial Y_2} \sigma_{Y_2} \right)^2 + \dots + \left(\frac{\partial f}{\partial Y_n} \sigma_{Y_n} \right)^2 \quad (7)$$

Although this formula can take more elegant form for the cases of specific form of linear systems, it will be used here in this generalized form to cover all different situations examined.

We will now discuss the problems of measurement selection, parameter selection and operating point selection, to demonstrate how the method is materialized for each type of problem.

Measurement Selection

Ideally, information for the condition of an engine component can be derived using sensors placed at its inlet and outlet, giving the full picture of the change that component causes to working fluid. Such an approach is not, however, acceptable for an engine on-duty, for several reasons: sensors and related systems are very expensive and increase engine complexity. Wall taps, pitot probes, thermocouples, cause flow disturbances. Measurements may not be possible at some locations, because of harsh local conditions (for example, turbine inlet). It is thus desirable to use a minimum number of sensors. The minimum set has to be chosen without sacrificing diagnostic ability. This type of situation is mainly of interest to the manufacturer for selecting the instruments to be placed on an engine for ensuring a good diagnostic ability. It can be also useful to the user who wants to modify an existing instrumentation set.

An indicative procedure was proposed by Stamatis et al. [2], using measurement sensitivity. Although the most sensitive measurements should be included in the monitoring set, one additional condition has to be fulfilled: the measurements chosen have to be linearly independent with respect to parameters deviations. A method to examine the degree of interdependence of measurements has been proposed by Provost [3], by evaluating angles between the vectors. When they are found sufficiently large, they indicate a weak interdependence. The method proposed here can deal with this problem in an efficient way, as explained in the following.

When N health parameters have to be estimated while M measurements are possible ($M > N$), we can select N out of these measurements to form a closed ($N \times N$) system. The ones that will be chosen have to ensure (a) that the system has a solution (b) that the solution of the system gives the minimum amplification to the measurement noise. The criterion thus introduced is: the set of measurements chosen is the one for which the condition number of the system expressed by Eq. (3) is minimum.

For determining which set satisfies this criterion we form a number of $N \times N$ submatrices of the $M \times N$ Jacobian. The number of these submatrices is given from the number of possible combinations of M available measurements taken N each time:

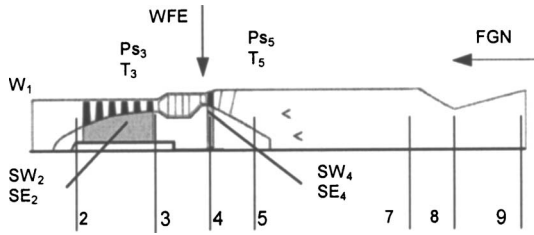


Fig. 1 Layout and station numbering for simple turbojet

$$L_{\text{combi}} = \binom{M}{N} = \frac{M!}{N! \cdot (M-N)!} \quad (8)$$

The combination with the minimum condition number is chosen.

At this point it must be said that the decision is taken using engineering judgment as well. Common practices in use, such as the desire to measure in the cold section of an engine, must be taken in to account, when the resulting combinations are inspected for selecting the most appropriate one.

Sample Application. Results from application to a case of turbojet engine are used to demonstrate the above principles. A computer model for a simple turbojet, resembling to the J79 engine, was used to simulate engine performance. The engine layout and the quantities measured are shown in Fig. 1. Even though this is a very simple engine configuration by today's standards, it lends itself as a good application example, to demonstrate the principles of the method.

A turbojet engine tested in a test cell has the possibility to provide measurements for compressor delivery pressure (P_{S3}) and temperature (T_3), turbine exhaust pressure (P_{S5}), and temperature (T_5), fuel flow rate (WFE), thrust (FGN), and air flow rate (W_1). We want to estimate the condition of compressor and turbine on the basis of these measurements and we want to select those that would provide an optimal diagnostic system. The health condition of the selected components is expressed through a flow factor SW_i and an efficiency factor SE_i .

First, the Jacobian matrix relating these measurements to compressor and turbine health parameters is evaluated and is as follows:

$$\begin{bmatrix} \Delta P_{S3} \\ \Delta T_3 \\ \Delta P_{S5} \\ \Delta T_5 \\ \Delta WFE \\ \Delta FGN \\ \Delta W_1 \end{bmatrix} = \begin{bmatrix} 1.11 & -0.49 & -0.80 & -0.39 \\ 0.21 & -0.89 & -0.14 & -0.07 \\ 1.53 & -0.62 & 0.37 & -0.80 \\ 0.36 & -0.85 & 0.41 & -1.07 \\ 1.50 & -1.33 & 0.69 & -1.68 \\ 1.82 & -0.71 & 0.43 & -0.91 \\ 0.94 & 0.03 & 0.04 & 0.02 \end{bmatrix} \cdot \begin{bmatrix} \Delta SW_2 \\ \Delta SE_2 \\ \Delta SW_4 \\ \Delta SE_4 \end{bmatrix}$$

The Jacobians corresponding to different possible combinations of the seven measured quantities by four (a total of 35) are formed. The condition numbers of these 4×4 matrices are evaluated and sorted in ascending order, as shown in Fig. 2.

For nine combinations the condition numbers are of very small magnitude (ten or less), one is an order of magnitude larger (~ 200) while the remaining ones are of several orders of magnitude larger. The ten combinations with the smaller values would be favorable for forming a diagnostic system, and are shown in Table 1.

We can further observe how uncertainty is propagated to the estimated parameters, depending on which measurement combination is employed. The uncertainties (3σ) considered for the different measurements are as follows:

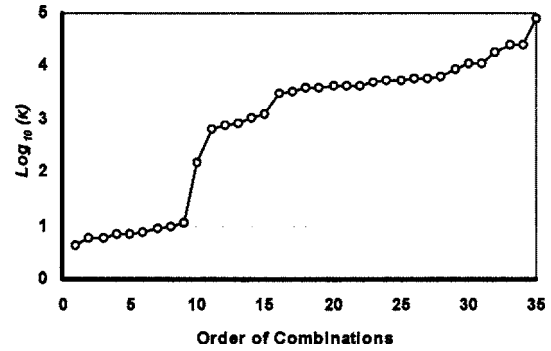


Fig. 2 Condition numbers of systems employing four measurements, for a turbojet

P_{S3}	T_3	P_{S5}	T_5	WFE	FGN	W_1
0.01	2	0.002	2	0.01	38	0.37
Bar	K	Bar	K	kg/s	Nt	kg/s

The uncertainties expressed by the standard deviation of each estimated parameter, for each one of the combinations of Fig. 2 are shown in Fig. 3. While the values remain small ($< 1\%$) for the first nine combinations, they become large for three of the parameters when the condition number approaches 10^3 or is larger. Such values are unacceptable from a practical point of view, since they would be of a magnitude that is much larger than deviations

Table 1 The 10 combinations with the lowest values for condition number. Turbojet engine.

Order	κ	P_{S3}	T_3	P_{S5}	T_5	WFE	FGN	W_1
1	4.31	•	•		•			•
2	5.84	•	•	•	•			
3	6.14	•	•		•		•	
4	6.89	•	•	•				•
5	6.95	•	•			•		•
6	7.63	•	•				•	•
7	9.15	•	•			•	•	
8	9.67	•	•	•		•		
9	11.18	•	•		•	•		
10	150.96	•	•	•			•	

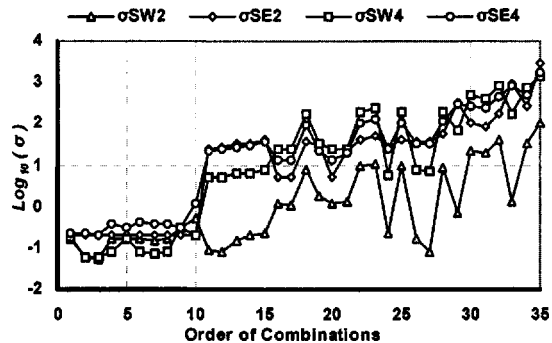


Fig. 3 Uncertainty in estimated parameters for the different measurement combinations

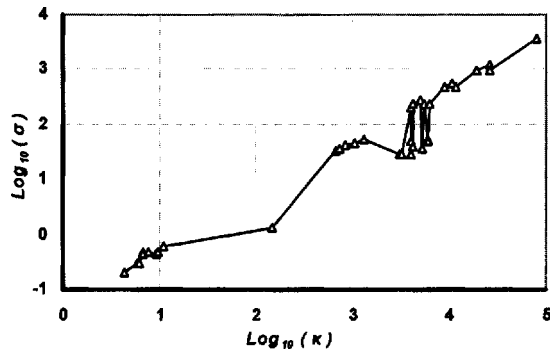


Fig. 4 Average parameter standard deviation ($\sigma = \sqrt{(\sigma_1^2 + \sigma_2^2 + \dots + \sigma_N^2)/N}$), as a function of the condition number of the system used for estimation

caused by practical component faults.

A global measure of parameter uncertainty is calculated as the RMS of the parameter σ 's and is shown as a function of the condition number in Fig. 4. When condition number becomes larger than 100, this global index indicates that at least one of the estimated parameters will be of unreasonably high magnitude.

Health Parameter Selection

A common feature of engines in service is the limited availability of instrumentation. This instrumentation is used primarily by the control of the engine, which ensures safe operation within its operating envelope. It is thus desirable to exploit the information provided from the sensors along the gas path in a way that ensures derivation of the maximum diagnostic information.

When the number M of measurements is less than the total number N of health parameters needed to be known for determining the health of all components, it is not possible to derive them by using only measurement-parameter relations (Eq. (1)). If an estimate of all the parameters is desirable, then additional information has to be used (as for example discussed by Mathioudakis [13]). If only measurement information has to be used, then only M ($<N$) health parameters can be estimated. Even though such an estimation does not provide a full picture of the engine condition, it can nevertheless be useful, in cases that faults are searched in some known engine subassembly. For example, existing experience may indicate that certain parts of the engine are more prone to damage than others. It is thus interesting to examine which health parameter combinations can be estimated best, in the same perspective as the measurement selection discussed in the previous section.

The full Jacobian matrix has M rows corresponding to measurements and N columns ($N > M$) corresponding to health parameters. In this case sub-matrices are formed by combining columns, producing $M \times M$ systems. The combinations, exhibiting the smaller condition numbers, are more suitable for estimation.

For the final selection engineering judgment should also be applied. If, for example, some specific component needs to be tracked, combinations containing this component's health indices should be solicited. The higher ones in the list should be chosen, not necessarily the top ones.

Sample Application. For this type of problem the case of a twin spool mixed turbofan that has been used as a test case in several previous publications of the authors ([9,14]) is used. Seven gas path measurement are available: low and high pressure spool speeds ($XNLP$, $XNHP$), fan delivery pressure and temperature, ($P13, T13$), compressor delivery pressure and temperature ($P3, T3$), turbine exit temperature, ($T6$).

A total of 11 health parameters are needed to establish the con-

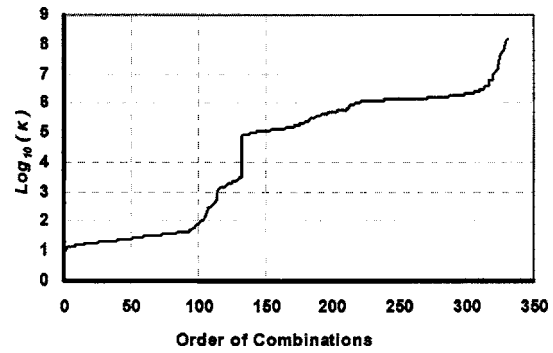


Fig. 5 Condition numbers for health parameter combinations (11×7) with 7 given measurements, for the case of a turbofan

dition of the components of the engine. It is desirable to know which combinations of health parameters are identifiable with a good accuracy.

The condition numbers of Jacobian matrices corresponding to combinations of the eleven health parameters by seven are shown in Fig. 5. Here there is a large number of combinations with condition numbers <100 , while the maximum values are up to eight orders of magnitude larger. For this case too, when condition number exceeds a value of about 100, the uncertainty interval for the estimated parameters becomes too large, as indicated by the results of error propagation shown in Fig. 6 for the turbofan engine.

It is noted here that the group of authors has proposed the use of the singular value decomposition method for selecting health parameters. As Stamatis et al. [2] have presented: "Health parameters with the greater projections in the direction of the greater singular vectors are estimated with greater accuracy" and this can be a criterion for choosing the most appropriate ones. This is not a strict quantitative measure however, as is the method employing the approach proposed in the present paper.

Operating Points in Multipoint Algorithms

The choice of operating points for multipoint diagnostic methods has been addressed by Zedda and Singh [6], Gronstead [7], and Pinelli et al. [8]. Although these methods provide some useful elements for choice, each one of them suffers from some deficiency. For example, Zedda and Singh [6] propose the use of a parameter that only accounts for the number of operating points and does not consider how far or closely they are spaced. For the same value of their parameter, a multipoint situation can be well or ill conditioned, depending on how close the points are. The method of Gronstead [7] is similar to the one proposed here, but it considers the Hessian matrix instead of the Jacobian, and does not

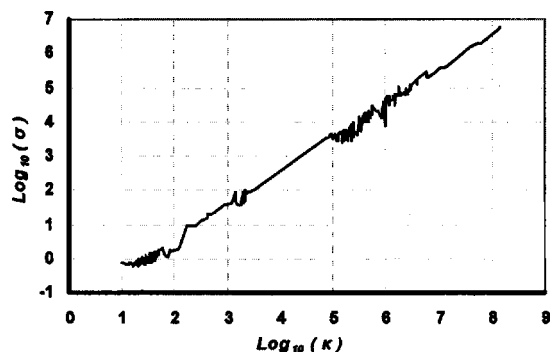


Fig. 6 Overall health parameter estimation uncertainty as a function of condition number for the different parameter combinations. Turbofan test case.

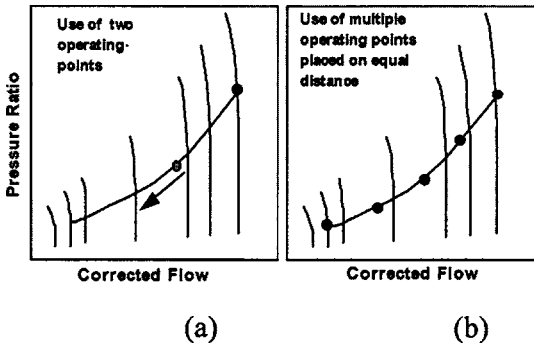


Fig. 7 Different operating points along the compressor of a turbofan engine

thus give the possibility of assessing uncertainty propagation. On the other hand, it does not provide a guide as to what magnitude of condition numbers could be considered small or large. Pinelli et al. [8] provide a number of parameters that have to be examined in a qualitative manner. No strict quantitative criterion is proposed.

The method proposed here is to formulate the linear multipoint model, by taking the Jacobian matrices at each operating point and composing an augmented Jacobian J_{augm} . Under the usual assumption of multipoint methods that the component deviations remain the same for all operating points, this produces a system with sufficient equations to solve for the unknown component condition parameters. For measurement vectors ΔY the linear system formed is

$$\begin{bmatrix} \Delta Y_1 \\ \Delta Y_2 \\ \vdots \\ \Delta Y_N \end{bmatrix} = \begin{bmatrix} J_1 \\ J_2 \\ \vdots \\ J_N \end{bmatrix} [\Delta f] \quad (9)$$

A solution exists if the augmented Jacobian is of rank N and is obtained by a least squares approach. For the purpose of the present analysis, SVD is applied on J_{augm} , its condition number is derived and is thus used as a criterion for the possibility to derive diagnostic information, as in the other cases previously discussed.

Sample Application. The turbofan test case is used to demonstrate this type of application as well. Measurements at two or more operating points are used to estimate the total set of eleven health parameters.

First, it is considered that data from two operating points are used. One of them is at the nominal speed of operation, while the other one can be at any point along the operating line, Fig. 7(a). The question is how close these two points should be, in order to achieve good estimation accuracy.

The condition numbers of augmented matrices for pairs of operating points spaced at different distances apart are evaluated and shown in Fig. 8. The distance of the operating points is expressed through the percentage deviation of XNLP from its datum value (at take off):

$$\text{Distance}(\%) = \frac{XNLP_D - XNLP}{XNLP_D} \cdot 100 \quad (10)$$

It is observed that when the points are very closely spaced, condition number is very high, decreasing monotonically as the distance between the points increases. The same trend is followed by the overall standard deviation. This representation can give the minimum operating point distance that would be needed for acceptable accuracies. For example, for an average of 1%, the points

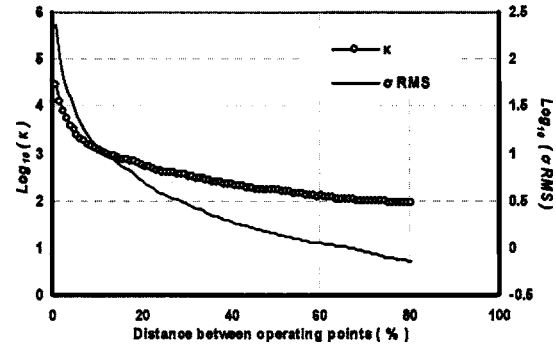


Fig. 8 Condition numbers of systems employing measurements at two operating points, and related overall estimation uncertainty

should be spaced by 60% or further apart.

This problem can be viewed from another perspective: what is the minimum number of operating points that have to be chosen over a given operating range, to achieve a better accuracy of estimation. For the case of the turbojet, different situations are considered, with various numbers of operating points between the points of nominal and minimum speed of the turbojet, as shown schematically in Fig. 7(b). In this case the augmented Jacobian is constituted by concatenating the Jacobian matrix for every additional operating point. The variation of condition number and the corresponding overall rms, as a function of the number of points are shown in Fig. 9. It is observed that while the increase of the number of points initially reduces the estimation uncertainty drastically, it then slows down and gives only marginal improvements with the addition of more operating points.

Discussion

Effectiveness of Weighted Least Squares Approaches. When fewer measurements than parameters are available, one approach that can be followed is to use a priori information on the health parameters to close the system of equations. This is applied either in linear methods (e.g., Doel [15]) or in nonlinear ones (e.g., Mathioudakis et al. [13]). Use of the present method reveals that the addition of this *a priori* information leads to a wellconditioned system. The linear relation employed is (see [9]):

$$\Delta f = \overbrace{[M^{-1} + J^T \cdot R^{-1} \cdot J]^{-1}}^D \cdot J^T \cdot R^{-1} \cdot \Delta Y \quad (11)$$

where J is the Jacobian matrix, $R = [\sigma_{Y_i}^2]$, is the matrix containing the weight coefficients for measurement terms (measurements uncertainty), and $M = [Cs/\sigma_{f_j}^2]$, is the matrix of *a priori* expected

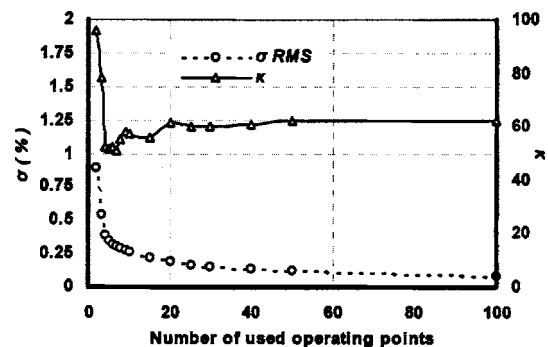


Fig. 9 Condition numbers of systems employing measurements at increasing number of operating points, and related overall estimation uncertainty

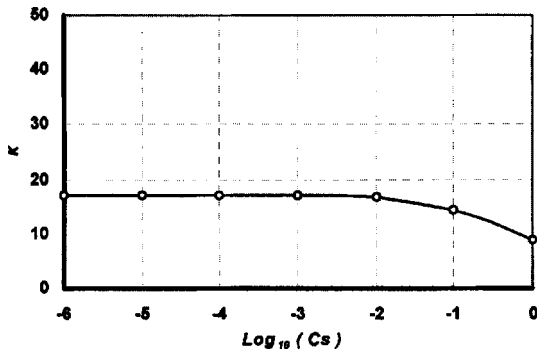


Fig. 10 Condition numbers for the WLS type of problems

values for health parameters, which is the matrix that permits the estimation. In Fig. 10 we present the condition of matrix D as function of coefficient C_s , which is the key element of the procedure. Figure 10 shows that for different values of the weight factor C_s , the condition number remains small. Of course it should be remembered that even though from a numerical point of view the estimation is stable, the solutions obtained are biased and do not necessarily represent correctly the existing health condition.

Stability of Nonlinear Algorithms. For nonlinear methods, examination of the condition number of the equivalent linear system provides an additional piece of information about the behavior of the method: it gives a criterion as to whether the nonlinear method can converge to a solution or not.

The reason that this is a piece of information different from the case of linear methods is that the nonlinear methods are based on an iterative approach that uses the nonlinear engine model. This model itself is a solution algorithm of a set of nonlinear relations, which are applied in successive steps. The update of health condition parameters during successive steps is based on some numerical scheme (see, for example, Stamatidis et al. [14]), whose behavior depends on the local properties of the nonlinear system. For example, for Newton-type methods, the inverse of the Jacobian is employed for successive updates.

The behavior of the update scheme depends on the condition of the matrix that forms the equivalent linear problem. Large condition numbers indicate that small corrections in the target value may lead to very large corrections of the independent variables. This for example means that the engine model may be required to operate with very high deviations of compressor or turbine condition, fact that may lead to inability for the model to converge, leading thus to failure of the method to obtain a solution. Convergence histories for two condition numbers from those of Table 1 are shown in Fig. 11. It is shown that for the larger condition

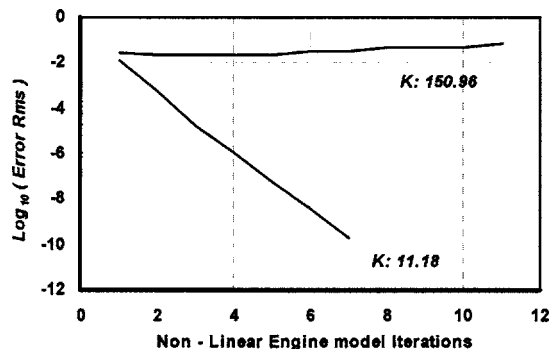


Fig. 11 Nonlinear diagnostic method convergence histories for a small and a large condition number, from Table 1

number the method does not have the possibility to reduce the error RMS and is thus unable to converge.

The Limit Values for Condition Numbers. A question that naturally arises from the previous discussions is whether it is possible to have some guide as to what condition numbers may be considered small or large.

Various answers to this question can be found in the literature. In linear algebra textbooks a level usually mentioned is related to the accuracy of the computing machine. Meyer [11], for example, mentions that if computing round-off are the only source of errors, then a t -digit floating point arithmetic will produce solutions accurate to $t-p$ significant digits, when the condition number is of the order of 10^p . In statistical textbooks, on the other hand, much lower values are encountered. Belsley et al. [16] reports that condition indices of 100 or more appear to be large and cause substantial variance inflation. This last observation is in line with observations made on the data presented above. The authors' experience from application of the method to several engine cases, shows that numbers above 100 are usually linked to bad condition. The way however to establish a threshold (which may vary for different engine designs and configurations) is to construct the uncertainty propagation charts that were presented in the applications discussed above. The limit values are then determined from the threshold in overall or partial standard deviation values (Figs. 4 and 6).

Conclusions

A method for assessing the effectiveness of diagnostic schemes has been presented. It is based on the evaluation of the condition number of a matrix of a linear system, characteristic of the diagnostic situation considered. Small values of the condition number are sought for choice of the optimal solution.

It was shown that the condition number is linked by direct analogy to the level of uncertainty in estimated parameters. The interdependence of the two can provide a guide for choice of threshold values for the condition numbers and thus define sets of acceptable combinations of the quantities of interest each time.

It was shown that this approach can be used for a variety of problems, such as measurement selection, parameter selection or operating point selection for multipoint methods. Additionally, it can be used for interpretation of the numerical behavior of nonlinear methods and indicate thus the limits of applicability of such methods, which may be narrower than corresponding linear ones.

Nomenclature

- a_{ij} = element of Jacobian matrix
- κ = condition number of Jacobian matrix
- F = prediction algorithm, Eq. (1)
- J = Jacobian matrix
- M = number of measurements
- L = number of possible combinations
- N = number of health parameters
- $XNLP$ = low pressure spool rotational speed
- $XNHP$ = high pressure spool rotational speed
- P = total pressure
- SE_i = efficiency health factor of component with entrance at station i , $SE_i = \eta_i / (\eta_i)_{ref}$
- SW_i = health factor for flow capacity of component with entrance at station i ,
 $SW_i = (W_i \cdot \sqrt{T_i / p_i}) / (W_i \cdot \sqrt{T_i / p_i})_{ref}$
- T = total temperature along the gas path
- u = vector of variables defining the operating point
- V = matrix containing the singular vectors of J
- W = diagonal matrix containing the singular values of J
- WFE = fuel flow
- $W\sqrt{\delta} / \delta$ = corrected gas mass flow rate

Y = vector of measurable quantities
 Δf = health parameter deviation from reference value $\Delta f_j = (f_j - f_j^{\text{ref}}) / f_j^{\text{ref}} \times 100$
 ΔY = measurement deviation from reference value, $\Delta Y_j = (Y_j - Y_j^{\text{ref}}) / Y_j^{\text{ref}} \times 100$
 η = efficiency
 σ = standard deviation

Subscripts

actual = actual parameter value on component performance map
 combi = combinations
 D = datum value
 ref = reference
 S = static pressure or temperature

References

- [1] Li, Y. G., 2002, "Performance Analysis Based Gas Turbine Diagnostics: A Review," *Proc. Inst. Mech. Eng., Part A*, **216**(A6), pp. 363–377.
- [2] Stamatis, A., Mathioudakis, K., and Papailiou, K. D., 1992, "Optimal Measurement and Health Index Selection for Gas Turbine Performance Status and Fault Diagnosis," *J. Eng. Gas Turbines Power*, **114**, pp. 209–216.
- [3] Provost, M. J., 1994, "The Use of Optimal Estimation Techniques in the Analysis of Gas Turbines," Ph.D. thesis, Cranfield University.
- [4] Provost, M. J., 2003, Observability Analysis for Successful Diagnosis of Gas Turbine Faults in Von Karman Institute Lecture Series, "Gas Turbine Condition Monitoring and Fault Diagnosis," VKI LS, Jan. 13–17.
- [5] Kamboukos, Ph., Oikonomou, P., Stamatis, A., and Mathioudakis, K., 2001, "Optimizing Diagnostic Effectiveness Of Mixed Turbofans By Means Of Adaptive Modelling And Choice Of Appropriate Monitoring Parameters," AVT Symposium on "Monitoring and Management of Gas Turbine Fleets for Extended Life and Reduced Costs," Oct. 8–11, Manchester, UK.
- [6] Zedda, M., Singh, R., 1999, "Gas Turbine Engine and Sensor Diagnostics," XIV ISABE, Sept. 5–10, Florence, Italy.
- [7] Groenstead, T., 2002, "Identifiability in Multi-Point Gas Turbine Parameter Estimation Problems," ASME Paper No. GT2002-30020.
- [8] Pinelli, M., Spina, P. R., Venturini, M., 2003, "Optimized Operating Point Selection for Gas Turbine Health State Analysis by Using a Multi-Point Technique," ASME Paper No. GT2003-38191.
- [9] Kamboukos, Ph., Mathioudakis, K., 2003, "Comparison Of Linear And Non-Linear Gas Turbine Performance Diagnostics," ASME Paper No. GT2003-38518.
- [10] Elgerd, O., 1967, *Control Systems Theory*, McGraw-Hill, New York.
- [11] Meyer, C., 2000, *Matrix Analysis and Applied Linear Algebra*, SIAM, New York.
- [12] Press, W., Teukolsky, S., Vetterling, W., and Flannery, B., 1992, *Numerical Recipes in FORTRAN 77: The Art of Scientific Computing*, 2nd ed., Cambridge University Press, Cambridge, UK.
- [13] Mathioudakis, K., 2003, "Nonlinear Methods for Gas Turbine Fault Diagnosis," Von Karman Institute Lecture Series "Gas Turbine Condition Monitoring and Fault Diagnosis," VKI LS 2003-01, Jan. 13–17.
- [14] Stamatis, A., Kamboukos, Ph., Aretakis, N., and Mathioudakis, K., 2002, "On Board Adaptive Models: A General Framework and Implementation Aspects," ASME Paper No. GT-2002-30622.
- [15] Doel, D., 1993, "A Weighted-Least-Squares Gas Path Analysis Method for Test Cell or on Wing Data," Von Karman Institute Lecture Series, Gas Turbine Condition Monitoring and Fault Diagnosis, VKI LS 2003-01, Jan. 13–17.
- [16] Belsley, D., Kuh, E., and Welsch, R., 1980, *Regression Diagnostics: Identifying Influential Data and Sources of Collinearity*, Wiley, New York.

Bayesian Network Approach for Gas Path Fault Diagnosis

C. Romessis

Research Assistant
e-mail: cristo@mail.ntua.gr

K. Mathioudakis

Associate Professor
e-mail: kmathiou@central.ntua.gr

Laboratory of Thermal Turbomachines,
National Technical University of Athens,
P. O. Box 64069,
Athens 15710, Greece

A method for solving the gas path analysis problem of jet engine diagnostics based on a probabilistic approach is presented. The method is materialized through the use of a Bayesian Belief Network (BBN). Building a BBN for gas turbine performance fault diagnosis requires information of a stochastic nature expressing the probability of whether a series of events occurred or not. This information can be extracted by a deterministic model and does not depend on hard to find flight data of different faulty operations of the engine. The diagnostic problem and the overall diagnostic procedure are first described. A detailed description of the way the diagnostic procedure is set-up, with focus on building the BBN from an engine performance model, follows. The case of a turbofan engine is used to evaluate the effectiveness of the method. Several simulated and benchmark fault case scenarios have been considered for this reason. The examined cases demonstrate that the proposed BBN-based diagnostic method composes a powerful tool. This work also shows that building a diagnostic tool, based on information provided by an engine performance model, is feasible and can be efficient as well.

[DOI: 10.1115/1.1924536]

Introduction

Fault detection and isolation in gas turbines can be achieved through the use of linearized gas path analysis methods, using approaches related to the Kalman filter and its derivatives (Doel [1], Volponi et al. [2,3]) or through nonlinear methods (Stamatis et al. [4,5], Mathioudakis et al. [6], Kamboukos et al. [7]).

During the last decade, diagnostic tools applying artificial intelligence methods have become very attractive. Among them, rule based expert systems (Breese et al. [8]) artificial neural networks (Kanelopoulos et al. [9], Volponi et al. [3]) and fuzzy logic (Healy et al. [10], Siu et al. [11]) are most common in use.

Recently, a new type of probabilistic expert system, the so-called Bayesian belief network (BBN), has been introduced, allowing the inclusion of information of a different nature and from different sources for diagnostics. Bayesian belief networks as a part of stochastic expert systems have been studied by several authors who describe methods for construction or inference with a BBN (Pearl [12], Castillo et al. [13]). It is common belief that, there is no "best" method for construction or inference with a BBN, only a "most suitable" one, with respect to the information available in each case.

To the authors' knowledge, such types of networks have been employed in the field of gas turbine diagnostics by few researchers. Breese et al. [8], present a method for detecting specific faults on large gas turbines that combines a thermodynamic model of the engine under examination and a BBN, constructed by use of statistical data of the engine. Palmer [14], presented a statistically constructed BBN for fault detection of the CF6 family of engines.

The first attempt to propose a general procedure of building a BBN for diagnostic reasons, has been presented by Romessis et al. [15]. The way of building diagnostic BBNs, allowing implementation into any type of engine, and the disengagement of the BBN from hard to find statistical data, were two elements that made the work interesting and promising. The heuristic way of building the BBN, however, put some question on its reliability and generality.

The BBN-based diagnostic procedure, described in the present

paper, overcomes this problem. A generalized way to set up the whole diagnostic procedure, from data acquisition to diagnostic conclusion, is presented.

Given the belief network that represents the relation among variables of aerothermodynamic nature of an engine, component faults can be detected anytime measurements of gas path variables are available. The effectiveness of the proposed diagnostic method is examined on benchmark fault case scenarios, in a typical modern turbofan engine of civil aviation. The flexibility of BBNs on including additional information and cooperating with other diagnostic methods is discussed.

Gas Path Fault Diagnosis Using the BBN

The Problem of Gas Path Fault Diagnosis. A formal description of the terms involved in the diagnostic problem can be given if the engine is considered as a system, whose operating point is defined by means of a set of variables, denoted as \mathbf{u}' . The health condition of its components is represented through the values of appropriate *health parameters*, contained in a vector \mathbf{f} . The engine is monitored through measured variables (speeds, pressures, temperatures, etc.), contained in a vector \mathbf{Y}' .

Health parameters can be given as

$$\mathbf{f} = \mathbf{f}_o + \delta_f$$

while measurements produce readings \mathbf{Y}' and \mathbf{u}' that are related to the actual quantity as follows:

$$\mathbf{Y}' = \mathbf{Y}_{\text{actual}} + \mathbf{n}_Y$$

$$\mathbf{u}' = \mathbf{u}_{\text{actual}} + \mathbf{n}_u$$

The operating engine establishes a relationship between the health parameters and the actual values of the measured quantities, which can be expressed through a functional relation:

$$\mathbf{Y}_{\text{actual}} = \mathbf{Y}(\mathbf{u}_{\text{actual}}, \mathbf{f}) \quad (1)$$

The problem examined here is the determination of δ_f from a set of measured \mathbf{Y}' and \mathbf{u}' from an engine. In cases usually encountered in practice, the available measurements, forming vector \mathbf{Y}' , are less than the health parameters, leading to an underdetermined system of equations, not allowing a unique determination of δ_f . On the other hand, the presence of noise on the measured quantities introduces some inaccuracy that, even in the case of the

Contributed by the International Gas Turbine Institute (IGTI) of ASME for publication in the JOURNAL OF ENGINEERING FOR GAS TURBINES AND POWER. Manuscript received by IGTI, October 1, 2003, final revision, March 1, 2004. IGTI Review Chair: A. J. Strazisar. Paper presented at the International Gas Turbine and Aeroengine Congress and Exhibition, Vienna, Austria, June 13–17, 2004, Paper No. GT2004-53801.

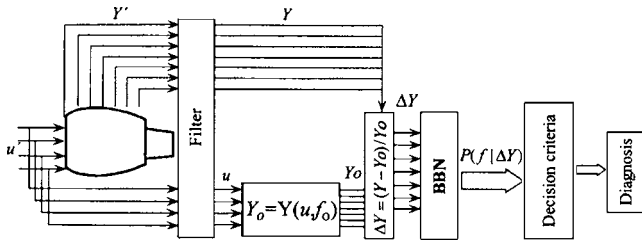


Fig. 1 Flowchart of the overall procedure of the proposed diagnostic method

determined problem, cannot lead to an exact determination of δ_f . All the above compose a problem highly linked with uncertainty. A procedure based on Bayesian belief networks (BBN), an efficient tool for application of probability theory principles, is proposed for handling this problem and is discussed in the following.

Overview of Diagnostic Procedure. The core of the proposed diagnostic method consists of a BBN accompanied by the functional relation of Eq. (1), materialized by a computer model for the engine under examination.

The BBN allows the estimation of probabilities for all possible health conditions of the engine given the measurements acquired from the engine. For a complete description of the BBN, the theory behind them and the corresponding algorithms, the reader is referred to Pearl [12] and Castillo et al. [13]. For reason of completeness some basic principles of BBN are presented in Appendix B.

A filtering procedure on the measurements acquired from the engine and suitable decision criteria on the output of the BBN, act as auxiliary but essential elements of the diagnostic procedure.

A schematic presentation of the overall procedure of the proposed diagnostic method is shown in Fig. 1.

A set of measurement readings (u' , Y') is preprocessed through a filtering procedure that minimizes the effect of the noise, providing with a set of measurements (u , Y) closer to the actual ones. Filtering methods for this purpose have been proposed by other researchers (Ganguli [16]). From these filtered measurements and through Eq. (1) applied for the fault-free operation of the engine, the percentage deviations of measurements Y from their nominal values are calculated. These percent deviations, which are called *deltas* in jet engine applications, are defined as

$$\Delta Y = \frac{Y - Y_o}{Y_o} \times 100 \quad (2)$$

The *deltas* are then presented to the BBN, from which the probabilities of all possible conditions of the engine are estimated. The use of *deltas* as input provides with data that have a weak dependence on operating conditions, as commented by Mathioudakis et al. [6].

Conclusions about the health condition of the engine are finally extracted from these probabilities and through use of goal-oriented decision criteria.

Setting up the BBN for Gas Path Fault Diagnosis

A way to built-up a diagnostic BBN has been presented by Romessis et al. [15]. It was based on a heuristic approach for defining the network elements.

The procedure proposed in the present paper overcomes this heuristic nature and allows BBN definition from given information about the engine under examination. The steps we follow are:

- (1) Acquire information that describes the specific diagnostic problem, namely: engine, configuration of our prior beliefs about its health condition, and the diagnostic goals;

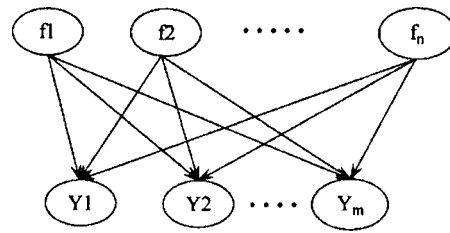


Fig. 2 The architecture of a diagnostic BBN

- (2) Define the network architecture that reflects the interrelation of the engine parameters and measured quantities;
- (3) Map out the structural elements of the network.

Network Settings for Diagnostic Problem Representation.

The diagnostic BBN can be constructed, once specific information about the engine under examination is given. The required information can be summarized in the following:

- (a) The operating conditions (u); for simplicity the diagnostic BBN is built using information at a specific operating point. This is a reasonable simplification since BBN can handle faults at different operating conditions. This feature of the BBN is discussed later in the paper.
- (b) The health parameters f representing the condition of the engine and the available measured quantities Y .
- (c) The relation among health parameters and measured quantities, for the chosen operating conditions: $Y = Y(u, f)$.
- (d) Regions of interest for each health parameter. Each region covers a range of *deltas* of a health parameter. The regions are exhaustive and mutually exclusive covering all possible values of *deltas*. They are chosen arbitrarily expressing the desired accuracy of estimation of the health condition of the engine.
- (e) The *a priori* probability for each region. These probabilities reflect our prior belief that the *delta* of a specific health parameter lies within the range of values of the specific region.
- (f) The standard deviations of the *deltas* of measured quantities: $\sigma_{\Delta Y}$, reflecting instrumentation accuracy. These deviations embed inaccuracies of measurements Y and measurements of the set point parameters u , affecting nominal values Y_o .

The way the above information is used for setting up the BBN is explained in the following two sections.

BBN Architecture. The BBN proposed for the specific kind of diagnostic problem, consists of nodes representing the *deltas* of health parameters and the measurements used for monitoring. Links lead from each health parameter node to each measurement node. A schematic presentation of the BBN, in the general case of n health parameters: $f = \{f_1, f_2, \dots, f_n\}$ and m measurements: $Y = \{Y_1, Y_2, \dots, Y_m\}$, is shown in Fig. 2.

For the specific architecture, the joint probability of network nodes [which is expressed in general form through Eq. (8)] is given:

$$P(Y_1, Y_2, \dots, Y_m, f_1, f_2, \dots, f_n) = \prod_{i=1}^n P(f_i) \cdot \prod_{j=1}^m P(Y_j | f_1, f_2, \dots, f_n) \quad (3)$$

This expression represents the probabilistic relationship that holds among variables Y and f , as expressed through the principles of probability theory (Romessis [17]).

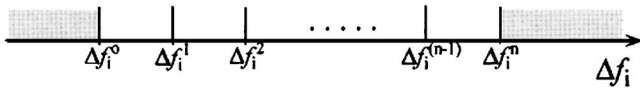


Fig. 3 Schematic presentation of the states of a health parameter node of the diagnostic BBN

During inference, the probabilities of all states of nodes f_1, f_2, \dots, f_n are estimated, from the given states of nodes Y_1, Y_2, \dots, Y_m , through measurements Y .

BBN Structural Elements. Structural elements of BBN are the discrete states and the Conditional Probability Tables (CPTs) of its nodes.

Since the nodes of the diagnostic BBN represent *deltas*, which take continuous values, a discretization is required and the resulting discrete states represent *deltas* within exhaustive and mutually exclusive intervals.

In the case of health parameter nodes, the states represent the regions of interest, introduced in the previous paragraph. A schematic presentation of the discretization of a health parameter f_i , is shown in Fig. 3, where its domain (ranging from Δf_i^0 to Δf_i^n) is divided into N states, each representing a region of interest. Any interval $[\Delta f_i^1, \Delta f_i^2]$, for instance, is a region of interest and constitutes the state of the f_i node of the network representing any deviation of the corresponding health parameter within this interval.

Each measurement node has three states. If we assume that the *delta* obtained from the engine of measurement Y_i is $\Delta Y_{i,G}$, and $\Delta Y_{i,min}, \Delta Y_{i,max}$ are the corresponding minimum and maximum expected values, respectively, the three states represent the regions of *deltas* (Fig. 4):

$$[\Delta Y_{i,min}, \Delta Y_{i,G} - 3\sigma_{\Delta Y_i}], [\Delta Y_{i,G} - 3\sigma_{\Delta Y_i}, \Delta Y_{i,G} + 3\sigma_{\Delta Y_i}], [\Delta Y_{i,G} + 3\sigma_{\Delta Y_i}, \Delta Y_{i,max}]$$

The second of the above states represents the interval the actual *delta* lies within with probability 99.73%, assuming normal distribution of measured *delta* around its actual value.

The conditional probability tables (CPTs) of the nodes express the quantitative relationship that holds among them.

The CPT for a health parameter node contains the *a priori* probabilities of its states. These probabilities are defined by the user and reflect existing knowledge on engine condition. For example, if no indication of tendency to a specific fault exists, it is reasonable to assume, with high probability that a component does not suffer from a fault. This will become clear through the numeric application presented in the following.

The CPT of a measurement node represents the *a posteriori* probability of its states, given the states of the health parameters. For the network of Fig. 2, the CPT of measurement Y_i , is expressed through the probabilities:

$$P(Y_i | f_1, f_2, \dots, f_n) \quad (4)$$

for all states of f_1, f_2, \dots, f_n and Y_i .

A schematic presentation of the procedure for calculating the above probability is shown in Fig. 5, given the state of one health

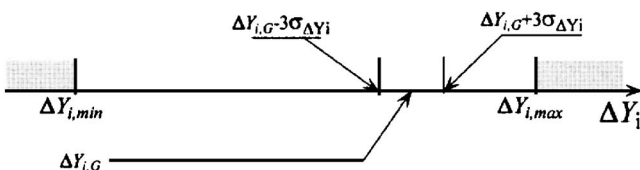


Fig. 4 Schematic presentation of the states of a measurement node of the diagnostic BBN

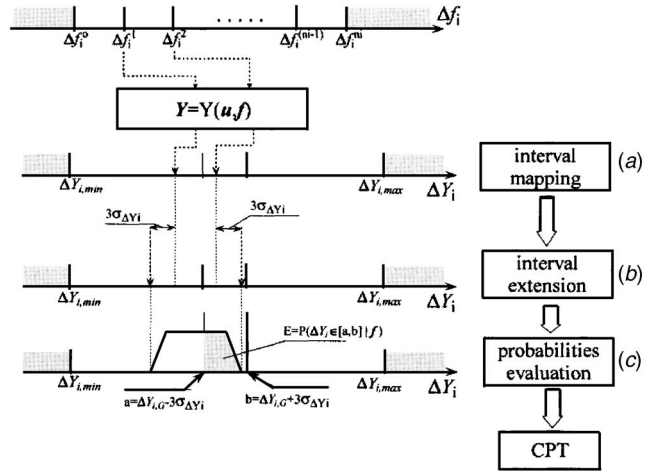


Fig. 5 Schematic presentation of the procedure for specifying the CPTs of the diagnostic BBN

parameter, for reasons of simplicity.

Deviations of f_i within the interval $[\Delta f_i^1, \Delta f_i^2]$ lead to an interval of *deltas* of measurement Y_i , through the relation: $Y = Y(u, f)$ [Fig. 5(a)]. Due to the presence of noise, this interval of *deltas* of Y_i , is extended by the value $3\sigma_{\Delta Y_i}$, resulting to the interval of all possible values of ΔY_i , that can be obtained in practice for the considered deviations of f_i (Fig. 5(b)). Assuming a trapezoid probability density function (pdf) of ΔY_i over this extended range of *deltas*, the required probability for a state of Y_i node is given as the area underneath the pdf function within the limits of this state of Y_i (Fig. 5(c)).

The trapezoid pdf has been chosen since it is a closer estimation of the actual type of pdf (as discussed by Romessis [17]).

Diagnostic Procedure for Turbofan Gas Path Faults

In order to give a clearer picture of the way the proposed method is set-up and to evaluate its effectiveness, application to a turbofan test case is presented. Apart from its illustrative nature, the test case represents also a situation of practical interest in today's jet engines applications. The type of engine for this application is described in Appendix A. It is selected as it has been used in applications of different diagnostic methods by the authors and other researchers and can be considered to constitute a benchmark case.

Network Definition for the Turbofan. The diagnostic BBN for the turbofan is defined by determination of the settings mentioned in the previous section.

The BBN is set for a typical cruise operating point and involves 11 health parameters and 7 quantities measured for monitoring, as described in Appendix A. The resulting architecture is shown in Fig. 6.

In the present case, we focus on the detection of small and moderate faults, represented by a maximum absolute deviation of

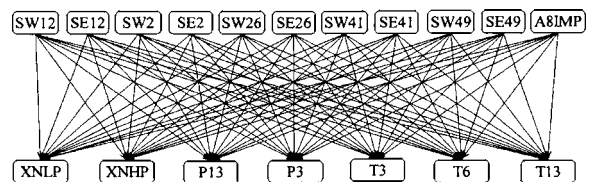


Fig. 6 The architecture of the diagnostic BBN for the considered turbofan case

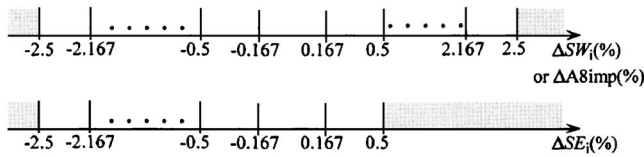


Fig. 7 Schematic presentation of the states of the flow and efficiency factor nodes of the diagnostic BBN

the health parameters from their nominal value equal to 2.5%.

A schematic presentation of the considered states of the health parameter nodes and their deviations is shown in Fig. 7.

The considered domain for each flow factor or the exhaust area is the interval of $[-2.5\%, +2.5\%]$, which has been divided into 15 continuous and nonoverlapping intervals, of the same width.

The considered domain for the efficiency factors is the interval of $[-2.5\%, +0.5\%]$, since component faults cannot possibly lead to an important increase of the efficiencies. Use of the same discretization with the flow factor nodes, at this domain, leads to a total of 9 states per efficiency factor node.

A deviation of the health parameters within the limits of $\pm 0.5\%$ is considered to represent healthy condition. The states corresponding to deviations within these limits represent healthy operation of the engine and are given a total *a priori* probability of 90% per health parameter, while the rest 10% is equally distributed to the other states. In Fig. 8, an example of the *a priori* probabilities assigned to the states of a flow factor node is shown, in the form of a probability distribution.

In order to define the states of the measurement nodes, the noise levels presented in Appendix A, have been considered.

Determination of the Auxiliary Elements of the Diagnostic Procedure. In order for the diagnostic procedure to be applied, appropriate filtering and decision criteria must be determined. For the turbofan diagnostic case, filtering is applied by averaging 50 raw readings, namely the values of u' and Y' acquired from the engine.

According to the considered decision criteria a fault occurs when at least one health parameter satisfies the rule:

$$P(\Delta f_i \in [-0.5\%, -0.167\%]) + P(\Delta f_i \in [-0.167\%, +0.167\%]) + P(\Delta f_i \in [+0.167\%, +0.5\%]) \leq 50\%$$

In that case we say that: "Health parameter f_i deviates significantly," since it is more probable to deviate from nominal by more than 0.5% which is the limit of healthy condition.

The set of significantly deviated health parameters represents the detected fault case. If no health parameters are found significantly deviated, the conclusion is that no fault occurs.

Evaluation of the Diagnostic Ability of the Method

In order to assess the diagnostic ability of the proposed method, fault cases covering situations expected to be encountered in practice are tested. They can be grouped in two major parts: (A) A set of benchmark fault cases, covering different possible faults in all

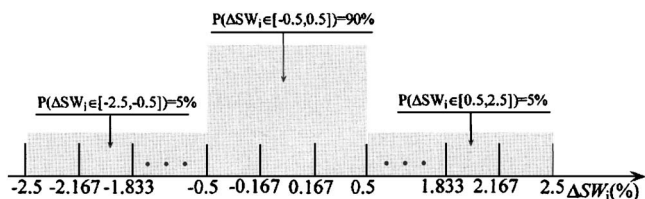


Fig. 8 Schematic presentation of the a priori probabilities given at a flow factor node of the diagnostic BBN

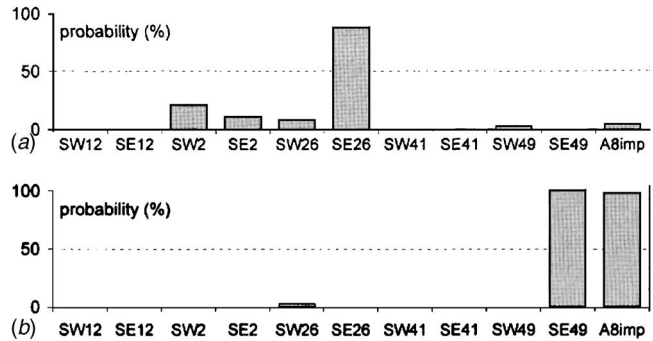


Fig. 9 (a) Example of a *FD* diagnosis (examined fault case: $\Delta SE_{26} = -1\%$). (b) Example of a *UD* diagnosis (examined fault case: $\Delta SE_{49} = -0.6\%$)

individual components on the engine. (B) Additional simulated fault cases, where data are generated through the EPM.

The situations that can be encountered are divided in the following classes:

- (i) If all factors are found not significantly deviated, the engine is considered healthy (symbolized as "Ok").
- (ii) If only the factors that actually deviate are found significantly deviated, the correct *Factor is Diagnosed (fD)*.
- (iii) If the factors found significantly deviated, belong to the same component with the actually deviated factor, the correct *Component is Diagnosed (cD)*.
- (iv) If the factor(s) found significantly deviated, belong to the same "section" with the actually deviated factor, the correct *Section is Diagnosed (sD)*. The compressors constitute the cold section, the turbines the hot section and the nozzle is considered as an individual section.
- (v) If two or more factors found significantly deviated, belong to different "sections" an *Unsafe Diagnosis (uD)* is made, since we claim that simultaneous presence of faults on both sections is rather rare.
- (vi) If the factors found significantly deviated, belong to a 'section' different from the actually faulty one, a *Wrong Diagnosis (wD)* is made.

In Figs. 9(a) and 9(b), examples of a *fD* and a *uD* class of diagnosis are shown, for illustration purposes. The actually deviated factor is identified to the one found by the BBN in Fig. 9(a) (and thus *fD* diagnosis). A nozzle deviation that is not actually present is found in the case of Fig. 9(b), and the *uD* diagnosis.

Benchmark Fault Cases. A set of fault scenarios has been examined, covering different possible faults in all individual components on the engine. This set of cases has been defined by Curnock [19] and the fault cases have been used for evaluation by several researchers and diagnostic methods (Mathioudakis et al. [6], Kamboukos et al. [7], Dewallef et al. [19]).

For each examined fault case data from a sequence of 50 operating points are used. They are typical readings taken every 5 min over the cruise sections of a flight.

The actual deviations that the examined fault cases represent and the evaluation of the diagnostic conclusion provided by the proposed diagnostic method are shown in Table 1.

From this figure it is concluded that in 12 out of 15 cases all actually deviated health parameters are identified correctly. In one case (case a), only one of the deviated parameters is identified since the deviation of the rest 3 parameters is close to or less than the healthy limit of $\pm 0.5\%$.

The remaining two fault cases not identified are a HPC fault expressed as a simultaneous reduction of efficiency and flow capacity (case c), and a LPT fault also expressed as a simultaneous reduction of efficiency and flow capacity (case j). These two cases

Table 1 Diagnostic performance on a set of 15 benchmark fault cases

Fault Case	Actual Deviations of Health Parameters	Factors found significantly deviated	Class Diagnosis
a	SW2=-0.7%, SE2=-0.4%, SW12=-1%, SE12=-0.5%	SW12	sD
b	SE12=-1%	SE12	fD
c	SW26=-1%, SE26=-0.7%	SE2	sD
d	SE26=-1%	SE26	fD
e	SW26=-1%	SW26	fD
f	SW41=+1%	SW41	fD
g	SW41=-1%, SE41=-1%	SW41, SE41	fD
h	SE41=-1%	SE41	fD
i	SE49=-1%	SE49	fD
j	SW49=-1%, SE49=-0.4%	SE41	sD
k	SW49=-1%	SW49	fD
l	SW49=+1%, SE49=-0.6%	SW49, SE49	fD
m	A8IMP=+1%	A8IMP	fD
n	A8IMP=-1%	A8IMP	fD
o	A8IMP=+2%	A8IMP	fD

of unsuccessful diagnosis occur due to parameter observability problems as reported by Kamboukos et al. [7]. It is nevertheless noted that even in these three cases, the faults are identified for the correct section of the engine (sD diagnosis).

If additional information is available, such problems can be confronted. This additional information can be included either as a priori knowledge, by modification of the a priori probability of the nodes, or as independent knowledge, by adding nodes to the network.

As an example, additional information has been included to the

Table 2 Diagnostic performance when additional information is available

Fault Case	BBN with 9 measurements		BBN with modified a-priori	
	Detected Factors	Class	Detected Factors	Class
a	SW12	sD	SW12	sD
b	SE12	fD	SE12	fD
c	SW26, SE2	sD	SW26, SE26	fD
d	SE26	fD	SE26	fD
e	SW26	fD	SW26	fD
f	SW41	fD	SW41	fD
g	SW41, SE41	fD	SW41, SE41	fD
h	SE41	fD	SE41	fD
i	SE49	fD	SE49	fD
j	SW49, SE49	fD	SE41	sD
k	SW49	fD	SW49	fD
l	SW49, SE49	fD	SW49, SE49	fD
m	A8IMP	fD	A8IMP	fD
n	A8IMP	fD	A8IMP	fD
o	A8IMP	fD	A8IMP	fD

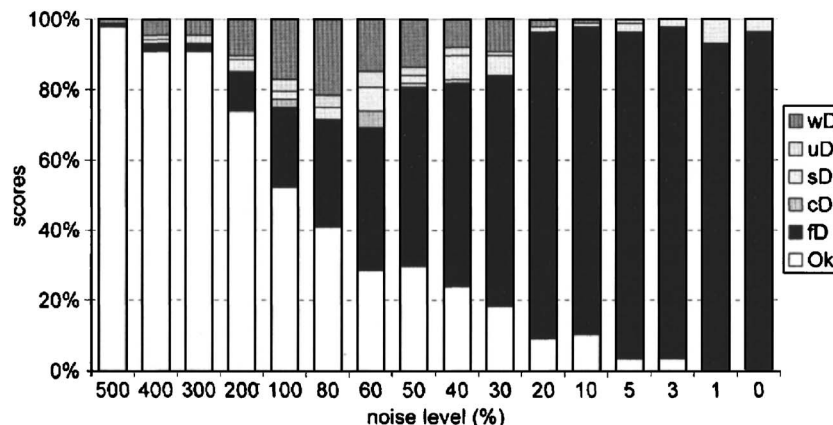


Fig. 10 Effect of noise on the diagnostic ability of the proposed method

considered BBN in two ways. First, additional measurements have been considered, resulting to a BBN with two more measurements nodes (P42 and T42). Second, the a priori probabilities of factors SW26 and SE26 have been modified to reflect a prior knowledge that these two factors are more probable to deviate than the others.

The BBN performance for the faults of Table 1, with the two alternatives is shown in Table 2. For both approaches an improved diagnostic ability is observed.

The addition of measurements P42 and T42 lead to a detection of both deviated parameters of case designated as fault J. In fault case C, also, health parameters SW26 has been detected.

The modification of the a priori probabilities leads to a detection of both deviated parameters in fault case C, while it did not influence the rest fault cases.

Examination of Simulated Data. Data for additional fault cases, presented in Appendix C, are examined to reveal the sensitivity of the proposed method on the measurement noise and the operating conditions of the engine.

Effect of Measurement Noise. An important aspect of the diagnostic performance of the proposed method is its behavior in the presence of noise. Data sets for the considered fault cases, contaminated with several noise levels, are tested. The performance of the method can be summarized in Fig. 10. Each column indicates the percentages of the examined fault cases, with a specific measurement noise level, that fall into each one of the six considered class of diagnosis. In total, 11 noise levels are considered, all expressed as percentage of those presented in Table 1.

The obvious conclusion is that decreasing noise levels lead to an increasing diagnostic performance of the method. The important to notice, however, is that for efficient diagnosis a filtering procedure, reducing the noise level, is required. The averaging of 50 readings, applied here for filtering, satisfies this need.

Effect of Operating Conditions on the Diagnostic Procedure. An important issue is how the proposed method, embedding information from a typical cruise condition, performs over a flight envelope, during which the operating point of the aircraft engine varies in the different flight segments.

Data sets of the considered fault cases, contaminated with noise level of Table 1, have been generated for the 287 operating points described in Appendix C. The percentages for each one of the six classes of diagnosis are shown in Fig. 11.

From this figure, we see that in all operating points, from ground roll until the descent starts, the diagnostic performance is high and almost unaffected by the operating condition of the engine. When descent starts, and until the landing of the aircraft, the diagnostic performance becomes poor. This is due to the fact that descent and deceleration of the aircraft is associated to an uneven reduction of the fuel consumption (WFE), in comparison to the

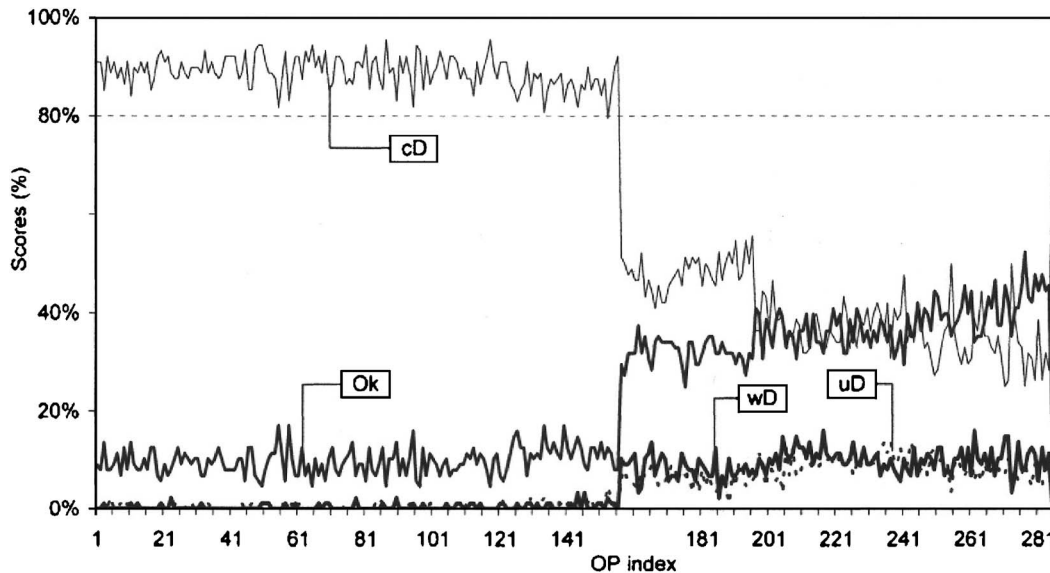


Fig. 11 Diagnostic performance of the method over a flight

other quantities defining the operating point of the engine (P_{amb} , $P1$, $T1$). This means that the engine operating point undergoes a shift that is significant in comparison to changes for other operating conditions, leading to a change of the interrelation among health parameters and measurements, as result of the nonlinear nature of engine response. The differentiation of interrelation among the involved parameters from those at cruise that are used for setting the BBN, leads to a poorer performance.

This problem is solved if an additional network is used, in which the BBN is setup at an operating point of a typical descent. The fuel consumption can be the decision parameter for selecting between the two networks. Following this procedure, the overall performance of the diagnostic method, using this pair of networks, one per region of operating points, is shown in Fig. 12. The improvement is obvious, though the diagnostic ability cannot reach the levels of the former part of the flight.

Discussion

The results presented above demonstrate that the proposed method has a strong diagnostic ability. In comparison with the BBN proposed by Romessis et al., [15], the current method is more efficient even in fault cases with smaller health parameters' deviations. This improvement is due to the way the BBN is constructed: probabilistic relationships among variables are more accurately represented.

Other popular methods allowing gas path fault diagnosis, demonstrate similar diagnostic ability with the one proposed here (Kamboukos et al. [7]). There are, however, some aspects making the present BBN-based method more attractive for application.

The diagnostic conclusions are derived through estimated probabilities. Therefore, apart from the diagnosis itself, the confidence level of the diagnostic conclusions are also provided.

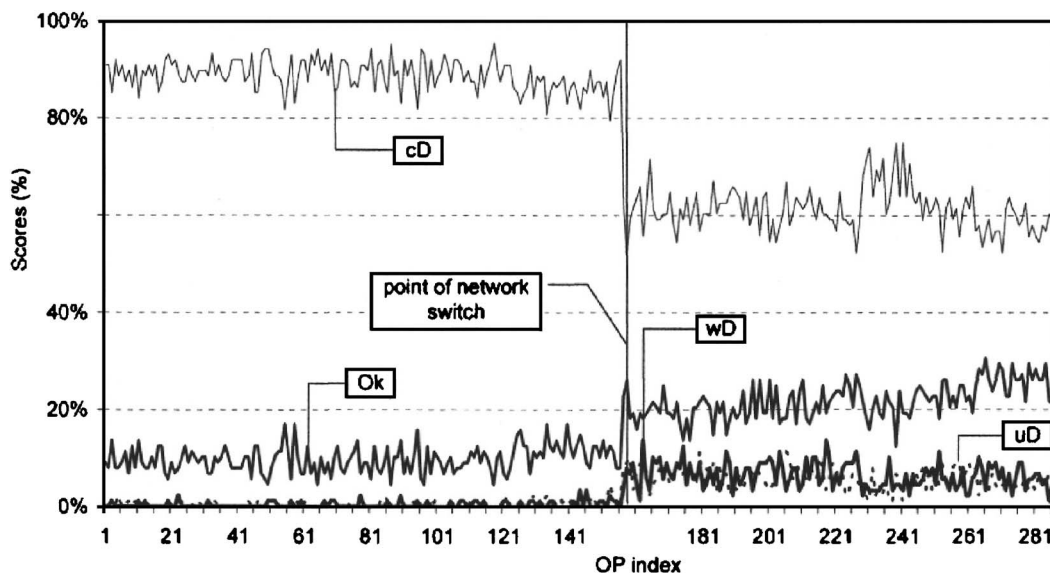


Fig. 12 Diagnostic performance of the method over a flight using two BBNs

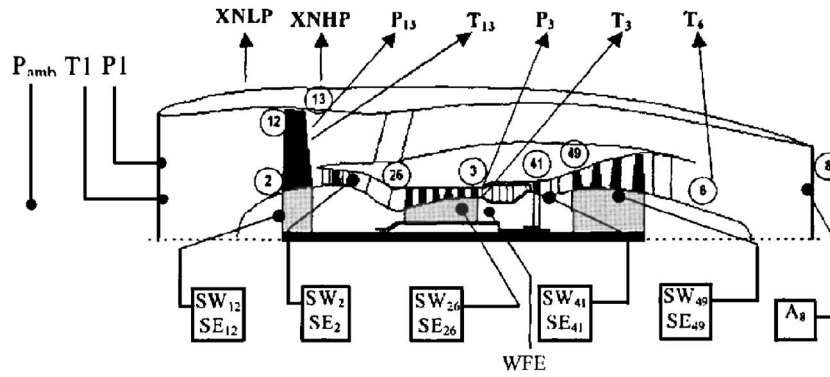


Fig. 13 Layout and station numbering and measurements of the considered turbofan engine

The ability to embed the proposed method into other diagnostic procedures, providing with more robust and accurate diagnosis is also a benefit. The presented method focuses on fault detection and isolation. Several “levels” of isolation (including isolation of the deviated health parameters, of the affected components or the affected section) have been considered. Once fault isolation at these levels is achieved, the deviation of the health parameters can be efficiently estimated by other existing diagnostic methods, leading to a more detailed diagnosis. A combination of the proposed method with other diagnostic tools is feasible and can be easily implemented as well. Dewallef et al. [19], present such a combination of Kalman filter techniques with a diagnostic BBN, for the case of a turbofan engine, demonstrating robust and detailed diagnosis.

Another important feature of the proposed BBN-based method is the convenience of inclusion of additional information, whenever available. As mentioned in a previous paragraph, the additional information can be included as an a priori knowledge, by modification of the a priori probability of the network nodes, or as independent knowledge, by adding nodes to the network. This inclusion is not a hard task since it does not require rebuild of the network. Information from other sources can be used, as for example vibration data or engine maintenance history. In this way, the present method offers an alternative to the known problem of gas path analysis (GPA), consisting of the determination of more health parameters than the available measurements. The BBN allows the inclusion of additional information from completely different sources for achieving this target, something that would be possible for GPA only by performing additional gas path measurements.

Table 3 Considered noise levels: $\sigma_{\Delta\gamma}\%$

XNLP	XNHP	P13	T3	P3	T6	T13
0.051	0.034	0.164	0.094	0.162	0.097	0.230

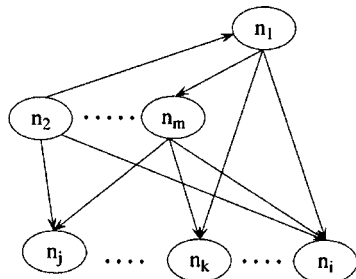


Fig. 14 Architecture of an example BBN

Concluding Remarks

The use of Bayesian belief networks for detection and isolation of component faults has been presented. The proposed diagnostic technique involves the use of an EPM, to produce the structural information of the network.

The way such a procedure can be set up is presented and application to a specific type of a turbofan engine is given.

The effectiveness of the proposed method has been demonstrated by its strong diagnostic ability with various fault scenarios and cases at several operating conditions, including coverage of an operational envelope of a typical flight.

The main conclusion concerning the performance of the presented method is its ability to handle efficiently the problem of fewer measurements than parameters in gas path analysis.

This conclusion becomes more important since it indicates that reliable diagnostic BBNs can be built from mathematical models, without the need of hard to find flight data of faulty operations on which other statistical methods are based, when dealing with uncertainty. An additional advantage of the proposed method is its ability to incorporate information from sources of different nature. It was shown that incorporating such information allows the extension of fault coverage, which was limited by the lack of sufficient gas path measurements.

Table 4 The considered fault cases of simulated test data

Fault Case	Affected f	deviation (%)	Fault Case	Affected f	deviation (%)
1	SW12	-2.0	17-24	SW2	-2.0 up to -0.6
2	SW12	-1.8	25-32	SE2	-2.0 up to -0.6
3	SW12	-1.6	33-40	SW26	-2.0 up to -0.6
4	SW12	-1.4	41-48	SE26	-2.0 up to -0.6
5	SW12	-1.2	49-56	SW41	-2.0 up to -0.6
6	SW12	-1.0	57-64	SE41	-2.0 up to -0.6
7	SW12	-0.8	65-72	SW49	-2.0 up to -0.6
8	SW12	-0.6	73-80	SE49	-2.0 up to -0.6
9-16	SE12	-2.0 up to -0.6	81-88	ABIMP	-2.0 up to -0.6

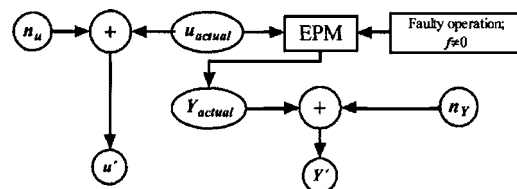


Fig. 15 Simulation of data of fault cases with the aid of EPM

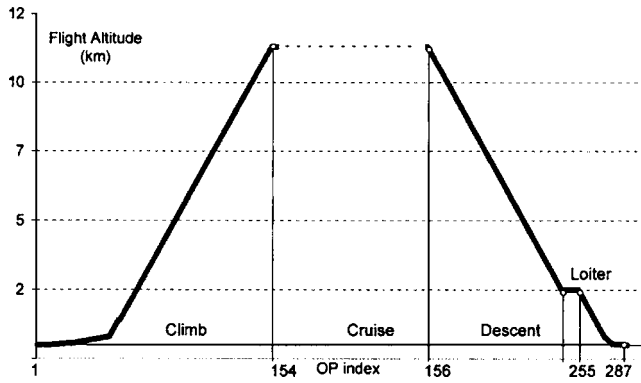


Fig. 16 The sections of a flight and the considered operating points

Nomenclature

- A8IMP = exhaust area
 EPM = Engine Performance Model
 f = vector of the health parameters of the engine
 f_o = nominal value of vector f
 HPC = high pressure compressor
 HPT = high pressure turbine
 LPT = low pressure turbine
 η_i = efficiency of component with entrance at station i
 n_u = random noise on the readings of vector u
 n_Y = random noise on the readings of vector Y
 P_{amb} = ambient pressure
 pdf = probability density function
 P_i = total pressure at station i of the engine
 $P(Y|f)$ = probability of Y given f
 $P(Y, f)$ = joint probability of Y and f
 $P(\Delta f_i \in [a, b])$ = probability of Δf_i to lie within limits $[a, b]$
 BBN = Bayesian belief network
 SE_i = efficiency factor at station i of the engine [Eq. (6)]
 SW_i = flow factor at station i of the engine (Eq. (5))
 T_i = total temperature at station i of the engine
 u = filtered values of u'
 u_{actual} = vector of actual values of u (noise free)
 u' = vector of measurements defining operating point
 W_i = gas mass flow rate at station i
 WFE = fuel flow rate
 XNHP = high pressure shaft rpm
 XNLP = low pressure shaft rpm
 Y = filtered values of Y'
 Y_{actual} = vector of actual values of Y (noise free)
 Y_o = nominal value of quantity Y
 Y' = vector of measured quantities on an engine
 δ = bias vector f
 ΔY = percentage deviation of Y ("delta") (Eq. (2))
 $\sigma_{\Delta Y}$ = standard deviations of vector ΔY
 $\sigma_{\Delta Y_i}$ = standard deviation of ΔY_i

Subscripts

- 1, 2, ..., 8 = station along the engine gas path, Fig. I-1
 ref = reference values (value in "healthy" engine)

Appendix A: Engine Layout and Representation

The layout of the considered turbofan engine, used as a test case, and the considered set of measurements for monitoring the

condition of the engine is shown in Fig. 13. The choice of this type of engine and instrumentation is discussed in (Mathioudakis et al. [6]).

The operating point of the engine is defined by measurement of the quantities: P_{amb} , $P1$, $T1$, and WFE, forming vector u , while rotating speeds of the two spools (XNLP and XNHP) and pressures and temperatures at several stations form vector Y .

Component faults are simulated by deviations of several health parameters from their nominal values. In the current work, flow and efficiency factors of each module of the engine at stations 12, 2, 26, 41, 49, 8, forming vector f are used as health parameters (see also Stamatis et al. [5]). For a component with entrance at station i of the engine we have:

$$\text{Flow factor: } SW_i = (W_i \cdot \sqrt{T_i/p_i}) / (W_i \cdot \sqrt{T_i/p_i})_{ref} \quad (5)$$

$$\text{Efficiency factor: } SE_i = \eta_i / (\eta_i)_{ref} \quad (6)$$

The quantitative interrelation among the health parameters and the measurements is expressed through an engine performance model (EPM) produced by Stamatis et al. [4] and adapted to individual engines to reproduce accurately their performance.

The measurements Y' obtained from the engine differ from those given by the EPM, since measured quantities are contaminated with noise. The considered noise levels, are those presented in Table 3 in the form of percentage of standard deviations from the nominal values at a typical cruise condition, and are those usually encountered for this type of instrumentation (as reported by Curnock [18]).

Appendix B: Basic Principles of Bayesian Belief Networks (BBN)

BBNs are probabilistic expert systems that combine the principles of probability theory and graph theory. They allow the estimation of probability of discrete variables even in complicated systems with many variables and strong relationship among them.

A BBN consists of nodes representing discrete variables, as defined in probability theory. All possible discrete values of a variable compose the set of states of the corresponding node. The interrelation among the variables is expressed through the links of the network. The quantitative relationship among the nodes is given through the conditional probability table (CPTs) of each node. The CPT of node n_i of a BBN is the set of probabilities:

$$P(n_i | \pi_i) \quad (7)$$

for all possible combination of states of the involved variables, where π_i is the set of nodes that are linked with node n_i , with direction to node n_i .

The nodes and links of a BBN represent its architecture. An example of BBN architecture is shown in Fig. 14.

The structure of a BBN consists of the states and the CPTs of its nodes.

Once the architecture and the structure of a BBN is defined, given the state of one or more nodes of the network, the probabilities of all states of the rest nodes can be estimated.

The estimated probabilities are function of the joint probability of the network nodes, given by:

$$P(n_1, n_2, \dots, n_n) = \prod_{i=1}^n P(n_i | \pi_i) \quad (8)$$

This estimation of probabilities with BBN has proven to be NP-hard (Cooper [20]), that is the required probabilities and computational time increase exponentially with the size (number of nodes, states and links) of the network. In order to overcome this problem, many approximating algorithms have been developed. For the needs of the current work, the algorithm of "systematic sampling method," described in details in Castillo et al. [13], has been applied.

Appendix C: Simulated Cases for Evaluation

The considered set of fault cases for evaluation consists of 88 cases each representing deviation of the health parameters from -0.6% to -2% , as shown in Table 4.

The corresponding measurements are derived from the EPM, applied for a specific operating point. These measurements are then contaminated with noise, to resemble actual measured data. A schematic presentation of this procedure for generating the set of testing measurements is shown in Fig. 15.

In order to reveal the behavior of the examined diagnostic method, under several operating conditions, the set of the 88 fault cases, has been considered for a total of 287 operating points, composing a flight envelope, covering all representative flight conditions, from ground roll to landing.

A schematic representation of the considered flight envelope is shown in Fig. 16.

References

- [1] Doel, D., 1992, "TEMPER-A Gas Path Analysis Tool for Commercial Jet Engines," ASME Paper No. 92-GT-315.
- [2] Volponi, A. J., and Urban, L. A., 1992, "Mathematical Methods of Relative Engine Performance Diagnostics," SAE 1992 Transactions, Journal of Aerospace, **101**, Technical Paper 922048.
- [3] Volponi, A. J., de Pold, H., Ganguli, R., and Daguang, C., 2000, "The Use of Kalman Filter and Neural Network Methodologies in Gas Turbine Performance Diagnostics: A Comparative Study," ASME Paper No. 2000-GT-547.
- [4] Stamatis, A., Mathioudakis, K., and Papailiou, K. D., 1990, "Adaptive Simulation of Gas Turbine Performance," J. Eng. Gas Turbines Power, **112**, pp. 168–175.
- [5] Stamatis, A., Mathioudakis, K., Ruiz, J., and Curnock, B., 2001, "Real Time Engine Model Implementation for Adaptive Control and Performance Monitoring of Large Civil Turbofans," ASME Paper No. 2001-GT-0362.
- [6] Mathioudakis, K., Kamboukos, Ph., and Stamatis, A., 2002, "Turbofan Performance Deterioration Tracking Using Nonlinear Models and Optimization Techniques," J. Turbomach., **124**, pp. 580-587
- [7] Mathioudakis, K., Kamboukos, Ph., and Stamatis, A., 2004, "Gas Turbine Component Fault Detection From a Limited Number of Measurements," Proc. Instn. Mech. Engrs., Part A: J. Power and Energy, **218**(Dec.), pp. 609–618.
- [8] Breese, J. S., Horvitz, E. J., Peot, M. A., Gay, R., and Quentin, G. H., 1992, "Automated Decision-Analytic Diagnosis of Thermal Performance in Gas Turbines," ASME Paper No. 92-GT-399.
- [9] Kanelopoulos, K., Stamatis, A., and Mathioudakis, K., 1997, "Incorporating Neural Networks Into Gas Turbine Performance Diagnostics," ASME Paper No. 97-GT-35.
- [10] Healy, T., Kerr, L., and Larkin, L., 1997, "Model Based Fuzzy Logic Sensor Fault Accommodation," ASME Paper No. 97-GT-222.
- [11] Siu, C., Shen, Q., and Milne, R., 1997, "TMDOCTOR: A Fuzzy Rule- and Case- Based Expert System for Turbomachinery Diagnosis," *Proceedings of the IFAC Symposium: SAFEPROCESS'97*, **1**, pp. 556–563.
- [12] Pearl, J., 1988, *Probabilistic Reasoning in Intelligent Systems: Networks of Plausible Inference*, 2nd ed., Morgan Kaufmann, San Mateo, CA.
- [13] Castillo, E., Gutierrez, J. M., and Hadi, A. S., 1997, *Expert Systems and Probabilistic Network Models* (Monographs in Computer Science), Springer, New York.
- [14] Palmer, C. A., 1998, "Combining Bayesian Belief Networks With Gas Path Analysis for Test Cell Diagnostics and Overhaul," ASME Paper No. 98-GT-168.
- [15] Romessis, C., Stamatis, A., and Mathioudakis, K., 2001, "Setting up a Belief Network for Turbofan Diagnosis With the Aid of an Engine Performance Model," ISABE Paper 2001, No. 1032.
- [16] Ganguli, R., 2003, "Jet Engine Gas-Path Measurement Filtering Using Center Weighted Idempotent Median Filters," J. Propul. Power, **19**, pp. 930–937.
- [17] Romessis, C., 2004, "Use of Stochastic Methods on Developing Systems for Condition Monitoring and Fault Diagnosis on Gas Turbines," Ph.D. thesis.
- [18] Curnock, B., 2001, OVIDICOTE Programme Work Package 4, "Steady-State Test Cases for Engine Deterioration," Rolls Royce Report, Document No. DNS78608, May.
- [19] Dewallef, P., Romessis, C., Mathioudakis, K., and Léonard, O., 2004, "Combining Classification Techniques with Kalman Filters for Aircraft Engine Diagnostics," ASME Paper No. GT-2004-53541.
- [20] Cooper, G. F., 1990, "The Computational Complexity of Probabilistic Inference Using Bayesian Belief Networks," *Artif. Intell.*, **42**, pp. 393–405.

Validation of CESI Blade Life Management System by Case Histories and in situ NDT

Claudia Rinaldi
Valerio Bicego
Pier Paolo Colombo

CESI,
Via Rubattino 54,
20134 Milano, Italy

A life management system was developed for hot components of large industrial gas turbines, in the form of a software tool for predicting component lives under typical operational transients (normal and also abnormal) and steady-state periods. The method utilizes results of previous thermo-mechanical finite element and finite volume fluid mechanics analyses. The basic idea of this method is using data from structural and aero-thermal analyses (pressures and temperatures), blade life theory, and material properties as an input to algorithms, and using operational and historical data to validate the predicted damage amounts. The software developed in this project, of general applicability to all GT models, has been implemented with reference to the geometries, materials, and service conditions of a Fiat-Westinghouse model. [DOI: 10.1115/1.2056534]

Introduction

To obtain a reliable, cost-effective, and efficient energy production with a low polluting level it is very important that the engine remains in a good condition as long as possible. Normally maintenance and overhaul intervals are prescribed by the gas turbine (GT) manufacturer based on the design know-how and on the feedback collated from users' experience. A sufficiently wide statistics to make reliable prediction of component lives is normally available only to the manufacturer; on the other hand, each individual user is generally unable to obtain a sufficient statistics on a particular GT model, unless he has several similar machines in his fleet and several years of operation experience.

Moreover, in several plants gas turbines are operated in variable conditions, so that the scheduled maintenance time intervals originally suggested by the OEM do not result to be the best ones to minimize maintenance costs while optimizing plant availability and safety. To obtain a convenient tool to optimize the life of hot parts in a GT, a code can be prepared which has the capability to calculate their residual life by combining turbine operational history with mechanical analysis algorithms and measured engine parameters. With the support of such a system it is possible for a user to predict the consequences of the different types of turbine operation (start/stop, baseload, trip, etc.). This concept [1–3] was originally proven with General Electric Frame 7 and 6 gas turbines in EPRI developments in the last decade, leading to the development of the so-called life management system (LMS) called REMLIF.

A life prediction methodology for large industrial gas turbines was developed also in CESI, dedicated at present to the first stage rotating blades of gas turbines widely used in Italy. In this study, the CESI approach is presented, implemented in a LMS as a PC software tool useful to calculate spent life fraction and to predict residual components lives under typical operational condition. Secondly, the application of this code is described to a number of real case histories, with the comparison between software predictions and experimental findings in the most damaged regions of the blades.

Finally, the results of in situ NDT measurements performed during maintenance plant stops with the frequency scanning eddy

current technique (F-SECT) were successfully compared with the prediction of the LMS software, run with the plant history as input.

These results will be described and the future perspectives of the use of this LMS tool will be discussed.

CESI LMS Approach

The life management system (LMS) developed at CESI is a PC software tool able to predict the gas turbine component lives under steady-state and transient conditions. The LMS development work was consisted of a comprehensive list of actions as follows.

(A) Damaged components and damage mechanisms identification: based on service experience, the critical regions on components and the relevant damage modes (creep, fatigue, TMF, coating damaged features, role of hot corrosion, embrittlement, etc.) are analyzed in order to identify the correct approach in the development of a LMS; attention has to be paid to the refurbishment cycles, repair and heat treatment features, and coating details.

(B) Computational fluid dynamics: geometrical parameters are retrieved for original component, including the inner cooling channel details, and the operating conditions are reviewed and collected, both normal steady-state service and the most typical start up and shut down transients; these data are then processed by means of fluid dynamics codes to obtain thermodynamic data distribution in gas flow around the component.

(C) Thermo-mechanical analyses: data obtained from the aero-thermal analyses (point B) are used as boundary conditions in a thermal-structural finite element (visco-elasto-plastic) code to provide patterns for temperature, stress, and strain at almost all locations in the component.

(D) Materials relevant data gathering: in a few cases, sufficient material information can be found in literature (traditional alloys and simple physical and mechanical parameters, such as thermal conductivity, Young modulus,...); on the other hand, material resistance to high temperature damage mechanisms, particularly for coated elements, has to be determined by important testing activities: creep, TMF, and cyclic oxidation mainly.

(E) Damage models: the materials data have then to be processed by suitable methods to provide all the numerical coefficient (temperature, stress, strain, and time dependent) in the damage growth rate models and end-life criteria, specific for the damage mechanisms and maintenance philosophy under consideration (e.g., end life defined as component failure, or maximum tolerated damage suitable to be repaired,...).

(F) LMS software: the several damage models and end life

Contributed by the International Gas Turbine Institute (IGTI) of ASME for publication in the JOURNAL OF ENGINEERING FOR GAS TURBINES AND POWER. Manuscript received October 1, 2003; final manuscript received March 1, 2004. IGTI Review Chair: A. J. Strazisar. Paper presented at the International Gas Turbine and Aeroengine Congress and Exhibition, Vienna, Austria, June 13–17, 2004, Paper No. GT2004-54217.

criteria are implemented in a software tool, also containing the input and output interfaces for a friendly use by the plant operator; it is pointed out that this software carries out a number of different damage evaluations, for a preselected grid of component conditions (new/refurbished) and operational scenarios (including transients), as provided by the user.

(G) Flexibility: within the LMS software, some options exist to take advantage of directly measured (or better to say, experimentally obtained) parameters; for example, the results from the aerothermal analysis can be tuned to the actual temperature values obtained by a pyrometer or estimated from metallurgical studies.

(H) Validation: at last, the code and its prediction capability have to be verified against actual case histories, namely damage evidence found after certain operational histories, for which the LMS tool is applied to derive comparative damage evaluations.

As regards point D, in CESI laboratories several cyclic oxidation tests were performed at different temperatures (1 h cycle); through metallography, quantitative image analysis, and x-ray microanalysis, an analytical model was formulated, taking into account all the aluminum depletion mechanisms active during operation and based on literature studies [4–8].

In this paper, aspects of the CESI activity for the development of LMS for the TG50D5 gas turbine are described. Due to space limitations, items A–D and G in the above list will not be further treated, short descriptions will be given of item F, and special focus will be put on the validation studies only (item H).

Damage Evaluation

The CESI life management system (LMS) takes into account three damage mechanisms:

- thermo-mechanical fatigue (coated blade material),
- creep (bare blade material), and
- cyclic oxidation (coated material).

The first two mechanisms act on mechanical properties of turbine component materials, while the last is related to protection capabilities of coatings.

The value D_{TMF} of damage for thermo-mechanical fatigue is given by the ratio between the number N of expended load cycles and the number N_f of cycles to rupture:

$$D_{TMF} = \frac{N}{N_f} \quad (1)$$

where N_f is a function of turbine operating conditions and mechanical properties of materials [3]:

$$N_f = C_1 (\Delta \varepsilon_m)^{C_2} (t_h)^{C_3} \exp(C_4 B) \quad (2)$$

In Eq. (2), C_i are function of material and load cycle shape, $\Delta \varepsilon_m$ is the total mechanical strain range during a load cycle, t_h is the hold time and B is given by

$$B = \frac{\varepsilon_{\max} + \varepsilon_{\min}}{\varepsilon_{\max} - \varepsilon_{\min}} \quad (3)$$

If turbine is subjected to different types of load cycles (transient speed, hold time, ...), for each of them Eq. (1) is applied and the total fatigue damage is the linear sum of partial damages:

$$D_{TMF} = \sum_i D_{TMF,i} = \sum_i \frac{N_i}{N_{f,i}} \quad (4)$$

The value D_{CR} of damage due to creep is given by the ratio between the exposure time t and the time t_r to creep rupture:

$$D_{cr} = \frac{t}{t_r} \quad (5)$$

Time t_r can be evaluated by means of the relation

$$t_r = C_1 \sigma^{C_2} \exp\left(\frac{Q}{RT}\right) \quad (6)$$

where C_i and Q are material parameters, R is the gas constant, and σ and T are, respectively, stress and temperature in steady-state condition. Again, when different types of load cycles are present, a linear sum of damage is adopted:

$$D_{cr} = \sum_i D_{cr,i} = \sum_i \frac{t_i}{t_{r,i}} \quad (7)$$

At present, fatigue and creep damages are treated separately, neglecting the influence of one mechanism on the other; the total mechanical damage $D_{m,tot}$ is then

$$D_{m,tot} = D_{TMF} + D_{cr} \quad (8)$$

At last, two models are implemented for cyclic oxidation damage. In the former, the value D_{OX} of cyclic oxidation damage is given by the ratio between the number N of expended load cycles and the number N_{ox} of cycles to get an Al content in coating insufficient to assure protection on base material:

$$D_{OX} = \frac{N}{N_{ox}} \quad (9)$$

The number N_{ox} is given by an empirical fit to published test results in literature [4,6,7] for a similar coating system:

$$N_{ox} = \left(\frac{C_4}{C_1 t_h \exp\left(\frac{-Q}{RT}\right)} \right)^{1/[C_2 + C_3 \exp(-Q/RT)]} \quad (10)$$

where C_i , are coating material parameters, and other parameters t_h , R , and T were defined above.

In the latter model, the value D_{OX} of cyclic oxidation damage is given by the ratio between the exposure time t and the time t_{ox} to the end of coating life (i.e., when coating aluminium content decreases to the value of the base material):

$$D_{OX} = \frac{t}{t_{ox}} \quad (11)$$

The value of t_{ox} , a function of a large number of parameters, has been evaluated by means of a computer code [9] for several operating conditions; in the LMS code data bank, the coefficients of a surface interpolating those t_{ox} values are stored.

Also for cyclic oxidation, the total damage is the sum of damages due to different load cycles:

$$D_{OX} = \sum_i D_{OX,i} \quad (12)$$

The Life Management System Computer Code

The LMS software was developed since the beginning as a small, flexible and self-contained software package for a personal computer, allowing efficient answers for any choice of scenarios asked by the user. Therefore it is running fast and providing great steps of view, based on a huge amount of preexisting knowledge and calculations. Such characteristics are provided by two features.

First of all, as already mentioned, the LMS software does not carry out any aerothermal or structural analysis to determine the needed values of temperature, stress, and strain at every point in the component; all such analyses were indeed made previously, during extensive simulations and modeling of several transients and steady-state operations; only their final results are stored in the LMS software. Moreover, in the code data bank also all needed material parameter values, temperature dependent, are contained.

Second, due to the wide variability of real operations, a scheme was adopted allowing a simple classification; not only simple for

the subsequent analysis by the LMS software, but also simple for the realistic possibility of the plant user to have the needed records of the operational data available. The simplifications here adopted were the following:

- Only two types of start up modes do exist, “normal” (as prescribed in the machine manual of operation) or “fast” (accelerated).
- Similarly the shut downs can be “normal” or “fast” (trips).

Before starting one run, the LMS software asks the user to choose a machine type, a component in it (first stage blade, vane, ...), and other data like new or refurbished material, coating type, and so on; all available component/material combinations are shown to the user by means of a tree view. In the current version, the software contains data and damage coefficients suitable for life analysis of first stage blades of two GTs, Fiat-Westinghouse TG50D5 and GE MS9001E; however, thanks to code modularity, as long as additional GTs and/or components will be investigated leading to the necessary algorithms matched to their characteristics (blade geometry, aerothermal conditions, stress-strain patterns, materials strength characteristics), the code can be implemented for such additions too.

Then the operational history is requested to be entered by the user:

- The past operation, in terms of percent normal transients and trips, percent of weekly operation ($t_h \cong 100$ h) or daily ($t_h \cong 15$ h), and so on, to be considered for the computation of the accumulated damage amounts (fatigue, creep and cyclic oxidation);
- the planned scenario of future GT utilization, in a form quite similar to one for the past operation (daily, or weekly, etc.), in order to evaluate damage accumulation rates specific for the planned future use.

Two options are available for planned future use: the user may wish to request the needed operational life up to the accumulation of a selected amount of component damage (e.g., up to a total damage of 100%, or coating damage up to 90% still suitable to allow blade refurbishment, any sort of special damage,...), or may wish to insert a desired plant operation period, and ask therefore what would be the damage accumulated in that period (this would be typically the residual component life, or the interval up to the next planned inspection during a major overhaul for maintenance).

Damage analysis results are provided by the LMS software in three formats:

(A) a simple text page with a summary of input data and of most relevant output results, namely the maximum levels of damage (creep, fatigue, cyclic oxidation, and total summed damage contributions) and the estimated remaining life for safe operation;

(B) detailed information in tabular form (a bit massive, so tedious to consult, essentially intended to allow special careful views when needed), presenting the values of the temperature, stress, strain, damages, etc., for each individual position in the component (the several nodes in the finite element mesh);

(C) dynamic graphical view of the component, in which the levels of the several quantities (e.g., the stresses, or the temperatures, or the cyclic oxidation accumulated damage,...) are displayed by means of iso-curves (in “banded form,” i.e., with regions between two iso-curves filled with a solid color).

When using graphical output, the view of turbine component can be panned, rotated, and zoomed simply by dragging the mouse; also available is an option to query all input and output data in a single point of the component by clicking in the desired position.

Table 1 Case histories for CESI LMS validation

Case history	Turbine inlet temperature	No. of start-ups	Trips %	Total firing hours	Mean hold time
1	Design	180	5	19,800	110
2A	Design	480	10	14,200	29
2B	Design	650	10	15,500	24
3	Design+50°C	450	40	8,800	19

Code Validation

The code validation was possible using several failure analysis studies performed on first stage blades in the first years of operation of the gas turbine fleet, before that the LMS system could be realized. In such studies metallographic analyses were performed on sections of the blades at different blade heights. Both optical microscopy and scanning electron microscopy and EDS (energy dispersive spectroscopy techniques) were used to evaluate coating damage and base material ageing (γ' coarsening and oxidation/corrosion). Among the different NDT techniques used in evaluating the blade after operation or during outages the F-SECT (frequency scanning eddy current technique [10–13]) resulted to be very powerful in measuring both coating thickness and coating damage.

In the following some applications of the code are described; the respective operating conditions introduced into the input screen of the LMS code are shown in Table 1, while summaries of analysis results (maximum value of each type of damage, usually happening at different positions on the component) are reported in Table 2. These are calculated with a mean value of coating thickness of 200 μm for case 1 (original new blade), while a mean coating value of about 170 μm was used for the other cases (refurbished blades), because this was the typical minimum thickness of the coating, measured in the hottest regions the by F-SECT technique in the coating shop.

Case History 1

This case history is representative of a TG50D5 turbine normal operating period with a prevalence of weekly operating cycles. The MCrAlY coating was produced by the OEM.

As shown in Table 2, the creep damage level is generally rather low, as expected, while the coating life (Fig. 1) is near its end along the leading edge and on a small region of the pressure side, near the trailing edge and at mid height of the blade, probably because of lower cooling as holes start to be placed only along one row instead of two. It can be noticed that these are the hottest zones of the calculated temperature distribution of the component (shown in Fig. 2). Secondly, a considerable thermo-mechanical fatigue damage is found at the platform edge in a particular position of the suction side (Fig. 3); relevant TMF damage is also observed along the leading edge.

The analyses performed by NDTs on operated components showed that in the regions indicated by the code, actually the coating was exhausted (very low equivalent beta thickness ob-

Table 2 Damage levels evaluated with CESI LMS for case histories in Table 1

Case history	Damage level (%)		
	Fatigue	Creep	Cyclic oxidation
1	24	18	80
2A	43	12	74
2B	54	14	84
3	59	8	81

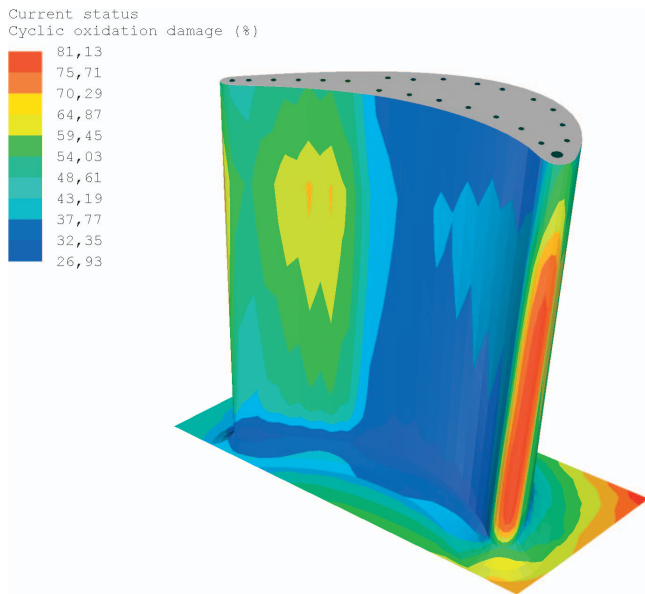


Fig. 1 Case history 1: distribution of cyclic oxidation damage

tained by measurement with the F-SECT system) in about 85% of the blades. A confirmation of the code results came also by residual stresses measurements performed on the component: significant tensile stress values were measured in the region of the platform around the position where the code indicates relevant thermomechanical fatigue damage. Moreover, the calculated plastic deformation levels and measured residual stresses gave the explanation of some accident (stress corrosion cracking of several millimetres) happening during the stripping process when this was performed without a previous solution heat treatment [14].

Case History 2A and 2B

Some GTs of the fleet were operated cycling more often (almost daily), so that the maximum equivalent operating hours (EOH)

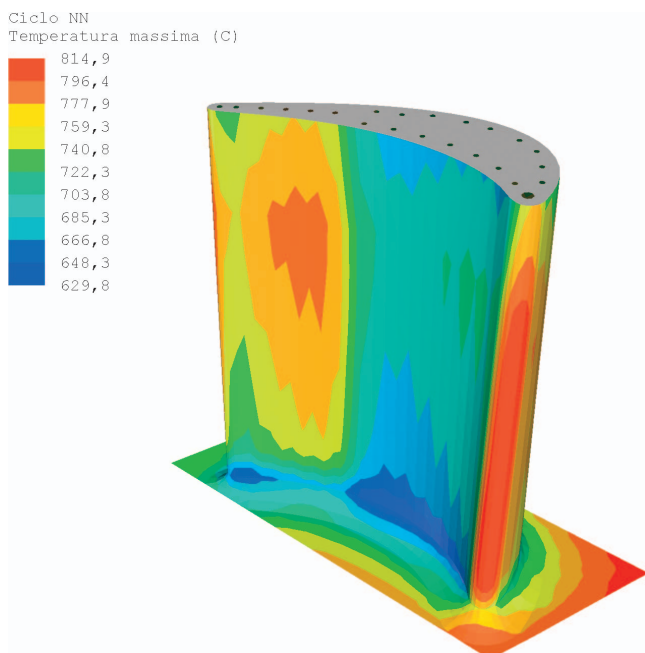


Fig. 2 Case history 1: distribution of steady-state temperature

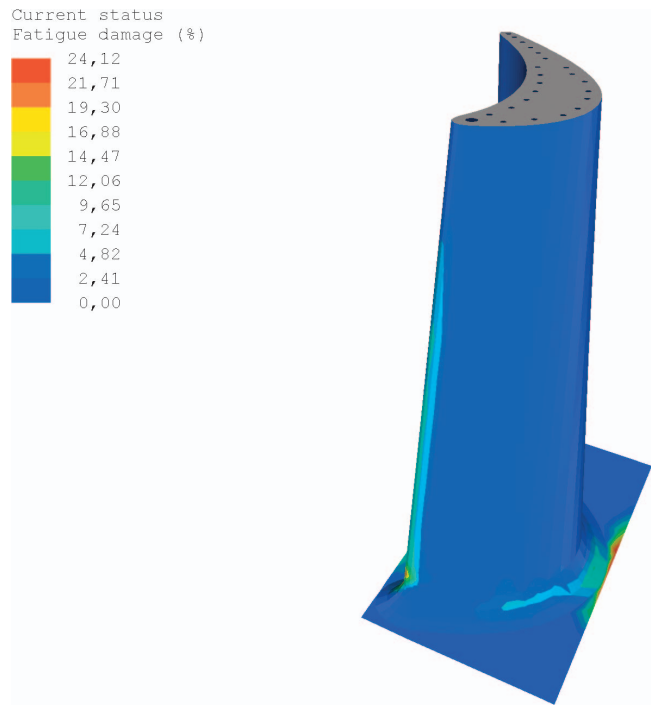


Fig. 3 Case history 1: distribution of thermo-mechanical fatigue damage

value indicated by the OEM was reached with about 14,000–15,500 firing hours and about 500–650 start-ups (see Table 1).

As shown in Table 2, in these cases the creep damage level is even lower than in the previous case, as expected due to the lower firing hours, while the coating life is near its end in regions located along the leading edge and on the pressure side (similar positions as in the previous case where cooling is reduced from two to one row of holes—Fig. 4).

At the platform edge in the position of the suction side previously noticed, the thermo-mechanical fatigue damage was about 50% (indication of possible crack presence—Fig. 5).

One blade (case 2A) was analyzed with F-SECT in several positions and after that sectioned to perform metallography;

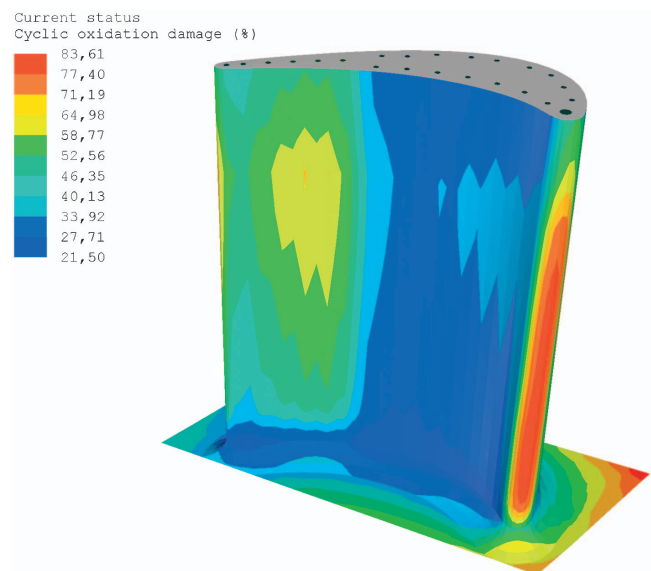


Fig. 4 Case history 2: distribution of cyclic oxidation damage

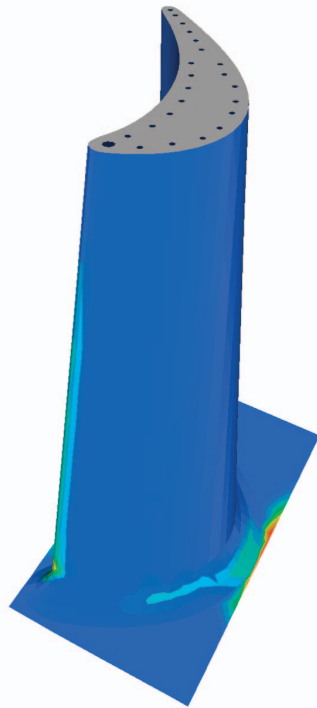
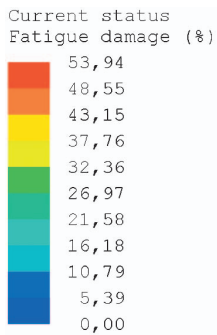


Fig. 5 Case history 2: distribution of thermomechanical fatigue damage

F-SECT results, shown in Fig. 6, confirm the level of coating damage calculated by the LMS. The comparison between Figs. 4 and 6 shows an interesting agreement between the coating damage level evaluated by the NDT technique F-SECT and the damage calculated by LMS:

- in positions 1 and 15 the coating is still protective (β phase is present) and the code evaluates about 50% of residual life;
- in the hottest positions (e.g., 12, and towards the leading edge) the coating is thin, no longer protective, and also base material is damaged;
- near the platform (position 23) the coating is present but no longer protective.

Moreover, the critical root position was analyzed. Very tiny transgranular oxidized cracks (some tenth of a millimeter deep) could actually be found. It must be noticed that usually such cracks are too small to be detectable with NDTs on the operated and sand blasted blade during the inspection for deciding component reparability after operation.

On some blades of case 2B (sent to refurbishment after the operation period) unacceptable platform cracks (longer than 2 mm) were found after stripping as shown in Fig. 7 (see also Fig. 8). Careful metallographic examination demonstrated the presence of preexistent small transgranular cracks due to thermo-mechanical fatigue (Fig. 9). This finding validates code calculations.

Case History 3

The third case is related to an abnormal operating period, with a lot of component scrapping due to heavy damage of the coating, its complete failure, and hot corrosion damage of the base alloy at the leading edge and on the pressure side (see the blades as operated and still mounted in Fig. 10). This happened at the beginning of the plant history, trying to reach the nominal efficiency levels and when the LMS code was not yet prepared.

Destructive metallographic examinations were performed on two scrapped blades (sections at 10%, 50%, and 90% of blade height). The coating was absent in two regions outlined in Fig. 11 (blade surface appearance after sand blasting). In the same picture examples of γ' morphology at different locations are shown: based on the measure of the γ' particle size and the reference curves of γ' coarsening versus temperature and time for UD 520 alloy [15] the evaluation of the operated metal temperature was performed. In the hottest regions of the blade an over temperature of about 50°C was estimated.

The code shows that actually the component life is passed over both for the cyclic oxidation and the fatigue damage mechanisms, even if in different regions. The damage maps are shown in Figs. 12 and 13. The comparison between Fig. 12 and the picture of the real component (Fig. 11) demonstrates a very good agreement between real and calculated damaged regions in the hottest zones of the component airfoil (pressure side) and at the leading edge. Some cracks were also found in some components at the platform edge in the same position of the suction side (see also previous cases) as shown in Fig. 14 for this case.

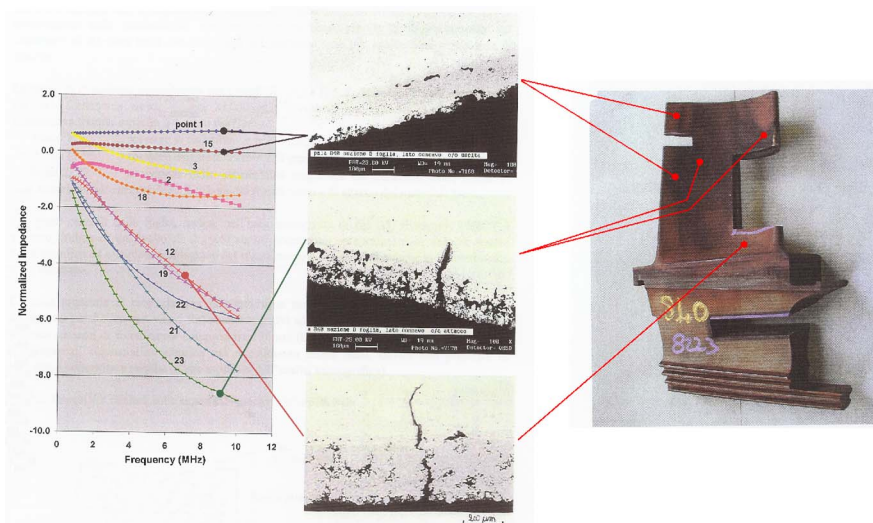


Fig. 6 F-SECT results for blade of case history 2A in Table 1

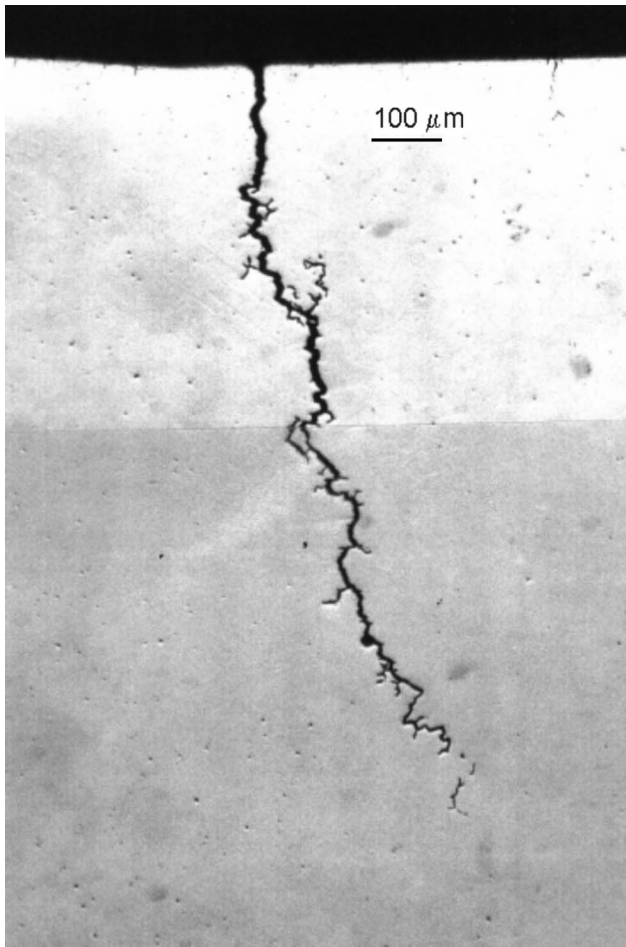


Fig. 7 Long intergranular stress corrosion cracks at platform edge of blade of case history 2B in Table 1 (see Fig. 8)

Discussion

Currently the LMS developed at CESI is still in the validation phase, i.e., it is intended that a number of details will be checked and progressively optimized by the feedback from experience gained in actual damage findings on service exposed GT components. Nevertheless, from the comparative analyses of predicted and actual damage amounts obtained in this paper, the prediction capability seems quite significant already at this stage. It has to be pointed out that creep and cyclic oxidation damage models are to be regarded as reasonably well established. On the other hand, the larger uncertainties might be expected within the TMF damage prediction part, as the TMF strength model presently included in the LMS software was determined from a limited source of TMF



Fig. 8 Position of platform crack shown in Fig. 7

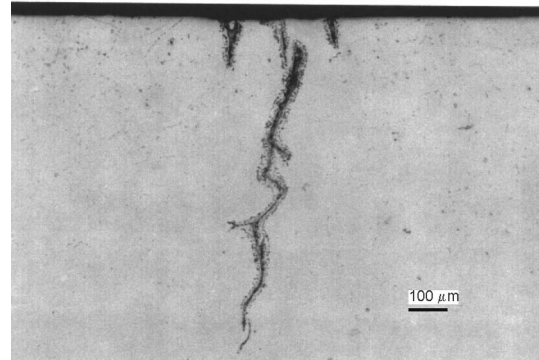


Fig. 9 Transgranular cracks at platform edge on blade of case history 2B in Table 1

data, from tests carried out at CESI in a previous program. As in that experiment no account was made for investigating hold time (t_h) nor strain ratio (B) effects, the numerical coefficients for such terms in Eq. (2) above for TMF life evaluations were not available for our alloy U520 and had to be taken identical to those reported in the EPRI [3], for another Ni-base alloy, in the noncoated condition (as most TMF cracking evidence were found in noncoated parts of the blades investigated). Predicted results were not bad in our TMF analyses, but clearly an experimental program devoted to define the t_h and B dependence of the TMF damage equation specifically for the alloy here considered, U520, is intended to remove this marginal lack of knowledge.

The LMS here developed was targeted to the main damage mechanisms for the first blades row in industrial gas turbines. Extending this package to other hot-parts would appear a useful development. However, this would require consideration of different damage phenomena not addressed here, e.g., aerothermal and mechanical vibrations which are often important for last stage rows blades performance.

Conclusions

The two tools (LMS and F-SECT technique) can be used together in a complementary and collaborative way to optimize GT maintenance policy (costs minimization and efficiency increase).



Fig. 10 Case history 3: cyclic oxidation damage on mounted first stage blades, leading edge side

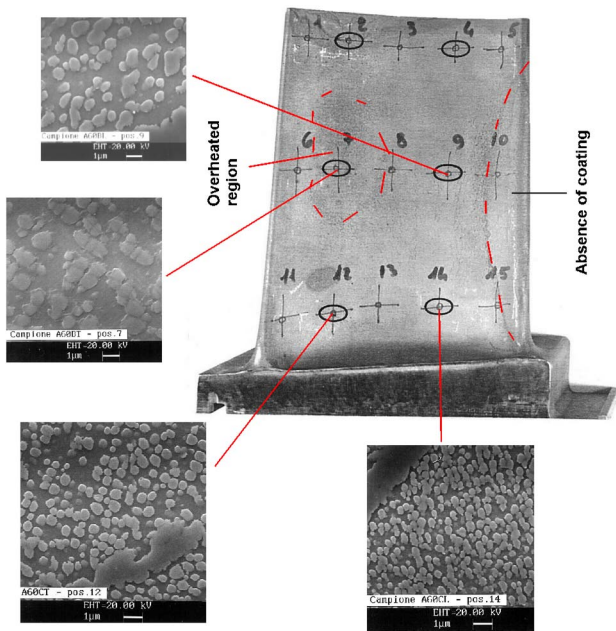


Fig. 11 Case history 3: damage on first stage blades

The capability of the LMS system coming out of the previous section can be summarized in the following:

- (A) prediction of different levels of cyclic oxidation and fatigue damage associated to different GT operation regimes (weekly, daily,...);
- (B) evaluation of life reduction (for thermo-mechanical fatigue) due to an unexpectedly high number of trips; and
- (C) residual life estimation for the actual conditions which the plant was operated in.

Most of all, the system is able to indicate the most critical locations on the components for each damage mechanism; this information can be a useful guide in several occasions:

- during quality control of the coating process, it allows a better choice of locations where the F-SECT measurements must be done to assure that a sufficient compact coating thickness is present;

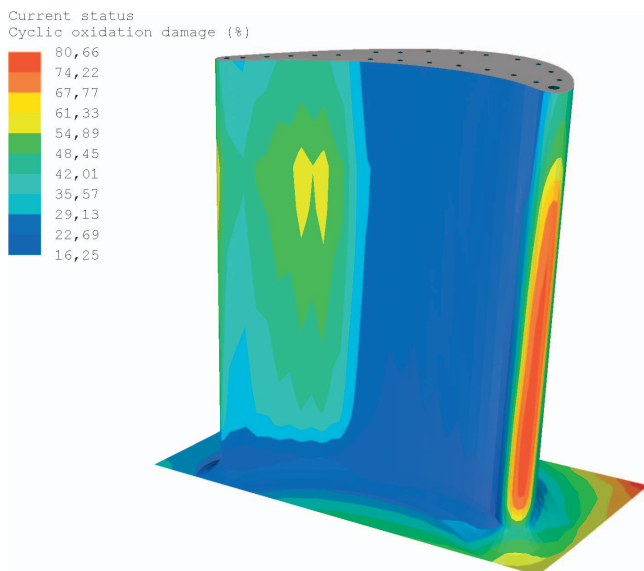


Fig. 12 Case history 3: distribution of cyclic oxidation damage

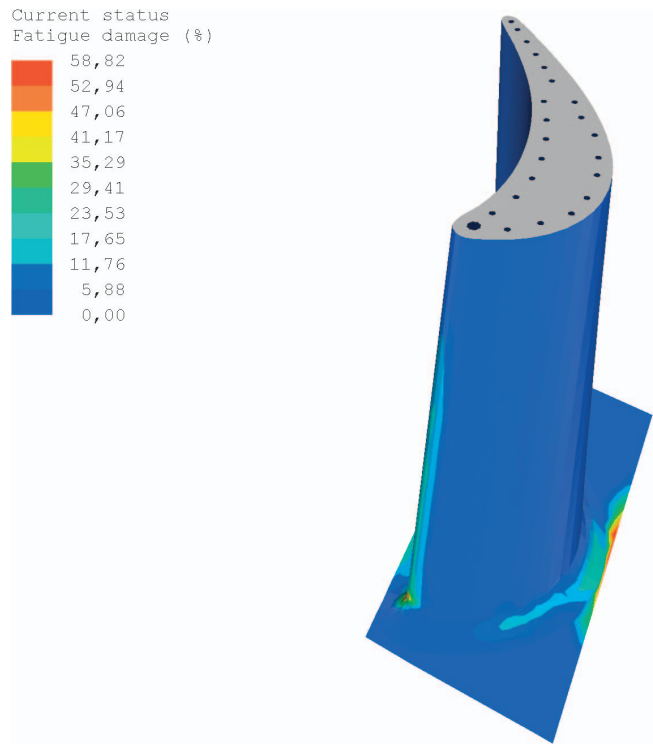


Fig. 13 Case history 3: distribution of thermo-mechanical fatigue damage

- during plant stops those critical positions will be more carefully observed by visual inspections and premature damage discovered;
- during the scheduled maintenance stops (open turbine case) the F-SECT control of the coating degradation by cyclic oxidation can be more effectively concentrated on the most critical positions; and
- decision to send components to refurbishment can be better supported by the use of code calculations and experimental measurements by F-SECT.

The experience done on the old machines analyzed in this paper gives a strong indication of how useful such a versatile LMS system can be and that it can be worthwhile to afford the big effort required to extend such methodology to the latest generation GTs.

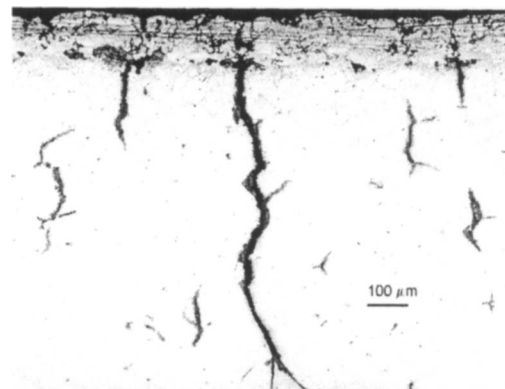


Fig. 14 Case history 3: platform TMF cracks at the same location where maximum fatigue damage is shown in Fig. 13

Acknowledgment

The basic studies required to prepare the frame of the code were performed in the frame of the Contract "Programma Ricerca di Sistema," established by the D-L-MICA 26 01 2000 of the Italian Government. The specific application to the GT model discussed in this paper was financially supported by a EUREKA contract, named TULIP.

Nomenclature

B	= strain ratio
C_i	= material parameters
D_{CR}	= creep damage
D_{OX}	= cyclic oxidation damage
D_{TMF}	= thermo-mechanical fatigue damage
$D_{m,tot}$	= total mechanical damage
N	= number of expended load cycles
N_f	= number of load cycles to failure for thermo-mechanical fatigue
N_{ox}	= number of load cycles to failure for cyclic oxidation
Q	= activation energy, J/mol K
R	= gas constant, J/mol
T	= absolute temperature, K
t	= expended time, h
t_h	= hold time, h
t_{ox}	= time to complete aluminium depletion, h
t_r	= creep time to rupture, h
$\Delta\epsilon_{mm}$	= range of mechanical strain in a load cycle
ϵ_{min}	= minimum value of mechanical strain in a load cycle
ϵ_{max}	= maximum value of mechanical strain in a load cycle
σ	= Von Mises equivalent stress, MPa

References

[1] Bernstein, H. L., 1990, "Life Management System for General Electric Frame

- 7E Gas Turbine," *Proc. of an Int. Conf. on Life Assessment and Repair Technology for Combustion Turbine Hot Section Components*, ASM, EPRI GS-7031, Phoenix, AZ, pp. 111–118.
- [2] Viswanathan, R., Scheibel, J., and Gandy, D. W., 1999, "Life Management System for Combustion Turbine Buckets and Nozzles," *Int. Conf. Life Assessment of Gas Turbine Hot Section Components*, Edinburgh, The Institute of Materials, London.
- [3] Berstein, H. L., Grant, T. S., McClung, M. C., and Allen, J. A., 1993, "Prediction of Thermal-Mechanical Fatigue Life for Gas Turbine Blades in Electric Power Generation," ASTM STP 1186, H. Sehitlogu, ed., Philadelphia, PA, pp. 212–238.
- [4] Chan, K. S., Cheruvu, N. S., and Leverant, G. R., 1999, "Coating Life Prediction for Combustion Turbine Blades," *ASME J. Eng. Gas Turbines Power*, **121**, pp. 484–488.
- [5] Lowell, C. E., Barrett, C. A., Palmer, R. W., and Auping, J. V., 1991, "COSP: a Computer Model of Cyclic Oxidation," *Oxid. Met.*, **36**(1/2), pp. S1–112.
- [6] Srinivasan, V., Cheruvu, N. S., Carr, T. J., and O'Brien, C. M., 1995, "Degradation of MCrAlY Coating and Substrate Superalloy During Long Term Thermal Exposure," *Mater. Manuf. Processes*, **10**, pp. 955–969.
- [7] Chan, K. S., Cheruvu, S., and Leverant, G. R., 1998, "Coating Life Prediction for Combustion Turbine Blades," *ASME Paper 98-GT-478*.
- [8] Nesbitt, J. A., 2000, "COSIM—A Finite Difference Computer Model to Predict Ternary Concentration Profiles Associated with Oxidation and Interdiffusion of Overlay Coated Substrates," NASA Report NASA/TM-2000-209271.
- [9] Mandelli, M., 2003, "Cyclic Oxidation Modelling of Coatings for Hot Parts of Gas Turbines," thesis (Prof. D. Colombo and S. Giananella), Trento University, Italy.
- [10] Antonelli, G., Ruzzier, M., and Necci, F., 1997, "Thickness Measurement of MCrAlY High-Temperature Coatings by Frequency Eddy Current Technique," *ASME Paper No. 97-GT-1*.
- [11] Antonelli, G., and Ruzzier, M., 1998, "A Calibration Free Electromagnetic Technique for NDT of Metallic Coatings," 7th European Conference on NDT, Copenhagen.
- [12] Antonelli, G., and Tirone, G., 2000, "Condition Assessment of Service Degraded High Temperature Blades, During Gas Turbine Overhauls," *Power. Gen Europe 2000*, Helsinki, Finland.
- [13] Antonelli, G., 2003, "Frequency Scanning Eddy Current System for Quality Control and in Field Life Assessment of High Temperature Coatings Applied on Gas Turbine Blading," *Turbine Forum*, Nice, France.
- [14] Colombo, P. P., Rinaldi, C., Sampietri, C., and Concari, S., 2001, "Failure Analysis of gas Turbine First Stage Blades," *Proc. EUROMAT 2001*, Conference on Materials for High Temperature, Rimini, Italy, paper 434.
- [15] Svinathan, V. P., Allen, J. M., and Touchton, G. L., 1996, "Temperature Estimation and Life Prediction of Turbine Blades with Post Service Oxidation measurements," *ASME Paper 96-GT-528*.

Proposal and Analysis of a Novel Zero CO₂ Emission Cycle With Liquid Natural Gas Cryogenic Exergy Utilization

Na Zhang

Institute of Engineering Thermophysics,
Chinese Academy of Sciences,
Beijing 100080, P. R. China
e-mail: zhangna@mail.etp.ac.cn

Noam Lior

Department of Mechanical Engineering and
Applied Mechanics,
University of Pennsylvania,
Philadelphia, PA 19104-6315

A novel liquefied natural gas (LNG) fueled power plant is proposed, which has virtually zero CO₂ and other emissions and a high efficiency. Natural gas is fired in highly enriched oxygen and recycled CO₂ flue gas. The plant operates in a quasi-combined cycle mode with a supercritical CO₂ Rankine type cycle and a CO₂ Brayton cycle, interconnected by the heat transfer process in the recuperation system. By coupling with the LNG evaporation system as the cycle cold sink, the cycle condensation process can be achieved at a temperature much lower than ambient, and high-pressure liquid CO₂ ready for disposal can be withdrawn from the cycle without consuming additional power. Good use of the coldness exergy and internal exergy recovery produced a net energy and exergy efficiencies of a base-case cycle over 65% and 50%, respectively, which can be increased up to 68% and 54% when reheat is used. Cycle variants incorporating reheat, intercooling, and reheat+intercooling, as well as no use of LNG coldness, are also defined and analyzed for comparison. The approximate heat transfer area needed for the different cycle variants is also computed. Besides electricity and condensed CO₂, the byproducts of the plant are H₂O, liquid N₂ and Ar. [DOI: 10.1115/1.2031228]

Introduction

Liquefied natural gas (LNG) is regarded as a relatively clean energy resource. During the process of its preparation, approximately 500 kWh energy per ton LNG is consumed for compression and refrigeration and a considerable portion of this invested exergy is preserved in the LNG [1], which has a final temperature of about 110 K, much lower than that of the ambient or of seawater. The liquefaction reduces its volume 600 fold, and thus makes long distance transportation convenient.

LNG is loaded into insulated tankers and transported to receiving terminals, where it is off loaded and first pumped to certain pressure, and then revaporized and heated, by contact with seawater or with ambient air, to approximately ambient temperature for pipeline transmission to the consumers. It is thus possible to withdraw cryogenic exergy from the LNG evaporation process which otherwise will be wasted by seawater heating. This can be achieved with a properly designed thermal power cycle using the LNG evaporator as the cold sink [1–13].

Use of the cryogenic exergy of LNG for power generation includes methods which use the LNG as the working fluid in natural gas direct expansion cycles, or its coldness as the heat sink in closed-loop Rankine cycles [1–5], Brayton cycles [6–9], and combinations thereof [10,11]. Other methods use the LNG coldness to improve the performance of conventional thermal power cycles. For example, LNG vaporization can be integrated with gas turbine inlet air cooling [5,12] or steam turbine condenser system (by cooling the recycled water [11]), etc. Some pilot plants have been established in Japan from the 1970s, combining closed-loop Rankine cycles (with pure or mixture organic working fluids) and direct expansion cycles [1].

Increasing concern about greenhouse effects on climatic change prompted a significant growth in research and practice of CO₂

emission mitigation in recent years. The technologies available for CO₂ capture in power plants are mainly physical and chemical absorption, cryogenic fractionation, and membrane separation. The amount of energy needed for CO₂ capture could lead to the reduction of power generation efficiency by up to 10 percentage points [14,15].

Besides the efforts for reduction of CO₂ emissions from existing power plants, concepts of power plants with zero CO₂ emission were proposed and studied. Particular attention has been paid to the research of trans-critical CO₂ cycle with fuel burning in highly enriched oxygen (99.5%+) and recycled CO₂ from the flue gas [16–25]. The common features of these cycles are the use of CO₂ as the working fluid and O₂ as the fuel oxidizer, produced by an air separation unit. With CO₂ condensation at a pressure of 60–70 bar (temperature 20–30 °C), efficiencies of 0.35–0.49 were reported for plants based on such cycles, despite the additional power use for O₂ production and CO₂ condensation. Staicovici [26] proposed an improvement to these cycles by coupling with a thermal absorption technology to lower the CO₂ condensation below ambient temperature (30 bar, 5.5 °C), and estimated a net power efficiency of 54%.

In a proposal by Velautham et al. [13], an LNG evaporation system is included in a gas-steam combined power plant just for captured CO₂ liquefaction and for air separation to provide oxygen for gas combustion. Deng et al. [9] proposed a gas turbine cycle with nitrogen as its main working fluid. The stoichiometric amount of air needed for the combustion is introduced at the compressor inlet, and mixed with the nitrogen. The turbine exhaust contains mainly nitrogen, combustion generated CO₂, and H₂O. With the cycle exothermic process being integrated with the LNG evaporation process, CO₂ and H₂O are separated from the mainstream by change of their phase, from gas to solid and liquid states, respectively, and the extra nitrogen is discharged. The main merit of this cycle is the absence of the air separation unit, but the combustion product may contain NO_x as well, and the collection and removal of solidified CO₂ may be difficult.

In this paper, a novel zero emission CO₂ capture system is

Contributed by the International Gas Turbine Institute of ASME for publication in the JOURNAL OF ENGINEERING FOR GAS TURBINES AND POWER. Manuscript received November 13, 2003; final revision received May 20, 2004. Associate Editor: R. F. Boehm.

Table 1 Main assumptions for the calculation

Cycle parameter	High pressure P_h^a [bar]	150
	Intermediate pressure P_m [bar]	30
	Low pressure P_l [bar]	1
	CO ₂ condensation pressure [bar]	6.5
	CO ₂ condensation temperature [°C]	-48.8
	Lowest temperature t_{13} [°C]	-70
	Mass flow rate ratio of Brayton cycle R_g [%]	30
Turbine	Methane LHV H_u [kJ/kg]	50,010
	LT Inlet temperature t_6 [°C]	1,300
Compressor	Isentropic efficiency [%]	88
	Pressure ratio	30.6
Combustor	Isentropic efficiency [%]	88
	Efficiency [%]	100
Recuperation system	Pressure loss [%]	3
	Water separator working temperature [°C]	10
ASU	Heat exchangers Pressure loss [%]	2
	Specific work for O ₂ production at 30.6 bar and 15°C [kJ/kg O ₂]	900
LNG vaporization system	LNG pump efficiency [%]	77
	Pressure loss [%]	3
	Evaporation pressure [bar]	30.6
	Delivery temperature [°C]	15

^aThe highest pressure of the cycle is $P_1=156$ bar, 6 bar is for pressure losses in the heat exchangers.

and then to evaporate the working fluid (CO₂) for the Rankine cycle by HE₁, the three-pass HE₂, and HE₃. The exhaust gas is then cooled further, by heating the LNG in HE₄, before compression by compressors LC and HC (this cooling reduces the compression work). The first compressor, LC, is used then to compress the working fluid to a pressure that would allow its condensation (in HE₅, the triple point of CO₂ is 5.18 bar and -56.6 °C), and some of the working fluid is withdrawn and first used to preheat combustion methane and oxygen in HE₇, and then condensed in HE₅. The remainder of the working fluid is compressed further in HC to the top pressure of the Brayton cycle, and then passed through the preheater HE₂ and combustor (*B*) before passing into the Brayton cycle turbine (LT). Assuming stoichiometric combustion, the exhaust gas of the Brayton cycle contains the combustion products CO₂ and H₂O through the path 6→7→8→9→10 only, with the H₂O separated from the CO₂ by condensation and withdrawal in *S*. A minute amount of CO₂ may be released along with water; but it is assumed here that the water and carbon dioxide are fully separated to simplify the calculation.

In the Rankine cycle, the Brayton cycle recuperators HE₁ and HE₂ serve as the 2-stage boiler of the working fluid (CO₂), HE₇ is a pre-condenser cooler and HE₅ is the condenser using the LNG as coolant, and P_C is the pump to raise the liquid CO₂ pressure to the top value of the Rankine cycle, and for the withdrawal of the excess liquid CO₂ for sequestration (at 19). The Rankine cycle turbine (HT) exhaust is preheated by the Brayton cycle exhaust recuperator HE₃ before being brought as additional working fluid into the combustor (*B*).

The air separator unit (ASU) is assumed here to produce oxygen for the combustor (*B*) at the combustor pressure. Liquid O₂ is pumped within the ASU to the combustor pressure by a cryogenic pump, and its cryogenic exergy is regenerated within the ASU (as in [26]). The O₂ (28) and fuel (25) are preheated in HE₇ before entering the combustor *B*. Further analysis is under way to explore the integration of the air separation process into the cycle, thus taking advantage of the coldness of its products.

LNG off loaded from its storage (20) is first pumped by pump P_L to its evaporation pressure (21), and then heated in the evaporation system (HE₄ (22) and HE₅ (23)) to near-ambient temperature. If the natural gas temperature at point 23 remains below that desired for distribution, the remaining coldness can be used for air conditioning or some other purposes in HE₆. A small portion (typically ~4%) of the natural gas (25) is preheated in HE₇ first and then sent to the combustor as fuel, and the remainder is sent

out to customers via pipeline. It is assumed in this paper that LNG is pure methane. It is noteworthy that both the thermal energy required for evaporation and the power that can be produced with the cryogenic cycle depend strongly on the LNG evaporation pressure. Different delivery pressures are typically made available at the receiving terminals: Supercritical (typically 70 bar) for long distance pipeline network supply, and subcritical (typically 30 bar) for local distribution and power stations based on heavy-duty combined cycles [10]. In this paper, only the subcritical natural gas evaporation process (30 bar) is considered, and the influence of different evaporation parameters will be investigated in forthcoming studies.

The placement of the heat exchangers in the cycle, and the choice of temperatures were made to reduce heat transfer irreversibilities. Furthermore, a combination of the higher-pressure (higher heat capacity) but lower mass flow rate fluid on the Rankine cycle side of the recuperators, with the lower-pressure (lower heat capacity) but higher mass flow rate fluid on the Brayton cycle side is also intended for reduction of irreversibilities.

The Cycle Performance

The simulations were carried out using the commercial Aspen Plus [27] code. To simplify computation, it was assumed that the system operates at steady state, the natural gas is pure methane, the combustion is stoichiometric with CO₂ and H₂O the only combustion products, no turbine blade cooling, and the stoichiometric amount of the water evacuated from the cycle does not contain dissolved CO₂. Besides, the outlet temperatures of the cold streams from HE₂ and HE₃ are set to be the same, i.e., $t_3 = t_{16} = t_5$, since the calculation results suggest a worse efficiency for $t_3 < t_{16} = t_5$. The most relevant assumptions for the calculations in this paper are summarized in Table 1.

The cycle minimal temperature is chosen as -70 °C to avoid gas condensation, since the saturated temperature of CO₂ under ambient pressure (1 bar) is -78.4 °C.

The energy efficiency is calculated as the ratio between overall power output and heat input in the topping cycle [11]:

$$\eta_1 = W_{net}/(m_f \cdot H_u) \quad (1)$$

where W_{net} is the overall power output from the turbines, reduced by the power input to the compressors (LC and HC) and pumps (P_C, P_L), m_f is the fuel mass flow rate input. This cycle employs both fuel and LNG coldness (via its evaporation) as its input resources, but we have used only the fuel energy in the definition of

Table 2 The stream parameters of CO₂ cycle

No.	<i>t</i> [°C]	<i>P</i> [bar]	<i>G</i> [kg/s]	<i>h</i> [kJ/kg]	<i>s</i> [kJ/kg K]	<i>a</i> [kJ/kg]	Mole Composition			
							CO ₂	H ₂ O	CH ₄	O ₂
1	-44.8	156	70	-9388.7	-2.289	255.9	1			
2	201.6	153	70	-8832.3	-0.555	295.1	1			
3	623.5	150	70	-8307.9	0.242	582.0	1			
4	442.7	30.6	70	-8522.2	0.284	355.3	1			
5	623.5	30	70	-8309.0	0.553	488.2	1			
6	1300	29.1	110.96	-7578.1	1.266	1194.8	0.9	0.1		
7	761.9	1.07	110.96	-8307.4	1.366	435.8	0.9	0.1		
8	656.2	1.05	110.96	-8441.8	1.233	341.0	0.9	0.1		
9	264.4	1.03	110.96	-8902.4	0.598	69.9	0.9	0.1		
10	10	1.01	110.96	-9253.1	-0.349	1.368	0.9	0.1		
11	10	1.01	4.93	-15,936.0	-9.298	1.677		1		
12	10	1.01	106.03	-8955.0	0.021	0.886	1			
13	-70	1	106.03	-9018.3	-0.239	15.18	1			
14	61.1	6.63	106.03	-8915.4	-0.202	106.8	1			
15	201.6	30.6	30	-8788.7	-0.169	223.8	1			
16	623.5	30	30	-8309.0	0.553	488.2	1			
17	53.8	6.565	76.03	-8922.0	-0.220	105.6	1			
18	-48.8	6.5	76.03	-9406.9	-2.309	243.5	1			
19	-44.8	156	6.03	-9388.7	-2.289	255.9	1			
20	-162	1	54.69	-5557.9	-11.721	1086.2				1
21	-160.5	31.5	54.69	-5548.5	-11.702	1089.9				1
22	-126.7	31.2	54.69	-5425.8	-10.75	928.8				1
23	-5	30.9	54.69	-4751.8	-7.143	527.4				1
24	15	30.6	52.49	-4702.4	-6.961	522.4				1
25	15	30.6	2.2	-4702.4	-6.961	522.4				1
26	51.1	30	2.2	-4613.3	-6.659	521.7				1
27	25	1	~37.76	/	/	/		air		
28	15	30.6	8.76	-17.5	-0.942	264.3				1
29	51.1	30	8.76	17.8	-0.821	263.7				1
30	/	/	~29.0	/	/	/		N ₂ , Ar,...		
31	25	1.01	130	-15,865.6	-9.056	0		1		
32	20	1	130	-15,886.4	-9.126	0.098		1		

Note: Combustor inlet CO₂ mass flow rate of 100 kg/s assumed as references.

η_1 , the energy efficiency, because the LNG coldness is free, and it is actually of benefit to the user. Both input resources are, however, used in defining η_2 , the exergy efficiency, which is the more appropriate criterion for performance evaluation than the fuel energy alone. It is defined here as the ratio between the net obtained and total consumed exergy

$$\eta_2 = W_{net} / (m_f \cdot H_u + m_L \cdot a_L) \quad (2)$$

assuming that the fuel exergy is approximately equal to its lower heating value H_u , m_L is the treated LNG mass flow rate, and a_L the exergy difference between the initial and the final states of the LNG evaporation process:

$$a_L = (h_{20} - h_{23}) - T_0(s_{20} - s_{23}) \quad (3)$$

and in the subcritical evaporation case (30.6 bar), it is about 560 kJ/kg_{LNG}, depending on the final temperature T_{23} .

For a given mass flow rate of the cycle working medium, the mass flow rates of needed fuel, of water and carbon dioxide recovered, and of LNG regasified can all be determined.

With 100 kg/s mass flow rate of CO₂ at the combustor inlet taken as reference, Table 2 summarizes the parameters, including temperature, pressure, flow rate and composition, and thermodynamic properties including exergy, of each stream for the subcritical pressure (30.6 bar) and temperature of 15 °C natural gas delivery. The mass flow rate of LNG regasified is found to be 54.69 kg/s, of which about 4% (2.2 kg/s) are sent to the combustor as fuel for the cycle; and the amount of water and CO₂ recovered are found to be 4.93 kg/s and 6.03 kg/s, respectively.

The computed performance of the cycle is summarized in Table 3 (first column). The total power produced is found to be 79.3

MW. Reduced by the power consumed for O₂ separation, which is roughly 7.9 MW (~10%), the net power output is 71.4 MW, resulting in an energy efficiency (η_1) of 65% and exergy efficiency (η_2) of 51%. The difference between the efficiencies is due to their definition (Eqs. (1) and (2)), where η_1 does not take into account the LNG coldness exergy, while η_2 does. Consequently, such a plant would produce about 124 MWE if installed with the first Chinese LNG receiving terminal that has an import capacity of 3,000,000 t per year (95 kg/s).

Figures 3 and 4 are the t - Q diagrams for the recuperation system and the LNG evaporation system, respectively, where Q is the heat duty of a heat exchanger. Heat load distribution is not even among the different heat exchangers. The minimal temperature differences are present in HE₁ and HE₅. The pinch point in HE₁ appears at the point where the H₂O vapor contained in the hot LT exhaust stream begins to condense. The minimal temperature difference, ΔT_{p1} , is 10 K in this case and one way to raise it is to increase the flue gas temperature out of HE₁(t_{10}), which will lead to more flue gas exhaust heat for LNG evaporation. The pinch point in HE₅ appears at the point where CO₂ begins to condense, and ΔT_{p5} is 5 K in this calculation. Reducing the pinch point temperatures will increase the thermal performance, but larger heat transfer surface area and more equipment investment will be required.

The NG temperature at the HE₅ outlet is -5 °C, still cold enough to be used for local applications such as refrigeration and air conditioning. The total heat duty of HE₆ is 2.7 MW, and if practical cooling can be accomplished up to $t_{24}=5$ °C (rather than

Table 3 Performance summary of different cycle configurations

	Base-case	No-LNG	Reheat	Intercooling	Reheat+ intercooling
LT turbine work [MW]	80.9	80.5	44.6	81.3	44.9
MT turbine work [MW]	0	0	43.0	0	43.2
HT turbine work [MW]	15.0	15.1	16.3	14.6	16.3
LC compressor work [MW]	10.9	14.0	11.0	10.9	11.0
MC compressor work [MW]	0	13.7	0	0	0
HC compressor work [MW]	3.8	4.6	3.9	2.6	2.6
LNG pump work [MW]	0.5	0	0.5	0.5	0.5
CO ₂ pump work [MW]	1.4	1.3	1.4	1.4	1.4
Fuel/O ₂ expander [MW]	0	0	0.6	0	0.6
O ₂ separation work [MW]	7.9	7.7	8.4	8.1	8.7
Net power output [MW]	71.4	54.1	79.4	72.4	80.8
LNG mass flow rate [kg/s]	54.7	0	54.9	54.7	55.0
Fuel ratio [%]	4.02	/	4.28	4.14	4.42
Fuel energy input $m_f \cdot H_u$ [MW]	109.9	107.2	117.6	113.3	121.5
LNG exergy input $m_L \cdot a_L$ [MW]	30.5	0	30.7	30.9	31.0
Energy efficiency [%]	65.0	50.5	67.5	63.9	66.5
Exergy efficiency [%]	50.9	50.5	53.6	50.2	53.0

all the way to 15 °C), a modest contribution of about 1.3 MW of cooling can be obtained and added to the overall useful output of the system.

Table 4 shows the heat duties of the heat exchangers, and the estimated required heat exchanger surface areas. There are seven

heat exchangers in the system: Recuperators (HE₁, HE₂, and HE₃), LNG evaporators (HE₄, HE₅, and HE₆), and a fuel/O₂ pre-heater, HE₇. The recuperators are conventional heat exchangers with gas streams flow through both sides (ignoring the small amount water condensation in HE₁). HE₄ is a CO₂ gas-to-CH₄ liquid heat exchanger. As shown in Fig. 4, HE₅ consists of two parts, in the first part heat is exchanged between CO₂ gas and natural gas, in the second part CO₂ is condensed due to cooling by liquid, boiling, and gaseous CH₄ with an overall heat transfer coefficient estimated as 600 W/m² K [28]¹. In the calculation in Table 4, the hot stream in HE₆ is assumed to be water with the inlet and outlet temperatures of 25 and 20 °C, respectively. The total heat transfer area for the cycle is estimated to be 27,856 m², nearly 80% of which are the recuperators, and 20% the LNG evaporators, the latter accommodating about 30% of the total heat duty.

The exergy inputs, outputs, and losses are shown in Fig. 5 and Table 5. Some important conclusions are: (1) The amount of coldness exergy of the LNG adds about 28% to the fuel exergy used in the cycle, and is 22% of the overall cycle exergy input ($m_f \cdot H_u + m_L \cdot a_L$), (2) the base-case cycle uses 54% of the coldness exergy of the LNG for power generation, (3) the largest exergy loss, 21%, is in the combustor, consistent with general values found in the literature [29]; this loss can be straightforwardly decreased only by increasing the inlet temperature of the LT turbine beyond the assumed 1300 °C, which would be possible if more advanced turbines are used, (4) obviously, the addition of any component for improving cycle efficiency introduces exergy losses associated with the component, here the most significant ones are in the heat exchangers HE₅ (8.2%), HE₄ (5.2%), and HE₁ (3.4%); these losses can be decreased by decreasing the temperature differences between the heat exchanging streams (Figs. 3 and 4), but this would obviously require larger or/and more complex heat exchangers. The LMTDs of different heat exchangers are shown in Table 4. HE₃ and HE₄ have the biggest LMTDs among the heat exchangers, while exergy loss in HE₃ is relatively smaller because of the high heat transfer temperature. To reduce the system exergy loss further calls for synthetic optimization of both cycle configu-

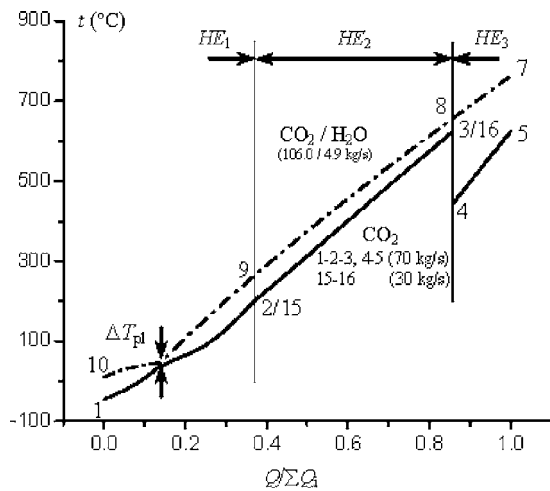


Fig. 3 t-Q diagram in CO₂ recuperation system

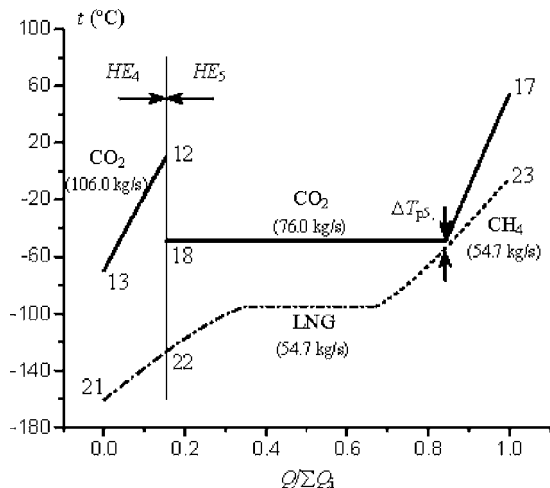


Fig. 4 t-Q diagram in LNG evaporation system

¹Precise determination of heat exchanger areas requires their detailed design specification. The estimates here are very rough, based on the assumption that the heat exchangers are of the shell-and-tube type, and using average typical overall heat transfer coefficient values for these heat exchanger processes and fluids as found in the process heat transfer literature [28]. Use of better heat exchangers, such as plate type, may reduce the required heat transfer area by as much as an order of magnitude.

Table 4 Heat exchanger surface area estimation

	Heat exchanger	Q [MW]	UA [kW/K]	LMTD [K]	U [28] [W/m ² K]	A [m ²]	A [%]	ΣA [m ²]
Recuperators	HE ₁	38.95	1005.76	38.7	99	10,159.2	36.5	21,968
	HE ₂	51.10	1011.75	50.5	93	10,879.0	39.0	
	HE ₃	14.93	86.47	172.7	93	929.8	3.3	
LNG evaporators	HE ₄	6.71	59.63	112.5	99	602.3	2.2	5,632
	HE ₅	36.86	1124.2	32.8	93/600	4645.6	16.7	
	HE ₆	2.699	164.97	16.4	429	384.6	1.4	
Fuel/O ₂ preheater	HE ₇	0.50	23.73	21.1	93	255.1	0.9	255

ration and stream parameters. (5) Figure 5 shows clearly that the proposed configuration of the cycle allows a large fraction of the exergy to be usefully reused internally.

Key Parameters and Discussion

The key parameters that have influence on the cycle performance include the Brayton cycle mass flow rate ratio R_g , the low-pressure turbine inlet temperature t_6 , the cycle high and intermediary pressure level P_h and P_m .

The Brayton cycle mass flow rate ratio R_g is defined as the ratio of the mass flow rate of stream 16 (Fig. 1) over that of the total CO₂ recycled in the system.

$$R_g = m_{16}/(m_5 + m_{16}) \quad (4)$$

If R_g equals 1, the plant becomes a pure Brayton cycle, and less flue gas exhaust heat will be recovered in the recuperation system due to the sizeable increase of the flue gas temperature at the inlet of the LNG evaporation system. This temperature equals to the sum of t_{15} and a temperature difference needed for heat transfer in HE₂. At the other extreme, if $R_g=0$, it is still a kind of quasi-combined cycle of a Brayton and a supercritical Rankine-type one, similar to the “MATIANT” cycle [25], and the higher heat capacity of the compressed liquid CO₂ will lead to a larger temperature difference between LT outlet flue gas and CO₂ entering the combustor, t_7-t_5 . Variation of R_g will thus not only change the flue gas heat distribution between the recuperation system and the LNG evaporation system, but also the heat balance inside the recuperation system itself. Calculation shows that both energy ef-

iciency and exergy efficiency increase by about 3 to 4 percentage points for every 100 °C increase of t_6 (LT inlet temperature) or 20% increase of R_g . Increasing R_g means that more flue gas waste heat is recovered in the recuperation system, and the pinch point temperature difference in HE₁(ΔT_{p1}) will drop accordingly, R_g reaches its upper limit when ΔT_{p1} drops to the accepted lowest value. The specific power output w increases with the increase of t_6 and with the decrease of R_g .

A relatively high level for P_h and P_m was employed in some past studies of power cycles with CO₂ separation, for example, they are 240 bar and 60 bar, respectively, in the “COOPERATE” [20,22] and “COOLENERG” cycles [26], and 300 bar and 40 bar in the “MATIANT” cycle [25]. To relieve the technical problems incurred by these high pressure levels, the pressure P_h and P_m is chosen in our cycle to be 150 and 30 bar for the design point.

Computations show that both P_h and P_m have positive impact on the efficiencies and specific power output within certain calculation range ($P_m=15-55$ bar and $P_h=100-200$ bar). When P_h increases from 150 bar to 200 bar for $P_m=25$ bar, the efficiencies increase by about 0.6 percentage point; and they increase by 1.7 percentage points when P_m increases from 15 to 25 bar for $P_h=150$ bar. Obviously P_m has a more notable influence on the cycle thermal performance than P_h , clearly because the power output of the LT turbine is several fold bigger than that of the HT turbine. Increasing P_h and P_m results in the lowering of the HT and LT turbine flue gas temperature, respectively, leading to the drop of

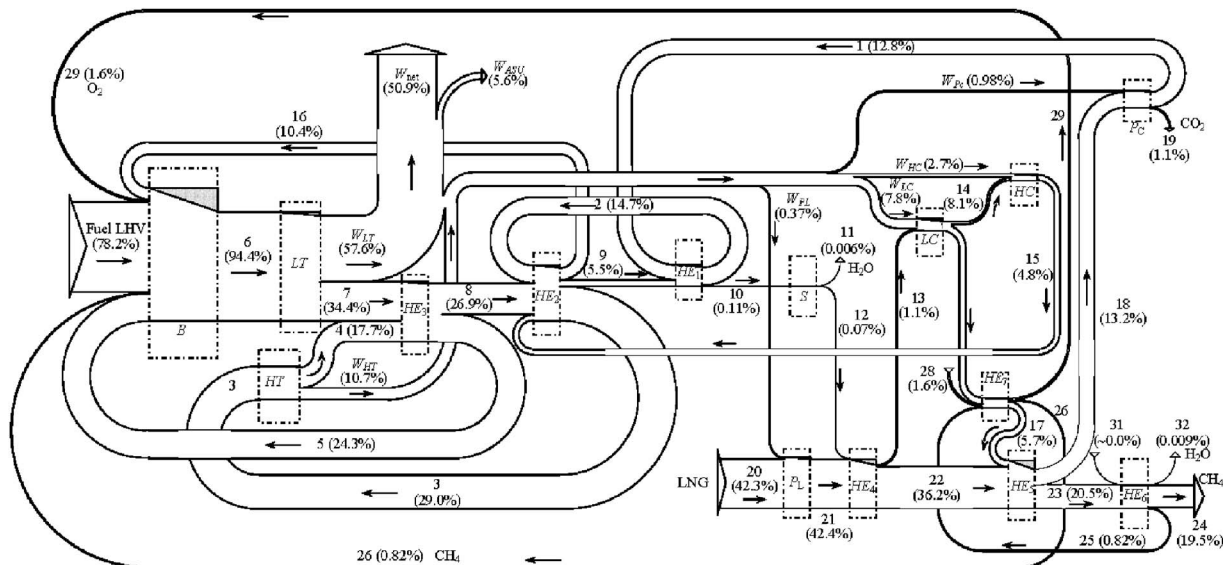


Fig. 5 The exergy flow diagram for the base-case cycle

Table 5 Exergy inputs, outputs, and losses decomposition in the cycle

Exergy input ^a (%)		
Chemical exergy	Fuel LHV	78.238
Physical exergy (stream in)	20; LNG	42.300
	28; O ₂	1.649
	31; H ₂ O	0.0
Sum		122.187
Exergy output ^a (%)		
Power output	W_{net}	50.860
	W_{ASU}	5.617
Physical exergy (stream out)	11; H ₂ O	0.0059
	19; CO ₂	1.099
	24; CH ₄	19.525
	32; H ₂ O	0.0091
Component exergy losses	B	21.058
	HE ₅	8.167
	HE ₄	5.194
	HE ₁	3.461
	LT	2.352
	HE ₂	1.471
	HE ₃	0.866
	LC	0.853
	HT	0.619
	P_c	0.312
	P_L	0.222
	HC	0.206
	HE ₆	0.186
	HE ₇	0.07
	S	0.035
Sum		122.188

^aValues are based on $(m_f \cdot Hu + m_{LNG}) = 78.238\% + (42.3 - 20.538)\% = 100\%$ (Eqs. (2) and (3)).

the pinch point temperature difference ΔT_{p1} , but it is not necessary to have very high values of P_h , since the HT turbine contributes less to the cycle power output.

Compared with the above-mentioned cycles, our cycle has two new features: first, while $R_g = 0$ (no HC compressor) in those cycles, $R_g > 0$ in our cycle, which allows a much better turbine exhaust heat recovery in the recuperation system; second, integration here with the LNG evaporation process accomplishes CO₂ condensation at a much lower pressure. As a result, the computed energy efficiency is as high as 65% with the enabling technologies (TIT=1300 °C, $P_h=150$ bar and $P_m=30$ bar), which is about 10 to 15 percentage points of increment compared with the other above-mentioned cycles.

The typical cryogenic equipment for air separation consumes about 0.2–0.28 kWh of electric power per kilogram of O₂ separated [13], depending on the product purity, production capacity and so on. It is found through the calculation that the power consumed for O₂ production is nearly 10% of the total power output, and every 10% reduction in the power needed for air separation will increase both efficiencies and power output by about 1.1%. Clearly, one way to improve system performance is to optimally integrate the air separation with the rest of the system.

Comparison of Different Cycle Configurations

With the base-case cycle described in Figs. 1 and 2 as reference, different system configurations were modeled and analyzed to further explore the effect of LNG exergy application and to examine the potential for performance improvement. These configurations include one where no LNG is used, one in which intercooling is used, one with reheat, and one with reheat and plus inter cooling. The corresponding t - s diagrams are shown in Figs. 6–9, respectively.

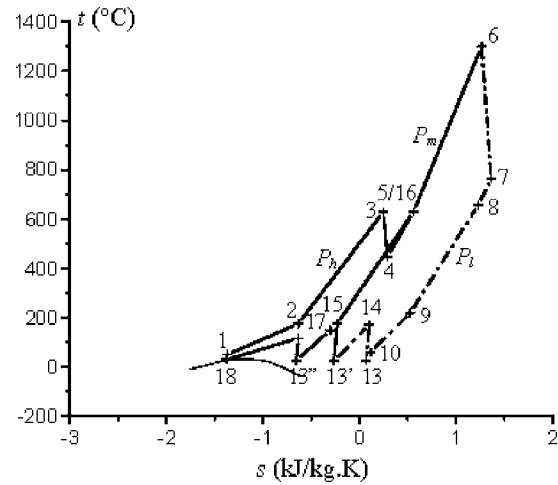


Fig. 6 t - s diagram for CO₂ cycle without LNG

Figures 10 and 11 show the cycle layout for the cycle without use of LNG coldness (no-LNG case), and the intercooling+reheat cycle, respectively. The reheat cycle is the combination of the left part of the schematic shown in Fig. 1 and the right part of that in Fig. 11. Similarly, the intercooling cycle is the combination of the right part of Fig. 1 and the left part of Fig. 11.

If LNG is not used for its coldness, as in reference [30], then a multi-stage compression process with intercooling $13 \rightarrow 14 \rightarrow 13' \rightarrow 15 \rightarrow 17 \rightarrow 13'' \rightarrow 14' \rightarrow 18$ (in Fig. 10) is adopted to bring the CO₂ up to a liquid state of 80 bar and 30 °C, instead of the CO₂ condensation process. This brings two advantages: Elimination of noncondensable gases and the associated problems, and elimination of the need for a condenser. The cycle in Fig. 6 can hence be regarded as a combination of the “MATIANT” cycle and a CO₂ Brayton cycle with intercooling. Unlike all the other ones, this cycle works above the ambient temperature. It uses cold water as the intercooler coolant with the temperature varying from 15 to 20 °C. The specific power output is about 76% of that of the base-case cycle, and it has the same energy efficiency and exergy efficiency, which can reach 50%.

When reheat is employed, the low-pressure turbine outlet temperature t_7 can be raised significantly (to over 1000 °C, Figs. 7 and 9), and the turbine exhaust heat is large, able to raise temperature of the cold streams in HE₂ to a higher magnitude. However, for practical turbine materials, the high pressure turbine HT inlet temperature is restricted to 700 °C in the calculations, and

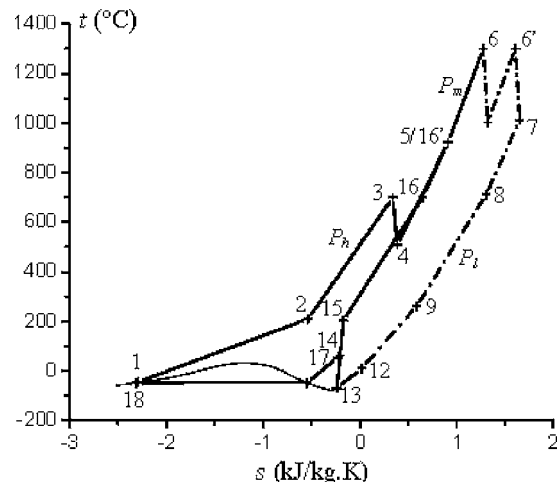


Fig. 7 t - s diagram for CO₂ cycle with reheat

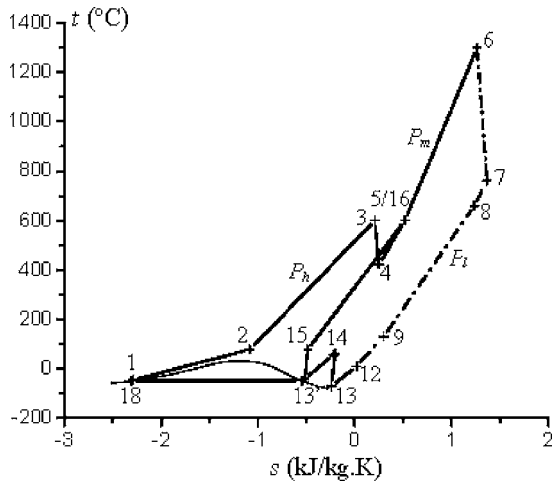


Fig. 8 t - s diagram for CO_2 cycle with intercooling

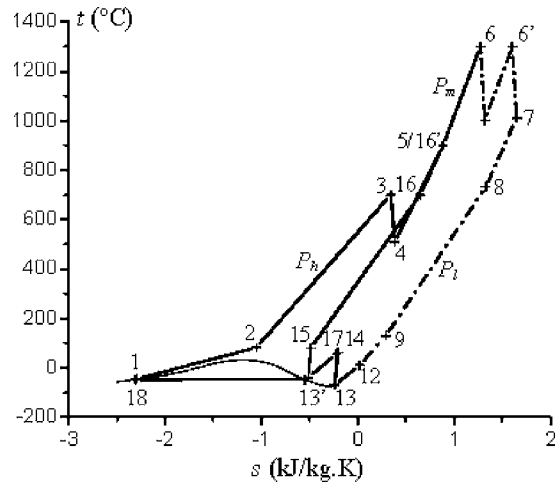


Fig. 9 t - s diagram for CO_2 cycle with intercooling and reheat

the excess amount of LT exhaust heat is used to raise the combustor inlet temperature to a higher level (point 5/16' in Figs. 7 and 9). The layouts of the cycles in Figs. 10 and 11 are somewhat different from that in Fig. 1 in terms of the number and the order of the heat exchangers).

The performances are summarized and compared in Table 3 and Figs. 12–14 as functions of the intermediary pressure P_m . A fuel compressor (or expander) is needed when the combustion pressure in B is higher (or lower) than the natural gas delivery pressure. The efficiencies and power output are found to increase monotonically with P_m within the whole calculation range of P_m (from 20 to 40 bar), with a diminishing rate.

Employing reheat is seen to improve performance: both the energy efficiency and exergy efficiency increase by 2 to 3 percentage points, and the specific power output increases by about 11%.

Employing intercooling increases the specific power output slightly, by 1.3% on average, but the energy and exergy efficiency coincidentally drop by more and less than 1 percentage point, respectively. From Figs. 8 and 9, in the intercooling cycle, the working fluid temperature after compression is lower, but the hot stream temperature at the recuperator outlet t_{10} is fixed. This results in a lower combustor inlet temperature and thus more fuel is needed to raise the temperature to the desired turbine inlet temperature, which explains the efficiency drop. In the intercooling

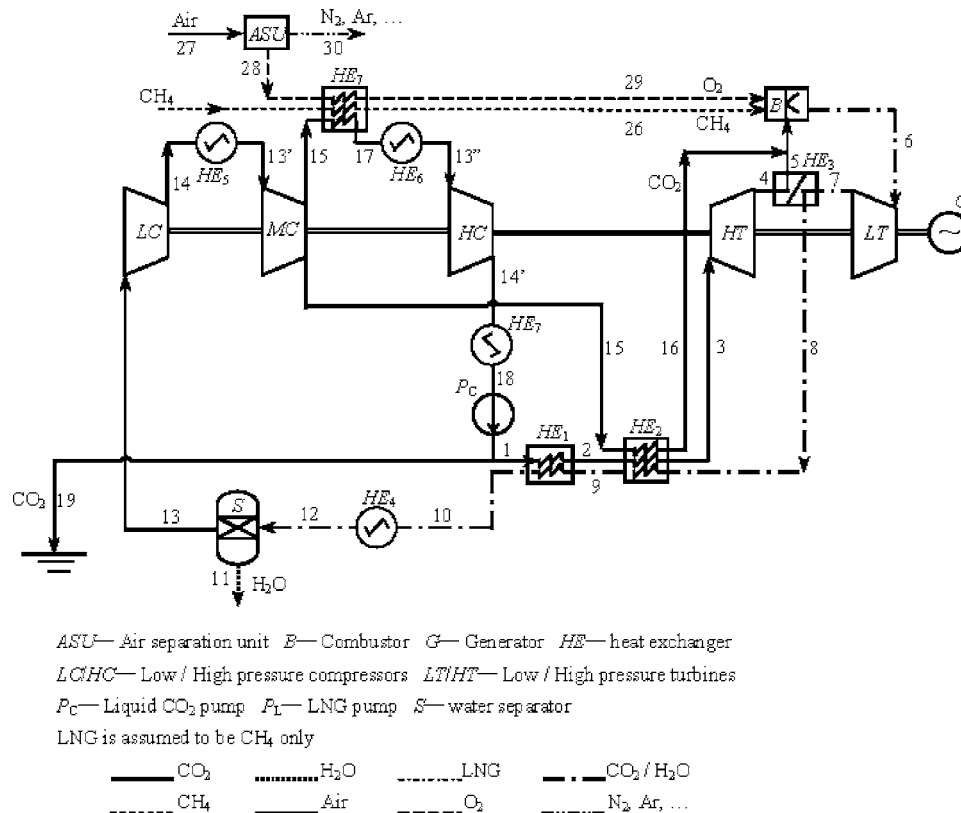


Fig. 10 CO_2 cycle flow sheet without LNG cold exergy utilization

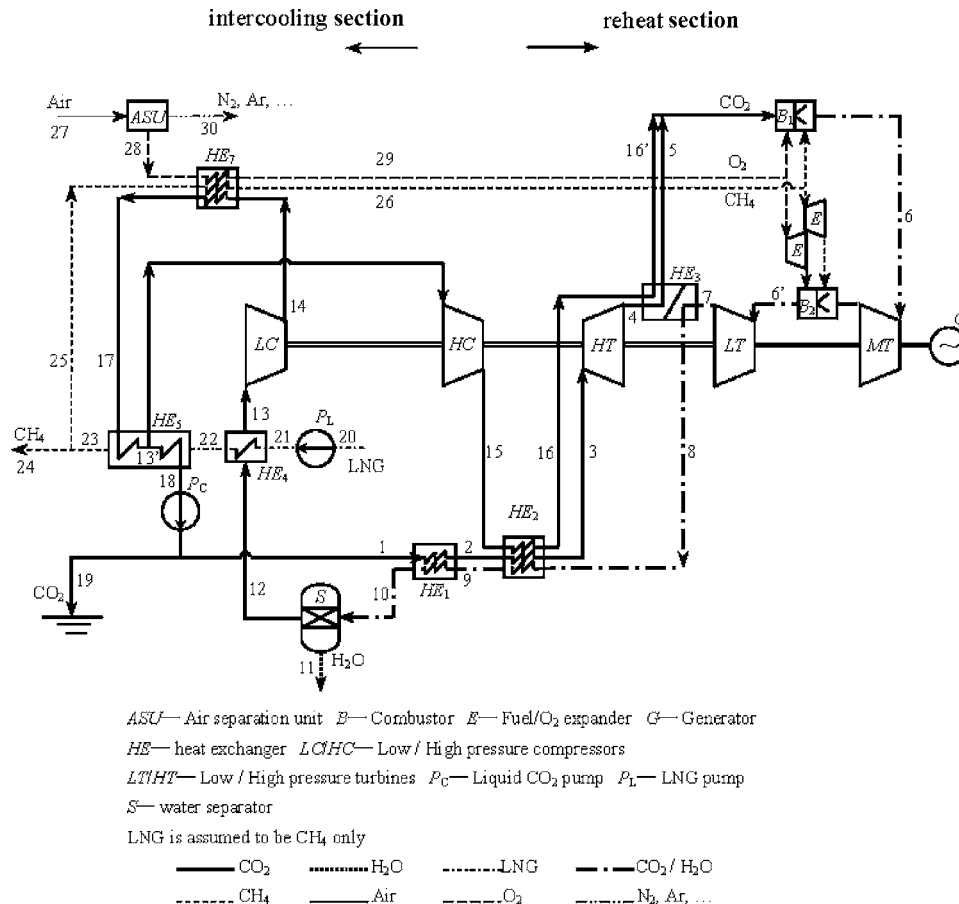


Fig. 11 CO₂ cycle flow sheet with reheat and intercooling

cycle, all of the working fluid needs to be cooled down by LNG after the first stage of compression (14→17→13' in Fig. 11). Therefore, the amount of heat available in the LNG evaporation system will bring the evaporated natural gas to the near-ambient temperature, leaving no extra coldness for air conditioning.

The comparison between the reheat+intercooling cycle with the reheat cycle is similar to the comparison between the intercooling cycle with the base-case cycle. As known in general, incorporation of reheat or intercooling alone can increase the cycle power output, but not necessarily improve the efficiency, because of the

higher turbine flue gas temperature in the cycle with reheat, or the lower compressor outlet temperature in the cycle with intercooling. It is also known that incorporation of recuperation (internal heat regeneration) may have other consequences. Unlike the situation in this paper, if the recuperator hot stream outlet temperature drops in the cycle with intercooling, it is possible to increase the overall efficiency as well.

Compared with the base-case cycle, the energy efficiency of the no-LNG case is lower by nearly 15 percentage points, but their exergy efficiencies are about the same. Its exergy efficiency is

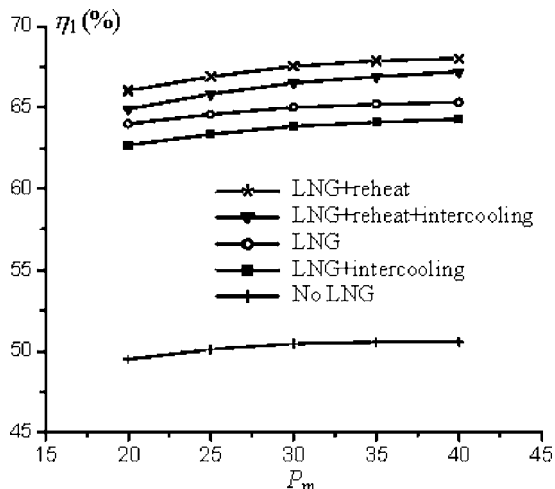


Fig. 12 The influence of P_m on thermal efficiency

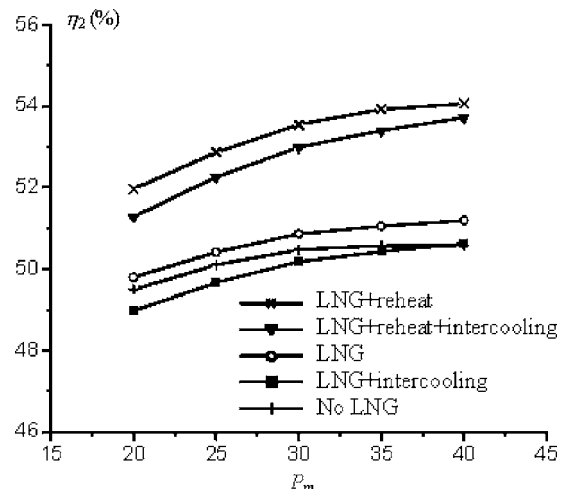


Fig. 13 The influence of P_m on exergy efficiency

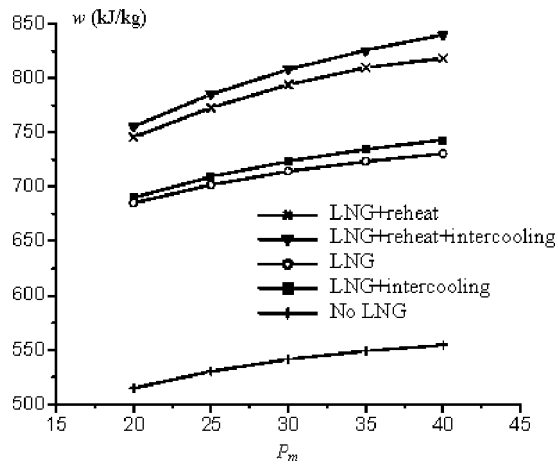


Fig. 14 The influence of P_m on specific power output

between that of the base-case cycle and the one with intercooling (Fig. 13). From Table 3, the LNG coldness contributes nearly 22% to the total base-case cycle exergy input, and it converts to power at almost the same efficiency as the fuel exergy does.

Among the cycle configurations studied in this paper, the reheat cycle has the highest efficiencies, while the reheat+intercooling cycle has the highest specific power output. It should, however, be noted that the recuperator material needs then to bear a temperature as high as 1000 °C.

The heat exchanger surface areas for different cycle configurations are also estimated and compared in Table 6. Differences mainly exist in the recuperation system. Compared with the base-case cycle, it was found that reheat cycle requires 54% additional heat transfer area, and the no-LNG cycle and intercooling cycle require 18% and 9% less, respectively.

Conclusions

A novel power cycle producing zero CO₂ emission by integration of LNG cryogenic exergy utilization is proposed and thermodynamically modeled. The main merits of the system include:

- (1) Good thermodynamic performance, with the energy and exergy efficiencies reaching 65% and 51%, respectively, using conventional technologies, despite the power consumed for air separation; this is in part because the amount of coldness exergy of the LNG adds about 28% to the fuel exergy used in the cycle, and
- (2) Negligible release of pollutants to the environment;
- (3) Removal of high-pressure liquid CO₂ ready for sale or disposal;
- (4) Valuable byproducts: condensed water, liquid N₂, and Ar; and
- (5) Full exploitation of the LNG evaporation process.

The exergy analysis identified the largest exergy loss, 21% (of the total exergy input), to be in the combustor, which can be straightforwardly decreased only by increasing the inlet temperature of the LT turbine beyond the assumed 1300 °C. The most significant other exergy losses are in the heat exchangers HE₅

(8.2%), HE₄ (5.2%), and HE₁ (3.4%), and these losses can be decreased by decreasing the temperature differences between the heat exchanging streams, but this would obviously require larger or/and more complex heat exchangers. The proposed configuration of the cycle allows a large fraction of the exergy to be usefully reused internally.

The influences of some key parameters on the cycle performance, including the Brayton cycle mass flow rate ratio, the low-pressure turbine inlet temperature and pressure levels, are discussed. Energy efficiency and exergy efficiency increase by about 3 to 4 percentage points for every 100 °C increase of t_6 (LT inlet temperature) or 20% increase of R_g . The specific power output w increases with the increase of t_6 and with the decrease of R_g . Both P_h and P_m have a positive impact on the efficiencies and specific power output within the calculation range; and P_m has a more notable influence on the cycle thermal performance than P_h . It is also found that every 10% reduction in the power needed for air separation will increase both efficiencies and power output by about 1.1%.

The total needed heat exchanger area is about 390 m²/MWe for the base-case cycle, ~75% of which are the recuperators HE₁ and HE₂. Employing larger heat transfer temperature differences can effectively reduce the heat transfer surface area, but will lead to a reduction of thermal efficiency. A formal thermoeconomic optimization is obviously called for. The pinch point temperature difference in the recuperation system is one of the main constraints to performance improvement, its influence and parameter optimization call for further study.

Among the different cycle schemes investigated, it was found that highest efficiencies' improvement over the base-case can be obtained by employing reheat but only by 2 to 3 percentage points, and this would also increase the specific power output by more than 10%. The major practical restrictions to employing reheat is the high recuperator inlet temperature for reheat cycle, and a 54% increase in the overall heat transfer surface. Compared with the base-case, incorporation of intercooling lowers efficiencies and slightly increases power output. If no LNG coldness is used, the cycle operates in the same temperature range as conventional power plants do, the required heat exchange area is reduced by 18% (only), the specific power output is reduced by one quarter, and the efficiency can reach 50%, about 15 percentage points lower than that of the base-case cycle.

Based on this analysis, the proposed base-case plant (which was not optimized yet) would produce 124 MWe if installed with the first LNG terminal in China that has an import capacity of 3,000,000 t/yr, and the capacity can be increased up to 137 MWe and 140 MWe for reheat cycle and reheat/intercooling cycle, respectively.

Acknowledgment

The authors gratefully acknowledge the support of the K. C. Wong Education Foundation, Hong Kong; the Chinese Natural Science Foundation Project (No. 50006013); and the Major International (Regional) Joint Research Program: Fundamental Study of CO₂ Control Technologies and Policies in China.

Nomenclature

A = heat exchanger surface area (m²)

Table 6 Heat exchanger surface area comparison of different cycle configurations

	No LNG	Reheat	Intercooling	Reheat/intercooling	Base-case
Recuperators [m ²]	18,664	36,940	18,742.5	28,551.2	21,968
Others [m ²]	4,225.6	5,967.3	6,702.1	6,804.8	5,887.6
Total area ΣA [m ²]	22,889.6	42,907.3	25,444.6	35,356.0	27,855.6
$\Sigma A / \Sigma A_{ref}$ [%]	82.2	154.0	91.3	126.9	1

a = specific exergy (kJ/kg)
 m = mass flow rate (kg/s)
 H_u = fuel LHV value (kJ/kg)
 h = specific enthalpy (kJ/kg)
 P = pressure (bar)
 R_g = mass flow rate ratio of Brayton cycle (%), Eq. (4)
 s = specific entropy (kJ/kg·K)
 T = temperature (K)
 t = temperature (°C)
 Q = heat duty (MW)
 U = overall heat transfer coefficient (W/m² K)
 W = power output (MW)
 w = specific power output (kJ/kg)
 ΔT_p = pinch point temperature difference (K)
 η_1 = energy efficiency
 η_2 = exergy efficiency

Subscripts

f = fuel
 h = high pressure
 m = intermediary pressure
 net = net output
 L = liquefied natural gas
 l = low pressure
 1...30 = states on the cycle flow sheet

References

- [1] Karashima, N., and Akutsu, T., 1982, "Development of LNG Cryogenic Power Generation Plant," *Proc. of 17th IECEC*, pp. 399–404.
- [2] Angelino, G., 1978, "The Use of Liquid Natural Gas as Heat Sink for Power Cycles," *J. Eng. Power*, **100**, pp. 169–177.
- [3] Kim, C. W., Chang, S. D., and Ro, S. T., 1995, "Analysis of the Power Cycle Utilizing the Cold Energy of LNG," *Int. J. Energy Res.*, **19**, pp. 741–749.
- [4] Najjar, Y. S. H., and Zaamout, M. S., 1993, "Cryogenic Power Conversion With Regasification of LNG in a Gas Turbine Plant," *Energy Convers. Manage.*, **34**, pp. 273–280.
- [5] Wong, W., 1994, "LNG Power Recovery," *Proc. Inst. Mech. Eng., Part A*, **208**, pp. 1–12.
- [6] Zhang, N., and Cai, R., 2002, "Principal Power Generation Schemes With LNG Cryogenic Exergy," *Proc. ECOS 2002 15th International Conference on Efficiency, Costs, Optimization, Simulation, and Environmental Impact of Energy Systems*, G. Tsatsaronis et al., eds., Berlin Technical University, Berlin, pp. 334–341.
- [7] Krey, G., 1980, "Utilization of the Cold by LNG Vaporization With Closed-Cycle Gas Turbine," *J. Eng. Power*, **102**, pp. 225–230.
- [8] Agazzani, A., and Massardo, A. F., 1999, "An Assessment of the Performance of Closed Cycles With and Without Heat Rejection at Cryogenic Temperatures," *ASME J. Eng. Gas Turbines Power*, **121**, pp. 458–465.
- [9] Deng, S., Jin, H., Cai, R., and Lin, R., 2004, "Novel Cogeneration Power System With Liquefied Natural Gas (LNG) Cryogenic Exergy Utilization,"

- Energy*, **29**, pp. 497–512.
- [10] Chiesa, P., 1997, "LNG Receiving Terminal Associated With Gas Cycle Power Plants," ASME Paper No. 97-GT-441.
- [11] Desideri, U., and Belli, C., 2000, "Assessment of LNG Regasification Systems With Cogeneration," ASME Paper No. 2000-GT-0165.
- [12] Kim, T. S., and Ro, S. T., 2000, "Power Augmentation of Combined Cycle Power Plants Using Cold Energy of Liquefied Natural Gas," *Energy*, **25**, pp. 841–856.
- [13] Velautham, S., Ito, T., and Takata, Y., 2001, "Zero-Emission Combined Power Cycle Using LNG Cold," *JSME Int. J., Ser. B*, **44**, pp. 668–674.
- [14] Riemer, P., 1996, "Greenhouse Gas Mitigation Technologies, an Overview of the CO₂ Capture, Storage and Future Activities of the IEA Greenhouse Gas R&D Program," *Energy Convers. Manage.*, **37**, pp. 665–670.
- [15] Haugen, H. A., and Eide, L. I., 1996, "CO₂ Capture and Disposal: the Realism of Large Scale Scenarios," *Energy Convers. Manage.*, **37**, pp. 1061–1066.
- [16] Yantovski, E. I., Zvagolsky, K. N., and Gavrilenko, V. A., 1992, "Computer Exergonomics of Power Plants Without Exhaust Gases," *Energy Convers. Manage.*, **33**, pp.405–412.
- [17] Shao, Y., and Golomb, D., 1996, "Power Plants With CO₂ Capture Using Integrated Air Separation and Flue Gas Recycling," *Energy Convers. Manage.*, **37**, pp. 903–908.
- [18] Shao, Y., Golomb, D., and Brown, G., 1995, "Natural Gas Fired Combined Cycle Power Plant With CO₂ Capture," *Energy Convers. Manage.*, **36**, pp. 1115–1128.
- [19] Wall, G., Yantovski, E., Lindquist, L., and Tryggstad, J., 1995, "A Zero Emission Combustion Power Plant for Enhanced Oil Recovery," *Energy*, **20**, pp. 823–828.
- [20] Yantovski, E. I., 1996, "Stack Downward Zero Emission Fuel-Fired Power Plants Concept," *Energy Convers. Manage.*, **37**, pp. 867–877.
- [21] Yantovski, E. I., and Gorski, J., 2000, "Further Elaboration of Quasi-combined Zero-Emission Power Cycle," *Proc. ECOS 2000 13th International Conference on Efficiency, Cost, Optimisation, Simulation and Environmental Aspects of Energy and Process Systems*, G. G. Hirs, ed., University of Twente, Enschede, Netherlands, pp. 1083–1092.
- [22] Yantovski, E. I., Zvagolsky, K. N., and Gavrilenko, V. A., 1995, "The COOPERATE-Demo Power Cycle," *Energy Convers. Manage.*, **36**, pp. 861–864.
- [23] Mathieu, P., Dubuisson, R., Houyou, S., and Nihart, R., 2000, "A Quasi Zero Emission O₂/CO₂ Combined Cycle," *Proc. ECOS 2000 13th International Conference on Efficiency, Cost, Optimisation, Simulation and Environmental Aspects of Energy and Process Systems*, G. G. Hirs, ed., University of Twente, Enschede, Netherlands, pp. 1071–1081.
- [24] Fioravanti, A., Lombardi, L., and Manfrida, G., 2000, "An Innovative Energy Cycle With Zero CO₂ Emissions," *Proc. ECOS 2000 13th International Conference on Efficiency, Cost, Optimisation, Simulation and Environmental Aspects of Energy and Process Systems*, G. G. Hirs, ed., University of Twente, Enschede, Netherlands, pp. 1059–1070.
- [25] Mathieu, P., and Nihart, R., 1999, "Zero-Emission MATIANT Cycle," *ASME J. Eng. Gas Turbines Power*, **121**, pp. 116–120.
- [26] Staicovici, M. D., 2002, "Further Research Zero CO₂ Emission Power Production: the 'COOLENERG' Process," *Energy*, **27**, pp. 831–844.
- [27] Aspen Plus®, Aspen Technology, Inc., version 11.1, <http://www.aspentech.com/>
- [28] Hewitt, G. F., Shires, G. L., and Bott, T. R., 1993, *Process Heat Transfer*, CRC Press and Begell House, Boca Raton, FL.
- [29] Dunbar, W. R., and Lior, N., 1994, "Sources of Combustion Irreversibility," *Combust. Sci. Technol.*, **103**, pp. 41–61.
- [30] Mathieu, P., and Nihart, R., 1999, "Sensitivity Analysis of the MATIANT Cycle," *Energy Convers. Manage.*, **40**, pp. 1687–1700.

Component Map Generation of a Gas Turbine Using Genetic Algorithms

Changduk Kong
e-mail: cdgong@mail.chosun.ac.kr

Seonghee Kho
e-mail: habari@paran.com

Jayoung Ki
e-mail: setgods@hotmail.com

Department of Aerospace Engineering,
Chosun University,
#375 Seosuk-dong, Dong-gu,
Gwangju 501-759, Korea

In order to estimate the precise performance of the existing gas turbine engine, the component maps with more realistic performance characteristics are needed. Because the component maps are the engine manufacturer's propriety obtained from very expensive experimental tests, they are not provided to the customers, generally. Therefore, because the engineers, who are working the performance simulation, have been mostly relying on component maps scaled from the similar existing maps, the accuracy of the performance analysis using the scaled maps may be relatively lower than that using the real component maps. Therefore, a component map generation method using experimental data and the genetic algorithms are newly proposed in this study. The engine test unit to be used for map generation has a free power turbine type small turboshaft engine. In order to generate the performance map for compressor of this engine, after obtaining engine performance data through experimental tests, and then the third order equations, which have relationships with the mass flow function, the pressure ratio, and the isentropic efficiency as to the engine rotational speed, were derived by using the genetic algorithms. A steady-state performance analysis was performed with the generated maps of the compressor by the commercial gas turbine performance analysis program GASTURB (Kurzke, 2001). In order to verify the proposed scheme, the experimental data for verification were compared with performance analysis results using traditional scaled component maps and performance analysis results using a generated compressor map by genetic algorithms (GAs). In comparison, it was found that the analysis results using the generated map by GAs were well agreed with experimental data. Therefore, it was confirmed that the component maps can be generated from the experimental data by using GAs and it may be considered that the more realistic component maps can be obtained if more various conditions and accurate sensors would be used. [DOI: 10.1115/1.2032431]

Introduction

Performance simulation is one of the most important activities not only to minimize risk and cost in the development phase but also to monitor engine health in the operation phase. In order to simulate gas turbine performance, it is absolutely needed that a condition, in which each engine performance must follow its own component characteristics, should be satisfied [1]. Generally, each component characteristic can be obtained from the component performance test at various operating and environmental conditions. However, it can be usually done in the case of the engine development stage. Moreover, it is not generally disclosed to engine users because of very expensive and important technical data. Obtaining the studying engine component map is a very important issue to engineers, who want to predict and diagnosis the engine performance. Engine users or engineers, who are observing engine performance, have been mostly utilizing the known engine component characteristics by scaling. Even though there are various scaling methods, current traditional methods are mostly using a technique in which first the scaling factors are derived from comparison between design point data and a new design point of the given original maps and then the scaled maps can be obtained by multiplying the derived scaling factors to off-design point map data of the original performance maps [2]. However, this technique may be reasonable if the derived scaling factors are close to 1.0 because it has similar performance between the original en-

gine and the scaled engine. Therefore, performance analysis results using this technique may usually agree well with the measured performance result of the scaled engine around the design point. However, if calculation at off-design points were performed from the on-design point, it would have a drawback that the calculation error of this technique may be increased.

A statistical analysis of many compressor maps was performed by Kurzke [3]. According to his study, a reference point on each map was employed to normalize its map. Then, the topology of the normalized map was captured with three characteristic numbers that describe the region at the highest efficiency, the mass flow-speed relationship, and the shape of the speed lines. However, if various kinds of component performance maps can exist for mating, it has a limitation in general use. In order to reduce the analyzed performance error, a scaling method for characteristics of gas turbine components using experimental data or partially given data from engine manufacturers was proposed by Kong [4]. This method can be realized by using the following procedure. First, after obtaining the scaling maps with the scaling factors of components from the known performance data or the known experimental data by engine manufacturers at some operation points, it can construct the new component maps using the system identification technique built by a mathematical model between input (scaling factors at some given conditions) and output parameters (pressure ratio, mass flow rate, and efficiency) with polynomial equations, and finally analyzing the engine performance with the identified maps. This method is able to obtain much closer component maps to the real engine component maps than the traditional scaling method with reference data from a design point at off-design points. Therefore, the method can reduce considerably the performance analysis error at off-design points. However, be-

Contributed by the International Gas Turbine Institute (IGTI) of ASME for publication in the JOURNAL OF ENGINEERING FOR GAS TURBINES AND POWER. Manuscript received October 1, 2003; final manuscript received March 1, 2004. IGTI Review Chair: A. J. Strazisar. Paper presented at the International Gas Turbine and Aeroengine Congress and Exhibition, Vienna, Austria, June 13 - 17, 2004, Paper No. GT2004-53736.

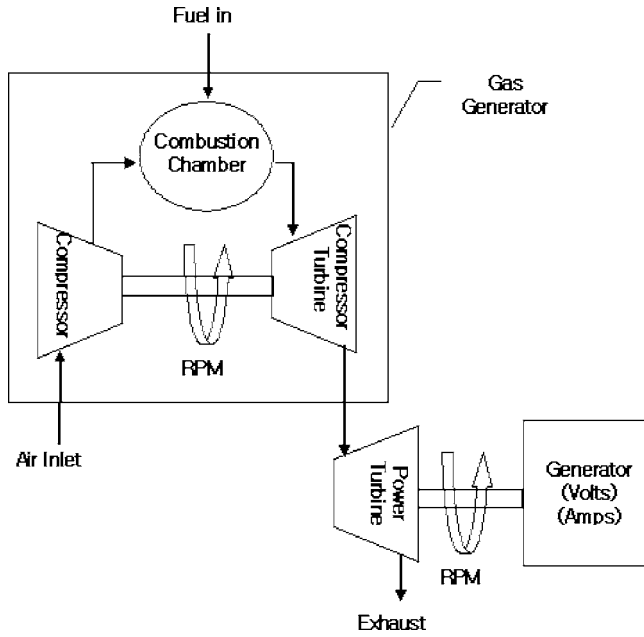


Fig. 1 Thermodynamic schematic diagram of the small turboshaft engine

cause this method cannot predict well the shape of the speed lines, there is a limitation in realization of the real component characteristics.

Therefore, this study proposes a method to generate the compressor map using the GAs (genetic algorithms) [5]. The GAs is a stochastic global search method that mimics the metaphor of natural biological evolution. The GAs operates a population of potential solutions by applying the principle of survival of the fittest to produce better approximations to a solution [6]. The gas turbine engine to acquire the experimental data was the maximum 4-kW class small turboshaft engine with a free power turbine. There were some difficulties to perform modeling the engine components and the performance analysis due to the very crude compressor map without turbine maps from the engine manufacturer. Moreover, the compressor is deteriorated due to long time use. Therefore, regeneration of component maps are needed to model and analyze the current engine. In order to generate the very precise maps for the compressor, the third-order equations with the relationships between the mass flow function, the pressure ratio, and the isentropic efficiency depending on the engine rotational speed were derived from performance data through experimental tests using the GAs. In order to evaluate the proposed scheme, the analysis results using the maps derived by the GAs were compared with them using the maps scaled maps from the commercial program GASTURB [7].

Derivation of Component Performance Parameters Through Experimental Test

The gas turbine used to obtain maps is a maximum 4-kW class small turboshaft engine with a free power turbine. It has a gas generator composed of a compressor, a combustor, and a compressor turbine, a power turbine, the loading system, the starting system, the ignition system, the lubrication system, and the measurement system. Figure 1 shows the thermodynamic schematic diagram of the small turboshaft engine [8].

Both wet gages, such as the bourden tube and the differential mercury manometer, and electronic transducers were used to measure various pressures, and the diode probes for low-temperature measurements of air and fuel and the NiCr/NiAl thermocouples

for high-temperature measurements of the combustion gas were used. The flow rate of the fuel was measured by the tapered tube float flow meter.

For measurement of the air flow rate, both the pitot-reverse tube and the differential manometer were used, and the tachometers were used for measurement of the rotational speeds.

After test data such as temperatures, pressures, fuel flows, air flows, rotor speeds, powers, etc., were acquired, and then the component characteristic parameters such as the pressure ratio, the mass flow parameter, and the isentropic efficiency of each component were calculated by using thermodynamic equations. The test was repeated, and the experimental data were finally corrected to the standard condition, and they were averaged for accurate calculation.

The following equations are used to calculate the characteristic parameters of compressor and turbine from the measured data:

$$PR_C = \frac{P_{02}}{P_{01}} \approx \frac{P_3}{P_a}, \quad (1)$$

$$MFP_C = m_1 \frac{1.0132}{P_1} \sqrt{\frac{T_1}{288.15}} = 6.7 \sqrt{h} \frac{1.0132}{P_1} \sqrt{\frac{T_1}{288.15}}, \quad (2)$$

$$\eta_C = \frac{\left(\frac{P_{02}}{P_{01}}\right)^{(\gamma-1)/\gamma} - 1}{\frac{T_{02}}{T_{01}} - 1} \approx \frac{\left(\frac{P_3}{P_{01}}\right)^{(\gamma-1)/\gamma} - 1}{\frac{T_{02}}{T_{01}} - 1}, \quad (3)$$

$$PR_T = \frac{P_3}{P_4}, \quad (4)$$

$$MFP_T = \frac{\dot{m}_3 \sqrt{T_{03}}}{P_3} = \frac{(\dot{m}_1 + \dot{m}_f) \sqrt{T_{03}}}{P_3}, \quad (5)$$

$$\eta_T = \frac{1 - \frac{T_{04}}{T_{03}}}{1 - \left(\frac{P_{04}}{P_{03}}\right)^{(\gamma-1)/\gamma}} \approx \frac{1 - \frac{T_{04}}{T_{03}}}{1 - \left(\frac{P_4}{P_3}\right)^{(\gamma-1)/\gamma}}. \quad (6)$$

The corrected rotational speed defines as follows:

$$CN = \frac{N}{\sqrt{\theta}}. \quad (7)$$

Traditional Components Scaling Method

In the commercial performance analysis program GASTURB, the design point calculation for the mass flow parameter, the pressure ratio, and the isentropic efficiency of the component can be matched with a reference point for scaling the original map.

The design point must be correlated with the map. This means that one point in the map has to be a reference point (subscript R,map), the design point (subscript dp). As a default, the reference point is defined to be $\beta_{R,map}=0.5$ and $N/\sqrt{\theta_{R,map}}=1.0$. The map scaling factors can be calculated as follows [6]:

$$f_{Mass} = \frac{(\dot{m} \sqrt{\theta_R / \delta})_{dp}}{(\dot{m} \sqrt{\theta_R / \delta})_{R,map} \times f_{w,RNI}}, \quad (8)$$

$$f_{Eff} = \frac{\eta_{dp}}{\eta_{R,map} \times f_{\eta,RNI}}, \quad (9)$$

$$f_{P_{exit}/P_{inlet}} = \frac{(P_{exit}/P_{inlet})_{dp} - 1}{(P_{exit}/P_{inlet})_{R,map} - 1}, \quad (10)$$

where assuming $f_{\eta,RNI}=0.99$ and consequently $f_{w,RNI}=0.995$.

In the steady-state performance analysis, the used compressor map was provided by the engine manufacturer, the compressor and power turbine maps were used by scaling the "ratur.map" of the GASTURB program.

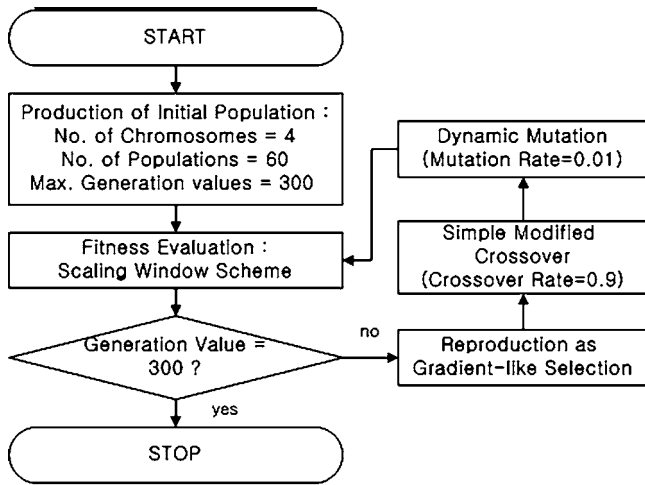


Fig. 2 Flow chart of genetic algorithm

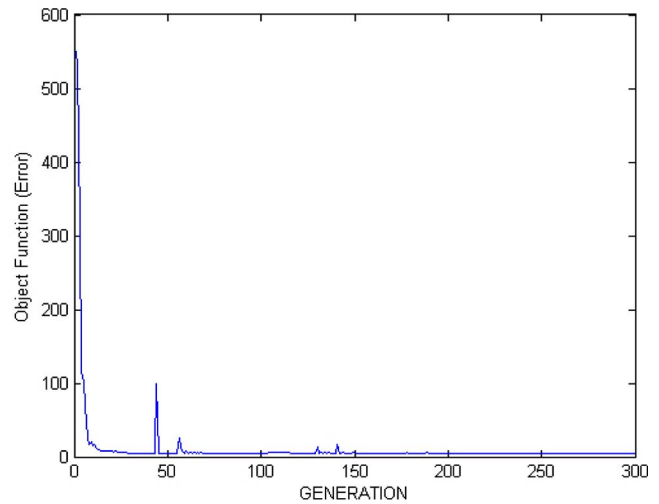


Fig. 3 Converge of object function as generation

Map Generation Using GAs

Genetic algorithms are stochastic search algorithms inspired by the principles of natural selection and genetics. A population of candidate solutions must be maintained, and individuals have to be made to compete with each other for survival. Once evaluated, stronger individuals are given by a greater chance of contributing to the production of new individuals (the offspring) than weaker ones, which may not even contribute at all. Offspring are produced through recombination, whereby they inherit features from each of the parents, and through mutation which can confer some truly innovative features as well. In the next selection step, offspring are made to compete with each other, and possibly also with their parents. Improvement of the population arises as a consequence of the repeated selection of the best parents, which are in turn more likely to produce good offspring, and the consequent elimination of low performers [9].

In this study, the component maps are identified from the experimental data using the genetic algorithm characteristics mentioned above. The maps for compressor can be expressed as the related functions of the engine rotational speed versus the pressure ratio, the mass flow function, and isentropic efficiency.

The mass flow parameter, the pressure ratio, and the efficiency for constructing the component map are calculated from the measured experimental data and these component parameters are corrected to the standard atmospheric condition. Here the mass flow function becomes a function of the pressure ratio and the rotational speed as follows:

$$MFP_N = aPR^3 + bPR^2 + cPR + d. \quad (11)$$

Additionally, the isentropic efficiency is a function of the mass flow parameter as follows:

$$EFF = aMFP^3 + bMFP^2 + cMFP + d. \quad (12)$$

A simple genetic algorithm is applied to find the unknown coefficients a , b , c , and d . After constructing “ n ” number data sets from Eqs. (11) and (12) through many tests, the absolute value of the following object function is minimized:

$$\text{Objetfuc} = \sqrt{\frac{\sum_{i=1}^n \text{error}_i^2}{n}}, \quad (13)$$

where, the “error” is defined as the percentage error about arbitrary a , b , c , and d , respectively.

In the GAs, individuals are considered at two levels: the phenotypic level and the genotypic level. An individual’s phenotype is its value in the domain over which the objective function is

defined, constituting a candidate setting for the decision variables of the problem. On the other hand, an individual’s genotype is a representation of its phenotype at a lower level, analogous to the genetic sequences contained in biological chromosomes, which the computer stores and the GA manipulate. The phenotype is therefore encoded in the genotype, as a real encoding in this study.

Random initialization is applied to produce initial population, so 60 populations and four chromosomes are used. Individuals are evaluated via the objective function which defines the problem. The fitness of each individual is normalized by using the scaling windows scheme. Selection, crossover, and mutation are used to obtain the genetic operator for reproduction. Selection is the process of choosing individuals to participate in the production of offspring proportionally to their fitness. In this study, a gradient-like selection scheme is used. The modified simple crossover technique is used to crossover operation. In mutation operation, the dynamic mutation method is applied. Crossover rate and mutation rate are 0.9 and 0.01 in this study, respectively [10].

Figure 2 shows the structure of the applied GAs for the study [10].

Figure 3 shows that the absolute value of the object function is finally converged to zero.

In this calculation, the number of generation is 300, and the range of unknown coefficients is assumed from -4 to 4 .

The compressor map generated by GAs is shown as Fig. 4.

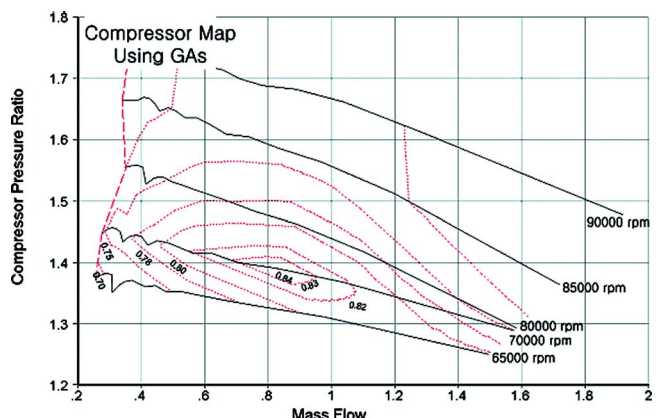


Fig. 4 Compressor map generated by GAs

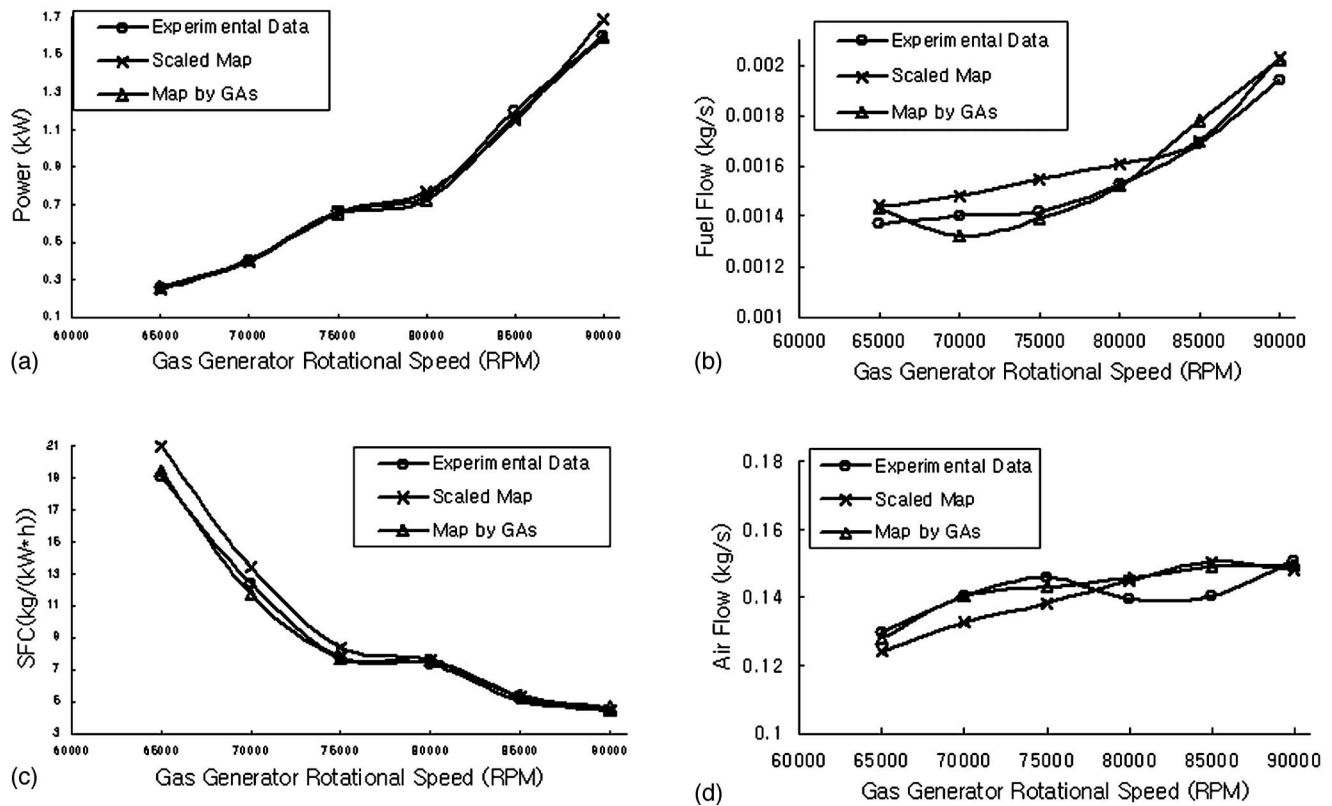


Fig. 5 Power, fuel flow, SFC, and air flow as to RPM

Verification of the Proposed Scheme

In order to verify the proposed scheme, the experimental data were selected at the ambient temperature condition of 296 K. And the selected experimental data for verification were compared with performance analysis using traditional scaled component maps and performance analysis using compressor map generated by GAs.

Figure 5 shows the comparison results of power, fuel flow, SFC, and air flow from 65,000 RPM to 90,000 RPM with 5000 RPM intervals. The experimental data seem of rather nonlinear character in this figure. It was considered that the error of measurement occurred due to old sensors and data of nonfiltered noise.

Table 1 shows the relative error for scaled method and GAs method to experimental data.

As performance analysis results were compared to experimental data, the total mean error of power, fuel flow, SFC, and air flow is respectively 3.2%, 5.4%, 6.0%, and 4.6% in using the scaled map and it is, respectively, 1.7%, 3.1%, 3.7%, and 2.5% in using the map by GAs. It was found that the analysis results using the map by GAs agreed well with experimental data. But the error still

remained. Therefore, it may be considered that the more realistic component maps can be obtained if more various conditions and accurate sensors would be used.

Conclusion

In this study, a component map generation method using experimental data and GAs was newly proposed. In order to generate the performance map for compressor of this engine, first we obtained engine performance data through experimental tests, and defined the relationships between the pressure ratio, the mass flow parameter, and isentropic efficiency of compressor as the third-order equation, then found unknown coefficients a , b , c , and d using GAs, finally generated compressor map using Polyval.m function of MATLAB. This compressor map was transformed into recognizable map type of GASTURB using SMOOTH-C. And the experimental data for verification were compared with performance analysis results using traditional scaled component maps and performance analysis results using a compressor map generated by GAs. In comparison, it was found that the analysis results using the map by GAs agreed well with experimental data.

Table 1 Relative error for scaled method and GAs method to experimental data

RPM	Power (kW)		MF (kg/s)		SFC [kg/(kW*h)]		MA (kg/s)	
	scaled map (%)	GAs map (%)	scaled map (%)	GAs map (%)	scaled map (%)	GAs map (%)	scaled map (%)	GAs map (%)
65,000	4.22	1.02	5.34	3.15	9.98	2.11	4.30	1.28
70,000	2.47	0.29	5.65	5.77	8.33	5.50	5.55	0.09
75,000	0.16	2.18	8.64	1.94	8.81	0.24	5.18	1.92
80,000	2.68	3.19	5.46	0.22	2.70	3.51	3.96	4.42
85,000	4.21	2.73	0.01	2.97	4.41	5.86	6.98	6.04
90,000	5.44	0.51	7.53	4.45	1.98	4.99	1.79	1.06

Therefore, it was confirmed that the component maps can be generated from the experimental data by using GAs and it may be considered that the more realistic component maps can be obtained if more various conditions and accurate sensors would be used.

Acknowledgment

This study was supported by research funds from Chosun University, 2004.

Nomenclature

CN	=	corrected rotational speed
C_p	=	specific heat at constant pressure
f	=	scaling factor
MFP	=	mass flow parameter
\dot{m}	=	mass flow rate
\dot{m}_f	=	fuel flow rate
N	=	true rotational speed
N.M.	=	new scaling method for component maps
PR	=	pressure ratio
RPM	=	revolution per minute
η	=	efficiency
θ	=	$T/288.15$ K
θ_R	=	$R^*T(R \text{ dry air}^*288.15 \text{ K})$
δ	=	$P/1.01325$ bars
h	=	$\Delta p/\rho_{H_2O}g$
a, b, c, d	=	unknown coefficients of a function
Objetfuc	=	object function

Error = percentage error for unknown coefficients
 β = auxiliary coordinate in maps

Subscripts

C	=	compressor
T	=	turbine
dp	=	design point
R	=	reference point
RNI	=	Reynolds number index
W	=	mass flow

References

- [1] Cohen, H., Rogers, G. F. C., and Saravanamuttoo, H. I. H., 2001, *Gas Turbine Theory*, 5th ed., Prentice-Hall, Englewood Cliffs, NJ.
- [2] Sellers, J. F., and Daniele, C. J., 1975, "DYNGEN—A Program for Calculating Steady-State and Transient Performance of Turbojet and Turbofan Engines," NASA TN D-7901.
- [3] Kurzke, J., and Riegler, C., 2000, "A New Compressor Map Scaling Procedure for Preliminary Conceptual Design of Gas Turbines," ASME Paper No. 2000-GT-0006.
- [4] Kong, C. D., and Ki, J. Y., 2003, "A New Scaling Method for Component Maps of Gas Turbine Using System Identification," ASME J. Eng. Gas Turbines Power, **125**(4), pp. 979–985.
- [5] Moon, B. L., 2001, *Genetic Algorithm*, Da Seong Pub. Co..
- [6] Chipperfield, A., Fleming, P., Pohlheim, H., and Fonseca, C., 1995, "Genetic Algorithm Toolbox for Use with MATLAB ver. 1.2," University of Sheffield.
- [7] Kurzke, J., 2001, "Manual GASTURB 9.0 for Windows - A Program to Calculate Design and Off-design Performance of Gas Turbines," Technical Report.
- [8] "CUSSONS Two Shaft Gas Turbine Unit P9005 Instruction Manual," CUSSONS Tech.
- [9] Fonseca, C., 1995, "Multiobjective Genetic Algorithms with Application to Control Engineering Problems," Ph.D thesis, The University of Sheffield, UK.
- [10] Jin, G. G., 2000, *Genetic Algorithms and Their Applications*, Kyowoo Sa.

The Effect of Water Injection on Multispool Gas Turbine Behavior

Background: The injection of water droplets into industrial gas turbines is now commonplace and is central to several proposed advanced cycles. These cycles benefit from the subsequent reduction in compressor work, the increase in turbine work, and (in the case of recuperated cycles) reduction in compressor delivery temperature, which all act to increase the efficiency and power output. An investigation is presented here into the effect such water droplets will have on the operating point and flow characteristics of an aeroderivative gas turbine cycle. Method of Approach: The paper first describes the development of a computer program to study the effects of water injection in multispool industrial gas turbines. The program can operate in two modes: the first uses predetermined nondimensional wet compressor maps to match the components and is instructive and fast but limited in scope; the second uses the compressor geometries as input and calculates the wet compressor operating conditions as and when required. As a result, it is more computationally demanding, but can cope with a wider range of circumstances. In both cases the compressor characteristics are calculated from a mean-line analysis using suitable loss, deviation and blockage models, coupled with Lagrangian-style droplet evaporation calculations. The program has been applied to a three-spool machine to address issues such as the effects of water injection on power output and overall efficiency, and the off-design nature of the compressor operation. Results: Preliminary results calculated on this basis show similar trends to predictions for single-shaft machines, namely that air mass flow rates and pressure ratios are increased by water injection, and that early stages of the compressor are shifted towards choke and rear stages towards stall. The LP compressor in particular operates at severely off-design conditions. Conclusions: The predicted overall performance of the three-spool machine shows a substantial power boost and a marginal increase in thermal efficiency.

[DOI: 10.1115/1.2032432]

A. J. Meacock
e-mail: ajm83@cantab.net

A. J. White

Hopkinson Laboratory,
Cambridge University Engineering Department,
Cambridge University,
Trumpington Street, CB2 1PZ, UK

1 Introduction

The injection of water into gas turbines is not a recent concept. As early as 1903 Ægidius Elling [1] came up with the idea of spraying water into the air stream before, and during, the compression process. Wilcox and Trout [2] have also described the benefits of water injection for jet engines. In more recent years further studies have been carried out as the pressure to reduce emissions and increase efficiencies and power outputs has mounted. Some of these are outlined below.

Several studies exist which explore the effects of water injection on the multistage compressors of single-shaft machines [3–6]. The general conclusion of these studies is that injection of water into a compressor operating at fixed speed results in a shifting of the characteristics to higher mass flow and higher pressure ratio, as if operating at higher speed. Individual stages, however, tend to operate at off-design conditions [7,8], thereby impairing the aerodynamic performance and offsetting some of the initial benefit of wet compression. In two- and three-spool machines, the HP and IP shaft speeds are not fixed, which provides some degree of flexibility. The possibility that this might alleviate the off-design difficulties, and the potential use of multispool aeroderivative engines for wet-compression cycles provide the motivation for the current study.

To date, there have been relatively few investigations of water-injected multispool gas turbines. Roumeliotis et al. [9] studied water injection for a twin-spool machine, but only for the case

where all the evaporation takes place in mixing chambers between compression stages. Bassily [10] also considered the effect of evaporative intercooling for a twin-spoiled gas turbine, and Sexton and Urbach [11] looked at the case of a single-spoiled machine with an additional power turbine. In the latter study, compressor characteristics were generated from mean-line calculations, coupled with a simple diffusion controlled droplet evaporation model (assuming no velocity slip) and correlations for off-design efficiencies. By redesigning the power turbine to maintain the same air-flow rate, Sexton and Urbach [11] reported a 10% increase in power output (with a small increase in efficiency) for a 1% water injection rate.

Regarding the issue of droplet size, Utamura et al. [12] and Sexton and Urbach [11] suggest that droplets of 10 μm diameter or less should remain entrained in the flow, though it would seem that such droplets would experience at least moderate velocity slip. Current technology for inlet fog boost (IFB) systems provides droplets upwards of 15 μm diameter, but van Liere et al. [13] report sprays with average sizes of less than 2 μm using the well established technique of preheating the water prior to injection. (This method was used in Whittle's engines to produce small fuel droplets, as reported by Lefebvre [14].) Essentially, both evaporation and inertial relaxation time scales scale as the square of droplet diameter, so that small droplets are beneficial both for reducing velocity slip (and hence deposition and erosion), and for maintaining conditions closer to saturated equilibrium, thereby reducing losses due to irreversible phase change. With this in mind, droplets with a diameter of 5 μm have been used in this study, and velocity slip has been neglected as a first approximation.

2 Compressor Mean-Line Calculations

The method used to determine wet-compression characteristics has been presented elsewhere [3], and is described here in outline

Contributed by the International Gas Turbine Institute (IGTI) of ASME for publication in the JOURNAL OF ENGINEERING FOR GAS TURBINES AND POWER. Manuscript received October 1, 2003; final manuscript received March 1, 2004. IGTI Review Chair: A. J. Strazisar. Paper presented at the International Gas Turbine and Aeroengine Congress and Exhibition, Vienna, Austria, June 13–17, 2004, Paper No. GT2004-53320.

only. Several improvements have, however, been made to the original method, and these are also described below.

One-dimensional, mean-line calculations are undertaken by applying the Euler work equation to each blade row in turn. Entropy increases due to aerodynamic effects and blade exit angles are determined by loss and deviation models, as described by Miller and Wasdell [15]. These calculations are then coupled to droplet evaporation routines via the thermodynamic form of the energy equation:

$$T ds_A = dh - v dp. \quad (1)$$

Note that the incremental change, ds_A , in this equation is the entropy increase due to aerodynamic effects alone, and as such does not include any contribution from irreversible phase change. (The latter is computed quite separately within the evaporation routines.) Quantities such as the specific enthalpy, h , and specific volume, v , are mixture properties (per unit mass of dry air), and thus include contributions from dry air, water vapor, and water droplets. In an initial dry step, the Euler work equation, loss, and deviation models thus furnish estimates for changes in entropy and pressure which enable Eq. (1) and the droplet evaporation equations to be integrated in a Lagrangian frame of reference. This in turn provides values of specific humidity and liquid mass fraction which are fed back into the standard mean-line calculations in an iterative fashion. The evaporation model used here is based on that due to Spalding [16], and assumes no velocity slip between droplets and the free stream. Further details are given in White and Meacock [3]. Semiperfect gas relations are assumed for computing all gas properties. New features introduced to the original method include the following:

1. Improved loss and deviation models. These are now fully based on models given by Wright and Miller [17] and are functions of inlet Mach number, Reynolds number, and incidence.
2. Blockage effects. Blockage of the annulus can have a significant effect so blockage factors are calculated to correct the annulus area. These factors are found from a two-dimensional (2D) semiempirical model for calculating the growth of the end-wall boundary layer momentum thickness as described by Wright and Miller [17].
3. Variable stator vanes (VSVs) and bleed flows. Realistic schedules for VSV angles and bleed flows have been incorporated. These are functions of the reduced speed, $N/\sqrt{T_o}$.

2.1 Computed Characteristics. Figure 1 reveals the agreement between the compressor mean-line computer program (in dry mode) and the experimental data for the IP compressor of an industrial gas turbine. Predicted compressor characteristics for 1% and 5% water injection rates are also shown for the same compressor. In both cases the droplets are injected at inlet with an initial diameter of $5 \mu\text{m}$ and a temperature of 300 K. It is evident that the characteristic has shifted to a higher air mass flow rate and to higher pressure ratios. In simple terms this trend can be attributed to the reduced stagnation temperatures throughout the compressor which result in an apparent increase in the reduced speed, $N/\sqrt{T_o}$.

Polytropic efficiencies (Fig. 1(b)) are difficult to define when phase change is occurring. The quantity plotted in the figure is an "effective" polytropic efficiency [3] which is essentially a dimensionless representation of the aerodynamic entropy increase, and equates to the true polytropic efficiency for a semiperfect gas of constant composition. Close to the design speed, the aerodynamic efficiency is seen to fall with the injection of water, and the curve is also observed to become more *peaky*. However, at the lower rotational speeds such a reduction in peak efficiency does not occur. This is because changes in incidence brought about by water injection can serve to reduce losses: for example, for the 82% speed curve, the incidence decreases with water addition which in this case tends to reduce the loss coefficient. However, this is

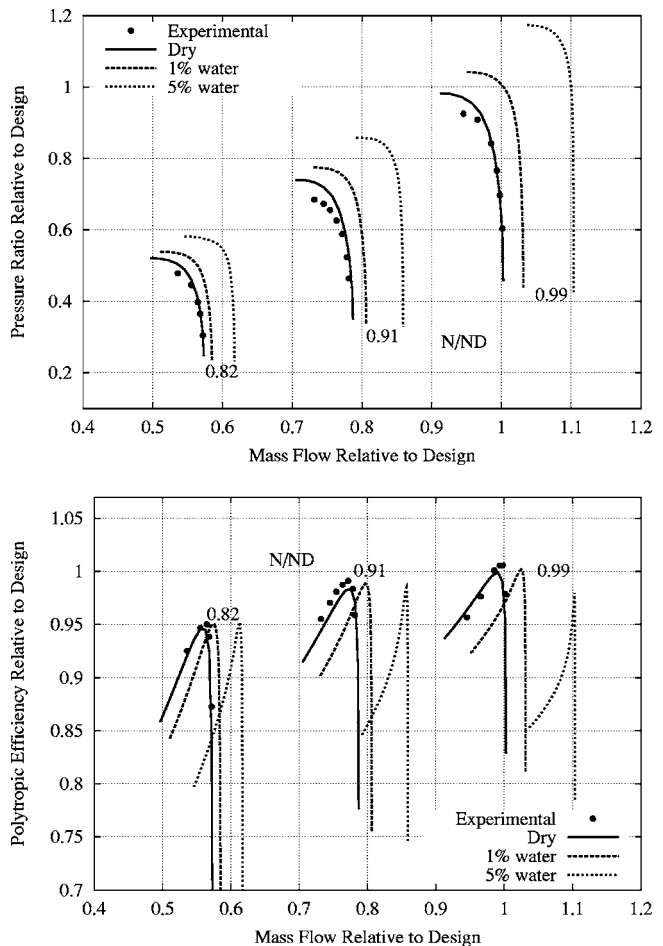


Fig. 1 Comparison between computational and experimental results and the shift in characteristics due to water injection

balanced by increased Mach numbers (which tend to increase the loss) such that the peak efficiency remains roughly constant. Such trends will obviously depend on the form of the loss and deviation models employed, but should be relatively trustworthy in the current case, given the level of agreement with the dry flow measurements.

2.2 Nondimensional Compressor Maps. The multispool calculation method discussed below is able to exploit the mean-line calculations directly, thus evaluating compressor operating points as and when required. This has the advantage of generality, and enables the full dependence of the compressor characteristics on all relevant parameters to be included. Alternatively, the computer program can operate in a second mode whereby a library of dimensionless wet compression maps is first compiled and spline routines are then used to interpolate between the curves. This approach is much faster, and has the additional advantage that the computer-generated characteristics can be replaced by measured wet compression data if and when they become available. It also provides considerably more insight into the work matching process. However, the scope of this method is restricted and in particular it cannot deal with situations where unevaporated droplets are carried over from one compressor to the next. This is because the characteristics are then dependent on additional parameters (i.e., the water content and droplet size distribution issuing from the previous compressor) and the interpolation procedure consequently becomes too cumbersome.

For a specified water injection rate and droplet spectrum, the compressor performance can be expressed in the dimensionless form:

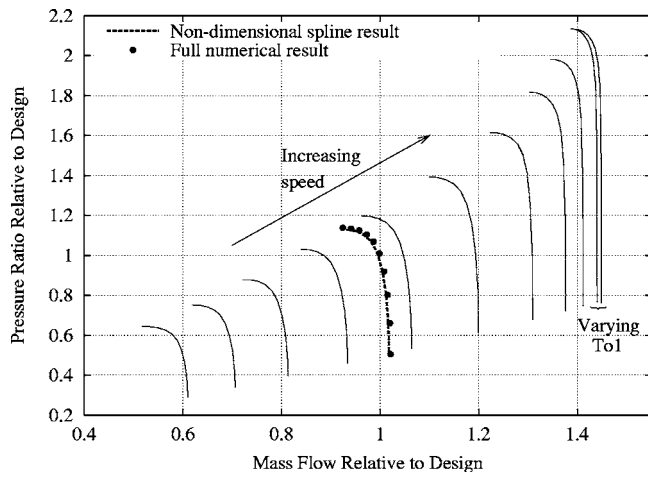


Fig. 2 Nondimensional compressor characteristics

$$\frac{P_{o_2}}{P_{o_1}} = f\left(\frac{\dot{m}\sqrt{c_{p_1}T_{o_1}}}{AP_{o_1}}, \frac{ND}{\sqrt{\gamma_1 R_1 T_{o_1}}}, \frac{T_{o_1}}{T_{o_1}^*}, \text{Re}, \omega_1, \alpha_1\right), \quad (2)$$

where subscripts 1 and 2 refer here to compressor inlet and exit, respectively. The same dependency is also true for the compressor efficiency and dimensionless work (defined as $\dot{W}_c/\dot{m}c_{p_1}T_{o_1}$). However, the effects of Reynolds number, Re , inlet flow angle, α_1 and inlet specific humidity, ω_1 , are small and have thus been neglected in compiling the dimensionless maps. (For the most part, the effect of ω_1 is accounted for by the values of c_p and γ included in the other dimensionless groups.) The functional dependency of Eq. (2) is thus reduced to the first three groups on the right-hand side. The term $T_{o_1}/T_{o_1}^*$ (where $T_{o_1}^*$ is the value of T_{o_1} at design conditions) accounts for real gas effects.

For each compressor, a library of maps is compiled consisting of ten nondimensional speed curves, each one evaluated at three values of $T_{o_1}/T_{o_1}^*$. A similar set of curves is generated for water injection rates in the range 0–2.5% at 0.5% intervals. Each curve is defined by ten computed points, distributed sinusoidally with respect to mass flow, through which variable power splines [18] are then fitted. A similar spline fit is also used to interpolate between curves.

Figure 2 shows an example of such a map (for clarity only two typical extreme values of T_{o_1} are shown on the highest speed line). A compressor characteristic reconstructed using the variable power splines is also shown and compares very favorably with that computed directly at the same inlet conditions and rotational speed. Similar characteristics for the dimensionless compressor work are also stored.

3 Multispool Calculation Methods

Compared with single shaft machines, computing the performance of multispool gas turbines is complicated by virtue of the IP and HP spools being free to rotate at any speed, so as to match turbine and compressor work. By contrast, the LP speed of most industrial machines is constrained by the generating frequency. Determining the overall operating point proceeds along the lines of standard work and mass-flow matching calculations (as described, for example, by Cohen et al. [19]), and is described here for a typical three-spool case (Fig. 3). For specified ambient conditions, combustor outlet temperature (COT) and spray characteristics (i.e., water mass flow rates and droplet size distributions upstream of each of the compressors), the following steps are involved:

1. The air mass flow rate, \dot{m}_a , is estimated and (since the LP

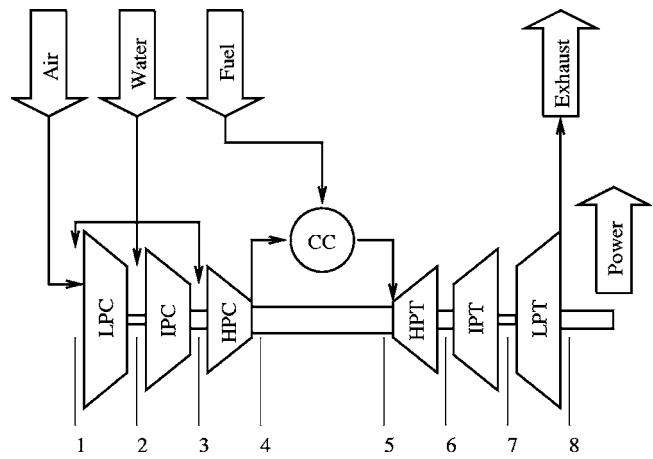


Fig. 3 Layout of multispool gas-turbine showing labeling of axial locations

shaft speed is fixed) conditions downstream of the LP compressor computed either directly or from the wet compressor map.

2. The fuel flow rate, \dot{m}_f , is estimated, thus providing an estimate for the turbine mass flow and gas composition. In the absence of more detailed data, each turbine is then modeled by assuming the first stage stators to be choked and the polytropic efficiencies to be constant. (These assumptions are reasonable provided the machine is not idling, and can be relaxed if turbine characteristics are available.) Thus, for the HP turbine,

$$\frac{\dot{m}\sqrt{c_{p_5}T_{o_5}}}{A_5P_{o_5}} = f\left(\gamma_5, \frac{T_{o_5}}{T_{o_5}^*}\right), \quad (3)$$

$$\frac{T_{o_6}}{T_{o_5}} = f\left(\frac{P_{o_6}}{P_{o_5}}, \gamma_5, \eta_{p_5}, \frac{T_{o_5}}{T_{o_5}^*}\right). \quad (4)$$

where the labeling of axial locations is as shown in Fig. 3. Expressions similar to Eqs. (3) and (4) for the IP and LP turbines provide a total of six equations in the six unknowns $P_{o_5}, T_{o_6}, P_{o_6}, T_{o_7}, P_{o_7}, T_{o_8}$ (T_{o_5} and P_{o_8} are known). Solution of this set of equations requires minor iteration due to the real gas effects. Once accomplished, conditions upstream and downstream of each turbine are known and the work outputs are then readily computed.

3. Matching the IP turbine and compressor work is undertaken as shown on the dimensionless wet compressor work map (Fig. 4): the estimated value of \dot{m}_a and the computed turbine work determine the compressor operating point, which then enables the rotational speed to be found by interpolation between characteristics on either side. The process is repeated for the HP compressor. The overall compressor pressure ratio and temperature ratio are thus known for the estimated values of \dot{m}_a and \dot{m}_f .
4. The fuel mass flow rate required to raise the temperature from the computed value of T_{o_4} to the specified T_{o_5} is calculated from a straightforward first law analysis, assuming adiabatic combustion. This provides an improved estimate of \dot{m}_f , and steps 2 to 4 are then repeated until \dot{m}_f converges (usually in two or three iterations).
5. With the estimated value of \dot{m}_a , the pressure at the combustor outlet (which is taken to be 5% below that of the compressor delivery) is generally incompatible with that obtained from Eq. (3). The air mass flow rate must therefore be adjusted, and in practice it is a straightforward matter to do so in a manner which rapidly converges upon a compatible

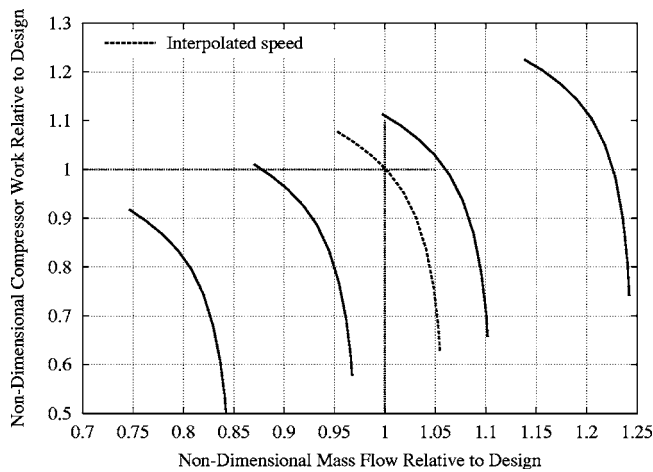


Fig. 4 Determining the compressor operating point from the dimensionless work characteristics

operating point. However, it is also instructive to compute the overall compressor characteristic (for fixed T_{05}) as discussed further below.

4 Industrial Gas Turbine Case Study

The methods described in Sec. 3 have been applied to a typical aeroderivative gas turbine. This is a three-spool machine with the LP shaft operating at a fixed speed. The IP compressor has variable inlet guide vanes and variable stator vanes. The HP compressor consists of six stages with a bleed flow point after the third stage. Full geometric data were available for the compressors, but the turbines were less well specified. Accordingly, estimates were made for the three first-row throat areas so as to give (dry) design operating points close to maximum efficiency for each compressor when the COT was set to 1700 K. Turbine polytropic efficiencies of 90% were assumed.

4.1 Comparison of Methods. Figure 5 shows overall compressor characteristics and turbine running lines computed both from the dimensionless compressor maps and from full numerical calculations. The two approaches compare well, with minor differences being attributable to the neglect of Reynolds number effects in the dimensionless maps and interpolation errors. The

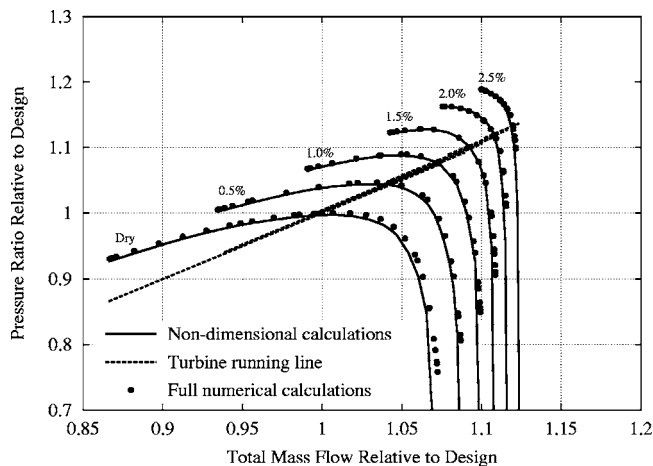


Fig. 5 Comparison between the dimensional and nondimensional methods for different water injection rates using 5- μ m-diameter droplets injected at inlet to the IP and HP compressors

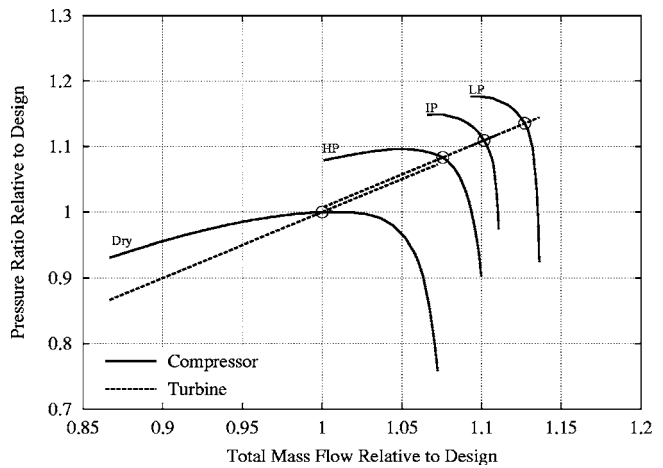


Fig. 6 Effects of water injection location on the multispool characteristic with a 1.5% water injection rate and 5- μ m-diameter droplets

agreement serves to provide confidence in the full numerical calculations which would otherwise be something of a numerical “black box” in nature. It should be noted that the compressor curves shown in the figure are for a fixed COT of 1700 K, with water injection equally divided between IP and HP inlets. Similar behavior as for single-shaft machines is observed, i.e., a shift to higher mass flow and pressure ratio.

4.2 Water Injection at LP Inlet. From a purely thermodynamic viewpoint, the cooling effect of droplet evaporation has a greater impact on compressor work reduction if more of the cooling occurs early on within the compressor [5]. Figure 6 shows the effect of varying the injection point between the LP the IP and HP inlet. 1.5% of water is injected in each case, and the results are produced using the full numerical calculations. The increases in mass flow rate and pressure ratio are clearly enhanced by bringing the injection point forward, and one would therefore expect the greatest power boost with injection at the engine intake.

A preliminary study has thus been made of the effect of increasing injection rate with all water added at the LP inlet and with the COT maintained at 1700 K. The results are summarized in Table 1. With an injection rate of 3%, an increase of power output of some 30% is achieved, with a slight improvement in thermal efficiency. This efficiency gain comes despite the impaired aerodynamic performance of the compressors, which is seen to be particularly severe for the LP compressor. (The slight increase in aerodynamic efficiency for the IP compressor is due to its dry “design” condition being below the peak efficiency point for the assumed turbine throat areas.) Figure 7 shows the evaporation profile through the machine, indicating that for this droplet size all water has evaporated before the HP inlet. With a 1% water injection rate and dry inlet air, the relative humidity in the inlet duct reaches a maximum of 75%, this reduces to just over 1% at the compressor outlet.

The dramatic reduction in aerodynamic efficiency of the LP compressor indicated in Table 1 stems chiefly from the increased mass flow rate, coupled with the fixed rotational speed of the LP shaft. This is evident from Fig. 8 which shows the flow coefficient $\phi = V_x / U$ relative to its design value at each point along the compressor. Due to the overall increase in air mass flow rate, the velocity (and hence ϕ) is initially higher than the design value. The LP compressor thus operates at significantly off design incidence angles, and so generates a lower than designed for pressure and density rise. This results in the flow coefficient increasing yet further. However, as the evaporative cooling takes effect, the density rises, thereby decreasing the velocity and ϕ . The relative increase in the flow coefficient in the duct before the IP compressor

Table 1 Variation of various parameters at the operating point with water injection rate (for 5- μm -diameter droplets injected at LP compressor inlet and a turbine inlet temperature of 1700 K). All values are expressed relative to the dry design value. The compressor and turbine are denoted by C and T , respectively. In addition, the compressor pressure and temperature ratios are represented by β and θ , respectively.

Water injection rate (%)		0.0	0.5	1.0	1.5	2.0	2.5	3.0
Overall	β	1.0	1.070	1.111	1.135	1.150	1.161	1.170
	θ	1.0	0.981	0.964	0.949	0.935	0.921	0.909
	\dot{W}_{net}	1.0	1.113	1.184	1.228	1.258	1.279	1.298
	η_{th}	1.0	1.020	1.026	1.025	1.020	1.014	1.007
	\dot{m}_a	1.0	1.062	1.095	1.110	1.117	1.120	1.121
LP	\dot{W}_C	1.0	0.932	0.861	0.810	0.776	0.755	0.741
	\dot{W}_T	1.0	1.101	1.162	1.200	1.225	1.244	1.261
	η_p	1.0	0.970	0.890	0.784	0.679	0.588	0.516
	β	1.0	0.950	0.896	0.850	0.815	0.789	0.771
IP	\dot{W}	1.0	1.072	1.115	1.141	1.158	1.171	1.182
	η_p	1.0	1.009	1.013	1.014	1.010	1.001	0.990
	N	1.0	1.006	1.017	1.029	1.041	1.051	1.060
	β	1.0	1.085	1.155	1.206	1.239	1.257	1.265
HP	\dot{W}	1.0	1.071	1.114	1.139	1.156	1.168	1.178
	η_p	1.0	0.999	0.998	0.995	0.992	0.988	0.984
	N	1.0	1.000	1.001	1.002	1.003	1.005	1.006
	β	1.0	1.038	1.074	1.108	1.140	1.170	1.200

is due to compressibility effects. With water injection the Mach numbers increase (as the temperatures are lower and velocities higher) and so in the duct the density falls more rapidly. This dominates any density increase due to evaporation and so the relative flow coefficient rises. The increased IP rotor speed also helps to maintain the IP compressor at closer-to-design flow angles. (Note that the sudden jump in ϕ at the HP compressor inlet is a consequence of a "change of reference" from the IP to HP rotational speed, the latter not being significantly different from its design value.)

4.3 Part Load Operation. The impact of water injection on part load performance is clearly of interest. Part load thermal efficiencies and power outputs have been computed by specifying values of COT in the range 1250–1700 K. The results are plotted in Fig. 9 and suggest that, for a given power output, the part-load efficiency is uniformly increased by water injection. The curves

for 1%, 2%, and 3% injection are close together at part load, but each power output will be achieved with a lower combustor temperature as the injection rate is increased.

5 Concluding Remarks

A method has been described for computing the performance of a multispool gas turbine with water injection. The method has been applied to a three-spool industrial machine, for which details of the compressor geometry and dry performance were available. The turbines were each modelled by assuming choked nozzle flow. Preliminary results calculated on this basis show similar trends to predictions for single-shaft machines, namely that air mass flow rates and pressure ratios are increased by water injection, and that early stages of the compressor are shifted towards choke and rear stages towards stall. The LP compressor in particular operates at severely off-design conditions, resulting in poor aerodynamic performance which compromises the benefits of

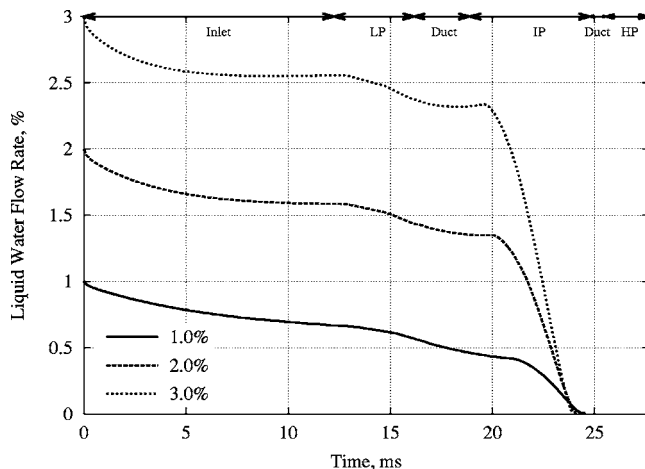


Fig. 7 Liquid water fraction during the compression process

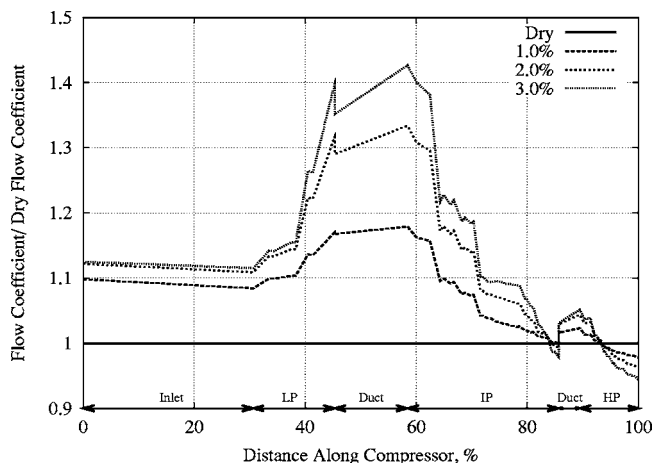


Fig. 8 Variation of flow coefficient throughout the compressor

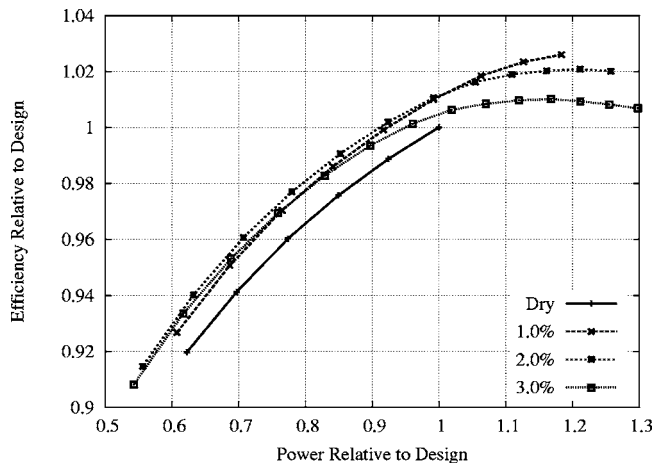


Fig. 9 Variation of overall efficiency with power output for several water injection rates (using 5- μm -diameter droplets)

evaporative cooling. However, the rotational speeds of the IP and HP shafts increase relative to their design values, thereby alleviating the adverse aerodynamic effects of the increased mass flow. It may be that adjustment to turbine throat areas and VGV schedules would also alleviate the off-design difficulties, and this clearly represents an area for future study.

The predicted overall performance of the three-spool machine shows a substantial power boost and a marginal increase in thermal efficiency, despite the impaired aerodynamic performance of the compressors. The precise values of computed efficiency and power output are, however, likely to be modified by improved modeling of the turbines. Furthermore, the analysis has been restricted to small droplets which travel with the gas stream without slip.

Acknowledgment

The authors would like to thank the Engineering and Physical Sciences Research Council and Rolls-Royce plc. for their generous funding and support. Thanks in particular to Peter Wright, John Bolger, Barry Curnock, and Richard Tunstall for their valuable help. The opinions expressed in this paper are those of the authors and not necessarily those of Rolls-Royce plc.

Nomenclature

A	= flow cross section (m^2)
c_p	= specific heat capacity (J/kgK)
D	= diameter (m)
h	= specific enthalpy (J/kg)
HP	= high pressure
IP	= intermediate pressure
LP	= low pressure
\dot{m}	= mass flow rate (kg/s)
N	= rotational speed (rpm)
P	= pressure (N/m^2)
R	= specific gas constant (J/kg)
Re	= Reynolds number
s	= specific entropy (J/kgK)
T	= temperature (K)
U	= blade speed (m/s)
ν	= specific volume (per unit mass of dry air) (m^3/kg)
V	= flow velocity (m/s)
VSV	= variable stator vane

\dot{W}	= power (W)
α	= flow angle
β	= pressure ratio
γ	= ratio of specific heats
η	= efficiency
θ	= temperature ratio
ϕ	= flow coefficient
ω	= absolute humidity

Subscripts and Superscripts

a	= dry air
A	= aerodynamic
C	= compressor
f	= fuel
o	= stagnation quantity
p	= polytropic
T	= turbine
th	= thermal
*	= reference value

References

- [1] Bolland, O., and Veer, T., 2003, "Centenary of the First Gas Turbine to Give Net Power Output: A Tribute to Ægidius Elling," presented (with no paper) at the ASME Turbo Expo, <http://www.tev.ntnu.no/Olav.Bolland/publica.htm>
- [2] Wilcox, E. C., and Trout, A. M., 1950, "Analysis of Thrust Augmentation of Turbojet Engines by Water Injection at Compressor Inlet Including Charts for Calculating Compression Processes With Water Injection," Technical Report No. 1006, NACA.
- [3] White, A. J., and Meacock, A. J., 2003, "An Evaluation of the Effects of Water Injection on Compressor Performance," ASME Paper GT-2003-38237.
- [4] Zhlukov, S. V., Bram, S., and De Ruyck, J., 2001, "Injection of Water Droplets in an Axial Compressor," *Proceedings of the Fifth World Conference on Experimental Heat Transfer, Fluid Mechanics, and Thermodynamics*, Thessaloniki, Greece, Sept., pp. 1415–1420.
- [5] Utamura, M., Takehara, I., and Karasawa, H., 1998, "MAT, A Novel, Open Cycle Gas Turbine for Power Augmentation," *Energy Convers. Manage.* **39**(16–18), pp. 1631–1642.
- [6] Karasawa, H., Utamura, M., and Murata, H., 2001, "Evaporation Behavior of Water Droplets Flowing Through Axial Flow Compressors," *Proceedings of International Conference on Power Engineering*, Oct.
- [7] Horlock, J. H., 2001, "Compressor Performance With Water Injection," ASME Paper 2001-GT-0343.
- [8] Hill, P. G., 1963, "Aerodynamic and Thermodynamic Effects of Coolant Injection on Axial Compressors," *Aeronaut. Q.*, Nov., pp. 331–348.
- [9] Roumeliotis, I., Aretakis, N., and Mathiodakis, K., 2003, "Performance Analysis of Twin-Spool Water Injected Gas Turbines Using Adaptive Modeling," ASME Paper GT-2003-38516.
- [10] Bassily, A. M., 2001, "Performance Improvements of the Intercooled Reheat Regenerative Gas Turbine Cycles Using Indirect Evaporative Cooling of the Inlet Air and Evaporative Cooling of the Compressor Discharge," *Proceedings of the Institution of Mechanical Engineers Part A—Journal of Power and Energy*, Vol. 215(A5), pp. 545–557.
- [11] Sexton, M. R., and Urbach, H. B., 1998, "Evaporative Compressor Cooling for NO_x Suppression and Enhanced Engine Performance for Naval Gas Turbine Propulsion Plants," ASME Paper 98-GT332.
- [12] Utamura, M., Kuwahara, T., Murata, H., and Horii, N., 1999, "Effects of Intensive Evaporative Cooling on Performance Characteristics of Land-Based Gas Turbine," *Joint Power Generation Conference*, Vol. PWR-34/2, ASME, New York, pp. 321–328.
- [13] van Liere, J., Meijer, C. G., Laagland, G. H. M., and Anemaat, C. A., 2000, *Swirlflash: One Year On*, Mod. Power Syst., Apr., pp. 26–27.
- [14] Lefebvre, A. H., 1983, *Gas Turbine Combustion*, Hemisphere Publishing, Washington, DC.
- [15] Miller, D. C., and Wasdell, D. L., 1987, "Off-Design Prediction of Compressor Blade Losses," *Proceedings of the Institution of Mechanical Engineers International Conference: Turbomachinery-Efficiency Prediction and Improvement*, pp. 249–260.
- [16] Spalding, D. B., 1979, *Combustion and Mass Transfer*, Pergamon Press, New York, Chaps. 2–5.
- [17] Wright, P. I., and Miller, D. C., 1991, "An Improved Compressor Performance Prediction Model," *Proceedings of the Institution of Mechanical Engineers European Conference: Turbomachinery-Latest Developments in a Changing Scene*, pp. 69–82.
- [18] Soanes, Jr., R. W., 1976, "Variable Power Splines, an Extension of Twice Differentiable Interpolation," *Proceedings of the Army Numerical Analysis and Computer Conference*, ARO Report No. 76-3.
- [19] Cohen, H., Rogers, G. F. C., and Saravanamuttoo, H. I. H., 1996, *Gas Turbine Theory*, 4th ed., Longman, London.

Influence of Operating Condition and Geometry on the Oil Film Thickness in Aeroengine Bearing Chambers

P. Gorse

Institut für Thermische Strömungsmaschinen,
University of Karlsruhe,
76128 Karlsruhe, Germany

S. Busam

MTU Aero-Engines GmbH,
Dachauer Strasse 665,
80995 München, Germany

K. Dullenkopf

Institut für Thermische Strömungsmaschinen,
University of Karlsruhe,
76128 Karlsruhe, Germany

Increasing the efficiency of modern jet engines does not only imply to the mainstream but also to the secondary air and oil system. Within the oil system the bearing chamber is one of the most challenging components. Oil films on the chamber walls are generated from oil droplets, ligaments, or film fragments, which emerge from bearings, seal plates and shafts, and enter the bearing chamber with an angular momentum. Furthermore, shear forces at its surface, gravity forces, and the design of scavenge and vent ports strongly impact the behavior of the liquid film. The present paper focuses on the experimental determination of the film thickness in various geometries of bearing chambers for a wide range of engine relevant conditions. Therefore, each configuration was equipped with five capacitive probes positioned at different circumferential locations. Two analytical approaches are used for a comprehensive discussion of the complex film flow.

[DOI: 10.1115/1.1924485]

Introduction

The oil system of an aero-engine has to lubricate and cool gears and bearings to ensure a high level of safety and reliability for many operating hours of an aircraft. Only a proper design of the oil system can avoid failures such as oil fire [1] or oil coking in the hot part of the engine. During the last decade many efforts were made to provide a better understanding of the heat transfer (e.g., [2,3]) and the two-phase flow (e.g., [4,5]) in the bearing compartments.

The bearing chamber is the interface between the pure oil flow and the secondary air system. Inside the chamber a complex mixing of the air and oil flow occurs. Pressurized labyrinths are commonly used to seal the chamber against the gaseous environment of the engine. Due to the sealing air flow and the rotation of the shaft a complex gas flow occurs in the chamber. Gorse et al. [6] experimentally investigated the pure air flow in a simplified geometry. Depending on the ratio between the rotational speed and the incoming sealing air flow different three dimensional flow patterns could be determined in the chamber. Furthermore, Gorse et al. [6] showed that increasing the sealing air flow rate caused a small reduction of the azimuthal velocity component in the chamber.

In addition to these two parameters the airflow is influenced by the oil which enters the chamber after it passed the bearings. Along the stationary or rotating walls a shear and gravity driven oil film can be observed whereas a droplet loaded gas flow occurs in the core of the chamber. Before the oil is fed back in a closed loop, the oil is discharged by the vent and scavenge system at the top and the bottom of the chamber, respectively.

Some information is available on analysis of droplet generation in bearing chambers. The bearings are one droplet source [5], where the oil is atomized by the motion of the roller elements and the cage and is then ejected into the bearing chamber. Glahn et al. [5] characterized these droplets and Farrall et al. [7,8] used these

data as initial conditions to calculate trajectories across the chamber. Numerical analysis [7] revealed that droplets are also generated due to splashing of droplets at the surface of the film. Wittig et al. [2] mentioned that above a certain rotational speed droplets are generated at the surface of the liquid wall film. Ebner et al. [9] investigated the effect of droplet entrainment from shear-driven liquid wall films under conditions typical for bearing chambers. Since existing correlations were not suitable, new correlations for the prediction of the entrainment rate and the film height were developed.

Many comprehensive studies were carried out to experimentally and theoretically investigate liquid wall films in bearing chambers [2,4,7,8,10]. Wittig et al. [2] determined for the first time the film thickness under engine relevant conditions using an ultrasonic gauge. The results revealed that gravitational forces as well as the rotational speed of the shaft have a strong impact on the film height. Glahn and Wittig [4] used the LDV technique to experimentally determine film velocity profiles. They showed that increasing the rotational speed causes increased interfacial shear forces and consequently increased film velocities. Using a three-dimensional CFD model Farrall et al. [7] analyzed the entire two-phase flow problem. Concerning the wall film, their numerical scheme took into account the effect of gravitation, interfacial shear and impinging droplets. Using experimental data included in the present paper also, the model could be validated successfully [8]. The features included and the results obtained make the CFD a powerful and accurate tool. But a lot of computational time is required for the CFD-modeling. Promising alternatives are analytical or empirical methods that require few computational efforts. Therefore, they are of great interest for an efficient development of bearing chambers. Based on experimental results, Glahn and Wittig [4] developed an analytical model to predict the film flow in the bearing chamber with a high degree of accuracy. Since the model is used in the present study a detailed description will be provided later in the paper.

In the scope of the present study the film thickness was experimentally determined for different rotational speeds, lubrication oil flow rates and different chamber geometries. The film thickness was measured as a function of the circumferential location by using capacitive sensors. At the beginning of the paper the three different configurations of bearing chambers are presented, before

Contributed by the International Gas Turbine Institute (IGTI) of ASME for publication in the JOURNAL OF ENGINEERING FOR GAS TURBINES AND POWER. Manuscript received October 1, 2003; final manuscript received March 1, 2004. IGTI Review Chair: A. J. Strazisar. Paper presented at the International Gas Turbine and Aeroengine Congress and Exhibition, Vienna, Austria, June 13–17, 2004, Paper No. GT2004-53708.

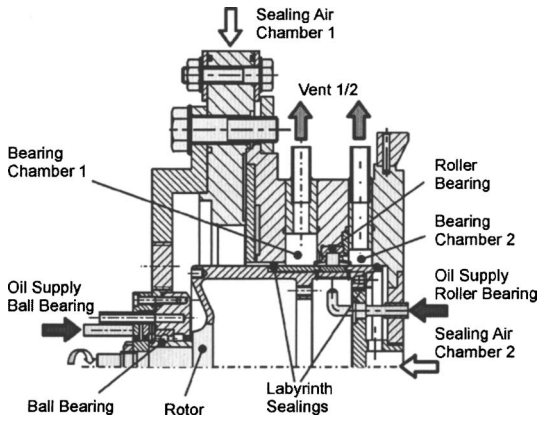


Fig. 1 High speed bearing chamber test rig

an analytical approach is developed, that allows the prediction of the azimuthal velocity of the pure air flow in bearing chambers. With this information the impact of the rotating gas flow on the wall film is estimated. Since the film flow is very complex and depends on many parameters, the analysis of the experimental data is very challenging. Based on several assumptions, an existing analytical approach [4] is extended to derive an enhanced understanding of the shear and gravity driven oil films. Then the experimental results are presented and discussed.

Compact High Speed Bearing Chamber Test Rig

A co-axial sectional view of the test rig is shown in Fig. 1. The rig was used first by Wittig et al. [2], who provided a detailed description of the test facility. Due to the compact and modular design, variations of bearing chamber geometries and roller bearings can be realized with relatively low financial and manufacturing effort.

The rotor ($n_{\max}=20,000$ rpm) is supported by two bearings. A ball bearing is used to prevent axial and radial displacements of the rotor. Due to the small size of the ball bearing only little amounts of oil were supplied for lubrication. The second bearing is a squeeze film damped roller bearing. Oil is supplied by an under race lubrication system and could be adjusted to maximum flow rates of $\dot{V}_{l,\max}=400$ l/h at temperatures of $T_{\ell,\max}=423$ K. The roller bearing separates the two bearing chambers, where the oil is ejected after cooling and lubricating the bearing. Both chambers are sealed by air pressurized labyrinths. The sealing air was provided by a compressor with a maximum mass flow rate of $\dot{m}_{g,\max}=0.5$ kg/s at a pressure ratio of $\Pi=10$ and a temperature of $T_{g,\max}=623$ K. The occurring two phase air-oil flow is discharged at the top and bottom of each chamber by the vent and scavenge system (not shown), respectively. Then the oil is separated from the air and returned into the tank.

The vent and scavenge ports of each design were positioned in the center of the chamber as shown in Fig. 2 and were flushed with the outer radial housing of the chambers.

In the present study, the film thickness was determined as a function of the circumferential position for three different geometries by using capacitive sensors. At one angular position film velocity profiles were measured with the LDV-method. The geometries and the instrumentation are shown in Fig. 2 and the main dimensions are summarized in Table 1.

Experimental Techniques

The experiments were focused on the characterization of the liquid wall film along the radial housing of the bearing chamber. Therefore, velocity profiles and the film thickness were determined using the LDV technique and capacitive sensors, respectively.

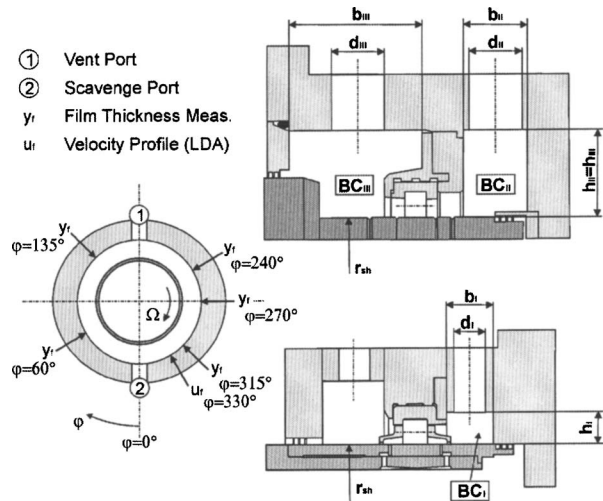


Fig. 2 Different configurations of bearing chambers and angular positions of film thickness and velocity measurements

Film velocity profiles were captured at an angular position of $\varphi=330$ deg in chamber BC_I (see Fig. 2). Since the LDV technique and the experimental setup for the present investigation did not differ from earlier studies [4] it is referred to the literature at this point.

Capacitive film thickness sensors were used to measure the local film thickness at five angular positions in each chamber BC_I - BC_{III} (see Fig. 2). A capacitive determination of a liquid film thickness is based on the dependence of the capacity on the specific dielectric coefficient. In general, the dielectric coefficient depends on material properties. Therefore, the measuring device is influenced by the volume fraction of the liquid located inside the probe volume. Measuring the capacity, the mean film thickness can be estimated [11]. An application inside the bearing chamber implies a sensor that can be adapted to the geometry without lapping into the chamber. This demand is fulfilled by the sensor shown in Fig. 3. Ground and shield electrode are located as concentric rings around the measuring electrode. Measuring and shield electrode are on the same electric potential, thus the homogeneity of the electric field in the short range of the sensor is given. Increasing the distance of the film surface from the sensor, the electric field becomes more and more inhomogeneous, so that the capacity C and in consequence the film thickness is determined by use of calibration functions. Therefore, the sensors were

Table 1 Geometries of bearing chamber

		BC_I	BC_{II}	BC_{III}
Radius of rotor	r_{sh} [mm]	64	62	62
Chamber height	h_{I-III} [mm]	10	28	28
Chamber width	b_{I-III} [mm]	15	20	46
Vent/Scavenge Pipe (\varnothing)	d_{I-III} [mm]	10	17	17

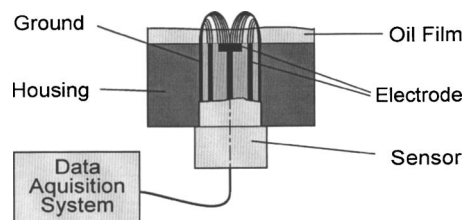


Fig. 3 Determination of film thickness using capacitive sensors

calibrated at static conditions down to a minimum film thickness of $\bar{h}_f \approx 0.2$ mm. The temperature dependency was compensated by calibrating the sensor at different oil temperature.

Even after a careful calibration, uncertainties remained due to the static calibration and the temperature compensation. Air bubbles in the film and unstable film surfaces also affect the accuracy of the sensors. In comparison, the waviness of the film has a negligible influence since the diameter of the sensor ($d = 2.3$ mm) is big compared to the wave-length and integration time of the sampled signal is sufficient long regarding the wave frequencies. All these effects lead to an estimated uncertainty of ± 25 μ m. Additionally, precise measurements using this method require a constant dielectric coefficient of the liquid. It can be affected by the temperature and the volume fraction of a component with higher dielectric coefficient (e.g., $\epsilon_{r,water} \gg \epsilon_{r,oil}$). Since the volume fraction of water in oil is in the range of 80–100 ppm, this effect could be neglected.

As confirmed by extensive preliminary tests, the described capacitive gauge has obvious advantages referring to an application in the bearing chamber rig. It is insensitive to vibrations, easy to handle and adaptable to the geometry. In addition, this technique is characterized by a high resolution (especially in the short range of the sensor) and can easily be linked to the data acquisition system of the test facility. For a comparison of the film flow inside the three different bearing chambers a criterion is required that can be used to estimate the effect of the gas flow on the film characteristics. Therefore, an analytical approach is derived in the next section.

Comparison of Different Geometries

Based on an angular momentum balance as given by Eq. (1), this approach is used to predict the averaged tangential velocity \bar{u}_g of the air flow, which is not affected by the oil flow.

$$M_r - M_s = \sum_{out} \dot{m}_{g,i} r_i (u_{g,t,i} - \bar{u}_g) - \sum_{in} \dot{m}_{g,i} r_i (u_{g,t,i} - \bar{u}_g) \quad (1)$$

Since this simplification is in contradiction to the real two phase flow in bearing chambers, this approach can only be used to estimate qualitatively the impact of the gas flow on the liquid wall film. But the advantage of such an approach is that the results can be compared to experimental data of the pure air flow in bearing chambers [6]. Similar approaches were used successfully for the characterization of secondary air system components [12,13].

The rotor and stator moment are determined as follows:

$$M_r = \frac{\lambda}{8} \rho_g (\Omega r_{sh} - \bar{u}_g)^2 \int_{Rotor} r dA_r \quad (2)$$

$$M_s = \frac{\lambda}{8} \rho_g \bar{u}_g^2 \int_{Stator} r dA_r \quad (3)$$

Due to the complex and differing geometries of bearing chambers, it was aimed to use a general expression for the friction factors. In the present study the Blasius correlation for turbulent flow in smooth pipes was chosen. Since the angular momentum balance is only used to estimate the influence of gas velocity on the film qualitatively, the Blasius approach can be used.

$$\lambda = 0.3164 Re^{-0.25} \quad (4)$$

$$Re = \frac{D_h \Delta u}{\nu_g} \quad (5)$$

$$\text{with } D_h = \frac{4A}{U} \text{ and } \Delta u = u_w - \bar{u}_g \quad (6)$$

The friction factors differ for the rotating and the stationary walls since the wall velocity u_w is equal to $u_w = \Omega r_{sh}$ and $u_w = 0$ for

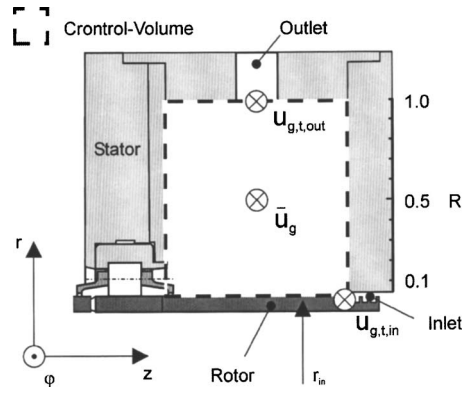


Fig. 4 Adaptation of angular momentum balance to the present configurations

the rotor and stator, respectively. The hydraulic diameter D_h is based on the cross section of the bearing chamber.

The adaptation of the one-dimensional (1D) approach to the present configurations is shown in Fig. 4. The air enters into the chamber with an angular momentum across the labyrinth seal. Depending on the tangential velocity or inlet swirl $u_{g,t,in}$ the sealing air flow either accelerates or decelerates the azimuthal velocity in the chamber. Further it is assumed, that the flow field is axisymmetric. Therefore, the outlet, which is originally a circular port at one angular location, is approximated by a slot along the circumference of the chamber, where the air has an azimuthal velocity equal to the swirl velocity $u_{g,t,out} = \bar{u}_g$. Therefore, the outlet has no impact on the angular momentum balance (see Eq. (1)). Since the outlet area is small compared to the surface of the stationary walls the outlet is neglected in the calculation of the stator moment. As a result, Eq. (1) can be simplified as follows:

$$M_r - M_s = -\dot{m}_{g,in} r_{in} (u_{g,t,in} - \bar{u}_g) \quad (7)$$

To validate the 1D-gas-model, it was compared to experimental data of tangential velocity profiles in bearing chamber for different sealing air flow rates [6]. The experiments were conducted in a geometry which was similar to the present configuration BC_I . Only the height and the width of the chamber differed and amounted $h_{BC} = 47$ mm and $b_{BC} = 44$ mm, respectively. In Fig. 5 examples of the experimentally determined profiles and predicted swirl velocity are shown. The tangential velocity was nondimensionalized by the surface velocity of the rotor. R denotes the radial position in the chamber (see Fig. 4) $-R = 0$ and $R = 1$ correspond to the rotor surface and the outer radial housing, respectively. Although the experimentally determined velocities are slightly reduced at increasing radii, a relatively flat velocity distribution occurred in the core region. Since the inlet swirl of the sealing air

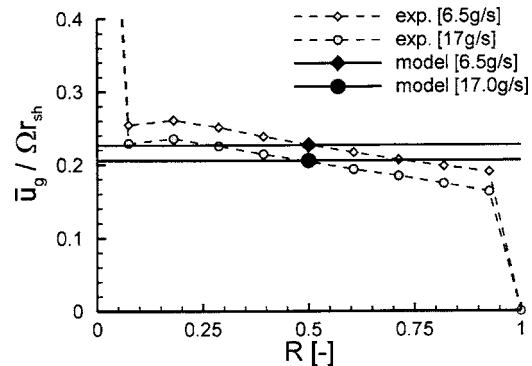


Fig. 5 Comparison of 1D gas model and experimentally determined velocity profile

Table 2 Predicted pure gas velocity for the different configurations

	BC_I	BC_{II}	BC_{III}
$\bar{u}_g/\Omega r_{sh}$	0.23	0.16	0.30

was not known from the experiments, the model was used to determine it. To simplify the calculation, the influence of the sealing air flow rate on the inlet swirl was neglected, so that a constant velocity ratio of $k=u_{g,t,in}/\Omega r_{sh}=0.13$ could be determined. The remaining deviation between the model and the experiments can be quantified with 0.7% in the center of the chamber ($R=0.5$). In addition, very few computational time is required to obtain reliable results, so that the angular momentum balance is an excellent approach to predict the tangential velocity of the pure air flow in bearing chambers. Due to a current gap in validation data this approach cannot be used to quantify gas velocities when the air flow interacts with the oil flow.

To predict the azimuthal pure gas velocity of the present configurations, the angular momentum balance was solved for each geometry at a rotational speed of $n=12,000$ rpm, a sealing air flow rate of $\dot{m}_{g,in}=10$ g/s and a temperature of $T_{g,in}=373$ K. Since the design of all labyrinth seals—validation geometry and BC_I – BC_{III} —was similar, the above determined velocity ratio of $k=0.13$ was used to predict inlet swirl $u_{g,t,in}$.

Table 2 summarizes the predicted velocity ratios $\bar{u}_g/\Omega r_{sh}$ for the three different configurations. Based on these assessments, the highest gas velocity occurs in BC_{III} . Thus, it can be assumed that the gas flow of BC_{III} has the strongest influence on the liquid wall film.

Before the results of the film thickness measurements are presented and discussed, a second analytical approach is introduced.

Modeling of Film Flow

In the following section an analytical approach to calculate liquid wall films along the outer wall of bearing chambers is presented. The approach is based on an existing model [4,14], which was used to characterize film velocity profiles under engine relevant conditions. In the present study this analytical model was extended to estimate the film thickness as a function of the circumferential position in the bearing chamber. Figure 6 explains how the film thickness distribution is determined and points out

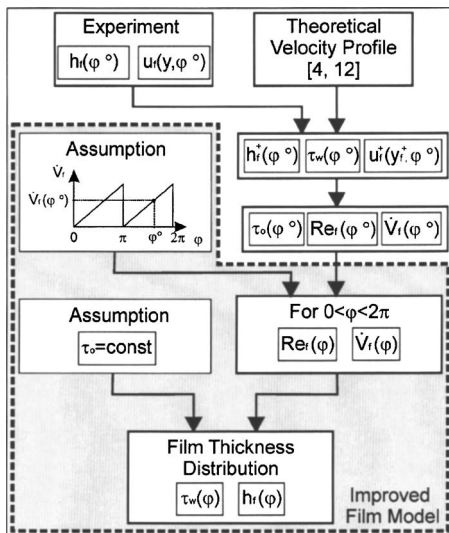


Fig. 6 Calculation scheme for the film thickness distribution in bearing chambers

the present improvements. Due to the complexity of the film flow in the bearing chamber the following assumptions were made in a first step:

- The film flow is two-dimensional, since effects in the axial direction are neglected.
- Interfacial shear and gravity forces mainly drive the oil film. Since it can be assumed, that the gas flow is axisymmetric—except at the outlets—accelerations of the film due to the air flow are neglected.
- The interfacial shear τ_0 at the surface of the film is assumed to be constant, $\tau_0 \neq f(\varphi)$.
- Any carry-over effect at the outlets is neglected. This is only possible if the vent pipe diameter is of the same size than the chamber width and the droplets are discharged with the air flow.
- The oil is supplied constantly along the circumference to the film, so that the film flow rate increases linearly along the chamber housing.
- The momentum transfer of the oil entraining into the film is neglected.
- Droplet entrainment from the film into the droplet loaded gas flow is neglected.

First the model requires the knowledge of the film thickness $\bar{h}_f(\varphi \text{ deg})$ and a velocity profile $\bar{u}_f(y, \varphi \text{ deg})$ at one angular position $\varphi \text{ deg}$. In the present study these parameters were determined experimentally.

A theoretical velocity profile is obtained from a nondimensional momentum equation (see Eq. (8)) which is derived from a force balance of a turbulent liquid film at an inclined plane [4,15]. Pressure forces and any acceleration of the fluid are neglected. Furthermore, it is assumed that the averaged film thickness \bar{h}_f is small compared to the curvature of the housing ($\bar{h}_f/r_l \leq 0.02$). The nondimensional velocity u_f^+ and coordinate y_f^+ are defined by Eqs. (9) and (10).

$$\frac{\tau}{\tau_w} = 1 - \sigma y_f^+ = \left(1 + \frac{v_f}{v_f}\right) \frac{du_f^+}{dy_f^+} \quad (8)$$

$$u_f^+ = \frac{u_f}{u_{\tau,f}} \quad \text{with} \quad u_{\tau,f} = \sqrt{\frac{\tau_w}{\rho_f}} \quad (9)$$

$$y_f^+ = y \frac{u_{\tau,f}}{v_f} \quad (10)$$

The superimposed effect of gravitational and shear forces is taken into account by σ in Eq. (8) and is defined as follows:

$$\sigma = \frac{-v_f g \sin \varphi}{u_{\tau,f}^{3/2}} \quad (11)$$

Glahn and Wittig [4] showed that the accuracy of the model strongly depends on the definition of the turbulent eddy viscosity. For bearing chamber applications the approach of Deissler [16] was used with great success.

$$\frac{v_f}{v_f} = m^2 u_f^+ y_f^+ [1 - \exp(-m^2 u_f^+ y_f^+)] \quad (12)$$

The parameter m was determined in Deissler's approach for water and amounts $m=0.109$. Glahn and Wittig [4] showed that the same value for the parameter m can be used for oil. To predict a velocity profile Eq. (8) must be integrated numerically. The wall shear stress τ_w has to be determined iteratively at the angular location $\varphi \text{ deg}$, where the velocity profile $u_f(y, \varphi \text{ deg})$ is known.

The local film Reynolds-number $Re_f(\varphi \text{ deg})$ and the film flow rate $\dot{V}_f(\varphi \text{ deg})$ are determined by Eqs. (13) and (8).

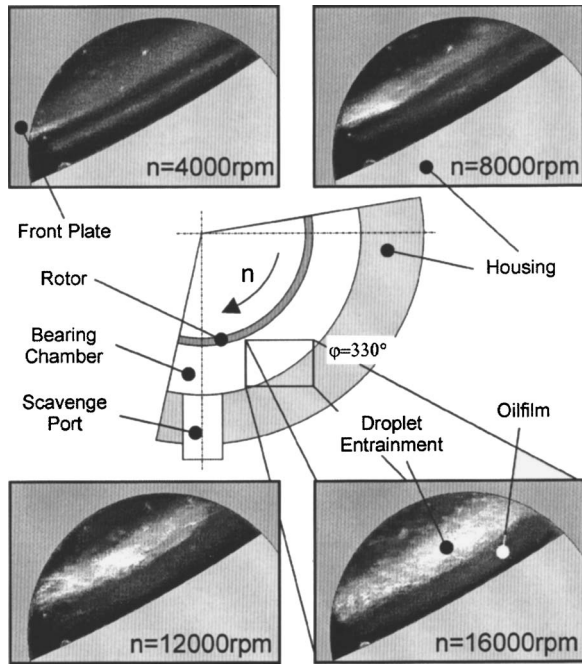


Fig. 7 Visualization of liquid wall film in configuration BC_I

$$Re_f = \frac{\dot{V}_f}{bv_f} = \int_0^{h_f} u_f^+ dy_f^+ \quad (13)$$

With the known flow rate $\dot{V}_f(\varphi \text{ deg})$ and the assumption that the film flow rate increases linearly between the two ports, the flow rates \dot{V}_f and the film Reynolds-numbers Re_f can be determined for any angular position φ . Together with the assumption that the interfacial shear stress τ_0 remains constant, the local film thickness $\bar{h}_f(\varphi)$ and local wall shear stress $\tau_w(\varphi)$ have to be determined iteratively.

In the present study this analytical model was compared to experiments and discussed for one bearing chamber configuration.

Results

The presentation and discussion of liquid wall films in bearing chambers is outlined as follows. First qualitative visualizations of the oil film at different rotational speeds are presented. Afterward the film thickness distribution in configuration BC_I is compared to the film model. At last the discussion of film flow is extended for different bearing chamber designs, including experimental results from Glahn [14]. He obtained the film thickness data in configurations BC_{II} and BC_{III} .

All experiments were conducted for a wide range of operating conditions. The rotational speed ranged between $4000 \text{ rpm} \leq n \leq 16,000 \text{ rpm}$ for configuration BC_I and $6000 \text{ rpm} \leq n \leq 16,000 \text{ rpm}$ for the other two configurations BC_{II} and BC_{III} . The liquid flow rate supplied to the bearing chamber ranged between $50 \text{ l/h} \leq \dot{V}_{l,in} \leq 150 \text{ l/h}$ for chambers BC_I and BC_{III} and $50 \text{ l/h} \leq \dot{V}_{l,in} \leq 200 \text{ l/h}$ for the other chamber. For all conditions the sealing air flow, the pressure in the chamber, and the oil and air inlet temperature were kept constant at $\dot{m}_{g,in} = 10 \text{ g/s}$, $p = 2.5 \text{ bar}$ and $T_l = T_g = 373 \text{ K}$, respectively.

In Fig. 7 the two phase flow was visualized in configuration BC_I at an angular position of $\varphi \approx 330 \text{ deg}$ for different rotational speeds. At $n = 4000 \text{ rpm}$ the flow field was characterized by a liquid wall film with a relatively smooth surface. Above the wall film few light was scattered indicating that the gas flow carried some oil droplets. At $n = 8000 \text{ rpm}$ the film characteristics did not

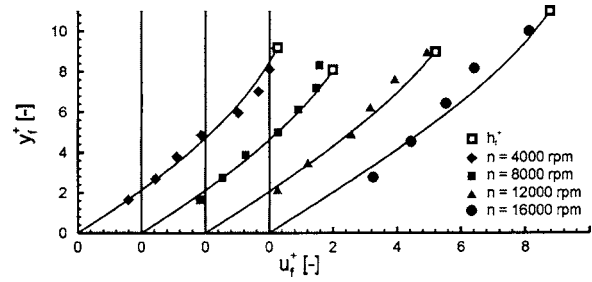


Fig. 8 Velocity profiles of liquid wall film at $\varphi = 330 \text{ deg}$ and $\dot{V}_{l,in} = 100 \text{ l/h}$

change significantly. But with further increasing rotational speeds more and more droplets occurred in the gas flow of the chamber. Based on these visualizations, it is not clear whether the droplets were shed from the bearing, entrained from the film into the gas flow, or both. Additionally, the film thickness was reduced as a consequence of higher gas velocities.

To calculate the circumferential film thickness distribution using the presented 1D film model, analysis of film velocity profiles were required and conducted as described by Glahn and Wittig [4]. These measurements were performed at an angular position of $\varphi = 330 \text{ deg}$. Profiles at different rotational speeds and at a constant oil flow rate $\dot{V}_{l,in} = 100 \text{ l/h}$ are shown in Fig. 8. The wall distance y_f^+ and the velocity u_f^+ are dimensionless values, which were calculated from Eqs. (9) and (10). Further, the wall shear stress was calculated iteratively for each measured data point until the predicted velocity profile matched the measured data. Then the averaged wall shear stress was used to calculate the velocity profiles, which are represented by the solid lines in Fig. 8. As a result, the film velocity increased when the rotational speed was increased.

The film thickness was measured at $\varphi = 315 \text{ deg}$ to avoid an influence of the capacitive film thickness sensor on the velocity measurements. Thus, a gap of $\Delta\varphi = 15 \text{ deg}$ between the measured values occurred. This gap can be neglected for the present analysis. The dimensionless film thickness h_f^+ is also given in Fig. 8.

Figure 9 shows the local measured film thickness \bar{h}_f and predicted quantities such as the interfacial shear τ_0 and the local film flow rate \dot{V}_f calculated by Eqs. (8) and (13), respectively. When the rotational speed was increased, τ_0 was increased. Consequently, the film velocities were increased too and tended to result in reduced film thicknesses. The effect of rotation on the film flow rate is more complex since several superimposed effects occur. The flow visualizations showed that the droplet concentration was increased with increasing rotational speed—especially above $n > 8000 \text{ rpm}$. Further, a characterization of the droplet flow in bearing chambers [5] showed that the droplet's diameters ranged

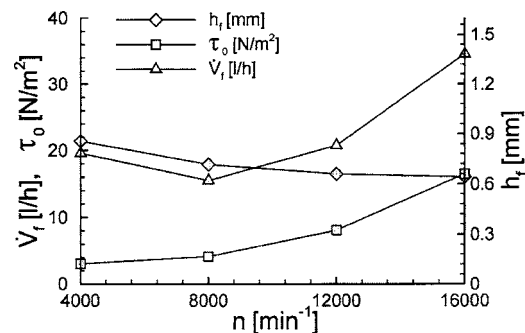


Fig. 9 Characterization of liquid wall film at $\varphi = 330 \text{ deg}$ and $\dot{V}_{l,in} = 100 \text{ l/h}$

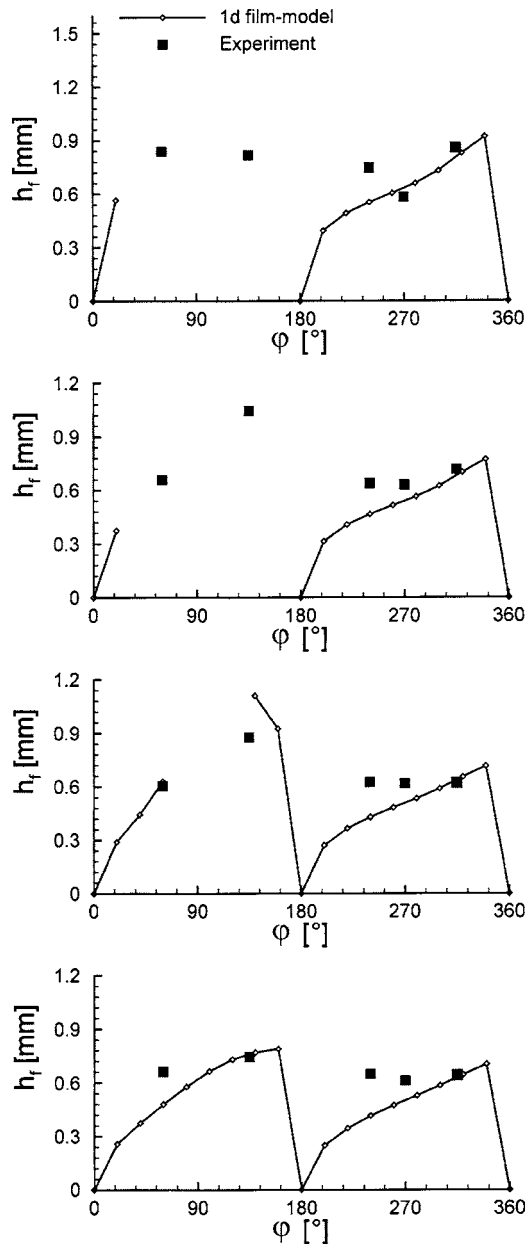


Fig. 10 Theoretical analysis of film flow depending on the angular position

between 14 and 500 μm . Based on this, it can be assumed, that especially bigger droplets were not discharged with the air flow and were fed back into the film downstream of the ports. As a result of this increased carry-over effect, the volume flow rate of the film was increased.

Another effect of increasing interfacial shear is a redistribution of local film flow rates within the bearing compartment. At low speeds, the majority of the oil will tend to settle in the bottom of the cavity. At higher speeds, the oil puddle will be pushed out of bottom-dead-center and shear forces will eventually lead to a more homogeneous film thickness distribution along the circumference.

With the knowledge of the interfacial shear the film model permits to predict the film thickness in bearing chamber BC_I as a function of the circumferential location. Figure 10 shows the measured and predicted film thickness distribution for an oil flow rate of $\dot{V}_{l,in}=100$ l/h through the chamber at different rotational speeds. The scavenge port at the bottom and the vent port at the

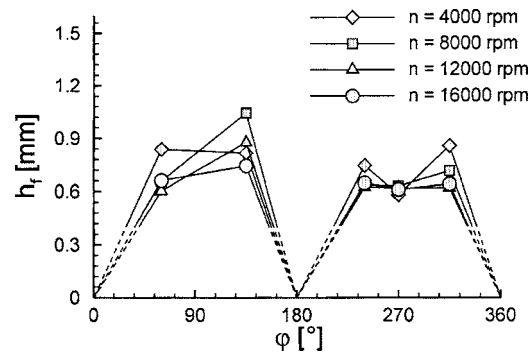


Fig. 11 Experimentally determined film thicknesses: Effect of rotational speed in configuration BC_I

top of the chamber are located at $\varphi=0$ deg and $\varphi=180$ deg, respectively. The angle φ increases in the direction of the rotation of the shaft (see Fig. 2), so that the interfacial shear and gravity forces act in the opposite direction for $0 \text{ deg} < \varphi < 180 \text{ deg}$ and in the same direction for $180 \text{ deg} < \varphi < 360 \text{ deg}$.

A current limitation of the film model can be seen in predicting film thicknesses at $n \leq 12,000$ rpm and $20 \text{ deg} < \varphi < 180 \text{ deg}$. Under these conditions the wall shear stress becomes $\tau_w \leq 0$ indicating that the oil starts to flow back along the wall. At higher shaft speeds $n=16,000$ rpm the interfacial shear is high enough so that $\tau_w > 0$ for all φ and the wall coordinate formulation of the model applies.

A comparison of the experimental and modeled results revealed, that the model has limitations in predicting the film flow accurately. It is obvious that the model and the experiments agree best at $\varphi=315$ deg since these data were used to calculate the interfacial shear and the liquid flow rate. The major deviation occurs at $n=4000$ rpm where a drop of the film thickness was measured between $\varphi=240$ deg and $\varphi=270$ deg. This effect was not displayed by the model and might occur due to the assumption that the interfacial shear remains constant [$\tau_0 \neq f(\varphi)$].

At high rotational speeds above $n \geq 12,000$ rpm constant film thicknesses were measured and not revealed by the model, which predicts a constantly increasing film thickness. This effect might be explained by a carry-over of oil at the ports.

The effect of rotational speed on film thickness is summarized for configuration BC_I in Fig. 11. The solid and dashed lines are only included to compare the experimental results conveniently. In general, the film thickness increased downstream of the scavenge port until the oil reached the vent port. At $n=4000$ rpm it can be assumed, that the interfacial shear τ_0 was too small to overcome gravity and a lot of the liquid remained in the oil sump. As a result, the film thickness decreased between $\varphi=60$ deg and $\varphi=135$ deg to the vent port. Since the effect of gravity decreased and the carry-over effect at the ports became more important when the shaft speed was increased, the circumferential distribution oil film thickness became more uniform, e.g., for $n=8000$ rpm the film thickness varied between $h_f=0.63$ mm and $h_f=1.04$ mm, whereas the film thickness varied between $h_f=0.61$ mm and $h_f=0.74$ mm at $n=12,000$ rpm.

The same effects were determined for configuration BC_{II} in Fig. 12. The major difference is that higher shaft speeds—at least $n \geq 12,000$ rpm—are necessary to overcome the effect of gravitation and to drive the oil film. At lower shaft speeds and especially at an angular position of $\varphi=315$ deg the film thickness increased to more than $h_f=1.5$ mm. These differences occurred due to the different gas velocities in the core region of the chamber. For configuration BC_I a velocity ratio of $Ru=0.23$ was predicted by the 1D gas-model whereas the velocity ratio was equal to $Ru=0.16$ for BC_{II} .

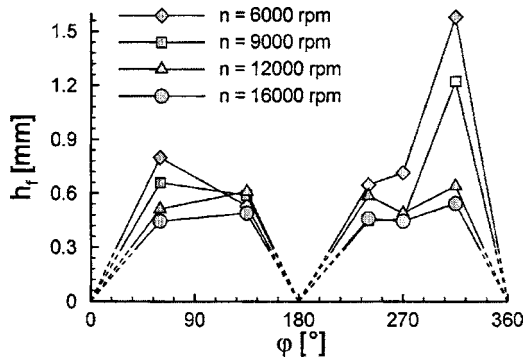


Fig. 12 Experimentally determined film thicknesses: Effect of rotational speed in configuration BC_{II}

A velocity ratio of $Ru=0.30$ was predicted for the third configuration BC_{III} in Fig. 13. Therefore, the wall film of BC_{III} was driven most by the interfacial shear. Opposite to the other geometries and the model, the film thickness decreased between $\varphi=60$ deg and $\varphi=135$ deg for all rotational speeds. Regarding the ratio between the width of the chamber and the diameter of the scavenge port, 66% and 85% of the chamber width were covered by the scavenge port in the configurations BC_I and BC_{II} , respectively. In contrast, only 37% were covered in configuration BC_{III} , leading to a large carry-over and higher film flow rates just downstream of the ports. This resulted in larger film thicknesses and in negative wall shear stresses $\tau_w \leq 0$ even at high rotational speeds.

The influence of the lubrication oil entering into the bearing chamber is shown in Fig. 14. An increased oil flow rate led to thicker films. As a result, gravitation had a stronger impact on the film, so that the gradient $dh_f/d\varphi$ decreased for the configurations BC_I and BC_{II} .

The present investigation revealed that the description of the film flow in bearing chambers is a very challenging task. The characteristics of the film strongly depend on the operating conditions and on the design of the bearing chamber also.

Conclusion

The present investigation focused on the characterization of the liquid wall film in bearing chambers. Film thickness and film velocity measurements were conducted by using capacitive probes and the LDV-technique, respectively. To permit a comparison of the different configurations and to predict the film flow as a function of the circumferential location, two analytical models were introduced. The first model estimated the tangential velocity the pure air flow in the chamber using an angular momentum balance. This velocity was used to estimate the impact of the air flow on the film for the different geometries. A comparison with experi-

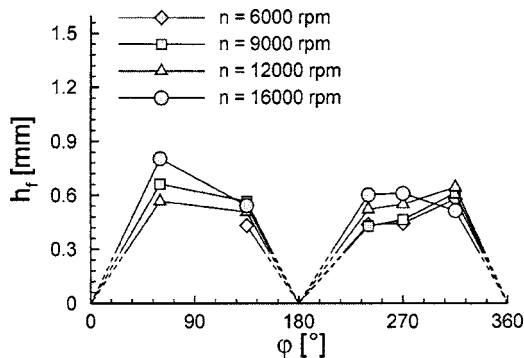


Fig. 13 Experimentally determined film thicknesses: Effect of rotational speed in configuration BC_{III}

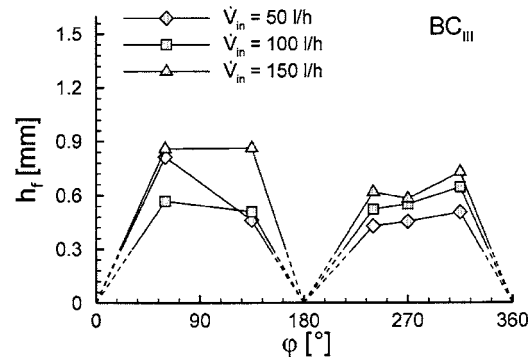
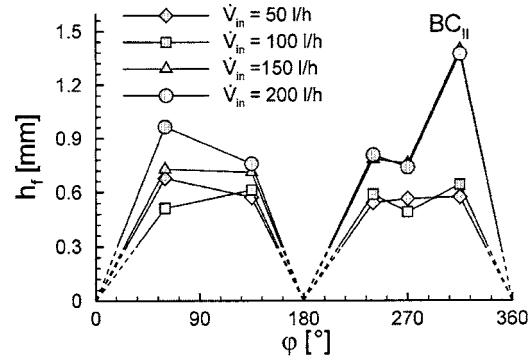
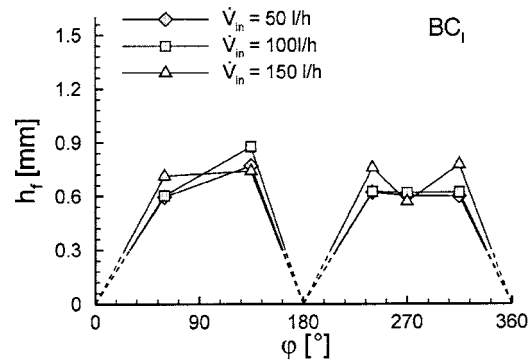


Fig. 14 Experimentally determined film thicknesses: Effect of lubrication oil in the different configurations

mental data revealed that this approach predicts the pure air flow with a very good accuracy. The second model was used to characterize the shear and gravity driven wall film. Due to the assumptions the model is limited for the prediction of the film, but helped to derive an enhanced understanding of the complex film flow in bearing chambers. The results revealed that the operating conditions as well as the design of the chamber strongly impact the complex film flow. The measurements showed that the film thickness ranged between $h_f \approx 0.5$ mm and $h_f \approx 1.5$ mm for all configurations investigated. Furthermore, the liquid wall film was strongly affected by the design of the vent and scavenge ports, which strongly impact the discharge-characteristics of the oil-air mixture. Additional and more generic research is necessary to further improve the understanding of two-phase flow phenomena in bearing chambers. Then more advanced analytical approaches and accurate design rules for future bearing chambers can be developed.

Acknowledgment

The authors would like to thank Dr. J. A. Glahn for the intensive and valuable discussions during the preparation of the paper.

Nomenclature

A	= surface (m^2)
b	= width of bearing chamber (m)
BC	= bearing chamber
d	= diameter (m)
D_h	= hydraulic diameter (m)
g	= acceleration of gravity (m/s^2)
h	= height (m)
k	= velocity ratio
m	= parameter
\dot{m}	= mass flow (kg/s)
M	= moment (Nm)
n	= rotational speed (rpm)
R	= radial position
r	= radius (m)
Re	= Reynolds-number
T	= temperature (K)
u	= velocity (m/s)
U	= circumference (m)
\dot{V}	= volume flow rate (l/h)
y	= wall distance (m)
ϵ_r	= specific dielectric coefficient
φ	= angle (deg)
λ	= friction factor
ν	= kinematic viscosity (m^2/s)
Ω	= angular velocity of rotor (s^{-1})
ρ	= density (kg/m^3)
σ	= parameter
τ	= shear (N/m^2)

Subscripts

f	= film
g	= gas
in	= inlet
I, II, III	= number of configuration
l	= liquid
r	= rotor
s	= stator
sh	= shaft
t	= turbulent
W	= wall
τ	= shear

0	= surface
+	= dimensionless

References

- [1] Willenborg, K., Busam, S., Roßkamp, H. and Wittig, S., 2002, "Experimental Studies of the Boundary Conditions Leading to the Oil Fire in the Bearing Chamber and in the Secondary Air System of Aeroengines," ASME Paper GT-2002-30241.
- [2] Wittig, S., Glahn, A. and Himmelsbach, J., 1994, "Influence of High Rotational Speeds on Heat Transfer and Oil Film Thickness in Aero Engine Bearing Chambers," J. Eng. Gas Turbines Power, **116**, pp. 395–401.
- [3] Busam, S., Glahn, A. and Wittig, S., 2000, "Internal Bearing Chamber Wall Heat Transfer as a Function of Operating Conditions and Chamber Geometry," ASME J. Eng. Gas Turbines Power, **122**, pp. 314–320.
- [4] Glahn, A. and Wittig, S., 1996, "Two-Phase Air/Oil Flow in Aero Engine Bearing Chambers: Characterization of Oil Film Flow," ASME J. Eng. Gas Turbines Power, **118**(3), pp. 578–583.
- [5] Glahn, A., Kurrek, M., Willmann, M. and Wittig, S., 1996, "Feasibility Study on Oil Droplet Flow Investigations Inside Aero Engine Bearing Chambers—PDDA Techniques in Combination with Numerical Approaches," ASME J. Eng. Gas Turbines Power, **118**(4), pp. 749–755.
- [6] Gorse, P., Willenborg, K., Busam, S., Ebner, J., Dullenkopf, K. and Wittig, S., 2003, "3D-LDA Measurements in an Aero-Engine Bearing Chamber," ASME Paper GT2003-38376.
- [7] Farrall, M., Hibberd, S. and Simmons, K., 2003, "Modelling of Droplet/Film Interaction in an Aero-Engine Bearing Chamber," ICLASS2003.
- [8] Farrall, M., Hibberd, S., Simmons, K., Busam, S., and Gorse, P., 2004, "A Numerical Model for Oil Film Flow in an Aero-Engine Bearing Chamber and Comparison with Experimental Data," ASME Paper GT2004-53698.
- [9] Ebner, J., Gerendas, M., Schäfer, O. and Wittig, S., 2001, "Droplet Entrainment from a Shear Driven Liquid Wall Film in Inclined ducts—Experimental Study and Correlation Comparison," ASME Paper 2001-GT-0115.
- [10] Chew, J. W., 1996, "Analysis of the Oil Film on a Bearing Chamber Housing," ASME 96-GT-300.
- [11] Marshall, B. W. and Tiederman, W. G., 1972, "A Capacitance Depth Gauge for Thin Liquid Films," Rev. Sci. Instrum., **43**, pp. 544–547.
- [12] Chew, J. W., Hills, N. J., Khalatov, S., Scanlon, T. and Turner, A. B., 2003, "Measurements and Analysis of Flow in a Pre-Swirled Cooling Air Delivery System," ASME Paper GT2003-38084.
- [13] Yucel, U. and Kazakia, J. Y., 2001, "Analytical Prediction Techniques for Axisymmetric Flow in Gas Labyrinth Seals," J. Eng. Gas Turbines Power, **123**, pp. 255–257.
- [14] Glahn, J. A., 1995, "Zweiphasenströmungen in Triebwerkslagerkammern—Charakterisierung der Ölfilmströmung und des Wärmeübergangs," Dissertation, Universität Karlsruhe.
- [15] Glahn, A. and Wittig, S., 1999, "Two-Phase Air/Oil Flow in Aero-Engine Bearing Chambers—Assessment of an Analytical Prediction Method for the Internal Wall Heat Transfer," Int. J. Rotating Mach., **5**(3), pp. 155–165.
- [16] Deissler, R., 1954, "Heat Transfer and Fluid Friction for Fully Developed Turbulent Flow of Air and Supercritical Water With Variable Fluid Properties," Trans. ASME, **76**, pp. 73–85.

A Numerical Model for Oil Film Flow in an Aeroengine Bearing Chamber and Comparison to Experimental Data

Mark Farrall

Kathy Simmons

Stephen Hibberd

University Technology Centre for Gas Turbine
Transmission Systems,
University of Nottingham,
University Park,
Nottingham, NG7 2RD, UK

Philippe Gorse

Institut für Thermische Strömungsmaschinen,
University of Karlsruhe,
76128 Karlsruhe, Germany

The work presented forms part of an ongoing investigation, focusing on modeling the motion of a wall oil film present in a bearing chamber and comparison to existing experimental data. The film is generated through the impingement of oil droplets shed from a roller bearing. Momentum resulting from the impact of oil droplets, interfacial shear from the airflow, and gravity cause the film to migrate around the chamber. Oil and air exit the chamber at scavenge and vent ports. A previously reported numerical approach to the simulation of steady-state two-phase flow in a bearing chamber, which includes in-house submodels for droplet-film interaction and oil film motion, has been extended. This paper includes the addition of boundary conditions for the vent and scavenge together with a comparison to experimental results obtained from ITS, University of Karlsruhe. The solution is found to be sensitive to the choice of boundary conditions applied to the vent and scavenge. [DOI: 10.1115/1.1924719]

Introduction

An understanding and optimization of three-dimensional oil flow and airflow in aeroengine transmission systems forms an integral part of future designs for aeroengines. This especially applies to bearing chambers, which contain a complex two-phase flow formed by the interaction of sealing airflow and lubrication oil. A model to compute the air and/or oil motion is presented and used to simulate the three-dimensional two-phase flow in an experimental bearing chamber. The intent of this study is to assess the validity of the approach for the modeling of oil films on bearing chamber housings.

The bearing chamber studied is formed by a combination of high-speed rotating components, a typical speed being 10,000 rpm, and stationary walls, inducing a strong azimuthal component of flow. This flow is modified by the presence of flow inlets, through an axisymmetric bearing and seal, and flow outlets, through vent and scavenge ports. Oil is supplied to the roller bearing for lubrication, and as a result discrete oil droplets are ejected into the rotating airflow. Because angular momentum is transferred to the droplets from the bearing and associated bearing cage, the droplets ultimately impinge on the outer chamber housing. The impingement may result in immediate deposition, in which case a wall film is formed that migrates around the chamber. Alternatively, droplets may break up on impact with smaller droplets being ejected back into the airflow, and further impingement may occur. Figure 1 shows a cross section through a chamber schematically indicating the various physical phenomena involved.

The two-phase flow in a bearing-chamber test facility has been studied extensively, with experimental and theoretical work focusing on the oil film motion [1–5] and heat transfer [1–3,6,7]. The variation in the oil film thickness with angular location and the velocity profile in the film have been measured experimentally by Wittig et al. [1] and Glahn and Wittig [2], respectively. Moreover,

a two-dimensional analytic model for the film flow derived by balancing the forces on the fluid and assuming a form for the shear stress within the film showed good agreement when compared to the experimental data for the velocity profile [2] for a prescribed film thickness.

In order to calculate film thickness distributions, an approach is to adopt an integral method. Chew [3] used this approach to investigate the effect of mass and momentum transfer to an oil film from impinging droplets but used simple axisymmetric source terms and neglected axial variations. Although yielding information about the dynamics of the oil film, this model is limited for most engineering applications, as knowledge of the flow is assumed in the calculations. To eliminate these limitations, Farrall et al. [4] and Farrall [8] developed a global modeling methodology for film flow, incorporating a calculation using the commercial computational fluid dynamics (CFD) code CFX4.3 to provide information regarding the distribution of the interfacial shear, mass, and momentum to the film. In this paper inclusion of vent and scavenge boundary conditions further extends the model and allows direct comparison to experimental data.

The interaction of oil droplets with any film present on the chamber housing is an important consideration when modeling the two-phase flow in bearing chambers. Little direct experimental data exist for bearing chambers at present, but analogous cases are the characterization of secondary droplets in direct injection (DI) diesel engines [9–13] and in prefilm atomizers [14–16]. Information from these studies was used by Farrall [8] and Farrall et al. [17] to develop a model for the interaction of oil droplets with an oil film for a simplified bearing chamber.

Experimental Setup

The model described in the following sections will be used to compute the two-phase airflow and oil flow in the high-speed bearing chamber test rig at the Institut für Thermische Strömungsmaschinen, University of Karlsruhe. A centerline section through the test rig is shown in Fig. 2. The rig was used first by Wittig et al. [1], who provided a detailed description of the test facility.

The rotor, capable of speeds up to 20,000 rpm, is supported by two bearings. The ball bearing is used to prevent axial and radial displacements of the rotor. Only a small amount of oil was supplied to this bearing, for lubrication. The second bearing is a

Contributed by the International Gas Turbine Institute (IGTI) of ASME for publication in the JOURNAL OF ENGINEERING FOR GAS TURBINES AND POWER. Manuscript received October 1, 2003; final manuscript received March 1, 2004. IGTI Review Chair: A. J. Strazisar. Paper presented at the International Gas Turbine and Aeroengine Congress and Exhibition, Vienna, Austria, June 13–17, 2004, Paper No. GT2004-53698.

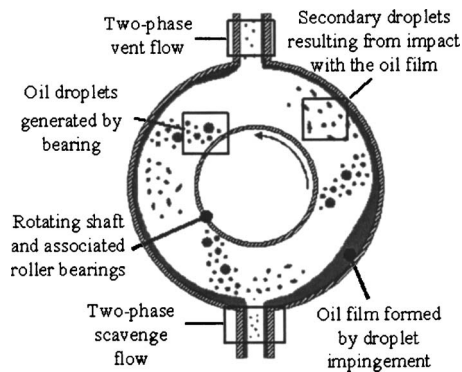


Fig. 1 Schematic of physical phenomena in chamber

squeeze film damped roller bearing. Oil is supplied by an under race lubrication system and can be adjusted to a maximum volume flow rate of 400 l/h at a temperature of 423 K. The roller bearing separates two bearing chambers, into which the oil is ejected after cooling and lubricating the bearing. Both chambers are sealed by air pressurized labyrinths. The sealing air was provided by an in-house compressor with a maximum mass flow rate of 0.5 kg s^{-1} at a pressure ratio of 10 and a temperature of 623 K. The two-phase airflow and oil flow formed in the chambers is discharged at the top and bottom of each through the vent and scavenge systems (not shown), respectively. The oil is then separated from the air and returned into the tank.

The present study is concerned with the flow in Chamber 2, having a height and width of 10 and 15 mm, respectively. The vent and scavenge ports are located diametrically opposite each other and have a diameter of 10 mm.

Computational Model

Methodology. The methodology for simulation of the two-phase flow in a bearing chamber involves implementation of successive stages. First, the airflow in the chamber is calculated using the commercial CFD package CFX-4.3. Oil droplets are then tracked through the chamber, employing the droplet-film interaction model where necessary. It is assumed in this calculation that the film thickness is negligible compared to the size of the chamber, so that the surface of the film is taken as corresponding to the chamber wall. Based on the results of Gorse et al. [5], the ratio of film thicknesses to chamber height is of the order of 0.01 and thus imposing this condition will only result in a small error in the impingement location. Finally, droplet data are gathered for the

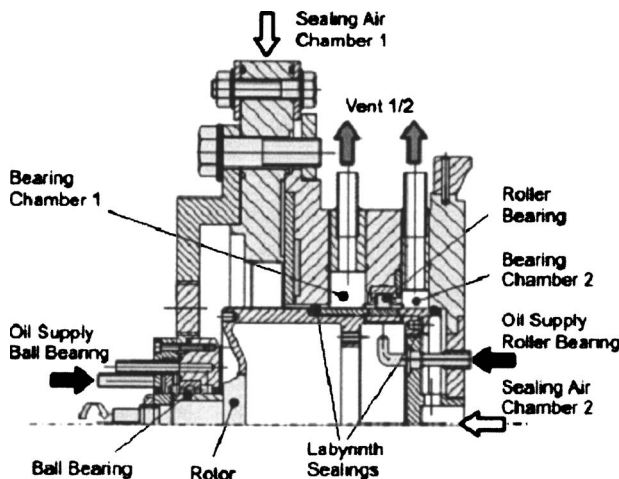


Fig. 2 High-speed bearing-chamber test rig

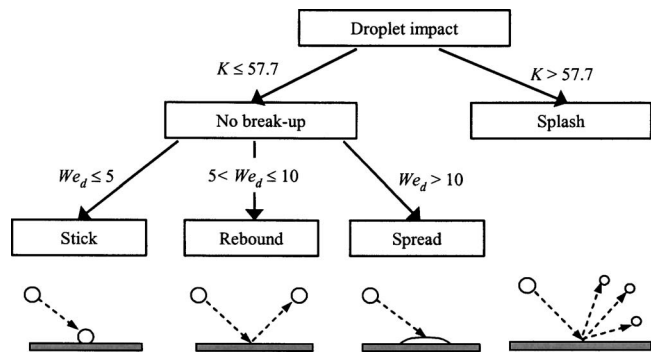


Fig. 3 Schematic showing the structure of droplet-film interaction model and the transition criteria for the various outcomes

input of mass and momentum to the oil film. These data are used together with a distribution of surface shear, obtained from the CFD solution, to provide required boundary information to the oil film model.

In the CFD calculation of the core airflow and oil droplet trajectories it is assumed that airflow through the scavenge port has negligible effect on the film flow and thus modeling of this geometric feature is omitted. The oil is released from the bearing cage as droplets and their motion numerically solved using the Lagrangian particle tracking model in CFX-4.3. At this stage in the study the droplets are modeled as rigid spheres with a low droplet loading in the chamber. Collisions between droplets and the modification of the airflow by the oil droplets' momentum are therefore omitted. In addition to this, the effect of turbulent dispersion on the droplets' motion has not been included. The focus here is on the oil film distribution and thus, while turbulent dispersion may influence the trajectories of small droplets with a low momentum, knowledge of the precise droplet trajectory and impingement location is not considered essential.

Submodels to describe the motion of the oil film present on the outer wall of the chamber and the interaction of the oil droplets with the oil film have been developed and incorporated into the overall bearing chamber model. Details of these are presented below.

Airflow in the Chamber. A three-dimensional calculation of the single-phase airflow in the chamber is performed on a body-fitted structured grid comprising 503,960 cells. The velocity field is solved in a Cartesian coordinate system using the standard $k-\epsilon$ turbulence model to calculate the turbulence quantities. The near-wall turbulence is modeled using standard log-law wall functions. The film's presence is accounted for by modifying the wall function using an equivalent sandgrain roughness [18]. The equations have been discretized using the higher-upwind differencing scheme, which extrapolates the face value using the two upstream points, and solved using the SIMPLE pressure-correction algorithm of Patankar and Spalding [19] as incorporated in CFX-4.3.

Oil Droplet Motion. The confined nature of aeroengine bearing chambers and the high-speed core airflow mean that oil droplet-film interactions are an important phenomenon and affect the size distribution of the droplets within the airflow as well as the heat transfer within the chamber. These interactions are accounted for using an in-house submodel based on experimental data and correlations obtained for DI diesel engines. The model, developed by Farrall [8] for the flow in a simplified bearing chamber, classifies each impact with the oil film primarily on whether the droplet breaks up. This is achieved through the evaluation of the splashing parameter $K(=We_d^{0.5}Re_d^{0.25})$. If the droplet does not splash the impact is further classified into the regimes of *stick*, *rebound*, and *spread*, shown schematically in Fig. 3 together with the associated

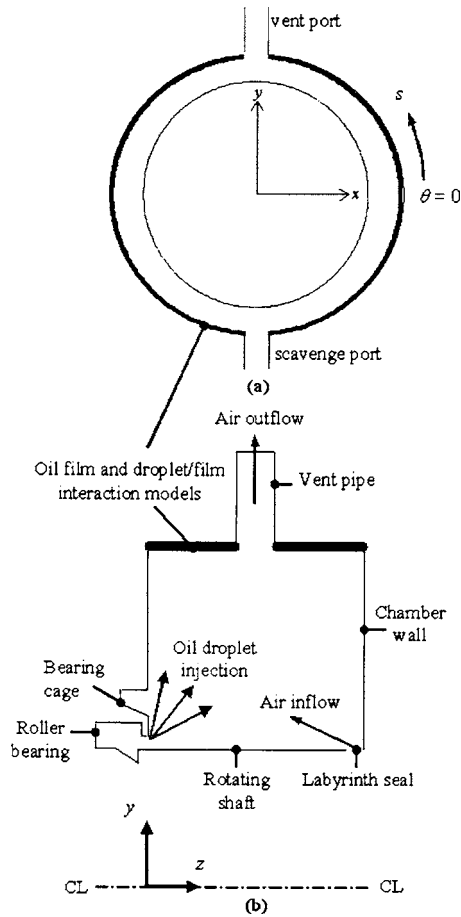


Fig. 4 Schematic diagram of chamber cross section through (a) an axial plane and (b) an angular plane through the vent port, indicating the model boundary conditions

parameter values. For specific details of the postimpingement characteristics, the reader is referred to Farrall [8]. To enable three-dimensional droplet impacts to be simulated, the in-plane turning angle ψ for droplets that are ejected back into the core flow must be calculated. The angle ψ is defined as the angle through which a droplet may turn on the film surface with respect to the tangential velocity vector of the impinging droplet. In the present work this angle is determined using the model suggested by Naber and Reitz [9].

The model provides a boundary condition for the Lagrangian particle-tracking routine in CFX-4.3, taking information regarding the droplet impingement and determining the outcome of the impact. Appropriate postimpingement characteristics are then calculated and new droplets sourced if required. In the present analysis the droplet-film interaction model has only been applied to the outer chamber housing where the motion of the film is to be calculated (see Fig. 4). Impacts with the side walls of the chamber are assumed to result in rebound of the droplets.

Oil Film Motion. Oil is deposited on the chamber housing as a result of oil droplet impacts and forms a wall film that migrates around the chamber. The two-dimensional (2D) integral model developed by Farrall et al. [4,17] has been employed to account for the dynamics of this wall film. The model assumes an incompressible, isothermal flow and accounts for the effects of gravity, shear forces on both the wall and the film's surface, and the addition of mass and momentum to the film from impinging oil droplets. The equations relating the film thickness, azimuthal volume flux, and axial volume flux are given by

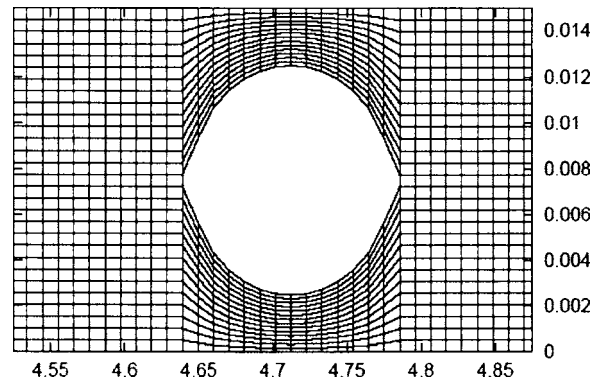


Fig. 5 Computational domain indicating the mesh density in the vicinity of the vent and scavenge ports

$$\frac{dh}{dt} + \frac{\partial q}{\partial s} + \frac{\partial Q}{\partial z} = \dot{V} \quad (1)$$

$$\frac{dq}{dt} + \frac{\partial}{\partial s} \left[\frac{q^2}{h} - \frac{1}{2}gh^2 \sin \theta \right] + \frac{\partial}{\partial z} \left[\frac{qQ}{h} \right] = \frac{1}{\rho} [\tau_s - \tau_{w,s}] - g \cos \theta + \dot{G} \quad (2)$$

$$\frac{dQ}{dt} + \frac{\partial}{\partial s} \left[\frac{qQ}{h} \right] + \frac{\partial}{\partial z} \left[\frac{Q^2}{h} - \frac{1}{2}gh^2 \sin \theta \right] = \frac{1}{\rho} [\tau_z - \tau_{w,z}] + \dot{H} \quad (3)$$

The derivation the above system of equations assumes:

- that the oil film is thin in comparison to the height of the chamber, i.e., $h/r \ll 1$
- hydrostatic pressure through the film thickness
- the horizontal velocity components have a uniform profile through the depth of the film

The model is based on a local coordinate system that is normal and tangential (z, s) to the wall, defined according to Fig. 4. Based on experimental film thickness and velocity measurements [2], the film has a Reynolds number of the order of 100. The wall shear τ_w in Eqs. (2) and (3) is thus calculated assuming a laminar quadratic profile for the tangential velocities across the film thickness. The distribution of mass and momentum added to the film as a result of droplet impingement is calculated using data regarding the loss of mass and momentum during the impact, obtained from the droplet-film interaction model.

For numerical calculations, Eqs. (1) and (3) are discretised on a trapezoidal computational domain according to the scheme of Liska and Wendroff [20], allowing for accurate representation of the circular boundaries corresponding to the vent and scavenge ports. This is illustrated in Fig. 5, which shows the computational grid in the vicinity of the scavenge port.

Conditions applied on the end walls of the chamber are given by

$$Q = \frac{\partial q}{\partial n} = \frac{\partial^2 h}{\partial n^2} = 0 \quad (4)$$

and correspond to zero flux out of the wall and a zero normal gradient in the flux parallel to the wall. The film thickness at the wall is obtained by a linear interpolation from the interior points.

Oil exiting the chamber at the vent port is given by a local analysis, where the tangential and normal components of the volume flux at the vent port boundary are taken as proportional to the respective normal gradient at the boundary, i.e.,

$$\frac{\partial^2 h}{\partial n^2} = 0, \quad \mathbf{F} = -\lambda \frac{\partial \mathbf{F}}{\partial n}, \quad \mathbf{F} = [f_r, f_n] \quad (5)$$

The vent parameter λ represents the local flow conditions in the vicinity of the vent port. The effect of this parameter on the solution is considered for the two extreme cases, $\lambda=0$ and $\lambda \rightarrow \infty$. The dynamics of the oil exiting the chamber through the scavenge port is extremely complex, and a number of possible flow patterns may exist [21]. Application of the results in [21,22] to the case of a bearing chamber suggest that, based on the radius of the scavenge port and the Froude number Fr of the incoming flow, the oil will tend to form a film on the scavenge port wall. For this reason the scavenge cannot be modeled using a simple mass sink in the continuity equation. To evaluate the effect the imposed boundary condition has on the resulting distribution of film thickness, two cases are considered: (a) a uniformly distributed exit flux condition where the mass out of the film is directly balanced to the droplet mass influx and (b) an unrestricted exit modeled by taking

$$\frac{\partial^2 h}{\partial n^2} = 0, \quad \frac{\partial f_s}{\partial n} = \frac{\partial f_z}{\partial n} = 0 \quad (6)$$

It is noted here that when a constant volume flux is prescribed (uniform exit condition) there is in general, no unique solution. In the current problem, however, the velocity of the film away from the scavenge port, and thus the solution obtained from the simulation, is determined by the velocity of the impinging droplets.

Modeling of any films on the side walls of the chamber has been omitted in the present study. Oil deposited on these walls will tend to be driven to the outer chamber wall providing sources of mass and momentum to the film currently being investigated. Inclusion of these films will be addressed at a future date.

Initial Data and Boundary Conditions

Incompressible, isothermal calculations of the two-phase airflow and oil flow were carried out to understand the steady-state dynamics of the oil film on the outer chamber housing of the bearing chamber. Initially the vent parameter λ was set to zero, corresponding physically to no flow exiting via the vent. To assess the sensitivity of the solution to the boundary condition imposed at the scavenge port, the value of λ was subsequently increased so that the restriction on the flow at the vent port was progressively removed. Data from the model is compared to experimental data for the film thickness to enable a conclusion to be drawn regarding the most appropriate boundary condition for the scavenge.

The physical dimensions of the model are chosen to match the experimental test facility. Figure 4 shows a schematic diagram of the chamber cross section indicating the model boundary conditions. Air, having a density of 2.92 kg m^{-3} and a dynamic viscosity of $1.84 \times 10^{-5} \text{ kg m}^{-1} \text{ s}^{-1}$, enters the chamber through the seal. The airflow rate was kept constant at 0.01 kg s^{-1} . The boundary condition applied at the seal is that the air enters the chamber at an angle of 15 deg to the rotating shaft with a tangential component of velocity equal to 25% that of the rotating shaft speed. The roller bearing and associated cage are taken to rotate at half the angular speed of the shaft with no leakage of air through the bearing. Oil, having a density of 954 kg m^{-3} and a dynamic viscosity of $9.5 \times 10^{-3} \text{ kg m}^{-1} \text{ s}^{-1}$, is released in the form of droplets from 10 angular locations, equally spaced around the bearing cage, with a total mass flow rate of oil of $2.65 \times 10^{-2} \text{ kg s}^{-1}$ being ejected into the chamber. Preliminary analysis suggests that this number of droplet-release locations is sufficient to distribute the oil droplet momentum around the chamber, although the influence of this number on the results will be addressed in greater depth at a later date. Using previous experimental results [23] the diameters are taken to satisfy a Rosin-Rammler distribution with a mean diameter of $480 \mu\text{m}$ and spread parameter of 3. The droplets are ejected with an initial azimuthal component of velocity equal to that of the bearing cage and an axial component of velocity equal to 2 ms^{-1} . In the simulation of the oil film on the chamber housing, as an initial condition, an initial volume flow rate per unit width is set prior to any droplet impact. Taking an average value

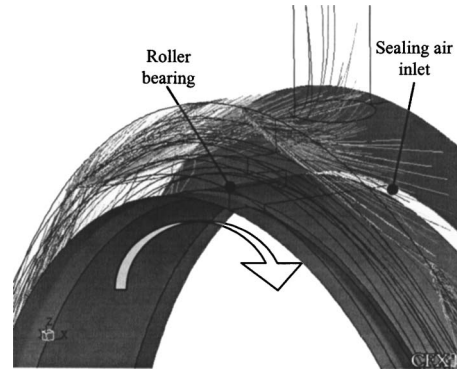


Fig. 6 Oil droplet tracks in the vicinity of the vent port. Indicated on the plot is the roller bearing and the inlet for the sealing airflow.

for the film thickness of $6.0 \times 10^{-4} \text{ m}$, as suggested by the experimental data shown in Fig. 8, traveling with a bulk velocity of 0.1 ms^{-1} , an initial volume flow rate per unit width of $6.0 \times 10^{-5} \text{ m}^2 \text{ s}^{-1}$ in the azimuthal direction is prescribed. In addition, it is assumed that initially there is no axial motion in the film.

Results and Discussion

Figure 6 shows typical computed particle tracks for the released oil droplets. On release the oil droplets travel largely unaffected by the airflow and impact on the chamber housing. The initial momentum of the droplets is great enough to promote splashing on primary impact, resulting in several smaller droplets being ejected back into the core flow as shown. This secondary splashing has the effect of distributing the input of momentum to the film over a wider area than the initial impact location.

The secondary airflow in the chamber consists of a single recirculation zone [17], producing an interfacial shear that drives the oil film axially away from the roller bearing. This, combined with the axial momentum supplied to the film by the impinging droplets, means there is a general increase in the film thickness across the width of the chamber. Figure 7 shows the variation in film thickness around the chamber wall for a shaft speed of 8000 rpm. The simulation was performed assuming zero flow exiting the chamber at the vent port.

The increase in film height with increasing distance from the bearing can be clearly identified. The vent boundary condition applied is equivalent to a cylindrical blockage in the film at that location. This leads to a buildup of oil around the vent location as

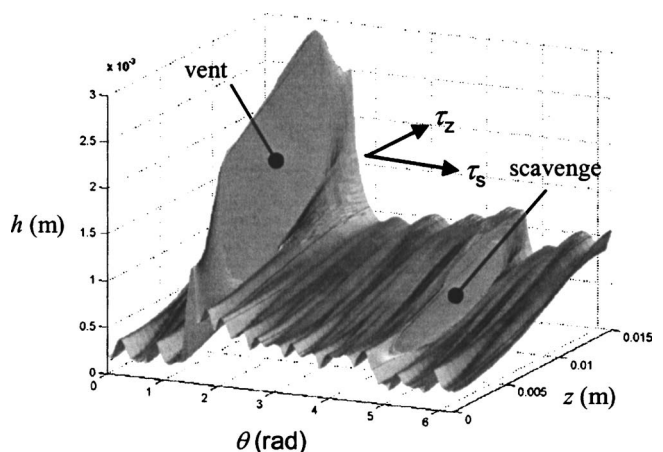


Fig. 7 Film thickness distribution on chamber housing. Arrows represent the principle directions for the interfacial shear.

shown in Fig. 7. The unrestricted scavenge condition leads to a local decrease in film height across the scavenge as expected. The surface of the film is visibly rippled, and this is a consequence of discrete droplet impact locations caused by the 10 discrete release locations applied in the model.

Effect of Scavenge Boundary Condition. Two scavenge boundary conditions have been applied and the resulting film thickness at the axial location $z=7.5$ mm are compared in Fig. 8(a). The associated average film velocity for each case is shown in Fig. 8(b). It is observed that when the scavenge port is modeled as a uniformly distributed exit flux (solid line), the film thickness increases on the rising side of the chamber ($4.76 < \theta < 2\pi$ and $0 < \theta < 1.5$), reaching a maximum at the top of the chamber, and then decreases on the downside reaching a minimum at the scavenge. In contrast, when a boundary condition corresponding to an unrestricted exit flow (dashed line) is imposed, the film thickness around the chamber housing shows a general increase starting from the scavenge in the direction of film motion. There is a step change across the scavenge port and local variations because of the influence of the vent port.

The assumption of a uniformly distributed exit flux means that the oil immediately after the scavenge port is drawn back toward the scavenge, shown in Fig. 8(b) by the negative velocity around $\theta=4.75$. This significantly retards the flow of the film, and, as a result, it is observed that the average velocity around the chamber is around 0.25 ms^{-1} , even with the additional momentum supplied to the film by the impinging droplets. In the case when the scavenge port is treated as an unrestricted exit, it is observed that the average velocity in the film is generally higher.

Correspondingly, the film thickness for the uniformly distributed exit flux is significantly greater than for the unrestricted exit. It is also observed that there is a slight increase in the film velocity as it travels between the scavenge and vent ports, on top of which small peaks occur because of the input of momentum from the droplets. At the vent, the velocity drops to zero as a result of the imposed no slip condition, resulting in a steep gradient in the velocity profile. This again explains the steeper gradient observed in the film thickness profile predicted when the scavenge is treated as an unrestricted exit.

Also shown on Fig. 8(a) are the experimental data of Gorse et al. [5], suggesting that the film thickness is relatively constant around the housing with a local build up prior to the vent port. This is more consistent with the numerical results obtained when the scavenge port is modeled using the unrestricted exit condition. However, it is observed that the extent of the buildup in the oil film thickness immediately upstream of the vent port is underpredicted in this case. A comparison of the experimental data and numerical results yields a maximum difference of 39% for the data point just prior to the vent port. For other points the maximum difference between experimental and computational data does not exceed 17%.

Some difference between the results is expected as within an integral model, variations in the radial direction are neglected and thus the model is not valid in the immediate vicinity of the side-walls or geometrical features, such as the vent and scavenge ports. In addition, the chamber studied includes a vent and scavenge whose diameter is two-thirds the width of the chamber. Ideally, experimental measurements for film thickness would be obtained in a wider chamber so that the effect of the vent and scavenge ports could be isolated. Furthermore, the shear stress at the wall is currently modeled assuming a quadratic velocity profile, whereas a flatter (turbulent) profile might be more representative. Using a turbulent profile would result in a lower wall friction, thus increasing the average velocity of the film, resulting in a decrease in the predicted film thickness.

Analysis of the numerical results for the two boundary conditions imposed at the scavenge suggests that the predictions could be brought more in line with the experimental data in the vicinity of the vent port by changing the boundary condition on the scav-

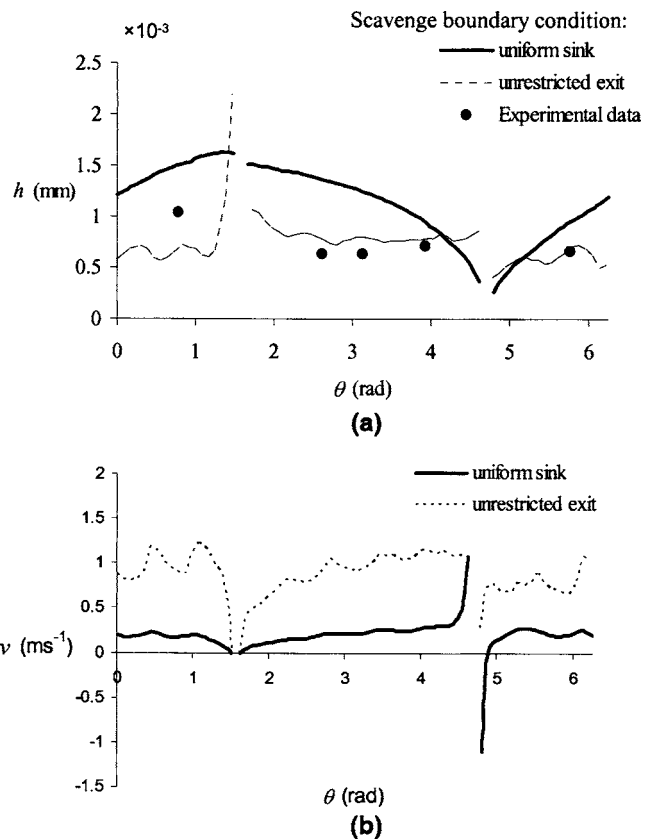


Fig. 8 Profiles showing the variation around the chamber housing of (a) the film thickness and (b) the average film velocity, at an axial location of 7.5 mm

enge. Adopting a condition similar to the vent and allowing the exit parameter to vary around the boundary would enable an unrestricted exit flow on the upstream side of the scavenge, while on the downstream side incorporating the effect of the force drawing the oil toward the drain.

Effect of Vent Boundary Condition. With the boundary condition at the scavenge port modeled as an unrestricted exit, the effect of the parameter λ on the vent port boundary condition is investigated. Figure 9 shows predicted variations in the film thickness and associated average film velocity with angular location, taken at an axial location corresponding to $z=7.5$ mm, for the extreme cases of zero flow out of the vent ($\lambda=0$), and an unrestricted exit flow ($\lambda \rightarrow \infty$). In terms of the film thickness, a small decrease is observed when the oil is no longer prevented from exiting the film via the vent port. The maximum difference between the two predictions occurs on the downside between the vent and scavenge ports. In the case when there is zero flow out of the vent port, the oil is forced between the boundary of the vent and the wall. After the vent port there is, thus, a region of low velocity corresponding to the wake, followed by a rapid increase in the velocity as the oil recovers and works its way to the center of the chamber once more. When the oil is allowed to exit via the vent port, the velocity of the oil flowing around the vent is maintained and thus when it flows back into the center of the chamber the resulting velocity is lower. The effect of varying the exit flow condition is thus to shift the general profile with local changes in the vicinity of the vent port.

Conclusions

Steady-state, three-dimensional, isothermal calculations have been performed using an integral model to describe the motion of

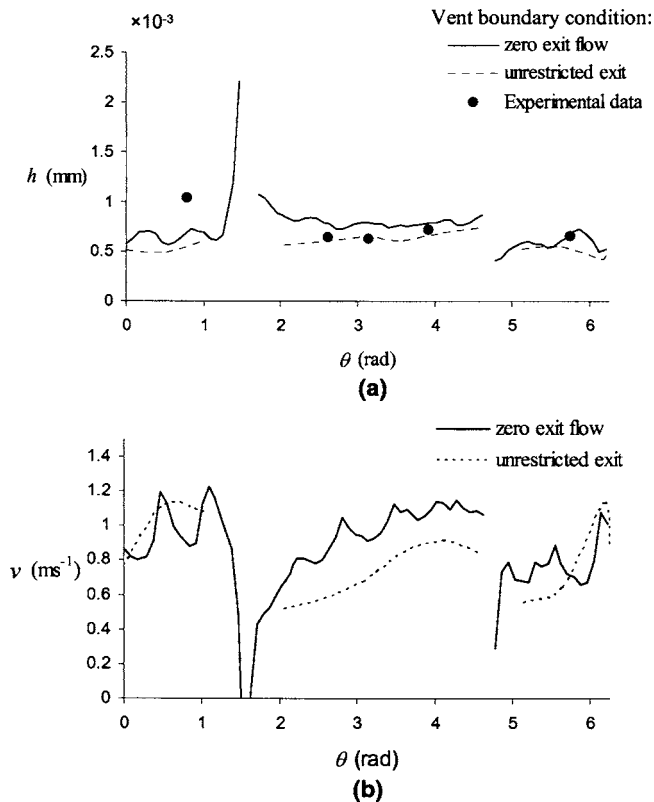


Fig. 9 Profiles showing the variation around the chamber housing of (a) the film thickness and (b) the average film velocity, at an axial location of 7.5 mm

an oil film on a bearing chamber housing. The exit of the oil at the scavenge port has been numerically calculated using two limiting forms of boundary condition and the results compared to available experimental data for the film thickness. Modeling the exit flow at the scavenge using a uniform exit flux results in an overprediction of the film thickness around the chamber housing. This is attributed to the large negative flow induced by the boundary condition downstream of the scavenge port, retarding the flow as the film travels up the rising side of the chamber. This retarding of the oil results in thickening of the film. When the scavenge is modeled as an unrestricted exit it is observed that because of the large unidirectional motion of the film there is a bias in the exit flow around the scavenge toward the upstream side. In this instance oil that flows past the scavenge is allowed to continue up the rising side of the chamber relatively unhindered. This results in the film having a higher average velocity and thus a thinner film thickness is predicted.

From these simulations it is observed that the distribution of film thickness around the chamber housing is sensitive to the boundary condition imposed at the scavenge port. Comparison of the predicted results to available experimental data suggests that imposing an unrestricted exit is the more physical boundary condition to adopt. Further development of the boundary condition is required in order to bring the numerical results more in line with the experimental data. It is proposed to combine the dynamics of the two cases so that an unrestricted exit is imposed on the upstream side of the scavenge while on the downstream side oil film is influenced by the scavenge and is drawn toward it.

The effect of the exit condition applied at the boundary of the vent port on the resulting distribution of film thickness has also been studied. It is found that changing the exit condition from a case of zero flow out of the vent to an unrestricted exit flow shifts the profile of the film thickness upwards (increased film height at

all locations) and increases the average film velocity. The general features in film height and velocity profiles are retained.

Acknowledgment

The work has been supported by the European Commission within the research project ATOS (Advanced Transmission and Oil System concepts), Contract No. G4RD-CT-2000-00391. This financial support is gratefully acknowledged.

Nomenclature

- d = diameter, m
- f = volume flux per unit length, $\text{m}^2 \text{s}^{-1}$
- F = volume flux per unit length vector
- Fr = Froude number $[=v/(gh)^{1/2}]$
- g = gravity, ms^{-2}
- \dot{G} = circumferential momentum flow rate per unit area, $\text{m}^2 \text{s}^{-2}$
- h = film thickness, m
- \dot{H} = axial momentum flow rate per unit area, $\text{m}^2 \text{s}^{-2}$
- k = turbulent kinetic energy, $\text{m}^2 \text{s}^{-2}$
- K = splashing parameter $(=We_d^{0.5} Re_d^{0.25})$
- n = normal coordinate
- q = azimuthal volume flow rate per unit length, $\text{m}^2 \text{s}^{-1}$
- Q = axial volume flow rate per unit length, $\text{m}^2 \text{s}^{-1}$
- r = radius, m
- Re = Reynolds number $[=q/v]$
- s = circumferential coordinate, m
- t = time, s
- v = velocity, ms^{-1}
- \dot{V} = volume flow rate per unit area, ms^{-1}
- We = Weber number $[=\rho d v_n^2 / \sigma]$
- z = axial coordinate, m

Greek Symbols

- ϵ = viscous dissipation rate, $\text{m}^2 \text{s}^{-3}$
- λ = vent exit flow parameter
- θ = angle, rad
- ρ = density, kg m^{-3}
- σ = surface tension, Nm^{-1}
- τ = shear stress, kg m^{-2}
- ν = kinematic viscosity, $\text{m}^2 \text{s}^{-1}$
- ψ = in-plane turning angle, rad

Subscripts

- n = normal component
- s = local tangential component
- t = tangential
- w = wall
- z = axial component

References

- [1] Wittig, S., Glahn, A., and Himmelsbach, J., 1994, "Influence of High Rotational Speeds on Heat Transfer and Oil Film Thickness in Aero Engine Bearing Chambers," *ASME J. Eng. Gas Turbines Power*, **116**, pp. 395–401.
- [2] Glahn, A., and Wittig, S., 1996, "Two-Phase Air/Oil Flow in Aero Engine Bearing Chambers: Characterisation of Oil Film Flows," *ASME J. Eng. Gas Turbines Power*, **118**(3), pp. 578–583.
- [3] Chew, J. W., 1996, "Analysis of the Oil Film on the Inside Surface of an Aero Engine Bearing Chamber Housing," ASME Paper No. 96-GT-300.
- [4] Farrall, M., Hibberd, S., and Simmons, K., 2000, "Computational Modelling of Two-Phase Air/Oil Flow Within an Aero-Engine Bearing Chamber," *Proc. of ASME FEDSM 2000*, Boston, June 11–15, ASME, New York.
- [5] Gorse, P., Busam, S., and Dullenkopf, K., 2004, "Influence of Operating Condition and Geometry on the Oil Film Thickness in Aero-Engine Bearing Chambers," *Proc. of ASME Turbo Expo 2004*, Vienna, Austria, June 14–17, ASME, New York.
- [6] Glahn, A., Busam, S., and Wittig, S., 1997, "Local and Mean Heat Transfer Coefficients Along the Internal Housing Walls of Aero Engine Bearing Chambers," ASME Paper No. 97-GT-261.

- [7] Busam, S., Glahn, A., and Wittig, S., 2000, "Internal Bearing Chamber Wall Heat Transfer as a Function of Operating Conditions and Chamber Geometry," *ASME J. Eng. Gas Turbines Power*, **122**, pp. 314–320.
- [8] Farrall, M., 2000, "Numerical Modelling of Two-Phase Flow in a Simplified Bearing Chamber," Ph.D. thesis, University of Nottingham, UK.
- [9] Naber, J. D., and Reitz, R. D., 1988, "Modelling Engine Spray/Wall Impingement," SAE Paper No. 880107.
- [10] Wang, D. M., and Watkins, A. P., 1993, "Numerical Modelling of Diesel Spray Wall Impaction Phenomena," *Int. J. Heat Mass Transfer*, **14**(3), pp. 301–312.
- [11] Senda, J., Kobayashi, M., and Fukimoto, H., 1994, "Modelling of Diesel Spray Impingement on a Flat Wall," SAE Paper No. 941894.
- [12] Bai, C., and Gosman, A. D., 1995, "Development of Methodology for Spray Impingement Simulation," SAE Paper 950283.
- [13] Stanton, D. W., and Rutland, R. J., 1996, "Modelling Fuel Film Formation and Wall Interaction in Diesel Engines," SAE Paper No. 960628.
- [14] Samenfink, W., Hallmann, M., Elsäßer, A., and Wittig, S., 1994, "Secondary Break-Up of Liquid Droplets: Experimental Investigation for a Numerical Description," *ICLASS-94*, July, Rouen, France.
- [15] Samenfink, W., Elsäßer, A., Dullenkopf, K., and Wittig, S., 1999, "Droplet Interaction With Shear-Driven Liquid Films: Analysis of Deposition and Secondary Droplet Characteristics," *Int. J. Heat Fluid Flow*, **20**, pp. 462–469.
- [16] Schmehl, R., Roskamp, H., Willmann, M., and Wittig, S., 1999, "CFD Analysis of Spray Propagation and Evaporation Including Wall Film Formation and Spray/Wall Interactions," *Int. J. Heat Fluid Flow*, **20**, pp. 520–529.
- [17] Farrall, M., Hibberd, S., and Simmons, K., 2003, "Modelling Oil Droplet/Film Interaction in an Aero-Engine Bearing Chamber," *ICLASS-2003*, Sorrento, Italy.
- [18] Wittig, S., Himmelsbach, J., Noll, B., Feld, H. J., and Samenfink, W., 1992, "Motion and Evaporation of Shear-Driven Liquid Films on Turbulent Gases," *ASME J. Eng. Gas Turbines Power*, **114**, pp. 395–400.
- [19] Patankar, S. V., and Spalding, D. B., 1972, "A Calculation Procedure for the Heat, Mass and Momentum Transfer in Three-Dimensional Parabolic Flows," *Int. J. Heat Mass Transfer*, **15**, pp. 1787–1806.
- [20] Liska, R., and Wendroff, B., 1999, "Two-Dimensional Shallow Water Equations by Composite Schemes," *Int. J. Numer. Methods Fluids*, **30**, pp. 461–479.
- [21] Hocking, G. C., and Vanden-Broeck, J. M., 1997, "Draining of a Fluid of Finite Depth Into a Vertical Slot," *Appl. Math. Model.*, **21**, pp. 643–649.
- [22] Merino, F., 1996, "Fluid Flow Through a Vertical Slot Under Gravity," *Appl. Math. Model.*, **20**, pp. 934–939.
- [23] Wittig, S., and Busam, S., 1997, "LUBSEAL Final Test Result Report," private communication.

Flow Characteristics and Stability Analysis of Variable-Density Rotating Flows in Compressor-Disk Cavities

Bruce V. Johnson
Heat Transfer Research Services,
Manchester, CT

J. D. Lin
University of Connecticut,
Storrs, CT

William A. Daniels

Roger Paolillo
Pratt & Whitney,
East Hartford, CT

Previous heat transfer experiments showed that significant differences in the flow and heat transfer characteristics can occur in models of aircraft gas-turbine, high-compressor drums. Experiments with heated disks and colder flow show large-scale instabilities that cause mixing between the cooling flow and the flow in the trapped cavities. The general result of this mixing is relatively high heat flux on the disks. Other heat transfer experiments, simulating the aircraft take-off condition with cold disks and hotter coolant, show decreased heat transfer due to the stabilizing effects of positive radial density gradients. A stability analysis for inviscid, variable-density flow was developed to quantify the effects of axial velocity, tangential velocity, and density profiles in the bore region of the disk cavities on the stabilizing or destabilizing characteristics of the flow. The criteria from the stability analysis were used to evaluate the axial velocity and density profile conditions required to stabilize three tangential-velocity profiles, obtained from previous experiments and analyses. The results from the parametric study showed that for Rossby numbers, the ratio of axial velocity to disk bore velocity, less than 0.1, the flow can be stabilized with ratios of cavity density to coolant density of less than 1.1. However, for Rossby numbers greater than 1, the flow in the bore region is unlikely to be stabilized with a positive radial density gradient. For Rossby numbers between 0.1 and 1.0, the flow stability is a more complex relationship between the velocity and density profiles. Results from the analysis can be used to guide the correlation of experimental heat transfer data for design systems. [DOI: 10.1115/1.1925648]

1 Introduction

The temperatures of the disks in high-pressure compressors of several aircraft gas turbines are thermally controlled by air from a compressor bleed location (Fig. 1). The cooling air passes by the bores of several disks between the inlet and exhaust locations. Each combination of disks and outer shroud form a rotating cavity with no net flow radially through the cavity. The thermal control of the disks is important to the gas turbine designer because the disk temperature has a strong influence on the compressor blade tip and the compressor hub radii. These locations and the outer case and vane radii determine the compressor blade and vane clearances. These blade tip clearances influence the compressor efficiency and compressor stall characteristics. A “zero” blade clearance or “rubbing” condition at one location in the flight cycle of idle, take-off, cruise, approach and the thermal history of the disks and outer case determines the clearances and performance at each point during this cycle. Hence, the control of the clearances through the thermal control of the disk temperature is critical to engine performance and life.

For aircraft engine startup and takeoff conditions, the compressor disks are cold and the cooling air along the bore of the disks is hot. Consequently the swirling flow tends to be stable and the core “cooling” air is not as likely to penetrate the trapped cavity region due to lack of flow instabilities. The result will be low heat transfer to the disks. For engine approach conditions, the disks are hot and the bore air temperature is decreased from cruise conditions.

Consequently, the swirling flow will be unstable and the heat transfer between the disks and compressor core air will be higher than for the stable condition. Previous flow visualization and heat transfer results will be shown to provide an understanding of the flow characteristics.

The axial velocities in the bore region are a function of the coolant flow rate and the distance between the center shaft and the disk bores and are characterized by a Rossby number; a ratio of axial velocity to the disk bore velocity. The tangential and axial flow Reynolds numbers for large engines are high enough that the viscous effects do not affect the stability characteristics. For engines, similar to that shown in Fig. 1, the Rossby numbers range from 0.05 to 0.5. For engines with disk bore diameters closer to the center shaft, the Rossby numbers can exceed 1.0.

Previous stability analyses have shown that the axial velocity, the tangential velocity, and the temperature/density/Mach number profiles influence the stability characteristics of swirling flow. These analyses are reviewed and an extension to a previous narrow-gap stability analysis is developed in the Appendix for variable-density and compressible flows. The stability criteria are applied locally in a parametric study with three tangential velocity profiles to obtain an understanding of the stability relationships resulting from the axial velocity, the tangential velocity, and the density profiles.

The principle objective of this study is to develop understanding about flow in compressor drum cavities that can be used to guide the correlation of experimental data for design systems and to provide criteria for changes in the heat transfer characteristics.

2 Background for Flow Characteristics

2.1 Previous Experiments. The flow and heat transfer characteristics of compressor disk cavities are discussed by Owen and Rogers [1]. Summaries of the compressor cavity flow and heat

Contributed by the International Gas Turbine Institute (IGTI) of ASME for publication in the JOURNAL OF ENGINEERING FOR GAS TURBINES AND POWER. Manuscript received by IGTI, October 1, 2003; final revision, March 1, 2004. IGTI Review Chair: A. J. Strazisar. Paper presented at the International Gas Turbine and Aeroengine Congress and Exhibition, Vienna, Austria, June 13–17, 2004, Paper No. 2004-GT-54279.

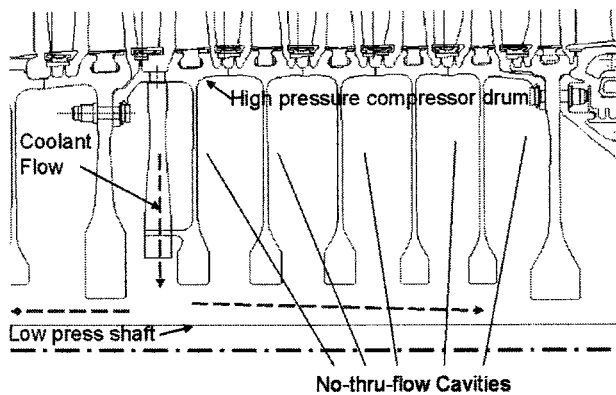


Fig. 1 Schematic of high-pressure compressor: drum and low-pressure shaft rotate at different RPM

transfer studies conducted at the University of Sussex prior to 1995 are included. This previous research included isothermal flow studies, heat transfer studies with heated disks and colder cooling flow and was conducted at lower Reynolds numbers than occur in large aircraft engines.

The following is a discussion of several additional experimental and numerical simulation studies of compressor drum heat transfer that are pertinent background for the present paper. In this paper, a cooling flow condition is defined as hot disks and cold coolant and occurs in the flight cycle during "approach." A heating flow condition is defined as cold disks and hot coolant and occurs during the flight cycle during "take-off." These operating conditions usually determine the minimum and maximum compressor blade clearances for aircraft engines.

Graber et al. [2] conducted isothermal flow studies in a five-cavity model at tangential Reynolds numbers of order 7×10^6 . These experiments were at Reynolds numbers, typical of aircraft gas turbine engines but at lower Mach numbers. The experiments were conducted with several injection locations typical of military and commercial aircraft engines. The flow injection location influenced the velocity distribution and hence the radial pressure variation in the cavities. The pressure difference between the bore and the outer shroud decreased with distance from the injection location. A limited number of transient heat transfer experiments were conducted for both heating and cooling flow conditions. The heat transfer coefficients at one location on the disk near the bore were approximately twice as great for the cooling condition as for the heating condition. The heat flux gauges also showed large temporal variations for cooling conditions and low temporal variations for heating conditions. Additional experiments were later conducted under Pratt & Whitney sponsorship and will be discussed in a following subsection.

Farthing et al. [3] conducted flow visualization experiments and showed the flow patterns in the rotating cavity are functions of Rossby number and the cavity geometry ratio. The experiments were conducted at Reynolds numbers to 3×10^5 .

Long [4] conducted isothermal flow experiments and cooling heat transfer experiments. The heat flux gauges showed the cyclic nature of the heat transfer for his cooling condition.

Kim et al. [5] conducted cooling heat transfer experiments in a single cavity with low inlet swirl, several thermal boundary conditions, and tangential Reynolds numbers to 5×10^5 . The results showed a complex relationship between axial Reynolds number, tangential Reynolds number, and the wall temperature distribution with Nusselt numbers varying by more than a factor of 10 for the same rotational Reynolds number.

Bohn et al. [6] conducted flow visualization experiments with tangential Reynolds numbers to 8×10^5 and for $0.27 < Ro < 0.97$. Their photographs showed strong secondary flows in the trapped cavities. The secondary flows were similar to Farthing et al. [3].

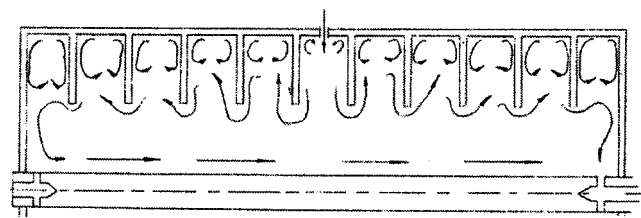


Fig. 2 Sketch of UTRC eleven-cavity compressor model: drum and shaft rotated at same RPM

The numerical simulation of Long et al. [7] for a turbulent flow in a cavity showed a wavy, periodic flow structure. The predicted heat transfer for the cavity with a central shaft differed in some regions from their experimental results.

The numerical prediction of Cao et al. [8] for flow between rotating and stationary disks showed a periodic structure moving at 90% of the disk speed. The secondary flow structure had four lobes, more than seen in the flow visualization of Long [4] or of Owen and Pincombe [9].

2.2 UTC Experiments. The preceding citations have shown that unsteady flow can occur in a rotating cavity. In a following section, data from previous United Technologies Research Center/Pratt & Whitney studies will be presented to show multi-lobed structures in a rotating cavity with a center shaft and unsteady heat transfer on disk walls. The experiments were conducted for a class of flows where the disk and the coolant tangential velocities were greater than the coolant axial velocities.

A number of aerodynamic and heat transfer experiments were conducted over an extended period to develop an understanding of the complex flow occurring within compressor drums. These experiments were conducted at tangential Reynolds numbers from 10^5 to 8×10^6 and with Rossby numbers that were less than 0.25. This flow range is significantly different from the Owen and Pincombe [9] experiments with $1 < Ro_b < 100$ and the Kim et al. [5] experiments with $0.8 < Ro_b < 25$. The heat transfer experiments were conducted at Reynolds numbers that are typical of large aircraft engines but at lower Mach numbers.

2.2.1 Flow Visualization Experiments. Experiments were conducted in the mid 1970s with an eleven-cavity compressor drum model (Fig. 2) using water as the working fluid and dye as a trace material. A sheet of light illuminates the dye forming the inner section of an unstable flow. For this model with $R_s/R_a=0.25$ and $R_b/R_a=0.5$, four to six lobes occurred. The number of lobes would vary during an experiment and with flow conditions (Fig. 3).

2.2.2 Heat Transfer Experiments. Heating and cooling heat transfer experiments were conducted with a five-cavity compressor model (Fig. 4). Reynolds numbers to 8×10^7 at 2000 rpm were obtained by operating the model in a ten-atmosphere chamber. Heat flux sensors with surface thermocouples were attached at several locations on both the upstream and downstream disks. The model was operated for several hours to obtain approximately constant temperatures on all the model surfaces. Transient heat transfer experiments were conducted with "step" changes in the coolant flow temperature. Because of the thermal mass of the components between the control valve and the coolant injection location, the "step" had a modest slope.

Results in Graber et al. [2] showed that the heat transfer coefficients for cooling conditions were greater than for heating conditions. For locations on the disk near the bore, the cooling coefficients were approximately twice those for heating. At locations further out on the disks, the ratio of cooling to heating coefficients varied by ten or more between heating and cooling flow conditions. The signal from the heat flux sensors at some locations varied considerably. The variations were much greater for cooling

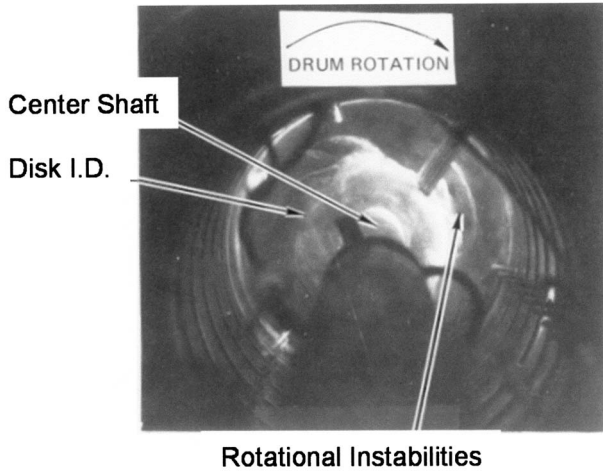


Fig. 3 Multi-lobed instability in cavity adjacent to bleed cavity

conditions than for heating conditions. Subsequent to Graber et al. [2], additional experiments were conducted to identify the cause of these variations. Monitoring one location with the data scanner showed that the variation was near periodic with approximately four cycles per drum revolution. This unsteady characteristic for the heat flux sensors was also described by Long [4].

Additional unpublished experiments were conducted to characterize the unsteadiness of the heat transfer process and the range of instantaneous heat transfer coefficients. The heat flux data (Fig. 5) were obtained with the "B" injection geometric, disk location near the bore and at the same dimensionless flow conditions for heating and cooling. Note that for heating, the data have a modest scatter, as expected for data systems with slip rings. For the cooling condition, the heat flux varies by as much as a factor of 10 and is greatest at the onset of the transient experiment when the temperature differences between the disks and the cooling air are the largest. Because of the thermal response of the heat flux gauges, the actual cooling variations will be somewhat larger.

The heat flux data (Fig. 5) were used to determine an "instantaneous" heat transfer coefficient Fig. 6. The results from both transient experiments are shown as a function of $\Delta T/T = (T_{\text{coolant}} - T_{\text{wall}})/T_{\text{wall}}$. Note that the range of instantaneous heat transfer coefficients decreases as $\Delta T/T$ increases from -0.08 to $+0.10$. From these data, it is not certain what value of $\Delta T/T$ is required to

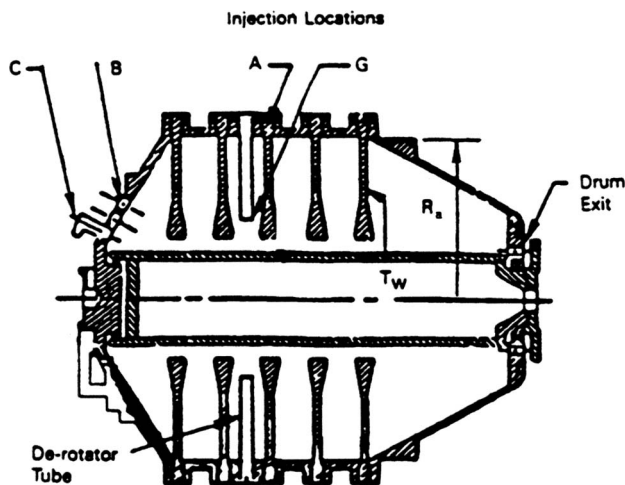


Fig. 4 Sketch of heat transfer model. Injection location "B" used for data and results in Figs. 5 and 6

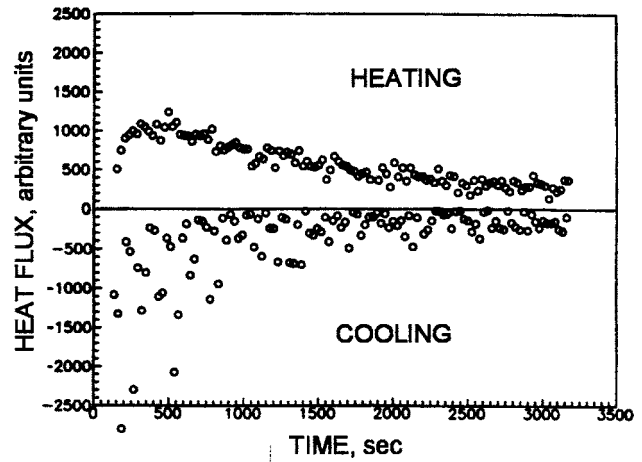


Fig. 5 Heat flux data from heating and cooling experiments at one disk location

cause the heat transfer coefficients to decrease to a minimum value, dependent only on the data acquisition system. Note that the range of coefficients for the heating condition with $\Delta T/T = +0.03$ is greater than the value at $\Delta T/T = +0.10$.

2.2.3 Comparison of UTC Flow Conditions with Previous Experiments. The range of Rossby numbers at the disk bore, $U_{z\text{-avg}}/(\Omega R_b)$, for the UTC experiments was 0.03 to 0.22 with tangential Reynolds numbers to 8×10^6 . For Kim et al. [5], the Rossby number range was 0.84 to 8.4 with tangential Reynolds numbers to 5×10^5 . For Owen and Pincombe [9], the Rossby number range was from 1 to ∞ (no disk rotation) with tangential Reynolds numbers to 3×10^5 . For Long [4], the Rossby numbers varied from 0.15 to 40 with tangential Reynolds numbers to 5×10^6 . For Rossby numbers ≥ 1 , the present authors expect the heat transfer on the downstream disk to be dominated by the impinging jet. For Rossby numbers ≤ 1 , the cavity flow and heat transfer are expected to be dominated (a) by the buoyant interaction of the "coolant" flow and the air temperature in the disk cavities and (b) by the stability characteristics of the swirling flow between the center shaft and the outer radius of the cavity. For Rossby numbers, $0.1 < Ro < 10$, the dominate mechanism influencing the cavity flow is expected to change from buoyancy or profile stability to impingement. For large aircraft engines with disk to shaft spacing shown in Fig. 1, the Rossby numbers are in

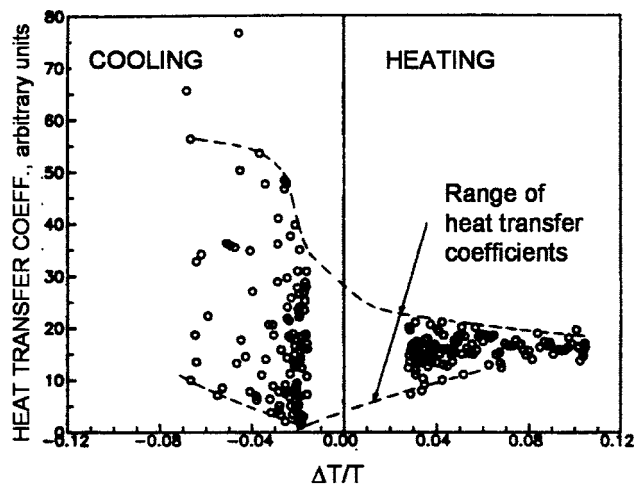


Fig. 6 "Instantaneous" heat transfer coefficients deduced from the data of Fig. 5

the range, $0.05 < Ro < 0.5$. The authors' conclusion is that the flow characteristics in these (Fig. 1) compressor disk cavities will be governed by buoyancy and axial velocity distribution rather than by impinging flow.

2.2.4 Conclusions From UTC Experiments. The flow visualization experiments showed that multi-lobed flow occurs within the trapped cavities for constant density conditions. The heat flux measurements indicate that the unsteadiness is almost periodic for some flow conditions and the unsteadiness decreases as the temperature of the coolant becomes significantly greater than the disks.

3 Stability Analysis

After reviewing the class of flows encountered in compressor disk cavities for Pratt & Whitney large aircraft engines, the authors concluded that the flow and heat transfer characteristics could be better predicted by understanding the influence of buoyancy on the large-scale mixing of the flow. This was driven by the significant differences in the heat transfer measured during heating or cooling conditions. There is also the possibility that relating the stability results may result in improved turbulence models for analysis of these complex flows.

The stability of axisymmetrical swirling, variable density flow is shown to be a function of the axial and tangential velocity profile, the density distribution, and the Mach number. The stability characteristics of curvilinear shear flows, including swirling coaxial shear flows, influence the transport of fluid momentum and scalar quantities within aircraft gas turbines and other rotating machinery. Studies have been conducted for over 70 years to obtain experimental data and analytical criteria that define the velocity and density distributions where instabilities in swirling flows will grow or stabilize.

The stability of the swirling flow is often complicated by the effects of non-parallel flow, compressibility and variable density, and combustion. Thus far, no general analytical criteria for stability have been developed. However, "sufficient" conditions for stability have been developed for certain classes of flow, which may be more restrictive than necessary. The present work is directed toward determining conditions for the stability of swirling, compressible and variable density shear flows that will more accurately predict the neutral stability conditions.

3.1 Background for Stability Analysis. In recent years, Rayleigh's criterion [10] for the stability of rotating flow, that the square of the circulation should nowhere decrease radially outward, has been extended by many investigators. Howard and Gupta [11] derived a sufficient condition for the stability of inviscid incompressible homogeneous swirling flow subject to axisymmetric disturbances. Ludwig [12,13] gave two criteria to delineate the neutral stability boundary for inviscid incompressible homogeneous flow in the narrow gap between concentric cylinders in terms of axial and azimuthal velocity gradient parameters. Leibovich [14] and Kurzweg [15] extended the results of Howard and Gupta [11] to inviscid incompressible flow with variable density subject to axisymmetric and asymmetric disturbances, respectively.

The stability of compressible and variable-density swirling flow is more complex than that of incompressible swirling flow. A sufficient condition for stability has been derived by Howard [16] for axisymmetric disturbances. Gans [17] also obtained a sufficient stability condition for near solid-body rotation in a pipe. Lalas [18] and Warren [19] extended Howard's [16] and Gans' [17] work, giving a sufficient condition for stability for non-axisymmetric disturbances. Eckhoff and Storesletten [20] derived a necessary condition for stability by a generalized progressive wave method. Leibovich and Stewartson [21] also provided a sufficient condition by using an asymptotic analysis for large azimuthal wave numbers.

3.2 Objectives of Present Analysis. The previous analyses above do not address the effects of radial temperature gradients in the interface between the flow in the core region along the center shaft and the flow in the rotating cavity. From Figs. 5 and 6, we interpret the variations of the heat flux and heat transfer coefficient with time and $\Delta T/T$, respectively, to be due to the stabilizing or destabilizing character of the flow in this interface. Therefore, the extension of the previous analyses to include radial gradients in the total temperature of the flow is warranted. In addition, a solution is desired that is relatively easy to use for the analysis of flow in rotating cavities with an axial flow near the core.

The present analytical study extends the work of Lalas [18] and Warren [19] and produces stability criteria for compressible, swirling, inviscid flow similar to those obtained by Ludwig [12,13] for incompressible inviscid swirling flows between concentric cylinders. The linearized stability equation is derived as a second-order ordinary differential equation for the complex amplitude function of the perturbed radial velocity component. Under the narrow-gap approximation, two stability criteria are derived analytically. Ludwig's two stability criteria for incompressible flow may be considered as special cases of the generalized compressible, variable-density results. The stability condition was obtained for basic swirling flows in terms of axial and azimuthal velocity gradient parameters. The neutral stability boundaries are derived as a family of curves for a stability parameter depending on the compressibility and density variation.

The criteria for the stability of the swirling, variable-density flow, derived from the analysis, are in a form that is related to the local flow conditions in the shear layer. Although the narrow gap results are not directly applicable for the full cavity shear and density layers, they are indicative of the stability characteristics for the flow as shown by Xia [22].

4 Stability Criteria

The governing equations for parallel axisymmetric swirling flows are developed in the Appendix. The equations used to demonstrate the present extensions from previous analysis are presented in the main text.

Small gap approximation. Two stability criteria are derived for compressible swirling flows, following the method used by Ludwig [12,13]. With the approximation of small annular gap, ($\Delta r/r \ll 1$), between rotating cylinders, (a) the term, G/r , in Eq. (A4) is neglected as compared with other terms, and (b) ρ , U , W , ρ' in Eqs. (A3)–(A5) are evaluated at a reference point, e.g., the mid point at $r_0 = (r_1 + r_2)/2$. With these approximations, the formulation can be made dimensionless by using r , ρ , and W at r_0 . By elimination from Eq. (A3), an ordinary differential equation for G can be obtained as

$$G'' - \alpha^2 \left\{ 1 + \left(\frac{n}{\alpha} \right)^2 + \frac{A}{\alpha^2} - \frac{2}{\gamma^2} \left[C_\theta + 1 - \left(\frac{n}{\alpha} \right) C_x \right. \right. \\ \left. \left. + 0.5N^2 \left(1 + \frac{n^2}{\alpha^2} \right) \right] \right\} G = 0 \quad (1)$$

where

$$A = \frac{2}{\alpha^2} \left[\frac{1}{\alpha^2} + N^2 + 2(1 + C_\theta) \right] \quad (2a)$$

$$N^2 = \frac{W^2}{r^2} \left(\frac{\rho'}{\rho} - \frac{M_\theta^2}{r} \right) \quad (2b)$$

$$M_\theta = \frac{W}{a} \quad (2c)$$

The local velocity profiles between the rotating cylinders may be approximated by

$$U \cong U_0 + C_x(r-1) \quad (3a)$$

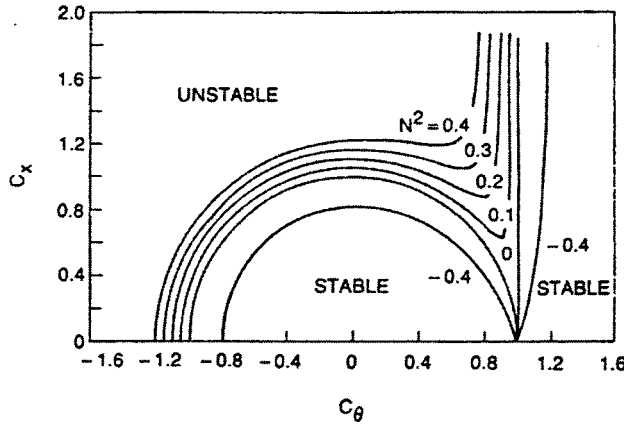


Fig. 7 First stability criterion of compressible swirling flow in narrow gap between concentric cylinders

$$W \cong 1 + C_\theta(r-1) \quad (3b)$$

Equation (A5) becomes

$$\gamma = (\alpha U_0 - \beta_r + n) + (\alpha C_x + n C_\theta - n)(r-1) - i\beta_i \quad (4)$$

where

$$\beta = \beta_r + \beta_i$$

The boundary condition remains the same as Eq. (A7).

For constant γ ,

$$\alpha C_x + n C_\theta - n = 0 \quad (5)$$

Ludwig [12,13] has shown that this condition describes a special disturbance, which has a definite direction in relation to the given basic swirling flow. The differential equation (1) admits sinus-shaped solutions only if the quantity in the square brackets is positive. Thus, the stability condition is

$$C_\theta + 1 - \frac{n}{\alpha} C_x + \frac{N^2}{2} \left(1 + \frac{n^2}{\alpha^2} \right) \geq 0 \quad (6)$$

Substituting Eq. (5) into Eq. (6), we get the first stability criterion,

$$(C_\theta - 1)(C_x^2 + C_\theta^2 - 1) + \frac{N^2}{2} [C_x^2 + (C_\theta - 1)^2] \geq 0 \quad (7)$$

The first term on the left-hand side implies the case of incompressible homogeneous fluid ($N^2=0$), which corresponds to Ludwig's [12] first stability criterion

$$(C_\theta - 1)(C_x^2 + C_\theta^2 - 1) \geq 0 \quad (8)$$

The second term describes the effect of compressibility on the neutral stability boundary. As N^2 increases, the stability region expands, particularly in the neighborhood of solid-body rotation ($C_\theta=1$).

The boundary between the stable and unstable regions of compressible swirling flow, based on Eq. (7), is shown in Fig. 7 for several values of the stability parameter N^2 . C_x and C_θ are the axial and azimuthal velocity gradient parameters defined in Eq. (A14). Ludwig's first criteria for the stability of swirling flow is identified by the curve with $N^2=0$. Note that a compressible flow is able to withstand larger axial velocity gradients before becoming unstable as N^2 increases. The value of N^2 for specific flow conditions can be obtained from Eq. (A7d) and (A12), or (A13). The increasing stability of the flow with increasing values of N^2 is compatible with the results of Howard [16], L alas [18], Warren [19], Eckhoff and Storesletten [20]. Because of the restriction of $\gamma=\text{constant}$, the first criterion should be considered only as a necessary condition for stability. Ludwig's comparison of analysis and his experiments are also shown in Schlichting [23]. This sta-

bility criteria is also compatible with swirling coaxial flow experiments of Roback and Johnson [24] that showed low levels of radial mixing for regions where $C_\theta=0$. Most turbulence models and CFD codes were unable to simulate the measured stabilizing effects.

Variable γ . A necessary and sufficient stability condition for the general case with variable density is obtained where γ is arbitrary, following Ludwig [13]. Let the radial coordinate be normalized by

$$\xi = \frac{r-1}{\Delta r}, \quad -1 \leq \xi \leq 1 \quad (9)$$

where

$$\Delta r = \frac{1}{2}(r_2 - r_1)$$

Equation (3) becomes

$$G''(\xi) - \alpha^2(\Delta r)^2 \left\{ 1 + \left(\frac{n}{\alpha} \right)^2 + \frac{A}{\alpha^2} - \frac{2}{\gamma^2} \left[C_\theta + 1 - \frac{n}{\alpha} C_x + 0.5N^2 \left[1 + \left(\frac{n}{\alpha} \right)^2 \right] \right] \right\} G(\xi) = 0 \quad (10)$$

where the prime denotes differentiation with respect to ξ . Let

$$L^2 = [1 + (\alpha/n)^2 + A/\alpha^2](\alpha\Delta r)^2 \quad (11)$$

$$Y = n/\alpha \quad (12)$$

$$P_1 = (1 - C_\theta)Y - C_x \quad (13)$$

$$M_1 = C_\theta + 1 - YC_x + 0.5N^2(1 + Y^2) \quad (14)$$

$$N_1 = -Y - U_0 + \beta_r/\alpha \quad (15)$$

$$K = M_1/P_1^2 \quad (16)$$

$$E = E_r + iE_i = (N_1 + i\beta_i/\alpha)/(P_1\Delta r) \quad (17)$$

so that

$$\gamma = -\alpha N_1 - \alpha P_1(r-1) - i\beta_i \quad (18)$$

Equation (10) is simplified to

$$G''(\xi) - [L^2 - 2K/(E + \xi)^2]G(\xi) = 0 \quad (19)$$

with boundary condition

$$G(-1) = G(1) = 0 \quad (20)$$

The general solution of the differential equation, (19), with the boundary condition, (20), can be expressed in terms of Bessel functions. Again, following Ludwig [13], it can be shown that the flow is stable ($E_i=0$ or $\beta_i=0$) if and only if

$$K = \frac{C_\theta + 1 - YC_x + 0.5N^2(1 + Y^2)}{[(C_\theta - 1)Y + C_x]^2} \geq -\frac{3}{8} \quad (21)$$

Given C_x , C_θ , and N , the value of Y which minimizes the value of K is given by

$$Y = C_x(7 - 3C_\theta)/[3(C_\theta - 1)^2 + 4N^2] \quad (22)$$

Then substituting Eq. (22) into Eq. (21), we obtained the second stability criterion

$$\begin{aligned} & [3(C_\theta - 1)^2 + 8N^2] \left[(C_\theta - 1)(C_\theta^2 - 1) - \left(\frac{5}{3} - C_\theta \right) C_x^2 \right] \\ & + \frac{3}{2} N^2 \left[(C_\theta - 1)^4 + \left(\frac{7}{3} - C_\theta \right)^2 C_x^2 \right] \\ & + 4N^4 \left[C_\theta^2 - \frac{2}{3} C_\theta + \frac{7}{3} + \frac{1}{2} C_x^2 \right] + \frac{8}{3} N^6 \geq 0. \end{aligned} \quad (23)$$

For $N^2=0$, Eq. (23) reduces to Ludwig's [13] second criterion

$$(C_\theta - 1)(C_\theta^2 - 1) - \left(\frac{5}{3} - C_\theta \right) C_x^2 \geq 0 \quad (24)$$

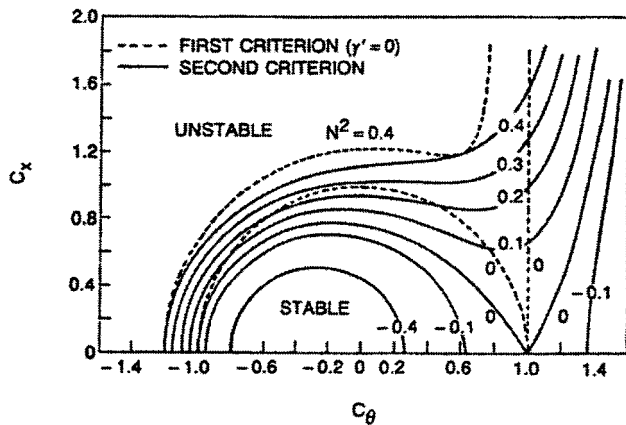


Fig. 8 Second stability criterion of compressible swirling flow in narrow gap between concentric cylinders

The variation of the neutral stability boundary with N^2 according to the second criterion is shown in Fig. 8. The general characteristics of the second criterion are similar to those of the first, i.e., the stability increases with increasing N^2 . However, there are several notable differences. The second criterion imposes a more stringent condition on the stability of compressible swirling flow than the first criterion, i.e., for a given swirl level and velocity gradient, C_θ , the flow becomes unstable at a lower value of the axial velocity gradient. For a value of $N^2=0$ and $C_\theta=0$, the maximum value of C_x for neutral stability is reduced from 1.0 to 0.77. The stability characteristics for $N^2>0$ are affected by the compressibility and variable density in a different manner, depending upon their location in the C_x - C_θ plane. The largest effects of increasing N^2 on the stability of the flow is found near $C_\theta=1$, solid-body rotation. For $N^2=0$ and $C_\theta=1$, the flow is unstable to any axial velocity gradient. Increasing N^2 allows the flow to remain stable at increasingly large values of N^2 of the axial logarithmic velocity gradient, C_x . For values of $N^2>0.3$, the maximum value of C_x , for stable flow increases with increasing C_θ rather than decreasing, near $C_\theta=1$.

The implication of the effect of temperature gradient or density gradient on the flow stability is evident in view of the stability parameter, N^2 , as presented by Eqs. (A7d) and (A12) and the experimental results shown in Fig. 6. The heating condition, $T'/T<0$ or $\rho'/\rho>0$, tends to increase the value of N^2 toward stability, while the cooling condition, $T'/T>0$ or $\rho'/\rho<0$, tends to decrease the value of N^2 toward instability. The second criterion may be used to investigate the flow stability in the compressor environment posed by various velocity, density, and temperature distributions.

In the Appendix and this section, the necessary and sufficient condition, the second stability criterion, for the stability of compressible inviscid swirling flows in a narrow gap between concentric cylinders was derived. In a parallel study, Xia [22], numerical solutions of Eq. (A6) were carried out for arbitrary velocity and density distributions in a wide gap. The second criterion in Eq. (23) was then used to verify a numerical solution and show that the application of the second stability criterion for narrow gaps at all locations in the radial profile was a good approximation for predicting the stability of wide gap profiles, at least for the cases of solid-body rotation and constant swirling velocities. Therefore, the local application of the second stability criterion will be used to study the effects of axial velocity (Rossby number) and density profiles on the stability characteristics of flow in rotating cavities with swirling flow in the bore region. Results from this parametric study provide an explanation for the heat transfer characteristics shown in Fig. 6 and the differences between heating and cooling conditions noted by Graber et al. [2].

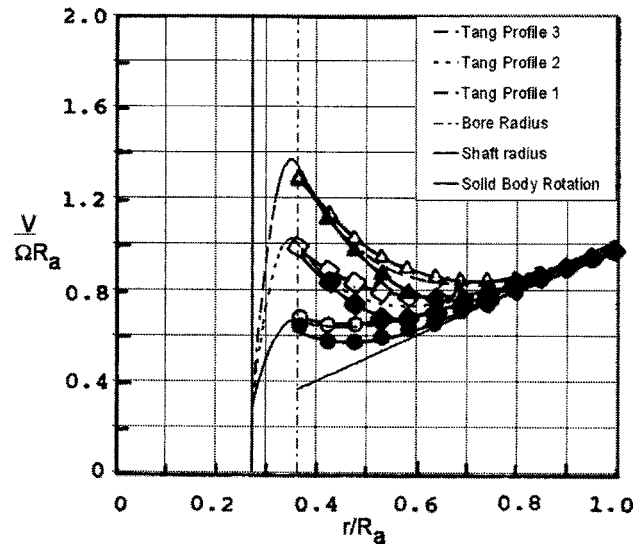


Fig. 9 Tangential velocity profiles used to determine stability of shear layer near bore radius of cavity. Symbols are calculated profiles from Johnson et al. [25].

5 Application to Rotating Cavity Flows

In this section, the stability criterion developed in the Appendix and the previous section for compressible flows between concentric rotating cylinders is applied to flow conditions similar to those in the compressor drum flow and heat transfer experiments of Graber et al. [2], Johnson et al. [25], and a subsequent Pratt & Whitney project (Figs. 5 and 6). In the present section, we use results from Eqs. (23) and (A7d) to demonstrate the effects of axial velocity profile and density profile on the stability of the shear layer between the axial-flowing cooling or heating flow in the region along a center shaft (Fig. 1) and the more quiescent rotating flow in the cavity. In this analysis, we assume

- (1) the shear layer will be stable if the stability criterion for narrow gaps is satisfied at all locations on the profile,
- (2) the approximation of velocity profiles, Eq. (3), can be relaxed by using local values of C_x, C_θ in Eq. (A14) from the profiles of previous UTC experiments. (See Fig. 9),
- (3) an axisymmetric shear layer that is centered at the bore radius of the cavity and is independent of distance from the upstream disk,
- (4) axial velocity and density profiles that have the form, $\tanh[2(r-R_b)/\delta]$, as shown in Eqs. (25) and (26).

Xia [22] has shown in a companion numerical study that assumption (1) shows correct trends but that modestly greater values of N^2 (of order 10%) are required for stability in some C_x - C_θ regions of Fig. 8 for large gaps of order $0.75 R_a$.

The stability analysis, formulated in the Appendix, is general in that the criteria for the radial density distribution are provided in terms of Mach number, temperature distribution, or directly in density distribution. Thus, the application of the analysis is applicable for a range of engine sizes and operating conditions, provided that the axial and tangential Reynolds numbers are relatively high.

The hyperbolic tangent and error function profiles are generally accepted as good representations of the velocity profiles in a developed shear layer, e.g., Schlichting [23]. The hyperbolic tangent profile was chosen for ease of use with velocity and density gradients.

The tangential velocity profiles used in the parametric study are shown in Fig. 9. Each dashed or solid line is a curve fit through two profiles with open and closed symbols. The two profiles were calculated, using a momentum integral code, with two different

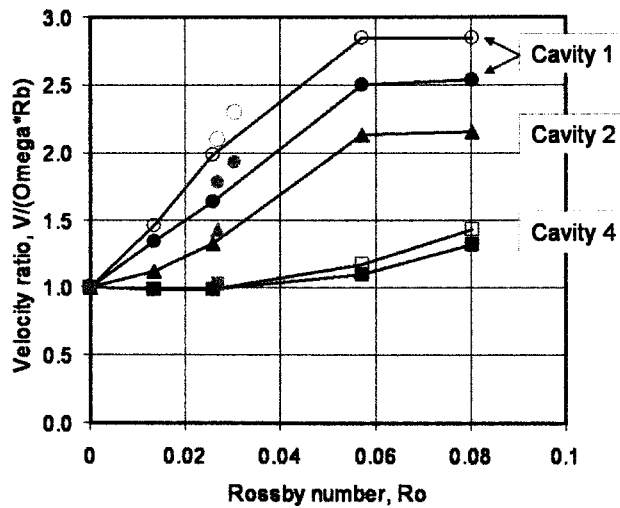


Fig. 10 Variation of $V_b/(\Omega R_b)$ with Rossby number for coolant injection location B; determined from radial pressure measurements and analysis with two turbulence models (Johnson et al. [25]). Symbols: Black- $Re=7 \times 10^6$; Gray- $Re=4 \times 10^6$; Open and closed—different turbulence models

assumed turbulence models for the core flow region. The integral method is outlined in Johnson et al. [25] and Graber et al. [2] and was used successfully to model the flows in Cavity 2 with injection location A (Fig. 4). The tangential velocity profiles in the cavity region were approximated with a combination of linear and exponential functions. The region between the shaft and the bore of the disk was modeled using a second-order curve with the shaft speed and the velocity and slope of the cavity region profile at the bore radius as boundary conditions.

The variations of bore tangential velocities with Rossby number (Fig. 10) for coolant flow from injection location “B” were determined from experimental pressure distributions of data from Graber et al. [2] and the momentum integral method described in the previous paragraph. Note that the estimated tangential velocity ratio at the bore varies by 10%, depending on the core viscosity model used. The swirl velocity ratio at the bore, $V_b/(\Omega R_b)$ varies from 1 at no coolant flow to more than 2.5 for Rossby numbers greater than 0.06. The bore swirl velocity ratio decreases with cavity distance from the injection location. For Cavity 4, the bore swirl velocity ratio is less than 1.5 for Rossby numbers of 0.08. Injecting coolant at radii greater than the bore radius causes a tangential velocity difference greater than zero in the bore region of the disk and guarantees that a portion of the disks will be cooled with forced rather than free convection. Forced convection on the disk will be important for conditions where a stable flow in the cavity could occur for portions of the aircraft flight cycle.

The stability analysis was conducted with assumed axial velocity and density profiles in the shear region and extending from the center shaft, R_s , to the cavity outside radius, R_a . A hyperbolic-tangent profile was assumed for both profiles, centered about the bore radius, R_b . The tanh profile was used to model mixing layers and has the characteristics of a developed mixing layer as follows:

$$U = \frac{1}{2} \{ 1 - \tanh[2(r - R_b)/\delta_U] \} Ro \frac{4}{11} \quad (25)$$

$$\rho = 1 + \frac{1}{2} \Delta\rho \{ 1 + \tanh[2(r - R_b)/\delta_\rho] \} \quad (26)$$

The axial velocity profiles are shown in Fig. 11 with three different shear layer thicknesses, δ . The thickness, δ , is defined in terms of the maximum slope and the difference between the maximum and minimum values of the profile. The nominal shear layer thickness for the parametric study, $\delta_\rho = \delta_U = 1/22^* R_a$, is 12.5% of

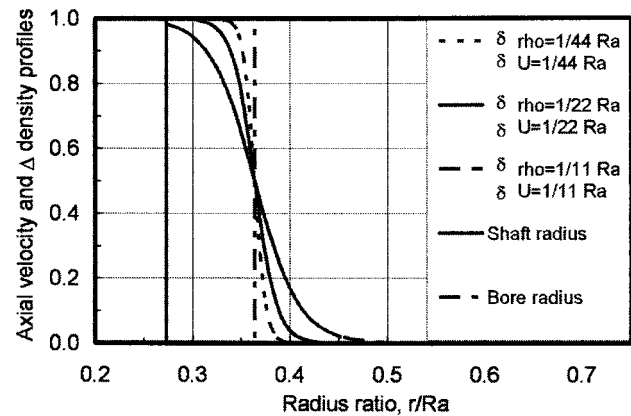


Fig. 11 Axial velocity ratio profiles used to determine stability of shear layer near bore radius of cavity

the bore radius, R_b . Additional profiles in Fig. 11 with half ($\delta_\rho = \delta_U = 1/44^* R_a$) and twice ($\delta_\rho = \delta_U = 1/11^* R_a$) that thickness were also used for additional stability calculations.

In the Appendix, the parameter, N^2 , was formulated for several conditions. The N^2 formulation of Eq. (A7d) with a negligible Mach number was used for the parametric analysis. With well-defined tangential velocity and temperature profiles in the shaft and cavity regions, a more exact analysis can be conducted, using the formulation of N^2 in Eq. (A12) or (A13).

The local values for all factors in Eq. (23) were examined with a worksheet for a set of tangential velocity, axial velocity, and density profiles at 40 locations between the shaft radius, R_s , and the outer radius, R_a . There was a concentration of points in the axial velocity shear layer where the instability tends to be greatest. The density ratio required for stability was iteratively found to two or three significant figures by selecting values of $\Delta\rho$ until Eq. (23) was greater than 0 at all locations

The stability characteristics of tangential velocity Profile 2 were evaluated with the three shear layer thicknesses (Fig. 11). The density ratios required for stability are shown in Fig. 12 as a variation with Rossby number, Ro . Both the axial-velocity and density layer thicknesses are identical for each curve. For Rossby numbers greater than 0.1, the stability characteristics are independent of shear layer thickness. For low Rossby numbers, the shear layer thickness affects the stability with the thinner shear layer requiring a greater density ratio than the thicker layers. A conclusion regarding assumption (2) is that when the width of the axial velocity and density profiles vary together, the stability is not significantly influenced by the shear layer thickness for Rossby numbers greater than 0.1.

For $Ro < 0.07$, the instability is a stronger function of the tangential velocity profile. A local density gradient is required to stabilize the flow. Because the gradients are less with the thicker density layer, $\delta_\rho = 1/11^* R_a$, a larger value of $\Delta\rho$ is required to stabilize the flow than for the standard condition, $\delta_\rho = \delta_U = 1/11^* R_a$.

The stability characteristics for the three tangential velocity profiles were evaluated for the shear layer thickness, $\delta = 1/22^* R_a$. The results are shown in Figs. 13(a) and 13(b) as the variation of $\Delta\rho$ with Rossby number. In Fig. 13(a), results show that the tangential velocity Profile 1 will permit stability with a negative density ratio (coolant denser than the cavity density) for Rossby numbers less than 0.03. Thus, the tangential velocity profile provides stability for both the axial shear and the negative density gradients. This result is compatible with the results shown in Fig. 8 for values of C_θ . Note that most of the stable flow conditions occur with $\Delta\rho > 0$, i.e., the coolant density is less than cavity density. For C_θ near 0, values of $C_\gamma > 0$ and $N^2 < 0$ can provide stability to the profile. This is also compatible with the experiments of Ro-

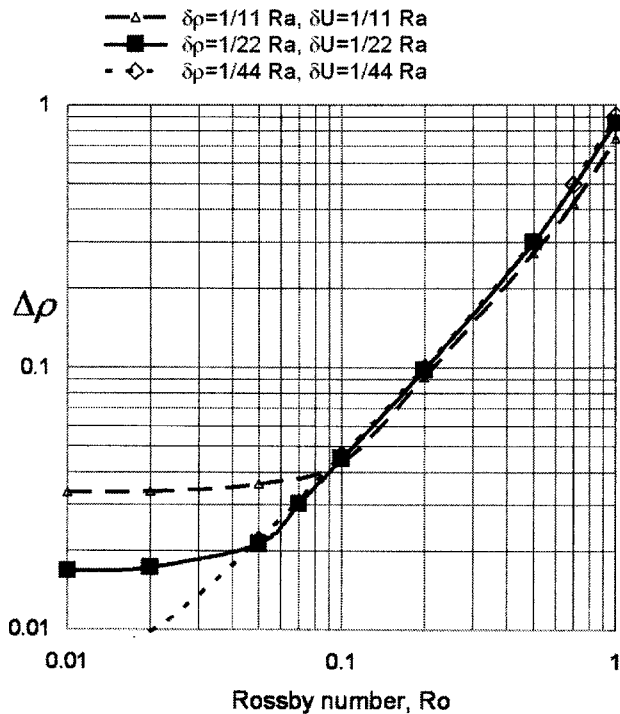


Fig. 12 Effect of shear layer width on variation of density ratio required for stability with Rossby number for tangential velocity Profile 2

back and Johnson [24] where the swirling flow with C_ρ near 0 inhibited radial mixing in a coaxial swirling flow experiment.

The results in Figs. 13(a) and 13(b) also show that profiles 2 and 3 require less density difference, $\Delta\rho$, for stability than Profile 1. For Rossby numbers greater than 0.07, the variations of density ratio, $\Delta\rho$, with Rossby number for each tangential velocity profile are parallel on Fig. 13(b) (log-log presentation). In this Rossby number range, the density ratio to stabilize Profiles 1 and 2 are three and two times greater, respectively, than for Profile 3. Thus, the coolant injection location with consequential swirl and the Rossby number can have a significant influence on the heat transfer characteristics for the condition where the "cooling" air is hotter than the disks and the cavity air.

Additional stability calculations were made for tangential velocity Profile 2 with different thicknesses for the axial velocity and density profiles. The four additional conditions, along with the Profile 2 results shown in Fig. 13, are shown in Fig. 14. For Rossby numbers greater than 0.1, the variations of density ratio with Rossby number required for stability are parallel on the log-log scale. For Rossby numbers greater than 0.1, increasing the density layer thickness by a factor of 2 or decreasing the axial velocity layer thickness by a factor of 2 results in a factor of 2 increases in the density ratio required for stability. Decreasing the density layer thickness or increasing the axial velocity layer thickness by a factor of 2 decreases the density ratio required for stability in the same Rossby number range. The conclusion from this comparison is that a strong density gradient at a critical location can suppress the instability due to the axial velocity gradient.

For Rossby numbers less than 0.1, the results are more complex. Varying the axial velocity thickness for a Rossby number of 0.01, showed that the same density ratio is required for stability, independent of density thickness. This value, 0.017, was required to stabilize tangential velocity Profile 2 for no axial flow. For a Rossby number of 0.01, increasing the density thickness by a factor of 2 also required an increase of 2 in the density ratio required to stabilize the flow. The conclusion is that the local density gradient required to stabilize tangential velocity Profile 2 is the dominant factor for these low Rossby numbers.

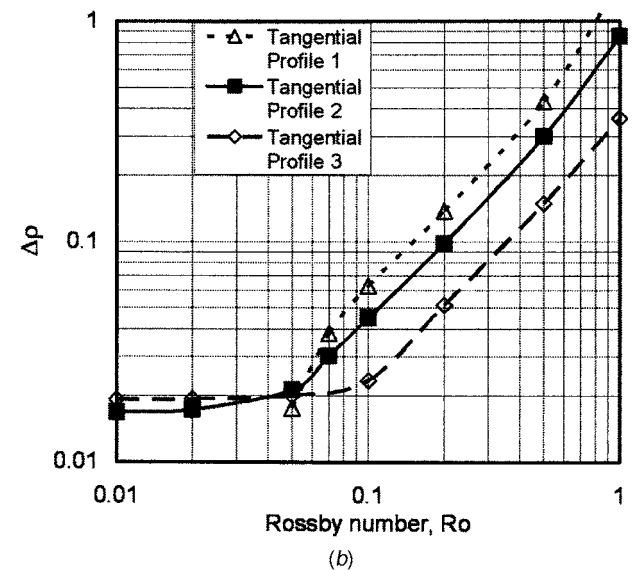
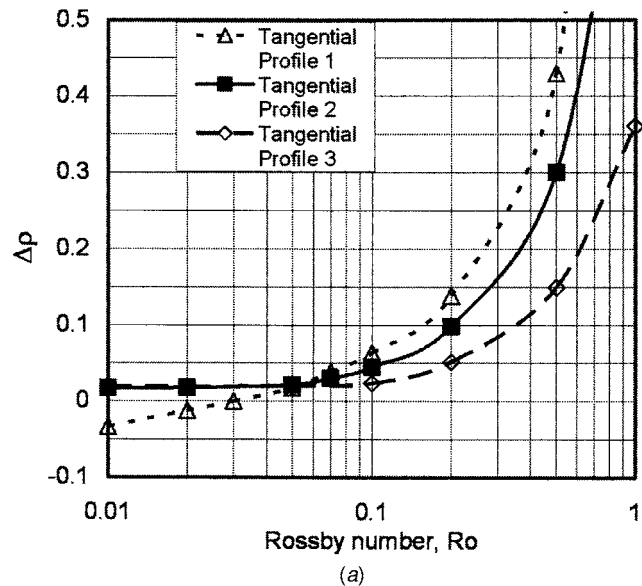


Fig. 13 Effect of tangential velocity profile on variation of density ratio required for stability with Rossby number for density and axial velocity profiles with $\delta\rho=\delta U=1/22 Ra$. Results for positive $\Delta\rho$ are identical for the upper log-linear (13a) and lower log-log presentations (13b) of $\Delta\rho$ with Rossby number.

6 Concluding Remarks

The necessary and sufficient condition, the second stability criterion, for the stability of compressible inviscid swirling flows in a narrow gap between concentric cylinders was derived. The second stability criterion for compressible flow significantly extended the stability criteria obtained by previous investigators. In a parallel project, this criterion was then used to verify a numerical solution and show that the application of the second stability criterion for narrow gaps at all locations in the radial profile was a good approximation for predicting the stability of wide gap profiles, especially for the cases of solid-body rotation and constant swirling velocities.

The stability characteristics shown in the parametric study provide a rational explanation for the differences in time-dependent and time-averaged heat transfer on compressor disk models with heating and cooling flow conditions. The results from the study also showed that flows with Rossby numbers greater than 0.5

$\delta\rho=1/22 Ra, \delta U=1/44 Ra$
 $\delta\rho=1/11 Ra, \delta U=1/22 Ra$
 $\delta\rho=1/22 Ra, \delta U=1/22 Ra$
 $\delta\rho=1/44 Ra, \delta U=1/22 Ra$
 $\delta\rho=1/22 Ra, \delta U=1/11 Ra$

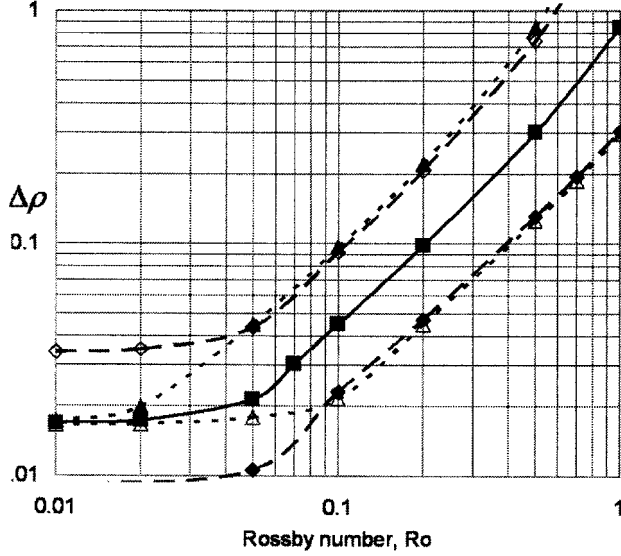


Fig. 14 Effects of density and axial velocity profile widths on variation of density ratio required for stability with Rossby number for tangential velocity Profile 2

would require density differences between the shaft region and the cavity region that are greater than could be expected to occur in aircraft operating cycles. Thus, for high Rossby number flow conditions, the flow in the cavity will always have instabilities as shown in previous studies at the Universities of Sussex and Bath. For Rossby numbers of order 0.1 or less, the flow characteristics in the rotating cavity and hence on the compressor disks will be influenced by the relationship between the tangential velocity, axial velocity, and density profiles within the shear region between the core flow and the cavity fluid.

The results of the parametric study and the explanation for the significant differences in heat transfer coefficients between heating and cooling flow conditions show that this parameter should be considered in cooling design correlations and practice for secondary flow systems.

Acknowledgment

The development of the stability theory and the UTC experiments were sponsored by Pratt & Whitney and United Technologies Research Center. The authors gratefully acknowledge Nan Xia (formerly at University of Science and Technology, Hefei, PRC) for work on the stability analyses when at the University of Connecticut as a Visiting Scholar.

Nomenclature

$C_x = C_x = rU'/W$ (' is differentiation with respect to r)
 $C_\theta = C_\theta = rW'/W$
 r = local radius, m
 R_a = outer radius of cavity, m
 R_b = bore radius of cavity, m
 R_s = center shaft radius, m
 Re_t = tangential Reynolds number, $\rho\Omega R_a^2/\mu$
 Re_z = axial Reynolds number, $\rho_{coolant}U_{z-avg}R_b/\mu$
 Ro = Rossby number, $U_{z-avg}/(\Omega R_b)$
 T = fluid temperature, K
 T_{cavity} = temperature of cavity fluid, K
 $T_{coolant}$ = temperature of coolant fluid, K

T_{wall} = temperature of disk wall, K

$\Delta T = T_{coolant} - T_{wall}$, K

U = axial velocity ratio, $U_z/(\Omega R_a)$

U_z = axial velocity, m/s

U_{z-avg} = average axial velocity between center shaft and bore radius, m/s

V = tangential velocity, m/s

W = tangential velocity ratio, $V/(\Omega R_a)$

ρ = local density ratio, $\rho_{local}/\rho_{coolant}$

ρ_{cavity} = density of fluid in cavity, kg/m^3

$\rho_{coolant}$ = density of coolant, kg/m^3

$\Delta\rho$ = density ratio, $(\rho_{cavity} - \rho_{coolant})/\rho_{coolant}$

Symbols used in the development of the stability analysis are defined in the Appendix and the Stability Criteria section as they are used.

Appendix

Governing Equations. The governing equations of an inviscid compressible flow are

$$\rho_t^* + \mathbf{V}^* \cdot \nabla \rho^* + \rho^* \nabla \cdot \mathbf{V}^* = 0 \quad (A1a)$$

$$\rho^* (\mathbf{V}_t^* + \mathbf{V}^* \cdot \nabla \mathbf{V}^*) = -\nabla p^* \quad (A1b)$$

and

$$\frac{dp^*}{dt} = -a^2 \rho^* \nabla \cdot \mathbf{V}^* \quad (A1c)$$

where \mathbf{V}^* is the velocity having (u^*, v^*, w^*) as the components in the cylindrical coordinates (x, r, θ) , ρ^* is the fluid density, p^* is the pressure, and a is the speed of sound. Let a steady, parallel axisymmetrical flow be subject to small disturbances such that

$$u^* = U(r) + F(r)e^{i(\alpha x + n\theta - \beta t)} \quad (A2a)$$

$$v^* = G(r)e^{i(\alpha x + n\theta - \beta t)} \quad (A2b)$$

$$w^* = W(r) + H(r)e^{i(\alpha x + n\theta - \beta t)} \quad (A2c)$$

$$p^* = p(r) + P(r)e^{i(\alpha x + n\theta - \beta t)} \quad (A2d)$$

$$\rho^* = \rho(r) + Q(r)e^{i(\alpha x + n\theta - \beta t)} \quad (A2e)$$

Substituting Eq. (A2) into Eq. (A1) and subtracting from the basic flow, which also satisfies Eq. (A1), the linearized inviscid stability equations can be rewritten as follows:

$$\gamma Q + \rho' G + \rho m = 0 \quad (A3a)$$

$$\gamma F + U' G + \frac{\alpha}{\rho} P = 0 \quad (A3b)$$

$$\gamma G + \frac{2W}{r} H + \frac{W^2}{\rho r} Q - \frac{1}{\rho} P' = 0 \quad (A3c)$$

$$\gamma H + \left(W' + \frac{W}{r} \right) G + \frac{n}{\rho r} P = 0 \quad (A3d)$$

$$\gamma P + \frac{\rho W^2}{r} G + a^2 \rho m = 0 \quad (A3e)$$

where

$$m = \alpha F + G' + \frac{G}{r} + \frac{n}{r} H \quad (A4)$$

$$\gamma = \alpha U - \beta + \frac{nW}{r} \quad (\text{A5})$$

and the prime denotes differentiation with respect to r . The variables, F , H , P , Q , and m can be eliminated from Eqs. (A3a)–(A3e) to yield a second-order differential equation for G ,

$$\gamma^2 \left[\frac{\rho S}{r} (rG)' \right]' - \left\{ \gamma r \left(\frac{\Gamma \rho S}{r} \right)' + \frac{2nW}{r^2} \Gamma \rho S - r \left(\frac{\gamma^2 M_\theta^2 \rho S}{r^2} \right)' - \left(\frac{4nW}{\gamma r} - M_\theta^2 \right) \frac{\gamma^2 M_\theta^2 \rho S}{r^2} + \rho (\gamma^2 - N^2 - \Phi) \right\} G = 0 \quad (\text{A6})$$

where

$$\Gamma = \gamma' + \frac{2nW}{r^2} \quad (\text{A7a})$$

$$\Phi = \frac{1}{r^3} (r^2 W^2)' \quad (\text{A7b})$$

$$S = \frac{r^2}{n^2 + \alpha^2 - \frac{r^2 \gamma^2}{\alpha^2}} \quad (\text{A7c})$$

$$N^2 = \frac{W^2}{r} \left(\frac{\rho'}{\rho} - \frac{M_\theta^2}{r} \right) \quad (\text{A7d})$$

$$M_\theta = \frac{W}{a} \quad (\text{A7e})$$

The boundary conditions are

$$G(r_1) = G(r_2) = 0, \quad (\text{A8})$$

where r_1 and r_2 are the radial locations of concentric cylinders. Note that $N^2 > 0$ in Eq. (A6) does not imply basic stability.

Constant Density Condition. For a constant density fluid, Eq. (A6) is reduced to the equation derived by Howard and Gupta [11]:

$$\gamma^2 \left[\frac{S}{r} (rG)' \right]' = \left\{ \gamma^2 + \gamma r \left[\frac{S}{r} \left(\gamma' + \frac{2nW}{r^2} \right) \right]' - \frac{2\alpha WS}{r^2} [\alpha (rW)' - nU'] \right\} G = 0 \quad (\text{A9})$$

Perfect Gas Condition. For a perfect gas, $p = \rho RT$ and $a^2 = \bar{\gamma} RT$ and

$$1/2(U^2 + W^2) + \frac{1}{\bar{\gamma}-1} a^2 = \frac{1}{\bar{\gamma}-1} a_0^2 \quad (\text{A10})$$

From the momentum equation, (A1b), a rotationally symmetric basic flow has the radial pressure gradient

$$p' = \frac{\rho W^2}{r} \quad (\text{A11})$$

The stability parameter, N^2 , can be derived as

$$N^2 = \frac{W^2}{r^2} \left[(\bar{\gamma}-1) M_\theta - \frac{rT'}{T} \right] \quad (\text{A12})$$

or in terms of total temperature, T_0 , Eq. (A12) becomes

$$N^2 = \frac{W^2}{r^2} (\bar{\gamma}-1) \left[\left(1 + C_\theta - \frac{rT'_0}{2T_0} \right) M_\theta^2 + C_x M_\theta M_x - \frac{rT'_0}{2T_0} M_x^2 - \frac{rT'_0}{(\bar{\gamma}-1)T_0} \right] \quad (\text{A13})$$

where

$$C_x = rU'/W, \quad C_\theta = rW'/W, \quad M_x = U/a \quad (\text{A14})$$

Perfect Gas at Constant Total Temperature. For $T'_0 = 0$, the stability parameter, N^2 , for the compressibility and density variation is

$$N^2 = \frac{W^2}{r^2} (\bar{\gamma}-1) [(1 + C_\theta) M_\theta^2 + C_x M_\theta M_x] \quad (\text{A15})$$

The Mach numbers play an intricate role on the stability depending on the parameters C_θ and C_x . For $C_\theta > -1$ and $C_x > 0$, an increase of the Mach number tends to increase the region of stability. Although applicable to other swirling flow applications, this condition is not usually applicable for compressor cavity applications because the cavity gas and cooling gas usually have different total temperatures.

Several constraints, conditions, and applications for Eq. (A6) are described in the main text.

References

- [1] Owen, J. M., and Rogers, R. H., 1995, *Rotating Cavities, Flow and Heat Transfer in Rotating-Disk Systems* Vol. 2, Wiley, New York.
- [2] Graber, D. J., Daniels, W. A., and Johnson, B. V., 1987, "Disk Pumping Test: Section VI-Compressor Drum Heat Transfer Experiments," U.S. Air Force Report No. AFWAL-TR-87-2050.
- [3] Farthing, P. R., Long, C. A., Owen, J. M., and Pincombe, J. R., 1992, "Rotating Cavity with Throughflow of Cooling Air: Heat Transfer," *ASME J. Turbomach.*, **114**, pp. 229–236.
- [4] Long, C. A., 1994, "Disk Heat Transfer in a Rotating Cavity with an Axial Throughflow of Cooling Air," *Int. J. Heat Fluid Flow*, **15**(4), pp. 307–316.
- [5] Kim, S. Y., Han, J. C., Morrison, G. L., and Elovic, E., 1994, "Local Heat Transfer in Enclosed Co-rotating Disks with Axial Throughflow," *ASME J. Heat Transfer*, **116**, pp. 66–72.
- [6] Bohn, D. E., Deutsch, G. N., Simon, B., and Burkhardt, C., 2000, "Flow Visualization in a Rotating Cavity with Axial Throughflow," *ASME Paper No. 2000-GT-0280*.
- [7] Long, C. S., Morse, A. P., and Tucker, P. G., 1995, "Measurement and Computation of Heat Transfer in High Pressure Compressor Drum Geometries with Axial Throughflow," *ASME J. Turbomach.*, **119**, pp. 51–60.
- [8] Cao, C., Chew, J. W., Millington, P. R., and Hogg, S. I., 2003, "Interaction of Rim Seal and Annulus Flows in an Axial Flow Turbine," *ASME Paper No. GT2003-38368*.
- [9] Owen, M. J., and Pincombe, J. R., 1979, "Vortex Breakdown in a Rotating Cylindrical Cavity," *J. Fluid Mech.*, **90**, pp. 109–127.
- [10] Rayleigh, J. W. S., 1916, "On the Dynamics of Revolving Fluids," *Proc. R. Soc. London, Ser. A*, **93**, pp. 148–154. (also in *Sci. Papers*, 6, 447).
- [11] Howard, L. N., and Gupta, A. S., 1962, "On the Hydrodynamic and Hydro-magnetic Stability of Swirling Flows," *J. Fluid Mech.*, **14**, pp. 463–476.
- [12] Ludwig, H., 1960, "Stabilität der Strömung, in Einem Zylindrischen Ringraum," *Z. Flugwiss.*, **8**, pp. 135–140.
- [13] Ludwig, H., 1961, "Ergänzung zu der Arbeit: Stabilität der Strömung in Einem Zylindrischen Ringraum," *Z. Flugwiss.*, **9**, pp. 359–361.
- [14] Leibovich, S., 1969, "Stability of Density Stratified Rotational Flows," *AIAA J.*, **7**, pp. 177–178.
- [15] Kurzweg, V. H., 1969, "A Criterion for the Stability of Heterogeneous Swirling Flows," *Z. Angew. Math. Phys.*, **20**, pp. 141–143.
- [16] Howard, L. N., 1973, "On the Stability of Compressible Swirling Flow," *Stud. Appl. Math.*, **52**, pp. 39–43.
- [17] Gans, R. F., 1975, "On the Stability of Shear Flow in a Rotating Gas," *J. Fluid Mech.*, **68**, pp. 403–412.
- [18] Lalas, D. P., 1975, "The 'Richardson' Criterion for Compressible Swirling Flows," *J. Fluid Mech.*, **69**, pp. 65–72.
- [19] Warren, F. W., 1975, "A Comment on Gans' Stability Criterion for Steady Inviscid Helical Gas Flow," *J. Fluid Mech.*, **68**, pp. 413–415.
- [20] Eckhoff, K. S., and Storesletten, L., 1978, "A Note on the Stability of Steady Inviscid Helical Gas Flows," *J. Fluid Mech.*, **89**, pp. 401–411.
- [21] Leibovich, S., and Stewartson, K., 1983, "A Sufficient Condition for the Instability of Columnar Vortices," *J. Fluid Mech.*, **126**, pp. 335–352.
- [22] Xia, N., 1987, private communication. (unpublished numerical study of instability of inviscid flows).
- [23] Schlichting, H., 1968, *Boundary-Layer Theory: Origin of Turbulence*, McGraw-Hill, New York, Chap. 17.
- [24] Roback, R. J., and Johnson, B. V., 1983, "Mass and Momentum Turbulent Transport Experiments with Confined Swirling Coaxial Jets," *NASA Contractor Report No. 168252*, Aug.
- [25] Johnson, B. V., Daniels, W. A., Kawecki, E. J., and Martin, R. J., 1991, "Compressor Drum Aerodynamic Experiments and Analysis With Coolant Injected at Selected Locations," *ASME J. Turbomach.*, **113**, pp. 272–280.

Buoyancy-Induced Flow in a Heated Rotating Cavity

J. Michael Owen
Department of Mechanical Engineering,
University of Bath,
Bath, UK

Jonathan Powell
Malvern Instruments Ltd.,
Malvern, UK

Experimental measurements were made in a rotating-cavity rig with an axial throughflow of cooling air at the center of the cavity, simulating the conditions that occur between corotating compressor disks of a gas-turbine engine. One of the disks in the rig was heated, and the other rotating surfaces were quasi-adiabatic; the temperature difference between the heated disk and the cooling air was between 40 and 100°C. Tests were conducted for axial Reynolds numbers, Re_z , of the cooling air between 1.4×10^3 and 5×10^4 , and for rotational Reynolds numbers, Re_ϕ , between 4×10^5 and 3.2×10^6 . Velocity measurements inside the rotating cavity were made using laser Doppler anemometry, and temperatures and heat flux measurements on the heated disk were made using thermocouples and fluxmeters. The velocity measurements were consistent with a three-dimensional, unsteady, buoyancy-induced flow in which there was a multicell structure comprising one, two, or three pairs of cyclonic and anticyclonic vortices. The core of fluid between the boundary layers on the disks rotated at a slower speed than the disks, as found by other experimenters. At the smaller values of Re_z , the radial distribution and magnitude of the local Nusselt numbers, Nu , were consistent with buoyancy-induced flow. At the larger values of Re_z , the distribution of Nu changed, and its magnitude increased, suggesting the dominance of the axial throughflow. [DOI: 10.1115/1.2032451]

1 Introduction

The work described here was conducted as part of a major European research project, entitled "The Internal Cooling Air Systems for Gas Turbines" (ICAS-GT). The project, which was sponsored by the European Commission, ran from 1998 to 2000 and involved ten gas turbine companies and four universities. The University of Bath was responsible for the measurements in an annular rotating cavity with an axial throughflow of cooling air, which is the subject of this paper.

Figure 1 shows a schematic diagram of a rotating cavity with an axial throughflow of cooling air. This provides a simple model of the flow that occurs between corotating, high-pressure compressor disks where air, extracted from an upstream compressor stage, passes through the center of the disks on its way to the turbine cooling system. Figure 1(a) shows the case where there is a central inlet, with no inner shaft. Figure 1(b) shows an annular inlet in which a central shaft corotates with the disks; in multishaft engines, the shaft rotates at a lower speed than the disks, but that case is not considered here.

In some engines, the compressor disks are sealed so that there can be no inflow or outflow of cooling air into the rotating cavity between the disks. If the solid boundaries of the system all had the same temperature then solid-body rotation would occur. In practice, the disks have radial temperature gradients, and the downstream disk is usually hotter than the upstream one. The rotating outer cylindrical surface (the shroud) is usually at a higher temperature than the inner cylindrical surface, particularly in steady-state operation or during the takeoff period of an aeroengine. Such temperature differences create buoyancy-induced flow in the rotating cavity, where the centripetal acceleration ($-\Omega^2 r$) can be around 10^4 times larger than the gravitational acceleration. Such buoyancy-induced rotating flows are usually three dimensional and unsteady, making measurements and computations difficult.

When there is an axial throughflow of cooling air, buoyancy-

induced flow in the outer part of the cavity interacts with the secondary flow of cooler air induced by the central throughflow; that case is considered here. In Sec. 2, some previous research studies are discussed; Sec. 3 describes the experimental apparatus and the measurement techniques; experimental results are presented and discussed in Sec. 4; and Sec. 5 contains the main conclusions.

2 Previous Research

The research described in this section was not part of ICAS-GT.

2.1 Sealed Cavities. The Aachen group (see Refs. [1–4]) made measurements in a sealed rotating annulus where the heat flow could be either axial (from a hot disk to a cold one) or radial (from a hot shroud to an inner cylinder). For axial heat flow, they defined the rotational Reynolds number as

$$Re_2 = \frac{\Omega r_m s}{\nu}, \quad (2.1)$$

where s is the axial space between the disks and r_m is the mean radius given by

$$r_m = 1/2(a + b). \quad (2.2)$$

For radial heat flow,

$$Re_3 = \frac{\Omega r_m b(1 - x_a)}{\nu}. \quad (2.3)$$

For the axial and radial heat flows, two different Grashof numbers (Gr_2 and Gr_3 , respectively) were used where

$$Gr_2 = \frac{\Omega^2 r_m s^3}{\nu^2} \beta (T_H - T_C) \quad (2.4)$$

and

$$Gr_3 = \frac{\Omega^2 r_m (b - a)^3}{\nu^2} \beta (T_H - T_C). \quad (2.5)$$

The temperatures correspond to the hot and cold disks or the hot shroud and cold inner cylinder.

The corresponding Nusselt numbers were defined as

Contributed by the International Gas Turbine Institute (IGTI) of ASME for publication in the JOURNAL OF ENGINEERING FOR GAS TURBINES AND POWER. Manuscript received October 1, 2003; final manuscript received March 1, 2004. IGTI Review Chair: A. J. Strazisar. Paper presented at the International Gas Turbine and Aeroengine Congress and Exhibition, Vienna, Austria, June 13–17, 2004, Paper No. GT2004-53210.

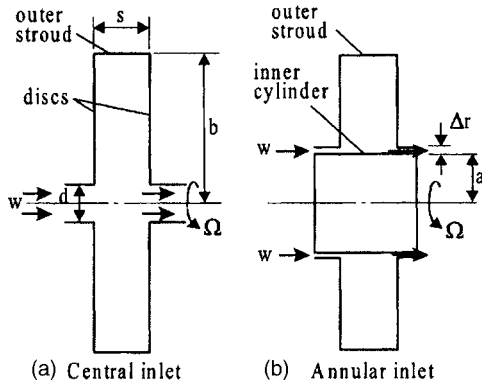


Fig. 1 Rotating cavity with axial throughflow of cooling air

$$Nu_2 = \frac{q_{av} s}{k(T_H - T_C)} \quad (2.6)$$

and

$$Nu_3 = \frac{q_{av} b \ln(b/a)}{k(T_H - T_C)}, \quad (2.7)$$

where q_{av} is the average heat flux. For pure conduction (as $Gr \rightarrow 0$), both Nusselt numbers tend to unity.

For the axial heat-flow case, their measurements of Nu_2 were correlated for $G=0.5$, $x_a=0.52$, and $2 \times 10^8 < Ra_2 < 5 \times 10^{10}$ by

$$Nu_2 = 0.346 Ra_2^{0.124}. \quad (2.8)$$

For the radial heat-flow case (with insulated disks), tests were conducted for $10^7 < Ra_3 < 10^{12}$ for three different geometries. Geometry A (axisymmetric annulus with $G=0.34$, $x_a=0.35$):

$$Nu_3 = 0.266 Ra_3^{0.228}. \quad (2.9)$$

Geometry B (axisymmetric annulus with $G=0.5$, $x_a=0.52$):

$$Nu_3 = 0.317 Ra_3^{0.211}. \quad (2.10)$$

Geometry C (annulus with eight 45 deg segments with $G=0.5$, $x_a=0.52$):

$$Nu_3 = 0.365 Ra_3^{0.213}. \quad (2.11)$$

That Nu_3 for geometry A is larger than for B is attributed to the fact that, for any value of Ra_3 , Re_3 for A is smaller than for B; buoyancy-induced flow is attenuated by Coriolis forces, and these increase as Re_2 increases. Nu_3 for the segmented annulus C were greater than for the axisymmetric annulus B. The radial walls in C provide the necessary circumferential pressure gradient needed to create the radial flow; increasing Re_3 has little adverse effect.

It is also worth noting that, for similar conditions, the Nusselt numbers for radial heat flow are larger than for axial heat flow. As shown by King [5], a radial temperature gradient creates unstable conditions resulting in pairs of cyclonic and anticyclonic vortices; these vortices are attenuated by the Coriolis forces. For the segmented cavity, a single anticyclonic vortex is formed.

2.2 Effect of Axial Throughflow. The Sussex group (see Refs. [6–11]) made measurements in a rotating cavity with an axial throughflow of cooling air (see Fig. 1(a)); either the disks or the shroud were heated. Their measurements were correlated using the dimensionless groups, defined below: Rotational Reynolds number:

$$Re_\phi = \frac{\Omega b^2}{\nu}. \quad (2.12)$$

Axial Reynolds number:

$$Re_z = \frac{WL}{\nu}, \quad (2.13)$$

where W is the bulk-average axial velocity given by $W = \dot{m} / \pi a^2 \rho$, and L is a characteristic length given by $L = d$. (For the annular inlet shown in Fig. 1(b), $W \approx \dot{m} / 2\pi a \Delta r \rho$ and $L = 2\Delta r$.) Rossby number:

$$Ro = \frac{W}{\Omega a} = \frac{Re_z b^2}{Re_\phi L a}. \quad (2.14)$$

Grashof number (for heated disks):

$$Gr_4 = \frac{\Omega^2 r (b-r)^3}{\nu^2} \beta (T_0 - T_1). \quad (2.15)$$

Nusselt number (for heated disks):

$$Nu_4 = \frac{q_o (b-r)}{k(T_0 - T_1)}. \quad (2.16)$$

In all cases, the fluid properties were based on the conditions at entry to the system.

The axial jet of fluid passing through the center of the cavity sets up a toroidal secondary flow inside the cavity, the strength and radial extent of which increases as Ro and G increase. The axial jet is susceptible to *vortex breakdown* (see Ref. [12]), the nature of which also depends on Ro and G . At the smaller radii, where the recirculation is strong, free-vortex flow occurs and $V_\phi / \Omega r$ can exceed unity: values of $V_\phi / \Omega r > 20$ have been measured. At the larger radii, where the effects of the axial throughflow are weak, quasi-solid-body rotation occurs; it is in this region that buoyancy effects are likely to be strong. Heat transfer is therefore due to mixed convection: forced convection (generated by the axial flow) at small radii, and free convection (generated by the buoyancy-induced flow) at large radii.

Flow visualization at Sussex revealed that the buoyancy-induced flow was nonaxisymmetric: regions of cyclonic and anticyclonic circulation, separated by so-called radial arms, were observed. As cyclonic and anticyclonic vortices generate regions of low and high pressure, respectively, they provide the circumferential variation of pressure required to create radial inflow and outflow in the cavity. Laser Doppler anemometry (LDA) measurements showed that the core of fluid between the boundary layers on the disks rotated at a speed lower than that of the disks. For example, for $G=0.24$, $Re_z=10^4$, $Re_\phi=4 \times 10^5$, $Ro=1.2$, and $x=0.63$, $V_\phi / \Omega r$ decreased from unity at $\Delta T=0^\circ\text{C}$ to around 0.93 at $\Delta T=80^\circ\text{C}$.

For the "symmetrically heated" case, where both disks were heated to similar temperatures (which increased radially), the Nusselt numbers were correlated for $G=0.138$ by

$$Nu_4 = 0.0054 Re_z^{0.30} Gr_4^{0.25}. \quad (2.17)$$

Long et al. [9] carried out a combined computational and experimental study for a simple cavity and for a compressor geometry. In the experiments, the disks and shrouds of the cavity could be independently heated; for the computations, they used an unsteady, three-dimensional (3D) elliptic solver with a mixing-length turbulence model. Their computations showed that some of the axial throughflow was ingested into the outer part of the cavity; in the outer region, near the heated shroud, cyclonic and anticyclonic vortices were observed.

In summary, it can be seen that heated rotating cavities, with or without an axial throughflow, produce complex flow structures. A radial gradient of temperature, produced by heating the disks or shroud, generates buoyancy effects that create three-dimensional unsteady flow. In addition, vortex breakdown, if it occurs in the axial jet, can further complicate the problem. A more detailed summary of buoyancy-induced flow in rotating cavities can be found in Ref. [13].

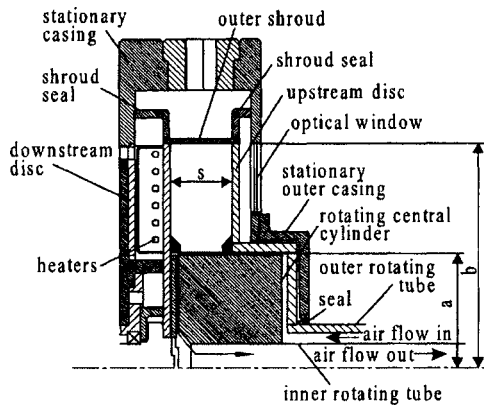


Fig. 2 Schematic diagram of rotating-cavity rig

3 Experimental Apparatus and Procedure

3.1 Experimental Rig. The rotating-cavity rig is shown in Fig. 2. The salient dimensions of the cavity were $a=150$ mm, $b=371$ mm, $\Delta r=4.8$ mm, and $s=75.2$ mm ($x_a=a/b=0.40$, $G=s/b=0.20$).

The downstream disk was made from 10-mm-thick steel, the back face of which was radiantly heated by a 21-kW stationary electric heater, and the front (cavity-side) face was covered by a 1-mm-thick glass-fiber mat in the outer surface of which 10 RDF fluxmeters and 10 thermocouples were embedded. The upstream disk, which was 12 mm thick, was made from transparent polycarbonate. The outer shroud was made from 5-mm-thick glass-fiber composite, the inner surface of which was thermally insulated by a 5-mm-thick layer of Rohacell foam. The inner cylinder, which was made from Rohacell foam, rotated synchronously with the two disks and the shroud. "Cobs," also made from Rohacell foam, were attached to the two disks; the cobs simulated the hubs found on compressor disks, and they also provided annular passages at inlet to and outlet from the cavity to encourage the air to enter and leave in the axial direction.

The rotating cavity and heater unit were enclosed by a stationary steel casing, designed to withstand a differential pressure of 3 bars. A window, in the upstream side of the casing, provided optical access for LDA measurements. Cooling air for the cavity, and pressurizing air for the outer casing, was supplied by a Bellis & Morcom compressor with a maximum output of around 1 kg/s at 4 bars absolute pressure. The cooling air was supplied, via stationary piping and an inlet volute, into the annular space between the rotating inner and outer tubes. The air then flowed radially outward through the axial and radial clearances between the rotating inner cylinder and the upstream disk. After flowing axially through the cavity, the air left the system, via the axial clearance between the inner cylinder and the downstream disk, through the rotating inner tube from where it flowed into a stationary tube. Radial vanes, attached to the upstream and downstream radial faces of the inner cylinder, ensured that the air entered the system with solid-body rotation. The "active" surfaces of the inner and outer rotating tubes were thermally insulated with a 5-mm-thick layer of Rohacell foam; this reduced the heat transfer to and from the air on its way to and from the rotating cavity.

Leakage of air between the rotating and stationary components was minimized by the use of five pressurized labyrinth seals. By feeding pressurized air to each seal, the pressure difference between the cooling air and the ambient air was minimized; this prevented, or reduced significantly, the loss of cooling air on its way to or from the rotating cavity. (The seal immediately downstream of the volute was the most difficult one to pressurize, and this resulted in loss of some of the inlet air. Consequently, the mass flow rates were based on the values measured at outlet from

the cavity.)

Owing to stress considerations, the maximum speed of the polycarbonate disk was limited to 1500 rev/min. The cavity was rotated by means of a combination of two thyristor-controlled dc motors (not shown in Fig. 2), with a total output of 26 kW, and the rotational speed of the cavity could be controlled to ± 1 rev/min. A toothed-belt and pulley system was used to transfer the power from the motors to the upstream and downstream disks; a layshaft ensured corotation of the two disks.

3.2 Instrumentation. As stated above, there were ten thermocouples and ten fluxmeters on the front (cavity-side) surface of the heated downstream disk. (Owing to failures, and to the fact that some of the instrumentation was covered by insulating foam, not all the fluxmeters were serviceable.) The signals from the rotating instrumentation were brought out through a 52-channel silver and silver-graphite slipring unit. The voltages were then measured using a computer-controlled Solartron data-logger and digital voltmeter with a resolution of ± 1 μ V. The uncertainty of the thermocouple measurements was estimated to be $\pm 0.3^\circ$ C. The uncertainty in the Nusselt numbers was dominated by the uncertainty in the radiation, as discussed in Sec. 4.1.

The temperatures of the air at inlet to and outlet from the system were measured using total-temperature probes inserted in the stationary tubing upstream and downstream, respectively, of the rig. The voltage outputs from the total-temperature probes were measured using the data logger. No instrumentation was attached to the shroud or to the inner cylinder, both of which were sensibly adiabatic, or to the polycarbonate disk, which was quasi-adiabatic.

The flow rates of the cooling air and sealing air were measured using orifice plates made to British Standards BS1042, and the estimated uncertainty was $\pm 3\%$ of the measured flow rate. The absolute pressures of the air, and the pressure drop across the orifice plates, were measured using a pair of absolute and differential pressure transducers multiplexed by a Scanivalve system, the outputs of which were recorded on the data logger.

The LDA system used was very similar to that described in Ref. [14], and only salient details are given here. The system used a 4-W Spectra-Physics argon-ion laser, the beam of which was transmitted to the optics through a fiber-optics cable with an efficiency of around 50%. The TSI optics, which were configured in a single-component back scatter mode, were mounted on an x - y traversing table, allowing movement in the radial and axial directions. By turning the transmitting optics through 90 deg, it was possible to measure either the radial or the tangential component of velocity. The transmitting optics included a Bragg cell which allowed frequency shifts of up to 40 MHz, and the beam spacing was 50 mm which, with a 250-mm focal-length lens, produced an optical probe volume around 1.4 mm long and 0.14 mm diameter. The Doppler signal from the receiving optics was processed by a TSI IFA-750 burst correlator, which could handle frequencies up to 90 MHz with signal-to-noise ratios as low as -5 dB. Micron-sized oil particles for the LDA measurements were injected into the cooling-air supply upstream of the rotating tubes in the rig. Table 1 shows the values of Re_ϕ , Re , and Ro for the test matrix.

4 Experimental Results

4.1 Analysis of Data. The rotational and axial Reynolds numbers, Re_ϕ and Re_z , are defined by Eqs. (2.12) and (2.13), with fluid properties based on conditions at inlet to the system. The local Nusselt number, Nu , used here is

$$Nu = \frac{qr}{k(T_o - T_i)} \quad (4.1)$$

where q is the convective heat flux, T_o is the disk temperature at radius r , and T_i is the temperature of the air at inlet.

The fluxmeters on the disk measured the total heat flux, comprising the convective and radiative fluxes. An approximate calculation for the radiation was used to estimate the radiative fluxes.

Table 1 Test matrix

Expt. no.	$Re_\phi(\div 10^6)$	$Re_z(\div 10^4)$	Ro
1	0.403	0.147	0.349
2	0.430	0.303	0.674
3	0.774	0.167	0.206
4	0.762	0.305	0.383
5	1.57	0.164	0.100
6	1.63	0.295	0.173
7	0.397	0.606	1.46
8	0.782	0.620	0.758
9	1.52	0.662	0.416
10	0.404	1.22	2.89
11	0.776	1.28	1.58
12	1.71	1.28	0.715
13	0.377	2.55	6.47
14	0.783	2.53	3.09
15	1.66	2.52	1.45
16	0.299	4.49	14.4
17	0.758	4.78	6.03
18	1.28	4.68	3.49
19	3.07	0.147	0.046
20	3.05	0.301	0.094
21	3.08	0.606	0.188
22	3.08	1.25	0.388
23	3.20	2.33	0.696
24	3.13	4.33	1.32

The calculation assumed blackbody radiation from the heated disk to the unheated one; the temperature of the unheated disk, which was not measured, was assumed to be equal to the temperature of the cooling air. This is likely to produce an overestimate of the radiation and an underestimate of the convective flux. The underestimate in the measured Nusselt numbers, Nu, is considered to be as high as 50; this is obviously significant for the smaller values of Nu presented below.

It should also be noted that the temperature of the heated disk varied from test to test. If the input power is left constant then the disk temperature will decrease as the Nusselt numbers increase. As the magnitude of Nu was unknown before the test was completed, it proved virtually impossible to control the power so as to produce a consistent temperature.

4.2 Velocity Measurements. Figure 3 shows the time-average radial variation of $V_\phi/\Omega r$, at $z/s=0.5$, for $Re_\phi=4.3 \times 10^5$, $Re_z=3000$, and $\Delta T \approx 75^\circ\text{C}$. It can be seen that $0.96 < V_\phi/\Omega r < 0.99$ for $0.67 < x < 0.97$; for these conditions, $|V_r/\Omega r| \leq 0.01$. These results, which were obtained in a thermal steady state approximately 3.5 h after the heaters had been switched on, are typical of those at other values of Re_ϕ and Re_z . The magnitude of $V_\phi/\Omega r$ is consistent with the Sussex measurements referred to in Sec. 2.

Figure 4 shows the variation of $V_\phi/\Omega r$ with ΔT , at $z/s=0.5$ and $x=0.674$, for the same values of Re_ϕ and Re_z used for Fig. 3. The time to reach the steady-state value of $V_\phi/\Omega r \approx 0.97$ at $\Delta T \approx 75^\circ\text{C}$ was approximately 3.5 h. Initially, before the heaters

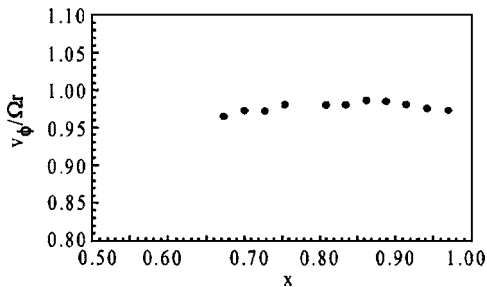


Fig. 3 Steady-state radial variation of $V_\phi/\Omega r$: $Re_\phi=0.43 \times 10^6$, $Re_z=0.30 \times 10^4$, $z/s=0.5$

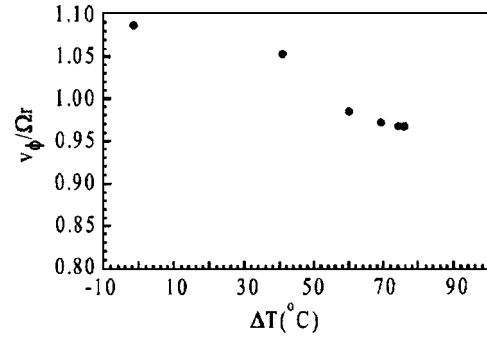


Fig. 4 Transient variation of $V_\phi/\Omega r$: $Re_\phi=0.43 \times 10^6$, $Re_z=0.30 \times 10^4$, $x=0.674$, $z/s=0.5$

were turned on, $V_\phi/\Omega r \approx 1.09$ at this value of x . The fact that $V_\phi/\Omega r > 1$ at $\Delta T=0$ and decreases as ΔT increases is consistent with the Sussex findings discussed in Sec. 2.

Figure 5 shows the instantaneous velocity measurements and power spectrum at different values of ΔT , for the same conditions as Fig. 4. For $\Delta T > 58^\circ\text{C}$, a dominant spike appears in the power spectrum at a frequency ratio of $f/f_o=1.92$, where f is the frequency of the spike and f_o the frequency of the rotating cavity. This is consistent with two pairs of cyclonic and anticyclonic vortices rotating at a speed approximately 4% slower than the disks.

Table 2 shows the spectral data derived from measurements of V_ϕ in the thermal steady states corresponding to the flow conditions given in Table 1. The ratio is the frequency ratio discussed above; PDS is the power density spectrum, which gives an indication of the relative strength of the dominant spike. It is considered that the data are most consistent for experiments 2, 4, 6, 7, 8, 9, 12, 14, 15, and 20, for which the number of vortex pairs are 2, 2, 2, 3, 2, 1, 2, 3, 2, and 3, respectively.

As stated in Sec. 1, this experimental work was conducted at the University of Bath as part of the ICAS-GT program, a summary of which is given in Ref. [15]. Complementary CFD studies

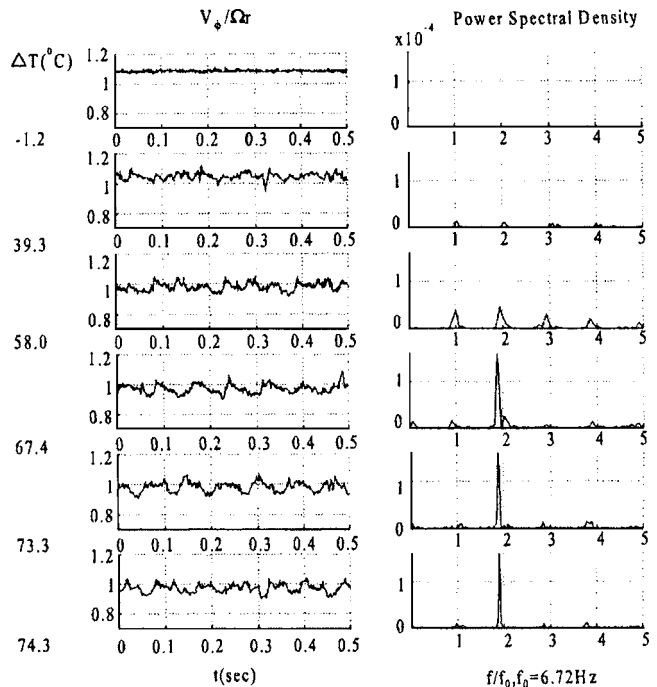


Fig. 5 Instantaneous and spectral velocity measurements for $Re_\phi=0.43 \times 10^6$, $Re_z=0.30 \times 10^4$, $x=0.674$, $z/s=0.5$

Table 2 Spectral data derived from V_ϕ measurements for thermal steady state

Normalized velocity and the highest peak in PDS							
Expt. 1, $f_0=6.72$ Hz				Expt. 2, $f_0=6.72$ Hz			
x	$V_\phi/\Omega r$	f/f_0	PDS	x	$V_\phi/\Omega r$	f/f_0	PDS
0.674	0.97	1.88	0.009	0.674	0.97	1.89	0.026
0.728	0.98	3.79	0.004	0.728	0.97	3.76	0.006
0.809	0.99	1.88	0.041	0.809	0.98	1.87	0.056
0.863	0.99	1.90	0.063	0.863	0.99	1.92	0.068
0.943	0.98	1.89	0.094	0.943	0.98	1.92	0.086
Expt. 4, $f_0=13.1$ Hz				Expt. 5, $f_0=26.3$ Hz			
x	$V_\phi/\Omega r$	f/f_0	PDS	x	$V_\phi/\Omega r$	f/f_0	PDS
0.674	0.97	1.90	0.051	0.674	0.77	0.03	0.004
0.728	0.98	3.78	0.012	0.728	0.78	0.85	0.007
0.809	0.98	1.88	0.104	0.809	0.83	0.85	0.081
0.863	0.98	1.90	0.133	0.863	0.84	0.02	0.055
0.943	0.98	1.88	0.168	0.943	0.89	0.01	0.079
Expt. 6, $f_0=26.3$ Hz				Expt. 7, $f_0=6.6$ Hz			
x	$V_\phi/\Omega r$	f/f_0	PDS	x	$V_\phi/\Omega r$	f/f_0	PDS
0.674	0.90	1.79	0.063	0.674	0.92	2.77	0.013
0.728	0.91	1.79	0.025	0.728	0.92	3.79	0.003
0.809	0.93	1.79	0.098	0.809	0.95	2.69	0.050
0.863	0.93	1.80	0.544	0.863	0.96	2.86	0.090
0.916	0.92	1.79	0.127	0.943	0.97	2.76	0.318
Expt. 8, $f_0=13.5$ Hz				Expt. 9, $f_0=26.2$ Hz			
x	$V_\phi/\Omega r$	f/f_0	PDS	x	$V_\phi/\Omega r$	f/f_0	PDS
0.674	0.92	1.84	0.078	0.674	0.75	0.81	0.027
0.728	0.93	3.69	0.016	0.728	0.77	1.57	0.063
0.809	0.95	1.84	0.212	0.809	0.82	0.83	0.188
0.863	0.94	1.84	0.249	0.863	0.85	0.82	0.105
Expt. 10, $f_0=6.65$ Hz				Expt. 11			
x	$V_\phi/\Omega r$	f/f_0	PDS	x	$V_\phi/\Omega r$	f/f_0	PDS
0.674	0.85	0.17	0.005	0.674	0.90	1.85	0.023
0.728	0.87	2.71	0.005	0.728	0.91	2.72	0.003
0.809	0.90	2.71	0.011	0.809	0.93	2.74	0.051
				0.863	0.94	0.27	0.046
				0.943	0.01	1.00	0.000
Expt. 12				Expt. 14			
x	$V_\phi/\Omega r$	f/f_0	PDS	x	$V_\phi/\Omega r$	f/f_0	PDS
0.674	0.85	1.75	0.164	0.674	0.81	2.66	0.108
0.728	0.85	0.01	0.112	0.728	0.82	2.66	0.019
0.809	0.88	1.75	0.203	0.809	0.86	2.66	0.022
0.863	0.90	1.75	0.900	0.863	0.88	2.68	0.125
0.943	0.93	0.88	0.229	0.943	0.93	2.66	0.204
Expt. 15				Expt. 16			
x	$V_\phi/\Omega r$	f/f_0	PDS	x	$V_\phi/\Omega r$	f/f_0	PDS
0.701	0.75	0.03	0.013	0.674	0.67	4.02	0.010
0.728	0.76	1.65	0.091	0.728	0.59	2.00	0.009
0.809	0.80	1.66	0.396	0.809	0.37	0.40	0.005
0.863	0.83	1.66	0.338	0.863	0.36	0.01	0.020
0.916	0.86	1.65	0.737				
Expt. 17				Expt. 19			
x	$V_\phi/\Omega r$	f/f_0	PDS	x	$V_\phi/\Omega r$	f/f_0	PDS
0.674	0.60	3.99	0.022	0.67	0.72	0.74	0.041
0.728	0.53	1.91	0.010	0.73	0.74	2.29	0.028
0.809	0.49	1.19	0.023	0.81	0.77	0.07	0.050
0.863	0.53	0.88	0.013	0.86	0.81	0.79	0.116
0.943	0.69	0.35	0.014	0.94	0.84	0.14	0.229
Expt. 20				Expt. 21			
x	$V_\phi/\Omega r$	f/f_0	PDS	x	$V_\phi/\Omega r$	f/f_0	PDS
0.674	0.61	1.18	0.031	0.674	0.56	1.36	0.034
0.728	0.62	2.05	0.138	0.728	0.58	1.36	0.053
0.809	0.67	2.05	0.291	0.809	0.60	0.02	0.070
0.863	0.70	2.06	0.342	0.863	0.65	1.37	0.023
0.943	0.75	2.05	0.086	0.916	0.68	0.18	0.023
Expt. 22				Expt. 23			
x	$V_\phi/\Omega r$	f/f_0	PDS	x	$V_\phi/\Omega r$	f/f_0	PDS
0.674	0.59	1.41	0.013	0.674	0.50	2.39	0.021
0.728	0.61	1.41	0.032	0.728	0.51	2.36	0.023
0.809	0.66	1.41	0.055	0.809	0.55	2.35	0.104
0.863	0.69	2.05	0.044	0.863	0.60	0.02	0.053
0.943	0.73	1.41	0.027	0.943	0.64	0.02	0.065

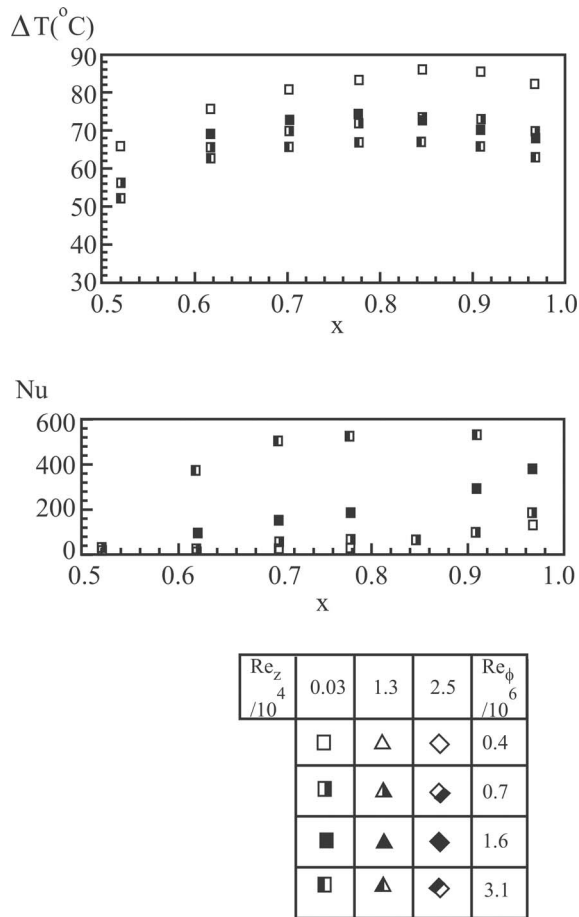


Fig. 6 Effect of Re_ϕ on ΔT and Nu for $Re_z=0.30 \times 10^4$

were conducted by Volvo Aero Corporation, MTU, and Rolls-Royce Deutschland; some of this work is also reported in Ref. [15]. The CFD code used by Volvo solved the 3D unsteady elliptic equations, using a $k-\epsilon$ turbulence model, with a grid of 2.6×10^6 cells. For experiment 2, the computed flow structure was consistent with that described above. For experiment 5, the other case computed, the computed flow became more unsteady with varying numbers of radial arms. The computations also produced heat fluxes that were in reasonably good agreement with the measurements. It should be pointed out, however, that these computations were computationally demanding, requiring around one month on an eight-node PC cluster or up to one year on a single PC.

4.3 Heat Transfer Measurements. Figures 6–8 show the effect of Re_ϕ on the steady-state values of ΔT and Nu for different values of Re_z . The values of Re_z and Re_ϕ are nominal, and precise figures are given in Table 1.

Figure 6 for $Re_z=0.3 \times 10^4$ shows that Nu increases as Re_ϕ increases and, in the main, as x increases. This is consistent with buoyancy-induced flow where there is a radial inflow of air on the heated disk, and the heat flux tends to decrease as x decreases. For $Re_z=0.16 \times 10^4$ (not shown here), the trends were similar but the magnitude of Nu was smaller. Figure 7 for $Re_z=1.3 \times 10^4$ shows similar trends to those shown in Fig. 6.

Figure 8 for $Re_z=2.5 \times 10^4$ shows different behavior for the larger values of Re_ϕ . In particular, for $Re_\phi=3.1 \times 10^6$, the magnitude of Nu is very large at the smaller values of x and Nu decreases as x increases. This effect, which was also observed at

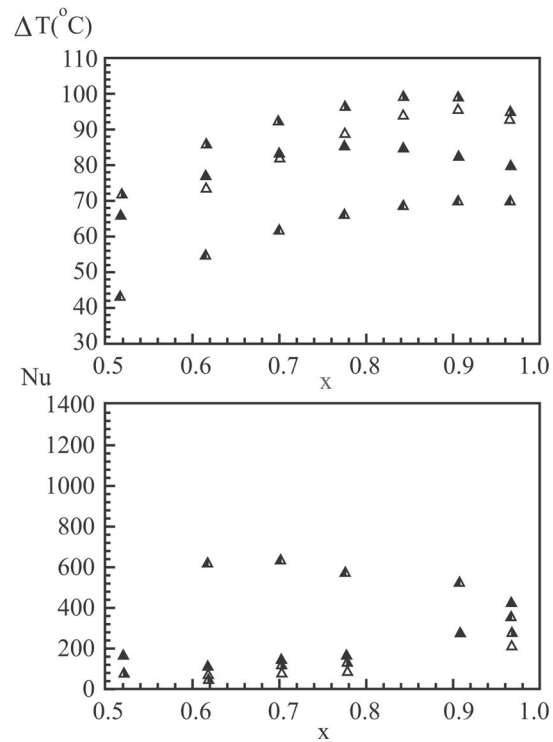


Fig. 7 Effect of Re_ϕ on ΔT and Nu for $Re_z=1.3 \times 10^4$ (for legend, see Fig. 6)

$Re_z=4.6 \times 10^4$, is believed to be caused by the penetration of the cooling air into the cavity, and it is possible that vortex breakdown has occurred.

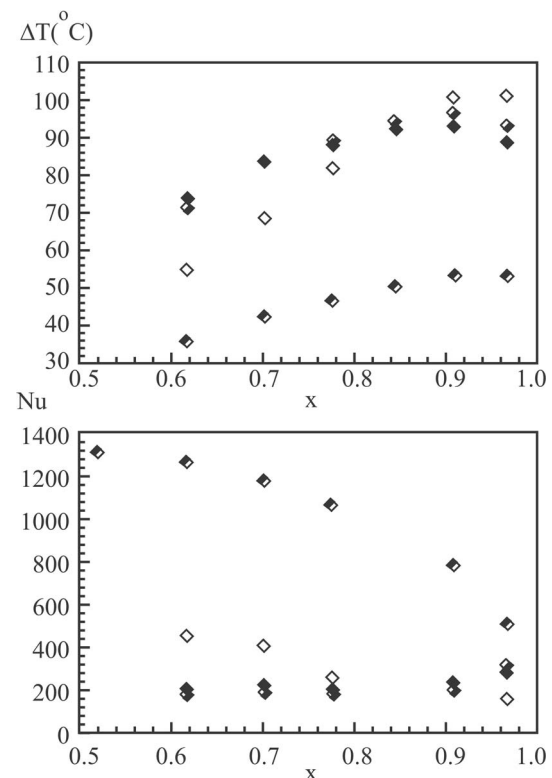


Fig. 8 Effect of Re_ϕ on ΔT and Nu for $Re_z=2.5 \times 10^4$ (for legend, see Fig. 6)

5 Conclusions

Velocity and heat-transfer measurements have been conducted in an annular rotating cavity with an axial throughflow of cooling air. The velocity measurements confirm that, when one disk is heated, the core of fluid outside the boundary layers rotates at a slower speed than the disks, and the ratio of the speed of the core to that of the disks decreases as ΔT increases. The velocity spectrum provides evidence of a multicell flow structure thought to comprise one, two, or three pairs of vortices. For $Re_z < 1.3 \times 10^4$, the measured Nusselt numbers tended to increase as x and Re_ϕ increased, which is consistent with buoyancy-induced flow. At the larger values of Re_z , a sharp increase in the magnitude of Nu was observed and Nu decreased radially; the effects were consistent with the circulation created by the cooling air dominating over the buoyancy-induced flow.

Acknowledgment

The authors wish to acknowledge the valuable contribution made by the consortium partners of ICAS-GT and to thank the industrial partners and the European Commission for their financial support.

Nomenclature

a	= inner radius of cavity (radius of inner cylinder)
b	= outer radius of cavity
d	= diameter of circular inlet
f	= frequency
f_0	= cavity frequency
\tilde{g}	= acceleration
G	= s/b , gap ratio
Gr	= $\tilde{g}L^3\beta\Delta T/\nu^2$, Grashof number
k	= thermal conductivity
L	= characteristic length
\dot{m}	= mass flow rate
n	= number of vortex pairs
Nu	= $qL/k\Delta T$, Nusselt number
Pr	= ν/α , Prandtl number
q	= heat flux
r	= radius
r_m	= $1/2(a+b)$, mean radius of annulus
Ra	= $PrGr$, Rayleigh number
Re_2	= $\Omega r_m s/\nu$, rotational Reynolds number
Re_3	= $\Omega r_m b(1-x_a)/\nu$, rotational Reynolds number
Re_ϕ	= $\Omega b^2/\nu$, rotational Reynolds number
Re_z	= WL/ν , axial Reynolds number
Ro	= $W/\Omega a$, Rossby number
s	= axial gap between disks
t	= time
T	= absolute temperature
V_r, V_ϕ	= radial, tangential components of velocity in stationary frame of reference
W	= bulk-average axial velocity
x	= r/b , nondimensional radius

x_a	= a/b , radius ratio of cavity
z	= axial distance from heated disk
α	= thermal diffusivity
β	= T_{ref}^{-1} volume expansion coefficient
Δr	= radial clearance of annular inlet
ΔT	= temperature difference
μ	= dynamic viscosity
ν	= kinematic viscosity
ρ	= density
Ω	= angular speed of cavity

Subscripts

av	= average value
C	= cold surface
H	= hot surface
I	= inlet value
o	= disk surface ref reference value
s	= shroud surface
2,3,4,5	= refer to Nu, Gr, Ra used in different definitions

References

- [1] Bohn, D., Dibelius, G. H., Deuker, E., and Emunds, R., 1994, "Flow Pattern and Heat Transfer in a Closed Rotating Annulus," *ASME J. Turbomach.*, **116**, pp. 542–547.
- [2] Bohn, D., Deuker, E., Emunds, R., and Gorzelitz, V., 1995, "Experimental and Theoretical Investigations of Heat Transfer in Closed Gas Filled Rotating Annuli," *ASME J. Turbomach.*, **117**, pp. 175–183.
- [3] Bohn, D., Edmunds, R., Gorzelitz, V., and Kruger, U., 1996, "Experimental and Theoretical Investigations of Heat Transfer in Closed Gas-Filled Rotating Annuli II," *ASME J. Turbomach.*, **118**, pp. 11–19.
- [4] Bohn, D., and Gier, J., 1998, "The Effect of Turbulence on the Heat Transfer in Closed Gas-Filled Rotating Annuli," *ASME J. Turbomach.*, **120**, pp. 824–830.
- [5] King, M. P., 2003, "Convective Heat Transfer in a Rotating Annulus," Ph.D. thesis, University of Bath, UK.
- [6] Farthing, P. R., Long, C. A., Owen, J. M., and Pincombe, J. R., 1992, "Rotating Cavity with Axial Throughflow of Cooling Air: Flow Structure," *ASME J. Turbomach.*, **114**, pp. 237–246.
- [7] Farthing, P. R., Long, C. A., Owen, J. M., and Pincombe, J. R., 1992, "Rotating Cavity with Axial Throughflow of Cooling Air: Heat Transfer," *ASME J. Turbomach.*, **114**, pp. 229–236.
- [8] Long, C. A., 1994, "Disk Heat Transfer in a Rotating Cavity with an Axial Throughflow of Cooling Air," *Int. J. Heat Fluid Flow*, **15**, pp. 307–316.
- [9] Long, C. A., Morse, A. P., and Tucker, P. G., 1997, "Measurement and Computation of Heat Transfer in High Pressure Compressor Drum Geometries with Axial Throughflow," *ASME J. Turbomach.*, **119**, 51–60.
- [10] Long, C. A., and Tucker, P. G., 1994, "Numerical Computation of Laminar Flow in a Heated Rotating Cavity with an Axial Throughflow of Air," *Int. J. Numer. Methods Heat Fluid Flow*, **4**, pp. 347–365.
- [11] Long, C. A., and Tucker, P. G., 1994, "Shroud Heat Transfer Measurements from a Rotating Cavity with an Axial Throughflow of Air," *ASME J. Turbomach.*, **116**, pp. 525–534.
- [12] Owen, J. M., and Pincombe, J. R., 1979, "Vortex Breakdown in a Rotating Cylindrical Cavity," *J. Fluid Mech.*, **90**, pp. 109–127.
- [13] Owen, J. M., and Rogers, R. H., 1995, *Flow and Heat Transfer in Rotating-disc Systems, Vol. 2: Rotating Cavities*, Research Studies Press, Taunton, Wiley, New York.
- [14] Kilic, M., Gan, X., and Owen, J. M., 1994, "Transitional Flow between Contra-Rotating Discs," *J. Fluid Mech.*, **281**, pp. 119–135.
- [15] Smout, P. D., Chew, J. W., and Childs, P. R. N., 2002, "ICAS-GT: A European Collaborative Research Programme on Internal Cooling Air Systems for Gas Turbines," ASME Paper No. 2002-30479.

Giovanni Cataldi

e-mail: giovanni.cataldi@power.alstom.com

Harald Güntner

Charles Matz

Tom McKay

Jürgen Hoffmann

Anton Nemet

ALSTOM (Switzerland) Ltd.,
Brown Boveri Strasse 7,
CH-5401 Baden, Switzerland

Stefan Lecheler

Universität der Bundeswehr München,
Werner-Heisenberg-Weg 39,
D-85577 Neubiberg, Germany

Jost Braun

Kempten University of Applied Sciences,
Bahnhofstrasse 61-63,
D-87435 Kempten, Germany

Influence of High Fogging Systems on Gas Turbine Engine Operation and Performance

High fogging is a power augmentation device where water is sprayed upstream of the compressor inlet with higher mass flow than that which would be needed to saturate the intake air. The main focus of this paper is on applications of high fogging on the ALSTOM gas turbine engines of the family GT24/GT26. Engine operation and performance are illustrated based on test results obtained from four different engines that have meanwhile accumulated more than 12,000 operating hours (OH) in commercial operation with ALSTOM's ALFog[®] high fogging system. The effect of internal cooling (water evaporation inside the compressor) is investigated considering actual compressor boundaries matched within the complete engine. Changes in the secondary air system (SAS) and corresponding movement of the engine operating line have been taken into account. Power output gain as high as 7.1% was experimentally demonstrated for injected water mass fraction ($f = m_{H_2O}/m_{air}$) equal to 1% and considering internal cooling effects only. Higher figures can be obtained for operation at low ambient relative humidity and partial evaporation upstream of the compressor inlet. [DOI: 10.1115/1.1926313]

1 Introduction

The effects of water ingestion and evaporation inside axial compressors have been subject to experimental and theoretical investigation since the early applications of turbojet engines for aircraft propulsion. There are two reasons for this: Aircraft engines are naturally subject to water ingestion in case of rain; water injection at the inlet of the compressor was recognized to be a convenient solution for increasing temporarily the engine thrust (for example, to allow faster take-off during hot days).

When liquid water is introduced at the compressor inlet, the compression of the gas-phase is no longer adiabatic: The injected water (liquid-phase) evaporates inside the compressor; the heat of evaporation is supplied by the gas-phase, which is consequently cooled down. Due to the "creation" of gas—in the form of water vapor—and to the (internal) cooling of the gas-phase, the volume flow distribution through the compressor varies. Consequently, the flow velocity triangles and the aerodynamic load of the compressor blades and vanes also change. In common literature the expression "internal cooling" is used to refer to the composition of these thermodynamic and aerodynamic phenomena.

Studying the early publications about internal cooling, remarkable is the work of Hill [1] published in 1963. The author described the effects of internal cooling including the load redistribution among the compressor stages and the corresponding variation of the compressor characteristics.

In recent years, internal cooling has gained renewed interest.

Major gas turbine manufacturers have started investigating its application as a means of power augmentation for stationary gas turbine engines.

Of particular significance are the results obtained by Utamura et al. [2] in 1998 and the analysis done by Horlock [3] in 2001. Two noteworthy papers have also been presented in the last ASME Turbo Expo 2003 by Härtel and Pfeiffer [4] as well as by White and Meacock [5].

Since the year 2000, ALSTOM (Switzerland) has been running a development program with the purpose of investigating the impact of conventional air inlet cooling systems and high fogging on heavy-duty gas turbine engines. A good summary of the development work has been presented by Lecheler and Hoffmann [6]. Preliminary results have been reported by Hoffmann [7] and by Hoffmann and Ojo [8].

Validation of high fogging on gas turbine engines of the type GT24/GT26 has been completed. This paper summarizes the results of this validation phase.

The first part of the paper deals with the integration of the ALFog[®] high fogging system within the gas turbine engine: The operation concept and the hot commissioning adjustments are described; the methods applied to evaluate the engine tests with high fogging are briefly explained.

The second part is mainly focused on the impact of internal cooling on the compressor and engine performance parameters. Furthermore, the reasons behind the required changes in the engine operation concept and the commissioning procedure are outlined. The figures presented are based on calculations made using a complete engine model fully calibrated and validated on the basis of the test results. The compressor behavior is also described for operation with real boundary conditions corresponding to a complete matching with the other engine components and, in particular, with the secondary air system (SAS). This has not been done so far in the open literature.

Contributed by the International Gas Turbine Institute (IGTI) of ASME for publication in the JOURNAL OF ENGINEERING FOR GAS TURBINES AND POWER. Manuscript received October 1, 2003; final manuscript received March 1, 2004. IGTI Review Chair: A. J. Strazisar. Paper presented at the International Gas Turbine and Aeroengine Congress and Exhibition, Vienna, Austria, June 13–17, 2004, Paper No. GT2004-53788.

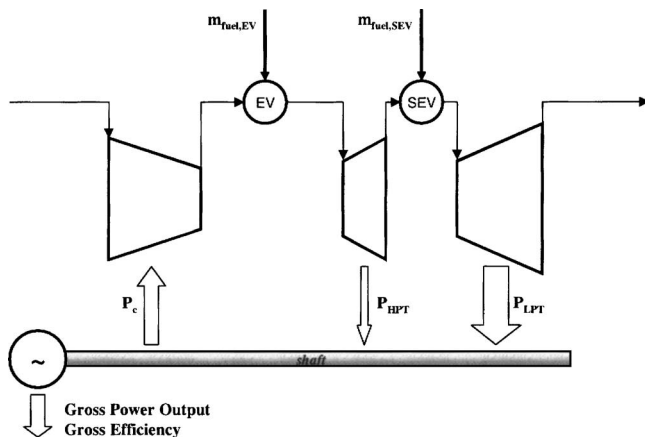


Fig. 1 Architecture of the GT24/GT26 engine family

1.1 Nozzle Type and Droplets Behavior. The engine tests have been carried out using nozzles with Sauter mean droplet diameter D_{Sauter} , see definition in Eq. (1), smaller than $30 \mu\text{m}$ as average of measurements over the whole plume conducted in still air.

$$D_{Sauter} = \left(\sum N_j \cdot D_j^3 \right) / \left(\sum N_j \cdot D_j^2 \right) \quad (1)$$

In order to obtain a performance benefit by a reduction of the initial droplet size (using different nozzles), the water droplets have to be small enough to remain entrained in the flow and follow the streamlines without impacting over the compressor blades. Based on preliminary calculations, White and Meacock [5] have pointed out that only droplets smaller than $\sim 5 \mu\text{m}$ are capable of doing so.

Droplets with a larger diameter impinge quickly upon the blade surface, consequently, there is a film evaporation, which is mainly driven by the extension of the blade surface area rather than by the initial droplet size (Hill [1]).

The nozzles currently available on the market, and suitable for gas turbine applications, are not capable of producing droplets smaller than $5 \mu\text{m}$ over the whole spray. Therefore, the results presented in this paper can be considered generally valid with respect to the present technology.

Together with droplet size, other factors characterize the quality of a nozzle and have to be taken into account to choose the best nozzle for high fogging applications. In particular: Robustness and performance stability over a lifetime; water mass flow at design supply pressure; specific purchase and installation costs with respect to nozzle water mass flow. At the same time, aspects associated to compressor blade and vane materials and to their resistance to erosion have to be considered as well.

1.2 Architecture and Performance of GT24 and GT26.

Readers not familiar with the architecture of the GT24/GT26 engine family can refer to the sketch in Fig. 1.

GT24 and GT26 are single-shaft engines that operate on a unique re-heated thermodynamic cycle making use of two individually controlled combustion chambers. The compressor inlet mass flow is regulated by means of three rows of variable inlet guide vanes (VIGV). All this results in high efficiency throughout the whole load range.

Table 1 shows the main performance parameters for operation on Natural Gas at ISO conditions [9].

2 High Fogging System

In order to ensure safe engine operation without affecting component lifetime, each high fogging system has to be well integrated within the gas turbine engine. This has been one of the

Table 1 GT24 and GT26 on Natural Gas at ISO conditions [9] (engines equipped with quench coolers in the secondary air system)

		GT24	GT26
Grid frequency	Hz	60	50
Shaft speed	Rpm	3600	3000
Gross electrical output	MW	187.7	280.9
Gross electrical efficiency	%	36.9	38.3
Gross heat rate	kJ/kWh	9756	9400
Compressor pressure ratio	-	32:1	32:1
Exhaust gas flow	kg/s	445	632
Exhaust gas temperature	$^{\circ}\text{C}$	612	615
NO_x emissions (corrected to 15% O_2 , dry)	vppm	<25	<25

main targets during the development of the ALFog[®] high fogging system.

As shown in Fig. 2, the hardware of the ALFog[®] high fogging system mainly consists of a nozzle rack installed in the engine air intake and connected to a pump skid. In order to avoid large secondary droplet formation (e.g., over the supporting structures inside the air intake), the nozzle rack is located relatively close to the compressor inlet.

The control of the ALFog[®] high fogging system is integrated into the gas turbine engine control logic. The local unit governs the pump skid and exchanges signals with the engine core controller (more details in Sec. 2.1).

The nozzle rack is divided into nozzle-groups. The sprayed water mass flow can be regulated by activating a certain number of nozzle-groups while keeping the water supply pressure constant ($\sim 140 \text{ bar}$ in typical installations).

The sprayed water evaporates mainly *inside* the compressor (“*internal cooling*”), but also partly *upstream* of it in the portion of air intake between the nozzle rack and the compressor inlet (“*evaporative air inlet cooling*”).

The effect of evaporative air inlet cooling is a reduction in temperature and an increase in humidity at the inlet of the compressor. Consequently the gas turbine engine reacts in a similarly way as it would for normal variations in ambient conditions.

Internal cooling, instead, introduces significant changes in the pressure and temperature build-up along the compressor (refer to Sec. 3). Specific engine adjustments are required for safe operation and in order not to affect component lifetime. These adjustments are described in Sec. 2.2.

In order to investigate and model high fogging properly, both *evaporative air inlet cooling* and *internal cooling* effects have to

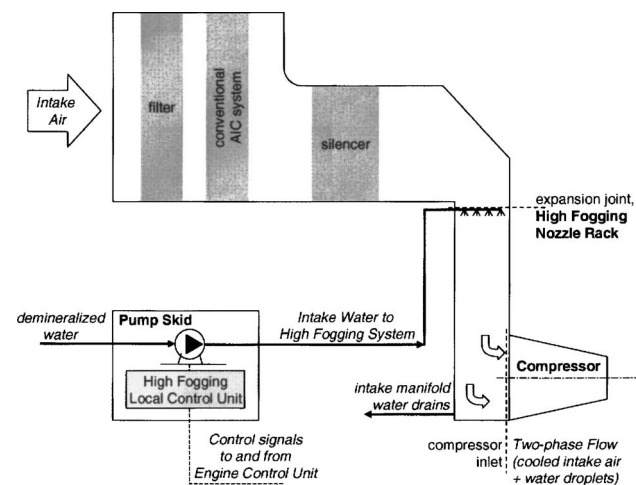


Fig. 2 High fogging system layout and engine air intake

be analyzed and quantified. More details about test evaluation and engine modeling are provided in Sec. 2.3.

2.1 Operation Concept. The expression “operation concept” is used to refer to a set of rules and physical values that describe the limits within which a certain system can operate and the way it reacts to external inputs and boundary conditions.

The ALFog[®] high fogging system operation concept is practically an extension of the overall engine concept. It determines the way the gas turbine and the high fogging system react to inputs from the operator of the power plant and to variable ambient conditions. Great attention has to be paid to the determination of the operation concept. Operation rules and settings will significantly influence the engine performance gain with high fogging, the availability of the high fogging system and the engine safety of operation.

This section illustrates the main aspects that require investigation and the corresponding changes that have been applied for updating the operation concept of the GT24/GT26 engine family.

2.1.1 ALFog[®] High Fogging System Operational Cycle. The plant operator sets the desired power output load set point of the plant (LSP) depending on the power demand that the plant is facing. In the case that the LSP is higher than what the plant can produce at base load, the operator can decide to activate a power augmentation device, e.g., high fogging. If the ambient relative humidity is low, the activation of a conventional AIC system is recommended beforehand to improve the uniformity of the temperature profile at the compressor inlet (see item “b” below for more information).

During operation, the high fogging system constantly regulates the water mass flow to the minimum amount sufficient for achieving the LSP. Variations of ambient conditions and possible changes of LSP are automatically compensated for. As the water mass flow can be regulated only in discrete steps, fine tuning of the power output is achieved by regulating the standard engine control parameters: VIGV and turbine inlet temperature (TIT).

In ALSTOM gas turbines, the TIT is calculated—in accordance with ISO 2314 [9]—from measured input parameters (i.e., turbine outlet temperature, turbine pressure ratio, and ambient temperature) as mixed turbine inlet reference temperature. The hot gas temperature corresponding to the TIT is evaluated by means of a heat balance in a performance measuring point.

Maximum engine power output is obtained with full water mass flow and with VIGV and hot gas temperature (at turbine inlet) corresponding to the same settings as for engine base load operation without high fogging.

High fogging shut down can be initiated manually by the operator or automatically by the engine control system when LSP is reduced below the values that the plant is capable to reach without high fogging.

2.1.2 Engine Protection Considering High Fogging. Several issues have to be considered concerning engine protection and safety of operation. Some of them are general and valid for all engine types, others are engine type specific. In the next paragraphs, five issues of particular importance are described together with their solutions:

- (a) *Ice formation in the first compressor vane and blade rows.* Because of the flow acceleration within the inlet guide vanes of the compressor, water condenses from the air stream and ice can be formed even with ambient temperature higher than 0°C and without high fogging. Air inlet cooling exacerbates this problem as it reduces the temperature at the compressor inlet and increases the water content of the flow. High fogging operation is, therefore, limited to a certain minimum ambient wet-bulb temperature. Figure 3 shows the corresponding limiting curve in terms of ambient temperature and relative humidity.

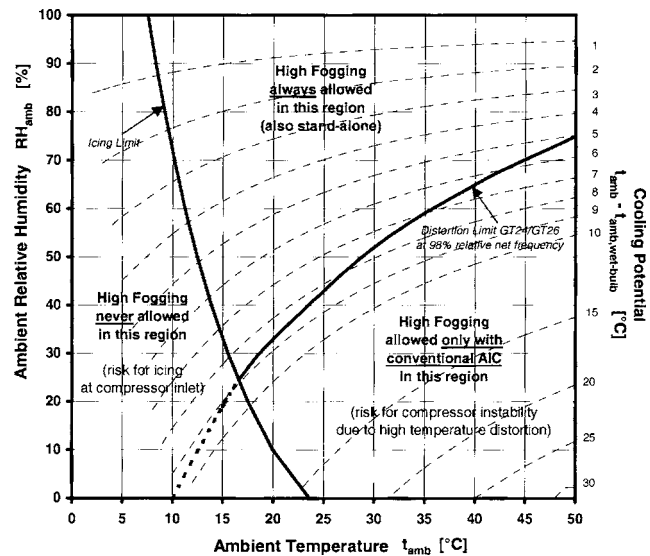


Fig. 3 Limits of operation with high fogging

- (b) *Induced distortion of the temperature profile at the compressor inlet.* When high fogging operates as a standalone system (without being assisted by conventional AIC) and at low water mass flow, only some of the nozzle-groups are activated. The cooling of the intake air is consequently not perfectly homogeneous. It is safe to assist high fogging with a conventional AIC system in case of ambient conditions with high cooling potential ($t_{\text{amb}} - t_{\text{amb,wetbulb}}$). Figure 3 shows the corresponding limiting curve. Its particular position is engine type specific, a conservative calculation approach has been applied. The cooling potential at each ambient condition is also represented in the diagram by means of dashed lines.
- (c) *Engine operation at low grid frequency.* Internal cooling modifies the aerodynamic loading along the compressor and can reduce the surge margin. Careful analysis of the flow stability through the compressor is therefore needed to determine the minimum compressor reduced speed (n_{in}^*) at which it can operate safely.

$$n_{\text{in}}^* = \frac{n}{\sqrt{R_{\text{air}} \cdot T_{\text{air}}}} \quad (2)$$

This results in a limitation on the minimum allowable grid frequency. Based on Eq. (2), it can be shown that this limitation has to be more stringent at high compressor inlet temperature T_{air} .

- (d) *Fuel mass flow regulation during transients.* As the fuel mass flow with high fogging is higher than during normal operation ($\sim 5.5\%$ more for $f=1\%$), special attention has to be paid to the controller capability during transient operation. Extensive test and calibration campaigns have proven the developed engine control system to be very robust and effective in keeping constant hot gas temperature during transients [8].
- (e) *Drain supervision.* Water aggregation at the bottom of the compressor bell-mouth can cause water sheets to be sucked into the compressor. The effect would be progressive erosion of compressor vanes and blades.

The problem has been solved by installing sensors for continuous monitoring of proper functioning of the water drain lines. Besides that, it is furthermore important to ensure a controlled flow pattern and sufficient distance between the lower edge of the bell-mouth and the actual position of the blades.

2.2 Hot Commissioning. The task of the hot commissioning is to adjust the engine according to the operational limits which are part of the operation concept (see Sec. 2.1). This is needed to fulfill the operational requirements of the engine. In addition, operation has to be safe with regard to combustion behavior (pulsations) and mechanical integrity.

For the three commercial GT24/GT26 engines equipped with high fogging, the hot commissioning consisted of the following main tests:

- *emission* measurements at varying hot gas temperatures up to base load in “dry” and in high fogging operation,
- performance measurements at *part load* in “dry” operation,
- *base load adjustments* by carrying out performance measurement points at base load in both “dry” and high fogging operation.

As part of the development program, two additional comprehensive test campaigns on the GT26 at the ALSTOM test center in Birr (Switzerland) were carried out beforehand.

The following tests have also been undertaken in order to validate mechanical integrity and operation of the high fogging system and its impact on transient engine operation:

- *transient loading and de-loading* tests with high fogging,
- traverse measurements of the *air intake flow velocity*,
- *vibration measurements of the nozzle rack*,
- optimization of the *positioning of the nozzles* on the high fogging nozzle rack.

The secondary air system (SAS) consists of all pipes and connections that are used to convey the cooling air from the compressor extractions to the combustor and turbine hot parts. As explained in Sec. 3, internal cooling changes the temperature, composition and mass flow at the compressor extractions. During hot commissioning, the SAS can be adjusted by modifying the diameter of orifices installed in the main cooling air pipes. For engines equipped with high fogging, special orifices settings have been designed according to the engine adjustment requirements (the engine base load adjustment has to be done for final orifice configuration, as any change in the SAS slightly modifies the relation between TIT and hot gas temperature).

With the help of the above mentioned tests, it was possible to determine and implement an optimized operation concept. The performance targets were reached while ensuring safe engine operation.

2.3 Experimental Tests and Models. The development program conducted within ALSTOM (Switzerland) included engine tests with evaporative coolers, chillers, fogging systems and high fogging systems.

A typical high fogging test run consists of a sequence of performance measurement points with increasing sprayed water mass flow from $f=0\%$ to approximately $f=1.2\%$. Each test run includes at least one “dry” point (PMP_{dry}) and several points with high fogging active (PMP_{HF}).

For the GT24/GT26 engine family, 35 measurement points with the ALFog[®] high fogging system at simple cycle base load operation have been taken (other measurement points at part load and in combined cycle operation have also been recorded). The points are uniformly distributed among the four tested engines and within the mass flow range specified above.

During the tests, the engines were equipped with performance test instrumentation, where the most important are listed below:

- t , p , RH of ambient air,
- VIGV position of compressor variable inlet guide vanes,
- n shaft rotational speed (grid frequency),
- t , p , m at the three compressor extractions,
- t , p at compressor and turbine outlets,
- p upstream of turbine inlets,

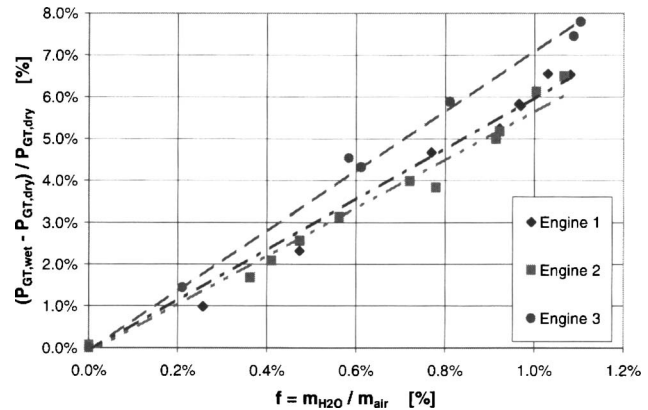


Fig. 4 Gross power output gain due to internal cooling, based on measurements with high fogging on the three commercial GT24/GT26 engines; all points corrected to ISO conditions

- P_{GT} gas turbine engine gross power output,
- t , p , m of fuel flows to EV and SEV combustors,
- fuel composition (based on analysis of fuel samples taken during each performance measurement point).

Additional validation instrumentation was installed inside the compressor and at its boundaries.

For each PMP_{HF} it is possible to determine the compressor inlet temperature and humidity on the basis of the knowledge about evaporative air inlet cooling previously gained at ALSTOM (based on complete engine tests with sprayed water mass flow below the saturation limit). In half of the cases, the air upstream of the high fogging system was already saturated or very close to saturation ($RH > 85\%$); for these points, the knowledge regarding evaporative air inlet cooling was not needed or had very little impact on the evaluation.

By using the measurements and the knowledge about evaporative air inlet cooling, it is possible to compute a complete heat balance in each PMP_{HF} . As a result, both the compressor inlet mass flow and the hot gas temperatures in each measurement point can be obtained.

In order to analyze the effect of internal cooling, it is necessary to determine and separate the effect of evaporative air inlet cooling. This has been done by simulating the dry engine behavior for operation at same compressor inlet conditions (t_{air} , RH_{air}) as in the points with high fogging and for no water entering the compressor in liquid state ($m_{H2O}=0$). In this way, for each PMP_{HF} , a “dry” point with evaporative air inlet cooling ($PMP_{dry+evapcooling}$) has been evaluated.

For each engine parameter, the differences between the values in the two heat balances ($PMP_{HF} - PMP_{dry+evapcooling}$) can be plotted versus the water mass fraction at the compressor inlet ($f = m_{H2O}/m_{air}$).

As an example, Fig. 4 shows the effect of internal cooling on the engine power output. When considering Fig. 4, two facts are particularly notable: The high measured power gain, and the linearity of the relation between power gain and water mass fraction. From this result, we can derive that, at least up to $f=1.2\%$, the alteration of the velocity triangles and the consequent mismatching among the compressor stages is not hurting the engine performance significantly.

Beside the performance improvement, the analysis of the experimental data revealed the following effects on the compressor due to internal cooling (refer also to Sec. 2):

- decreases of m_{air} by $\sim 0.5\%$ for $f=1\%$,
- decrease of t_{ex} and t_{out} ,
- decrease of (p_{ex}/p_{out}) with consequent reduction of m_{ex} .

2.3.1 *Thermodynamic Engine Model and Detailed Compressor Model.* During the development work, mainly two types of models have been updated and used to evaluate the measurements.

- Thermodynamic engine model:
It makes use of characteristic-based simplified modules for each engine component and is used for computation of engine heat balances and for complete engine prediction calculations. Each simplified module is calibrated on the basis of the detailed model of the corresponding component.
- Detailed compressor model:
It is used to gain more insight in the flow properties along the compressor. It is also needed to extrapolate predictions to other compressors with different geometry and positioning of the extractions.

The improvement in the thermodynamic engine model mainly consisted in the introduction of an evaporative air inlet cooling module, and in the upgrade of the compressor module with the two following modifications (more details in [8]):

- the thermodynamic equations now include the liquid water mass flow through the compressor;
- empirical correction factors have been introduced in the equations used for the calculations of inlet air mass flow and extraction temperatures and pressures.

The detailed compressor model has also been upgraded. New functions to perform heat transfer and water evaporation calculations along the compressor mean streamline have been introduced.

The focus of this paper is on the overall engine. Therefore, it deals mainly with results obtained using the thermodynamic engine model.

3 Internal Cooling

This second part of the paper gives a description of the physical phenomena involved in internal cooling and their impact on the engine performance. All diagrams and illustrations are based on the thermodynamic engine model of an engine of the family GT24/GT26. All parts of the model (including the internal cooling features of the compressor module and the pressure losses through the SAS) have been calibrated beforehand based on engine test results.

All calculations are done at engine base load operation and ISO ambient conditions ($T_{\text{air}}=15^\circ\text{C}$, $\text{RH}_{\text{air}}=60\%$). The scope is to illustrate the effect of internal cooling. Therefore, it is assumed that all the sprayed water enters the compressor in liquid state (no drains and no evaporative air inlet cooling) as if the spray-nozzles were installed immediately upstream of the compressor inlet.

A brief description of internal cooling has already been given in the introduction. The topic has also been investigated in Ref. [1–5]. It is convenient to divide the physical phenomena that take place inside the compressor with internal cooling into two categories:

- (a) Thermodynamic phenomena:
 - heat extraction from the gas-phase in order to supply the heat of evaporation to the liquid water with reduction of the temperature build-up along the compressor;
 - increase of the gas-phase mass flow along the compressor due to the evaporation of the liquid water and generation of superheated water vapor;
 - change of the composition of the gas-phase with associated increase of c_p .
- (b) Aerodynamic phenomena:
 - change of the volume flow along the compressor with increase in the front stages and reduction in the rear part (well illustrated in [5]), corresponding alteration of the velocity triangles and consequently rearward shifting of the pressure build-up along the compressor;

- shifting of the aerodynamic loading towards the rear stages;
- increased airfoil trailing edge flow angle deviations on wet blades (resulting in a weakening of the stage characteristics in the first blade rows);
- alteration of the overall compressor characteristics and of the surge limit.

The phenomena listed above are connected with one another. The links are the balances of mass flow, mechanical momentum, and energy; the corresponding equations have to be fulfilled in each compressor stage. The mentioned changes in pressure, temperature and volume flow along the compressor can be calculated as solution to this system of equations. The topic is treated in detail also in Refs. [1,3,5].

A complete solution of the flow field allows evaluations of the compressor stability and of the mechanical stresses in the blades, both dependent on the particular compressor design. During the development of the ALFog[®] high fogging system, an upgraded detailed compressor model (refer to Sec. 2.3) has been used to solve the flow field along the compressor.

The changes inside of the compressor propagate to all other engine components, physical equilibrium has to be fulfilled. In particular:

- (c) Variation of mass flows and physical properties of the secondary cooling air flows from the compressor to combustor and turbine hot parts.
- (d) Movement of the operating line in the compressor map, due to the variation of the relative compressor outlet mass flow ($m_{\text{out}}/m_{\text{in}}$) while the turbine swallowing capacity remains practically constant.
- (e) Variation of the power input to the compressor and of the power output from the turbines as well as change of simple cycle performance and of energy input to a possible bottoming steam cycle.

These latter issues (items (c)–(e)) have been addressed by using the upgraded thermodynamic engine model (refer to Sec. 2.3).

Item (c) is mainly due to the rearward shifting of the pressure build-up along the compressor, see item (b): The relative extraction pressures ($p_{\text{ex}}/p_{\text{out}}$) decrease and the cooling air mass flows through the secondary air system (SAS) are affected. Particular engine adjustments are needed to avoid undesired reduction of lifetime as described in Sec. 2.2.

The variation of the SAS mass flows has significant impact on the whole engine, e.g., item (d) is basically determined by it. Therefore, it is efficient to divide the analysis into two sections with similar structure but with different assumptions on the SAS hardware.

In Sec. 3.1, it is assumed that the SAS hardware contains variable components (e.g., valves instead of the orifices) that can be automatically regulated in order to maintain the relative cooling air mass flows constant:

$$m_{\text{ex}}/m_{\text{in}} = \text{constant} \quad (3)$$

In this way, it is possible to investigate the so-called “pure” effects of internal cooling (refer also to [1–5]).

In Sec. 3.2, the SAS hardware consists of fixed components only which is usually the case for heavy-duty gas turbine engines. In that case, Eq. (3) cannot be fulfilled for all operating points and the calculated effects are the sum of the “pure” internal cooling and of the changed relative mass flows at the compressor extractions. This has not yet been shown in the open literature.

The engine behavior is also affected by the operation concept settings (refer to Sec. 2.1). The analysis in this paper is based on the two following boundary conditions:

- The position of the variable inlet guide vanes (VIGV) is

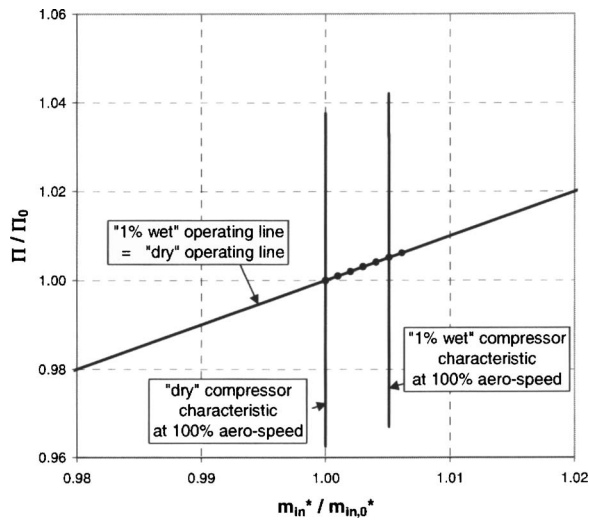


Fig. 5 Compressor characteristics and engine operating line considering variable SAS hardware

kept constant at engine base load independently of the sprayed water mass flow.

- The fuel mass flows are controlled in order to keep constant hot gas temperatures at the turbine inlets.

3.1 Variable SAS Hardware, “Pure” Internal Cooling. By virtually fixing the value of m_{ex}/m_{in} at each compressor extraction in the model, it is possible to simulate the “pure” effect of internal cooling. On a real engine, this kind of operation could be made possible by installing control valves in the SAS in order to maintain constant relative supply pressures after the valves. Consequently, the relative cooling air mass flows to combustor and turbine hot parts will also remain constant independently of the injected water mass flow.

With variable SAS hardware, the engine operating point moves within the compressor map as shown in Fig. 5 for injected water mass flow varying from $f=0\%$ to $f=1.2\%$.

The shift in the compressor characteristics is represented for $f=1\%$ and compressor reduced speed (n_{in}^*) constant and equal to the nominal value (100% aero-speed). All points are at same inlet air conditions ($t_{air}=15^\circ\text{C}$, $\text{RH}_{air}=60\%$).

With water injection, the compressor characteristics move towards higher values of the reduced inlet mass flow (m_{in}^*).

$$m_{in} = m_{air} + m_{H_2O} \quad (4)$$

$$\frac{m_{in}^*}{m_{in}} = \frac{m_{in} \cdot \sqrt{R_{air} \cdot T_{air}}}{P_{air}} \quad (5)$$

For 1% water injection, the increase in reduced mass flow is only $\sim 0.5\%$. This means that the air inlet mass flow m_{air} actually decreases by approximately 0.5%. This result has been obtained by evaluating the experimental tests and computing engine heat balances (refer to Sec. 2.3). This has been confirmed by evaluating static pressure measurements in the compressor bell-mouth applying the method described by Biesinger in [10].

This result differs from what has been observed and predicted in [1] and [5]. The reason for that has probably to be looked for in the differences between the GT24/GT26 compressors and those considered in [1] and [5].

Within the detailed compressor model, this problem is addressed by modeling the impact of water injection on the airfoil trailing edge flow angle deviations. In particular, these deviations are expected to be higher in the case of wet blades than in normal “dry” operation.

The engine operating line in Fig. 5 is calculated for constant

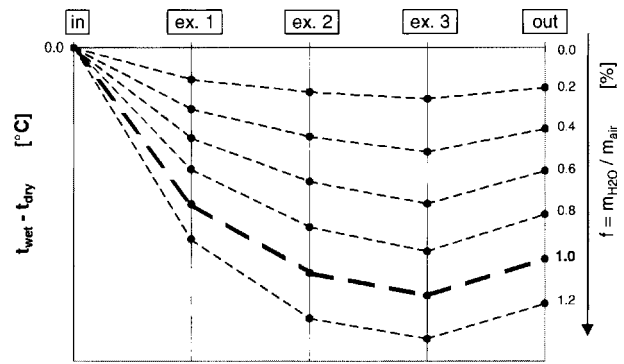


Fig. 6 Temperature variation along compressor considering variable SAS hardware

ambient conditions, constant n_{in}^* and assuming an engine controlled by constant hot gas temperatures (during “dry” operation, the operating point of such an engine would move along this line according to variations of VIGV). With “pure” internal cooling, this operating line is not influenced by the injected water mass flow. This result is due to the congruence between compressor outlet and turbine inlet mass flows together with the fact that Eq. (3) is fulfilled for all compressor extractions and consequently (m_{out}/m_{in}) remains constant at each operating point.

For all engine components (i.e., compressor, combustor, and turbine), the overall mass flow (liquid-phase+gas-phase) increases by 0.5%.

Temperatures and pressures along the compressor are also affected by the evaporation of water inside of the compressor. The two figures below show, with respect to the “dry” case ($f=0\%$), the variation of temperatures and pressures at the compressor extractions and outlet.

The temperature reduction in Fig. 6 is due to the fact that the gas-phase has to supply the heat of evaporation to the liquid-phase. The rearward shifting of the pressure build-up along the compressor is shown in Fig. 7. With internal cooling, the first stages of the compressor produce less pressure rise than in dry operation (opposite behavior for the rear stages).

With water injection, the specific enthalpy increase of the water–air mixture is also reduced, i.e., the specific work of compression (L_c) decreases being L_c defined as:

$$L_c = \frac{P_c}{m_{in}} = \frac{\sum_i m_i \cdot \Delta h_i}{\sum_i m_i} \quad (6)$$

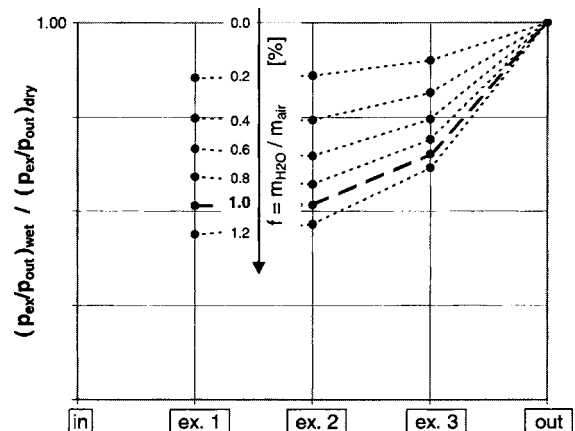


Fig. 7 Pressure variation along compressor considering variable SAS hardware

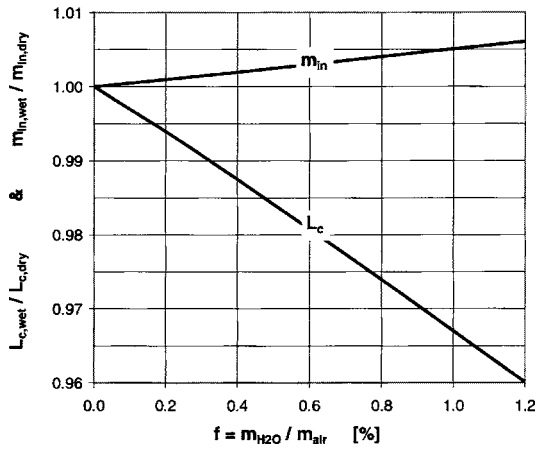


Fig. 8 Specific work of compression and inlet mass flow considering variable SAS hardware

For $f=1\%$, L_c is reduced by 3.3% compared to the “dry” case (see Fig. 8).

As shown in Fig. 5, the pressure ratio Π increases with internal cooling in the same way as m_{in} . The relative work of compression normalized with respect to this effect ($L_{c,\Pi=constant}$) would decrease by approximately 3.5% for $f=1\%$ when using the following definition:

$$L_{c,\Pi=constant} = L_c \cdot \frac{(\Pi_0^{(\gamma_0-1)/\gamma_0} - 1)}{(\Pi^{(\gamma-1)/\gamma} - 1)} \quad (7)$$

Finally, Fig. 9 shows the “pure” effect of internal cooling on the overall engine performance for $f=1\%$. Engine power output and efficiency increase both linearly with f .

As for mass flow, gross power, efficiency and specific heat, the values in the parenthesis are relative changes with respect to the “dry” case, e.g., $(m_{wet} - m_{dry}) / m_{dry}$. As for the temperature absolute changes are used, $(t_{wet} - t_{dry})$.

The gas specific heat at constant pressure (c_p) increases with the amount of water in the gas composition and contributes to an equivalent increase of the engine power output. The gain in turbine power output is slightly lower than what would correspond to the augmentation of m and c_p . This happens because of the temperature reduction of some of the cooling air mass flows reaching the turbines.

The gain in gross power output is distributed almost equally

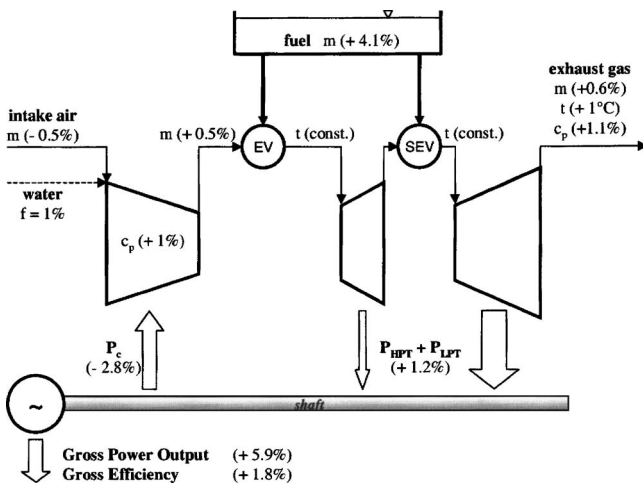


Fig. 9 Effect on overall engine performance considering variable SAS hardware

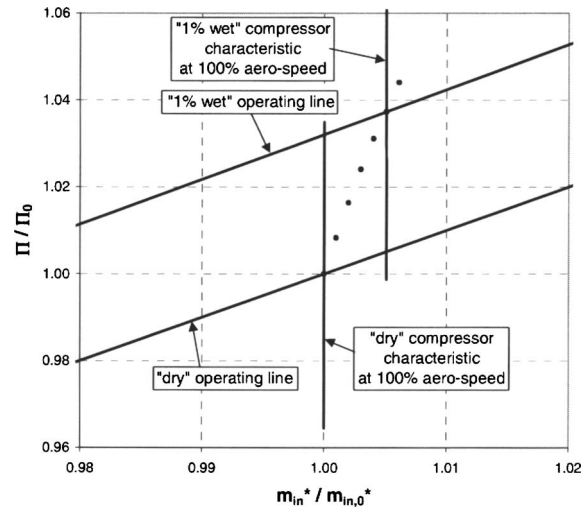


Fig. 10 Compressor characteristics and engine operating line considering fixed SAS hardware

between reduction of compressor power and increase of turbine power. This figure changes significantly when fixed SAS hardware is considered (refer to the next Sec. 3.2).

3.2 Fixed SAS Hardware, “Real” Internal Cooling. The calculation in this section corresponds to fixed SAS hardware (optimized and adjusted for high fogging, refer to Sec. 2.2). This is the usual situation in heavy-duty gas turbine engines. Consequently, the “real” effect of internal cooling is illustrated, i.e., a combination between the “pure” effect in Sec. 3.1 and the changes in the secondary air cooling mass flows induced by internal cooling.

Compared to “dry” operation with the same SAS hardware, all the three relative cooling air flows (m_{ex} / m_{in}) decrease due to the decrease of (p_{ex} / p_{out}) . Consequently, the compressor outlet mass flow increases significantly and the engine operating line moves to a higher level of pressure ratio as illustrated in Fig. 10.

In particular, the right shift with respect to m_{in}^* remains the same as in Fig. 5. This phenomenon is located in the first part of the compressor, therefore, it is not influenced by the mass flows at the extractions.

As for the temperature along the compressor, with fixed SAS hardware, the higher increase of Π partly compensates the temperature reduction due to internal cooling. Consequently, the reduction in Fig. 11 is lower than what is shown in Fig. 6.

Similarly, the rearward shifting of the pressure build-up differs

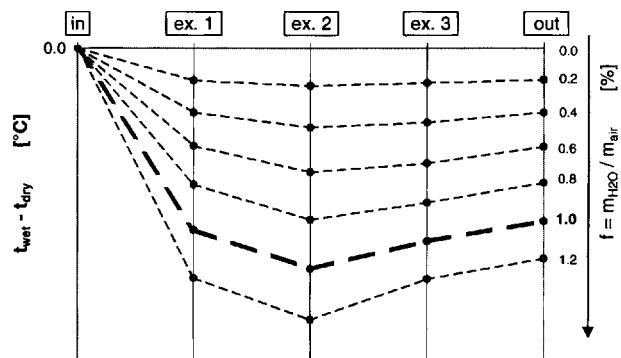


Fig. 11 Temperature variation along compressor considering fixed SAS hardware (same scale as Fig. 6)

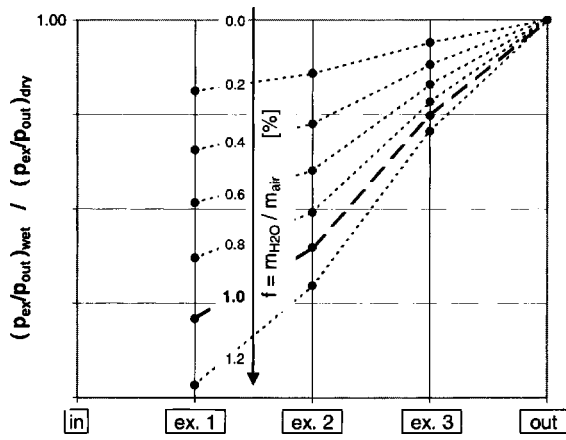


Fig. 12 Pressure variation along compressor considering fixed SAS hardware (same scale as Fig. 7)

between Figs. 12 and 7. With fixed SAS hardware, it is further exacerbated by the reduced extracted mass flows (m_{ex}) and by the resulting higher mass flow through each section of the compressor.

Figure 13 shows the variation of the specific work of compression. For $f=1\%$, L_c is 1% smaller than in the “dry” case. The effect on the value of $L_{c,II=constant}$, see definition in Eq. (7), is a reduction of 2.6% for the same amount of water. The differences with respect to Fig. 8 are again explained by the smaller extraction mass flows.

Finally, Fig. 14 shows the “real” effect of internal cooling with fixed SAS hardware on the overall engine.

Also in this case, the increase of c_p due to water evaporation has a beneficial impact on the engine power output.

As shown in the compressor map in Fig. 10, for $f=1\%$, the total inlet mass flow m_{in} increases by 0.5%. The mass flow at the compressor outlet, however, increases more significantly due to the reduction of the mass flows at the extractions. Consequently, the mass flow increase through combustors and turbines is significantly above 0.5%.

Considering these facts, the result of “balanced contributions” of compressor and turbine to the total power gain changes considerably compared to the previous Sec. 3.1. When the real behavior of the SAS hardware is taken into account (i.e., fixed SAS hardware), the major portion of the power gain comes from the turbines whereas the reduction of compressor power contributes by relatively small extent.

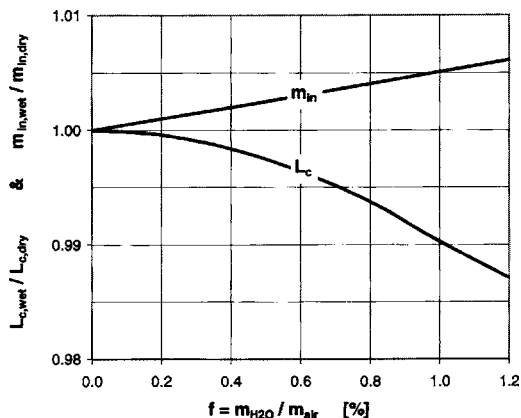


Fig. 13 Specific work of compression and inlet mass flow

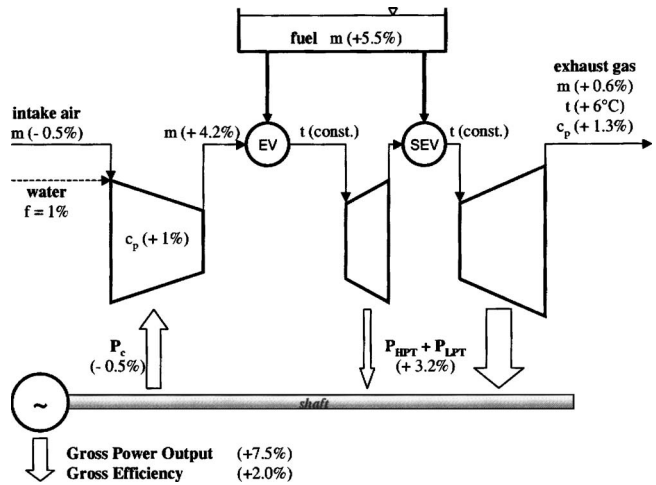


Fig. 14 Effect on overall engine performance considering fixed SAS hardware

4 Discussion and Future Research

The authors want to emphasize the fact that the effect of internal cooling on the operating conditions of compressor stages “is appreciable even for very small quantities of water injection” (quoted from Horlock [3]).

Working for the development of the ALFog[®] high fogging system, we have often been asked the following question by our colleagues:

«(What is the maximum water mass flow that our engine can withstand without hurting safety and lifetime?)»

This topic has long been subject to the attention of many authors. It is possible to address this question by referring to practical issues and by taking the word “engine” as the central one in the question. In fact, the effect of internal cooling on the compressor propagates to all the other engine components. Consequently, the limiting factors have to be analyzed not only for the compressor, but for the whole engine. On the basis of ALSTOM’s experience, it is possible to establish a ranking among various issues that could restrict the acceptable water mass fraction. The most important ones are indicated below:

- The secondary air cooling mass flows decrease with internal cooling. The water mass fraction has to be limited and the engine needs to be adjusted with proper SAS hardware modifications.
- Compressor aerodynamic loading varies as well as the engine operating line in the compressor map. As a result, the surge margin could be reduced. Careful analysis is needed to define the limits for safe compressor operation.
- The temperature at the inlet of the EV combustor is significantly reduced. Effects on emission levels and operation stability have to be investigated in case of high water mass fractions.

When high fogging is applied on engines that have been designed for “dry” operation only, the acceptable water mass fraction (in terms of safety and lifetime) is limited by one of the three factors mentioned above. Injection rates as high as $f=6\%$ or even $f=10\%$ appear to be practically not possible without substantial hardware re-design not only of the compressor, but also of the whole SAS.

Water mass fractions as high as 1% and 2% (considering internal cooling only) appear, instead, to be applicable without major changes to the engine design. Anyway, specific engine adjustments and protections are needed.

For new design of engines, the choice of the location of the water injection system (and the possible installation of additional

heat exchangers) opens the way to many combinations and engine architectures. The publications of Ågren [11], Lindquist [12], Macchi et al. [13], and Chiesa et al. [14] provide extensive information about these innovative thermodynamic cycles with high water injection rates. In these cases, water recovery from the exhaust flue gas (Cataldi [15]) is shown to be a worthwhile consideration.

Conclusions

The target of developing a high fogging system for the gas turbine engines of the family GT24/GT26 has been successfully achieved and resulted in the establishment of the ALFog[®] high fogging system. Issues concerning engine safety, lifetime, operability, and performance have been carefully investigated and effective solutions have been found and tested (refer also to [6]). A power gain of 7.1% has been experimentally demonstrated for $f=1\%$ water injection (see Fig. 4).

Although the investigation is limited to small water mass fractions, the results published by other authors have substantially been confirmed. In particular, it is possible to refer to the work of Hill [1] and Horlock [3] as for the variation of the temperature and pressure build-up along the compressor, and to the results of Hill [1], Utamura et al. [2], Härtel and Pfeiffer [4], and White and Meacock [5] as for the reduction of compression work. The increase in compressor inlet mass flow predicted by other authors has not been observed.

The analysis of the effect of internal cooling on the overall engine (considering a complete matching of the compressor with the other engine components) has shown significant variations in the behavior of the SAS. These changes have an impact on the position of the engine operating line within the compressor map and on compressor and turbine power. Additionally, specific hardware adjustments are needed to avoid any impact on components lifetime.

Acknowledgment

The authors wish to thank all the people who have participated in the development of the ALSTOM ALFog[®] high fogging system: The members of the development team, technical review board, project management, commissioning, and customer service. We are also grateful to Dr. M. Utamura for his valuable discussions during the preparation of this paper.

Nomenclature

AIC	= conventional air inlet cooling system such as evaporative cooler, fogging, or chiller
EV	= environmental burner (standard ALSTOM technology for low emissions in exhaust)
LSP	= load set point (dependent on external power demand)
PMP	= performance measurement point
SAS	= secondary air system (turbine and combustor cooling)
SEV	= sequential environmental burner (see also EV), as part of ALSTOM's unique sequential combustion system used in GT24/GT26 engine family
TIT	= mixed turbine inlet reference temperature according to ISO 2314 [9]
D	= droplet diameter (μm)
L	= specific work (kJ/kg)
N	= number of droplets
P	= power (kW)
R	= specific gas constant (kJ/(kg K))
RH	= relative humidity (%)
T	= total temperature (K)
VIGV	= variable inlet guide vane position (deg)
c	= specific heat (kJ/(kg K))

f	= water mass fraction ($m_{\text{H}_2\text{O}}/m_{\text{air}}$) at compressor inlet (%)
h	= specific enthalpy (kJ/kg)
m	= mass flow (kg/s)
n	= shaft rotational speed (rpm)
p	= total pressure (bar)
t	= total temperature ($^{\circ}\text{C}$)
Π	= compressor pressure ratio ($p_{\text{out}}/p_{\text{in}}$)
γ	= ratio of specific heats (c_p/c_v)
D_{Sauter}	= Sauter mean droplet diameter, see Eq. (1)
$L_{c,\Pi=\text{constant}}$	= corrected specific work of compression, see Eq. (7)
m_{in}^*	= compressor reduced mass flow, see Eq. (5)
n_{in}^*	= compressor reduced speed, see Eq. (2)

Subscripts

0	= engine "dry" operation at ISO base load
air	= intake air at compressor inlet
c	= compressor
dry	= engine "dry" operation ($f=0$)
ex	= compressor air extraction
GT	= gas turbine engine
H ₂ O	= water at compressor inlet
HF	= high fogging system
HPT	= high pressure turbine
i	= i th stream of air in Eq. (6)
j	= j th class of droplets of equal size in Eq. (1)
in	= compressor inlet
LPT	= low pressure turbine
out	= compressor outlet
p	= constant pressure
v	= constant volume
wet	= engine "wet" operation with internal cooling ($f > 0$)

References

- Hill, P. J., 1963, "Aerodynamic and Thermodynamic Effects of Coolant Injection on Axial Compressors," *Aeronaut. Q.*, **14**, pp. 331–348.
- Utamura, M., Takehara, I., and Karasawa, H., 1998, "MAT, a Novel, Open Cycle Gas Turbine for Power Augmentation," *Energy Convers. Manage.*, **39**, pp. 1631–1642.
- Horlock, J. H., 2001, "Compressor Performance with Water Injection," ASME Paper No. 2001-GT-0343.
- Härtel, C., and Pfeiffer, P., 2003, "Model Analysis of High-Fogging Effects on The Work of Compression," ASME Paper No. GT 2003-38117.
- White, A. J., and Meacock, A. J., 2003, "An Evaluation of the Effects of Water Injection on Compressor Performance," ASME Paper No. GT 2003-38237.
- Lecheler, S., and Hoffmann, J., 2003, "The Power of Water in Gas Turbines: ALSTOM's Experience With Air Inlet Cooling," *Proc., PowerGen 2003*, São Paulo, Brasil, November 11–13.
- Hoffmann, J., 2002, "Inlet Air Cooling Performance and Operation," *Proc., CEPSI 2002*, Fukuoka, Japan, November 5–8.
- Hoffmann, J., and Ojo, C., 2003, "High Fogging Tests and Performance Model," *Proc., IGTC 2003*, Tokyo, Japan, Paper TS-091.
- International Standard ISO 2314: 1989, "Gas Turbines—Acceptance Tests," 2nd ed. 1989-05-01, Sec. 8.6.
- Biesinger, T., 2003, "Flow Field Investigations in Intake Manifolds of Industrial Gas Turbines," *Proc., 5th European Turbomachinery Conference*, Prague, Czech Republic, March 17–22.
- Ågren, N., 2000, "Advanced Gas Turbine Cycles with Water–Air Mixtures as Working Fluid," Ph.D. thesis, Royal Institute of Technology, Stockholm, Sweden, ISSN 1104-3466.
- Lindquist, T., 2002, "Evaluation, Experience and Potential of Gas Turbine Based Cycles with Humidification," Ph.D. thesis, Lund University, Lund, Sweden, ISBN 91-628-5330-9.
- Macchi, E., Consonni, S., Lozza, G., and Chiesa, P., 1995, "An Assessment of the Thermodynamic Performance of Mixed Gas–Steam Cycles—Part I: Intercooled and Steam-Injected Cycles," *ASME J. Eng. Gas Turbines Power*, **117**, pp. 489–498.
- Chiesa, P., Lozza, G., Macchi, E., and Consonni, S., 1995, "An Assessment of the Thermodynamic Performance of Mixed Gas–Steam Cycles: Part—Water-Injected and HAT Cycles," *ASME J. Eng. Gas Turbines Power*, **117**, pp. 499–508.
- Cataldi, G., 2001, "Dry Air-Cooling for Water Recovery in Humidified Gas Turbine Cycles," Master thesis, Dept. of Chemical Engineering and Technology, Div. Energy Processes, Royal Institute of Technology, Stockholm, Sweden.

Basil R. Marple¹

e-mail: basil.marple@nrc.ca

Joël Voyer²

Michel Thibodeau

National Research Council Canada,
Industrial Materials Institute,
75 de Mortagne Boulevard,
Boucherville, QC J4B 6Y4, Canada

Douglas R. Nagy

Liburdi Engineering Limited,
400 Highway 6 North,
Dundas, ON L9H 7K4, Canada

Robert Vassen

Institute for Materials
and Processes in Energy Systems,
Forschungszentrum Jülich GmbH,
D-52425 Jülich, Germany

Hot Corrosion of Lanthanum Zirconate and Partially Stabilized Zirconia Thermal Barrier Coatings

The hot corrosion resistance of lanthanum zirconate and 8 wt. % yttria-stabilized zirconia coatings produced by thermal spraying for use as thermal barriers on industrial gas turbines or in aerospace applications was evaluated. The two ceramic oxide coatings were exposed for various periods of time at temperatures up to 1000°C to vanadium- and sulfur-containing compounds, species often produced during the combustion of typical fuels used in these applications. Changes in the coatings were studied using a scanning electron microscope to observe the microstructure and x-ray diffraction techniques to analyze the phase composition. The results showed different behaviors for the two materials: the zirconia-based coating being rapidly degraded by the vanadium compounds and resistant to attack by the sulfur materials while the lanthanum zirconate was less damaged by exposure to vanadia but severely attacked in the presence of sulfur-containing species. [DOI: 10.1115/1.1924534]

1 Introduction

Thermal barrier coatings (TBCs) are widely used in jet engines and land-based turbines as insulating layers to shield the underlying components from the high temperatures arising from combustion. The TBCs consist of a duplex structure comprised of a metallic bond coat and a ceramic top coat. The bond coat is applied directly to the roughened surface of the component and plays an important role in reducing oxidation of the high temperature metal alloy in the underlying part. The top coat is normally a porous layer of a ceramic oxide applied either by thermal spraying or by an electron beam physical vapor deposition (EB-PVD) process. It serves as a thermal insulator, reducing the temperature experienced by the surface of the underlying component during operation. The combination of internal air cooling using channels both within and at the back face of the component together with the insulating effect of the TBC can result in a temperature drop of approximately 150°C across the coating [1].

Because of the protection offered by the TBC, it is possible to extend the life of the underlying component and increase the cycle time between stoppages for overhaul and repair. This cycle time has been reported to be approximately 8000 h for commercial aircraft and 24,000 h for turbines used for power generation [2]. In these applications, TBCs are not currently required to serve as the “last line of defense” and most components can function for at least a short time without them. However, it is projected that new, higher-performance engines will be developed having higher operating temperatures and larger temperature drops across the TBC [1]. It is expected that at some point TBCs will become “prime reliant” parts of the system. In other words, failure of the coating would lead to failure, in some cases in a catastrophic fashion, of the underlying component.

The requirement for increased insulation to protect components

from hotter combustion gases will necessitate a change in the TBC system to achieve a higher temperature drop across the coating. Thicker ceramic coatings are one possible approach to improving the insulating value of the TBC [3,4]. However, producing thicker coatings presents challenges, particularly when deposited using plasma spraying, because of the build up of stresses that can cause the coating to spall. There are also concerns associated with the increased weight of thicker coatings and the possibility of creep at higher temperatures when the coatings are being employed on rotating components. And even if thicker coatings can be produced and employed on rotating components, there is a question concerning the ability of the most widely used top coat composition, 8 wt. % $Y_2O_3-ZrO_2$, to resist sintering at the higher temperatures to which it will be exposed. Sintering and densification can degrade the coating [5] and raise the thermal conductivity, making it a less effective thermal barrier.

There is a need, therefore, for the development of new design strategies or new materials for TBCs in order to address the challenges of more demanding operating environments. One composition that has been shown to possess some very interesting properties for this application is lanthanum zirconate, $La_2Zr_2O_7$ [6,7]. The results of early work have shown that this material has a stable phase structure and, when engineered correctly, can outperform a standard yttria-stabilized zirconia TBC in high-temperature thermal cycling tests [8].

The present study focuses on another aspect of the performance of these materials—resistance to hot corrosion. This is one of several degradation processes identified as contributing to the deterioration of TBCs [9]. Much of the body of work performed in the area of hot corrosion of TBCs was reviewed and summarized in a relatively recent paper by Jones [10]. Under normal operating conditions, hot corrosion of TBCs used in power generation and jet engine components arises due to reactions involving impurities, particularly vanadium, sulfur and sodium, present in the fuel. The present study compares the hot corrosion performance of ZrO_2-8 wt. % Y_2O_3 and $La_2Zr_2O_7$ in the presence of vanadium and sulfur compounds.

¹To whom correspondence should be addressed.

²Currently at ARC Leichtmetallkompetenzzentrum GmbH, Ranshofen, Austria.

Contributed by the IGTI Manufacturing Materials and Metallurgy Committee of ASME for publication in the JOURNAL OF ENGINEERING FOR GAS TURBINES AND POWER. Manuscript received by the MM&M Committee February 8, 2004; final revision received July 30, 2004. IGTI Review Chair: W. Miglietti.

Table 1 Spray parameters used to deposit the various TBC materials

Spray conditions	Coating			
	Bond coat for 8YSZ	8YSZ top coat	Bond coat for La ₂ Zr ₂ O ₇	La ₂ Zr ₂ O ₇ top coat
Process	APS ^a	APS ^a	VPS ^b	APS ^c
Voltage (V)	37	43	76	69
Current (A)	700	400	650	300
Primary Gas	Ar	Ar	Ar	Ar
Flow (lpm)	50.0	38.7	40	20
Secondary Gas	He	H ₂	H ₂	He
Flow (lpm)	23.6	2.0	15	13
Carrier Gas	Ar	Ar	Ar	Ar
Flow (lpm)	6.5	8.6	1.7	2.5
Powder Feed Rate (g/min)	17.0	22.6	38.4	27.0
Spray Distance (cm)	6.4	6.4	27.5	9.0

^aSG-100 plasma spray gun, Praxair Surface Technologies, Concord, NH.

^bF4 Plasma Spray Gun, Sulzer Metco, Wohlen, Switzerland.

^cTriplex I Plasma Spray Gun, Sulzer Metco, Wohlen, Switzerland.

2 Experimental Procedure

2.1 Thermal Spray Processing. Coatings were produced by plasma spraying onto 19 mm diameter metal substrates containing Ni as the major element and Cr, Mo, Nb, and Fe as the principal minor constituents (IN-625, Rolled Alloys, Mississauga, Canada). Before depositing the coatings, the surface of the substrate was roughened by grit blasting with alumina particles. To produce the bond coat, a Ni–Cr–Al–Y alloy (Ni-164-2, Praxair Surface Technologies, Indianapolis, IN) was deposited to a thickness of ap-

proximately 150–220 μm using two different processes. For the TBC system designed to have a zirconia-based top coat, the bond coat was produced by atmospheric plasma spraying (APS) (SG-100 Plasma Spray Gun, Praxair Surface Technologies, Concord, NH). The bond coat for the TBC system involving La₂Zr₂O₇ as the ceramic top coat was deposited using vacuum plasma spraying (VPS). This was accomplished using a plasma spray gun (Model F4, Sulzer Metco, Wohlen, Switzerland) mounted in a VPS unit manufactured by the same company.

The ceramic top coats were deposited onto the bond coat to a thickness of approximately 250 μm using two different APS systems. The zirconia-based TBC top coat was produced using a yttria-stabilized zirconia powder containing 8 wt. % yttrium oxide and having a reported size distribution in the range 10–106 μm (204NS, Sulzer Metco, Westbury, NY). This was accomplished using the same APS gun as used for depositing the bond coat for this TBC system. In the remaining sections of this paper this yttria-stabilized zirconia top coat will be referred to as 8YSZ, a designation now widely used in the TBC literature. The lanthanum zirconate top coat was deposited using a second APS system (Triplex I Plasma Spray Gun, Sulzer Metco, Wohlen, Switzerland) and an experimental powder being developed and evaluated for use as a TBC material [6–8]. The spray conditions employed for depositing the various coatings are shown in Table 1.

2.2 Hot Corrosion Testing. Testing was performed to compare the changes in these coatings when exposed to compounds containing either vanadium or sulfur at elevated temperatures. A detailed description of the approach used to perform these types of tests is presented elsewhere [11]. To briefly summarize, the corrosion tests in the presence of vanadium compounds were performed by placing approximately 3.5 mg of high-purity V₂O₅ powder on a 0.25 cm² area of the surface of the TBC and heating

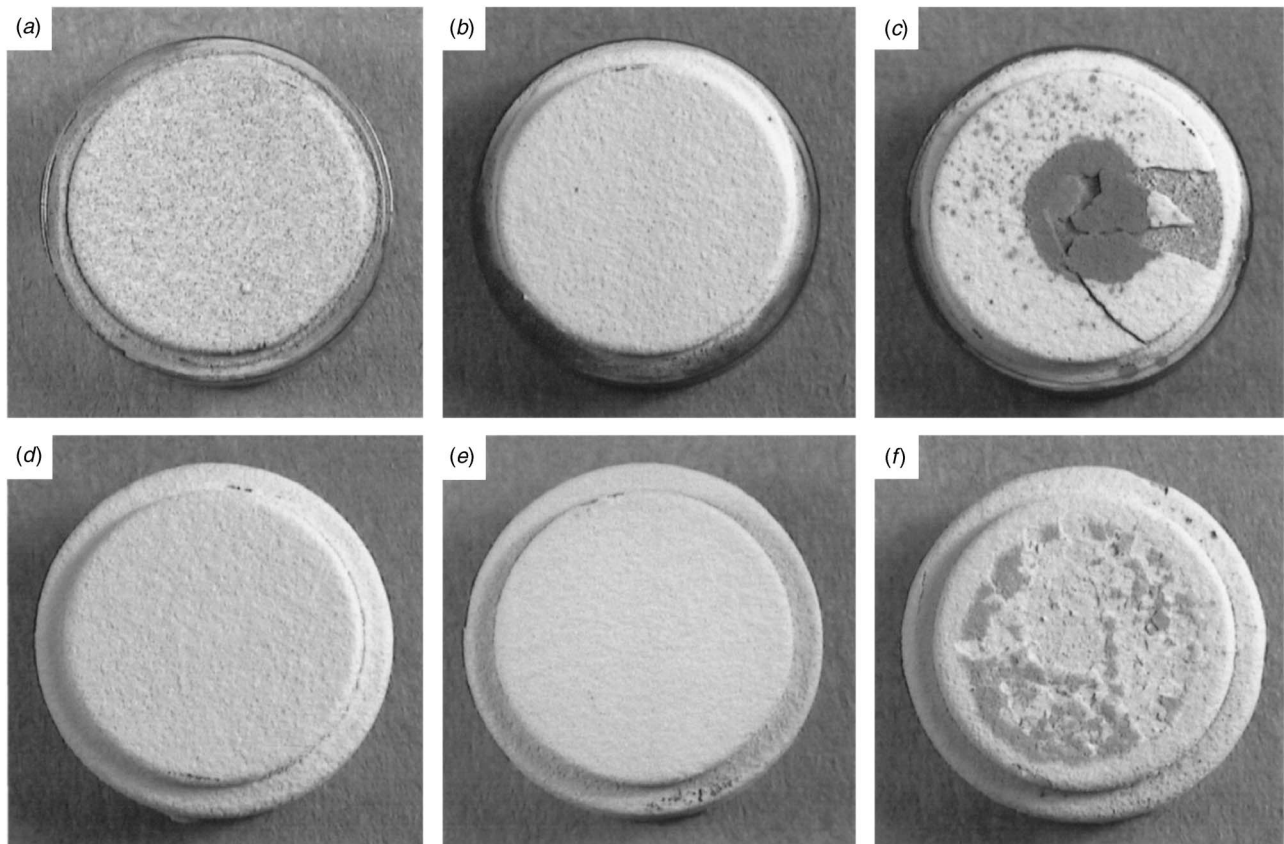


Fig. 1 Overall appearance of the 8YSZ (a–c) and La₂Zr₂O₇ (d–f) TBCs at various stages: in the as-deposited state (a) and (d), after a 3-h dwell at 1000 °C (b) and (e), and following a 3-h corrosion test at 1000 °C in contact with V₂O₅ (c) and (f)

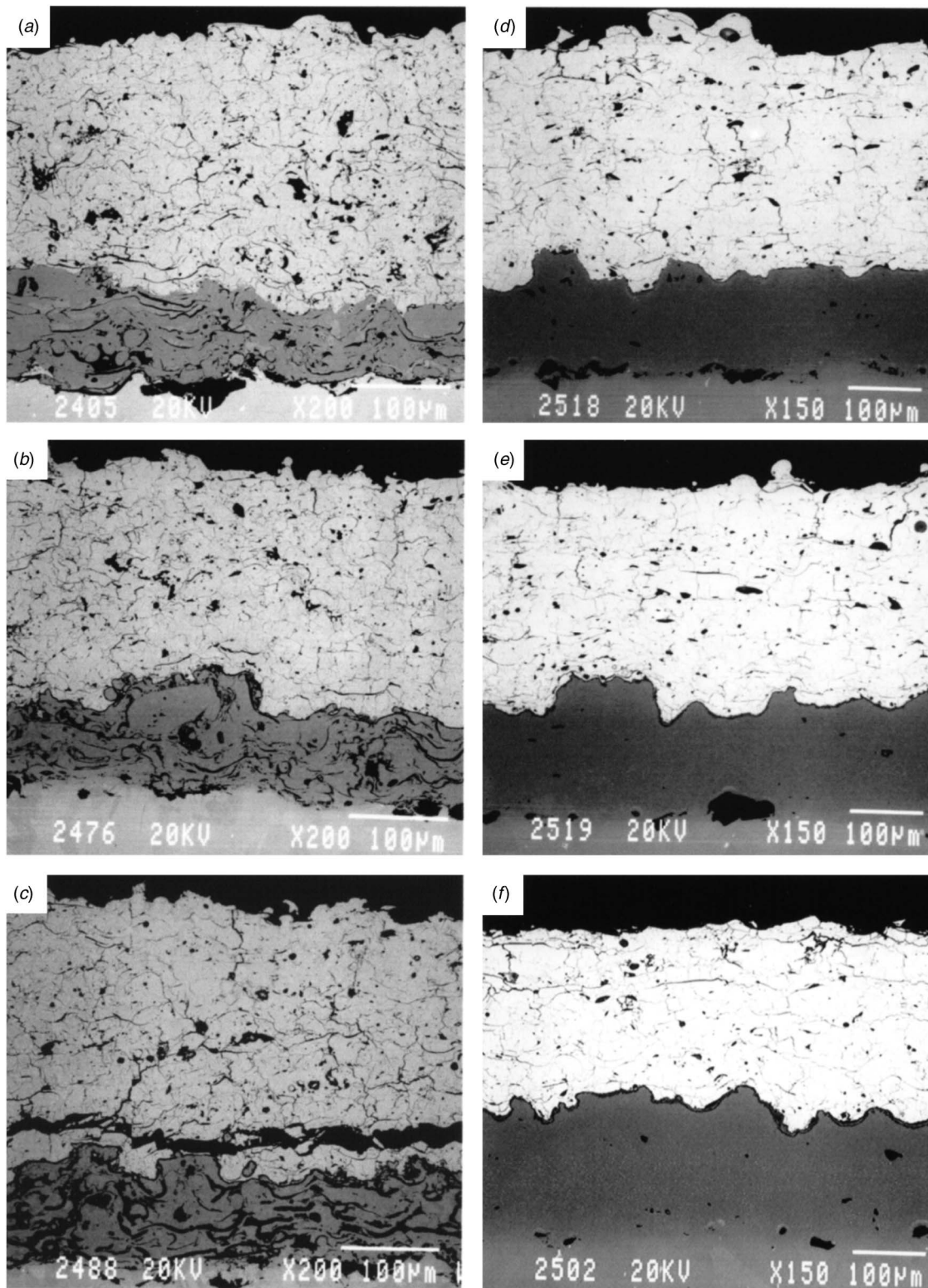


Fig. 2 Structure of 8YSZ (a–c) and $\text{La}_2\text{Zr}_2\text{O}_7$ (d–f) coatings in the as-sprayed state (a and d), after 3 h at 1000°C (b and e), and following contact with V_2O_5 at 1000°C for 3 h (c and f)

($600^\circ\text{C}/\text{h}$) the sample in a furnace to 1000°C in ambient air. Following a 3-h dwell under these conditions, the samples were left to cool in the furnace. Samples that had not been treated with V_2O_5 powder were subjected to an identical heat treatment.

Exposure of the TBCs to sulfur compounds was performed by applying sulfate salts and then heating the samples in a furnace to 900°C under a flow of SO_2 -containing dried air. This was accom-

plished by first cleaning the TBC and then performing a salting procedure involving heating the samples in a furnace to 300°C and then spraying the hot coating with a salt solution (containing sulfate salts in a mole ratio of $3\text{Na}_2\text{SO}_4:2\text{MgSO}_4$) to achieve a salt coverage of $4\text{ mg}/\text{cm}^2$. These samples (two from each composition) were then heated in a furnace at 900°C under a gas flow consisting of $2000\text{ ml}/\text{min}$ of dried air and $5\text{ ml}/\text{min}$ of SO_2 . An

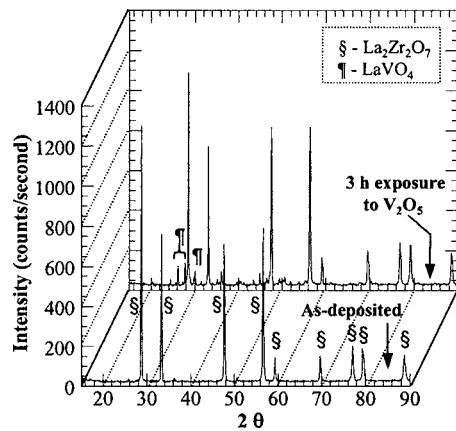


Fig. 3 X-ray diffraction spectra for the $\text{La}_2\text{Zr}_2\text{O}_7$ coating in the as-sprayed state and following a 3-h treatment at 1000°C in contact with V_2O_5

exposure interval of 20 h was employed, following which the samples were removed, inspected and resalted. The samples were then reinserted into the furnace for another 20-h interval. When significant degradation of a coating was observed during the inspection step, one of the samples of that composition was removed from the corrosion test for further analysis. A total exposure at 900°C of up to 360 h was employed for some samples.

Another test was performed to determine the combined effect of sulfur and vanadium compounds on these TBC materials when exposed simultaneously to these two substances at elevated temperatures. For this test, a dry mixture comprised of 85 wt. % Na_2SO_4 and 15 wt. % V_2O_5 was placed on the TBC to a coverage of $4\text{ mg}/\text{cm}^2$. These samples were heated in a furnace at 900°C under the same gas flow described above using an exposure interval of 20 h. After each interval, the samples were inspected, resalted and then reinserted into the furnace. However, if there was significant degradation of a coating, the sample was not subjected to any further exposure to the corrosive conditions. Maximum exposure time for these samples was 60 h.

2.3 Characterization. Coatings were studied using a scanning electron microscope (SEM) and x-ray diffraction (XRD) techniques. To characterize the changes in microstructure during the hot corrosion tests, polished cross sections of resin vacuum-impregnated samples of the as-sprayed, heat-treated and corroded samples were observed under an SEM (JSM-6100, JEOL, Tokyo, Japan). The SEM was equipped with an energy dispersive x-ray spectrometer (EDS) (Analyzer eXL, Link Systems, High Wycombe, U.K.), which was used to obtain information on the distribution of the various elements within the samples. The phases present in the various samples were identified by XRD (Model D8, Bruker AXS, Karlsruhe, Germany) using $\text{Cu } K\alpha$ radiation, a step size of 0.1 deg, a step time of 0.5 s and a 2θ scan window from 15 deg to 90 deg.

3 Results

3.1 Corrosion by Vanadium Compounds. The overall appearance of the two groups of samples used to determine the effect of exposure to vanadium compounds is shown in Fig. 1. It is apparent that, as observed in earlier work [11], the presence of V_2O_5 has a negative effect on the 8YSZ coating, which results in a serious degradation. Whereas the as-sprayed (Fig. 1(a)) and heat-treated (Fig. 1(b)) 8YSZ coatings appeared to be well bonded to the substrate, delamination and spalling of the ceramic top coat is apparent in Fig. 1(c). The dark stain seen on this coating was maroon in color and was caused by the reaction and spreading of

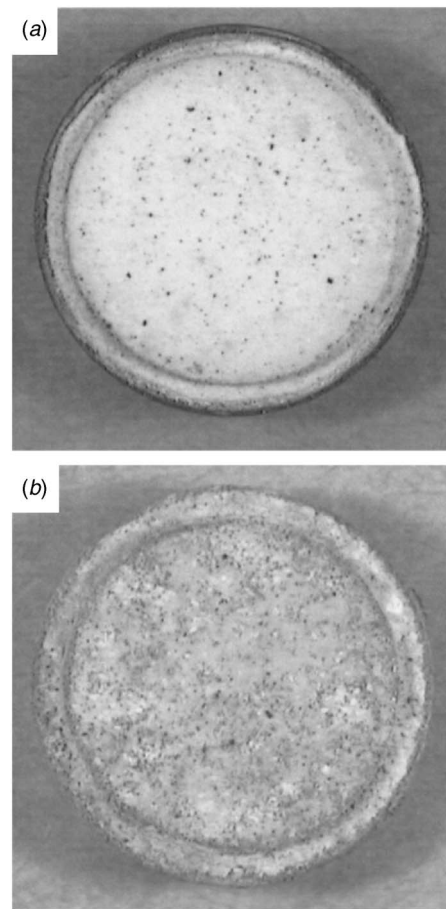


Fig. 4 Photographs of the coated test specimens following 360 h of exposure to sulfur-containing salts at 900°C : (a) ZrO_2 -8 wt. % Y_2O_3 and (b) $\text{La}_2\text{Zr}_2\text{O}_7$

the V_2O_5 .

In the case of the $\text{La}_2\text{Zr}_2\text{O}_7$ top coat, a simple heat treatment at 1000°C did not appear to cause a significant change in the coating or lead to debonding (Figs. 1(d) and 1(e)). When this treatment was performed in the presence of V_2O_5 , a green-colored substance (gray deposits seen in Fig. 1(f)) was observed on the surface of the coating following the test. However, any reactions that may have occurred during the corrosion test did not appear to have affected the bonding of the TBC to the substrate.

Micrographs of the cross sections of the six samples shown in Fig. 1 are presented in Fig. 2. The micrographs show that both top coat compositions have a stable microstructure, exhibiting little change when subjected to a heat treatment at 1000°C (compare Figs. 2(a), 2(b), 2(d), and 2(e)). This was also observed at higher magnifications (not shown). The micrographs shown in Figs. 2(c) and 2(f) confirm the observation from Fig. 1 concerning the effect of exposure of the TBCs to V_2O_5 at 1000°C on bonding; delamination of the 8YSZ occurs in the ceramic layer just above the bond coat (Fig. 2(c)) and the $\text{La}_2\text{Zr}_2\text{O}_7$ remains well bonded to the substrate (Fig. 2(f)).

Results of element mapping for the samples exposed to V_2O_5 indicated that, in the case of 8YSZ, significant infiltration of the vanadium compound into the top coat had occurred. In the case of $\text{La}_2\text{Zr}_2\text{O}_7$, overlap of the $K\alpha$ peak for vanadium and the $L\beta_1$ peak for lanthanum made it difficult to determine the distribution of vanadium using this technique.

Earlier XRD work showed that for 8YSZ, the phase present in the as-sprayed coating and in a coating heated at 1000°C was tetragonal zirconia. However, heating in contact with V_2O_5 , pro-

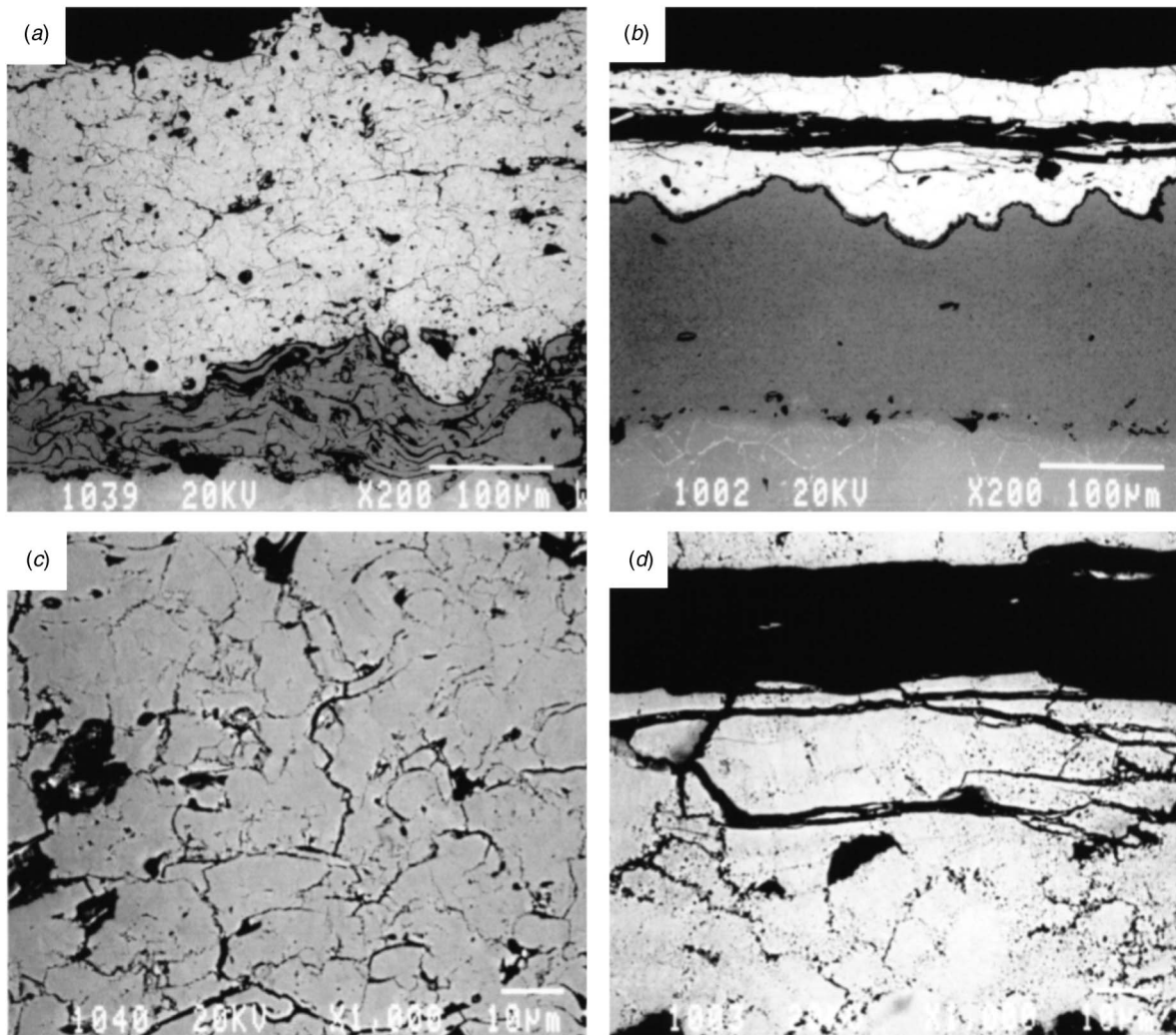


Fig. 5 Micrographs of the coated test specimens following 360 h of exposure to sulfur-containing salts at 900°C: (a) and (c) ZrO_2 -8 wt. % Y_2O_3 and (b) and (d) $\text{La}_2\text{Zr}_2\text{O}_7$

duced peaks attributed to monoclinic zirconia and to YVO_4 . These results, presented elsewhere [11], were reconfirmed in the present work.

For the coating produced using a lanthanum zirconate powder, XRD analysis indicated that the as-sprayed coating exhibited peaks of a defect fluorite structure while the feedstock showed peaks characteristic of a stoichiometric $\text{La}_2\text{Zr}_2\text{O}_7$ pyrochlore. As found earlier, the as-sprayed coatings transform into the pyrochlore structure after annealing at 1400°C and below [12]. Exposure of the coating to V_2O_5 at 1000°C resulted in the appearance of peaks attributed to LaVO_4 together with the additional pyrochlore peaks (Fig. 3). However, this new LaVO_4 phase was present as a minor component and its appearance did not have the disruptive effect on the integrity of the coating as that observed with the YSZ material.

3.2 Corrosion by Sulfur Compounds. The overall appearance of the YSZ and the $\text{La}_2\text{Zr}_2\text{O}_7$ coatings following the hot corrosion test in the presence of sulfur compounds can be seen in Fig. 4. While the $\text{La}_2\text{Zr}_2\text{O}_7$ material experienced severe attack, the YSZ underwent little change following this 360-h treatment at 900°C. More detailed information on the level of attack can be obtained by observing the micrographs presented in Fig. 5 showing a cross-sectional view of the coatings at two levels of magnification. The YSZ coating has remained intact, with little change in the microstructure (compare to Fig. 2(a)). No major changes

were observed in the XRD spectra from that of the as-sprayed coating except for the appearance of very minor peaks at 2θ values in the range 28 deg to 29 deg and 31 deg to 32 deg. These peaks were attributed to the presence of monoclinic ZrO_2 produced during the high-temperature corrosion test.

The $\text{La}_2\text{Zr}_2\text{O}_7$ coating shown in Fig. 5(b) experienced severe cracking and delamination, reducing its thickness by more than half during the test (compare to Fig. 2(d)). As shown in Fig. 6 for a sample subjected to a 4.5-h test, degradation of this coating occurred rapidly under the conditions used in this study. The X-ray spectrum for the coating shown in Fig. 5(b) is presented in Fig. 7. By comparing this result to the spectrum of the as-sprayed coating shown in Fig. 3, it can be observed that the major change following heat treatment is the presence of peaks attributed to MgO. This material is the residue from decomposition of the sulfate salts used in the corrosion test. The absence of other compounds or phases suggests that either the coating was degraded by reactions producing volatile phases, if the attack was of a chemical nature, or, other factors contributed to deterioration of the coating.

3.3 Corrosion in the Presence of both Vanadium and Sulfur Compounds. The condition of the two coatings following exposure to a combination of sulfur and vanadium compounds can be seen in Fig. 8. Due to the significant degradation of the $\text{La}_2\text{Zr}_2\text{O}_7$ material following the first 20 h of exposure, the test

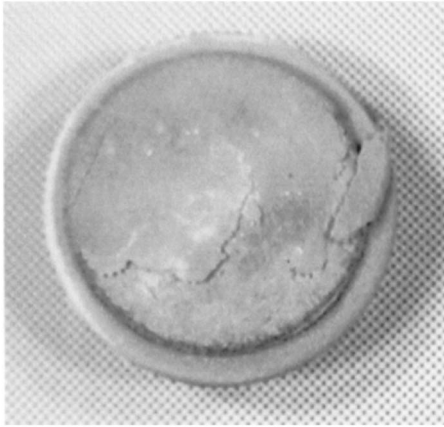


Fig. 6 Photograph of a $\text{La}_2\text{Zr}_2\text{O}_7$ coating following only 4.5 h of exposure to sulfur-containing compounds at 900°C

was terminated for this sample at that point. The YSZ sample was subjected to two additional 20-h intervals, for a total exposure time of 60 h. Micrographs of the polished cross-sections of these samples are shown in Fig. 9. It is clear that both coatings were affected by this treatment. Although the bulk of the YSZ sample has remained on the substrate, delamination has begun, as evidenced by the relatively large crack located near the surface of the coating. The $\text{La}_2\text{Zr}_2\text{O}_7$ material was much more severely degraded, with more than half of the coating having been removed (compare Figs. 1(b) and 2(d)). The EDS maps shown in Fig. 10 indicate that vanadium is present within both coatings. Similar maps for sulfur did not reveal the presence of this material within the coatings.

The x-ray spectra for these coatings together with those for the as-sprayed coatings are shown in Fig. 11. The spectra for YSZ (Fig. 11(a)) show that the zirconia has been almost completely transformed from the tetragonal to the monoclinic phase during the corrosion test. In the case of $\text{La}_2\text{Zr}_2\text{O}_7$ (Fig. 11(b)), the material that remains following the corrosion test exhibits diffraction peaks little changed from the as-sprayed coating. Peaks are also found for a minor new phase identified as LaVO_4 .

4 Discussion

The results indicate that there are important differences between the hot corrosion resistance of 8YSZ and that of $\text{La}_2\text{Zr}_2\text{O}_7$. An 8YSZ coating is quite prone to attack by V_2O_5 but relatively stable in the presence of sulfur-containing compounds. In contrast, $\text{La}_2\text{Zr}_2\text{O}_7$ coatings are rapidly degraded when exposed to sulfur-containing compounds at 900°C ; however, contact with V_2O_5

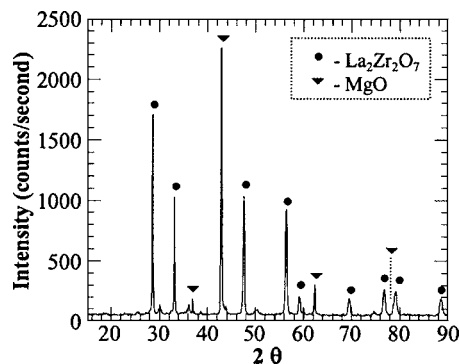


Fig. 7 X-ray diffraction spectra for the $\text{La}_2\text{Zr}_2\text{O}_7$ coating following 360 h of exposure to sulfur-containing salts at 900°C [sample shown in Fig. 5(b)].

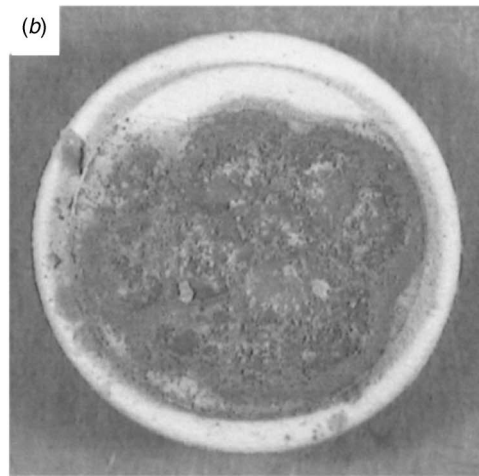
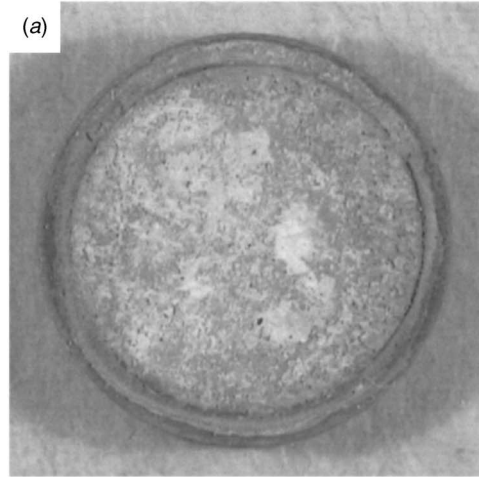


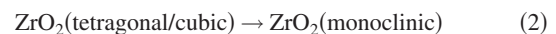
Fig. 8 Appearance of the coatings following exposure to a combination of sulfur- and vanadium-containing compounds at 900°C : (a) YSZ after 60 h and (b) $\text{La}_2\text{Zr}_2\text{O}_7$ after 20 h.

causes only very limited reaction at 1000°C . It is believed that the differences in performance of the two TBC systems can be explained solely on the basis of the difference in chemical composition of the tops coats and are not caused by the different thermal spray processes used to produce the bond coats and top coats.

The reactions that lead to the high-temperature degradation of yttria-stabilized zirconia coatings in the presence of vanadium compounds have been studied and explained by various other groups of researchers including Hamilton and Nagelberg [13] and Hertl [14] and discussed in earlier work by some of the present authors [11]. The yttria, added to zirconia to stabilize the tetragonal (and, in some cases, the cubic) zirconia structure, is attacked by vanadia via the following reaction:



As this reaction progresses, the amount of yttria remaining to serve as a stabilizing agent diminishes. Below a threshold yttria level, phase transformation of the zirconia will occur as represented by



This transformation would normally occur upon cooling and is accompanied by a volume expansion. These structural changes generate stresses that can cause cracking and fragmentation of the coating. In the present study it was shown that the V_2O_5 (which melts at approximately 690°C) infiltrated the porous ceramic layer to reach the bond coat. The subsequent reactions led to an

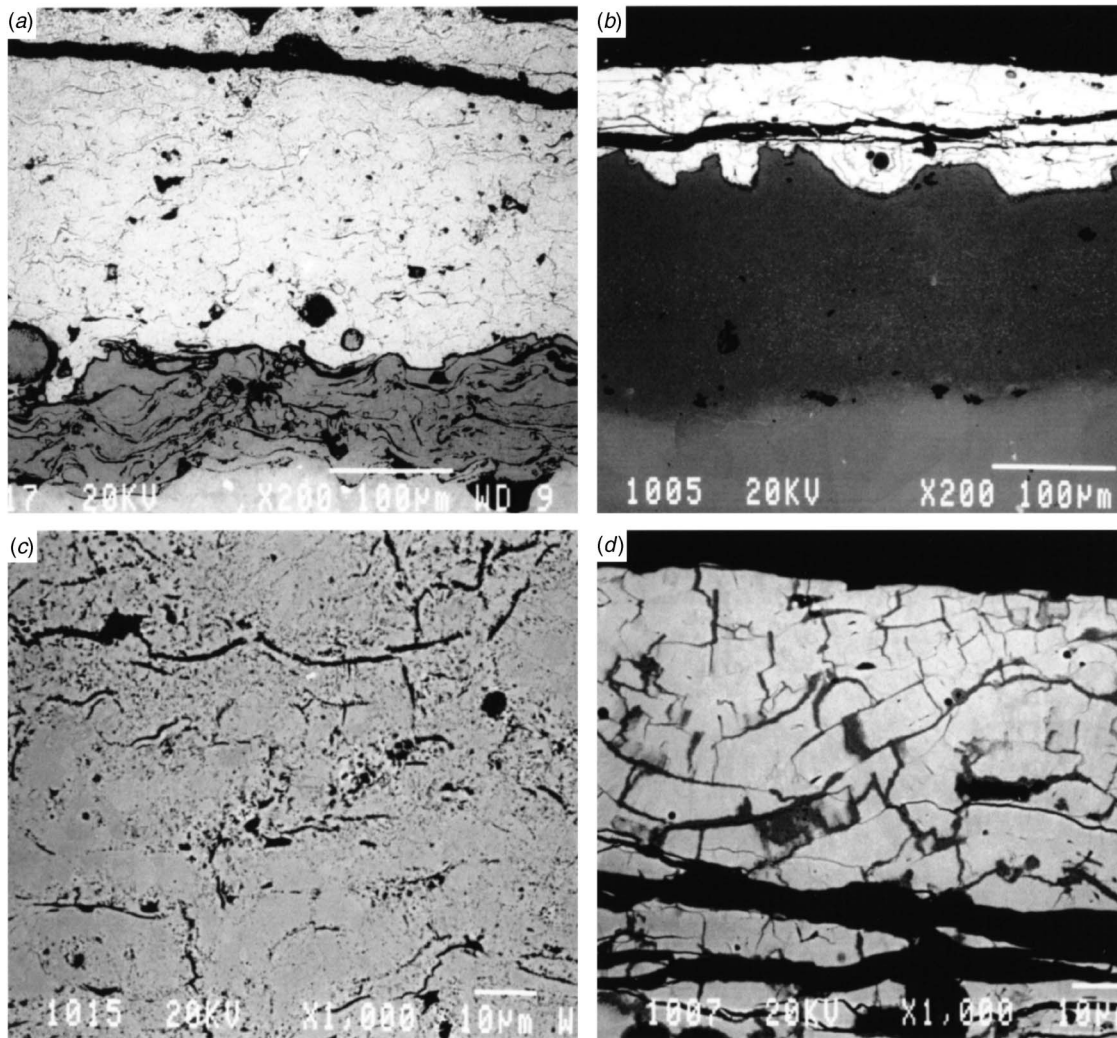


Fig. 9 Micrographs of the cross section of coatings exposed to a combination of sulfur- and vanadium-containing compounds at 900°C: (a) and (c) YSZ after 60 h and (b) and (d) La₂Zr₂O₇ after 20 h

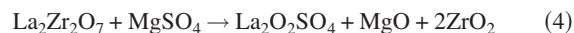
increased level of microcracking through the thickness of the coating (see Fig. 2(c)) and eventual spallation. The level of severity of attack was similar to that observed in earlier work [11]. It is worth noting that for YSZ samples in contact with vanadia, spallation typically occurred within 50 µm of the interface between the top coat and the bond coat, indicating that the maximum (delamination) stresses generated by the changes occurring during the corrosion test were concentrated in this region. For the YSZ sample exposed to both sulfur- and vanadium-containing compounds, delamination was observed much nearer the surface of the top coat.

In the case of lanthanum zirconate only minor amounts of a new phase, LaVO₄, were detected following exposure to V₂O₅. A possible reaction that would have produced this phase can be written as



In contrast to the deleterious effect of vanadia on the 8YSZ coating, this reaction did not appear to have any major effect on the coating microstructure and did not lead to spallation of the coating. These preliminary results suggest that if resistance to exposure to vanadia, as might be the case when fuels containing a relatively high concentration of vanadium are employed, is a prime factor in selecting a TBC, then La₂Zr₂O₇ would probably be a better candidate than 8YSZ.

The reactions with sulfur-containing compounds that led to the rapid degradation of the La₂Zr₂O₇ coating could not be fully identified. In general the x-ray spectra (see Fig. 7) did not reveal the presence of new phases in the coating following the high-temperature tests in contact with sulfur salts. However, in one case, following a 40-h test, the oxysulfate La₂O₂SO₄ was detected in the coating. A reaction leading to the formation of this species could be



It has been reported that at these temperatures (900°C) the oxysulfate rather than the sulfate, La₂(SO₄)₃, is the dominant species [15].

The occurrence of reaction (4) as part of the degradation sequence remains to be confirmed. However, these findings clearly show that, regardless of the mechanism of attack, in its current state this coating does not appear to be suitable for use in high-sulfur environments. Additional work is required to develop strategies such as the use of sealants or protective layers to improve the resistance of this material to hot corrosion by sulfur-containing compounds. Therefore, if one of the prime considerations in selecting a TBC material is high-temperature resistance to sulfur compounds (e.g., for use in applications involving the combustion

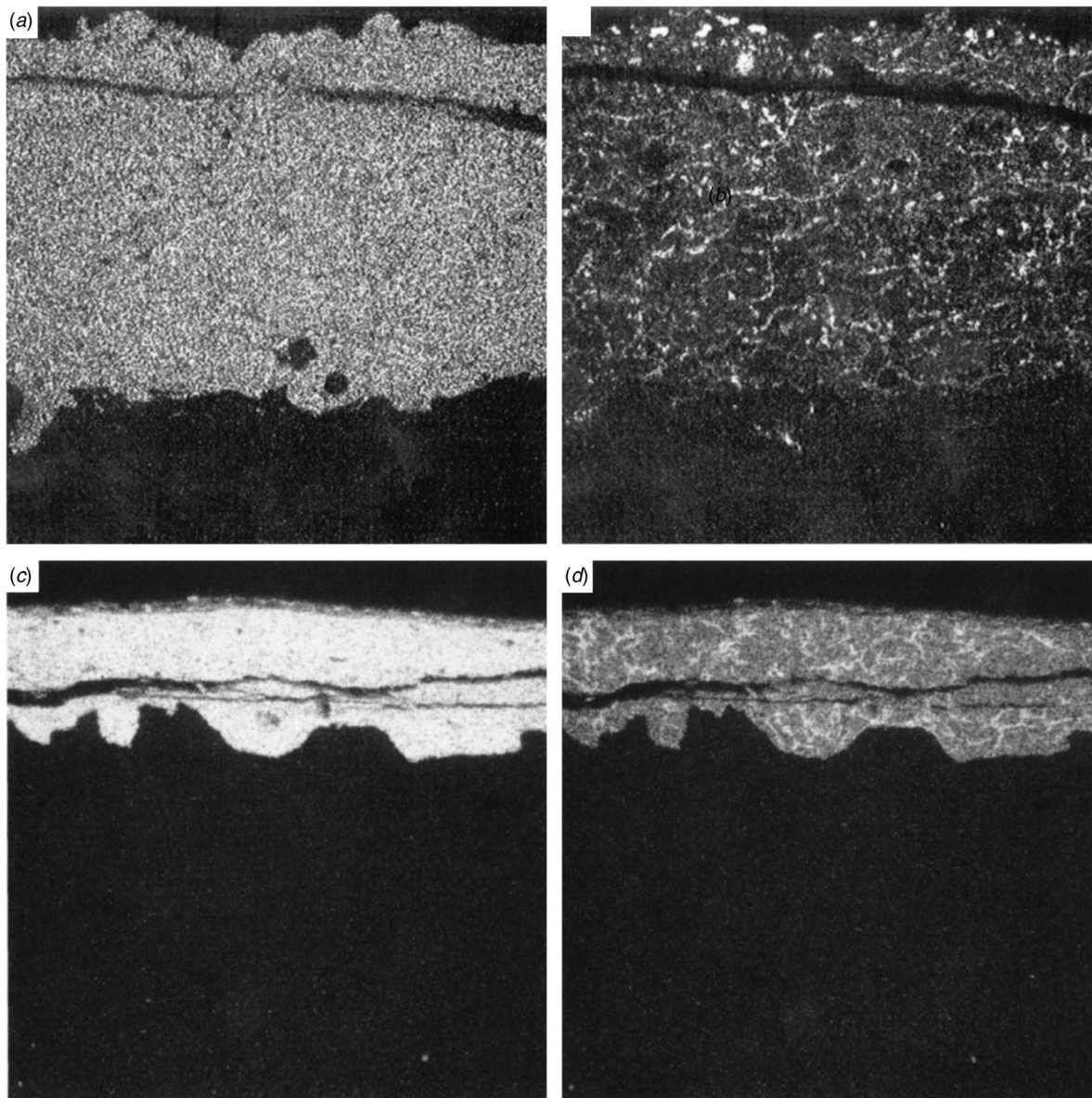


Fig. 10 EDS dot maps showing the distribution of (a) zirconium and (b) vanadium in a region of the YSZ coating from the micrograph shown in Fig. 9(a) and maps for lanthanum (c) and vanadium (d) for a region of the $\text{La}_2\text{Zr}_2\text{O}_7$ coating shown in Fig. 9(b). It is important to note that, due to the similarity of the energies for the $V_{K\alpha}$ and $\text{La}_{L\beta 1}$ peaks, the V map for the $\text{La}_2\text{Zr}_2\text{O}_7$ coating has a component due to La.

of high-sulfur fuels), the results of this study indicate that 8YSZ would be a more suitable candidate than $\text{La}_2\text{Zr}_2\text{O}_7$.

It should be noted that in the search for new TBC materials to meet the needs of increasingly demanding operating conditions, hot corrosion is only one of the many factors that must be taken into account. Other aspects such as thermal conductivity, high-temperature phase stability, resistance to sintering/densification, compatibility with bond coat and substrate materials (in terms of both thermal expansion coefficient and chemistry), and mechanical properties are among those that must also be considered. Therefore, when designing TBC systems for specific service conditions, the results of this research on the hot corrosion resistance must be used in conjunction with those from studies in which other aspects of these materials were evaluated.

5 Summary and Conclusions

This study on the hot corrosion of $\text{La}_2\text{Zr}_2\text{O}_7$ and yttria-stabilized zirconia thermal barrier coatings by vanadium- and

sulfur-containing compounds has shown a significant difference in the resistance of these materials to degradation by these two species. Lanthanum zirconate was relatively resistant to attack by vanadia. These coatings remained well bonded to the substrate following high-temperature exposure to this vanadium compound, contained only minor amounts of a new phase, LaVO_4 , and exhibited a microstructure little changed from the as-sprayed state. For this same $\text{La}_2\text{Zr}_2\text{O}_7$ material, contact with sulfate salts at 900°C resulted in very rapid disintegration of the coating, which occurred within 4 h under the conditions used in this work.

The performance of 8YSZ in the same tests was markedly different. Exposure to vanadia resulted in increased microcracking within the coating, reaction with the yttria stabilizer to produce YVO_4 , an increase in the amount of monoclinic zirconia, and spallation of the coating. In contrast, this material exhibited excellent resistance to high-temperature attack by sulfate salts. Following 360 h of exposure to these species, the 8YSZ coating ap-

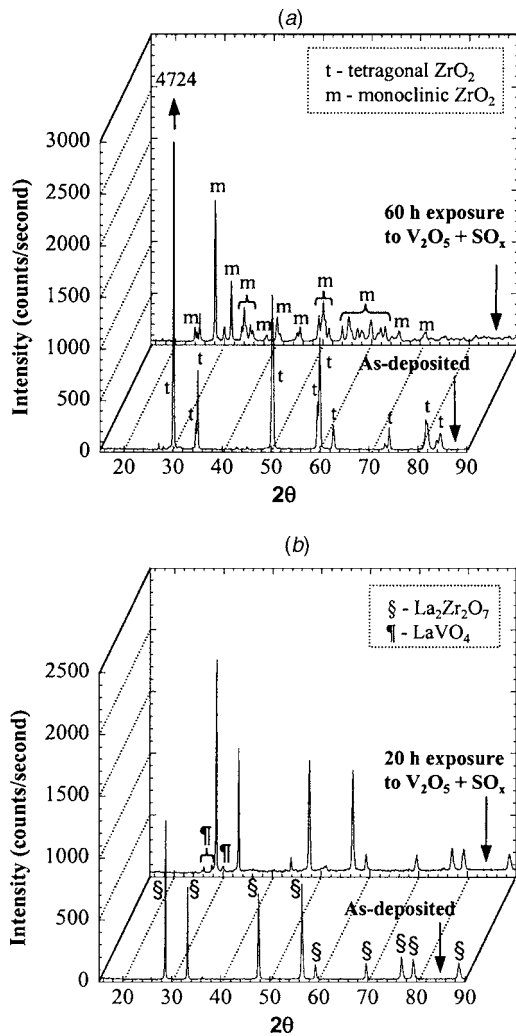


Fig. 11 X-ray spectra for coatings in the as-sprayed state and following exposure to a combination of sulfur- and vanadium-containing compounds at 900°C: (a) YSZ and (b) $\text{La}_2\text{Zr}_2\text{O}_7$

peared to have maintained its structural integrity and remained well bonded to the substrate.

Not surprisingly, when the $\text{La}_2\text{Zr}_2\text{O}_7$ and 8YSZ coatings were exposed to a mixture of vanadia and sulfate salts, both coatings

were degraded, the 8YSZ by vanadia and the $\text{La}_2\text{Zr}_2\text{O}_7$ by the sulfate. These results underline the need for designing thermal barrier coatings taking into account the level of impurities in the fuel being used in the application and the operating conditions during service.

Acknowledgment

The technical support of S. Bélanger, É. Poirier, and K. H. Rauwald during plasma spraying and sample preparation is gratefully acknowledged.

References

- [1] Wigren, J., and Pejryd, L., 1998, "Thermal Barrier Coatings—Why, How, Where and Where To," *Thermal Spray—Meeting the Challenges of the 21st Century*, C. Coddet, ed., ASM International, Materials Park, OH, Vol. 2, pp. 1531–1542.
- [2] Nelson, W. A., and Orenstein, R. M., 1997, "TBC Experience in Land-Based Gas Turbines," *J. Therm. Spray Technol.*, **6**(2), pp. 176–180.
- [3] Beardsley, M. B., 1997, "Thick Thermal Barrier Coatings for Diesel Engines," *J. Therm. Spray Technol.*, **6**(2), pp. 181–186.
- [4] Steffens, H.-D., Babiak, Z., and Gramlich, M., 1999, "Some Aspects of Thick Thermal Barrier Coating Lifetime Prolongation," *J. Therm. Spray Technol.*, **8**(4), pp. 517–522.
- [5] Bose, S., and DeMasi-Marcin, J., 1997, "Thermal Barrier Coating Experience in Gas Turbine Engines at Pratt & Whitney," *J. Therm. Spray Technol.*, **6**(1), pp. 99–104.
- [6] Vaßen, R., Cao, X., Tietz, F., Kerkhoff, G., and Stöver, D., 1999, " $\text{La}_2\text{Zr}_2\text{O}_7$ —A New Candidate for Thermal Barrier Coatings," in *Proceedings of the United Thermal Spray Conference-UTSC'99*, E. Lugscheider and P. A. Kammer, eds., DVS-Verlag, Düsseldorf, Germany, pp. 830–834.
- [7] Vaßen, R., Cao, X., Tietz, F., Basu, D., and Stöver, D., 2000, "Zirconates as New Materials for Thermal Barrier Coatings," *J. Am. Ceram. Soc.*, **83**(8), pp. 2023–2028.
- [8] Vaßen, R., Cao, X., and Stöver, D., 2001, "Improvement of New Thermal Barrier Coating Systems Using a Layered or Graded Structure," *Ceram. Eng. Sci. Proc.*, **22**(4), pp. 435–442.
- [9] Lee, W. Y., Stinton, D. P., Berndt, C. C., Erdogan, F., Lee, Y.-D., and Mutasim, Z., 1996, "Concept of Functionally Graded Materials for Advanced Thermal Barrier Coating Applications," *J. Am. Ceram. Soc.*, **79**, pp. 3003–3012.
- [10] Jones, R. L., 1997, "Some Aspects of the Hot Corrosion of Thermal Barrier Coatings," *J. Therm. Spray Technol.*, **6**(1), pp. 77–84.
- [11] Marple, B. R., Voyer, J., Moreau, C., and Nagy, D. R., 2000, "Corrosion of Thermal Barrier Coatings by Vanadium and Sulfur Compounds," *Mater. High Temp.*, **17**(3), pp. 397–412.
- [12] Cao, X. Q., Vaßen, R., Jungen, W., Schwartz, S., Tietz, F., and Stöver, D., 2001, "Thermal Stability of Lanthanum Zirconate Plasma-Sprayed Coatings," *J. Am. Chem. Soc.*, **84**, pp. 2086–2090.
- [13] Hamilton, J. C., and Nagelberg, A. S., 1984, "In situ Raman Spectroscopic Study of Yttria-Stabilized Zirconia Attack by Molten Sodium Vanadate," *J. Am. Chem. Soc.*, **67**(10), pp. 686–690.
- [14] Hertl, W., 1988, "Vanadia Reactions with Yttria Stabilized Zirconia," *J. Appl. Phys.*, **63**(11), pp. 5514–5520.
- [15] Poston Jr., J. A., Siriwardane, R. V., Fisher, E. P., and Miltz, A. L., 2003, "Thermal Decomposition of the Rare Earth Sulfates of Cerium (III), Cerium (IV), Lanthanum (III), and Samarium (III)," *Appl. Surf. Sci.*, **214**, pp. 83–102.

Understanding Royal Navy Gas Turbine Sea Water Lubricating Oil Cooler Failures When Caused by Microbial Induced Corrosion (“SRB”)

Richard Bolwell

Warship Support Agency,
UK MoD,
Marine Propulsion Systems Integrated Project
Team,
Abbeywood Filton, Bristol BS34 8JH, UK

A managed program to review engine failures and take necessary preventative measures has been in place successfully in the Royal Navy since the introduction of gas turbines into service in the 1970s. One of the more prominent failure mechanisms with the Tyne RMIC and Spey SM1A engines has been the degradation of main line bearings accounting for 25% of all engines rejected. Historically, since the first recorded incident in March 1987, the failures pointed to poor performance of the bearings themselves. However, maintenance studies and recent analysis indicates that a vast proportion have occurred through previously unidentified chloride corrosion as a result of contamination of the lubricating oil system with salt water from the seawater lubricating oil cooler (SWLO cooler). Despite joint ownership of both engine variants with the Royal Netherlands Navy, there was no clear evidence until about five years ago to suggest why tube perforation was occurring. Indeed, the fact that failures have only occurred in Royal Navy service is an interesting twist to the problem. This paper summarizes the phenomenon of SWLO cooler corrosion caused by Microbial Induced Corrosion (principally Sulphate Reducing Bacteria—SRB). It highlights the conditions in which SRB occurs along with demonstrated prevention in Royal Navy gas turbine service through the combined efforts of maintenance and development of a new titanium tubestack. The fault finding and remedial recovery experience may well be of interest to operators of marine gas turbines, both naval and commercial, who use tube type heat exchangers, especially when operating or undertaking work in estuarial waters and nontidal basins or when undertaking littoral duties. This is a practical view of the issue from an operators perspective and while utilizing a wealth of research and technical data available on the subject, it relates the issues at hand to the particular corrosion problem and is not intended as an introduction into organic chemistry. [DOI: 10.1115/1.1926315]

Introduction

The UK Warship Support Agency provides overarching in-service gas turbine support and cooperation through two Memoranda of Understanding involving four European nations, 21 years of collaboration and three million shared running hours of operation. The membership of the Olympus and Tyne MoU, in place since 1980, comprises the navies of the UK (RN), The Netherlands (RNLN), France (FN), and Belgium (BN) (Table 1). The MoU for the Spey SM1A, signed in 1989, is between the UK and The Netherlands. In addition, the Royal Navy also operates the Rolls Royce Spey SM1C and since 2002 it has been accompanied by The Royal Netherlands Navy under the Spey SM1C MoU to encompass the engines installed in the RNLN's new class of Air Defense and Command Frigate (LCF).

Marine gas turbines have been used for many decades in a diverse range of commercial and naval marine vessels almost exclusively for main propulsion duties in a number of different configurations. Seawater is a naturally available cooling medium and is extensively used in marine vessels, however, its use brings about many difficult decisions and complications; (a) choice of





materials that can be used, (b) system architecture, and (c) cost and maintenance loading throughout the life of the vessel due to material corrosion and wastage. There are trade-offs in choosing sea water over other conventional cooling media such as a closed loop system using fresh water or ethylene glycol.

In a warship, however, the seawater cooling system plays an even more vital role in successful achievement of the mission. Clearly it is important for capability and maintainability reasons to employ the most cost effective means of cooling using materials that resist known failure mechanisms of corrosion and erosion. The degree to which this occurs is a juggling act between many environmental factors [1] including;

- **Sea water temperature:** Corrosion generally increases with increased temperature but there are exceptions.
- **pH level:** Corrosion increases as pH decreases, however, a pH less than 7 provides good protective oxide scaling.
- **Marine growth:** This can either act as a barrier to prevent corrosion or gives rise to crevice conditions creating increased corrosion and effects from corrosive products.
- **Salinity:** Chloride ion concentration increases as salinity increases giving greater corrosion rate.
- **Metal ion concentration:** As metal ion concentration increases, corrosion in copper alloys increases. The presence of dissolved copper ions which are converted into an aggressive (cupric) form causes further corrosion.
- **Dissolved gasses:** Sufficiently high oxygen content can in-

Contributed by the International Gas Turbine Institute (IGTI) of ASME for publication in the JOURNAL OF ENGINEERING FOR GAS TURBINES AND POWER. Manuscript received October 1, 2003; final manuscript March 1, 2004. IGTI Review Chair: A. J. Strazisar. Paper presented at the International Gas Turbine and Aeroengine Congress and Exhibition, Vienna, Austria, June 13–17, 2004, Paper No. 2004-GT-54063.

Table 1 Gas turbine population within the two MoU's (Mar 04)

Engines within the MOU's						
Engine Variant	Fleet Seats				Spare Engines	Total
						
	RN	RNLN	BN	FN		
Olympus	29	4	3	14	10	60
Tyne	31	4	-	-	17	52
Spey 1A	25	16	-	-	10	51
Spey 1C	16	6	-	-	5	27

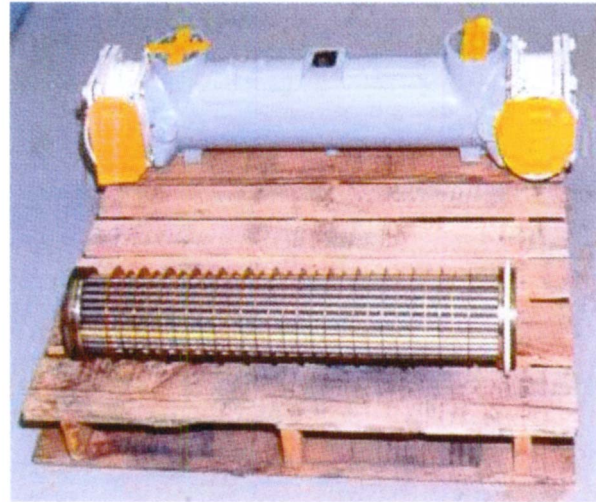


Fig. 2 Cooler on pallet with CuNi tubestack in foreground

crease corrosion but adequate levels provide good oxide film production, other gasses also cause an increase, especially carbon dioxide CO₂ and sulphur dioxide SO₂.

- **Pollutants:** As pollutant levels increase, corrosion usually increases. Sulphide and ammonia are particularly corrosive towards copper based alloys.
- **Suspended solids:** Increased solids content create higher corrosion rates usually through “erosion corrosion” and the effects of removal of the oxide film.
- **Season:** Greater corrosion can occur in Summer months with increased seawater temperatures.
- **Stray electrical currents:** The effect on corrosion depends on the polarity and magnitude of the current—this can sometimes be put to good use.
- **Water velocity:** Higher water velocities give rise to increased erosion and can remove the oxide film giving rise to increased erosion corrosion, particularly where there is a high level of debris and suspended solids.

Tyne and Spey Gas Turbine Engine Failures

This paper specifically concentrates on the successful measures put in place by the UK to counteract a corrosion problem with the design of copper nickel (CuNi) heat exchanger tubestacks used to cool the lubricating oil of the main propulsion Tyne and Spey gas turbines, shown in Figs. 1 and 2. This design of cooler is also in general ship use in other systems such as weapons, steering systems, and refrigeration. The gas turbine coolers differ slightly in

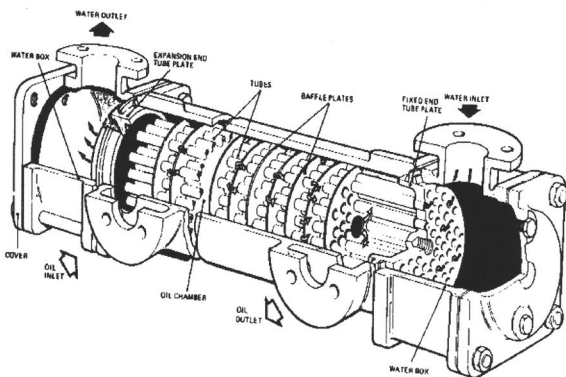


Fig. 1 Schematic representation of SWLO cooler

that they have control valves fitted on the oil inlet to regulate the GT oil supply temperature. Similar failures have occurred to a degree in all systems but the consequences are more severe for the main engines as SW contaminates the lubricating oil supply to the bearings.

Propulsion and Cooling System Design

The Tyne RM1C gas turbine entered RN service in the mid 1970s and is in use extensively as a 4 MW “cruise” engine alongside the more powerful Olympus and Spey “boost” engines used for sprints and when high speeds of advance are required. The 12.75 MW Spey SM1A is used in two configurations, one of which is alongside the Tyne and the other is in a diesel or electric motor arrangement. This engine entered RN service in the mid 1980s.

The Tyne arrangement in particular, relies on designs that were produced as far back as 1968 with much “technology” being inherited from previous classes of warship, including the engine cooling arrangements. The Spey is of similar parentage, however, the oil cooler used is the same unit as the Tyne with no design changes.

Historically, nonferrous copper alloys are favored in naval marine SW cooling systems. Based on many years of operation, the RN and the bulk of other marine operators are no different in this respect and there is a significant level of past commitment to copper based materials. Neither has there been a radical use of newer materials such as Titanium. That said, there is evidence of increasing popularity in this material perhaps because the material is now considered to be more available and has developed a short but positive history. Peacock [2] refers to sighted examples being Soviet submarines, the use by the Royal Norwegian Navy, the offshore oil industry and the US Navy. Progress with the use of Titanium in RN service is relatively slower and evaluation programs are known to be in place to generate design data on Titanium and selected alloys. The inherent corrosion and erosion resistance of all these materials is derived from the ability to quickly develop a natural, hard, and inert oxide surface film when exposed to oxygen present in the seawater.

Engine Cooling

The cooling arrangement for each engine relies on a dedicated SWLO cooler solidly mounted to the base plate of each gas turbine and connected by rubber flexibles to the respective seawater and lubricating oil systems. It is worthy to note that no arrange-

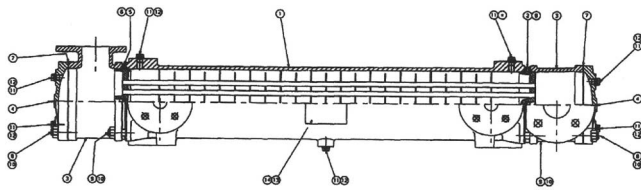


Fig. 3 Sectional arrangement through SWLO cooler

ments have been made to electrically isolate the cooler body from the SW system, despite rubber flexibles being used.

The standard multipass tube type heat exchanger used is capable of providing 48°C of oil cooling at full power. This is a Rolls Royce original design manufactured by Serck Heat Transfer Ltd. in the UK. A sectional arrangement is shown in Fig. 3.

“Multipass” is achieved by the use of 14 large baffles and 13 small baffles which fit over the tubes on the oil side thereby causing 27 directional changes in the oil over the tubestack [3]. Interestingly, the complete assembly is of mixed metal construction with an aluminum alloy shell (body), tin bronze inlet and outlet water boxes and cover plates, 70/30 copper–nickel alloy tubestack (SW through tubes), steel leakage ring and aluminum bronze fasteners. The overall length is 1.3 m and fully charged it weighs 81 kg. The tubestack contains 78 in number 70/30 CuNi tubes which have roller expanded ends to provide a 25 mm seal within the endplates and it is designed to withstand MoD UK Grade 1 shock requirements.

In terms of performance criteria, Table 2 demonstrates that the unit is designed to remove 60 kW from the lubricating oil (NATO OX22/OX28) under maximum operating conditions and that the SW velocity of 0.59 m/s is less than the recommended maximum of 0.7 m/s for tubes less than 10 mm diameter [4].

Naval Operation

Depending on deployment and mission profile, Tyne and Spey operation is generally one of mixed running or long periods spent at medium to high power followed by prolonged periods of inactivity when in leave or maintenance periods unlike most other systems which remain operative. As the engines are not used during these periods, fuel system components become sticky, SWLO oil coolers can corrode and oil wetted internal surfaces and bearings are more prone to humidity corrosion and “drain down.” This has led to an increased incidence of bearing rejections at overhaul due to surface corrosion and measures are in place to address this, including a better anti-corrosion additive package within the oil and de-humidification of engine enclosures and gas paths.

The modes of operation described place increased demands on the thermal performance and shut-down capabilities of the SWLO coolers, in particular their ability to respond well to: (a) changes in seawater temperature, (b) thermal load dissipation rate, (c) periods of inactivity, and (d) ability to reject marine organisms and plant life contained in the SW cooling water supply.

Failure Modes and Frequency

A study by UK MoD in 1999 [5] revealed that 21 Tyne and Spey engines (mainly in the RN fleet) had been rejected from service in the preceding five-year period due to “bearing related issues.” Fleet size at this time was 60 engines so this represented a severe drain on resource and operational availability. Of the 21 engines, Price [3] identified 15 failures as directly attributable to bearing corrosion rather than an inherent defect which was also evident in this period and later resolved at overhaul. The corrosion problem alone is estimated to have cost nearly £4.0 m due to unplanned repairs and unrecoverable hours lost to shortened intervals between overhauls.

Despite specialist assistance at the time, the primary reason for failure had been largely unresolved until the RN conducted a

Table 2 Gas turbine SWLO cooler performance criteria

One pass horizontal tubestack.	Shell side (Oil)	Tube side (Seawater)
Surface area per shell = 2.73 m ²		
Fluid Circulating	Synthetic Lubricating Oil NATO Grades OX22 & OX28	Natural Seawater pH 7.2 - 8.5
Flow Rate	2.5 m ³ /hr (540 UK gall/hr)	10.9 m ³ /hr (2400 UK gall/hr)
Temperature IN	118 °C Max	35 °C Max
Temperature OUT	70 °C Max	40 °C Max
Velocity	-	0.59 m/s
Heat Exchanged	60 kW	-

study of the sources of contamination and linked this with two other key areas; (a) the dates of SWLO cooler maintenance and (b) work underway by Price [3] to investigate the high incidence of submarine fuel tank corrosion. Price concluded that there was no discernible difference between age or history of cooler and the mean time to failure. The failures had occurred platform wide in new, used, or overhauled tubestacks at various points in time but, importantly, an alarming number of failures had occurred after major maintenance periods where the ships SW system had been closed down. Three of four engines in particular failed from bearing and gearbox corrosion problems on one ship alone, HMS Cumberland in 1997, within some 200 engine hours after refit. Price observed that in all cases, the tubestacks that had failed prematurely up to two years after a refit were generally caused by corrosion pitting and those that had failed after two years were mostly caused by localized impingement erosion due to high operational hours. Although strip reports indicate the failures shared the same chloride corrosion mechanism, no early evidence from the failures was available to explain why tube perforation was occurring. Chemical and/or galvanic attack of the oxide film was suspected but required proof.

In-Service SWLO Cooler Failure Indicators. Arguably it is questionable why automatic SW detectors in the oil system are not fitted and, although it is clear this is not ideal, there has never been a reason to doubt the resistance of this design of cooler or even that such a system is warranted.

Where ship staff were available for comment at the study point and based on the length of operation of the engines with the problem concerned, failure of the SWLO coolers was indicated by one or more of the following observations:

- fluctuating engine oil pressure (due to the SW having a higher pressure than the scavenge oil pressure of the engine),
- loss of lubricating oil from the oil header tank,
- oil overflowing the engine air–oil breather pipe to the ships sullage tank,
- presence of sea water in the auxiliary high speed gearbox (HSG),
- visible surface corrosion of the gearwheels in the HSG,
- crystallized salt deposits clogging HP and LP oil filters,
- high water content detectable in the engines lub oil supply (increasing at point of engine),
- increased vibration levels,
- reduced spool run-down times.

Saltwater removal from main machinery oil systems is not considered a science but relies on reacting quickly to undertake fresh water flushing of the system to dissolve the salt, followed by copious clean oil flushes to purge the water. In all events tried, this technique failed and bearing life was short lived. It was concluded that the bearings were extremely sensitive to SW contamination



Fig. 4 Corrosion of the CuNi fixed end plate and deposits in the exposed tube ends

regardless of whether the failure had just occurred or had been undetected for some time (for example, on the occasion that only one tube had failed).

One of the prime observations when draining and removing some of the tubestacks was evidence of Hydrogen Sulphide, characterized by the strikingly unpleasant smell of “rotten eggs.” This was accompanied by general corrosion of the tubestacks with localized deeper attacks and internal pitting within the tubes. The surface in the thinned areas of the pits appeared to have a rippled discolored surface with a distinctive black surface surrounded by a brown oxide film. Corrosion of the naval brass fixed end tube plate was generally extensive. Tube end thinning and slotting was present at the sliding end with evidence of marine growth. Figures 4–8 show this in more detail. This evidence is vital in the identification of the particular corrosion mechanism presented in this paper. To understand the problem, a three pronged investigation was undertaken by UK MoD with the assistance of Rolls Royce (who undertook a number of whole engine Defect Investigations), Serck Heat Transfer (who, as the OEM, undertook failure investigations on a number of rejected tubestacks) and SGS UK Ltd. (an independent technical consultant who looked at the specific corrosion mechanisms involved).

Installation, Commissioning, and Upkeep

As discussed, the ability for a CuNi tubestack to resist corrosion is directly proportional to the build up and stability of the brown protective copper oxide film on the inside surface of the tubes (Fig. 8). Manufacturers call this process the “burn-in” phase. Film thickness is established more quickly when in contact with clean, flowing, naturally occurring seawater that is high in dis-

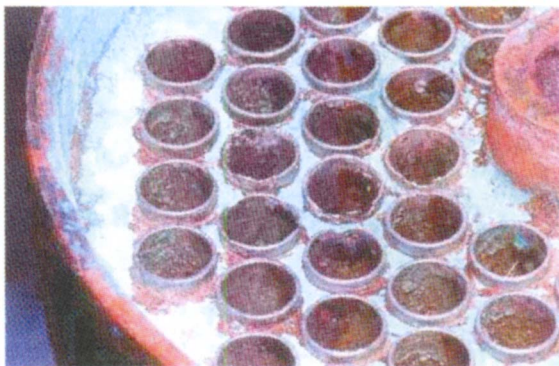


Fig. 5 Corrosion of the CuNi sliding end. Tubes exhibiting end slotting and wall thinning

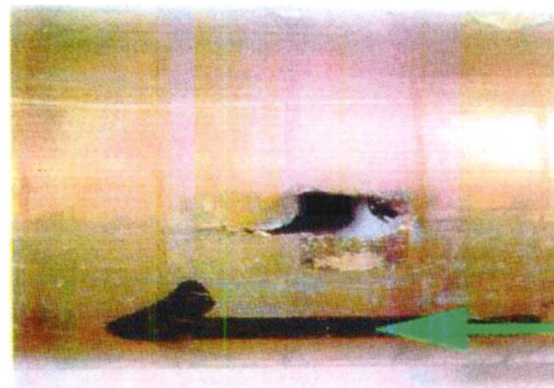


Fig. 6 CuNi tubestack showing through hole perforation

solved oxygen and low in debris or marine growth. Although only a few microns thick, the thin adherent film matures to full strength in most 70/30 CuNi systems in approximately 90 days but published literature makes reference to a considerable variation in this figure. Furthermore, formation can be dramatically reduced when (a) much shorter periods are used, (b) when the process is interrupted, or (c) where any of the previously identified negative factors are encountered such as increased salinity, increased pollutants, entrapped solids and deposits, etc.

The degree of protection that the film offers is crucial to the longevity of the cooler tubestack and, in this case, the ultimate life of the gas turbine bearings (there is no “fail safe” mode for tube leakage).



Fig. 7 CuNi tubestack through hole perforation, wall thinning, presence of black deposit, and oxide film

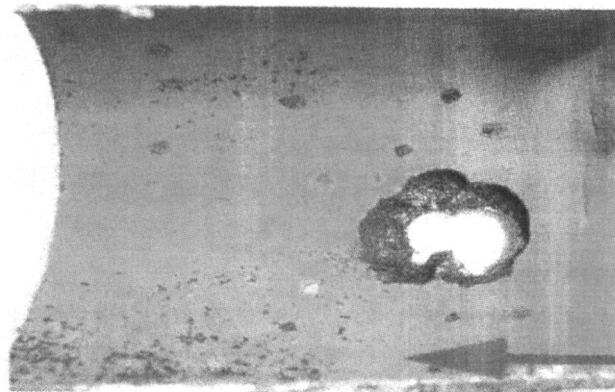


Fig. 8 CuNi tubestack through hole perforation localized pitting and brown copper oxide

All very well, but this relies on dockyards being alert to “best practice” at the commissioning stage of the ship or the strategy relies heavily on ship staff awareness of the issues during replacement of a tubestack while at sea.

This practical advice has uncovered a known weak point with cooler installation and upkeep on gas turbine ships at the point of commissioning or following a period of maintenance. The evidence ties in well with the previously discussed problems on ships whose coolers had failed within two years of a refit period such as that shown on HMS Cumberland.

A chemical dosing agent such as Ferrous Sulphate or Sodium Dimethyldithiocarbamate can be introduced upstream of the equipment to be protected to accelerate protective film formation. Additionally, a biocide such as Hydrogen Peroxide can usually deter attachment of organic matter. Both would be used in a “total loss” capacity, usually with severe environmental restrictions.

Failure Observations. *Type “A” Failures* (i.e., those that had occurred following refit, repair, or essential Dockyard maintenance):

- Three UK dockyards are contracted to undertake ship refits. A high number of Type “A” failures had occurred in one particular dockyard where post refit flood-up was physically undertaken at the end of an estuarial basin found later to be high in pollutants, nitrates, sulphates, and marine organisms. Combined with this, it is known that a second yard used for earlier ship building was based immediately on the Clyde Estuary. This is a significant clue to the identification of the corrosion mechanism discussed later.
- It was common for ship’s SW systems to be commissioned and then remain flooded for long periods, in excess of three to four weeks. Some of the failures were observed to have occurred where the SW systems were inactive in order to prepare for refit milestones or completion dates. On the occasions where the SW system was isolated and drained down, it was not customary practice at the time to open up the coolers and air dry them. However, there is substantial evidence [6] to suggest that the practice of using clean seawater to burn-in tube type heat exchanges was well known, despite a lack of documented servicing advice and maintenance history available to support this in RN operation.
- At one time, the MoD specified the use of Sodium Dimethyldithiocarbamate as a pre-treatment dosing agent. However, any chemical treatment appears to be in decline, especially as newer corrosion resistant materials come on line which have better anti-corrosion properties and do not require the expense of an injection system.

EU Marine Pollution Legislation appears to have tightened in the mid 1990s. Certain SW dosing compounds were discontinued but Tuthill [7] reports that commercial shipping operating with Ferrous Sulphate still do so to strict port turn round times and rarely experience significant corrosion problems, even in polluted harbors.

There are few cited examples where dosing systems are used in RN service, HMS Endurance being the only example the author investigated having a mixed metal galvanized steel and 90/10 CuNi SW system. Generally, dosing has historically been precluded from naval warship operation for environmental, cost and maintenance reasons even under intermittent operation.

- Neither the cooler manufacturer or Rolls Royce had originally recommended periodic inspections of the tubestack upon entry of the gas turbines into service. Uneasy with such a policy and having no firm knowledge of the effect of the conditions on the growth rate of marine crustacean that can take place within the tubes, the UK MoD decision at this point was to adopt a two-year maintenance operation to remove, clean (by freshwater lance and dedicated rodding equipment) and inspect the tubestack and end plates in order

to maintain longevity and thermal performance. If significant corrosion or erosion was evident then tube plugging or complete unit replacement was specified. The procedure has been in place for many years.

A maximum of eight tubes (representing 10%) could be plugged in this manner without significantly effecting heat transfer rate. This routine was adopted until 1997 when questions started to be asked about the cost effectiveness of the strategy and the level of risk involved in sending repaired units back into service (£1000 per item compared to a typical cost of £100,000 to undertake a Tyne bearing replacement due to chloride corrosion).

Risk of failure increases with depth of corrosion. Arguably, a major concern was that a successful pressure test with plugged tubes did not ensure leak free operation after re-introduction back into service.

Type “B” Failures (i.e., those that had occurred in-service following ship staff maintenance):

- Some ships had followed maintenance procedures strictly to the BR, while others had to minimize activities due to reduced compliment or higher priorities (an example is the continued operation of the SW Circ system through the coolers even when engines are shut down);
- Up until 1997, guidance relating to the mandatory draining, flushing and drying of CuNi coolers during periods of extended inactivity had not been promulgated to GT vessels. As a consequence, a number of ships reported their cooler failures directly after routine shutdown or after a period of crew leave. This was particularly evident where the ship was berthed in estuarial water for the duration of its stay or if it had previously undertaken littoral duties operating within sight of shore.

Results of Studies: The Corrosion Mechanism

Prior to drawing up conclusions as to the corrosion mechanisms involved with the CuNi tubestack and the post failure remedial activity undertaken, a summary of the key observations are presented;

- Installation, commissioning, operating, and refit procedures were considered too relaxed—there was risk of insufficient “burn-in” for new coolers, risk of water stagnation occurring during shut down (oxygen is depleted), and poor on-board maintenance,
- A step reduction had occurred in the preference for oxidation and biocide dosing of SW systems,
- The tubestack failure trend favors ships that have undergone maintenance in estuarial waters exposed to high amounts of organic activity, pollutants and effluent followed by operation at sea in aerated un-polluted seawater,
- Failed tubestacks showed:
 - significant corrosion and erosion of the SW inlet tube-plates and general corrosion of the bores accompanied by tube clogging, black deposits, localized pitting, and through holes in one or more tube walls,
 - visual proliferation of mussels, crustacean, and seaweed attachment within end plates and tube ends,
 - smell of “rotten eggs” upon withdrawal of the tubestack indicating the presence of dissolved hydrogen sulphide gas.

The evidence indicated the combined presence of two major failure mechanisms; (a) localized impingement erosion at the tube plate faces caused by turbulent flow around partial tube blockages (mussel shells, sediment, and entrapped debris) leading to erosion of the parent metal and depletion of the protective oxide film Fig. 5 and (b) the presence of sulphide corrosion within the tubes caused by the acid secretion from Sulphate Reducing Bacteria

(SRB) through a mechanism of Microbial Induced Corrosion (MIC). This was detected by Price when spot testing samples using the sodium azide chemical test [3]. This test is specific to sulphides and can detect their presence with good repeatability.

Compared to open water, sulphides are found in higher concentrations around outflows rich in nitrates and phosphates or when water conditions support the growth of Sulphate Reducing Bacteria (SRB). These areas are typically industrial outlets to main waterways where effluent and a rise in water temperature is apparent. Both these conditions were supported from the evidence collected.

SRB thrive on the slow decomposition and decay of micro organisms which release nutrients back into solution in the form of nitrogen and phosphorous. Depending on the strain, this can occur under oxygenated or de-aerated conditions but pollution level plays a critical role. They tend to be prolific and voracious reproducing with dramatic intensity, especially when seawater is still and stagnant over an appreciable time scale, but reportedly as short as three to four days [7].

Under depleted oxygen conditions, such as in the case of a tubestack flooded with seawater during periods of commissioning or shut down inactivity, sulphides form under a black slime corrosion product which is less adherent and protective than the normal copper oxide film. During research, Syrett found that when oxygen was not present to form a stable oxide film, concentrations of sulphide as high as 55 mg/ltr would still provide acceptable corrosion resistance in conditions up to 5 m/s [8]. This slime and discoloration was detected in all RN cases investigated by Price and McCann [5].

Once a system is re-commissioned with aerated pollution free seawater, the sulphide deposits are washed away to expose clean bright metal which will eventually regain a protective oxide film but on this occasion, the film takes considerably longer to form and corrosion rates are reported to be considerably higher as there is an element of galvanic corrosion over the newly exposed anodic regions [7]. In addition, water that contains significant hydrogen sulphide can be very corrosive towards all copper alloys, acting as a corrosion accelerator even in very small concentrations [5].

Substantial evidence supports this pattern of events in the cooler failures which occurred, especially those within 200 h of leaving a refit period despite renewal or repair of the tubestack.

The RNLN conduct refit and maintenance activity away from a primary source of estuarial or pollutant rich seawater using a commissioning and drain down philosophy more advanced than that of the Royal Navy, hence the reason for the lack of cooler incidents within the Royal Netherlands Navy.

Recovery Actions Employed

For the purposes of identification, 1998 was a turning point in the identification of the problems and the implementation of a vast array of recovery actions. These are classified as; *short term* “quick wins” (immediate actions with the chance of instant results at low cost) and those that required *long term* investigation and implementation.

Short Term Recovery. Investigation of the cooler failures revealed the importance of correct maintenance and care of the coolers in order to establish the protective oxide coatings in the tubestack.

It was clearly undesirable that coolers remain full of stagnant polluted sea water, particularly if they were new or had been repaired by acid cleaning and pressure testing. Ships and maintenance authorities were instructed to;

- (a) Flush new or replacement tubestacks continuously with clean aerated sea water for a minimum of 14 consecutive days to establish a protective oxide layer to resist subsequent attack. Evidence showed that the most critical period was the first two to three weeks of service, this being

the minimum period to provide protection for the normal working life of the tubestack against subsequent encounters with polluted water.

- (b) Maintenance instructions [9] were re-written to include an annual routine instead of bi-annually.
- (c) More detailed inspections were employed to look for signs of tube end slotting, wall thinning and corrosion, prior to cleaning in order to raise awareness of the corrosion problem.
- (d) The significance of a sulphurous odor was highlighted as characteristic of SRB.
- (e) Personnel were made aware of the very serious health consequences of exposure to hydrogen sulphide gas, a fact not previously published to operators undertaking tubestack replacement.
- (f) Acid cleaning, mechanical de-scaling (rodding), high pressure water jetting and tube plugging was deleted for tubestacks below 10 in diameter.
- (g) Correct commissioning procedures were stipulated. If symptoms of unreasonable levels of corrosion were present, the tubestack would now be replaced with a new item.
- (h) The re-introduction of overhauled tubestacks was discontinued as it carried unnecessary risk of failure.
- (i) Tubestacks less than 10 in diameter were reclassified as “consumable” rather than “repairable” items.
- (j) Cast Naval Brass endplates were discontinued as they permitted increased erosion corrosion and leakage.
- (k) During refits or inactive periods over 14 days duration, coolers would now be isolated, drained and, end caps removed, flushed with fresh water and left to dry out.
- (l) Ships and bases were made aware of the need to operate within correct seawater circulating parameters for pressure, flow, etc., especially in estuarial waters where there is an increased risk of erosion from suspended solids.
- (m) Tubestacks were immediately replaced on ships deploying on extended duties. Without question, this action alone was considered an immediate priority and responsible for saving at least £800,000 of premature repair arisings and lost operational life between overhauls.

Longer Term Potential. Longer term alternatives to the use of a CuNi tubestack were investigated. The emphasis on assessment was to highlight viable options that would lead to a positive increase in engine reliability whilst representing value for money alongside a short and recoverable “pay back” period. Out of service dates also needed to be considered. Dosing and treatment of the entire SW system were again revisited and discounted for the reasons outlined earlier.

The “Leak Free” Cooler. An interesting design of “inherently safe leak free cooler” manufactured by Aberdeen Radiators Ltd. in the UK was also investigated. The design features a tube-within-tube principle utilising a material of the customers choice. The cooling medium and the medium to be cooled are effectively separated by a thin layer of ethylene glycol antifreeze solution within an annular space. As a minimum requirement, a differential pressure gauge is fitted to this cavity to indicate the rise in glycol pressure above a set operational limit. Leakage from one of the other fluids into the annular space is immediately apparent by a rising pressure on the gauge. More significantly this prevents contamination of the fluid being cooled irrespective of the type of fluid.

Furthermore, the cooler can be run to failure without fear of contaminating machinery coolant or lubricating oil if this is a desirable and cost effective strategy. Whilst the cooler design fully met the requirements for GT cooling and costs appeared to provide value for money, the increase in overall size required to meet

Table 3 Comparison of material properties of titanium grades 2 and 5 against CuNi grades 90/10 and 70/30

Material Property	Copper Nickel Alloy		Titanium Alloy	
	90/10	70/30	Grade 5	Grade 2
	Density (kg/m ³)	8900	8950	4420
Specific Heat (J/kg K)	377	377	560	519
Melting range (°C)	1122	1205	1650	-
Thermal conductivity (W/mK)	50	29	6.7	22
Coefficient of linear expansion: 10 to 300 °C (10 ⁻⁶ /K)	17	16	9.2	8.9
Electrical resistivity (microhm cm)	19	34	0.170	-
Modulus of Elasticity (GN/m ²)	130	148	114	103
Relative Shock Resistance	0.36	0.24	2.5	1
Yield Strength (MN/m ²)	90	105	828	275

the desired thermal performance was a significant constraint in terms of the additional work required to modify the gas turbine base plate.

This option was, therefore, not considered further, however, may well be of interest to other operators where space is not at such of a premium.

The Titanium Cooler Tubestack. Price and McCann's discussions with the original cooler manufacturer, Serck, led to interest in a titanium cooler tubestack that was being offered for use in submarines to resist MIC. Interestingly, around this time, Peacock had reported that Titanium had "comparatively little use" by the RN [2]. Indeed, progress with the use of titanium in the RN was relatively slower than that in other navies such as the Royal Norwegian Navy or the US Navy. Nowadays, the position has improved somewhat with the assistance of outside research agencies such as the UK's QinetiQ organisation to build up extensive data and evaluation programs.

The process by which titanium claims increased corrosion resistance over a CuNi alloy depends on the similar build up of a protective oxide film. Titanium oxide is also reportedly more inert and tenacious than copper oxide, forming rapidly on contact with oxygen within seconds rather than weeks and its higher strength increases resistance to erosion, cavitation and crevice corrosion along with reduced density, lighter products, and better resistance to shock. The oxide film is also self healing if damaged. Published material properties for two widely used commercially available titanium alloys are compared to CuNi in Table 3 [10].

The material's availability and use is gradually improving, especially within the offshore oil industry. Despite this, however, titanium still suffers from crevice attack, hydrogen uptake and galvanic effects when coupled to dissimilar metals as in a ships SW system. The advice by Peacock is that it should never simply be used to directly replace a lesser material without realistic validation or testing [2]. There are however, a vast number of long established titanium heat exchanger and condenser programmes in the Process and Petrochemical industries which are of great interest. Reports on the use of titanium in seawater environments indicate very favorable resistance to debris erosion, SRB and the vast majority of known failure mechanisms [10]. With this in mind, UK MoD set out with a primary aim to establish:

- **Feasibility and Costs:** for 70 in-service CuNi units—clearly a primary objective before undertaking fleet wide replacement.

- **Galvanic Performance:** back to back rig testing of the titanium cooler verses the CuNi item undertaken by members of the Nuclear Department of the School of Air and Marine Engineering, HMS Sultan.
- **Thermal Performance:** back to back testing involving in situ trials on three operational vessels.
- **Manufacturing timescale:** post test introduction of 70 units to the Tyne and Spey fleets.

Through Life Costs. In terms of direct hardware costs, the results were surprising. A direct replacement tubestack in Grade 2 titanium alloy compared well with the existing 70/30 CuNi item at a cost ratio of only 3.5:1. Due to their own perception, the RN had wrongly anticipated this multiplier to have been between 8 and 10 so were pleasantly encouraged by the reality. Additionally, there was scope for further reduction in costs if tubestacks could be ordered in sufficient batch quantities to provide economies of scale during manufacture.

To replace all RN tubestacks and provide a sufficient level of support stock, 70 titanium units are required at a cost of approximately £200 k. To put this into perspective, the modification to embody a titanium cooler into the RN fleet could be accommodated at less cost than would occur due to a single Tyne bearing failure. Additionally, titanium coolers would be fitted for the remaining lives of the vessels. This could provide significant increase in engine reliability and substantial cost savings in terms of spares, maintenance and reduction in engine premature failure rate.

This is an entirely credible financial argument for the introduction of the new material into the RN but the option has not been met with open arms by the Royal Netherlands Navy on the grounds that similar failure modes have never been experienced in RNLN service for the reasons highlighted earlier in this paper. This may prove to be a high risk decision and places additional responsibility on UK MoD and the OEM to ensure CuNi tubestacks remain available for use by the RNLN Spey vessels.

Trial to Establish the Galvanic Performance of a Titanium Cooler. One of the main concerns with the new titanium tubestack when in contact with the original aluminum alloy cooler body and bronze end plates is that titanium is more protected (more noble) than the items it is to be coupled to. This led to suspicion that there could be system related corrosion problems due to the coupling effects. It would be pointless using a titanium cooler tubestack if the rest of the ship dissolved around it [11].

Metals which are galvanically close to titanium are reported to perform satisfactory, as shown in the abridged galvanic series shown in Table 4.

To investigate the problem, research was undertaken using two separate tests;

Rig Test. The first tubestack was tested in a purpose built rig designed and manufactured by students undertaking project work as part of SEMC Training at HMS Sultan, the RN's School of Air and Marine Engineering. The trial was conducted using back-to-back galvanic testing with a CuNi tubestack to record and assess the open circuit potentials at specific points around the cooler assembly and, in so doing, confirm that the corrosion rate was acceptable both in conditions of flow and when shut down with stagnant sea water [12].

The Rig Test revealed that:

- by using the standard "O" seals and gaskets both CuNi and Titanium tubestacks were isolated from the water boxes and end covers with no intimate electrical contact observed by either unit,
- the static testing of the galvanic potential ranged from 175 to 220 mV, discounting temperatures over 90°C, Fig. 9 refers.
- with SW flowing, the measured potential of the CuNi tubestack was 0.25 mV p-p bandwidth with a mean of

Table 4 Galvanic series in clean, oxygenated seawater at 35° C based on electrode potential measurements

Material	Steady State Electrode Potential (vs.SCE) (volts)
Graphite	+ 0.25
Zeron 100 Super Duplex Steel	- 0.01
316 Stainless Steel passive	- 0.05
22%Cr Duplex SAF2205	- 0.07
Monel 400	- 0.08
Hastelloy C	- 0.08
Titanium	- 0.10
13%Cr Stainless Steel passive	- 0.15
316 Stainless Steel active	- 0.18
Nickel Aluminium Bronze	- 0.20
70/30 Copper Nickel alloy	- 0.25
13%Cr Stainless Steel active	- 0.52
Carbon Steel	- 0.61
Aluminium	- 0.79
Zinc	- 1.03
Magnesium	- 1.70

0.37 mV, that for the titanium tubestack was markedly different with a greater bandwidth of 5.0 mV p-p about a mean of 0.30 mV.

- despite the titanium tubestack cooler assembly standing for 8 weeks in stagnant sea water, no significant changes in potential compared to flowing sea water conditions were noted,
- following 8 weeks of inactivity, the titanium tubestack was clean and bright with no corrosion or deposits, Fig. 10–12 describe.
- a stable, green oxide film was present on exposed cooler box surfaces with no evidence of biological activity,
- the annular crevice region around the inlet box “O” seal showed negligible evidence of corrosion,
- there was no degradation of the titanium tubestack.

Under the inherent measuring interference of the hardware, significant harmful potentials could not be detected. Although it was not possible to calculate a corrosion rate, testing concluded no adverse electrochemical corrosion existed with the introduction of

Basic cell potential (variation with temperature)

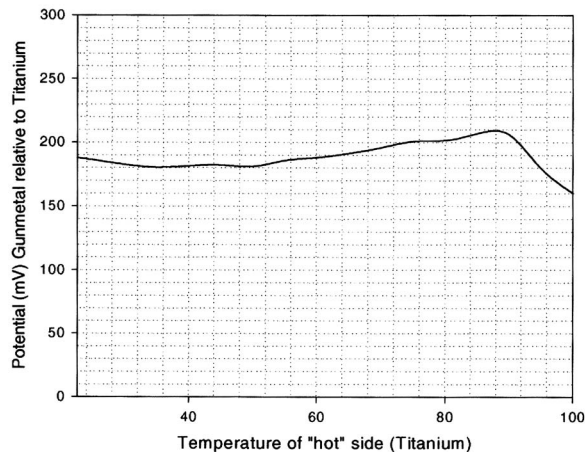


Fig. 9 Temperature dependence of electro chemical potentials. HMS Sultan Titanium SWLO cooler static testing.



Fig. 10 Overview of HMS Sultan test rig water box inlet side assembly, after 8 weeks standing

the titanium cooler under test conditions.

Ship Test. The second tubestack for the galvanic trial was operated in HMS Edinburgh (Tyne powered ship) for a period of 2 years. The ships program involved littoral duty and operation in a tropical climate [13].

The Ship Test revealed that after two successful years in service under a wide variety of conditions:

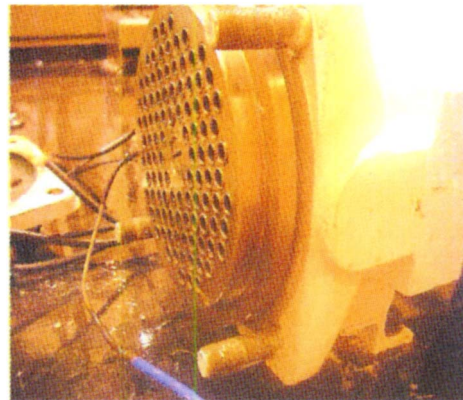


Fig. 11 Absence of notable corrosion on titanium tubestack, remaining shiny throughout

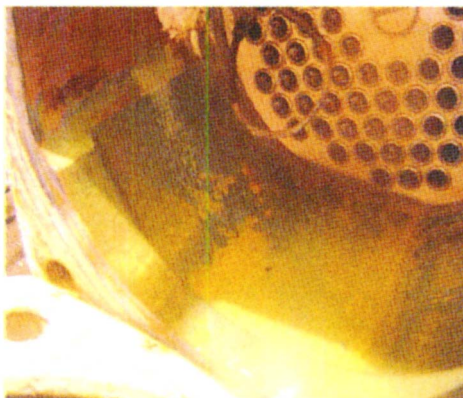


Fig. 12 Crevice region shows slight discoloration but it is not deteriorated

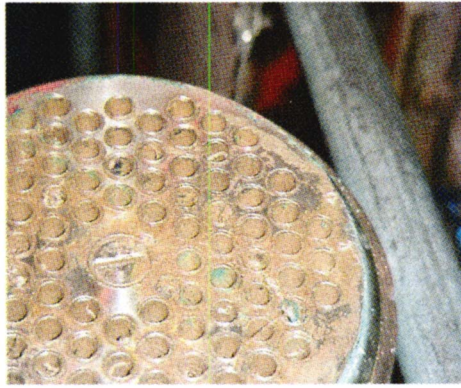


Fig. 13 Titanium tubenest in service on HMS Edinburgh showing end plate original machining marks still intact

- a stable oxide film had passivated the tubestacks and despite theoretical expectations, galvanic pitting was not evident to any significant effect, the titanium surfaces were clean and almost free from biofouling, exceptions being a number of established crustaceans resembling barnacles, Fig. 13 refers,
- the water boxes were free from biofouling with an even coating of green oxide film,
- at tube entry, the tubestack showed no signs of localized impingement corrosion or crevice attack,
- cleaning revealed a maximum depth of material wastage of 1 mm around the periphery of the endplate over a 120 deg arc extending no more than 10 mm from the gasket face, evident in Fig. 14.

A condition based maintenance strategy could be explored by monitoring the performance and SW pressure drop. This was considered a favorable inspection with no system problems reported, however, a recommendation was made to undertake an annual strip and clean of the tubestack and cooler body followed by a 2 annual "system check-up."

Trial to Establish the Thermal Performance of a Titanium Cooler. The second concern was with the thermal performance of the Grade 2 titanium cooler over the CuNi item due to its lower thermal conductivity, see Table 3. In reality, the Titanium Information Group advises that wall thickness for titanium tubing can normally be reduced by as much as 30% over the equivalent diameter of CuNi material [10], however, in the case of the gas turbine tubestack, it was thought that this may adversely effect heat transfer take up from the surface of the stack to the seawater.

Using a conservative approach, the titanium unit was designed



Fig. 14 Water box inner surface

with an equal number of tubes as the CuNi item, 78 in all, with an equal outer diameter of 10 mm. Tube thickness was increased only slightly from 0.9 to 1.00 mm from the titanium unit thereby allowing an increased corrosion allowance.

Two ships; HMS Montrose (Spey powered ship) and HMS Southampton (Tyne powered ship), each installed two titanium tubestacks to monitor temperature profiles and material conditions over mixed periods of operation during a timescale of 18 months. During this period, no reported incidents of excessive oil temperature were recorded. Furthermore, upon stripping, the material condition of the tubestacks were very similar to that of HMS Edinburgh.

Marine crustacea were certainly present but they do not so readily attach to a titanium oxide film so were easily removed by cleaning to leave a bright corrosion free surface on tubes, endplates and water boxes. Tube baffle plate fretting under vibration and shock was not a feature in any of the tubestacks inspected.

Investigation Closing Recommendations

Based upon the evidence provided, UK MoD were content that the failure mechanisms had been fully investigated and that sufficient evidence existed to commence an embodiment program to replace CuNi tubestacks with those manufactured from Titanium Grade 2.

The ship trials have been closed, however, the titanium units will remain in operation following the recommendations to explore the periodicity of inspections and Condition Based Maintenance. Initial assessment will be undertaken at one-year intervals until sufficient knowledge has been built up to relax this periodicity. This is considered achievable within two to three years.

Despite the increase in wall thickness of the titanium unit over the equivalent CuNi tubestack, no further changes are planned.

Remedial recovery actions for the CuNi tubestack previously outlined will remain in place until full fleet wide introduction has been accomplished.

Summary and Conclusions

UK MoD have embarked upon two parallel programs to understand the phenomenon of gas turbine main line bearing failures in RN Tyne and Spey operation and to investigate and implement an alternative course of action with a Titanium cooler that is considered to provide a lifetime, value for money, retrofit solution.

Analysis of the problems experienced with the auxiliary mounted CuNi SWLO cooler tubestack used in the GT lubricating oil supply, has identified a principle corrosion mechanism and many other additional factors which combine for failure events to occur.

This has generated a wealth of understanding of the effects and actions necessary to prevent Microbial Induced Corrosion, in particular that due to Sulphate Reducing Bacteria. The work has also benefited those responsible for lubricating oil maintenance and a number of key points, particularly regarding contamination testing, have been learnt. A greater understanding of these type of issues relies on continual education and retraining of designers, on-board operators, support officers, and dockyard maintenance staff.

Furthermore, where dosing and biocide is an environmental concern and cannot be accommodated, there is a real need for taught commissioning and operating procedures which accommodate shut down periods lasting more than a few days. This needs to become standard practice, regardless of the materials involved.

As RN operations move to more littoral waters and as pollutants around coastlines gradually increase, there is a shared view of an upsurge in SRB activity for the foreseeable future. This is alarming as many vessels (commercial ones included), will still be in operation in the next 20–30 years. Certainly food for thought.

Finally, any views expressed are those of the author and do not necessarily represent those of the Department/Agency.

Acknowledgment

Lt. Cdr. A. Schaap (RNLN)/Mr. R. Bolwell (UK MoD MPS214); Experience with Aero-Derivative Gas Turbines as Marine Propulsion Machinery, NATO RTO Paper, Symposium on Gas Turbine Operation and Technology for Land, Sea and Air, Ottawa 1999. Mr. R. Bolwell (UK MoD MPS214); Through Life Management of Naval Gas Turbines for Extended Service Lives and Reduced Lifetime Costs (GT-2002-30269), ASME Turbo Expo 2002, June 3–6 2002, Netherlands.

Nomenclature

BR = Book of Reference (Gas Turbine handbook)
CuNi = Copper Nickel alloy, grade 70/30 or 90/10
HMS = Her Majesty's Ship
MIC = Microbial Induced Corrosion
MoU = Memorandum of Understanding
OEM = Original Equipment Manufacturer
RN = Royal Navy
RNLN = Royal Netherlands Navy
SEMC = System Engineering Management Course
SRB = Sulphate Reducing Bacteria
SW = sea water
SWLO = Sea Water Lubricating Oil
WSA = UK Warship Support Agency

References

- [1] "Factors Affecting the Corrosion and Fouling of Metal Condenser Tubes of Copper Alloys and Titanium," 1978, Sumitomo Light Metal Technical Reports, Vol 19, Nos. 3/4.
- [2] Peacock, D. K., 1998, "Effective Design of Marine High Performance Corrosion Resistant Systems Using Titanium," *TransIMarE*, **110**, Pt. 3, pp. 155–170.
- [3] Price, R., 2000, "Investigation into Failures of Tyne and Spey Lubricating Oil Coolers," Unpublished UK MoD Report, Apr. 27.
- [4] British Standards Institute, 1973, "Code of Practice for Salt Water Piping Systems in Ships (Obsolete)," British Standard BS MA18.
- [5] McCann, A. J., 1998, "Failure Investigation into HMS Cumberland Tyne and Spey GT Sea Water Lub Oil Coolers," Unpublished UK MoD report, Feb. 13.
- [6] Mistry, A. J., 1992, HMS Argyll Cooler Failure Investigation, Spey Development Technical Report SDTR 232, Mar. 24.
- [7] Powell, Carol A., 1992, "CuNi Alloys-Resistance to Corrosion and Biofouling," Copper Development Association Seminar Technical Report 7044-1919.
- [8] Tuthill, A. H., 1987, *Guidelines for the Use of Copper Alloys in Seawater*, Copper Development Association, Materials Performance Manual, pp. 155–170.
- [9] Defect Acquaint Form S/No. 4528V1, 2001, unpublished UK MoD S2022a (1998 original revised and updated).
- [10] "Titanium for Offshore and Marine Applications," 1999, *A Designers and Users handbook*, 2nd ed., Titanium Information Group.
- [11] Todd, B., and Lovett, P. A., 2000, *Selecting Materials for Sea Water Systems*, Marine Engineers Practice, **2**, Pt. 10, June.
- [12] Jarman, S. E., Winzar, J., Chard-Tuckey, P. R., Dickinson, P., Heron, B., Kilmartin, A., and McGregor, C., 2003, "An Electrochemical Performance Investigation of Polymetallic Seawater/Lube Oil Heat Exchangers Used in Spey and Tyne Gas Turbine Installations," unpublished UK MoD Report.
- [13] Jarman, S. E., and Chard-Tuckey, P. R., 2002, HMS Sultan Nuclear Department, In Service Inspection of Ti oil cooler fitted to HMS Edinburgh, unpublished UK MoD Report.

Vladimir D. Weinstock

Propulsion Engineer
Northrop Grumman,
One Space Park Drive,
m/s 140/2134C
Redondo Beach, CA 90278
e-mail: vladi.weinstock@ngc.com

Stephen D. Heister

Professor
School of Aeronautics and Astronautics,
Purdue University,
1282 Grissom Hall,
West Lafayette, IN 47907-1282
e-mail: heister@ecn.purdue.edu

Modeling Oil Flows in Engine Sumps: Drop Dynamics and Wall Impact Simulation

A computational preliminary design tool has been developed to help simulate drop-related processes that take place in an oil sump of a gas turbine engine accounting for drop motion, deformation, breakup, and drop/wall interactions including wall film impact and potential splashing. Aerodynamic interactions with the gas phase are considered using an exact solution of the Navier–Stokes equations to approximate the annular gas flow. Detailed results for the baseline case that attempts to replicate the conditions found in a typical oil sump of a turbofan engine are presented. In addition, the results of more general parametric studies utilizing a simplified geometry that investigated the effects of changing various parameters are discussed. [DOI: 10.1115/1.1924432]

Introduction

The lubrication system of a typical gas turbine engine consists of a pump that supplies oil to many different portions of the engine that require lubrication and cooling. A special oil scavenging system is designed to collect the oil after it has fulfilled its function and return it to the oil tank in order to be filtered, cooled, and reused. The oil is often injected in areas where high-speed rotating machinery is present that results in extremely complex two-phase air/oil flows for which it is difficult to obtain experimental data. Nevertheless, understanding these processes is very important in order to design reliable and efficient lubrication systems that supply the necessary amounts of oil while minimizing leakage.

Several factors contribute to the complexity of flow processes in the lubrication subsystem of gas turbine engines. Forces due to aerodynamic interaction of the oil with the spinning gas (windage), viscosity, gravity, and drop/film or drop/wall interactions can all affect the oil behavior and the draining characteristics of the sump. Drops shed from seal runners and bearings contain some of the most energetic fluid as they can exit at a significant fraction of the shaft speed. For this reason, mass and momentum interactions with the wall and other components in the bearing chamber are largely dependent on drop behavior.

The present work is concerned with simulating oil drop trajectories and drop/wall interactions in oil sump geometries similar to that found in the Rolls-Royce AE3007 gas turbine engine. Specifically, the center oil sump of the AE3007 was chosen as the baseline case in the present work. Figure 1 shows a schematic of the sump. Oil is delivered via a pressurized pipe and is sprayed through a nozzle onto the rotating seal runner with the goal of providing lubrication and cooling to the engine seal. The oil is then driven along the seal runner by its momentum and centrifugal forces and develops into a thin liquid film due to the rotation of the seal runner. Upon reaching the edge of the seal runner, the oil is flung off as a train of drops in the direction of the outer sump wall. Experiments of Radocaj [1] suggest that typical drop diameters are in the range of 100 to 1000 μm . These drops interact with surrounding airflow (induced by the high rotational speed of the shaft), which leads to their deformation and possible in-flight breakup. Finally, drops impact the outer sump wall and transfer a portion of their momentum to the liquid film that covers the wall. If the impact is strong enough, drops splash and create a large

number of secondary droplets that eventually also impact the wall at some other location and transfer a portion of their momentum to the liquid film. The film migrates around the sump and eventually is scavenged out by using a combination of gravity and a fixed displacement pump.

The objective of the present work is to use the best available knowledge in the areas of drop deformation, breakup, and drop/wall interactions in order to develop a preliminary design tool to rapidly track the drops from the moment of separation from the edge of the rotating seal runner to the point of impact with the outer sump wall, to simulate the drop/wall impact event, and to assess the effects of changes in various parameters on the amount of momentum that is eventually transferred to the liquid film at the wall. Shimo [2] considered oil film behavior along the seal runner and the outer sump wall concurrently with the present effort. The model is described in the next two sections, followed by results of baseline and parametric studies aimed at identifying the influence of design parameters on drop momentum transfer to the wall film.

Drop Tracking Model

The main purposes of the drop tracking model are to determine the motion of a single parent drop from the edge of the rotating seal runner to the point of impact with the outer sump wall and to determine impact parameters needed for the drop/wall impact simulation. In addition, the core of the drop tracking model is subsequently used to individually track secondary droplets that are formed after the parent drop impacts the wall.

The airflow between the rotating shaft and the stationary outer sump wall is nonuniform and fairly complex. Because the main goal of this work is to develop a preliminary design tool, it is very important to keep the run time as short as possible, so an exact solution of the laminar Navier–Stokes equations for flow between rotating and stationary cylinders was employed:

$$V_g = R1\omega \left[\frac{R1/R2}{1 - (R1/R2)^2} \right] \left[\frac{1 - (r/R2)^2}{r/R2} \right] \quad (1)$$

where V_g is the tangential gas velocity magnitude, $R1$ is the radius of the inner rotating cylinder, $R2$ is the radius of the outer stationary cylinder, ω is the rotational speed in rad/s, and r is the radial coordinate. Physical properties of the oil (density ρ_o , dynamic viscosity μ_o , and surface tension σ_o) are computed as a function of oil temperature using available data from the oil manufacturers as described by Weinstock [3].

As a typical 100–1000 μm drop moves through a gas, aerodynamic forces cause it to distort. Larger, aerodynamically unstable

Contributed by the Structures and Dynamics Division of ASME for publication in the JOURNAL OF ENGINEERING FOR GAS TURBINES AND POWER. Manuscript received September 3, 2003; final manuscript received December 13, 2004. Editor: N. Arakere.

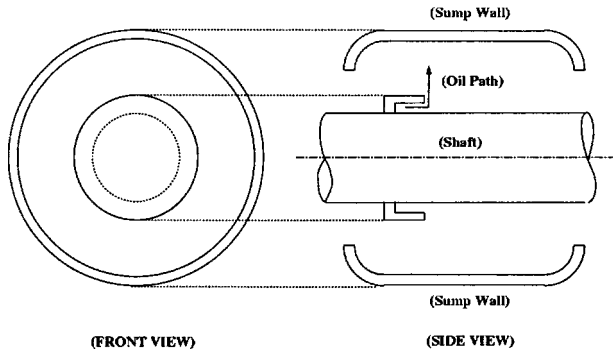


Fig. 1 Schematic of the oil sump

drops eventually can deform into a thin liquid ellipsoid. This distortion significantly affects the drop's drag coefficient and thus has an important influence on the drop's trajectory. In addition, sufficiently high deformations can lead to a breakup of the parent drop into many secondary droplets.

One of the earliest and most widely used drop deformation models is the Taylor Analogy Breakup (TAB) model of O'Rourke and Amsden [4] used in the KIVA hydrodynamics code [5]. The model is based on an analogy between an oscillating and distorting drop and a spring-mass system first suggested by Taylor [6]. The drop deformation and breakup (DDB) model proposed by Ibrahim et al. [7] is used in the present work. It is similar to the TAB model but is formulated in terms of the motion of the center of mass of the half-drop (the TAB model is formulated in terms of the displacement of the drop's equator). It is assumed that the liquid drop is deformed due to a pure extensional flow from an initial spherical shape of radius r into an oblate spheroid of an ellipsoidal cross section with semimajor axis a and semiminor axis b . Defining the dimensionless time $\bar{t} = tV_r/r$ and center of mass motion $\bar{y}_c = y_c/r$, where V_r is the drop/gas relative velocity, the dimensionless DDB equation can be written as follows:

$$\left(\frac{\rho_l}{\rho_g}\right) \frac{d^2 \bar{y}_c}{d\bar{t}^2} + \left(\frac{8}{\text{Re} \bar{y}_c^2}\right) \left(\frac{\mu_l}{\mu_g}\right) \frac{d\bar{y}_c}{d\bar{t}} + \left(\frac{27}{8} \frac{\pi^2}{\text{We}}\right) \bar{y}_c \left[1 - 2 \left(\frac{3\pi}{4} \bar{y}_c\right)^{-6}\right] = 3/8 \quad (2)$$

where ρ is the fluid density, μ is the fluid viscosity, and Re and We are the Reynolds and Weber numbers based on the relative velocity between the two fluids and the initial drop diameter:

$$\text{We} = \rho_g V_r^2 d / \sigma_l \quad \text{Re} = \rho_g V_r d / \mu_g \quad (3)$$

The initial conditions for the dimensionless form of the DDB model are $\bar{y}_c = 4/(3\pi)$ and $d\bar{y}_c/d\bar{t} = 0$ at $\bar{t} = 0$. The authors also state that the model is applicable to shear-type (typically at $\text{We} > 40$) deformation of spray drops in pure extensional flows.

Deformation of the drop has an important effect on its drag coefficient. Usually, the drop drag coefficient is specified as a function of the drop Reynolds number using a standard solid-sphere correlation:

$$C_{D,S} = \begin{cases} \frac{24}{\text{Re}} \left(1 + \frac{1}{6} \text{Re}^{2/3}\right) & \rightarrow \text{Re} \leq 1000 \\ 0.424 & \rightarrow \text{Re} > 1000 \end{cases} \quad (4)$$

Liu and Reitz [8] and Liu et al. [9] found that the drop drag coefficient was related to the magnitude of the drop deformation as follows:

$$C_D = C_{D,S} (1 + 2.632 y_1) \quad (5)$$

where parameter y_1 for the case of the DDB model is calculated as proposed by Hwang et al. [10]:

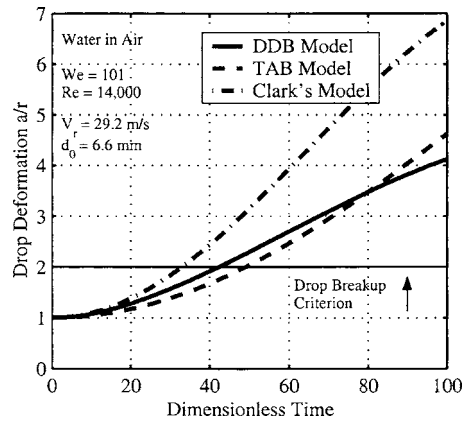


Fig. 2 Comparison of various drop deformation models

$$y_1 = \min(1, [a/r - 1]) \quad (6)$$

where $a = (3\pi/4)y_c$ is the semimajor axis of the deformed drop. Equation (5) reflects the fact that the drag coefficient of a deformed drop should lie between that of rigid sphere and that of a disk. Drag coefficients of a spherical drop and a disk are recovered in the undistorted and fully distorted limits. In addition, Hwang et al. proposed that the projected area of the drop based on the semimajor axis, $A_p = \pi a^2$, should be used in drag force calculations.

Figure 2 compares the TAB, DDB, and Clark's [11] drop deformation models, with the drop deformation a/r plotted versus the dimensionless time \bar{t} . The specific set of initial conditions was chosen to match the figure presented by Ibrahim et al. [7]. All integrations were performed using a fourth-order Runge-Kutta scheme. It should be noted, however, that while drop deformation curves obtained by using the TAB and Clark's models match those in Ref. [7], results based on the DDB model do not. Pham [12] reached a similar conclusion. It appears that, at least for the conditions relevant to gas turbine oil systems, the TAB and DDB models give similar results.

Sufficiently high drop deformations can lead to a breakup of the parent drop into many secondary droplets. Several criteria have been proposed to help determine the onset of breakup as well as to characterize the size of the resulting secondary droplets. The issue is additionally complicated by the fact that most of the previous theoretical and experimental investigations focused on drop breakup in uniform gas flows, which is not the case in the present work. Some authors [4,13,14] proposed a time for the onset of breakup in terms of a dimensionless breakup time, while others [7,10] proposed a breakup criterion based on the drop deformation a/r exceeding a critical value. All of the breakup criteria based on the dimensionless breakup time were derived assuming uniform gas flows; hence their applicability to the current work is limited. Dai and Faeth [13] reported that drop deformations do not proceed much higher than $a/r = 2$ before breakup process takes over and therefore this breakup criterion was chosen for the present work; the same criterion was also used by Hwang et al. [10]. In order to determine the size of the secondary droplets that are formed as a result of a parent drop breakup, an expression proposed by O'Rourke and Amsden in their TAB model [4] is used:

$$d_s = 12\sigma_l / (\rho_g V_r^2) \quad (7)$$

where d_s is the Sauter Mean Diameter (SMD) of the secondary droplets.

Drop acceleration is integrated in time subject to aerodynamic interactions, drop deformation, and drop breakup. A standard three-dimensional cartesian coordinate system is used as shown in Fig. 3. The z direction is along the shaft centerline from the front toward the aft of the gas turbine engine, the y direction is verti-

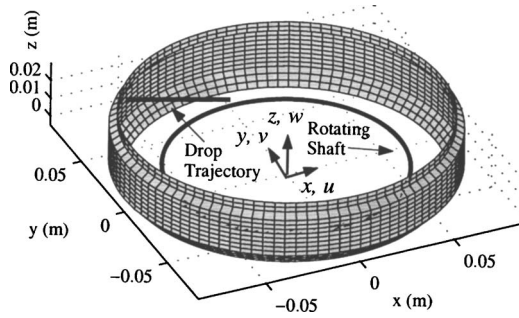


Fig. 3 Cartesian coordinate system and sample drop trajectory

cally from bottom to top, and the x direction is to the right when standing aft and looking forward. The shaft is rotating counter-clockwise (aft looking forward) and the drop is assumed to separate off the edge of the seal runner, which is located slightly above the shaft. Weinstock [3] describes geometry generation and details of the drop/wall impact checking logic. Using Newton's second law, drop's equations of motion can be written in the following form:

$$\frac{du}{dt} = 3C_D \frac{\rho_g a^2}{\rho_l d^3} |\mathbf{V}_g - \mathbf{V}| (u_g - u) \quad (8)$$

$$\frac{dv}{dt} = 3C_D \frac{\rho_g a^2}{\rho_l d^3} |\mathbf{V}_g - \mathbf{V}| (v_g - v) - |g| \quad (9)$$

$$\frac{dw}{dt} = 3C_D \frac{\rho_g a^2}{\rho_l d^3} |\mathbf{V}_g - \mathbf{V}| (-w) \quad (10)$$

where d is the original drop diameter, a is the semimajor axis of the deformed drop, and u , v , w are the x , y , z components of the velocity, respectively. Gas velocity magnitude is given by Eq. (1) and drag coefficient by Eq. (5). Notice that gas velocity is assumed to have no axial component, therefore there is no w_g term in Eq. (10). Equations (8)–(10) are solved simultaneously with the drop deformation Eq. (2) by using a fourth-order Runge–Kutta numerical integration scheme.

Drop/Wall Impact Model

A number of models were proposed and applied to study spray/wall and drop/wall impact processes over the last decade [15–23]. Most of these models were created to help better understand spray/wall interactions that take place inside diesel and gasoline engines. Until recently, various researchers' approaches to solving the drop/wall impact problem have been fairly inconsistent. Several of the recently proposed models point to a more general agreement; nevertheless, wall impact modeling remains a very complicated problem and an active area of research. A brief summary is presented here while Weinstock [3] provides a more detailed literature review.

Drop Impact Regimes and Splash Criterion. The collision of a drop with a wall may result in several different regimes. At low impact energy, the drop sticks to the wall; at slightly higher energy levels, a rebound mode is encountered in which the drop bounces off the surface. At higher impact energies, a spreading mode is encountered and the drop forms a film on a dry wall or merges with an existing film on a wet wall. At even higher impact energies, the drop will splash and atomize into smaller droplets. Generally, all four regimes can be observed when the wall temperature is less than the boiling temperature of the liquid, which is always the case in the present work. A good overview of the various regimes and their dependence on wall temperature is given by Bai and Gosman [16]. The existence of these regimes is governed by

a number of parameters which include liquid properties (density, viscosity, surface tension), drop properties at the moment of impact (size, velocity, angle with respect to the wall), and wall conditions (temperature, surface roughness, liquid film thickness). The effect of some of these parameters on the process of drop splashing was investigated in detail by Stow and Stainer [24]. Many of the above parameters can be combined into Weber and Reynolds numbers based on the normal component of the drop's velocity with respect to the wall, drop diameter, and liquid properties. The normal component of the drop's impact velocity is used because numerous previous experiments showed it to be more important in predicting the outcome of a drop/wall collision than the total magnitude of the impact velocity.

Wachters and Westerling [25] investigated the behavior of drops impinging on very hot dry walls. Their experiments, as well as those of others [26–28] showed that the first two impact regimes, sticking and rebounding, occur at very low impact Weber numbers, typically at $We < 10$. Based on preliminary calculations it was determined that splashing will be the primary regime of interest in the present work because of high magnitude of the drop's normal velocity component at impact (on the order of 30 m/s) and relatively large drop diameters (hundreds of microns). Therefore, drop sticking and rebounding regimes are ignored in the present work, and all attention is focused on the spread/splash transition criterion and modeling of the splashing process.

Mundo et al. [29] investigated liquid spray drops impinging on dry smooth and rough surfaces. The authors varied liquid properties, drop sizes, and impingement angles and velocities while also measuring the sizes and velocities of the secondary droplets using phase-Doppler particle analyzer (PDPA). They found a correlation for the onset of the splashing regime in terms of a certain dimensionless parameter K :

$$K = We^{0.5} Re^{0.25} = 57.7 \quad (11)$$

Values of $K < 57.7$ lead to a complete deposition of the impinging drop, while $K > 57.7$ corresponds to drop splashing into many secondary droplets. A larger value of the parameter K causes a larger mass fraction of the impinging drop to be splashed. Size and velocity distributions of the secondary droplets reported by Mundo et al. in the form of probability density functions (pdf) serve as a basis for several drop/wall impact models.

O'Rourke and Amsden [23] used the work of Mundo et al. [29] and Yarin and Weiss [30] to come up with a slightly modified splash criterion that is subsequently used in their drop/wall impact model. The authors proposed that the splash criterion should depend on the wall film thickness, thus requiring a modification of Eq. (11). They used theoretical justification given by Yarin and Weiss in order to modify the Mundo splash criterion to account for the presence of a liquid film. O'Rourke and Amsden splash criterion is based on the impact parameter E exceeding a critical value:

$$E^2 = We / (\min(h_0/d, 1) + 1/\sqrt{Re}) > (57.7)^2 \quad (12)$$

where h_0 is the film thickness. Equation (12) is the splash criterion used in the present work.

Impact Model Description. A recently developed impact model of O'Rourke and Amsden [23] is used in the present work. The model appears to combine the best available experimental data with sound theoretical considerations and ease of implementation. Simulating a drop/wall impact consists of the following steps. First, a single parent drop is tracked until it hits the wall. If the impact is not energetic enough to cause a splash as determined by Eq. (12), it is assumed that the drop's mass and preimpact tangential momentum are transferred to the liquid film while the normal component of the momentum is assumed to be completely dissipated. Otherwise, secondary droplet properties are determined as a function of the impact parameter E and impact veloc-

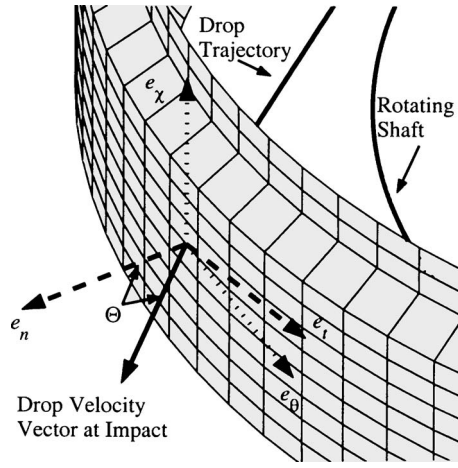


Fig. 4 Parent drop impact geometry

ity. All secondary droplets are then tracked separately in the same manner as the parent drop until they hit the wall. Secondary droplet impacts are far less energetic and do not result in a splash, so it is assumed that they simply merge with the liquid film and transfer their tangential momentum upon impact. Parent drop impact geometry is shown in Fig. 4.

Secondary droplet properties are chosen to conform to the experimental results [29,30] using an energy consistency result [23] and splash direction results of Naber and Reitz [15]. The total mass fraction of the secondary droplets m_s/m is chosen to conform to the results of Yarin and Weiss [30]:

$$\frac{m_s}{m} = \begin{cases} 1.8 \times 10^{-4} (E^2 - E_{\text{crit}}^2) & \rightarrow E^2 < 7500 \\ 0.75 & \rightarrow E^2 > 7500 \end{cases} \quad (13)$$

where $E_{\text{crit}}=57.7$ corresponds to the splashing threshold. With known m_s/m the mass and momentum additions to the liquid film at the original impact point can be determined. For example, momentum added in the circumferential (θ) direction along the grid at a given grid point (i, j) closest to the impact location is given by

$$M_{\hat{e}_\theta}(i, j) = (1 - m_s/m)m(\mathbf{V} \cdot \hat{e}_\theta) \quad (14)$$

where m and \mathbf{V} are the mass and velocity of the parent drop at the moment of impact.

Size distributions of the secondary droplets are reported by both Mundo et al. [29] and Yarin and Weiss [30] in the form of probability density functions (pdf) of secondary droplet radius r_s divided by the parent drop radius r . O'Rourke and Amsden proposed using a Nukiyama-Tanasawa size distribution [31] of the form

$$\text{pdf}(r_s) = \frac{4}{\sqrt{\pi}} \frac{r_s^2}{r_{\text{max}}^3} \exp \left[- \left(\frac{r_s}{r_{\text{max}}} \right)^2 \right] \quad (15)$$

where r_{max} is the droplet radius at which the pdf achieves its maximum value. The value of r_{max}/r is a function of E that O'Rourke and Amsden approximate by the following expression:

$$r_{\text{max}}/r = \max(E_{\text{crit}}^2/E^2, 6.4/\text{We}, 0.06) \quad (16)$$

The first argument in Eq. (16) approximates experimental results of Mundo et al. who only reported size distributions near the splashing threshold. The second argument limits the sizes of secondary droplets at high impact Weber numbers and is obtained from an energy consistency requirement that the total energy of the secondary droplets (including their surface energy) cannot exceed the incident drop energy [23]. Finally, the results of Mundo et al. and Yarin and Weiss indicate that r_{max}/r is never less than

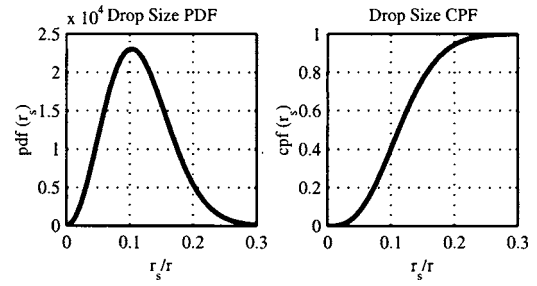


Fig. 5 Typical secondary droplet size distributions

0.06, which is approximated by the third argument in Eq. (16).

Usually the sizes of individual secondary droplets are determined by integrating Eq. (15) to obtain a cumulative probability function (cpf):

$$\text{cpf}(r_s) = \frac{-2}{\sqrt{\pi}} \frac{r_s}{r_{\text{max}}} \exp \left[- \left(\frac{r_s}{r_{\text{max}}} \right)^2 \right] + \text{erf} \left(\frac{r_s}{r_{\text{max}}} \right) \quad (17)$$

where erf is the error function. Figure 5 depicts typical pdf and cpf functions for the distribution chosen. Secondary droplet sizes could then be computed by selecting a random number p from the interval (0,1) and r_s is chosen such that $\text{cpf}(r_s)=p$.

Using the above approach in the present work, however, results in a problem: if the size of a particular secondary droplet is too small, then there exists a possibility that the droplet will be trapped by the rotating airflow and will continue moving along with it indefinitely without either hitting the wall nor traveling outside the computational domain. To avoid this difficulty, a different approach is used: all secondary droplets are replaced with the same number of droplets of identical size equal to the distribution's Sauter Mean Diameter (SMD) or d_{32} :

$$d_{32,s} = 2 \left(\int_{r_{s,\text{min}}}^{r_{s,\text{max}}} r_s^3 \text{pdf}(r_s) dr_s \right) / \left(\int_{r_{s,\text{min}}}^{r_{s,\text{max}}} r_s^2 \text{pdf}(r_s) dr_s \right) \quad (18)$$

where $r_{s,\text{min}}$ and $r_{s,\text{max}}$ define the interval of pdf secondary droplet radii over which the integral is being evaluated. Knowing $d_{32,s}$ allows determination of the total number of secondary droplets formed after impact $N_s = (m_s/m) (d/d_{32,s})^3$ from mass conservation. The actual number of secondary droplets simulated during impact event, N_{sim} , is a user input. All results are later adjusted for the actual number of secondary droplets formed after impact. This is done in order to have statistically representative results even in the event the number of actual secondary droplets is small and to simulate the average of a large number of parent drop impacts. A value for N_{sim} is recommended after each time the model is run using a statistical analysis of secondary droplet impact properties that relies on confidence-interval approach [3]. Typical values of N_{sim} used in the present work are in the range of 500–1000.

Secondary droplet velocity distributions were reported by Mundo et al. [29]. O'Rourke and Amsden approximate the observed distributions by choosing secondary droplet velocities \mathbf{V}_s according to the following expression:

$$\mathbf{V}_s = (-\bar{w})\hat{e}_n + [0.12(\mathbf{V} \cdot \hat{e}_n) + \bar{v}][(\cos \bar{\psi})\hat{e}_t + (\sin \bar{\psi})\hat{e}_p] + [0.8(\mathbf{V} \cdot \hat{e}_t)]\hat{e}_r, \quad (19)$$

where $\hat{e}_p = (-\hat{e}_n) \times \hat{e}_t$, \mathbf{V} is the parent drop impact velocity, and \bar{w} , \bar{v} , and $\bar{\psi}$ are random variables chosen as follows. Quantity \bar{w} is the normal component of the secondary droplet velocity and is chosen from the Nukiyama-Tanasawa distribution:

$$\text{pdf}(\bar{w}) = \frac{4}{\sqrt{\pi}} \frac{\bar{w}^2}{\bar{w}_{\max}^3} \exp \left[- \left(\frac{\bar{w}}{\bar{w}_{\max}} \right)^2 \right] \quad (20)$$

where $\bar{w}_{\max} = 0.2(\mathbf{V} \cdot \hat{e}_n)$. Quantity \bar{v} is the fluctuating component of the secondary droplet tangential velocity chosen from the Gaussian distribution:

$$\text{pdf}(\bar{v}) = \frac{1}{\sqrt{2\pi}\delta^2} \exp \left[- \frac{\bar{v}^2}{2\delta^2} \right] \quad (21)$$

where $\delta = 0.1(\mathbf{V} \cdot \hat{e}_n)$. The final random variable, $\bar{\psi}$, represents the angle that the fluctuating tangential velocity makes with the vector \hat{e}_t in the plane of the wall. It takes on values in the interval $(-\pi, \pi)$ and is chosen according to the distribution suggested by Naber and Reitz [15]:

$$\text{pdf}(\bar{\psi}) = \frac{\beta}{2\pi(e^\beta - 1)} \exp \left[\beta \left(1 - \frac{|\bar{\psi}|}{\pi} \right) \right] \quad (22)$$

where $\beta > 0$ is a parameter related to the drop/wall impact angle Θ (measured with respect to \hat{e}_n) by the following expression:

$$\sin \Theta = \left[\frac{e^\beta + 1}{e^\beta - 1} \right] \left[\frac{1}{1 + (\pi/\beta)^2} \right] \quad (23)$$

Expression for the cumulative probability function of $\bar{\psi}$ cannot be obtained analytically because of the $|\bar{\psi}|$ term in Eq. (22), so cumulative trapezoidal numerical integration is employed instead, while Eq. (23) is solved for β iteratively by using Newton's method.

Secondary Droplet Tracking. Secondary droplet tracking is analogous to tracking of parent drops using the droplet size and velocity distribution functions as initial conditions for the simulation. Parent drop impact point is assumed to be the launch point for secondary droplets. The drop breakup model is disabled during secondary droplet tracking because the droplets are not expected to breakup due to their already small size. Drop deformation model can be either enabled or disabled depending on the options set by the user. Secondary droplet impacts with the wall are not energetic enough to cause a splash, thus it is assumed that droplets simply merge with the liquid film at the wall. Droplet tangential momentum is transferred to the film while the normal momentum is assumed to be completely dissipated. Mass and momentum additions at the impact grid points are determined in a manner similar to that of the parent drop [Eq. (14)] but adjusted for the actual number of secondary droplets formed after impact versus the number being simulated.

Finally, a major output of the impact simulation is a measure of how much momentum is transferred to the liquid film at the outer wall as a result of both parent and secondary droplet impacts. For the purposes of this work, it has been decided to use the initial momentum of the parent drop when it leaves the seal runner as a reference. Momentum transferred to the liquid film in the circumferential direction along the grid is used for comparison because it is larger in magnitude and is more significant than the grid-axial momentum. The degree of momentum transfer to the liquid film is measured by an efficiency η defined as follows:

$$\eta = \left(\sum_{i=1}^{i \max} \sum_{j=1}^{j \max} M_{\hat{e}_\theta}(i,j) \right) \left(\frac{N_{\text{drops}}}{m_0 |\mathbf{V}_0|} \right) \quad (24)$$

where m_0 and $|\mathbf{V}_0|$ are the initial mass and velocity of the parent drop as it leaves the seal runner, and N_{drops} accounts for the fact that the original parent drop can break up in flight prior to hitting the wall, resulting in several "miniparent" drop impacts. Physically, the momentum transfer efficiency measures the drop momentum losses due to drag, secondary atomization events and wall collisions. If the bearing chamber annulus is large, drops will decelerate significantly and may break up in flight. If secondary

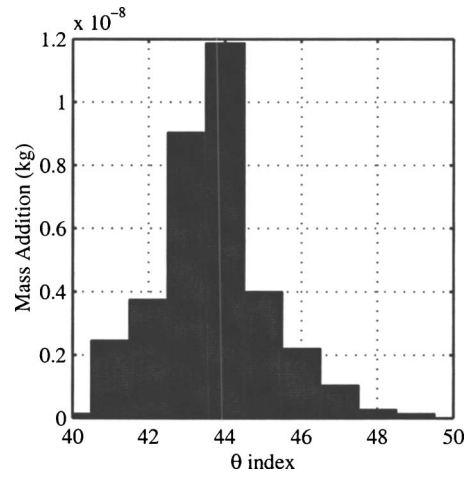


Fig. 6 Typical mass distribution following a single parent drop impact at a fixed axial distance

atomization does occur, then aerodynamic drag becomes even more important for these smaller droplets. The resultant momentum transfer efficiency permits designers to estimate the remaining momentum/velocity in the film formed on the outer sump wall.

Extension of a Single Drop Impact Simulation. All of the preceding discussion centered on predicting the outcome of a single parent drop impact at a given point on the outer wall. In a practical situation such as that found inside a gas turbine engine sump, it is necessary to extend the results of a single drop impact in order to match the total oil mass flow rate. Central to this effort is the assumption that all drops contained in a given mass flow rate will undergo identical impacts uniformly spaced along the circumferential (θ) direction. If this approach is extended and it is assumed that there is at least one parent drop that impinges at every grid point along the θ direction, then calculating the total mass deposited at a given point (i,j) adjusted for the effect of neighboring drop impacts simply amounts to integrating the results of a single drop impact along the θ direction at a fixed axial location (Fig. 6) and then assigning this value to all grid points with the same axial location. Lastly, the results need to be multiplied by a correction factor that specifies how many parent drops will impact at each θ location per unit time, adjusted for the possibility of in-flight breakup, in order to match the total mass flow rate. The procedure for determining momentum addition per unit time is analogous.

Other values of interest include the mass and momentum addition fluxes. Therefore, it becomes necessary to determine the area of the outer wall that should be used in the flux calculation. Only the area affected by droplet impacts is used in computing the mass and momentum fluxes. Specifically, the area of a grid cell is added to the total flux area if the total mass deposited at all grid cells with the same axial location exceeds one percent of the total mass flow rate. Mass flux is calculated as follows:

$$m_{\text{flux}} = \left(\sum_{i=1}^{i \max} \sum_{j=1}^{j \max} \dot{m}_{\text{tot}}(i,j) \right) / A_{\text{flux}}, \quad (25)$$

where A_{flux} is the outer wall area affected by droplet impacts and $\dot{m}_{\text{tot}}(i,j)$ is the total mass addition per unit time at a given grid point. The procedure for determining momentum fluxes in the grid-circumferential and grid-axial directions is analogous.

Results and Discussion

Drop tracking and impact simulations were conducted for a variety of initial conditions. Most of the attention was focused on

Table 1 Initial conditions for the baseline case

Grid size ($i \max \times j \max$)	15 × 101
Shaft radius $R1$ (m)	0.060
Sump wall to shaft radius ratio $R2/R1$	1.43
Shaft rotational speed ω (RPM)	15 000
Oil mass (volume) flow rate (kg/s) (gal/min)	0.0211 (0.35)
Gas pressure (kPa)	101.3 (1 atm)
Liquid and gas temperature ($^{\circ}\text{C}$) ($^{\circ}\text{F}$)	82.2 (180)
Sump wall oil film thickness (μm)	1000
Initial parent drop diameter (μm)	700
Initial parent drop velocity (m/s)	$u=-60, v=0, w=15$
Initial parent drop position (m)	$x=0, y=0.065, z=0$
Parent drop tracking time step (s)	1.0×10^{-5}
Secondary droplet tracking time step (s)	1.0×10^{-5}
Number of secondary droplets simulated	1000

the baseline case that closely resembles the geometry and operating conditions found in the Rolls-Royce AE3007 gas turbine engine. In addition, parametric studies were conducted that investigated the effect of changing specific parameters on overall results.

Baseline Case. Initial conditions for the baseline case are intended to match the conditions inside the Rolls-Royce AE3007 turbine engine center oil sump. Table 1 shows a detailed list of all initial conditions for the baseline case. Most of the values in Table 1 come from known engine operating conditions and physical characteristics of the center oil sump. Parent drop initial diameter and velocity components are assumed to be the same as the properties of the liquid film at the edge of the rotating seal runner. Shimo [2] developed a detailed model of film behavior from the moment of injection to the point of separation from the edge of the seal runner concurrently with the present work. It should be noted, however, that at the time of this writing there still was a general lack of experimental data to help validate the initial conditions and/or the results presented here.

Although the code contains provisions for handling in-flight parent drop breakup, it was decided to disable this feature in the present work. This was dictated by the fact that in the baseline case drop deformation never reaches the breakup criterion of $a/r=2$ as will be shown shortly. In some of the parametric studies it is possible that the breakup criterion is reached; however, because of the extremely short time scales, it is argued that the drop breakup process still will not be complete by the time parent drop impacts the outer sump wall. For the baseline case it takes slightly less than 1 ms for the parent drop to reach the outer sump wall. In addition, having the breakup feature turned off allows for a better comparison with the baseline case where drop breakup does not occur. Secondary droplets that are formed after parent drop impacts the outer sump wall experience much less deformation because of their smaller size and therefore the breakup model is always disabled during secondary droplet tracking regardless of whether or not it is used to track the parent drop.

Figures 7–9 show parent drop tracking results for the baseline case. In order to conserve space and ease comparison, parent drop tracking results are shown for a range of possible drop sizes: 100 μm , 400 μm , 700 μm , and 1000 μm . Figure 7 shows a simplified two-dimensional view with outlines of the shaft and the outer sump wall. Note that since parent drop separates off the edge of the rotating seal runner, its starting radial position is slightly larger than shaft radius $R1$. For complex outer wall geometry, wall radius $R2$ is taken as being equal to the wall radius in the middle of the grid. It is these values of $R1$ and $R2$ that are used to compute the gas velocity. From Fig. 7 it is clear that parent drops travel in virtually straight lines. The trajectory of the 100 μm drop is more affected by interactions with the gas because of the drop's smaller mass and thus larger acceleration.

Figure 8 shows velocity, radial distance, and relative Weber number histories of the parent drops. Again, velocity and position

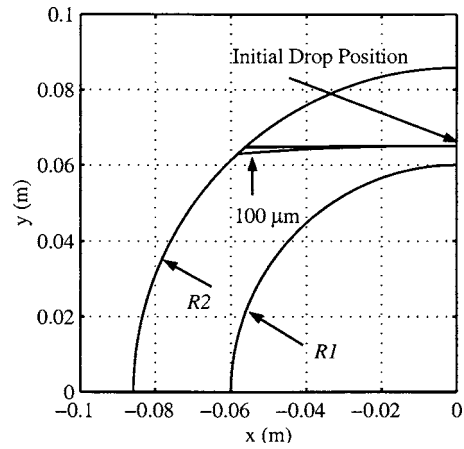


Fig. 7 Parent drop trajectories (baseline case)

histories of the larger drops are nearly identical, and only the results for the 100 μm drop continue to stand slightly apart from the rest. An interesting insight can be gained from the relative velocity history plot: initially, the magnitude of the relative velocity is low because both the drop and the gas have fairly high velocities near the shaft that are roughly in the same direction. As the drop travels farther away from the shaft, gas velocity magnitude decreases much more rapidly than that of the drop, and therefore the relative velocity of the drop with respect to the gas continuously increases. Weber number histories are very different for all drops because the Weber number directly depends on drop size.

Drop deformation histories are shown in Fig. 9. None of the drops reach the breakup criterion of $a/r=2$ before impacting the

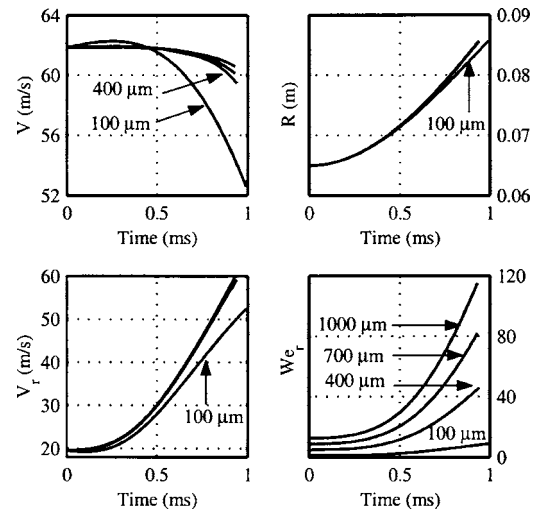


Fig. 8 Parent drop trajectory details (baseline case)

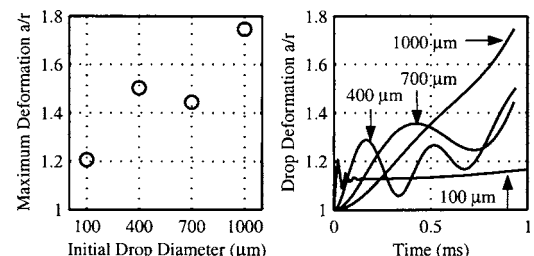


Fig. 9 Parent drop deformation histories (baseline case)

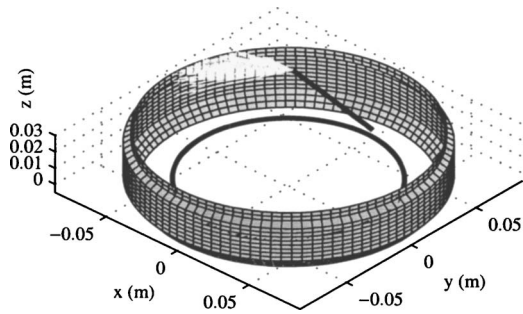


Fig. 10 Secondary droplet trajectories as a result of a 700 μm parent drop impact (baseline case)

wall. The smaller 100 μm drop remains virtually undeformed throughout. Larger drops are much more easily deformed and thus show the importance of including the drop deformation model in the calculations, even though its effects in the baseline case are probably small because of extremely short flight times. The oscillations are present because the drop deformation model is based on an analogy between an oscillating and distorting drop and a spring-mass system.

Results of the parent drop impact with the outer sump wall for the baseline case are shown in Figs. 10–13. These results are for the impact of a 700 μm parent drop only as it is difficult to show the results for multiple drop sizes on the same plot as was done with parent drop trajectories. The results of the impact simulation are summarized in Table 2. Only 55% of the parent drop's initial

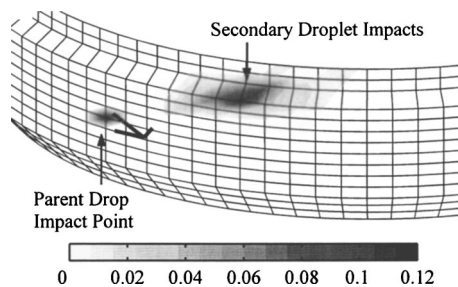


Fig. 11 Mass distribution following a 700 μm parent drop impact as a fraction of the parent drop mass

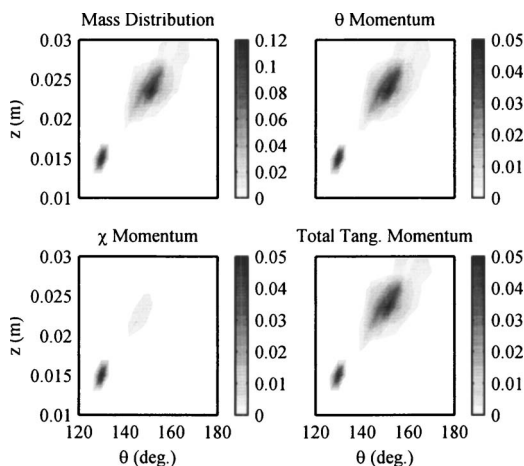


Fig. 12 Mass and momentum distributions following a 700 μm parent drop impact. Mass and momentum values are shown as a fraction of the parent drop mass and momentum when it leaves the seal runner.

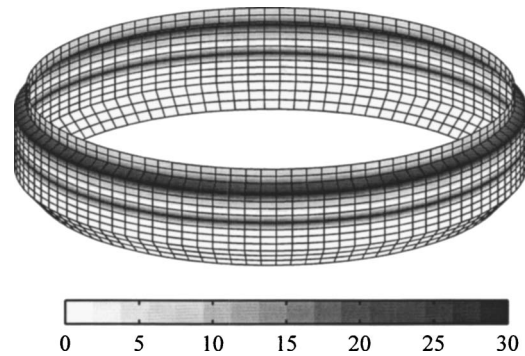


Fig. 13 Extension of single drop impact results: mass distribution around the circumference of the sump at a fixed axial location as percentage of the total mass flow rate

momentum (when it separates from the edge of the seal runner) is eventually transferred to the liquid film at the outer sump wall in the grid-circumferential direction.

Figure 10 shows the trajectories of all secondary droplets that were formed after impact. Dark lines show droplets that traveled outside the computational domain and are considered lost. Figure 11 shows a mass distribution footprint. Large arrow near the original impact point indicates the direction in which the parent drop struck the wall. It should be noted that 25% of the parent drop's mass (or 0.25 on a fractional basis) is deposited at the original impact point; however, in order to resolve the fine details in the footprint it was necessary to modify the color scale and restrict it to the range of 0–0.12.

Figure 12 shows the same mass distribution footprint as in Fig. 11, only in a 2D projection. Also shown are the tangential momentum distribution footprints in both θ and χ directions as well as their combined magnitude. Similarly to Fig. 11, all color scales were adjusted in order to resolve fine details in the footprints. Momentum distribution is shown as a fraction of the parent drop's initial momentum.

Results of extending a single drop impact simulation in order to match the total oil mass flow rate are shown in Fig. 13. Overlapping footprints of individual drop impacts create continuous bands of constant mass addition around the circumference of the sump. The location of parent drop impacts clearly stands out as a thin band in the middle of Fig. 13. The largest amount of mass addition, however, takes place at a location where the curvature of the sump changes abruptly, thus creating a barrier for many secondary droplets that would have otherwise impacted at some other location further away from the original impact point. This effect is clearly a result of the specific geometry considered in the present

Table 2 Results of a 700 μm parent drop impact simulation (baseline case)

Drop velocity magnitude at impact (m/s)	60.6
Impact angle Θ (deg)	50.5
Impact Weber number	32 881
Impact Reynolds number	3 671
Impact parameter E	179.9
Splashed mass fraction m_s/m	0.75
Number of secondary droplets formed	202
Secondary droplet d_{32} (μm)	108
Amount of secondary droplets lost outside the domain (%)	0.5
Total outer sump wall area (m^2)	0.0211
Sump wall area used for flux calculations (m^2)	0.0091
Average mass flux ($\text{kg}/(\text{m}^2 \text{s})$)	2.32
Average θ momentum flux ($\text{kg}/(\text{m}^2 \text{s})$)	79.9
Average χ momentum flux ($\text{kg}/(\text{m}^2 \text{s})$)	16.3
Momentum transfer efficiency η (%)	55.6

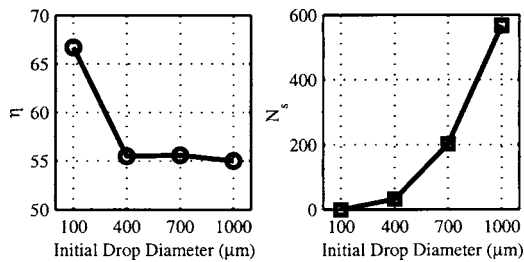


Fig. 14 Effect of parent drop size on impact results (baseline case)

work.

Concluding the description of the baseline case is Fig. 14 that shows how the most important impact simulation results (number of secondary droplets formed after impact N_s and momentum transfer efficiency η) change as a function of the parent drop size. Larger parent drops result in more violent wall impacts and therefore more secondary droplets. However, parent drop size seems to have very little effect on η except for the 100 μm drop which does not splash at all and thus has by far the highest momentum transfer efficiency.

Parametric Studies. Several parametric studies were performed to find out how the number of secondary droplets N_s and momentum transfer efficiency η are affected by the changes in the radius ratio $R2/R1$, shaft rotational speed, temperature, pressure, and liquid film thickness. All of these studies utilized a simple cylinder instead of the geometry used for the baseline case in order to make the results more general. Cylinder radius $R2$ was chosen such that the sump wall to shaft radius ratio $R2/R1$ was the same as for the baseline case (except, of course, for the radius ratio parametric study where $R2/R1$ was allowed to vary by changing $R2$). Cylinder length in the axial direction was chosen to be 0.15 m—long enough to make sure that none of the secondary droplets travel outside the computational domain. Other than the geometry and the parameter being varied, all other initial conditions were exactly the same as for the baseline case (see Table 1).

Changing the radius ratio has a dramatic effect as shown in Fig. 15. Increasing the radius ratio increases the time that the drop is subject to aerodynamic drag forces that tend to slow it down.

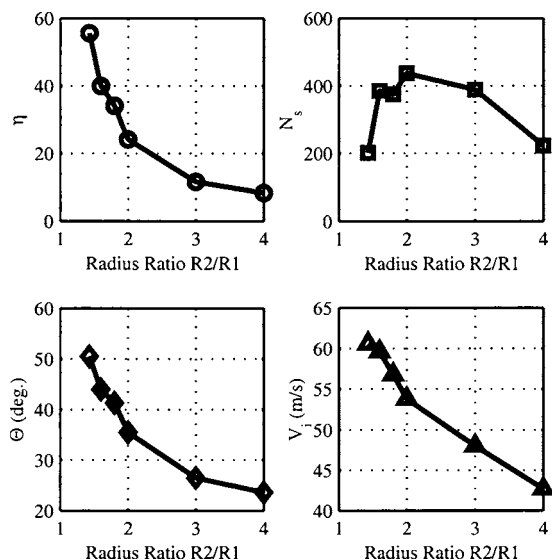


Fig. 15 Results of the radius ratio parametric study: number of secondary droplets, momentum transfer efficiency, impact angle and the magnitude of impact velocity

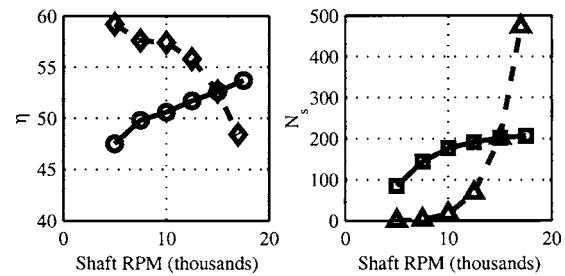


Fig. 16 Results of the shaft speed parametric study

Slower-moving parent drops cause η to decrease. Normally this would also lead to less energetic impacts, but there is another factor that comes into play: impact angle Θ that decreases with increasing radius ratio (see Fig. 15). This means that parent drops impact the wall at angles that are increasingly closer to being normal to the surface, thus increasing the normal component of the drop's velocity at impact and resulting in more energetic impacts. The effects of slower-moving parent drops and decreasing Θ compete with each other and thus explain why the number of secondary droplets formed after impact does not correlate easily with changes in the radius ratio.

Figure 16 shows the effect of changes in the shaft rotational speed. Two cases were investigated: one where the initial drop velocity was held constant at the values shown in Table 1, and one where the circumferential component of the initial drop velocity was scaled with shaft speed.

Solid lines in Fig. 16 correspond to the case of constant drop initial velocity. Increasing the shaft rotational speed decreases the amount of time that the parent drop is exposed to high relative Weber numbers because gas velocity magnitude remains high at a farther distance away from the shaft, lowering the drop-gas relative velocity. Lower relative velocities and Weber numbers mean the drop is not decelerated as much resulting in more violent impacts and a higher number of secondary droplets. The fact that η increases steadily with shaft speed is also due to smaller parent drop and secondary droplet deceleration. Changes in η of only $\sim 6\%$ for this case result from extremely short drop flight times—there simply is not enough time for aerodynamic forces to appreciably change drop trajectories as the shaft speed is varied at these conditions.

Dashed lines in Fig. 16 correspond to the case where drop initial velocity is scaled with shaft speed. At shaft speeds below 5000 rpm drop impact velocity is so low that it does not have enough energy to splash and simply merges with the liquid film at the wall, which results in the highest momentum transfer efficiency. As the shaft speed increases, so do drop initial as well as impact velocities, resulting in progressively more energetic impacts and exponentially rising number of secondary droplets. At high shaft speeds secondary droplets become very small, which makes them more easily influenced by aerodynamic deceleration and results in lower η . Overall, the transfer efficiencies for this case are of similar magnitude to those in the constant drop velocity case (solid lines in Fig. 16).

Figure 17 shows the effect of changes in the temperature. In the present work it is assumed that both air and oil have identical temperatures. The number of secondary droplets seems to increase linearly with temperature while η decreases almost linearly. It is difficult to single out a reason for this behavior because the temperature affects several parameters simultaneously: increase in temperature decreases oil viscosity, surface tension, and density while increasing viscosity of the air. However, it seems that the parent drop trajectory is virtually unaffected by the temperature: the changes in the results come in because of the difference in impact parameter E which depends on the Weber and Reynolds numbers and, therefore, liquid surface tension and viscosity. Pa-

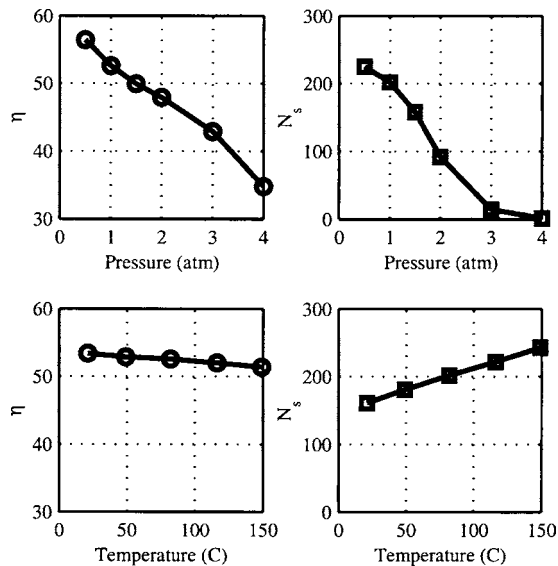


Fig. 17 Results of the bearing chamber temperature and pressure parametric study

parameter E increases with increased temperature resulting in more secondary droplets being formed. At the same time, η decreases because a larger number of secondary droplets means they are smaller in size and thus are more easily decelerated by the almost stagnant air near the outer sump wall.

Effects of air pressure variations are also shown in Fig. 17. Increase in pressure causes an immediate increase in air density and consequently the aerodynamic drag forces acting on the drop. Parent drops are more rapidly decelerated and result in less violent impacts, smaller number of secondary droplets, and smaller momentum transfer efficiency. At higher pressures the possibility of in-flight drop breakup rapidly increases even with short flight times and potentially could be an important factor to investigate in future studies.

Finally, Fig. 18 shows the effect of changes in the thickness of the liquid film that covers the outer sump wall. As the film thickness decreases, impact parameter E increases and in the limit approaches the dry-wall splash criterion of Mundo et al. [Eq. (11)]. Film thickness of less than 400 μm has no effect on impact results because the size distribution of secondary droplets stops varying—it becomes limited by the third argument of Eq. (16), which is constant. Because of the assumption that film thicknesses larger than the impacting drop's diameter do not affect the splash event [23], the results for film thicknesses greater than 700 μm are also constant. Between 400 μm and 700 μm the increasingly higher film thickness dampens the splash event resulting in smaller number of secondary droplets and higher momentum transfer efficiency.

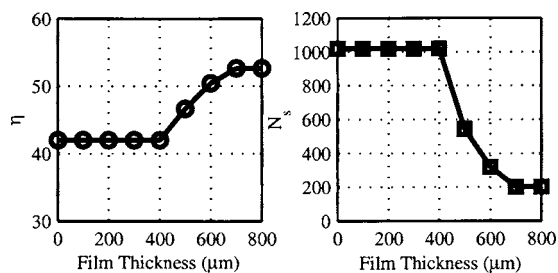


Fig. 18 Results of the sump wall film thickness parametric study

Conclusions

A computational preliminary design tool has been developed to help simulate the processes that take place in an oil sump of a gas turbine engine based on the best available knowledge in the areas of drop tracking, deformation, breakup, and drop/wall interactions. Results for the baseline case that attempts to replicate the conditions found the center oil sump of the Rolls-Royce AE3007 turbofan indicate that only about half of the oil drop's initial momentum (when it leaves the edge of the rotating seal runner) is eventually transferred to the liquid film at the outer sump wall. In addition, the drops do not reach high enough deformations to order to initiate the in-flight breakup process due to aerodynamic forces. Initial drop size has a very small effect on the amount of momentum eventually transferred to the liquid film at the wall except for the smallest of drops (less than 100 μm in diameter) that do not have enough energy to splash and simply merge with the liquid film upon impact, resulting in significantly higher momentum transfer efficiency (the fraction of the drop momentum transferred to the wall film). Because of the high initial axial velocity component of the parent drops it appears that none of them interact with the secondary droplets from earlier impacts.

Parametric studies indicate that the sump wall-to-shaft radius ratio and air pressure have the largest effect on the momentum transfer efficiency. Increasing both radius ratio and air pressure results in significantly lower amount of momentum transfer to the film due to deceleration of parent drops by aerodynamic drag forces.

In the shaft speed parametric study, momentum transfer efficiency was analyzed for two cases: (i) a constant drop speed from the baseline conditions; (ii) a variable drop speed that increased with shaft speed. Results from both cases showed different trends, but gave comparable transfer efficiencies in the 45%–60% range. This insensitivity demonstrates the utility in using the transfer efficiency parameter. Changes in temperature have very small effect on the amount of momentum transfer and this effect can be ignored for most practical purposes.

Changes in the thickness of the liquid film do not affect the amount of momentum transfer if the thickness is higher than the impacting drop's diameter or lower than about half of the impacting drop's diameter. When the film thickness is 50%–100% of the drop's diameter, the momentum transfer efficiency increases with increasing film thickness.

One of the problems with efficient scavenging of oil out of the sump is a result of high velocity of the liquid film on the outer sump wall that causes the oil to skip past the drain location. Based on the results from the present work it appears that the best way to slow the oil film down is to move the outer sump wall farther out (increasing the radius ratio) and/or to increase the air pressure inside the sump. However, both solutions may be difficult to implement. Increasing the radius ratio means that the area of the outer sump wall is increased thus potentially requiring a larger amount of oil flow for adequate cooling. Increasing the pressure means higher leakage rates through engine seals, which in turn can affect the overall engine efficiency. Nevertheless, with the help of the computational tool developed in the present work it becomes possible to predict the changes in oil film behavior as a result of design modifications without having to rely purely on experimental data or guess work.

Nomenclature

- C_D = drag coefficient
- E = impact parameter
- M = momentum
- Re = Reynolds number
- $R1, R2$ = radii of the shaft and sump outer wall, respectively
- V = velocity
- We = Weber number

d = drop diameter
 d_{32} = drop Sauter Mean Diameter (SMD)
 \hat{e}_n, \hat{e}_t = unit vectors in the wall-normal and tangential directions
 $\hat{e}_\chi, \hat{e}_\theta$ = unit vectors in the grid-axial and circumferential directions
 g = gravitational acceleration
 h_0 = liquid film thickness
 m = mass
 r = drop radius, or radial coordinate
 t = time
 u, v, w = velocity components in $x, y,$ and z directions
 \bar{v}, \bar{w} = fluctuating tangential and normal velocity components of the secondary droplet
 x, y, z = Cartesian coordinates
 y_c = distance to the center of mass of upper-half of distorted drop from its equator

Greek Symbols

Θ = drop/wall impact angle with respect to \hat{e}_n
 η = momentum transfer efficiency
 χ = axial direction along the grid
 θ = circumferential direction along the grid
 μ = dynamic viscosity
 ρ = density
 σ = surface tension
 ω = shaft rotational speed
 $\bar{\psi}$ = angle of the secondary droplet's fluctuating tangential velocity component in the plane of the wall

Subscripts

$()_r$ = relative gas/liquid conditions
 $()_g$ = gas
 $()_l$ = liquid
 $()_s$ = secondary

References

- [1] Radocaj, D., 2001, "Characterization of a Simple Aero Engine Sump Geometry," M.S. thesis, Purdue University, West Lafayette, IN.
- [2] Shimo, M., 2001, "Modeling of Oil Film Behavior on a Seal Runner and Sump Wall," M.S. thesis, Purdue University, West Lafayette, IN.
- [3] Weinstock, V. D., 2001, "Modeling of Drop Trajectories and Drop/Wall Interactions in Gas Turbine Engine Sumps," M.S. thesis, Purdue University, West Lafayette, IN.
- [4] O'Rourke, P. J. and Amsden, A. A., 1987, "The TAB Method for Numerical Calculation of Spray Droplet Breakup," SAE Paper No. 872089.
- [5] Amsden, A. A., O'Rourke, P. J., and Butler, T. D., 1989, "KIVA-II: A Computer Program for Chemically Reactive Flows with Sprays," Technical Report LA-11560-MS, Los Alamos National Laboratory, Los Alamos, NM.
- [6] Taylor, G. I., 1963, "The Shape and Acceleration of a Drop in a High Speed Air Stream," *The Scientific Papers of G. I. Taylor*, G. K. Batchelor, ed., University Press, Cambridge, MA, Vol. III.
- [7] Ibrahim, E. A., Yang, H. Q., and Przekwas, A. J., 1993, "Modeling of Spray Droplets Deformation and Breakup," *AIAA J. Propul. Power*, **9**(4), pp. 651–654.
- [8] Liu, A. B. and Reitz, R. D., 1993, "Mechanism of Air Assisted Liquid Atomization," *Atomization Sprays*, **3**, pp. 55–75.
- [9] Liu, A. B., Mather, D., and Reitz, R. D., 1993, "Effects of Drop Drag and Breakup on Fuel Sprays," SAE Paper No. 930072.
- [10] Hwang, S. S., Liu, Z., and Reitz, R. D., 1996, "Breakup Mechanisms and Drag Coefficients of High-Speed Vaporizing Liquid Drops," *Atomization Sprays*, **6**, pp. 353–376.
- [11] Clark, M. M., 1988, "Drop Breakup in a Turbulent Flow-I: Conceptual and Modeling Considerations," *Chem. Eng. Sci.*, **43**(3), pp. 671–679.
- [12] Pham, T. L., 2000, "A Computational Tool for Spray Modeling Using Lagrangian Droplet Tracking in a Homogeneous Flow Model," Ph.D. dissertation, Purdue University, West Lafayette, IN.
- [13] Dai, Z., and Faeth, G. M., 2001, "Temporal Properties of Secondary Drop Breakup in the Multimode Breakup Regime," *Int. J. Multiphase Flow*, **27**, pp. 217–236.
- [14] Ranger, A. A., and Nicholls, J. A., 1969, "The Aerodynamic Shattering of Liquid Drops," *AIAA J.*, **7**, pp. 285–290.
- [15] Naber, J. D., and Reitz, R. D., 1988, "Modeling Engine Spray/Wall Impingement," SAE Paper No. 880107.
- [16] Bai, C., and Gosman, A. D., 1995, "Development of Methodology for Spray Impingement Simulation," SAE Paper No. 950283.
- [17] Stanton, D. W., and Rutland, C. J., 1996, "Modeling Fuel Film Formation and Wall Interaction in Diesel Engines," SAE Paper No. 960628.
- [18] Stanton, D. W., and Rutland, C. J., 1998, "Multi-Dimensional Modeling of Heat and Mass Transfer of Fuel Films Resulting from Impinging Sprays," SAE Paper No. 980132.
- [19] Mundo, C., Sommerfeld, M., and Tropea, C., 1997, "Numerical and Experimental Investigation of Spray Characteristics in the Vicinity of a Rigid Wall," *Exp. Therm. Fluid Sci.*, **15**, pp. 228–237.
- [20] Mundo, C., Sommerfeld, M., and Tropea, C., 1998, "On the Modeling of Liquid Sprays Impinging on Surfaces," *Atomization Sprays*, **8**, pp. 625–652.
- [21] Roisman, I. V., Araneo, L., Marengo, M., and Tropea, C., 1999, "Evaluation of Drop Impingement Models: Experimental and Numerical Analysis of a Spray Impact," Thirteenth Annual Conference on Liquid Atomization and Spray Systems ILASS-Europe, Florence, Italy.
- [22] Tropea, C., and Roisman, I. V., 2000, "Modeling of Spray Impact on Solid Surfaces," *Atomization Sprays*, **10**, pp. 387–408.
- [23] O'Rourke, P. J., and Amsden, A. A., 2000, "A Spray/Wall Interaction Sub-model for the KIVA-3 Wall Film Model," SAE Paper No. 2000-01-0271.
- [24] Stow, C. D., and Stainer, R. D., 1977, "The Physical Products of a Splashing Water Drop," *J. Meteorol. Soc. Jpn.*, **55**(5), pp. 518–532.
- [25] Wachters, L. H. J., and Westerling, N. A. J., 1966, "The Heat Transfer from a Hot Wall to Impinging Water Drops in the Spheroidal State," *Chem. Eng. Sci.*, **21**, pp. 1047–1056.
- [26] Jayaratne, O. W., and Mason, B. J., 1964, "The Coalescence and Bouncing of Water Drops at an Air/Water Interface," *Proc. R. Soc. London, Ser. A*, **280**, pp. 545–565.
- [27] Rodriguez, F., and Mesler, R., 1985, "Some Drops Don't Splash," *J. Colloid Interface Sci.*, **106**(2), pp. 347–352.
- [28] Kolpakov, A. V., Romanov, K. V., and Titova, E. I., 1985, "Calculation of the Conditions for Rebound Upon Collisions Between Droplets of Different Sizes," *Colloid J. USSR*, **47**, pp. 817–820.
- [29] Mundo, C., Sommerfeld, M., and Tropea, C., 1995, "Droplet-Wall Collisions: Experimental Studies of the Deformation and Breakup Process," *Int. J. Multiphase Flow*, **21**(2), pp. 151–173.
- [30] Yarin, A. L., and Weiss, D. A., 1995, "Impact of Drops on Solid Surfaces: Self-Similar Capillary Waves, and Splashing as a New Type of Kinematic Discontinuity," *J. Fluid Mech.*, **283**, pp. 141–173.
- [31] Lefebvre, A. H., 1989, *Atomization and Sprays*, Hemisphere Publishing, New York.

Jing JianPing
e-mail: jianpj@sjtu.edu.cn

Meng Guang

The State Key Laboratory of Vibration, Shock &
Noise,
Shanghai JiaoTong University,
Shanghai 200030, P. R. China

Sun Yi

Xia SongBo

School of Energy Science and Engineering,
Harbin Institute of Technology,
Harbin 150001, P. R. China

A Continuum Damage Mechanics Model on Creep Rupture Life Assessment of a Steam Turbine Rotor

A nonlinear continuum damage mechanics model is proposed to assess the high temperature creep life of a steam turbine rotor, in which the effect of mean stress is taken into account and the damage is accumulated nonlinearly. The model is applied to a 300 MW steam turbine under hot start operation. The results are compared with those from the linear accumulation theory that is dominant in the creep life assessment of steam turbine rotors at present. The comparison results show that the nonlinear continuum damage mechanics model describes the accumulation and development of damage better than the linear accumulation theory. [DOI: 10.1115/1.1924483]

1 Introduction

The development of modern industry require the parts of steam turbine to operate in higher temperature and under heavier working loads. Much concern has been paid on the creep damage behavior and the failure mechanism. At present, the linear damage accumulation (LDA) theory is widely used in the creep life assessment of steam turbine parts. As it contains uniaxial assumptions, the effect of multiaxial stress is ignored and the damage accumulation calculation is rather crude. The predicted results are usually quite different from practice. The continuum damage mechanics (CDM) developed in the past decades has not only a stronger theoretical foundation but also is a better method than LDA. It has been used successfully in many engineering fields such as creep, fatigue, ductile fracture and composite failure [1–3].

Being an important part of the steam turbine, the rotor operates in high temperature and high-pressure environment. Creep damage plays an important role in the rotor damage. Generally the low cycle fatigue wears off approximately seventy percent of the life of the rotor and creep accounts for the remaining thirty percent [6]. Therefore, the high temperature creep damage must be examined carefully in the fatigue design and the life prediction of steam turbine rotors.

In this paper, the transient temperature and the stress field of a 300 MW steam turbine rotor are investigated. The nonlinear CDM model is employed to predict the creep life of the steam turbine rotor and the results are compared with those from LDA theory. Finally, the advantages of the nonlinear CDM model are discussed.

2 Theoretical Model

2.1 Linear Damage Accumulation Theory. At present, the LDA theory is mainly used in the creep life assessment of steam turbine parts. The damage accumulation is considered as a linear process. The structure fails as the damage amounts to 1. It can be expressed as follows

$$\frac{\Delta t_1}{t_{r1}} + \frac{\Delta t_2}{t_{r2}} + \dots + \frac{\Delta t_i}{t_{ri}} = 1 \quad (1)$$

The creep damage is generally defined as

$$D = \frac{\Delta t}{t_r} \quad (2)$$

The creep life, t_r , can be obtained from following equation

$$t_r = \left(\frac{\sigma_{eq}}{A} \right)^B \quad (3)$$

the A , B are material constants.

The LDA theory is based on the following assumptions:

- (1) For any stress level, at the beginning or at the end, each creep process leads to the same damage.
- (2) Loading sequence does not affect life prediction.

The above theory is based on the tests of uniaxially loaded specimens. It may lead to a satisfying life prediction for a uniaxial loaded component. The majority of components and structures in service, however, are generally subjected to multiaxial loading conditions resulting in biaxial–triaxial states of stress. Pressure vessels, turbine blades, and turbine rotor are common examples. Therefore, the life prediction for these components from LDA often deviate largely from practice. To predict creep life of such components and structures using laboratory test data, a suitable multiaxial creep theory or criterion is required in order to relate complex multiaxial stress states to laboratory test data.

2.2 Continuum Damage Mechanics Theory. For a nominal stress of σ , [1,4] the damage parameter D is zero for material containing no cracks and unity when rupture takes place. Also $\sigma/(1-D)$ is the “effective” stress, takes into account the weakness of the material due to the presence of voids or micro-cracks. From a thermodynamic point of view, D is an internal variable of an irreversible damage process. Generally, a creep process includes three stages, in the first stage the strain rate reduces with the time elapsing; in the second stage, creep develops stably and the strain rate is nearly a constant; in the third stage, creep develops quickly. Many tests demonstrate that creep damage takes place mainly in the third stage of creep. If $\dot{\epsilon}_p^*$ is the strain rate in the second stage of creep and $\dot{\epsilon}_p$ is the strain rate of tertiary stage, then the creep damage can be defined as follows:

Contributed by the Structures and Dynamics Committee of ASME for publication in the JOURNAL OF ENGINEERING FOR GAS TURBINES AND POWER. Manuscript received July 30, 2003; final manuscript received February 15, 2005. Editor: M. Mignolet.

$$D = 1 - \left(\frac{\dot{\epsilon}_p^*}{\dot{\epsilon}_p} \right)^{1/n} \quad (4)$$

n is a material constant related to temperature. From a uniaxial stress-controlled creep test, the strain rates of the second stage and the third stage of creep can be obtained and the damage at any time of the third creep stage can be obtained by Eq. (4). Many tests have proved that the creep strain always increases with the time elapsing. The strain rate is positive in all the creep stages, and the strain rate of the first stage is always greater than the strain rate of second stage. Therefore, the ratio of the two strain rates in Eq. (4) is positive, and D is less 1. Damage may also be related to the variation in density, resistivity, or other material properties.

The equation of damage evolution of inter-granular creep cracking based on thermodynamic principles has been proposed by Lemaitre [1,4] who took into account the effects of nonlinear damage accumulation and multi-axial stress

$$dD = \frac{R_V}{(1-D)^\beta} \left(\frac{\sigma_{eq}}{\Omega} \right)^r dt \quad (5)$$

Where R_V is the triaxial coefficient and is expressed as

$$R_V = \frac{2}{3}(1+\nu) + 3(1-2\nu) \left(\frac{\sigma_H}{\sigma_{eq}} \right)^2 \quad (6)$$

and

$$\sigma_{eq} = \left(\frac{3}{2} S_{ij} S_{ij} \right)^{1/2}, \quad S_{ij} = \sigma_{ij} - \sigma_H \delta_{ij}, \quad \sigma_H = \frac{1}{3} \sigma_{kk}$$

β , Ω , and r are material constants adjusted to fit the experimental result. In Eq. (5), the mean stress σ_H is related and the effects of multiaxial stress state are considered. Let $t=0$ and $D=0$, integrating equation (5), then it can be obtained that

$$D = 1 - \left(1 - R_V(1+\beta) \left(\frac{\sigma_{eq}}{\Omega} \right)^r t \right)^{1/1+\beta} \quad (7)$$

Under uniaxial load, the $R_V=1$, and Eq. (3) becomes

$$D = 1 - \left(1 - (1+\beta) \left(\frac{\sigma_{eq}}{\Omega} \right)^r t \right)^{1/1+\beta} \quad (8)$$

Let $t=t_r$ and $D=1$, from Eq. (7), it can be obtained that

$$t_r = \frac{1}{R_V(\beta+1)} \left(\frac{\sigma_{eq}}{\Omega} \right)^{-r} \quad (9)$$

Under uniaxial load, $R_V=1$, then

$$t_r = \frac{1}{\beta+1} \left(\frac{\sigma_{eq}}{\Omega} \right)^{-r} \quad (10)$$

Substituting Eq. (9) into Eq. (7), the general damage form is

$$D = 1 - \left(1 - \frac{t}{t_r} \right)^{1/1+\beta} \quad (11)$$

Notice that in the present continuum damage model, the damage accumulates nonlinearly and the triaxiality is included, which can reflect the effects of multiaxial stress.

The material constants β , Ω , and r in the above equations can be obtained by a uni-axial stress-controlled creep test. Via the creep test, the creep life equation (3) can be achieved. Substituting it into Eq. (10), it can be deduced that $r=-B$ and

$$A^{-B} = 1/(1+\beta) \cdot \Omega^{-B} \quad (12)$$

Via the $\dot{\epsilon}_p^*$ and $\dot{\epsilon}_p$ obtained by a creep test and using Eq. (4), the damage can be determined. Using the damage and the t_r from the creep test, and Eq. (11), the parameter β can be determined. Take it into Eq. (12), the Ω can then be calculated.

In theory, the structure fails when damage amounts to 1, i.e., the critical damage $D_r=1$. However, tests show that when damage is

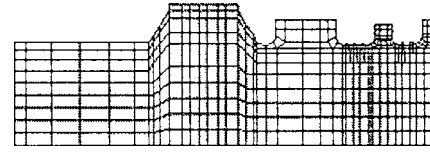


Fig. 1 Finite element mesh of high pressure rotor of 300 MW steam turbine

still at a low value, cracks have initiated and the structure will fracture in very less cycles. Therefore, in CDM, the critical damage is not set to 1. Many tests show show that $0.2 \leq D_r \leq 0.8$. It can be obtained by uniaxial tension tests as follows [3]

$$D_r = 1 - \sigma_r / \sqrt{2EY_r} \quad (13)$$

where σ_r and Y_r are the critical stress and critical release rate of strain energy when structure rupture.

3 Temperature and Stress Field Analysis of a 300 MW Steam Turbine Rotor

In the control stage and first compressor stage of the High-Pressure (HP) rotor of a 300 MW steam turbine, the temperature and pressure of the steam are much higher than other areas and creep usually occurs. Therefore, the creep life of a turbine depends mainly on the damage evolution in these stages. In this paper, the transient temperature field and the thermal stress field under a start operation are calculated by the finite element software ADINA. The finite element model is shown in Fig. 1. The start curves are shown in Fig. 2 [5].

In the calculation all related parameters are considered as functions of time and temperature, they are given in Table 1. The convection coefficients adopted in the analysis is given in Eqs. (14) and (15) [6]. The convection coefficients on the surface of shaft are

$$N_u = 0.1 Re^{0.68}$$

$$Re = uR/v$$

$$\alpha = N_u \lambda / r \quad (14)$$

The convection coefficients on the surface of impeller

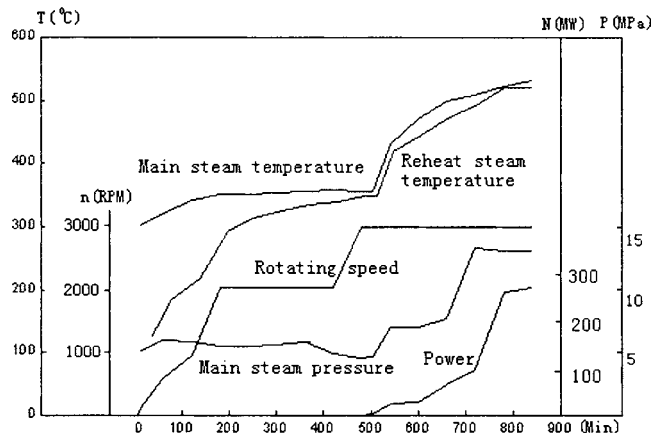


Fig. 2 Start operation curves [5]

Table 1 Parameters at several temperatures

Temperature (°C)	100	200	300	400	500	600
Specific heat (J/kg·°C)	487.4	507.6	565.2	622.8	669.6	716.4
Dilation coefficient (10 ⁻⁶ /°C)	11.49	12.03	12.43	12.80	13.23	13.32
Heat conduction coefficient W/(m·k)	38.9	38.1	33.9	33.1	30.1	26.4

$$\begin{cases} N_u = 0.675 Re^{0.5} & (Re \leq 2.4 \times 10^5) \\ N_u = 0.0217 Re^{0.8} & (Re > 2.4 \times 10^5) \\ Re = \omega R^2 / \nu \\ \alpha = N_u \lambda / R \end{cases} \quad (15)$$

In the analysis, the centrifugal force of the rotor is also taken into account.

As the load of the steam turbine nearly reach the maximum rating, the steam temperature also nearly reaches the rated value. The creep usually comes into function at this time. The maximum stress and temperature of the rotor at the rated load are given in Table 2. The corresponding temperature field and effective stress field are shown in Figs. 3 and 4.

4 Damage and Life Analysis and Model Comparison

The traditional creep life prediction equation of 30Cr1Mo1V rotor steel at 530°C is given by [8]:

$$t_r = \left(\frac{\sigma_{eq}}{381.6} \right)^{-8.596} \quad (16)$$

In terms of the CDM theory (Sec. 2) and the test data from Ref. [8], the multiaxial creep life prediction equation of 30Cr1Mo1V rotor steel at 530°C is written as

Table 2 Effective stress, temperature, and triaxial coefficients at dangerous points at rated load

Dangerous points	σ (MPa)	T (°C)	R_v (ν)
Front root of control stage	66.87	519.3	1.63
Back root of control stage	72.98	509.6	1.86

UNIT: MPa

1-72.9 2-61.4 3-50.7 4-39.9
5-29.1 6-18.3 7-7.50 8-2.72



Fig. 3 Stress field of high pressure rotor of 300 MW steam turbine at rated load

UNIT: °C

1-519 2-500 3-481 4-463
5-444 6-425 7-407 8-388



Fig. 4 Temperature field of high pressure rotor of 300 MW steam turbine at rated load

$$t_r = \frac{1}{R_v \cdot 7.02} \left(\frac{\sigma_{eq}}{478.8} \right)^{-8.596} \quad (17)$$

under uni-axial load, $R_v = 1$, then Eq. (17) becomes

$$t_r = \frac{1}{7.02} \left(\frac{\sigma_{eq}}{478.8} \right)^{-8.596} \quad (18)$$

The damage evolution model can be written as

$$D = 1 - \left(1 - \frac{t}{t_r} \right)^{0.1423} \quad (19)$$

In terms of the stress-controlled creep test data and the definition of damage by Eq. (4), the experimental damage evolution process can be obtained and it is shown in Fig. 5. The damage evolutions obtained from LDA by Eq. (2) and CDM by Eq. (19) are also presented in Fig. 5. It demonstrates that the above CDM model fits very well with the uniaxial creep test data. Although the life prediction from LDA (the dashed line result in Fig. 5) is coincide with the test data in uniaxial loading condition, the description for damage evolution is rather coarse and deviates from the test data greatly. The test data also shows that for a same load, damage does not develop with a same speed in the creep process, which is not like that described by LDA. It can be observed that damage develops slowly at the beginning of the creep process, however, quickly at the end. For a multistage load process, it means that load sequence may affect the damage evolution in some extent, which has been proved by many experiments [2,3]. However, the CDM model can describe this mechanism reasonably. It can be illustrated by Fig. 6: For a two stage loading process, if stress σ_1 and σ_2 all function as long as Δt , then there are two possible cases: (1) σ_1 loads firstly and then σ_2 follows; (2) σ_2 loads firstly and then σ_1 follows. For case (1), after σ_1 loading as long as Δt , damage develops from zero to *point 1* along the *Curve 1* and the corresponding damage value is D_1 (see Fig. 6). At this time, σ_2 comes to load, the damage develops from *points 2* to *3* along the *Curve 2* and the final damage corresponding point 3 is D_2 (shown in Fig. 6); For case (2), σ_2 loads firstly and the damage changes

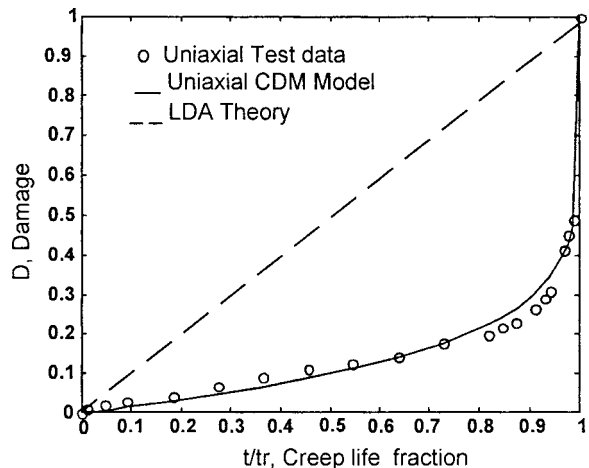


Fig. 5 Damage evolution for creep of 30Cr1Mo1V at 525°C and $\sigma=200$ MPa

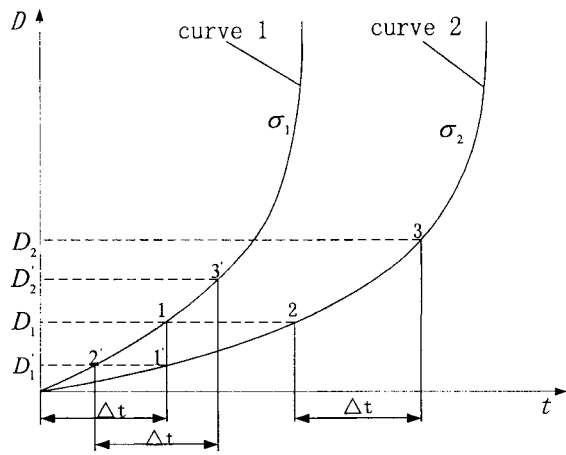


Fig. 6 Diagram of effects of load sequence for CDM model

from zero to point 1' along Curve 2, its corresponding damage value is D_1' , (see Fig. 6). Then σ_1 loads as long as Δt . The damage changes along curve 1 from points 2' to 3' and the final damage value corresponding to point 3' is D_2' (shown in Fig. 6). Apparently, different loading sequences lead to different damage value D_2 and D_2' . It is easy to know that the bigger the difference of loads has the bigger effects the loading sequence does on damage. The present LDA, however, assumes that load sequence does not affect the damage and it certainly will lead to a deviating result for a multistage loading process.

By using the traditional creep life prediction of Eq. (16) and the continuum damage mechanics model of Eqs. (17) and (18), the creep life predictions of high pressure rotor of a 300 MW steam turbine under hot start are calculated, respectively. The results are listed in Table 3. It is shown that the life predictions of the LDA model coincide with those of a uniaxial CDM model, but are quite different from the results of the multiaxial CDM model. The inherent weakness of the LDA model in not dealing well with the multiaxial problem is reflected in the table. The triaxial coefficient is adopted in the multiaxial CDM model, and the effects of complex stress state are considered. It is, therefore, expected that the multiaxial CDM model could predict the life and damage evolution more accurately [9].

In the life predictions of the multiaxial CDM model, the triaxial coefficient affects the results greatly and Eq. (9) shows that creep life t_r is inverse proportional to the triaxial coefficient R_V . In Fig. 7, the triaxial coefficient field corresponding to the stress field in Fig. 3 is plotted. It shows that the complex multiaxial stress state is widely scattered in steam turbine rotor. The results demonstrate that the creep life predictions in the turbine rotor design may change greatly if the effects of multiaxial loading are considered.

In Fig. 8 the damage evolution of the back root of the rotor from the multiaxial CDM model, at which the triaxial coefficient (R_V) value is 1.86, is compared with that from the uniaxial CDM model. The results show that the multiaxial complex stress accelerates the damage accumulation greatly. Therefore, in damage analysis of a steam turbine rotor, the effects of multiaxial complex stress must be considered.

The average design life of a large capacity steam turbine is usually 30 years. In assuming that the frequency of the start and

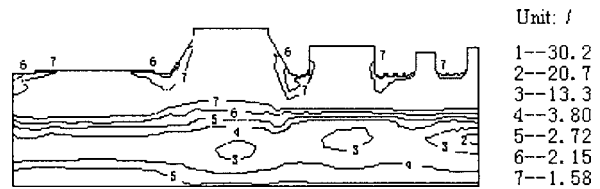


Fig. 7 Distribution of triaxial coefficient of 300 MW steam turbine at rated load

stop operations is one time per year, and the stable running time is 300 days [11] during each start–stop process, at which creep damage usually takes place. Finally, the total damages of creep in 30 years of the back root of the control stage, which is most dangerous, are calculated by applying the LDA theory and the multiaxial CDM model. The results are shown in Table 4.

In this study, for CDM model, $D_r=0.24$ is obtained by uniaxial test [7]. Figure 8 shows that the life of the back root of the control stage impeller under multiaxial load has nearly been exhausted when the damage is as low as 0.24. It demonstrates that because damage evolves nonlinearly, damage can be low when there is little remanent life. If life-used ratio is written as $\delta=D/D_r$, because the difference of the fracture criteria of CDM and LDA ($D_r=0.24$ for CDM in this study and $D_r=1$ for LDA), although the estimated damage from the multiaxial CDM model is 0.0437 shown in Table 4, at this time 18.21% ($\delta=0.0437/0.24$) of the life has been used. It seems more reasonable than the result from the LDA theory of 14.42% ($\delta=0.1442/1$). It is suggested that although the LDA theory may overestimate the damage evolution, it is not always a conservative estimation in life prediction. This should be important in practical rotor design.

The above analyses show that, compared with the LDA theory, the nonlinear CDM model cannot only describe the damage accumulation more precisely but also takes into account the effects of multiaxial complex stress and load sequence. Therefore, both the life prediction and the damage accumulation are expected to be in better agreement with the practical case.

5 Conclusions

In this paper, a nonlinear continuum damage mechanics model is employed to predict the creep damage and the life of a 300 MW steam turbine high pressure rotor, and the results are compared with those from a linear damage accumulation theory. The conclusions drawn from the study can be summarized as follows:

- (1) Since the linear damage accumulation Theory uses a uniaxial assumption, the effects of multiaxial complex stress are not considered. The life is over evaluated.
- (2) The LDA theory has overestimated the damage of the material. The nonlinear continuum damage mechanics model can describe the damage accumulation more accurately and can also consider the effect of loading sequence.
- (3) Multiaxial complex stress makes the life shorter and accelerates damage accumulation. Therefore, in the creep analysis of a steam turbine rotor, the effects of multiaxial complex stress must be considered.

Table 3 Creep life at dangerous points (h)

Dangerous points	LDA theory	Uniaxial CDM model	Multiaxial CDM model
Front root of control stage	3.1772×10^6	3.1811×10^6	1.9516×10^6
Back root of control stage	1.4978×10^6	1.5003×10^6	8.066×10^5

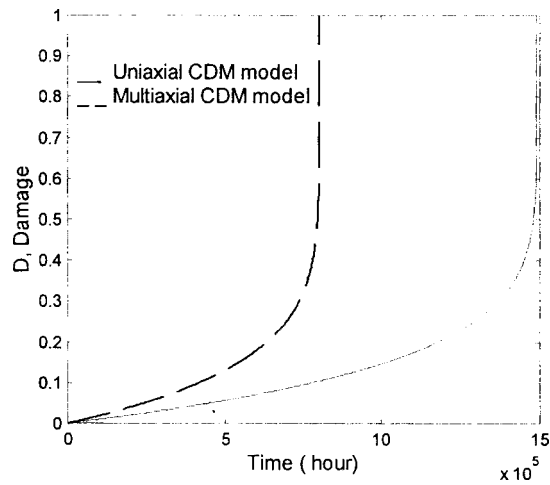


Fig. 8 Creep damage comparison of uniaxial and multiaxial CDM model

Acknowledgment

The supports from China “863” Project (No.2002AA412410), China Postdoctoral Science Foundation and The Doctor Subjects Research Founding of China University (No.20020248053) are greatly acknowledged.

Nomenclature

- E = Young’s modulus
- R_V = triaxial coefficient
- ν = Poisson’s ratio
- δ_{ij} = δ -function

Table 4 Total damage of back root of control stage in 30 years

Damage theory	Front root of control stage	Back root of control stage
LDA theory	0.0680	0.1442
CDM Model	0.0165	0.0437

- S_{ij} = component of deviatoric stress
- σ_{kk} = component of normal stress
- t = time
- u = line velocity of rotor surface
- ν = dynamic viscosity of steam
- α = coefficient of convection
- $\dot{\epsilon}_p^*$ = strain rate of the second creep process
- D_r = critical damage for rupture
- Y_r = release rate of strain energy for rupture
- t_{ri} = times to failure under a creep load σ_i
- Δt = time of loading
- σ_{eq} = effective stress
- σ_H = mean stress
- σ_{ij} = component of cauchy stress
- A, B, Ω, β, r = temperature dependent material constants under creep conditions
- R_e = Reynold number
- R = radius of rotor
- λ = coefficient of heat conduction of steam
- ω = rotating speed of rotor
- $\dot{\epsilon}_p$ = strain rate of the third creep process
- σ_r = critical stress for rupture

References

- [1] Sedmak, A., and Sedmak, S., 1995, “Critical Crack Assessment Procedure for High Pressure Steam Turbine Rotors,” *Fatigue Fract. Eng. Mater. Struct.* **18**, pp. 923–934.
- [2] Chaboche, J. L., 1987, “Continuum Damage Mechanics: Present State and Future Trends,” *Nucl. Eng. Des.*, **105**, pp. 19–33.
- [3] Lemaitre, J., 1984, “How to Use Damage Mechanics,” *Nucl. Eng. Des.* **80**, 233–245.
- [4] Lemaitre, J., 1979, “Application of Damage Concepts to Predict Creep-Fatigue failures, Transaction of the ASME,” *J. Eng. Mater. Technol.* **101**, 284–292.
- [5] Wang X. J., and Shi K. Z., 1998, “Life Prediction of 300 MW Steam Turbine Under Cold Start,” *Turbine Technology* **40**(5), 269–271.
- [6] Zhang B. H., 1988, “Life Management and Load-Peak Adjustment Running of Large Capacity Fossil Power Generator,” Water Power and Electric Power Publishing Company, Peking, China, pp. 19–27.
- [7] Li J., and Zhou J. L., 2000, “Investigation on Creep Performance of 30Cr1Mo1V Rotor Steel,” *Physical & Chemical Test-Physics Fascicule.* **36**(1), 10–12
- [8] Li. Y. W., and Li C. B., 1998, “Investigation on Low-Cycle Performance of 30Cr1Mo1V Rotor Steel and Damage Evolution,” *Turbine Technology.* **40**(4), 248–250
- [9] Chaboche J. L., 1988, “Continuum Damage Mechanics: Part II,” *Trans. ASME, J. Appl. Mech.* **55**(1), 65–72

Reduction of Power Losses in Bearing Chambers Using Porous Screens Surrounding a Ball Bearing

Michael Flouros

MTU Aeroengines,
Air and Oil Systems,
Dachauer Strasse 665,
80995 Munich, Germany
e-mail: michael.flouros@muc.mtu.de

Trends in aircraft engine design have caused an increase in mechanical stress requirements for rolling bearings. Consequently, a high amount of heat is rejected, which results in high oil scavenge temperatures. An RB199 turbofan bearing and its associated chamber were modified to carry out a survey aiming to reduce power losses in bearing chambers. The test bearing was a 124 mm PCD ball bearing with a split inner ring employing under-race lubrication by two individual jets. The survey was carried out in two parts. In the first part, the investigations were focused on the impact on the power losses in the bearing chamber of the operating parameters, such as oil flow, oil temperature, sealing air flow, bearing chamber pressure, and shaft speed. In the second part, the investigations focused on the reduction of the dwell time of the air and oil mixture in the bearing compartment and its impact on the power losses. In this part, porous screens were introduced around the bearing. These screens would aid the oil to flow out of the compartment and reduce droplet-droplet interactions as well as droplet-bearing chamber wall interactions. The performance of the screens was evaluated by torque measurements. A high-speed camera was used to visualize the flow in the chamber. Considerable reduction in power loss was achieved. This work is part of the European Research programme GROWTH ATOS (Advanced Transmission and Oil Systems). [DOI: 10.1115/1.1995769]

1 Introduction

Highly loaded bearings generate heat in the contact areas between the rolling elements and the race, the rolling elements and the cage, and in the annular gaps between the cage and the races. The generated heat is caused by friction in the contact areas and by churning and windage as a result of dissipation of Euler work (acceleration to circumferential speed). Within the scope of the ATOS program the impact of the operating parameters affecting power losses in the bearing chamber were investigated [1]. These were the oil and sealing air flow, the temperature, the axial load, the rotor speed, and the bearing chamber pressure. Power losses in bearings have been investigated by several authors. Specifically [2–6] can be highlighted. The bearing chamber is shown in Fig. 1, and the schematic of the test facility is depicted in Fig. 2. The bearing chamber is a vented chamber with the vent being at top position (12 o'clock) and the scavenge port at the bottom position. Two vent configurations were tested; the first introduced a vent that was protruding 15 mm into the chamber, and the second, a flush vent. The chamber was sealed by a straight labyrinth seal. The ball bearing shown in Fig. 1 has an inner land riding cage with a split inner ring and under-race lubrication. Each half of the inner ring has 18 1 mm holes, which centrifugally direct the oil to the cage scoop and from there to the rolling elements (Figs. 1 and 3, rear-half design). Two additional 1 mm holes on each half of the inner ring are used to guide the cage (Figs. 1 and 3, front-half design). The cage guiding holes are at a circumferential distance of 180 deg to each other and are placed toward the edge of the inner ring so that they face the cage land. The lubricant is supplied to the bearing by two jets which individually lubricate the front and rear sides of the bearing.

The condition of the bearing was monitored by accelerometers,

chip detectors, and thermocouples. The latter recorded the temperature of the outer ring at different circumferential locations (Fig. 1, TOR). The heat rejection of the bearing was monitored by thermocouples, which recorded the temperature of the oil leaving the bearing. A row of three thermocouples was placed adjacent to the bearing on each side (Fig. 1, positions A and B). These recorded the temperature of the oil leaving the bearing through the gap between the outer ring and the cage. Two additional rows of thermocouples were installed at a distance of 1 cm on either side of the bearing for additional monitoring. In order to visualize the bearing, an endoscope was used, which could be connected to a high-speed camera (Fig. 4). In order to avoid the oil droplets that smear the lens of the endoscope during operation, a tube was placed around it and purge air was conducted through the tube. The purge air pressure was regulated. A pressure of about 3 KPa above chamber pressure was adequate to maintain a clean lens. Also Plexiglas windows were introduced into the bearing chamber front cover (Fig. 1), which enabled additional view of the interior.

Pressure transducers were used to monitor the chamber pressure. Additionally, the torque on the bearing shaft was measured. Torque measurements were used to assess the power consumption of the bearing and, therefore, enable comparisons among different operating conditions. The estimated power consumption values were nondimensionalized by the parameter P_0 . This equals 7.0 KW of power consumption and corresponds to an operating condition at 15,000 rpm, 14.7 KN thrust, 350 L/hr oil flow, 2.6 bar bearing chamber pressure, and 80 °C air and oil inlet temperature. Torque measurements were preferred to calorimetric measurements of the heat transfer because the latter is difficult to assess since, during operation, the oil distribution through the scavenge and vent is not known and other secondary heat losses (i.e., convection through the chamber walls) are difficult to estimate.

Figure 5 shows the screens which were used around the ball bearing. The screens were selected with pore diameters (PD) of 3, 4, and 6 mm. The porosity of the screens was about 29%. This is the ratio analogous of the free to the total area. The screens were

Contributed by the IGTI Structures and Dynamics Committee of ASME for publication in the JOURNAL OF ENGINEERING FOR GAS TURBINES AND POWER. Manuscript received April 2, 2004; final manuscript received May 1, 2005. Assoc. Editor: W. Miglietti.

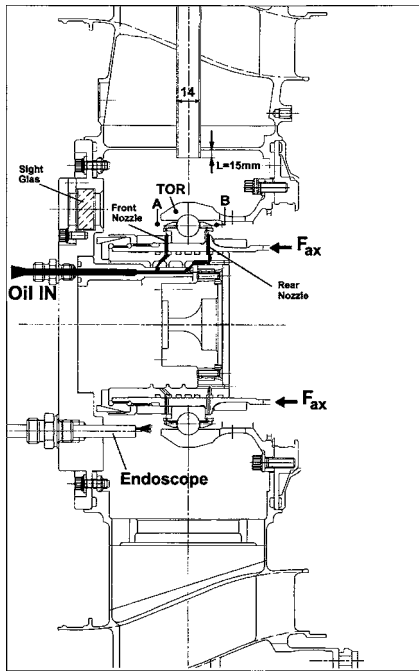


Fig. 1 Schematic of the bearing chamber with the rear and front nozzles, the endoscope, the thermocouple positions adjacent to the bearing, and the immersed vent

attached to the outer ring (Fig. 3), and the distance to the cage was about 10 mm (Fig. 3, front screen). In a later test the distance to the cage was reduced to about 3 mm, as schematically shown in Fig. 3 by the rear screen. The screen with 3 mm pore diameter was selected to be the baseline screen.

The oil flow was varied between 200 and 450 L/hr, the sealing air flow between 6 and 80 Kg/hr, the chamber pressure between 0.9 and 4.8 bar, and the temperatures for air and oil were 80 °C and 130 °C. The shaft speed was varied between 6000 and 19,000 rpm. The lubricant was Mobil Jet II, which corresponds to the MIL-L-23699 standard.

As has already been mentioned, the tests were evaluated based on torque-power measurements. In order to increase accuracy, the same measurements were repeated several times. The deviation was less than ±1.5% of the average value. In addition to the torque measurements, video pictures were taken with the high-speed camera, both with and without the screens. These pictures were used to assess the calming of the oil flow and the spray

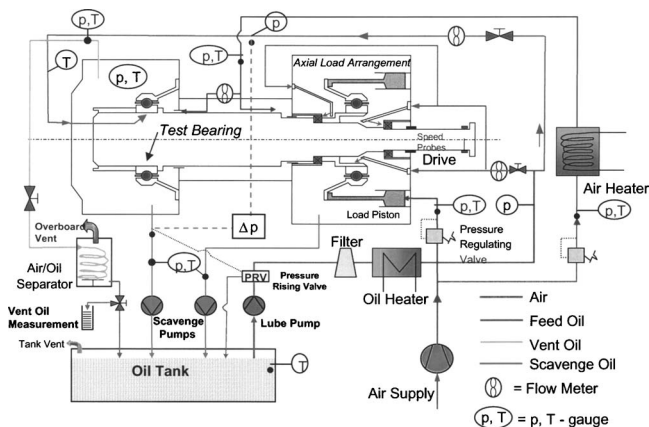


Fig. 2 Schematic of the test facility with the test bearing and the axial load arrangement

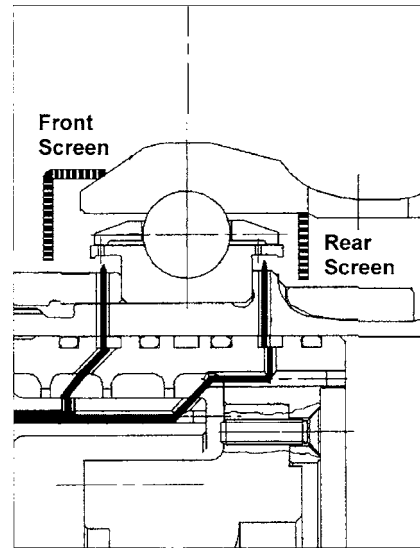


Fig. 3 Rear and front screen arrangement

generation in the chamber. Finally, oil-quantity measurements through the chamber vent were carried out. These measurements would enable one to conclude whether the oil is aided out of the compartment through the scavenge when screens are used, consequently, reducing the dwell time of the air and oil mixture.

2 Results

Figure 6 shows the bearing power consumption, with and without the screens, as a function of sealing air, pressure in the chamber, and oil flow. A power-consumption reduction of ~5–6 % is achieved. Figure 7 depicts variations of the shaft speed, the oil and air inlet temperature, the pore diameter, and the distance between the front and rear screens to the cage. At a shaft speed of 19,200 rpm, a power-loss reduction of ~11% is achieved. The introduction of screens with pores of 6 mm diam yielded to a

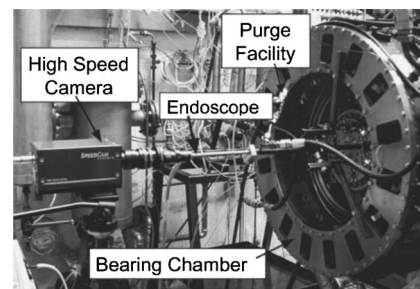


Fig. 4 Bearing chamber with the high-speed camera, endoscope, and purge facility



Fig. 5 Screens used at the front side of the ball bearing

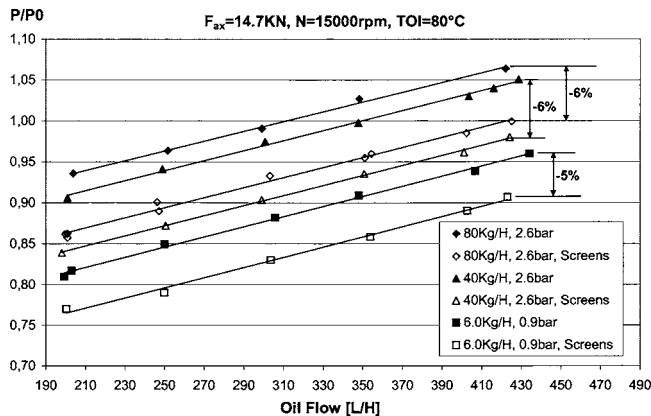


Fig. 6 Impact of screens as a function of the oil and air flow. The presence of screens results in significantly lower power loss to the bearing compartment.

deterioration compared to screens with pores of 3 mm. This implied that with increasing pore diameters, the performance of the screens has deteriorated. As a consequence, testing with screens having a 4 mm pore diameter was skipped. When the distance of the screens to the cage was reduced from 10 to 3 mm, no considerable difference in the bearing power consumption was detected (bottom curves, Fig. 7). The reduction in power consumption between using oil-air inlet temperatures of 80 °C and 130 °C is ~13%.

These measurements showed that an obvious reduction of the power losses is achieved when screens are used. This benefit increases with increasing rotor speed, as this is shown in Fig. 7.

As already mentioned in the Introduction, a visualization of the bearing running with and without the screens using the high-speed camera was carried out. The visualization tests were performed at different speeds between 10,000 and 19,260 rpm. Additionally, the camera shutter speed was varied between 360 and 4000 fps.

Above 4000 fps, the picture quality became very poor because the illumination of the picture deteriorated. The first video pictures were taken at 15,000 rpm, 200 L/hr, 80 °C oil inlet temperature, 14.7 KN axial load, and 2.6 bar chamber pressure. Figure 8 is a frame from the video and shows how the oil is leaving the bearing at the above conditions. Even though the oil was ingested under the the cage through the inner ring, no oil was observed leaving through the gap between inner ring and cage. On the contrary, the oil was observed leaving through the gap between the cage and the outer ring. This behavior was observed at all operating conditions, even when the direction of the axial load was reversed.

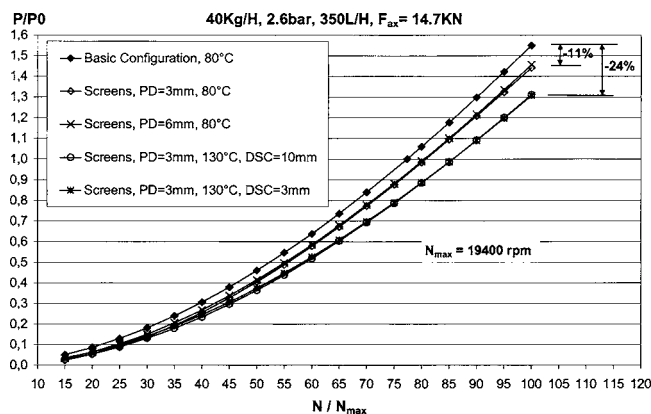


Fig. 7 Impact of screens on the power loss as a function of shaft speed, PD, DSC, and temperature

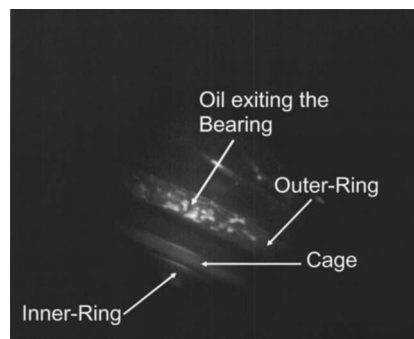


Fig. 8 Oil exiting the bearing between cage and outer ring at 15,000 rpm, 200 L/H

Apparently there is a mechanism that draws the oil from under the cage inside the bearing and then the oil is centrifuged outward between cage and outer ring.

Figure 9 shows the front screen with the nonrotating bearing behind it. The endoscope was placed in a tube that was purged with air to avoid oil contamination of the lens. Part of this purge tube inner wall can also be seen in the figure.

Figure 10 compares the basic and the screen configuration of the bearing at 17,300 rpm, 200 L/hr oil flow, 40 Kg/hr sealing air flow, 14.7 KN axial load, and 80 °C oil and air inlet temperature. The pore diameter of the screen was selected at 3 mm. The frames were taken from the video movie, which runs at 360 fps. The pictures from the top to the bottom are consecutive pictures. The top picture is the “reference” at “zero milliseconds.” The next appears five frames (13.9 ms) later, followed by the next two, 15 and 30 frames later, respectively. As can be seen by comparing the left with the right column, more fine spay is generated without the screens than with screens. This observation was done regardless of the operating condition or camera shutter speed. Particularly at a shutter speed of 4000 fps it could be observed how liquid oil and not spray was exiting through the pores of the screen. This is shown in Fig. 11. Above 1000 fps, no video was possible with the basic configuration because of the strong spray generation and the low light conditions due to the higher shutter speed.

If most of the oil leaving the screens is liquid and not spray, the liquid should, aided by gravitation, run toward the scavenge port rather than toward the vent. This would imply that in this case the amount of oil leaving through the vent should be less. The results of the vent oil-quantity measurements are depicted in Fig. 12. Two vent configurations were tested in this program. The first configuration introduced a flush vent, the second a vent protruding 15 mm into the chamber. The idea of the protruded vent was to prevent the rotating oil film along the bearing chamber’s walls from exiting the chamber through the vent. Consequently, the air and oil particle loaded core of the chamber can be evacuated through the

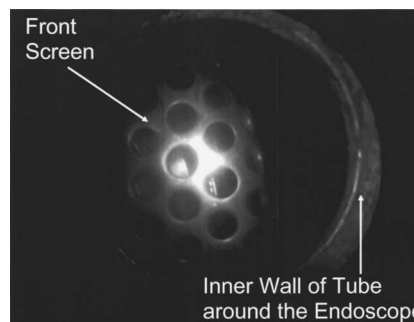


Fig. 9 View of the front screen with the nonrotating bearing behind it

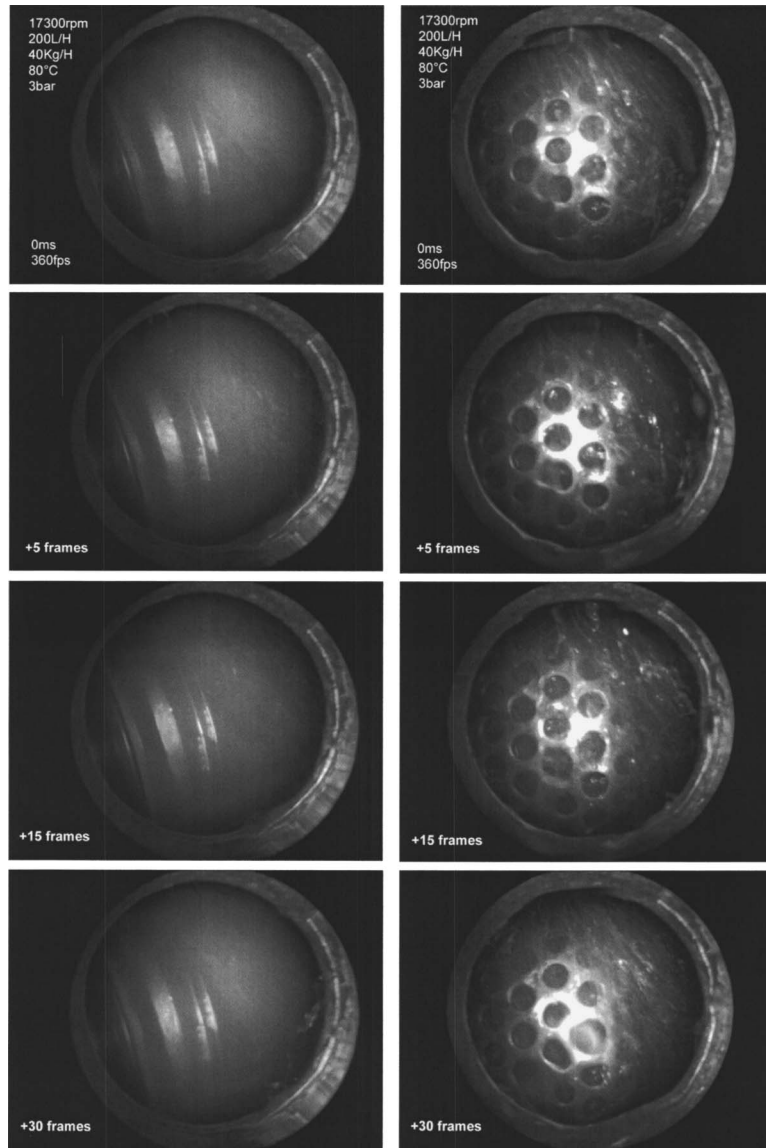


Fig. 10 Comparison of the spay generation between the basic configuration and the screens at 360 fps. Less spray is created when screens are used.

vent more efficiently. The vent oil was collected into a container, and the quantity was measured. The same measurement was repeated several times to ensure repeatability. The oil flow was 350 L/hr at an air-oil inlet temperature of 80 °C, and the screens had pores of 3 mm.

Both the flush and protruded vent configurations resulted in a much lower vent oil quantity with the screens compared to the basic bearing configuration. The impact of the vent protrusion is also shown in Fig. 12. Generally, the amount of oil leaving through the vent rapidly increases with shaft speed. It also in-

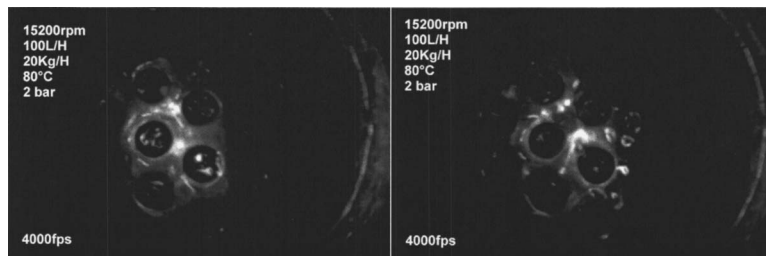


Fig. 11 High-speed camera images showing liquid oil emerging through the pores

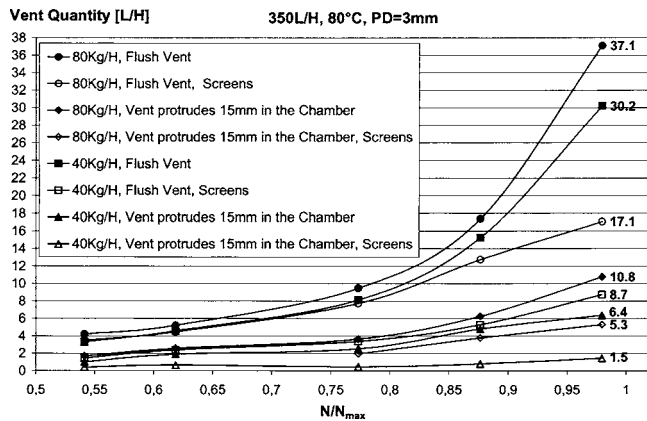


Fig. 12 Vent-oil quantity measurements at different bearing and vent configurations, sealing air flows and shaft speeds. Screens always result to lower vent-oil quantity.

creases with the sealing air flow. The difference in vent oil quantity, which results between the bearing without and with surrounding screens, rapidly increases with the rotor speed.

3 Conclusions

The power consumption in a bearing chamber is generally affected by the operating conditions, such as oil and sealing air flow, temperature, chamber pressure, axial load, and rotor speed. However considerable reduction in the power loss can be achieved if the dwell time of the air and oil mixture in a bearing chamber is reduced. This has been demonstrated in this study by the introduction of porous screens placed 10 mm away from the bearing. These were selected to have a porosity of 29% but having pore diameters of 3 and 6 mm. The best result was achieved with the screens having 3 mm pores. Compared to the basic configuration, 11% less power consumption was measured at the maximum shaft speed. The savings in power consumption rapidly increased with the rotor speed. Visualization of the bearing with a high-speed camera showed that much less spray was produced when the bearing was surrounded by the screens. The visualization also showed that, for this particular bearing, the oil leaves the bearing through the gap between the cage and the outer-ring.

Vent oil-quantity measurements also showed that more oil leaves the chamber through the scavenge line when screens are used. All these findings combined indicate that the dwell time of the air and oil mixture in the chamber is reduced with the consequence of less power consumption.

Reduction of the power losses in bearing chambers leads to better engine performance reduced mechanical or cost requirements on pumps, coolers, and piping.

This study will be continued by using screens of different porosities so that maximum performance of the screens is assessed. It can also be extended on roller bearings.

Acknowledgment

The author and MTU Aeroengines gratefully acknowledge the support of the European Commission within the GROWTH Research Project "Advanced Transmission and Oil System Concepts" (ATOS), Contract No. G4RD-CT-2000-00391.

Nomenclature

- D = bearing bore diameter, mm
- DSC = distance of screen from the bearing cage, mm
- F_{ax} = axial force on the bearing (axial load), KN
- fps = frames per second,
- N = rotor speed, rpm
- N_{max} = maximum rotor speed (=19,400), rpm
- p = pressure, bar
- P = power consumption, KW
- PCD = pitch circle diameter, mm
- PD = pore diameter of the screen, mm
- $P0$ = reference value for power loss, KW
- T = temperature, °C
- T_{OI} = oil inlet temperature, °C
- T_{OR} = outer ring temperature, °C

Units for Flow

- L/hr = liters per hour
- Kg/hr = Kilograms per hour

References

- [1] Flouros, M., 2005, "The Impact of Oil and Sealing Air Flow, Chamber Pressure, Rotor Speed and Axial Load on the Power Consumption in an Aeroengine Bearing Chamber," ASME J. Eng. Gas Turbines Power **127**, pp. 182–186.
- [2] Signer, H., Bamberger, E. N., and Zaretsky, E. V., 1974, "Parametric Study of the Lubrication of Thrust Loaded 120-MM Bore Ball Bearings to 3 Million DN," ASME J. Lubr. Technol., **96**(3), pp. 515–525.
- [3] Scibbe, H. W., and Munson, H. E., 1973, "Experimental Evaluation of 150-Millimeter Bore Ball Bearings to 3-Million DN Using Either Solid or Drilled Balls," ASME J. Lubr. Technol., **73-LUB-24**, pp. 1–10.
- [4] Nemath, Z., Macks, E. F., and Anderson, W. J., 1952, "Investigation of 75-Millimeter-Bore Deep-Groove Ball Bearings Under Radial Load at High Speeds, Oil-Flow-Studies," NACA Tech. Note 2841.
- [5] Trippet, R. J., 1978, "A High-Speed Rolling Element Bearing Loss Investigation," ASME J. Eng. Power, **100**(1), pp. 40–47.
- [6] Harris, T. A., 2001, *Rolling Bearing Analysis*, 4th ed., Wiley, New York.

Mihai C. Duta

e-mail: mihai.duta@comlab.ox.ac.uk

Michelle S. Campobasso

e-mail: sergio.campobasso@comlab.ox.ac.uk

Michael B. Giles

e-mail: mike.giles@comlab.ox.ac.uk

Oxford University Computing Laboratory,
University of Oxford,
Oxford OX1 2QD, UK

Leigh B. Lapworth

Aerothermal Methods Group,
Rolls-Royce plc., P.O. Box 31,
Derby DE24 8BJ, UK
e-mail: leigh.lapworth@rolls-royce.com

Adjoint Harmonic Sensitivities for Forced Response Minimization

This paper presents an adjoint analysis for three-dimensional unsteady viscous flows aimed at the calculation of linear worksum sensitivities involved in turbomachinery forced response predictions. The worksum values are normally obtained from linear harmonic flow calculations but can also be computed using the solution to the adjoint of the linear harmonic flow equations. The adjoint method has a clear advantage over the linear approach if used within a rotor forced vibration minimization procedure which requires the structural response to a large number of different flow excitation sources characterized by a unique frequency and interblade phase angle. Whereas the linear approach requires a number of linear flow calculations at least equal to the number of excitation sources, the adjoint method reduces this cost to a single adjoint solution for each structural mode of rotor response. A practical example is given to illustrate the dramatic computational saving associated with the adjoint approach.

[DOI: 10.1115/1.2031227]

Introduction

The demand for greater efficiency in modern turbomachinery has resulted in engine blading with low weight and high unsteady loadings. As a consequence, the vibratory stress levels have increased and high cycle fatigue failure caused by excessive vibration at high frequencies has become a serious design concern. Over the last two decades, an increasing number of turbomachinery aeroelasticity methods have emerged to address this need; overviews of this field of activity are given in references [1,2]. The state-of-the-art in modeling aeroelastic phenomena are the fully coupled three-dimensional (3D) nonlinear unsteady viscous methods which compute the interaction between structures and fluids using time-accurate integration [3]. Nevertheless, however accurate the physical models, these methods are prohibitively expensive for routine design.

Increasingly, uncoupled linearized unsteady methods are preferred as an optimal compromise between model accuracy and computational efficiency in industrial aeroelastic predictions. These methods treat fluid and structural dynamics independently and analyze the fluid unsteady motion in the frequency domain at a number of fixed frequencies of unsteadiness, known a priori. In this treatment, fluid unsteadiness is assumed to be a small amplitude harmonic variation superposed on a baseline steady flow and is computed as the solution to the linearized equations of fluid motion [4]. There is satisfying evidence that linearized calculations are adequate for a surprisingly large range of applications [5–10]. In particular, a series of studies have demonstrated the suitability of the linear harmonic approach to turbomachinery forced response by comparison with nonlinear time-accurate calculations and with experimental data [8,11–14].

The use of the adjoint method in aeronautical optimization of steady-state performance has been pioneered by Jameson [15–17] and advanced by a number of other authors; an overview is given by Giles [18]. In this approach, the sensitivities of a steady-state objective functional (typically lift or drag) to a large number of underlying design parameters are obtained using a single steady adjoint solution. Whereas the cost of the sensitivity analysis

through linearization or finite differencing is proportional to the number of design parameters, that of the adjoint sensitivity analysis is independent of it. Recently, the adjoint method has been extended to linear sensitivities of objective functionals of harmonic unsteady flows. Florea [19] formulated a two-dimensional (2D) inviscid adjoint method for the sensitivities of unsteady aerodynamic forces and radiated noise to geometric variations. Using automatic differentiation, Hall and Thomas developed adjoint sensitivity analyses of aerodynamic forces for 3D inviscid [20] and 2D viscous harmonic balance calculations [21].

The present paper builds on previous work [22–24] to introduce a 3D turbulent viscous adjoint harmonic method for the computation of aerodynamic forcing and aerodynamic damping in the context of turbomachinery forced response. The adjoint harmonic analysis is discussed starting from the equations of structural vibration and the definition of the aerodynamic forces as linear worksum functionals, the main figure of engineering merit in uncoupled aeroelastic calculations. The emphasis is on the implications of the adjoint approach to engineering practice. Thus, the adjoint method computes the aerodynamic forcing worksums associated with one rotor vibration mode and a number of different flow excitation sources of fixed frequency and interblade phase angle at the cost of a single adjoint harmonic calculation whereas the traditional approach requires a separate linear harmonic calculation for each excitation. Moreover, the aerodynamic damping worksums can be obtained using the same adjoint solution at no additional cost. A numerical example based on the wake shaping minimization method is also provided to illustrate the strength of the adjoint harmonic method.

Analysis of Forced Response

Forced response in turbomachinery is defined as the vibration of rotor blades excited by time-periodic aerodynamic forcing induced by engine flow unsteadiness which is independent from the blade vibration. Aerodynamic forcing of frequencies close to the natural frequencies of rotor vibration is of particular concern as they could result in blade response of excessive amplitude. The aim of the forced response analysis is to predict the amplitude of blade vibration, usually in order to determine whether a resonant engine excitation is acceptable or not [2].

Chiefly responsible for forced vibration problems is the vane passing excitation, i.e., the excitation from the relative rotation of stator vanes [4]. Vane passing excitation is defined by two important parameters: the frequency ω of excitation and the interblade

Contributed by the International Gas Turbine Institute (IGTI) of ASME for publication in the JOURNAL OF ENGINEERING FOR GAS TURBINES AND POWER. Manuscript received by IGTI October 1, 2002; final revision received March 1, 2003. Associate Editor: H. R. Simmons. Paper presented at the International Gas Turbine and Aeroengine Congress and Exhibition, Atlanta, GA, June 16–19, 2003, Paper No. GT2003-38904.

phase angle (IBPA) ϕ . The latter represents the fixed difference of phase between the unsteady flow quantities corresponding to neighboring blades in a rotor row and is generally nonzero because of unequal stator and rotor pitches. Both parameters depend solely on the rotor speed Ω , the rotor blade pitch θ_r , and the vane pitch θ_s of the adjacent stator [4]:

$$\omega = 2\pi \frac{|\Omega|}{\theta_s}; \phi = \frac{\omega\theta_r}{\Omega} = 2\pi \cdot \text{sign}(\Omega) \frac{\theta_r}{\theta_s} \quad (1)$$

Analysis of turbomachinery forced response is commonly based on the observation that the blade-to-air mass ratio is relatively high and, as a consequence, the aerodynamic forces do not alter the frequencies or the mode shapes of free rotor vibration significantly [13]. Let \mathbf{q} be the vector of blade surface nodal displacements in a particular structural mode and let ω_0 denote the corresponding natural frequency. Both \mathbf{q} and ω_0 are the output of a finite element analysis of the blade vibration in a vacuum at the rotor speed of the studied resonant crossing. Using modal decomposition for the structural response, let the scalar \tilde{r} be the time-dependent response of the rotor in the vibration mode \mathbf{q} ; the product $\tilde{r}\mathbf{q}$ thus represents the vector of instantaneous nodal displacements from the blade equilibrium. Choosing \tilde{r} as a generalized coordinate, Lagrangian mechanics yields the well-known differential equation of forced response

$$\ddot{\tilde{r}} + \sigma\dot{\tilde{r}} + \omega_0^2\tilde{r} = \int_S \tilde{p}(t)q_n^* dS \quad (2)$$

In general, mechanical damping present in the rotor structure comes from complex nonlinear sources, e.g., root friction and underplatform dampers. However, the present study is concerned with the calculation of linear worksum functionals which are independent of mechanical damping. For simplicity, damping has been assumed of proportional type and modeled through the constant coefficient σ .

The right-hand side of Eq. (2) is the generalized unsteady force which, neglecting Coriolis effects, is defined as the integral on the blade surface S of the product between the unsteady pressure \tilde{p} on the blade and the complex conjugate of the amplitude q_n of vibration in the direction normal to the blade surface at its equilibrium position. For a single frequency ω of fluid unsteadiness, this generalized force is discretized as the sum over the fluid mesh nodes on the blade surface of the products between the harmonic fluid pressure force on the discrete surface associated with each node and the complex conjugate of the modal displacement at the respective node. Further, this is the inner product between the mode \mathbf{q} and a vector \mathbf{p} of fluid pressure force amplitudes times the harmonic time variation, i.e., $\mathbf{q}^H \mathbf{p} \exp(i\omega t)$. (H represents complex conjugation and transposition.) The inner product between a vector of modal displacements and a vector of harmonic aerodynamic force amplitudes is termed the *worksum functional*.

The unsteady flow field about the blade is generated by two coexisting sources characterized by the same frequency ω : the excitation from the passing stator vanes and blade vibration. In general, turbomachinery forced response is not clearly a linear phenomenon and the amplitude \mathbf{p} of fluid harmonic forces is a nonlinear function of both the prescribed vane passing flow disturbance and the vibration mode \mathbf{q} . However, fluid unsteadiness is in many cases sufficiently small to be computed using a linear harmonic flow analysis. In a linearized treatment, the effects of the two sources of unsteadiness are independent and additive. Then, the amplitude \mathbf{p} of the fluid pressure forces decomposes into an amplitude \mathbf{p}_f of *aerodynamic forcing* generated by the passing stator vanes and an amplitude \mathbf{p}_d of *aerodynamic damping* induced by (and generally opposing) the vibration of the blade: $\mathbf{p} = \mathbf{p}_f + \mathbf{p}_d$. While the term \mathbf{p}_f depends only on the prescribed flow excitation from vane passing, the amplitude \mathbf{p}_d of aerodynamic damping is a linear function of the unknown blade response. Let

$P(\omega)$ denote the matrix of aerodynamic coefficients relating the motion of the blade at a fixed frequency ω to the amplitude of the aerodynamic damping forces arising on the blade as a cause of that motion; with this notation, the amplitude of aerodynamic damping becomes $\mathbf{p}_d = P(\omega)\tilde{r}\mathbf{q}$.

Due to linearity, the rotor structural response is harmonic with unknown amplitude r and frequency equal to that of the excitation: $\tilde{r}(t) = r \exp(i\omega t)$. Replacing this along with the aerodynamic force decomposition into Eq. (2), the final frequency-domain equation of forced response becomes

$$(\omega_0^2 - \omega^2 + i\omega\sigma - \mathbf{q}^H P(\omega)\mathbf{q})r = \mathbf{q}^H \mathbf{p}_f \quad (3)$$

If there are more than one mode of vibration close to resonance with ω , the modal response of the rotor structure to vane passing is coupled through aerodynamic damping [23]. The amplitude $\mathbf{q}^H P(\omega)\mathbf{q}'$ of the aerodynamic damping force arising on the blade in mode \mathbf{q} due to own vibration in mode \mathbf{q}' is generally nonzero and the resonant vibration modes have to be treated collectively.

Worksum Functionals and Forced Response

The two independent worksum functionals involved in Eq. (3), the aerodynamic forcing and the aerodynamic damping, are the output of independent linear harmonic analyses. Because the vector \mathbf{p}_f of pressure forces is a linear function of the amplitude of the harmonic pressure field on the blade, the aerodynamic forcing worksum can be equated to the inner product between a constant vector \mathbf{s} and the amplitude of the harmonic flow unsteadiness: $\mathbf{q}^H \mathbf{p}_f = \mathbf{s}^H \mathbf{u}_f$. In this expression, \mathbf{s} is a linear function of the structural mode \mathbf{q} and is a sparse vector whose nonzero entries correspond to the fluid mesh nodes belonging to the blade surface. Also, \mathbf{u}_f is a vector of amplitudes of linear harmonic flow variables defined at the nodes of the fluid mesh and represents the response of the fluid motion to the harmonic excitation in the response of the fluid motion to the harmonic excitation in the passing vanes. Similarly, \mathbf{p}_d is the amplitude of the harmonic pressure forces acting on the blade due to own vibration in mode \mathbf{q} and is a linear function of the amplitude of the corresponding pressure field. Therefore, the aerodynamic damping worksum can be written as the inner product between the same constant vector \mathbf{s} and the amplitude \mathbf{u}_d of harmonic fluid unsteadiness due to blade vibration: $\mathbf{q}^H P(\omega)\mathbf{q} = \mathbf{s}^H \mathbf{u}_d$.

Analysis of Linear Harmonic Flow

The analysis of linear harmonic fluid motion is derived from the time-dependent Reynolds-averaged Navier–Stokes equations in conservative form, discretized using a finite volume edge-based formulation [25] into the system of nonlinear ordinary differential equations:

$$M \frac{d\mathbf{U}}{dt} + \mathbf{R}(\mathbf{U}, \mathbf{U}_b, \mathbf{X}, \dot{\mathbf{X}}) = 0 \quad (4)$$

M is the Jacobian of the transformation from the discrete conservative variables to the primitive, \mathbf{U} is the vector of discrete primitive flow variables at the nodes of the fluid mesh, \mathbf{R} is the vector of spatial discretization residuals, \mathbf{X} and $\dot{\mathbf{X}}$ are the respective nodal coordinates and velocities, and \mathbf{U}_b the time-dependent data of the far-field (i.e., inflow and outflow) boundary conditions. The discrete equations (4) express the conservation laws for viscous flow at the grid nodes, include Coriolis and centrifugal effects and may also include a turbulence model. The residual dependence on mesh nodal velocities occurs due to the motion of the discretization cells following the possible motion of the blades. In turbomachinery, the boundary conditions closing the flow equations are no-slip flow at the blade and end-wall solid surfaces, prescribed thermodynamic quantities (e.g., total pressure) at the far-field boundaries and a periodicity condition at the periodic boundaries of the flow domain. The far-field boundary conditions model the interaction of the studied rotor with the rest of the engine and

represent a set of discrete flux balance equations which depend on the boundary data \mathbf{U}_b . The periodicity condition equates the flow quantities at corresponding grid nodes on the lower and upper periodic boundaries (a rotation of the vector of fluid velocity is necessary in the case of an annular cascade). This condition is due to the circumferential periodicity of the flow; a period equal to the blade pitch is assumed in the steady-state case and the steady flow past the entire row of blades is computed as the flow within a single blade-to-blade passage. In the notation adopted here, all these boundary conditions are viewed as integral part of the discrete nonlinear flow equations [23].

Flow unsteadiness in turbomachines is assumed to be relatively small and time-periodic at the same time [4] and is treated as a harmonic variation of small amplitude \mathbf{u} and known frequency ω about a steady and nonuniform baseline flow field $\bar{\mathbf{U}}: \mathbf{U}(t) = \bar{\mathbf{U}} + \Re[\mathbf{u} \exp(i\omega t)]$. Introducing this into Eq. (4) and linearizing, the baseline steady flow becomes the solution of the set of discrete nonlinear equations $\mathbf{R}(\bar{\mathbf{U}}) = 0$ while the amplitude \mathbf{u} of harmonic flow unsteadiness is the complex-valued solution of the algebraic system

$$A\mathbf{u} = \mathbf{r} \quad (5)$$

The matrix A is the sum between the sensitivity of the steady discrete residuals to the primitive flow variables and a harmonic unsteady term depending on the frequency

$$A = \frac{\partial \mathbf{R}}{\partial \mathbf{U}} + i\omega M \quad (6)$$

At the same time, A represents a linearization of the boundary conditions and of the turbulence model. The matrix A is constant as depends only on the baseline flow field $\bar{\mathbf{U}}$, the frequency ω and the IBPA ϕ and is the same for both flow excitation sources, vane passing, and blade vibration. The distinction between these two cases comes from different nonhomogeneous terms \mathbf{r} and different boundary data. Thus, the excitation from the passing stator vanes is modeled as a linear harmonic perturbation to the far-field boundary data about a steady-state: $\mathbf{U}_b(t) = \bar{\mathbf{U}}_b + \Re[\mathbf{u}_b \exp(i\omega t)]$. Then, the amplitude \mathbf{u}_f of the harmonic flow unsteadiness due to vane passing is obtained as the solution of Eq. (5) in which the nonhomogeneous term \mathbf{r}_f represents the linear variation of the steady residuals due to a harmonic perturbation of amplitude \mathbf{u}_b in the far-field data:

$$\mathbf{r}_f = - \frac{\partial \mathbf{R}}{\partial \mathbf{U}_b} \mathbf{u}_b \quad (7)$$

Similarly, blade vibration is modeled using a mesh which conforms to the motion of the blade by deforming harmonically with a prescribed amplitude \mathbf{x} about the coordinates of the fixed mesh of the steady-state calculation [5]: $\mathbf{X}(t) = \bar{\mathbf{X}} + \Re[\mathbf{x} \exp(i\omega t)]$. The amplitude of flow unsteadiness arising due to blade vibration is the solution of the linear system (5) with a nonhomogeneous term which represents the linearized effect of the harmonic mesh nodal motion through the baseline flow field $\bar{\mathbf{U}}$:

$$\mathbf{r}_d = - \left(\frac{\partial \mathbf{R}}{\partial \mathbf{X}} + i\omega \frac{\partial \mathbf{R}}{\partial \dot{\mathbf{X}}} \right) \mathbf{x} \quad (8)$$

The viscous wall boundary condition for the linear harmonic flow Eq. (5) is identical with that for the nonlinear flow analysis and imposes either zero (vane passing) or the wall harmonic velocity (blade vibration) to the linear velocity field at the blade surface and end walls. The linear harmonic farfield boundary conditions are applied through the vector \mathbf{r} . In the vane passing case, the only nonzero entries of \mathbf{r} are at the farfield mesh nodes where Eq. (5) represents a linearization of the flux balance across the boundary using the prescribed data perturbation \mathbf{u}_b . In the case of blade vibration, the boundary perturbation is zero and the term \mathbf{r}

is homogeneous at the far-field mesh nodes. The implementation of the harmonic far-field conditions is based on the one-dimensional (1D) nonreflective boundary conditions of Giles [26]. Lastly, the periodicity condition is common to the treatment of both sources of unsteadiness and is similar to that for the steady analysis. This condition equates the linear flow quantities at corresponding grid nodes on the lower and upper periodic boundaries, including the rotation of the linear fluid velocity vector. In addition to this, the linear harmonic periodicity condition imposes a difference of phase equal to the IBPA of the vane passing excitation between the lower and upper periodic linear variables. This phase-lagged periodicity condition allows the linear harmonic calculation to be carried out on a single blade-to-blade passage.

Worksum Functionals Using the Adjoint Method

The adjoint approach is based on the observation that any worksum inner product $\mathbf{s}^H \mathbf{u}$ can be computed either starting from the linear flow solution \mathbf{u} or from the solution to the equations adjoint to the linearized flow equations [18]. Indeed,

$$\mathbf{s}^H \mathbf{u} = \mathbf{s}^H (A^{-1} \mathbf{r}) = (A^{-H} \mathbf{s})^H \mathbf{r} = \mathbf{v}^H \mathbf{r}, \quad (9)$$

where \mathbf{v} is the solution to the adjoint harmonic equation

$$A^H \mathbf{v} = \mathbf{s} \quad (10)$$

The adjoint harmonic equation is therefore given by the adjoint of the matrix A of the linearized equations and by the vector \mathbf{s} determined by the structural mode involved in the worksum product. The adjoint harmonic solution \mathbf{v} represents the sensitivity of the linear worksum functional with respect to the linear source term \mathbf{r} which models the harmonic flow excitation. In the adjoint calculation, the vector \mathbf{r} of the linear problem and the vector \mathbf{s} from the worksum expression exchange roles; what is a nonhomogeneous term in one calculation becomes a term of the inner product in the other. The derivation of the adjoint analysis as the adjoint of the linearized discrete equations of flow motion is called the *fully discrete approach* [18].

The wall boundary condition and the periodicity condition of the adjoint harmonic analysis are identical with the respective conditions of the linear harmonic analysis [23]; the adjoint momentum variables are set to zero at the blade surface and end walls and periodicity is imposed with the same IBPA. The adjoint harmonic condition at the far-field boundary is given by the adjoint of the linearized flux balance across the far-field boundary using zero boundary data and the nonreflective boundary treatment of the linearized code.

To understand the advantage of the adjoint approach, consider that m different constant vectors \mathbf{s} are given and the worksum product is required for n different terms \mathbf{r} . The direct approach needs the solution of n linear systems (5) and m inner products for each of these solutions. The adjoint approach requires the solution of m adjoint systems (10) and n inner products for each adjoint solution. Therefore, because the evaluation cost of the vectors \mathbf{s} and \mathbf{r} is negligible compared with the cost of a single linear or adjoint calculation, if m is a much smaller integer than n , then it is much less expensive to get the required worksum inner products by solving m adjoint systems rather than n linear.

This idea can be applied to a design scenario which requires the rotor response in a small number m of structural modes to a large number n of specified flow excitations of fixed frequency and IBPA. In such a case, the direct linear approach requires $n+m$ independent linear harmonic flow solutions; n linear harmonic flow fields \mathbf{u}_f correspond to each flow excitation to obtain the aerodynamic forcing worksums as $\mathbf{q}^H \mathbf{p}_f = \mathbf{s}^H \mathbf{u}_f$ and m linear harmonic flow fields \mathbf{u}'_d are associated with rotor vibration in each mode \mathbf{q}' to compute the aerodynamic damping worksums as $\mathbf{q}^H P(\omega) \mathbf{q}' = \mathbf{q}^H \mathbf{p}'_d = \mathbf{s}^H \mathbf{u}'_d$. To obtain the same worksum values, the adjoint approach requires by contrast only m adjoint solutions of (10) with \mathbf{s} corresponding to each mode of vibration. Indeed, the

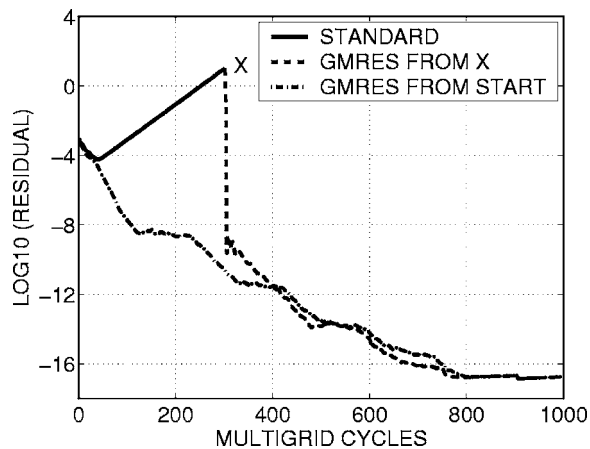


Fig. 1 Comparison between the standard iteration and GMRES convergence histories for a turbine flutter case; GMRES (applied either from the initial conditions or from a restart) is a stable solver

aerodynamic forcing worksums associated with one structural mode \mathbf{q} are computed as $\mathbf{v}^H \mathbf{r}_f$ where \mathbf{r}_f are the nonhomogeneous terms defined by Eq. (7) and correspond to each flow excitation source. Also, the aerodynamic damping in the same mode \mathbf{q} due to vibration in any mode \mathbf{q}' is obtained as $\mathbf{v}^H \mathbf{r}'_d$ using the same adjoint solution \mathbf{v} and the nonhomogeneous term \mathbf{r}'_d defined by Eq. (8) and corresponding to \mathbf{q}' . Therefore, the cost reduction achieved by the adjoint approach is proportional to the number n of flow excitation sources considered.

Computer Implementation and Validation

Both the linear harmonic solver and its adjoint counterpart are derived from a steady nonlinear code [25] which solves the steady Reynolds-averaged Navier–Stokes equations and incorporate the Spalart–Allmaras one-equation turbulence model [27]. The solver uses an edge-based finite volume space discretization on unstructured hybrid grids and a five-stage Runge–Kutta algorithm to time march the discrete flow equations to steady state. Jacobi preconditioning, multiple grids, and parallel computing are employed to accelerate convergence. The emerging linear harmonic solver is a direct code-level linearization of the nonlinear solver; each nonlinear routine which computes a contribution to the nonlinear discrete residual has a correspondent in the linear code which gives the exact linearization of that contribution. Likewise, each linear routine has an adjoint counterpart which computes the corresponding adjoint residual contribution.

Both the linear and adjoint harmonic codes inherit the iterative features of the nonlinear solver and use the Runge–Kutta scheme together with Jacobi preconditioning and multigrid. Although the linear and adjoint iterations normally converge without difficulty, problems have been encountered if the steady flow calculation itself failed to converge to a steady state but instead finished in a low-level limit cycle, often related to some physical phenomenon such as vortex shedding at a blunt trailing edge. This limit cycle results in a small number of eigenvalues of the preconditioned matrix A lying outside the unit circle centered at 1 in the complex plane and thus causing an exponential growth of the linear residual with the standard iteration. To overcome this difficulty, the GMRES algorithm has been implemented to solve the linear and the adjoint systems using the standard multigrid iteration as a preconditioner [28]. Figure 1 shows a comparison between the convergence histories of the standard iteration and of the GMRES solver; GMRES is stable and insensitive to the outlying eigenvalues.

The linear harmonic solver has been validated using a comprehensive suite of tests: The details are covered in reference [23].

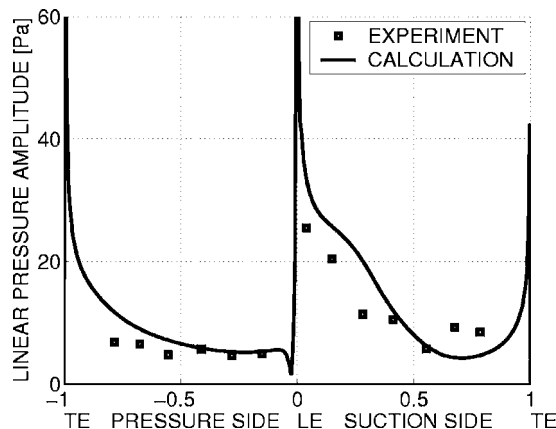


Fig. 2 Comparison between the measured and the computed midspan distribution of the unsteady pressure amplitude for the 11th standard configuration at the subsonic flow condition

Validation has started with the classical inviscid subsonic linearized theory by Smith [29] and the related code (LINSUB) due to Whitehead [30]. The agreement between the linear harmonic and the LINSUB results has been very good over the full range of IBPAs for both fluttering cascades and forced response at representative values of reduced frequency. The viscous capability of the linear harmonic code has been checked on the analytical solution of the Stokes layer problem [31] with excellent agreement. Further, the measurement data from the 11th Standard Configuration database [32] has been used to test the capacity of the linear harmonic code to predict a complex unsteady flow condition. There has been a good agreement with the measured data, especially for the subsonic flow case and it has been concluded that the present code predicted the measured data at least as well as the other codes assessed in the paper by Fransson. For instance, Fig. 2 depicts the comparison between the computed midspan distribution of the unsteady pressure amplitude and the measured data at the subsonic condition. Another test has compared the worksum values output by the linear harmonic code as a function of the IBPA with the corresponding results from an independent time-accurate unsteady nonlinear flow solver [33] for the flutter of a research Rolls Royce fan rotor, Fig. 3. Both codes have used turbulence modeling, and the good agreement between results indicates the suitability of the linearized approach for 3D turbulent viscous turbomachinery applications. Lastly, the correctness of the adjoint code has been verified against the linear harmonic solver

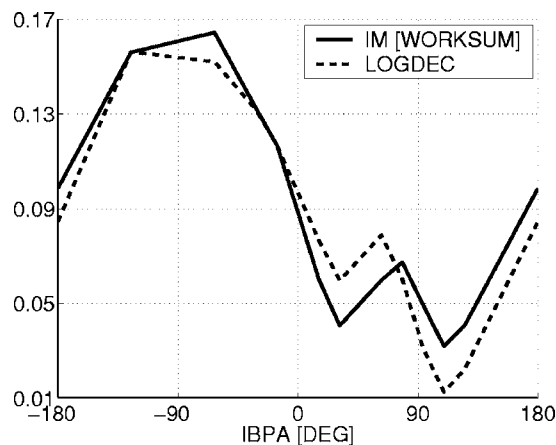


Fig. 3 Comparison between the imaginary part of the worksum value and the logarithmic decrement output by an independent nonlinear viscous code

first by checking routine level compatibility. Then, the linear-adjoint worksum equivalence (9) and the equality of the convergence rates of the two harmonic solvers have been examined for a number of representative cases. As expected from the fully discrete design of the adjoint method, excellent agreement has been observed in all cases.

Wake Shaping Using the Adjoint Method

Wake shaping is a method for reducing the forced vibration of a rotor blade row at a problematic vane passing resonance by choosing an optimum from a relatively large set of n possible designs of the upstream stator vanes. The designs in this set differ through the radial stacking of fixed profiles defined at an earlier stage; the choice of the different stacking designs is largely based on past experience. The optimum is that vane stacking design which gives the minimum forced response in the downstream rotor blading. The traditional variant of the method first involves the use of the steady nonlinear flow solver to compute the steady flow around each particular vane stacking. This is followed by a circumferential Fourier decomposition of the nonlinear flow fields to obtain the vane passing perturbation \mathbf{u}_b corresponding to each stacking design as the amplitude of the fundamental circumferential harmonic [23]. The magnitude of rotor forced response in a single structural mode to the flow perturbation from each vane design is estimated in the second part of the method using a unique nonlinear flow solution $\bar{\mathbf{U}}$ as the baseline rotor flow but one linear harmonic flow response \mathbf{u}_f to each flow perturbation. An extra linear harmonic solution \mathbf{u}_d corresponding to the rotor vibration in that mode is also necessary for the calculation of aerodynamic damping. If m structural modes are considered, wake shaping requires $n+m$ independent linear harmonic calculations: n for the determination of the harmonic unsteady flow fields \mathbf{u}_f responding to the passing of each vane design plus m to determine the “self-induced” harmonic unsteadiness \mathbf{u}_d corresponding to each structural mode. Adopting the adjoint approach, the $n+m$ linear harmonic flow fields are replaced by m adjoint harmonic solutions, each adjoint calculation corresponding to one structural mode. Since the computational costs of the linear and adjoint codes are comparable, the cost reduction achieved by using the adjoint approach within wake shaping is proportional to the size n of the optimization space.

The test case chosen to illustrate the above idea is one stage of a HP turbine rotor operating at an engine speed of 7346.3 rpm (70% of the design speed). This test case was studied in the past [12] to demonstrate a good agreement between forced response predictions using a linearized uncoupled approach and the results from a nonlinear method coupling fluid and structural dynamics. The turbine stage has 36 stator vanes and 92 turbine blades; this corresponds to a vane passing frequency of 4407.8 Hz and an IBPA equal to 140.87 deg. The first torsion (1T) and the second flap (2F) modes of rotor vibration have natural frequencies close to resonance (5038.9 Hz and 5107.2 Hz at 70% part speed, respectively) and are considered together.

In order to generate the set of flow perturbations \mathbf{u}_b corresponding to different vane designs, a linearized relationship has been used between the variation of the vane stacking about a given initial design and the phase shift of the flow perturbation corresponding to this datum. It is assumed that a restacking of the vane changes the shape of the downstream wake at the vane exit through a pitchwise displacement but leaves the wake “strength” largely unaffected. Then, at any radial position on the rotor inlet plane, only the phase of the vane passing harmonic perturbation \mathbf{u}_b varies significantly with the vane restacking while its amplitude remains approximately the same. Thus, the initial vane design produces a flow perturbation which becomes the basis for the minimization process and the optimal phase shift about this perturbation represents the result of wake shaping. Then, the inverse

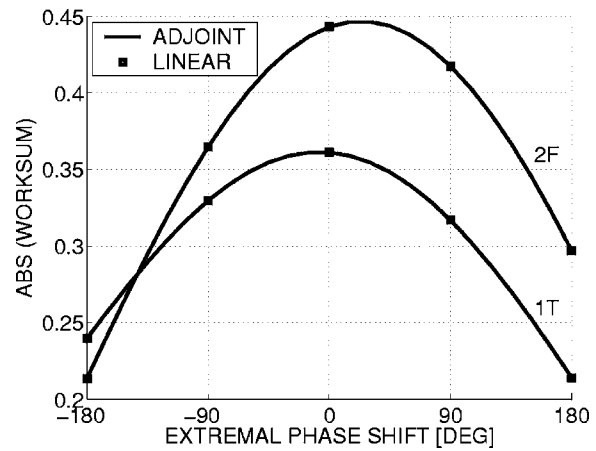


Fig. 4 Variation of the absolute value of the aerodynamic forcing worksum with the value of the extremal phase shift for the 1T and 2F modes of rotor vibration

of the linearized relationship relates the optimal perturbation phasing to the optimal variation of the vane stacking about the datum.

The application of a linearized relationship between stacking variations and perturbation phase shifts is limited in principle to small variations of the vane design. If employed in a real vane design module, it should be first validated against a vane exit nonlinear flow study; in cases in which the highly nonlinear radial flow effects are important, the relationship is probably invalid. However, the validity of this linearized relationship is independent of the adjoint analysis and is used in this study only thanks to its ease of implementation in order to illustrate the strength of the adjoint approach. In other words, if the flow perturbations \mathbf{u}_b are the result of independent steady viscous flow calculations about different vane geometries rather than obtained through phase shifting a datum, the above discussion in favor of the adjoint approach remains unchanged.

A linear radial variation from zero at the hub to an extremal value at the casing is assumed for the phase shift and this extremal value is used as the coordinate of a one-dimensional optimization space. The interval of variation for the extremal phase shift has been chosen between -180 deg and 180 deg and 25 discrete points along this variation have been set using a constant step size of 15 deg. Each of the resulting 25 points corresponds to a particular vane passing disturbance (and to a particular vane stacking, as far as design is concerned) and yields a different magnitude of rotor response. Figure 4 depicts the dependence of the absolute value of the aerodynamic forcing worksum for the respective 1T and 2F structural modes on the extremal phase shift. These two variations have been obtained using one adjoint harmonic solution for each structural mode rather than one linear calculation for each mode at each discrete point. The adjoint values have been verified against the corresponding linear harmonic results at a number of phase shift values (datum 0 deg, ± 90 deg, and ± 180 deg) and the agreement has been found to be excellent.

Shown in Fig. 5 is the midspan distribution of the linear pressure amplitude on the turbine blade as induced by the datum inflow perturbation as well as by the perturbations corresponding to the phase shifts ± 180 deg. This plot reveals the fact that the reduction in the absolute value of aerodynamic forcing toward the ends of the interval of phase shift variation is due to the “rephasing” of the inlet flow perturbation as well as to a reduction in the level of flow unsteadiness. Thus, while the general level of unsteadiness (measured as the linear pressure amplitude squared and integrated over the blade surface) has reduced with only about 15% from datum to 180 deg, the worksum absolute values have dropped with over 30% for both modes and the difference is accounted for by the phase shift of the flow perturbation.

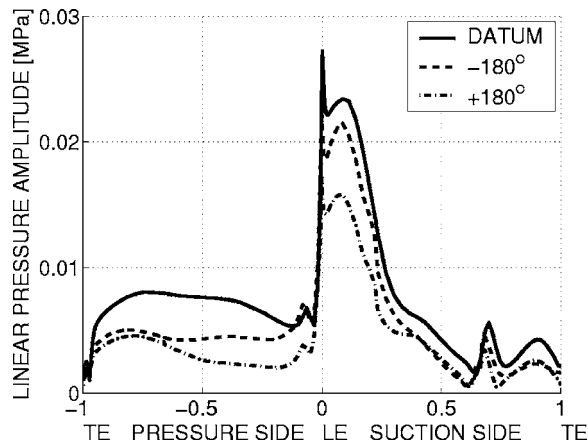


Fig. 5 The midspan distribution of the unsteady pressure amplitude computed as a response to the datum inlet flow harmonic perturbation and to the perturbations phase shifted with ± 180 deg

Finally, the same two adjoint solutions have been used to compute the aerodynamic damping terms as $\mathbf{q}^H P(\omega) \mathbf{q}' = \mathbf{v}^H \mathbf{r}'_d$ in which \mathbf{v} is the adjoint solution associated with mode \mathbf{q} while \mathbf{q} and \mathbf{q}' independently represent the 1T and 2F modes in turn. Table 1 tabulates these four aerodynamic damping values along with the corresponding worksums from linear calculations for comparison; a very good agreement is observed.

Conclusions

The adjoint method has been successfully applied in the past to steady-state aeronautical optimization to compute efficiently the sensitivities of objective functions to the underlying design parameters. This paper has introduced a new 3D viscous harmonic unsteady adjoint method for the calculation of the aerodynamic forcing and aerodynamic damping worksum functionals occurring in turbomachinery forced response predictions. Following the fully discrete approach, the harmonic adjoint method has been derived from the discrete linear harmonic equations of flow motion. The adjoint method is particularly suited to the wake shaping minimization, in which the worksum values associated with m modes of rotor vibration and a large number n of different stacking designs of the upstream vanes are computed efficiently using a single adjoint harmonic solution for each vibration mode. The benefit from using the adjoint harmonic method is thus a reduction in the computational cost of the wake shaping method proportional to the number of vane designs considered in the optimization space. This benefit has been clearly demonstrated on a HP turbine rotor test case.

Acknowledgment

The present research has been supported by the Engineering and Physical Sciences Research Council under Grant No. GR/L95700, and by Rolls Royce plc. (technical monitor: L. Lapworth), DERA (technical monitor: J. Calvert), and BAE Systems

Table 1 Comparison between the aerodynamic damping terms for the 1T and 2F structural modes as computed by the linear and adjoint harmonic codes

	Linear	Adjoint
$\mathbf{q}_{1T}^H P \mathbf{q}_{1T}$	-6.86799-15.17130 i	-6.86793-15.17133 i
$\mathbf{q}_{1T}^H P \mathbf{q}_{2F}$	1.17416+4.47028 i	1.17415+4.47029 i
$\mathbf{q}_{2F}^H P \mathbf{q}_{1T}$	5.60554+5.47400 i	5.60549+5.47398 i
$\mathbf{q}_{2F}^H P \mathbf{q}_{2F}$	-0.82541-7.59087 i	-0.82539-7.59086 i

plc. (technical monitor: D. Standingford). We also acknowledge the contributions of P. Moinier, J.-D. Müller, N. A. Pierce, and M. West to the development of the HYDRA suite of nonlinear, linear, and adjoint codes.

Nomenclature

- A = matrix of linear harmonic problem
- d = subscript for aerodynamic damping quantities
- f = subscript for aerodynamic forcing quantities
- M = conservative to primitive variable transformation Jacobian
- P = matrix of aerodynamic influence coefficients
- \tilde{p} = time-dependent pressure at blade surface
- \mathbf{p} = amplitude of harmonic aerodynamic forces
- q_n = amplitude of modal vibration normal to blade
- \mathbf{q} = mode of free structural vibration
- \mathbf{R} = vector of discrete nonlinear residuals
- \tilde{r} = instantaneous value of modal response
- r = amplitude of modal response
- \mathbf{r} = nonhomogeneous term of linear problem
- \mathbf{s} = nonhomogeneous term of adjoint problem
- \mathbf{U} = vector of time-dependent discrete flow variables
- \mathbf{U}_b = vector of time-dependent far-field boundary data
- $\bar{\mathbf{U}}_b$ = vector of steady far-field boundary data
- $\bar{\mathbf{U}}$ = vector of steady discrete flow variables
- \mathbf{u} = amplitude of harmonic fluid unsteadiness
- \mathbf{u}_b = amplitude of farfield data perturbation
- \mathbf{v} = adjoint harmonic solution
- \mathbf{X} = vector of mesh nodal coordinates
- $\dot{\mathbf{X}}$ = vector of mesh nodal velocities
- ϕ = inter-blade phase angle
- θ_r = rotor blade pitch
- θ_s = stator vane pitch
- ω = frequency of forcing
- ω_0 = natural frequency of blade vibration
- σ = mechanical damping coefficient
- Ω = rotor speed

References

- [1] Verdon, J. M., 1993, "Review of Unsteady Aerodynamic Methods for Turbomachinery Aeroelastic and Aeroacoustic Applications," *AIAA J.*, **31**(2), pp. 235-250.
- [2] Marshall, J. G., and Imregun, M., 1996, "A Review of Aeroelasticity Methods With Emphasis on Turbomachinery Applications," *J. Fluids Struct.*, **10**(3), pp. 237-267.
- [3] Vahdati, M., Sayma, A. I., and Imregun, M., 2000, "An Integrated Nonlinear Approach for Turbomachinery Forced Response Prediction. Part II: Case Studies," *J. Fluids Struct.*, **14**(1), pp. 103-125.
- [4] Giles, M. B., 1992, "An Approach for Multi-Stage Calculations Incorporating Unsteadiness," ASME Paper No. 92-GT-282.
- [5] Hall, K. C., 1993, "Deforming Grid Variational Principle for Unsteady Small Disturbance Flows in Cascades," *AIAA J.* **31**(5), pp. 891-900.
- [6] Hall, K. C., Clark, W. S., and Lorence, C. B., 1994, "A Linearized Euler Analysis of Unsteady Transonic Flows in Turbomachinery," *ASME J. Turbomach.*, **116**(3), pp. 477-488.
- [7] Clark, W. S., and Hall, K. C., 1995, "A Numerical Model of the Onset of Stall Flutter in Cascades," ASME Paper No. 95-GT-0377.
- [8] Marshall, J. G., and Giles, M. B., 1998, "Some Applications of a Time-Linearized Euler Method to Flutter and Forced Response in Turbomachinery," *Proc., 8th ISUAAT, Stockholm, Sweden*, T. H. Fransson, ed., Kluwer Academic, Dordrecht, The Netherlands, pp. 225-240.
- [9] Panovsky, J., and Carson, S. M., 1998, "Prediction of Turbine Blade Vibratory Response Due to Upstream Vane Distress," *ASME J. Turbomach.*, **120**(3), pp. 515-521.
- [10] Hoyniak, D., and Clark, W. S., 1999, "Aerodynamic Damping Predictions Using a Linearized Navier-Stokes Analysis," ASME Paper No. 99-GT-207.
- [11] Suddho, A., Giles, M. B., and Stow, P., 2003, "Simulation of Inviscid Blade Row Interaction Using a Linear and a NonLinear Method." ISABE Paper 91-7049.
- [12] Vahdati, M., Green, J. S., Marshall, J. G., and Imregun, M., 1998, "Forced Response Predictions for a HP Turbine Rotor Blade," *Proc. RTO Applied Ve-*

- hicle Technology Panel Symposium on Design Principles and Methods for Aircraft Gas Turbine Engines, NATO Research Technology Organization, Neuilly-sur-Seine, France.
- [13] Green, J. S., and Marshall, J. G., 1999, "Forced Response Predictions Within the Design Process," *Proc., 3rd European Conference on Turbomachinery-Fluid Dynamics and Thermodynamics*, von Karman Institute for Fluid Dynamics, Rhode Saint-Genese, Belgium.
- [14] Sbardella, L., and Imregun, M., 2001, "Linearized Unsteady Viscous Turbomachinery Flows Using Hybrid Grids," *ASME J. Turbomach.*, **123**(3), pp. 568–582.
- [15] Jameson, A., 1988, "Aerodynamic Design via Control Theory," *J. Sci. Comput.*, pp. 233–260.
- [16] Jameson, A., 1995, "Optimum Aerodynamic Design Using CFD and Control Theory," AIAA Paper 1995-1729.
- [17] Jameson, A., 1999, "Re-Engineering the Design Process Through Computation," *AIAA J. Aircr.*, **36**(1), pp. 36–50.
- [18] Giles, M. B., and Pierce, N. A., 2000, "An Introduction to the Adjoint Approach to Design," *Flow, Turbul. Combust.*, **65**(3–4), pp. 393–415.
- [19] Florea, R., and Hall, K. C., 2001, "Sensitivity Analysis of Unsteady Inviscid Flow Through Turbomachinery Cascades," *AIAA J.*, **39**(6), pp. 1047–1056.
- [20] Hall, K. C., and Thomas, J. P., 2002, "Sensitivity Analysis of Coupled Aerodynamic/Structural Dynamic Behavior of Blade Rows," *Proc., 7th National Turbine Engine HCF Conference*.
- [21] Thomas, J. P., Hall, K. C., and Dowell, E. H., 2003, "A Discrete Adjoint Approach for Modeling Unsteady Aerodynamic Design Sensitivities," AIAA Paper 2003-0041.
- [22] Giles, M. B., Duta, M. C., Müller, J.-D., and Pierce, N. A., 2003, "Algorithm Developments for Discrete Adjoint Methods," *AIAA J.*, **41**(2), pp. 198–205.
- [23] Duta, M. C., 2002, "The Use of The Adjoint Method for the Minimisation of Forced Vibration in Turbomachinery," PhD thesis, University of Oxford, United Kingdom.
- [24] Duta, M. C., Giles, M. B., and Campobasso, M. S., 2002, "The Harmonic Adjoint Approach to Unsteady Turbomachinery Design," *Int. J. Numer. Methods Fluids*, **40**(3–4), pp. 323–332.
- [25] Moinier, P., 1999, "Algorithm Developments for an Unstructured Viscous Flow Solver," PhD thesis, University of Oxford, United Kingdom.
- [26] Giles, M. B., 1990, "Nonreflecting Boundary Conditions for Euler Equation Calculations," *AIAA J.*, **28**(12), pp. 2050–2058.
- [27] Spalart, P. R., and Allmaras, S. R., 1994, "A One-Equation Turbulence Model for Aerodynamic Flows," *Rech. Aerosp.*, pp. 5–21.
- [28] Campobasso, M. S., and Giles, M. B., 2003, "Effect of Flow Instabilities on the Linear Analysis of Turbomachinery Aeroelasticity," *AIAA J. Propul. Power*, **19**(2), pp. 250–259.
- [29] Smith, S. N., 1971, "Discrete Frequency Sound Generation in Axial Flow Turbomachines," Tech. Rep. CUED/A-Turbo/TR 29, University of Cambridge, Department of Engineering, Cambridge, United Kingdom.
- [30] Whitehead, D. S., 1988, "Classic Two-Dimensional Methods," *AGARD Manual on Aeroelasticity in Axial-Flow Turbomachines*, AGARD-AG-298, M. Platzer and F. O. Carta, eds., Vol. 1, NATO Advisory Group for Aerospace Research and Development, Neuilly-sur-Seine, France.
- [31] Telionis, D. P., 1981, *Unsteady Viscous Flows*, Springer, New York, pp. 156–158, Chap. 4.
- [32] Fransson, T. H., et al., 1999, "Viscous and Inviscid Linear/Nonlinear Calculations Versus Quasi Three-Dimensional Experimental Cascade Data for a New Aeroelastic Turbine Standard Configuration," *ASME J. Turbomach.*, **121**, pp. 717–725.
- [33] Vahdati, M., Sayma, A. I., Marshall, J. G., and Imregun, M., 2001, "Mechanisms and Prediction Methods for Fan Blade Stall Flutter," *AIAA J. Propul. Power*, **17**(5), pp. 1100–1108.

Pezhman Akbari

Department of Mechanical Engineering,
Michigan State University,
2500 Engineering Building,
East Lansing, MI 48824-1226
e-mail: akbari@egr.msu.edu

Razi Nalim

Department of Mechanical Engineering,
Indiana University–Purdue University
Indianapolis (IUPUI),
Indianapolis, IN 46202-5132
e-mail: mnalim@iupui.edu

Norbert Müller

Department of Mechanical Engineering,
Michigan State University,
2455 Engineering Building,
East Lansing, MI 48824-1226
e-mail: Mueller@egr.msu.edu

Performance Enhancement of Microturbine Engines Topped With Wave Rotors

Significant performance enhancement of microturbines is predicted by implementing various wave-rotor-topped cycles. Five different advantageous cases are considered for implementation of a four-port wave rotor into two given baseline engines. In these thermodynamic analyses, the compressor and turbine pressure ratios and the turbine inlet temperatures are varied, according to the anticipated design objectives of the cases. Advantages and disadvantages are discussed. Comparison between the theoretic performance of wave-rotor-topped and baseline engines shows a performance enhancement up to 34%. General design maps are generated for the small gas turbines, showing the design space and optima for baseline and topped engines. Also, the impact of ambient temperature on the performance of both baseline and topped engines is investigated. It is shown that the wave-rotor-topped engines are less prone to performance degradation under hot-weather conditions than the baseline engines. [DOI: 10.1115/1.1924484]

Introduction

A growing market for distributed power generation and propulsion of small vehicles has motivated a strong interest in design of small gas turbine systems in the range of 30–300 kW. Known as microturbines, they are now widely used in the US for distributed power generation, shaving peak loads, and providing backup power for critical needs. They propel small commercial aircraft, unmanned air vehicles (UAV), and terrestrial vehicles. Microturbines are often the preferred alternative to IC engines, because of their higher power density and robustness. They present several advantageous features such as compact size, simple operability, ease of installation, low maintenance, fuel flexibility, and low NO_x emissions. Furthermore, recent electric-power crises and environmental concerns have stimulated a strong interest in the research, development, and application of microturbines.

Despite their attractive features, compared with larger gas turbines, microturbines suffer from lower thermal efficiency and their relative output power, due to their (lower) component efficiencies, limited cycle pressure ratio, and peak cycle temperature. For example, experimental and theoretical research has shown that microturbines with pressure ratios of 3–5 without recuperation systems achieve only about 15%–20% efficiency [1,2]. For many applications improvement of their performance is desirable to enhance advantages over competing technologies. To achieve such improvements, current efforts are mainly focused on utilizing heat recovery devices, developing new high-strength, high-temperature materials for turbine blades, and improving the aerodynamic quality of turbomachinery components [3]. The aerodynamics of turbomachinery has already yielded very high component efficiencies up to around 90% [4]. Further improvement is possible, but huge gains seem unlikely especially for small compressors with unavoidable tip leakage. Geometries of microturbines make blade cooling very difficult and internal cooling methods applied to larger engines are often impractical for smaller turbines. Hence, their lifetimes are shorter when using materials typical of larger gas turbines [5]. Therefore, there is significant research toward developing advanced metallic alloys and ceramics for high-thermal-resistance turbine wheels used in

microturbines [6,7]. Utilizing conventional recuperators based on the use of existing materials can improve the overall efficiency of microturbines up to 30% [2,8–10]. Despite the attractive feature of the recuperator concept, a recuperator adds about 25%–30% to the overall engine manufacturing cost, which is a challenge for commercialization of microturbines [11–13]. The current trend of the microturbine market is to reduce the investment cost. Therefore, alternative devices need to be considered to achieve higher performance at lower component costs. Topping a microturbine with a wave rotor device is an appropriate solution.

In a wave-rotor-topped cycle, the combustion can take place at a higher temperature while the turbine inlet temperature can be equal to that of the baseline cycle. Also, a pressure gain additional to that provided by the compressor is obtained by the wave rotor. Thus, the wave rotor can increase the overall pressure ratio and peak cycle temperature beyond the limits of ordinary turbomachinery. The performance enhancement is achieved by increasing both thermal efficiency and output work, hence reducing specific fuel consumption rate considerably. This enhancement is especially favorable for smaller gas turbines often used for distributed power generation or propulsion of small vehicles [14–17].

Wave Rotor History. The first successful wave rotor was tested by Brown Boveri Company (BBC), later Asea Brown Boveri (ABB), in Switzerland in the beginning of the 1940s [18] as a topping stage for a locomotive gas turbine engine [19–22], based on the patents of Seippel [23–26]. This first unit suffered from inefficient design and crude integration [21]. Later, BBC focused on the development of pressure wave superchargers for diesel engines, anticipating greater payoff [27]. By 1987, their Compresx® supercharger appeared in the Mazda 626 Capella passenger car [28,29]. Since then, the Compresx® has been commercialized for heavy diesel engines, and also tested successfully on vehicles such as Mercedes-Benz [30], Peugeot, and Ferrari [27]. Such a pressure-wave supercharger offers rapid load response and scale-independent efficiency, making its light weight and compact size attractive for supercharging small engines (below about 75 kW or 100 hp) [31,32].

Propulsion applications resumed in the 1960s, with General Electric Company (GE), General Power Corporation (GPC), Mathematical Science Northwest (MSNW), and Rolls Royce developing prototypes [27,33]. In the 1980s, US agencies like the Defense Advanced Research Projects Agency (DARPA) and the Navy sponsored research programs on wave rotor science and

Contributed by the IGTI Microturbines and Small Turbomachinery Committee of the ASME for publication in the JOURNAL OF ENGINEERING FOR GAS TURBINES AND POWER. Manuscript received March 12, 2004; final manuscript received December 13, 2004. Committee Chair: D. Haught.

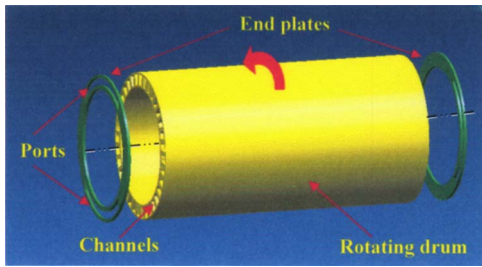


Fig. 1 Schematic configuration of a typical wave rotor

technology. The 1985 ONR/NAVAIR Wave Rotor Research and Technology Workshop [33] offered a comprehensive review of prior work.

Since the late 1980s, a sustained research program at NASA Glenn Research Center (GRC) collaborating with the US Army Research Laboratory (ARL) and Rolls-Royce Allison has aimed to develop and demonstrate the benefits of wave rotor technology for future aircraft propulsion systems [34–40]. Experimental studies at NASA on four-port [41] and three-port [42–44] wave rotors enabled the estimation of loss budgets [45,46] and simulation code validation [47]. Initially, a simple three-port flow divider wave rotor was built and tested to evaluate loss mechanisms and calibrate the simulation code. Next, a four-port pressure exchanger was built and was tested to evaluate the pressure-gain performance for application to a small gas turbine (Allison 250). Wave rotor cycles with lower thermal loads have been proposed [48,49], and mechanical design issues are being addressed in current NASA-sponsored research.

The French National Aerospace Research Establishment (ONERA) has also investigated wave rotor enhancement of gas turbines in auxiliary power units, turboshaft, turbojet, and turbofan engines [15]. Consistent with NASA studies [50], ONERA anticipates the largest gains and efficiency for engines with a low compressor pressure ratio and high turbine inlet temperature, such as turboshaft engines and auxiliary power units.

The objective of the present work is a comprehensive and systematic performance analysis of two actual microturbines known as the C-30 and C-60 engines which are topped with a four-port wave rotor in various wave-rotor-topping cycles. The challenges and advantages associated with the different implementation cases are discussed. While the performance evaluation of several gas turbine engines has been studied extensively [14,15,50], to the knowledge of the author, there exists no comprehensive work investigating the potential benefits of various implementation cases of wave rotor topping cycles for small gas turbines. The presented results have been obtained using basic thermodynamic equations along with the wave-rotor characteristic equation previously validated using computational tools [14]. The model can be employed to predict the performance improvement of various wave-rotor-topping cycles without the need for knowing the details of the complex fluid mechanics within the wave rotor.

Wave Rotor Description

Wave rotors do not use mechanical components such as pistons or vaned impellers to compress the fluid. Instead, the pressure rise is obtained by generating compression waves in appropriate geometries. It has been proven that for the same inlet and outlet Mach numbers the pressure gain in time-dependent flow devices can be much greater than in steady flow devices [51–53].

The essential feature of wave rotors is an array of channels arranged around the axis of a cylindrical drum. As schematically shown in Fig. 1, the drum rotates between two end plates each of which has a few ports or manifolds, controlling the fluid flow through the channels. The number of ports and their positions vary for different applications. By carefully selecting their locations

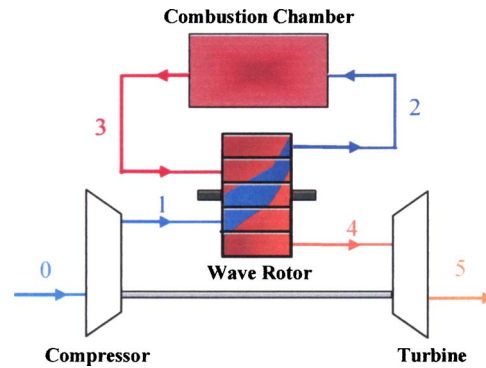


Fig. 2 Schematic of a gas turbine topped by a four-port wave rotor

and widths to generate and utilize wave processes, a significant and efficient transfer of energy can be obtained between flows in the connected ducts. Through rotation, the channel ends are periodically exposed to the ports located on the stationary end plates initiating compression and expansion waves within the wave rotor channels. Thus, pressure is exchanged dynamically between fluids by utilizing unsteady pressure waves. Unlike a steady-flow turbomachine that either compresses or expands the fluid, the wave rotor accomplishes both compression and expansion within a single component. Even though the wave rotor is internally unsteady, the flows in the ports are almost steady, aside from the fluctuations due to the opening and closing of the channels as they enter and exit port regions. Therefore, the wave rotor outflow shows very low pulsating behavior. To minimize leakage, the gap between the end plates and the rotor has to be very small, but without contact under all operating and thermal expansion conditions.

With axial channels and matched port flow alignment, the power required to keep the rotor at a correctly designed speed is negligible [54,55]. It only needs to overcome rotor windage and friction. In such a configuration, the rotor may be gear or belt driven or preferably direct driven by an electrical motor (not shown). Alternatively, a self-driving configuration, known as the “free-running rotor,” can drive itself by using port flow incidence on channel walls to turn the rotor [28,30].

In a conventional arrangement, the wave rotor is embedded between the compressor and turbine “parallel” to the combustion chamber. Figure 2 illustrates how a four-port wave rotor is used to top an unrecuperated (simple) gas turbine cycle. Figure 3 schematically shows how the wave rotor could be embedded physically into an unrecuperated baseline engine that uses single-stage radial compressor and turbine. Two practical design arrangements of installation of a four-port wave rotor in such a gas turbine engine are described in detail in Ref. [56].

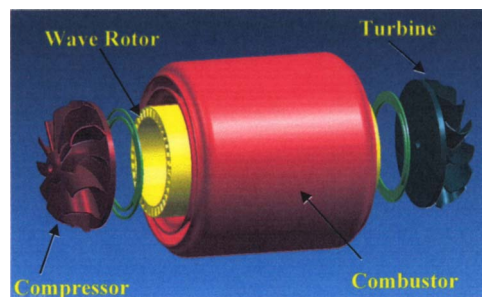


Fig. 3 Schematic example of the physical implementation of a wave rotor in a gas turbine (exploded view, piping not shown)

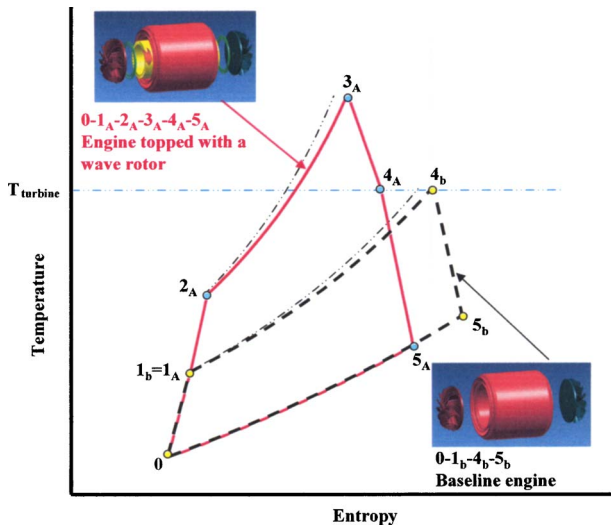


Fig. 4 Schematic T-s diagrams for a gas turbine baseline engine and the most common implementation case of a topping wave rotor

Following the flow path shown in Fig. 2, air from the compressor enters the wave rotor (state 1) and is further compressed inside the wave rotor channels. After the additional compression of the air in the wave rotor, it discharges into the combustion chamber (state 2). The hot gas leaving the combustion chamber (state 3) enters the wave rotor and compresses the air received from the compressor (state 1). To provide the energy transfer to compress the air, the burned gas partially expands in the wave rotor en route to the turbine (state 4). Due to the pre-expansion in the wave rotor, the burned gas enters the turbine with a lower temperature than that of the combustor exit. However, the turbine inlet total pressure is typically 15%–20% higher than the air pressure delivered by the compressor [40]. This pressure gain is in contrast to the untopped engine, where the turbine inlet pressure is always lower than the compressor discharge pressure, due to the pressure loss across the combustion chamber. As a result of the wave rotor pressure gain, more work can be extracted from the turbine increasing engine thermal efficiency and specific work. Finally, the channels are re-connected to the compressor outlet, allowing fresh pre-compressed air to flow into the wave rotor channels and the cycle repeats.

The general advantage of using a wave rotor becomes apparent when comparing the thermodynamic cycles of baseline and wave-rotor-enhanced engines. Figure 4 shows schematic T-s diagrams of the baseline engine and the corresponding wave-rotor-topped engine. The shown wave rotor implementation is the one most commonly discussed in references, referred to as Case A in this study. It is evident that both gas turbines are operating with the same turbine inlet temperature and compressor pressure ratio. Each wave rotor investigated in this work has zero shaft work. Therefore, the wave rotor compression work is equal to the wave rotor expansion work. Thus, the energy increase from state “1_b” to “4_b” in the baseline engine and from state “1_A” to “4_A” in the wave-rotor-topped engine is the same. This results in the same heat addition for both cycles. However, the output work of the topped engine is higher than that of the baseline engine due to the pressure gain across the wave rotor ($p_{t4A} > p_{t4b}$, where subscript “t” indicates total values). Therefore, the thermal efficiency for the topped engine is higher than that of the baseline engine. The inherent gas dynamic design of the wave rotor compensates for the combustor pressure loss from state “2_A” to “3_A,” meaning that the compressed air leaving the wave rotor is at higher pressure than the hot gas entering the wave rotor.

There are several other important advantages of wave rotor ma-

Table 1 Baseline engine data, assuming $T_0=300$ K, $Cp_{air}=1.005$ kJ/kgK, $Cp_{gas}=1.148$ kJ/kgK, $\gamma_{air}=1.4$, $\gamma_{gas}=1.33$

Baseline engine		C-30	C-60
turbine inlet temperature	T_{t4b}	1116.5 K (1550° F)	1227.6 K (1750° F)
compressor outlet temperature	T_{t1b}	466.5 K (380° F)	505.4 K (450° F)
compressor pressure ratio	P_{t1b}/P_0	3.6	4.8
compressor isentropic efficiency	η_C	79.6%	82.6%
turbine isentropic efficiency	η_T	84%	85%
compressor polytropic efficiency	η_{PC}	82.9%	85.9%
turbine polytropic efficiency	η_{PT}	81.7%	82.3%

chines. Their rotational speed is low compared with turbomachines, which results in low material stresses. They can respond on the time scale of pressure waves with no rotor inertial lag. From a mechanical point of view, their geometries can be simpler than those of turbomachines. Therefore, they can be manufactured relatively inexpensively. Also, the rotor channels are less prone to erosion damage than the blades of turbomachines. This is mainly due to the lower velocity of the working fluid in the channels, which is about one-third of what is typical within turbomachines [55]. Another important advantage of wave rotors is their self-cooling capabilities. In heat engine applications, the rotor channels pass both air (being compressed) and hot gas (being expanded) in the cycle at least once per rotor revolution, alternating faster than thermal diffusion rates. The rotor temperature equilibrates between the temperature of the cooler air and the hotter gas, allowing peak cycle temperature above materials limits.

Thermodynamic Calculations

To evaluate the performance enhancement of topping small gas turbines with wave rotors, a computer program based on a thermodynamic approach was created to determine the thermodynamic properties of the gases in different states of the cycles. The results are used to calculate the theoretical performance (expressed by specific cycle work w , thermal efficiency η , and specific fuel consumption SFC) and the actual T-s diagrams of both wave-rotor-topped and baseline engines. The methodology is similar to that introduced by Wilson and Paxson [14] with some modifications.

For thermodynamic calculations, two unrecuperated microturbine engines called C-30 and C-60 made by Capstone Turbine Corporation are considered here. The component performance parameters for the baseline engines are based on information provided by the manufacturer and are listed in Table 1. For each engine it is assumed that the compressor inlet condition is known and is the same for both baseline and wave-rotor-enhanced engines. Considering the same “aerodynamic quality” of the wheels, the polytropic efficiencies are kept the same for the enhanced and baseline engine, for the compressor and turbine, respectively. Incomplete combustion of the fuel is reflected by a combustor efficiency of 98% ($\eta_C=0.98$). Also a 2% pressure drop in the combustion chamber is considered ($\Pi_{comb}=0.98$). Air enters the compressor at 300 K. For both air and burned gas constant values of specific heat coefficients ($Cp_{air}=1.005$ kJ/kgK, $Cp_{gas}=1.148$ kJ/kgK) and specific heat ratios ($\gamma_{air}=1.4$, $\gamma_{gas}=1.33$) are considered. This assumption simplifies the performance calculations significantly without affecting the qualitative nature of the results. Consistently with previous wave rotor investigations [14,15,57], the wave rotor compression and expansion efficiencies are assumed as $\eta_{WC}=\eta_{WE}=0.83$. These efficiencies take into account irreversible effects such as friction. In addition, a wave rotor compression ratio of $PR_W=p_{t2}/p_{t1}=1.8$ appears to be conceivable for the envisioned application [14,15,57] and is chosen for the

following discussion. In this work all performance plots are shown for various wave rotor pressure ratios indicating its effect on the performance enhancement.

Implementation Cases. There are several possibilities to top a gas turbine with a wave rotor. Considering possible design restrictions and preferences, five different advantageous implementation cases for a wave rotor into a given baseline engine can be introduced as follows:

Case A: same compressor, same turbine inlet temperature

Case B: same overall pressure ratio, same turbine inlet temperature

Case C: same combustor

Case D: same turbine

Case E: same compressor, same combustion end temperature

Case A: In Case A the pressure ratio of the compressor is kept unchanged, so the physical compressor of the baseline engine can also be used for the wave-rotor-enhanced engine provided the mass flow is kept approximately the same. The pressure in the combustion chamber of the enhanced engine is increased by the compression ratio of the wave rotor. This may require modifications to the structure of the combustion chamber and to the fuel injection system. The heat addition in the combustor is the same as for the baseline engine, but it takes place after the energy exchange in the wave rotor, hence the heat addition starts at a higher temperature. Thus, the combustion end temperature is even higher than that of the baseline engine, possibly requiring additionally a thermal enhancement of the combustor structure. The turbine of the topped engine might need to be adapted to efficiently utilize the higher pressure ratio. The turbine inlet temperature, however, is the same as that of the baseline engine. As will be shown later, this implementation case provides the highest thermal efficiency and specific work and the lowest value of *SFC*. However, concerns may be raised concerning emissions and combustor design due to the elevation of combustor pressure and temperature. Therefore, other topping cycles might be preferred which are discussed below.

Case B: In Case B the overall pressure ratio for the wave-rotor-enhanced engine is kept equal to that of the baseline engine, so that the combustor works under the same pressure. However, for the wave-rotor-topped engine, the heat addition in the combustor and the combustion end temperature are greater than those of the baseline engine. This may require some adaptation of the combustor, especially in the outlet region. The turbine and compressor work with lower pressure ratios, reducing the design challenges. Thus, both may be adapted advantageously. This might reduce the cost of the compressor and turbine due to reduction of stages in multistage types (mostly axial), or due to reduction of the tip diameter in radial types (mostly single-stage). With a smaller tip diameter the wheels can be manufactured more economically over a shorter time from cheaper materials with less strength and on smaller machines. Besides an attractive performance enhancement, this case additionally provides the highest turbine outlet temperature of all five cases investigated. The temperature of the leaving exhaust gas is much higher than that of the baseline engine. Therefore, this case is attractive for an external heat recovery application or for internal recuperation that can enhance the performance further.

Case C: Case C assumes that it is desirable for the wave-rotor-enhanced engine to use the unmodified combustor of the baseline engine. So the overall pressure ratio and combustor inlet and outlet temperatures for the wave-rotor-enhanced engine are kept equal to those of the baseline engine. The heat addition in the combustor is consequently the same.¹ The implementation of the wave rotor considerably reduces the pressure ratio of the turbine

¹The wave rotor compression efficiency is greater than the compressor efficiency. Therefore, the combustor inlet temperature is in fact negligibly smaller and hence the heat addition is negligibly greater than that in the baseline engine.

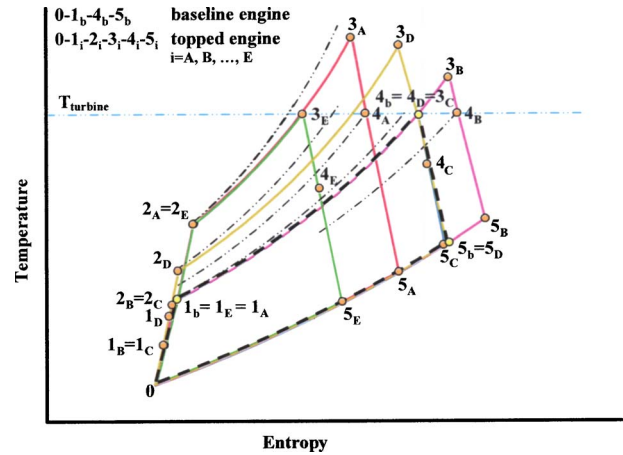


Fig. 5 Schematic T-s diagrams for a baseline cycle and five different wave-rotor-topped cycles

and compressor. The compressor pressure ratio is as low as in Case B, and the turbine pressure ratio and turbine inlet temperature are even lower than those in Case B. Thus, the turbine and compressor could be made from less thermally resistant material. Compared to the baseline engine, they also could be smaller and hence less expensive, as discussed in Case B. This might be the main implementation reason because unfortunately, but not surprisingly, the unambitious combustor constrains the performance enhancement. It is nearly negligible for the smaller C-30 engine and even negative for the C-60 engine.

Case D: Case D employs the same physical turbine as the baseline engine. Due to the wave-rotor-topping, the compressor needs to produce a lower pressure ratio than that of the baseline engine. This allows for a smaller and less expensive compressor as discussed for Cases B and C. The pressure in the combustion chamber and the combustion end temperature are higher than those of the baseline engine, but lower than those of Case A. Hence, less effort might be required to adapt the structure and fuel injection of the combustion chamber. As a result of the lower pressure ratio in the compressor, hence lower compressor discharge temperature, the heat addition in the combustor has to be more than that for the baseline engine to utilize the same allowed turbine inlet temperature. This case gives the second highest performance increase for both baseline engines.

Case E: Case E is similar to Case A but the combustion end temperature (the cycle peak temperature) is restricted to the turbine inlet temperature of the baseline engine in order to avoid additional thermal requirements on the combustor design. The overall pressure ratio is the same as in Case A because this case employs the same physical compressor as for the baseline engine. Thus, the overall pressure ratio is greater than that of the baseline engine, by the wave rotor pressure ratio. The heat addition in the combustor is less than that for the baseline engine because to the wave rotor compression work is added to the fluid before combustion. The turbine in the topped cycle works with a slightly greater pressure ratio than the turbine of the baseline engine, but the turbine inlet temperature is less than that for the baseline engine. In fact, it is the lowest of all cases investigated. This may give the option to produce the turbine wheel at a lower cost out of less thermally resistant material.

According to the state numbering introduced in Fig. 2, Fig. 5 visualizes all five cases in schematic T-s diagrams. Path 0-1_b-4_b-5_b represents the baseline cycle and 0-1_i-2_i-3_i-4_i-5_i (i = A, B, C, D, E) indicates the wave-rotor-topped cycles, where the subscripts indicate the case. One of the five cases might be preferable for a practical design, however, intermediate design cases

are possible. In the following it is assessed how the wave-rotor-topping enhances the performance of C-30 and C-60 baseline gas turbine engines.

Analytical Procedure. According to state numbering introduced in Fig. 2, the following steps are taken to calculate the thermodynamic properties of the gases in different states of the topped cycle:

Path 0-1: Compressor. With the given compressor inlet temperature ($T_0=T_{t0}$), the compressor outlet total temperature and pressure are calculated from the adiabatic relations:

$$T_{t1} = T_{t0} + \frac{T_{t0}}{\eta_C} \left(\Pi_C^{\frac{\gamma_{\text{air}}-1}{\gamma_{\text{air}}}} - 1 \right) \quad (1)$$

$$\frac{p_{t1}}{p_0} = \frac{p_{t1}}{p_{t0}} = \Pi_C \quad (2)$$

where the compressor isentropic efficiency (η_C) relates the compressor pressure ratio (Π_C) to the compressor polytropic efficiency (η_{pC}) through:

$$\eta_C = \frac{\Pi_C^{\frac{\gamma_{\text{air}}-1}{\gamma_{\text{air}}}} - 1}{\Pi_C^{\frac{\gamma_{\text{air}}-1}{\gamma_{\text{air}}}} \eta_{pC} - 1} \quad (3)$$

For Cases A and E, the compressor pressure ratio is equal to that of the baseline engine (e.g., for C-30 engine $\Pi_C=3.6$ and for C-60 engine $\Pi_C=4.8$). However, for Cases B and C its value is calculated by dividing the baseline compressor pressure ratio with the wave rotor compression ratio (PR_W). For Case E, the value of Π_C is calculated in a way that keeps the pressure at the turbine inlet equal for both baseline and topped engines. This calculation can be performed by inversely solving of Eqs. (1)–(21). The compressor specific work is obtained by:

$$w_C = Cp_{\text{air}}(T_{t1} - T_{t0}) = \frac{Cp_{\text{air}}T_{t0}}{\eta_C} (\Pi_C^{\frac{\gamma_{\text{air}}-1}{\gamma_{\text{air}}}} - 1) \quad (4)$$

Path 1-2: Compression in the Wave Rotor. The flow properties after the wave rotor compression process are obtained from the adiabatic relations similarly to those of the compressor:

$$T_{t2} = T_{t1} + \frac{T_{t1}}{\eta_{WC}} (PR_W^{\frac{\gamma_{\text{air}}-1}{\gamma_{\text{air}}}} - 1) \quad (5)$$

$$\frac{p_{t2}}{p_{t0}} = \frac{p_{t2} p_{t1}}{p_{t1} p_{t0}} = PR_W \cdot \Pi_C \quad (6)$$

Path 2-3: Combustion Chamber. The value of fuel–air ratio ($f=m_f/m_{\text{air}}$) can be obtained by applying the energy (first law) equation to the combustion chamber:

$$\eta_Q f h_{PR} = (1+f)Cp_{\text{gas}}T_{t3} - Cp_{\text{air}}T_{t2} \quad (7)$$

where $h_{PR}=43,000$ kJ/kg is the heating value used for all calculations here. This equation gives f as:

$$f = \frac{Cp_{\text{gas}}T_{t3} - Cp_{\text{air}}T_{t2}}{\eta_Q h_{PR} - Cp_{\text{gas}}T_{t3}} \quad (8)$$

Alternatively, f can be expressed based on the turbine total inlet temperature (T_{t4}) and the compressor total exit temperature (T_{t1}). For this purpose, the wave rotor compression and expansion specific work (per unit mass of air flow) are defined, respectively, as follows:

$$w_{WC} = Cp_{\text{air}}(T_{t2} - T_{t1}) \quad (9)$$

$$w_{WE} = (1+f)Cp_{\text{gas}}(T_{t3} - T_{t4}) \quad (10)$$

Here, it is considered that $\dot{m}_1=\dot{m}_2=\dot{m}_{\text{air}}$ and $\dot{m}_3=\dot{m}_4=\dot{m}_{\text{air}}+\dot{m}_f$. Other cycles exist in which the mass flow rates \dot{m}_1 and \dot{m}_2 are not the same, and, correspondingly the mass flow rates \dot{m}_3 and \dot{m}_4 may not be equal either. These cycles are not considered here. Using Eqs. (9) and (10), Eq. (7) can be expressed as:

$$\eta_Q f h_{PR} = (1+f)Cp_{\text{gas}}T_{t4} + w_{WE} - w_{WC} - Cp_{\text{air}}T_{t1} \quad (11)$$

Because the net output work of the wave rotor is zero ($w_{WC}=w_{WE}$), solving for f leads to:

$$f = \frac{Cp_{\text{gas}}T_{t4} - Cp_{\text{air}}T_{t1}}{\eta_Q h_{PR} - Cp_{\text{gas}}T_{t4}} \quad (12)$$

For Cases C and E, T_{t3} is equal to the baseline inlet turbine temperature, therefore, Eq. (8) is used to calculate f . For Cases A, B, and D, where T_{t4} is a known value and is equal to the baseline inlet turbine temperature, f can be obtained from Eq. (12). The relation between T_{t3} and T_{t4} can be found by equating Eqs. (9) and (10):

$$T_{t3} = T_{t4} + \left[\frac{T_{t1}}{\eta_{WC}} (PR_W^{\frac{\gamma_{\text{air}}-1}{\gamma_{\text{air}}}} - 1) \right] \frac{Cp_{\text{air}}}{(1+f)Cp_{\text{gas}}} \quad (13)$$

Finally, the total pressure after the combustion chamber is obtained by:

$$\frac{p_{t3}}{p_{t0}} = \frac{p_{t3} p_{t2}}{p_{t2} p_{t0}} = \Pi_{\text{comb}} \cdot PR_W \cdot \Pi_C \quad (14)$$

Path 3-4: Expansion in the Wave Rotor. To obtain the turbine inlet total pressure (p_{t4}), it is convenient to express the wave rotor compression work and the expansion work in terms of pressure ratios:

$$\dot{W}_{WC} = \dot{m}_{\text{air}} Cp_{\text{air}}(T_{t2} - T_{t1}) = \frac{\dot{m}_{\text{air}} Cp_{\text{air}} T_{t1}}{\eta_{WC}} (PR_W^{\frac{\gamma_{\text{air}}-1}{\gamma_{\text{air}}}} - 1) \quad (15)$$

$$\begin{aligned} \dot{W}_{WE} &= (\dot{m}_{\text{air}} + \dot{m}_f) Cp_{\text{gas}}(T_{t3} - T_{t4}) = (\dot{m}_{\text{air}} + \dot{m}_f) Cp_{\text{gas}} \eta_{WE} T_{t3} \\ &\times \left[1 - \left(\frac{PO}{\Pi_{\text{comb}} PR_W} \right)^{\frac{\gamma_{\text{gas}}-1}{\gamma_{\text{gas}}}} \right] \end{aligned} \quad (16)$$

where $PO=p_{t4}/p_{t1}$ is the gain pressure ratio across the wave rotor. Equating the compression work to the expansion work leads to:

$$\begin{aligned} \frac{Cp_{\text{air}} T_{t1}}{\eta_{WC}} (PR_W^{\frac{\gamma_{\text{air}}-1}{\gamma_{\text{air}}}} - 1) &= (1+f)Cp_{\text{gas}} \eta_{WE} T_{t3} \\ &\times \left[1 - \left(\frac{PO}{\Pi_{\text{comb}} PR_W} \right)^{\frac{\gamma_{\text{gas}}-1}{\gamma_{\text{gas}}}} \right] \end{aligned} \quad (17)$$

Substituting T_{t3} from Eq. (13) into Eq. (17) and some algebra gives:

$$PO = \Pi_{\text{comb}} PR_W \left\{ 1 - \frac{A \frac{1}{\eta_{WE} \eta_{WC}} B}{1 + A \frac{1}{\eta_{WC}} B} \right\}^{\frac{\gamma_{\text{gas}}}{\gamma_{\text{gas}}-1}} \quad (18)$$

where

$$A = \frac{Cp_{\text{air}}}{(1+f)Cp_{\text{gas}}} \quad (19)$$

$$B = \frac{T_{t1}}{T_{t4}} [PR_W^{(\gamma_{\text{air}}-1)/\gamma_{\text{air}}} - 1] \quad (20)$$

Equation (18) is a modified version of the “wave-rotor characteristic” equation introduced in the literature [14]. This equation represents the performance of the wave rotor. By using Eq. (18), the turbine inlet total pressure is obtained by:

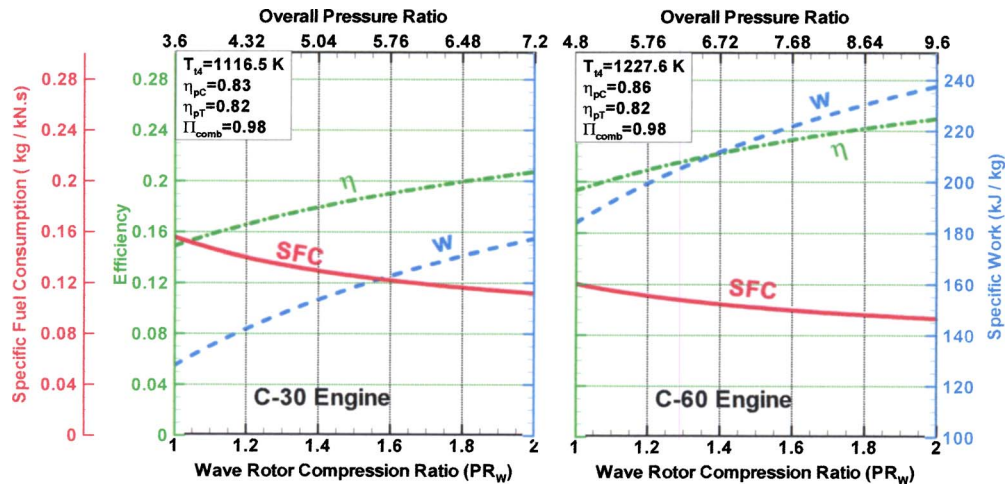


Fig. 6 Thermal efficiency, specific work, and *SFC* for the wave-rotor-topped engines versus the wave rotor pressure ratio and overall pressure ratio, Case A consideration

$$\frac{p_{t4}}{p_{t0}} = \frac{p_{t4} p_{t1}}{p_{t1} p_{t0}} = PO \cdot \Pi_C \quad (21)$$

Path 3-4: Turbine. The turbine specific work (per unit mass of air flow) can be calculated knowing the pressure ratio across the turbine:

$$W_T = (1 + f) C_p p_{\text{gas}} (T_{t4} - T_{t5}) = (1 + f) \eta_T C_p p_{\text{gas}} T_{t4} \left[1 - \left(\frac{p_{t0}}{p_{t4}} \right)^{\frac{\gamma_{\text{gas}} - 1}{\gamma_{\text{gas}}}} \right] \quad (22)$$

Assuming the turbine expands the hot gas leaving the wave rotor to atmospheric pressure ($p_{t5} = p_{t0}$). As a result, the total temperature of the gas leaving the turbine (T_{t5}) can be calculated from the above equation.

After calculating the thermodynamic properties of all states in the cycle, it is possible to calculate the engine performance parameters. The net specific output work produced by the engine can be calculated by subtracting the turbine specific work from the compressor work as $w = w_T - w_C$. With the amount of specific heat addition through the combustion process being defined as $q = f \cdot h_{PR}$, the thermal efficiency can be written as $\eta = w/q$. Finally, the specific fuel consumption (*SFC*) is calculated by $SFC = f/w$.

Predicted Performance Results

Case A is the most common case discussed in the literature and it gives mostly the best performance enhancement. Therefore, it is discussed here in more details. Figure 6 illustrates the increase of cycle thermal efficiency (dash dot) and specific work (dashed), and the decrease of specific fuel consumption (solid) with increasing wave rotor pressure ratio PR_W for both C-30 and C-60 topped engines. The plot visualizes how the effect develops from the baseline engine with $PR_W = 1$ until $PR_W = 2$ which might be a practical limit for the investigated application. However, if the wave rotor pressure ratio increases beyond this limit, the trend already shows that the rate of increase of the effect diminishes while technical problems may increase. With a conceivable wave rotor pressure ratio of 1.8, the thermal efficiency of the baseline cycle increases from 14.9% to 20.0% for the C-30 engine and from 19.4% to 24.2% for the C-60 engine. Simultaneously, the specific work increases from 128 to 171 kJ/kg for the C-30 engine and from 184 to 231 kJ/kg for the C-60 engine. The specific fuel consumption (*SFC*) of the C-30 engine decreases from 0.156 to 0.116 kg/kN.s and it reduces from 0.120 to 0.095 kg/kN.s for the C-60 engine.

A better picture of the performance improvement is obtained by calculating the relative increases of thermal efficiency, specific work, and the relative decrease of *SFC* as shown in Fig. 7. For Case A, the relative increases of thermal efficiency and specific work (dash-dot) are precisely the same as it is obvious from $\eta = w/q$ where the heat addition $q = f \cdot h_{PR}$ is the same for both topped and baseline engines. For a wave rotor pressure ratio of 1.8, Fig. 7 indicates an attractive relative performance improvement in thermal efficiency and specific work of about 33.8% and a 25.2% reduction in *SFC* (solid) for the C-30 engine. The C-60 engine shows a 25.1% enhancement in thermal efficiency and specific work and a 20.1% reduction in *SFC*.

More detailed documentation of these cases are not presented here. The reader is referred to Ref. [16]. Instead, numerical values of the predicted performance enhancement of all five investigated cases with a wave rotor pressure ratio of 1.8 are summarized in Table 2. In this table, Π_T represents the turbine pressure ratio. Subscript “gain” indicates the relative increase of thermal efficiency and specific work and decrease of *SFC*. Table 2 shows that Case A gives the highest performance increase for both baseline engines. After Case A, Case D gives the highest overall performance for the C-30 engine as for the C-60 engine. However, Case E provides the second highest thermal efficiency and the lowest *SFC* for the C-60 engine.

Figure 8 shows maps of the relevant design space for Cases A, B, and D for each engine. The only fixed parameters are turbine inlet temperature, the polytropic efficiencies of the compressor and turbine corresponding to the respective baseline engine, and the combustion chamber pressure loss as indicated in the upper-right hand corner legend of each map. Performance maps valid for Cases C and E of the C-30 and the C-60 engines are shown in Fig. 9 which have lower turbine inlet temperatures than that indicated in Fig. 8. Instead, Cases C and E have the same combustion end temperature as the baseline engine, as indicated in the upper-right hand corner of these maps.

The maps allow predicting the performance of the wave-rotor-enhanced engine in terms of thermal efficiency (green), specific work (blue), and *SFC* (red) for any combination of the compressor pressure ratio (abscissa) and the wave rotor pressure ratio PR_W (parameter labeled in black). In these maps, the multiplication of compressor pressure ratio p_{t1}/p_0 and wave rotor pressure ratio PR_W determines the overall cycle pressure ratio p_{t2}/p_0 (orange). The locus of optimum compressor pressure ratio points (for highest thermal efficiency and specific work at each achievable wave rotor pressure ratio) are connected by black solid lines. The optima for *SFC* are found at the same combination of the compres-

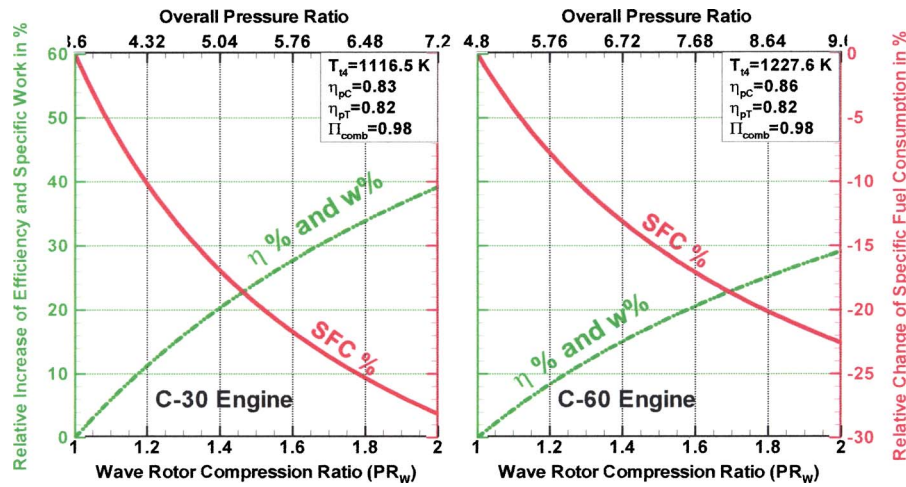


Fig. 7 Relative values of thermal efficiency, specific work, and SFC for the wave-rotor-topped engines versus the wave rotor pressure ratio and overall pressure ratio, Case A consideration

sor pressure ratio and PR_W as the optima of the thermal efficiency.

Such maps are not only very useful to explore the possible enhancement of already existing baseline engines, but they also serve well for selecting a design point or region for designing a new wave-rotor-topped engine. In all plots, the performance points of the baseline engine ($PR_W=1$) and the wave-rotor-enhanced engines of all cases with a wave rotor pressure ratio of $PR_W=1.8$ can be found. For instance in Fig. 8, starting from the performance point of the baseline engine, the performance values for Case A are found by moving vertically upwards (e.g., along the dashed line for constant compressor pressure ratio p_{t1}/p_0) until the corresponding performance curve of the expected wave rotor pressure ratio is crossed. Case B is found by moving along a line of constant overall pressure ratio p_{t2}/p_0 (orange).

The results indicate that for every compressor pressure ratio in each design space shown here, the performance of the topped engine is always higher than that of the corresponding baseline engine with the same compressor pressure ratio (Case A consideration). The increase of PR_W always increases the performance. However, for higher compressor pressure ratios the benefit of using a wave rotor progressively diminishes. In fact, for compressor

pressure ratios greater than around 11, almost no benefit can be obtained for the C-30 engine. An identical statement applies to the C-60 engine for compressor pressure ratios above around 15. The benefit is clearly the greatest for lower compressor pressure ratios. This suggests that the wave-rotor-topping for microturbines with low compressor pressure ratios can produce the greatest relative benefit. Moreover, as expected and known for baseline engines ($PR_W=1$), it is also true for wave-rotor-topped engines that the compressor pressure ratio for the maximum specific work is always less than that of the maximum thermal cycle efficiency. However, with increasing wave rotor pressure ratio, the optima come closer together, while moving towards lower compressor pressure ratio. This can be viewed as an additional advantage for applying wave rotors to small gas turbines with low compressor pressure ratios. So as the plots show, adding a wave rotor with a 1.8 pressure ratio to C-30 or C-60 baseline engines with a compressor pressure ratio $p_{t1}/p_0=3.6$ or $p_{t1}/p_0=4.8$, respectively, already brings the design point into the optimum range for highest specific work and nearly half way closer to the optimum for highest thermal efficiency.

Table 2 Performance comparison between baseline engines and five cases of wave-rotor-topping with a wave rotor pressure ratio of 1.8

Identical to baseline engine are:	Case A		Case B		Case C		Case D		Case E		Baseline	
	• compressor • turbine inlet temp. p_{t1}, T_{t1}, T_{t4}		• overall press. ratio • turbine inlet temp. $p_{t2} = p_{t1b}, T_{t4}$		• combustor $p_{t2} = p_{t1b}, T_{t2}, T_{t3}$		• turbine $p_{t2} = p_{t1b}, p_{t4}, T_{t4}$		• compressor • combustion end temp. $p_{t1}, T_{t1}, T_{t3} = T_{t4b}$		C-30	C-60
Engines	C-30	C-60	C-30	C-60	C-30	C-60	C-30	C-60	C-30	C-60	C-30	C-60
T_{t4} [K]	1116	1228	1116	1228	1044	1149	1116	1228	1027	1132	1116	1228
q [kJ/kg]	855	952	946	1047	857	950	894	993	747	833	855	952
II_c	3.60	4.80	2.00	2.67	2.00	2.67	2.84	3.77	3.60	4.80	3.60	4.80
II_T	4.38	5.87	2.60	3.48	2.55	3.41	3.53	4.70	4.24	5.70	3.53	4.70
w_c [kJ/kg]	167	206	81	116	81	116	131	167	167	206	167	206
w_r [kJ/kg]	338	437	231	324	211	298	295	391	305	396	295	391
w [kJ/kg]	171	231	150	208	130	182	165	224	137	190	128	184
SFC[kg/kN.s]	0.116	0.095	0.147	0.117	0.153	0.121	0.126	0.103	0.126	0.102	0.156	0.120
η	0.200	0.242	0.158	0.199	0.151	0.192	0.184	0.225	0.184	0.227	0.149	0.194
$(w)_{gain}$ [%]	33.8	25.1	17.1	13.0	1.7	-1.1	29.1	21.5	7.7	2.9		
$(SFC)_{gain}$ [%]	25.2	20.1	5.5	2.6	1.4	-0.8	19.0	14.1	18.9	14.9		
$(\eta)_{gain}$ [%]	33.8	25.1	5.9	2.7	1.5	-1.8	23.5	16.5	23.4	17.5		

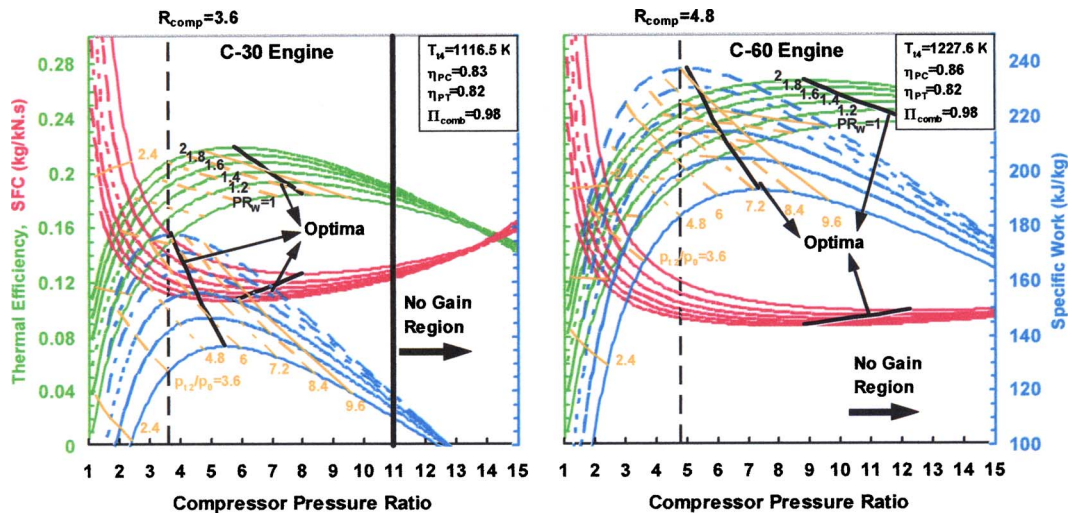


Fig. 8 Performance map for wave-rotor-topping of gas turbines, Cases A, B, and D

Comparison Between Adding a Second Compressor Stage and Wave-Rotor-Topping. The wave-rotor-topping competes mainly against adding a second compressor stage to the single stage baseline engine. In this competition one major advantage of the wave-rotor-topping is that the wave rotor favorably operates mechanically independently from the high-speed engine shaft. Therefore, adding a retrofit wave rotor does not require the redesign of the challenging dynamic system. Even if the compressor or turbine wheel is adapted subsequently to utilize the full potential of the wave-rotor-topping, the dynamic system may change but not as dramatically as if a second compressor stage was added. Thus, by default the wave rotor is a system for achieving similar thermodynamic advantages as by adding a second compressor stage or a high pressure spool, but with many fewer dynamic challenges.

To justify the wave-rotor-topping approach further, the performance results of both competing solutions are compared below. For the addition of a second compressor stage, performance data are calculated for the five most probably relevant pressure ratios of the second stage described here:

$$\Pi_{c2} = PR_W$$

A (perhaps) logical way to compare both systems would be to assume the same compression ratio for the second compressor

stage as for the wave rotor. Hence the compression ratio of the second compressor stage would be $\Pi_{c2} = 1.8$, because the assumed wave rotor compression ratio is $PR_W = 1.8$.

$$w_{C2} = w_{C1}$$

More likely, when the effort of adding a second compressor stage is undertaken, the designer would not limit the pressure ratio of the second stage to $\Pi_{c2} = 1.8$. It might be desired to add a second compressor wheel that is similar to the existing first stage (or the same) for reasons such as using existing experience, or producing both wheels cost effectively as identical wheels, or producing them geometrically similar using the same or slightly modified tools. This approach can be modeled by setting the compressor shaft work of the second stage equal to that of the first stage, simulating the same angular momentum change of the flow in both stages at the same shaft. Because the inlet air temperature for the second stage is much higher, the pressure ratio of the second stage is less than that of the first stage $\Pi_{c2} < \Pi_{c1}$.

$$\Pi_{c2} = \Pi_C$$

Alternatively, it could simply be assumed that the pressure ratio of the second stage is equal to the pressure ratio in the first stage. This is a common design approach.

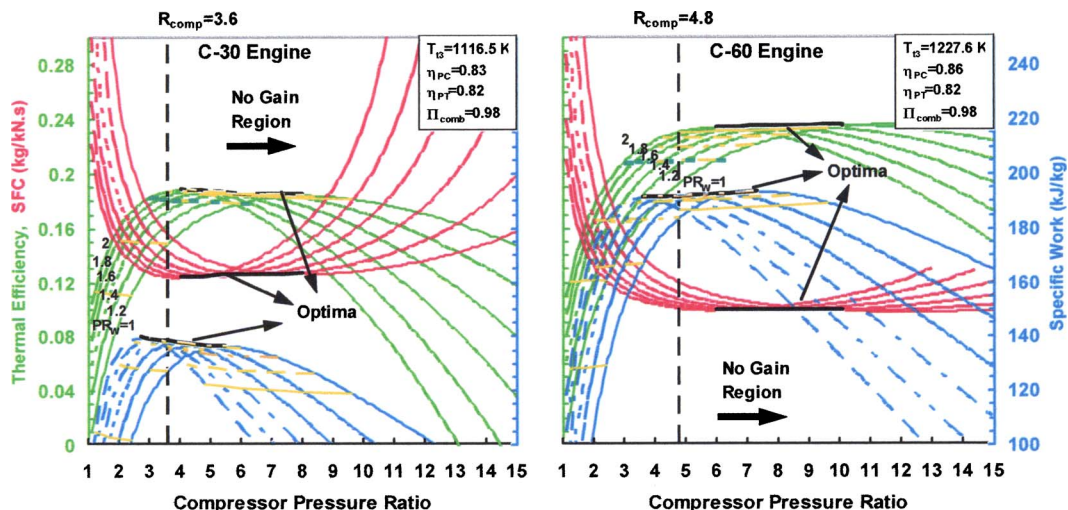


Fig. 9 Performance map for wave-rotor-topping of gas turbines, Cases C and E

Table 3 Performance comparison between adding a conventional second compressor stage and wave-rotor-topping Cases A and E with a wave rotor pressure ratio of 1.8; baseline engine C-30

C-30 Feature	Two-Stage Compressor					Wave Rotor Topped		Baseline
	$\Pi_C(w)_{opt}$	$\Pi_{C2}=PR_W$	$\Pi_C(\eta)_{opt}$	$w_{C2}=w_{C1}$	$\Pi_{C2}=\Pi_{C1}$	Case A	Case E	
Π_{C2}	1.52	1.8	2.22	2.42	3.6	1.8	1.8	
w [kJ/kg]	136	135	129	125	95	171	137	128
SFC [kg/kN.s]	0.133	0.128	0.126	0.127	0.141	0.116	0.126	0.156
η	0.175	0.181	0.184	0.183	0.164	0.200	0.184	0.149
$(w)_{gain}$ [%]	6.3	5.5	0.8	-2.3	-25.8	33.8	7.7	
$(SFC)_{gain}$ [%]	14.5	17.9	18.9	18.6	9.6	25.2	18.9	
$(\eta)_{gain}$ [%]	17.5	21.5	23.4	22.8	10.1	33.8	23.4	

$$\Pi_C(w_{net})_{opt} \text{ and } \Pi_C(\eta)_{opt}$$

It might be desirable to compare the wave-rotor-topped engine with a two-stage compressor engine that has an overall pressure ratio $\Pi_{C2} \cdot \Pi_{C1}$ corresponding to the optimum for maximum specific work $\Pi_C(w)_{opt}$ or the optimum for maximum efficiency $\Pi_C(\eta)_{opt}$. The resulting values for specific work and thermal efficiency, respectively, are the maximum values actually obtainable by enhancing the pressure ratio of a conventional compressor. The values of $\Pi(w)_{opt}$ and $\Pi(\eta)_{opt}$ can be found by using performance maps in Figs. 8 and 9 and following the curves for $PR_W = 1$ to their optimum points.

In all performance calculations above, it is assumed that the polytropic compression efficiency of the second stage is equal to that of the single stage baseline compressor. The performance values of all these two-stage-compressor cases as well as intermediate cases can also be read off the performance maps in Figs. 8 and 9 following the curves for $PR_W = 1$. The compressor pressure ratio at the abscissa then corresponds to the overall pressure ratio $\Pi_{C2} \cdot \Pi_{C1}$.

The performance results are compiled for the C-30 engine in Table 3 and for the C-60 engine in Table 4 for all five two-stage-compressor cases described above. The two-stage-compressor engines are compared with the wave-rotor-topped engine Case A and Case E. These cases are more suitable to be compared with two-stage-compressor engines for a few reasons. Both cases employ the same compressor as the first stage of the baseline engines. Case A has shown the highest performance improvement and it represents the maximum performance achievable for a wave-rotor-topping cycle. In Case E, the baseline compressor is the same and the combustion end temperature is the same as for the baseline engine (not requiring any thermal enhancement of the combustor). It can be understood that this is exactly the case for the two-stage-compressor engine, where the combustion end tem-

perature is simultaneously the turbine inlet temperature (which is never the case for wave-rotor-topping). The two-stage-compressor values may also be compared with the wave-rotor-topping Cases B, C, and D using the supplied data in Table 2.

Tables 3 and 4 show that the gain in predicted overall efficiency, specific shaft work, and SFC of the wave-rotor-topped engine in Case A is always greater than any obtainable values for the two-stage-compressor engine. A look at the maps in Fig. 8 easily verifies this for the relevant design space. In Fig. 8 the performance points for Case A lie well above any point at the curves for $PR_W = 1$ where all the performance data of the two-stage-compressor engine can be found. For the C-30 engine, Case E in Table 3 still shows a higher performance than any two-stage-compressor configuration. For the C-60 engine, however, Case E in Table 4 achieves nearly the same performance as a two-stage-compressor engine with a second-stage compression ratio in the range between the two optima for maximum specific work and maximum overall efficiency (minimum SFC), $\Pi_{C2} = 1.52, \dots, 2.55$. Finally, the results show again that the compressor pressure ratio for the maximum specific work is always less than that of the maximum overall cycle efficiency (minimum SFC).

Besides the drawbacks of the two-stage-compressor implementation already mentioned, a second compressor stage adds not only a second compressor wheel, it always requires an enhanced combustor capable for higher combustion pressure and a turbine adapted to considerably higher pressure ratio. Finally, it requires an enhanced engine shaft, transmitting much more compression work. Quite opposite for the wave-rotor-enhanced engine, the transmitted compression work for all considered wave-rotor-topping cases is always either less (Cases B, C, D) or the same as for the baseline engine (Cases A and D). The combustion pressure ratio can be kept the same (Cases B and C). Furthermore, the

Table 4 Performance comparison between adding a conventional second compressor stage and wave-rotor-topping Cases A and E with a wave rotor pressure ratio of 1.8; baseline engine C-60

C-60 Feature	Two-Stage Compressor					Wave Rotor Topped		Baseline
	$\Pi_C(w)_{opt}$	$\Pi_{C2}=PR_W$	$\Pi_C(\eta)_{opt}$	$w_{C2}=w_{C1}$	$\Pi_{C2}=\Pi_{C1}$	Case A	Case E	
Π_{C2}	1.52	1.8	2.55	2.79	4.8	1.8	1.8	
w [kJ/kg]	193	192	179	173	118	231	190	184
SFC [kg/kN.s]	0.105	0.101	0.098	0.098	0.115	0.095	0.102	0.120
η	0.222	0.229	0.236	0.236	0.203	0.242	0.227	0.194
$(w)_{gain}$ [%]	4.9	4.3	-2.7	-6.0	-35.9	25.1	2.9	
$(SFC)_{gain}$ [%]	12.5	15.8	18.3	18.3	4.2	20.1	14.9	
$(\eta)_{gain}$ [%]	14.4	18.0	21.6	21.6	4.6	25.1	17.5	

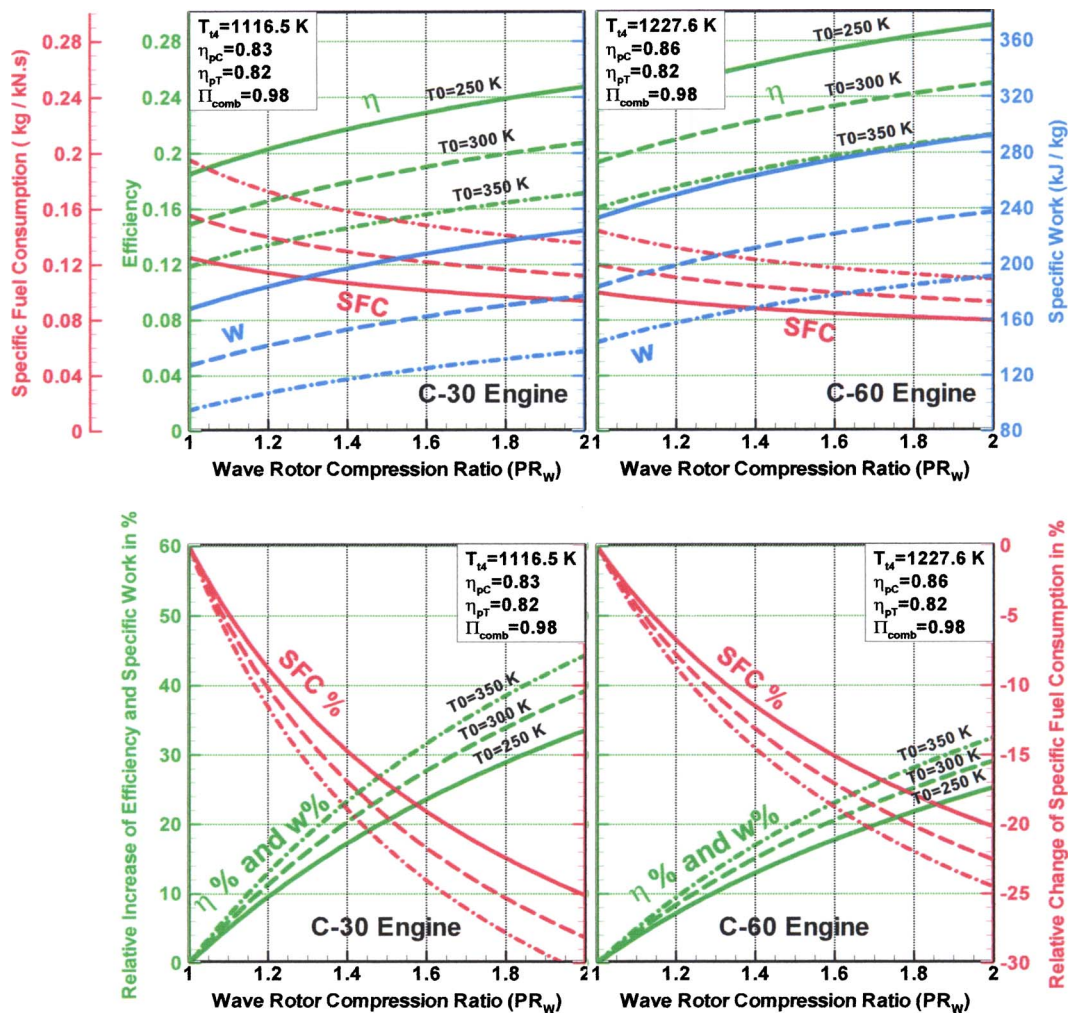


Fig. 10 Effect of ambient temperature—overall thermal efficiency, specific work, and specific fuel consumption versus wave rotor pressure ratio and overall pressure ratio for Case A

pressure ratio that has to be accommodated in the turbine is always less for the wave-rotor-topped engine than for the two-stage-compressor engine with the same or greater overall pressure ratio, causing likely fewer problems when adapting the turbine. For the wave-rotor-topping Cases B and C, the turbine pressure ratio is even less than that of the single stage baseline engine. Additionally, in Cases C and E the wave-rotor-topping even lowers the turbine inlet temperature, which allows the designer to use a turbine made of a lower cost material.

Effect of Compressor Inlet Temperature. It is well known that the performance of gas turbines is affected by varying ambient conditions [58]. For instance, both thermal efficiency and output power of a gas turbine engine with a fixed turbine inlet temperature decrease when the compressor inlet temperature rises. This is disadvantageous if a stationary gas turbine is installed in hot-weather locations. Under this consideration, it is proved in the following that for such conditions the wave-rotor-topping is even more advantageous.

For simulation, it is assumed that the compressor isentropic efficiency stays constant although a slight decrease might be expected. It is furthermore assumed that the specific compression work stays constant since the compressor geometry does not change. Hence, the compressor pressure ratio decreases by increasing ambient temperature due to basic thermodynamics. For the baseline engine it is obvious this results in a lower turbine pressure ratio and less specific work produced by the engine.

The performance values of the wave-rotor-enhanced engines of Cases A and B, which are the most considered cases discussed in the literature, for compressor inlet temperatures of 250, 300, and 350 K are shown in Figs. 10 and 11, respectively, for a range of wave rotor compression ratios $PR_w = 1, \dots, 2$.

For the wave-rotor-enhanced engines, the general performance trend is the same as baseline engines. However, while the absolute performance degrades at higher ambient temperatures for baseline and topped engines, performance gains of the enhanced engines relative to the baseline engines increase, making this technology even more desirable for applications under hot-weather conditions. This reversed effect is visualized in the figures especially in the lower part showing the relative gains of the topped engines.

Wave Rotors for Gas Turbines with Recuperations. Figure 12 shows a block diagram of a recuperated gas turbine topped with a four-port wave rotor. The wave rotor is placed after the compressor and before the recuperator. Figure 13 shows a schematic T-s diagram of the baseline engine and the corresponding wave-rotor-topped engine for Cases A and B. Path 0-1_b-2_b*-4_b-5_b-5_b* represents the baseline cycle and path 0-1_i-2_i*-3_i-4_i-5_i-5_i* (i=A and B) indicates the wave-rotor-topped cycles. Only Cases A and B are considered in this study due to their high potential for performance improvement under recuperated conditions. All calculations have been presented only for the C-30 engine, while the conclusions are valid for the C-60 engine, too.

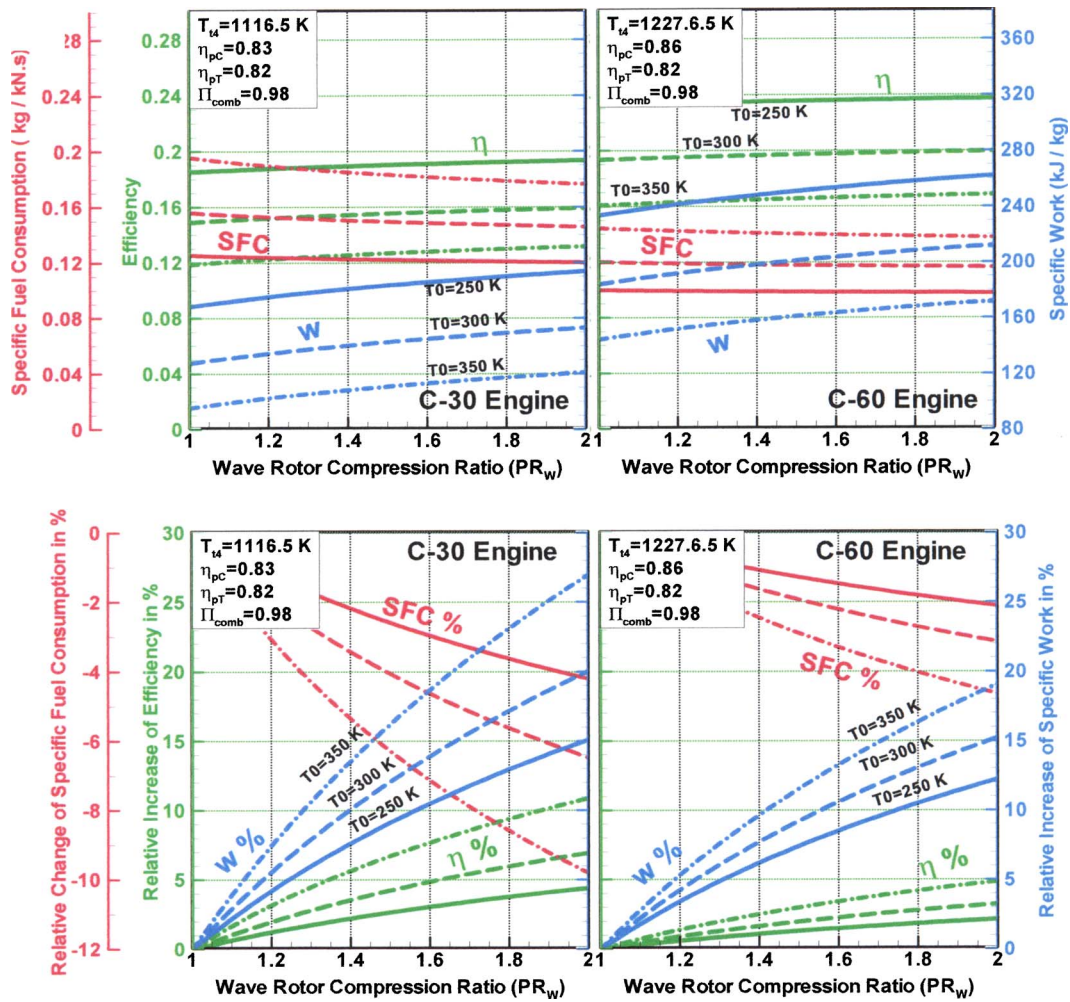


Fig. 11 Effect of ambient temperature—overall thermal efficiency, specific work, and specific fuel consumption versus wave rotor pressure ratio and overall pressure ratio for Case B

The analytical approach to analysis such wave-rotor-topped recuperated cycles has been introduced by the authors in previous work [59] and is not stated here. Instead, Table 5 summarizes the obtained results and shows a comparison between performance improvements of the simple and recuperated engines for implementations of both Cases A and B. It is seen from the table that the baseline engine (C-30 without the wave rotor) with recuperation has much higher efficiency (about twice) and lower *SFC* than those of the unrecuperated baseline engine due to the reduction of

heat addition in the combustion process, as expected. As explained before, implementation of Case A into the baseline engine results in a significant performance improvement of the unrecuperated engine, however, the thermal efficiency and *SFC* improve-

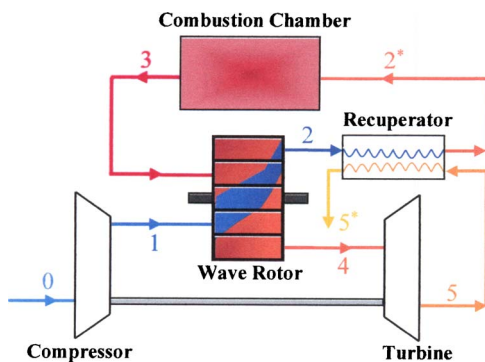


Fig. 12 Schematic of a recuperated gas turbine topped by a four-port wave rotor

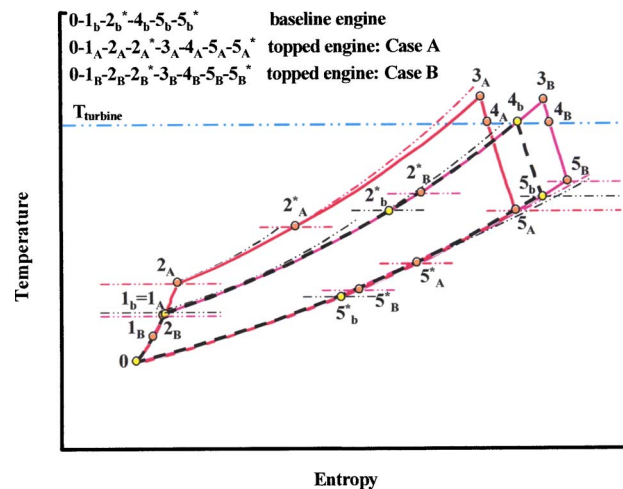


Fig. 13 Schematic T-s diagram for a recuperated baseline cycle and two wave-rotor-topped cycles

Table 5 Performance comparison between simple and recuperated engines and two cases of wave-rotor-topping with a wave rotor pressure ratio of 1.8, C-30 engine

Engines	Case A		Case B		Baseline	
	Simple	Recuperated	Simple	Recuperated	Simple	Recuperated
Π_c	3.60	3.60	2.00	2.00	3.60	3.60
Π_T	4.38	4.19	2.60	2.49	3.53	3.39
q [kJ/kg]	855	603	946	505	855	470
w_c [kJ/kg]	167	167	81	81	167	167
w_T [kJ/kg]	338	328	231	219	295	284
w [kJ/kg]	171	161	150	138	128	117
SFC [kg/kN.s]	0.116	0.087	0.147	0.085	0.156	0.094
η	0.200	0.266	0.158	0.273	0.149	0.248
$(w)_{gain}$ [%]	33.8	37.6	17.1	18.0		
$(SFC)_{gain}$ [%]	25.2	6.7	5.5	8.7		
$(\eta)_{gain}$ [%]	33.8	7.2	5.9	9.7		

ments of the recuperated engine are much less than that of the specific work. In Case B, however, the topped recuperated cycle has higher performance compared to the unrecuperated engine and its thermal efficiency and SFC gains are even more than those of Case A. Case B takes advantage of the fact that the temperature difference between the air and the gas entering the recuperator of the topped engine ($T_{15B}-T_{12B}$) is more than that of Case A ($T_{15A}-T_{12A}$). This results in a higher recuperation effect for Case B. The results clearly demonstrate the advantage of implementing Case A for unrecuperated engines and implementing Case B for recuperated engines. The results also indicate that the recuperator enhances thermal efficiency and SFC better, while the wave-rotor is mostly better for enhancing the specific work output. Therefore, substituting a recuperator with a wave rotor may be guided by a preference for high power output and reduced unit cost, considering that a recuperator contributes about 25%–30% to the unit cost [11–13] and a wave rotor may be cheaper.

Conclusion

For the implementation of a wave rotor into two simple-cycle microturbines C-30 and C-60, the present investigation predicts an attractive performance enhancement for both baseline engines. The smaller C-30 engine would benefit more from the wave-rotor-topping than the C-60 engine. The C-30 engine overall efficiency and specific work may increase by up to 34% and for the C-60 engine by up to 25%. Five different cases of implementing a wave rotor into the existing baseline engines are investigated. Ideally, one of the three main components (compressor, combustor, or turbine) would remain unchanged when a wave rotor is implemented. However, compromises may be considered for tests or cost-effective prototype development, keeping two or even all three main components unchanged. Case A, in which the baseline compressor remains completely unchanged, appears to be the most beneficial case. However, the combustor works under higher pressure and with higher combustion end temperature. The turbine pressure ratio increases as well. Thus, an adaptation of the turbine wheel may be desired to utilize the obtained potential optimally. Other cases with unchanged overall pressure ratio (Cases B and C), with unchanged combustion end temperature (Cases D and E) or unmodified turbine (Case D) are investigated as well. Case B gives an increased turbine exit temperature and is therefore especially attractive for external heat recovery applications or internal recuperation, which would enhance the performance even more. Sacrificing some performance enhancement, the wave-rotor implementation can yield other advantages like decreased turbine inlet temperature (Cases C and E), reduced compressor pressure ratio (Cases B, C, and D) or reduced turbine pressure ratio (Cases B and C), which can reduce the gas turbine cost. Further, adding a wave rotor instead of a second compressor stage results in better

or similar performance enhancement and has many other advantages. While a second compressor stage alters the dynamic system tremendously and always increases the combustion pressure, turbine inlet pressure and compressor work transmitted through the shaft, a wave-rotor implementation requires no or only minor changes to the dynamic system of the gas turbine spool. It can keep the combustion pressure the same, can even reduce the turbine inlet pressure or temperature and the transmitted shaft work for the compressor. Furthermore, it is shown that the performance degradation at higher temperatures is much less for the wave-rotor-topped engines than for the baseline engines, making this technology even more desirable for applications under hot-weather conditions. Finally, it is shown that the recuperator is better for improving overall thermal efficiency and specific fuel consumption, while the wave-rotor-topping is better for increasing the specific work output. Cost considerations may additionally favor the wave-rotor.

Acknowledgment

The authors wish to acknowledge the cooperation of Capstone Turbine Corporation, providing the baseline engine data. The assistance of A. Behinfar in sketching Figs. 1 and 3 is acknowledged.

References

- [1] Craig, P., 1997, "The Capstone Turbogenerator as an Alternative Power Source" SAE Paper 970292.
- [2] Kang, Y., McKeirnan, R., 2003, "Annular Recuperator Development and Performance Test for 200 kW Microturbine" ASME Paper GT-2003-38522.
- [3] Benini, E., Toffolo, A., and Lazzaretto, A., 2003, "Centrifugal Compressor of A 100 KW Microturbine: Part 1-Experimental and Numerical Investigations on Overall Performance" ASME Paper GT2003-38152.
- [4] Zauner, E., Chyou, Y. P., Walraven, F., and Althaus, R., 1993, "Gas Turbine Topping Stage Based on Energy Exchangers: Process and Performance" ASME Paper 93-GT-58.
- [5] Rogers, C., 2003, "Some Effects of Size on the Performance of Small Gas Turbine" ASME Paper GT2003-38027.
- [6] Shi, J., Venkata, R., Vedula, J. H., Connie, E. B., Scott, S. O., Bertuccioli, L., and Bombara, D. J., 2002, "Preliminary Design of Ceramic Components for the ST5+ Advanced Microturbine Engine" ASME Paper GT-2002-30547.
- [7] Walsh, C., An, C., Kapat, J. S., and Chow, L. C., 2002, "Feasibility of a High-Temperature Polymer-Derived-Ceramic Turbine Fabricated Through Micro-Stereolithography" ASME Paper GT-2002-30548.
- [8] McDonald, C. F., 1996, "Heat Recovery Exchanger Technology for Very Small Gas Turbine" Journal of Turbo and Jet Engines, **13**, pp. 239–261.
- [9] Proeschel, R. A., 2002, "Proe 90TM Recuperator for Microturbine Applications" ASME Paper GT-2002-30406.
- [10] Carman, B. G., Kapat, J. S., Chow, L. C., and An, L., 2002, "Impact of a Ceramic Microchannel Heat Exchanger on a Microturbine" ASME Paper GT2002-30544.
- [11] McDonald, C. F., 2000, "Low Cost Recuperator Concept for Microturbine Applications" ASME Paper GT2000-167.
- [12] Utraienen, E., and Sunden, B., 2001, "A Comparison of Some Heat Transfer Surfaces for Small Gas Turbine Recuperators" ASME Paper GT2001-0474.
- [13] Maziasz, P. J., Pint, B. A., Swindeman, R. W., More, K. L., and Lara-Curzio,

- E., 2003, "Selection, Development and Testing of Stainless Steel and Alloys for High-Temperature Recuperator Applications" ASME Paper GT2003-38762.
- [14] Wilson, J. and Paxson, D. E., 1993, "Jet Engine Performance Enhancement Through Use of a Wave-Rotor Topping Cycle" NASA TM-4486.
- [15] Fatsis A., and Ribaud Y., 1999, "Thermodynamic Analysis of Gas Turbines Topped with Wave Rotors" *Aerosp. Sci. Technol.*, **3**, No. 5, pp. 293–299.
- [16] Akbari, P., and Müller, N., 2003, "Performance Improvement of Small Gas Turbines Through Use of Wave Rotor Topping Cycles" ASME Paper GT2003-38772.
- [17] Akbari, P., and Müller, N., 2003, "Performance Investigation of Small Gas Turbine Engines Topped with Wave Rotors" AIAA Pap. 2003-4414.
- [18] Meyer, A., 1947, "Recent Developments in Gas Turbines" *Chin. J. Mech. Eng.*, **69**, No. 4, pp. 273–277.
- [19] Real, R., 1946, "The 3000 kW Gas Turbine Locomotive Unit" *Brown Boveri Rev.*, **33**, No. 10, pp. 270–271.
- [20] Meyer, A., 1947, "Swiss Develop New Gas Turbine Units" *Electr. World*, **127**, pp. 38–40.
- [21] Azoury P. H., 1992, *Engineering Applications of Unsteady Fluid Flow*, John Wiley and Sons, New York.
- [22] Rose, P. H., 1979, "Potential Applications of Wave Machinery to Energy and Chemical Processes" *Proceedings of the 12th International Symposium on Shock Tubes and Waves*, pp. 3–30.
- [23] Seippel, C., 1940, Swiss Patent No. 225426.
- [24] Seippel, C., 1942, Swiss Patent No. 229280.
- [25] Seippel, C., 1946, "Pressure Exchanger" US Patent 2399394.
- [26] Seippel, C., 1949, "Gas Turbine Installation" US Patent 2461186.
- [27] Taussig, R. T., Hertzberg, A., 1984, "Wave Rotors for Turbomachinery" *Winter Annual Meeting of the ASME*, edited by Sladky, J. F., Machinery for Direct Fluid-Fluid Energy Exchange, AD-07, pp. 1–7.
- [28] Zehnder, G., Mayer, A. and Mathews, L., 1989, "The Free Running Compress®" SAE Paper 890452.
- [29] Mayer, A., Oda, J., Kato, K., Haase, W. and Fried, R., 1989, "Extruded Ceramic-A New Technology for the Compress® Rotor" SAE Paper 890453.
- [30] Hiereth, H., 1989, "Car Tests With a Free-Running Pressure-Wave Charger-A Study for an Advanced Supercharging System" SAE Paper 890 453.
- [31] Azoury, P. H., 1965-66, "An Introduction to the Dynamic Pressure Exchanger" *Proc. Inst. Mech. Eng.*, **180**, Part 1, No. 18, pp. 451–480.
- [32] Guzzella, L., Wenger, U., and Martin, R., 2000, "IC-Engine Downsizing and Pressure-Wave Supercharging for Fuel Economy" SAE Paper 2000-01-1019.
- [33] Shreeve, R. P., Mathur, A., 1985, *Proceeding ONR/NAVAIR Wave Rotor Research and Technology Workshop*, Report NPS-67-85-008, Naval Postgraduate School, Monterey, CA.
- [34] Paxson, D. E., 1992, "A General Numerical Model for Wave-Rotor Analysis" NASA TM-105740.
- [35] Paxson, D. E., 1996, "Numerical Simulation of Dynamic Wave Rotor Performance" *J. Propul. Power*, **12**, No. 5, pp. 949-957.
- [36] Welch, G. E., Jones, S. M., and Paxson, D. E., 1997, "Wave Rotor-Enhanced Gas Turbine Engines" *J. Eng. Gas Turbines Power*, **119**, No. 2, pp. 469–477.
- [37] Welch, G. E., 1997, "Macroscopic Balance Model for Wave Rotors" *J. Propul. Power*, **13**, No. 4, pp. 508–516.
- [38] Welch, G. E., 1997, "Two-Dimensional Computational Model for Wave Rotor Flow Dynamics" *J. Eng. Gas Turbines Power*, **119**, No. 4, pp. 978–985.
- [39] Wilson, J., and Paxson, D. E., 1996, "Wave Rotor Optimization for Gas Turbine Topping Cycles" *J. Propul. Power*, **12**, No. 4, pp. 778–785. See SAE Paper 951411, and NASA TM 106951.
- [40] Welch, G. E., 2000, "Overview of Wave-Rotor Technology for Gas Turbine Engine Topping Cycles" *Novel Aero Propulsion Systems International Symposium, The Institution of Mechanical Engineers*, pp. 2–17.
- [41] Wilson, J., 1997, "Design of NASA Lewis 4-Port Wave Rotor Experiment" AIAA Pap. 97-3139. Also NASA CR-202351.
- [42] Wilson J., and Fronek, D., 1993, "Initial Results from the NASA-Lewis Wave Rotor Experiment" AIAA Pap. 93-2521. Also NASA TM-106148.
- [43] Wilson, J., 1997, "An Experiment on Losses in a Three Port Wave-Rotor" NASA CR-198508.
- [44] Wilson, J., 1998, "An Experimental Determination of Loses in a Three-Port Wave Rotor" *J. Eng. Gas Turbines Power*, **120**, pp. 833–842. Also ASME Paper 96- GT-117, and NASA CR-198456.
- [45] Paxson, D. E., 1993, "A Comparison Between Numerically Modeled and Experimentally Measured Loss Mechanisms in Wave Rotors" AIAA Pap. 93-2522.
- [46] Paxson, D. E., 1995, "Comparison Between Numerically Modeled and Experimentally Measured Wave-Rotor Loss Mechanism" *J. Propul. Power*, **11**, No. 5, pp. 908–914. Also NASA TM-106279.
- [47] Paxson D. E., and Wilson, J., 1995, "Recent Improvements to and Validation of the One Dimensional NASA Wave Rotor Model" NASA TM-106913.
- [48] Paxson, D. E., and Nalim, M. R., 1999, "Modified Through-Flow Wave-Rotor Cycle with Combustor Bypass Ducts" *J. Propul. Power*, **15**, No. 3, pp. 462–467. Also AIAA Paper 97-3140, and NASA TM-206971.
- [49] Nalim, M. R., and Paxson, D. E., 1999, "Method and Apparatus for Cold-Gas ReInjection in Through-Flow and Reverse-Flow Wave Rotors" US Patent 5,894,719.
- [50] Jones, S. M., and Welch, G. E., 1996, "Performance Benefits for Wave Rotor-Topped Gas Turbine Engines" ASME Paper 96-GT-075.
- [51] Weber, H. E., 1986, "Shock-Expansion Wave Engines: New Directions for Power Production" ASME Paper 86-GT-62.
- [52] Weber, H. E., 1995, *Shock Wave Engine Design*, John Wiley and Sons, New York.
- [53] Akbari, P., Kharazi, A. A., and Müller, N., 2003, "Utilizing Wave Rotor Technology to Enhance the Turbo Compression in Power and Refrigeration Cycles" ASME Paper IMECE2003-44222.
- [54] Gyarmathy, G., 1983, "How Does the Compress Pressure-Wave Supercharger Work?" SAE Paper 830234.
- [55] Kentfield, J. A. C., 1993, *Nonsteady, One-Dimensional, Internal, Compressible Flows*, Oxford University Press, Oxford.
- [56] Taussig, R. T., 1984, "Wave Rotor Turbofan Engines for Aircraft" *Winter Annual Meeting of the ASME*, edited by Sladky, J. F., Machinery for Direct Fluid-Fluid Energy Exchange, AD-07, pp. 9–45.
- [57] Welch, G. E., 1996, "Two-Dimensional Computational Model for Wave Rotor Flow Dynamics" ASME Paper 96-GT-550.
- [58] El Hadik, A. A., 1990, "The Impact of Atmospheric Conditions on Gas Turbine Performance" *J. Eng. Gas Turbines Power*, **112**, No. 4, pp. 590–595.
- [59] Akbari, P., Müller, N., and Nalim, M. R., 2004, "Performance Improvement of Recuperated and Unrecuperated Microturbines Using Wave Rotor Machines," 2004 ASME-ICED Spring Technical Conference, Japan.

The Development of a Dual-Injection Hydrogen-Fueled Engine With High Power and High Efficiency

Y. Y. Kim

Jong T. Lee

School of Mechanical Engineering,
Sungkyunkwan University,
Jangan-gu, Suwon 440-746, Korea

J. A. Caton

Department of Mechanical Engineering,
Texas A&M University,
College Station, TX 77840

To achieve high power and high efficiency in a hydrogen-fueled engine for all load conditions, the dual-injection hydrogen-fueled engine, which can derive the advantages of both high efficiency from external mixture hydrogen engine and high power from direct cylinder injection was developed. For verifying the feasibility of the above engine, a high-pressure hydrogen injector of ball-valve type and actuated by a solenoid was developed. A systematic experimental study was conducted by using a modified single-cylinder dual-injection hydrogen-fueled engine, which was equipped with both an intake injector and high-pressure in-cylinder injector. The results showed that (i) the developed high pressure hydrogen injector with a solenoid actuator had good gas tightness and fine control performance, (ii) the transient injection region, in which injection methods are changed from external fuel injection to direct-cylinder injection, ranged from 59 to 74% of the load, and (iii) the dual-injection hydrogen-fueled engine had the maximum torque of direct-cylinder fuel injection and the maximum efficiency of external fuel mixture hydrogen engines. [DOI: 10.1115/1.1805551]

Introduction

Two major types of hydrogen-fueled engines have been developed over the years. These two types are (i) those using external fuel mixture preparation and (ii) those using direct-cylinder fuel injection [1–4]. The use of an external fuel mixture preparation has the advantages of a simple configuration and high efficiency [5], but low power due to backfire occurrence at high load [6,7]. On the other hand, a direct-cylinder fuel-injection engine in which only air is induced during the intake process can obtain high power by avoidance of backfire occurrence [8]; but its thermal efficiency becomes relatively lower due to a poor hydrogen-air mixing rate, hydrogen leakage in the high-pressure injector, and the losses associated with the injection system [9,10].

The final goal of the engine development is to achieve high power and high efficiency simultaneously for practical use. It is difficult for the case of external mixture preparation and for direct-cylinder injection to meet these requirements because of the above reasons [11]. The dual-injection hydrogen-fueled engine, which can derive the advantages of both high efficiency from external mixture and high power from direct-cylinder injection, was introduced by the authors [12]. The dual-injection hydrogen-fueled engine uses only external mixture under idling and low load because no backfire occurs. For the case of high load, most of the fuel is injected directly into the cylinder during the compression process and the rest, which guarantees that the intake mixture is lean enough so that no backfire occurs, is supplied into the intake pipe to increase the mixing rate [13].

To realize the dual-injection hydrogen-fueled engine, a high-pressure hydrogen direct-cylinder injector installed in the cylinder head is necessary. This injector has to be capable of good gas tightness against injected high-pressure hydrogen gas, and it also has to accurately control the amount of fuel injection correspond-

ing with that of an intake injector under high engine speed. Most of the hydrogen injectors used in previous hydrogen engines have not met the above requirements.

The fuel-injection regions of dual-injection hydrogen-fueled engines are divided into external fuel-injection, transient-injection, and direct-cylinder fuel-injection regions. The transient-injection region is one in which the injection methods are varied from external fuel injection to direct-cylinder fuel injection. If the injection method is shifted rapidly in this transient-injection region, it may affect unfavorably on the hydrogen-air mixing rate and, therefore, on the combustion performance. This may result in unstable operation, such as higher cycle variations and more torque fluctuations. The suitable injection conditions in the transient injection region, therefore, have to be established to obtain stable combustion and high performance for the dual-injection hydrogen-fueled engine.

At the beginning of this study, a high-pressure hydrogen injector using a poppet valve of ball-valve type and actuated by a solenoid was developed to verify the feasibility of the dual-injection hydrogen-fueled engine development. An experimental single-cylinder engine was modified into the dual-injection hydrogen-fueled engine by equipping this engine with both this high-pressure injector and a low-pressure injector. The proper injection timing for the direct-cylinder injection was determined by cycle analyses of the two kinds of dual-injection hydrogen-fueled engines. The suitable operating conditions, including the transient-injection region and engine performances, were established by using the experimental dual-injection hydrogen-fueled engine. The feasibility of this engine, which can achieve high power or high efficiency according to load conditions, was also evaluated by comparing with the performance characteristics of typical hydrogen engines.

Cycle Analyses and Determining the Proper Dual Injection Cycle

Cycle Analyses of the Dual Injection Hydrogen Engines. The method of direct-cylinder injection is divided by injection timing into two types. The first type is the method of injection early in the compression process, and the other type is that of

Contributed by the Internal Combustion Engine Division of THE AMERICAN SOCIETY OF MECHANICAL ENGINEERS for publication in the ASME JOURNAL OF ENGINEERING FOR GAS TURBINES AND POWER. Manuscript received by the ICE Division January 20, 2003; final revision received by the ASME Headquarters April 23, 2004. Associate Editor: D. Assanis.

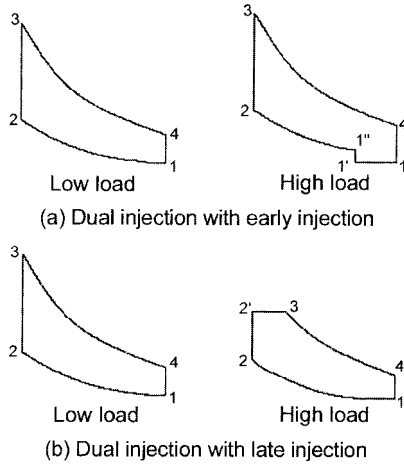


Fig. 1 Theoretical p-V diagrams of the dual-injection hydrogen engine cycle for early and late direct-injection timing

injection late in the compression process. Since direct-cylinder injection is adopted at high load for the dual-injection hydrogen-fueled engine, there are also two types of the dual-injection hydrogen-fueled engines injecting at early compression process and at late compression process. These engines are called the dual-injection hydrogen engines with early direct-cylinder injection and with late direct-cylinder injection, respectively.

For the purpose of investigating the proper cycle for dual-injection hydrogen engines, both cycles of early direct-cylinder injection and late direct-cylinder injection were examined. This examination is based on theoretical, idealized cycles.

Early Direct-Cylinder Injection. Figure 1(a) shows the p-V diagrams of the theoretical cycle of the dual-injection hydrogen engine with early direct-cylinder injection. For the case of low load, hydrogen fuel is only supplied into the intake pipe and the fuel-air mixture is burned under near-constant volume combustion, like the 2–3 processes. The cycle diagram for this case is equal to the Otto cycle. For high load, the in-cylinder pressure is increased, due to the supplied energy, by direct-cylinder injection; hydrogen and air are pre-mixed and then burned under near-constant volume combustion. So, the theoretical cycle of the dual-injection hydrogen engine with early direct-cylinder injection is the same as for the typical Otto cycle for all load conditions.

Because hydrogen gas is induced quickly by direct-cylinder injection, the temperature and the pressure of the working fluid during the constant volume process, 1'–1'', are changed under an adiabatic process. Define R_{fe} (=mass of external fuel/mass of total fuel) as the ratio of the amount of fuel supplied into intake pipe to the amount of total fuel supplied in the cycle. A value of zero for R_{fe} means only direct in-cylinder injection, and a value of 100% for R_{fe} means only external mixture. The theoretical thermodynamic thermal efficiency η_{de} of the dual-injection hydrogen engine with early direct-cylinder injection is given by

$$\eta_{de} = 1 - \varepsilon^{1-k} \frac{B^{k-1} \alpha_{de} - 1}{B^{k-1} (\alpha_{de} - 1)} \quad (1)$$

where,

$$\begin{aligned} \rightarrow \alpha_{de} &= 1 + \frac{H_{uf}}{(\gamma_{af} C v_a + C v_f) T_1 \varepsilon^{k-1} B^{k-1}} \\ B &= \frac{m''_1}{m'_1} = \frac{\gamma_{af} + 1}{\gamma_{af} + R_{fe}} \end{aligned}$$

where ε is compression ratio, k is the specific heat ratio, H_{uf} is the lower heating value of hydrogen, $C v_a$ and $C v_f$ are the specific heats at constant volume for air and hydrogen, γ_{af} is the air-fuel mass ratio, and T_1 is the initial temperature.

The theoretical mean effective pressure $p_{mi(de)}$ is

$$p_{mi(de)} = \eta_{de} \frac{p_1 \varepsilon^k B^{k-1} (\alpha_{de} - 1)}{S_c (k-1) (\varepsilon - 1)} \quad (2)$$

where p_1 is initial pressure, and $S_c = (\gamma_{af} C v_a + R_{fe} C v) / (\gamma_{af} C v_a + C v_f)$.

Late Direct-Cylinder Injection. The theoretical p-V diagram of the dual-injection hydrogen engine with late direct-cylinder injection is shown in Fig. 1(b). The cycle for low load is the same as for the early direct-cylinder injection due to only using external mixture. But, for high-load operating conditions, a lean hydrogen-air mixture is induced into the cylinder during the intake process. This mixture undergoes a near-constant volume premixture combustion process and most of the hydrogen fuel injected into the cylinder undergoes a near-constant pressure-combustion process. The dual-injection hydrogen engine with late direct-cylinder injection, therefore, theoretically works on the Dual cycle having both constant volume and constant pressure combustion processes at high load.

The pressure ratio, $\alpha_{dl} (= p'_2 / p_2)$, and the shut off ratio, $\sigma (= V_3 / V'_2)$, meaning the quantity of supplied heat energy in the 2–2' and the 2–3' processes are concerned with the ratio of the amount of fuel injection R_{fe} . The theoretical thermal efficiency for the above engine η_{dl} is as follows:

$$\eta_{dl} = 1 - \varepsilon^{1-k} \left(\frac{\alpha_{dl} \sigma^k S_R - 1}{S_c (\alpha_{dl} - 1) + k \alpha_{dl} (\sigma S_R - 1)} \right) \quad (3)$$

where

$$\begin{aligned} \rightarrow \alpha_{dl} &= 1 + \frac{R_{fe} H_{uf}}{(\gamma_{af} C v_a + R_{fe} C v_f) T_1 \varepsilon^{k-1}} \\ \sigma &= \left\{ 1 + \frac{(1 - R_{fe}) H_{uf}}{[\gamma_{af} C v_a + (1 - R_{fe}) C v_f] T_1 \varepsilon^{k-1} \alpha_{dl}} \right\} / S_R \\ S_R &= \frac{\gamma_{af} R_a + R_{fe} R_f}{\gamma_{af} R_a + R_f} \end{aligned}$$

And the theoretical mean effective pressure $p_{mi(dl)}$ is given by

$$p_{mi(dl)} = \eta_{dl} \frac{p_1 \varepsilon^k \{ (\alpha_{dl} - 1) + S_c^{-1} \alpha_{dl} (\sigma S_R - 1) \}}{(k-1) (\varepsilon - 1)} \quad (4)$$

Considering hydrogen and air as ideal gases of diatomic molecules, the theoretical specific heat ratios of hydrogen and air are equal in Eqs. (3) and (4). So, S_R is equivalent to S_c .

Determining the Proper Dual-Injection Cycle. Compression ratios of conventional SI engines are mainly limited by knock occurrence, but compression ratios for hydrogen engines depend on backfire as well as knock due to the fast burning velocity, low ignition energy, and wide flammability of hydrogen gas.

Backfire phenomenon is generally attributed to a fresh mixture in the cylinder being ignited by any ignition source while the intake valve is open. For the case of low load, fuel injection into the intake pipe is used, and then the fresh mixture related to backfire exists in the intake pipe and in-cylinder for both types of dual-injection hydrogen engines. This means that the compression ratios for these engines are subject to backfire occurring under external injection region, though the compression ratio of the Dual cycle is basically higher than that of the Otto cycle. So, compression ratios for the two types of the dual-injection hydrogen-fueled engines may be similar to each other. For the same compression ratio, the dual-injection hydrogen engine with early direct-

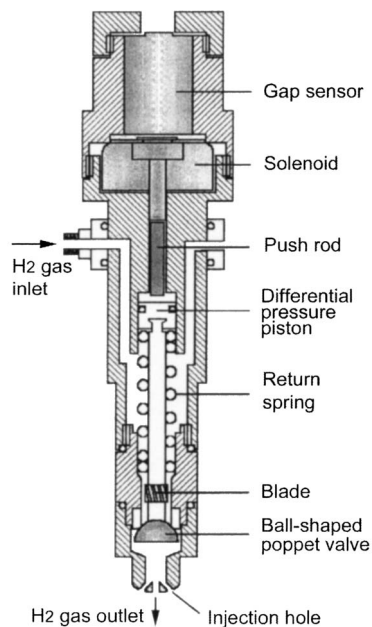


Fig. 2 Schematic cutaway diagram of the high-pressure hydrogen injector of ball-valve type with solenoid actuator

cylinder injection is more favorable than that with late direct-cylinder injection because the thermal efficiency of the Otto cycle is higher than that of the Dual cycle.

In general, the thermal efficiency of a direct-injection hydrogen engine becomes relatively lower compared to an external-mixture hydrogen engine due to the short hydrogen-air mixing duration and less mass of hydrogen gas [14]. To enhance the poor mixing rate due to the above reasons, a portion of the hydrogen gas is induced by auxiliary external injection into the intake pipe in the case of high load for the two types of dual-injection hydrogen engines. Though the enhancement effect of the mixing rate is aided by the auxiliary injection, the mixing of hydrogen and air in the cylinder for the direct-cylinder injection mainly relies on the mixing duration, which is the period after fuel injection and up until ignition. The dual-injection hydrogen engine with early direct-cylinder injection, which has a longer mixing duration, is also more favorable than that with late direct-cylinder injection with respect to the mixing rate.

Furthermore, the higher injection pressure (for the dual-injection hydrogen engine with late direct-cylinder injection) has disadvantages in a practical application due to the difficulties of keeping gas tightness, use of a high-pressure hydrogen gas, and fuel supply system. The early direct-cylinder injection, therefore, is employed as the proper direct-injection method for the dual-injection hydrogen-fueled engine for the above reasons.

Experimental Apparatus and Methods

High-Pressure Hydrogen Injector of Ball-Valve Type Actuated by a Solenoid. A high-pressure hydrogen injector for the dual-injection hydrogen engine should be capable of keeping gas tightness against high-pressure hydrogen gas. Its driving parts, which are in contact with the hydrogen gas, must not wear out by the nonlubricant property of hydrogen. In addition, a high-pressure hydrogen direct-cylinder injector interlocking with an intake injector has to control the amount of fuel injection under high-speed operation.

A high-pressure hydrogen injector of the ball-valve type and actuated by a solenoid was developed to meet the above requirements. Figure 2 shows a schematic cutaway diagram of this high-pressure hydrogen, direct-cylinder injector. It consists of a sole-

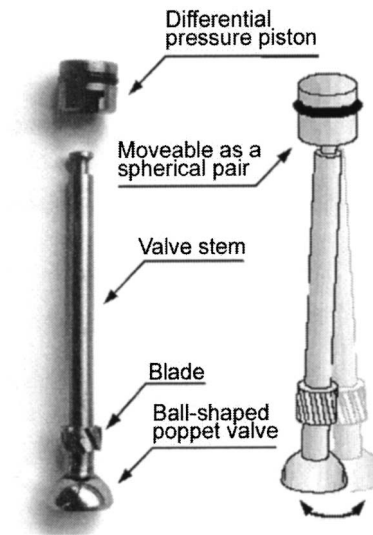


Fig. 3 The poppet valve face with a shape of ball in the high-pressure hydrogen injector

noid actuating part, push-rod, and injection valve part of ball type and a holder with injection holes. The design concept of this injector is based on those of poppet-valve-type and ball-valve-type high-pressure hydrogen injectors, which are actuated by a hydraulic driving system. This type of injector has been developed by the authors in preceding research, which was concerned with the direct-cylinder injection hydrogen engine [15,16].

The solenoid actuator, compared to the hydraulic actuator, can easily control the injection parameters and has a faster response under high-speed operation. Due to the high pressure of the supplied hydrogen gas and the high spring tension acting on the poppet valve, the driving force generated from a conventional solenoid is not enough to actuate a high-pressure hydrogen injector. For adopting a solenoid actuator, it is necessary to decrease the driving force required by the hydrogen injector. This driving force has been reduced by using the principle of pressure-offset due to the area difference between the poppet valve fillet and the piston for generating the differential pressure. The piston for generating the differential pressure is installed at the valve stem end, and its area is a little larger than that of the poppet valve fillet.

The differential pressure due to the area difference automatically closes the poppet valve. The O-ring is inserted in the piston to prevent hydrogen leakage. The valve spring installed below the piston has the primary role of keeping the hydrogen injector closing, even though the hydrogen supplement is shut off, and it has the secondary role of helping the poppet valve to return back to the valve seat. The wear between the valve stem and the stem guide due to the nonlubricant property of hydrogen gas will cause the valve center to be eccentric and results in poor gas tightness. In general, the ball valve is always apt to be fitted with the valve seat because it has a spherical geometric surface. Furthermore, the rotation of the ball valve during its operation has an effect to polish the valve seat. This can lead to better gas tightness. To further improve the gas tightness of the high-pressure hydrogen direct-cylinder injector, the poppet valve face is formed into a ball shape as shown in Fig. 3. To rotate the poppet valve, the blade is installed in a valve-head direction of the valve stem. The piston and the valve stem end are linked by a spherical pair structure to prevent the valve stem from being eccentric. The valve rotation force is generated by the kinetic energy of the hydrogen jet flow passing through the blade in the valve stem. The blade is located 10 mm from the valve head. Its geometric configurations are 1.5 mm wide, 1.5 mm high, 3.5 mm long and 30 deg deflection angle.

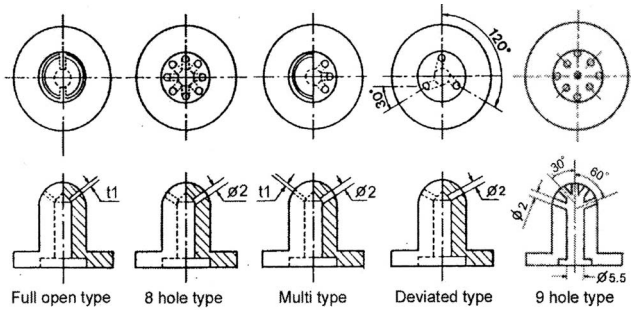


Fig. 4 Five types of the injection hole configurations

The shape of entrance passage toward the blade is a nozzle type for the conversion of the hydrogen pressure energy to kinetic energy.

The combustion and performance of the hydrogen engine with direct-cylinder injection mainly depends on the homogeneity of the hydrogen-air mixture, which is affected by the injection pressure, the configuration of the injection holes, the combustion chamber shape, and the in-cylinder flow pattern. The hydrogen momentum decreases rapidly after injection due to its low density. For the cases of constant engine operating conditions, therefore, a configuration of the injection holes should be a very important factor to enhance the in-cylinder mixing rate of the. The visualization of the mixing process and the analysis of engine performance have been carried out to determine the suitable configuration of the injection holes in the previous studies. The nine-hole type, which is the most favorable among the proposed five types as shown in Fig. 4 [17], is used in this hydrogen injector.

Figure 5 shows the leakage flow rate of hydrogen gas as a function of the number of injections. The leakage flow rate increased to about 800 injections and then rapidly decreased as the number of injections is further increased. The leakage rate becomes as low as 50 cc/min for over 1600 injections. This may be caused by the fact that the gas tightness of the hydrogen injector is improved by the polishing effect of the valve seat due to valve rotation. This leakage rate is negligible as it is estimated to be less than about 0.5% of the lean flammable limit of the hydrogen mixture at 1000 rpm engine speed. The increasing and decreasing

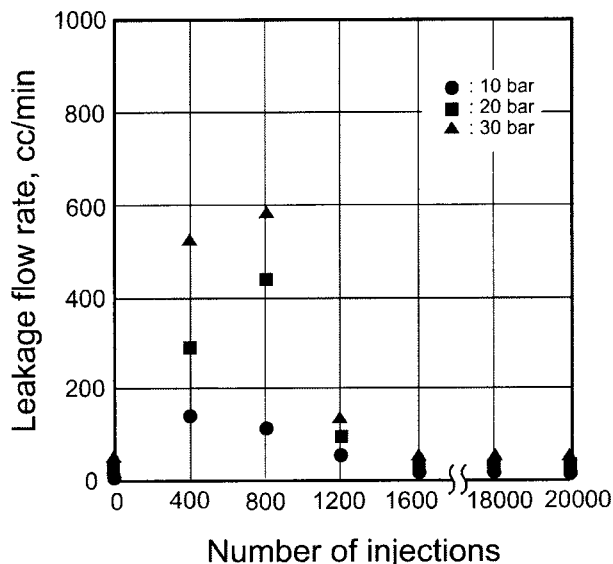


Fig. 5 The leakage flow rate of the high-pressure hydrogen injector as a function of the number of injections

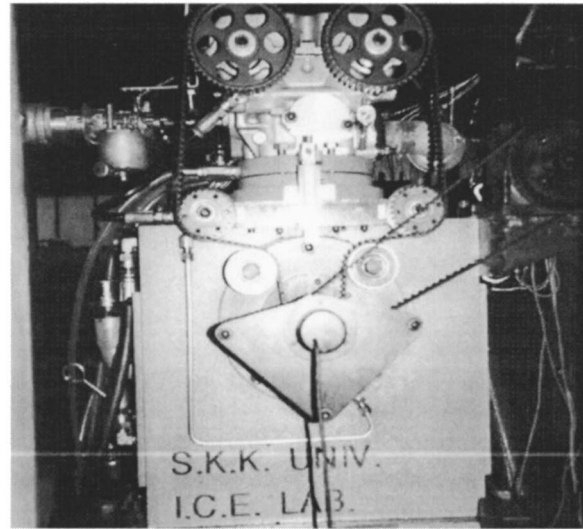


Fig. 6 Photograph of the dual-injection hydrogen engine

tendencies of the leakage rate mean that the polishing effect by the poppet valve rotating contributes to the improvement of the gas tightness of the hydrogen injector.

Dual Injection Hydrogen Fueled Engine. Figure 6 shows the experimental dual-injection hydrogen-fueled engine. It is a single-cylinder 500 cc engine with 9:1 compression ratio, and made by modifying conventional engine parts. Table 1 lists the main engine specifications for this engine.

For proper use of the external mixture or the direct-cylinder injection according to the load conditions, the low-pressure intake injector and the high-pressure direct-cylinder injector as mentioned above are installed in the intake pipe and cylinder head, respectively. The low-pressure hydrogen injector is modified from a conventional CNG injector (SPI). The installed location of the low-pressure intake injector is 100 mm from the intake valve stem, and the installed location of the high-pressure direct-cylinder injector is at the flywheel end of cylinder head with a 60 deg slope.

Because of the low ion density of hydrogen-air mixture flames, much residual electric energy may remain in the ignition system of a hydrogen engine after normal ignition [18]. Discharging this residual energy abnormally during the intake process or valve overlap would lead to backfire occurrence [19]. For preventing abnormal ignition, a high value of earth resistance is connected to a secondary coil of a full transistor-type ignition system.

The coolant is supplied into the cylinder head, the cylinder block and the oil cooler separately. The coolant temperature is controlled by using a solenoid valve installed at the coolant passage outlet.

Experimental Apparatus and Method. Figure 7 is a schematic diagram of the experimental apparatus, including the dual-injection hydrogen-fueled engine, the hydrogen supply system,

Table 1 Specifications of the dual injection hydrogen engine

Engine	Single cylinder
Bore	86.0 mm
Stroke	86.0 mm
Displacement volume	500 cc
Combustion chamber	Pent-roof type
Compression ratio	9:1
Ignition system	Full transistor type
Cooling type	Water cooling
Spark-plug	Cold rating type

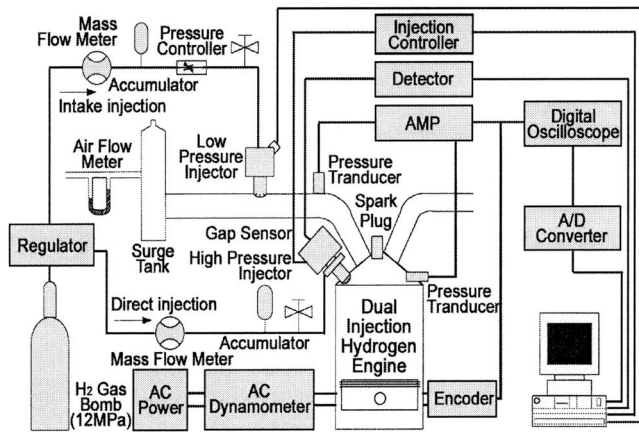


Fig. 7 Schematic diagram of experimental apparatus

the dynamometer unit, the injector control system, and the data acquisition system. Hydrogen gas (decompressed from a high-pressure cylinder by a two-stage regulator) is induced into the low-pressure intake injector and high-pressure direct-cylinder injector. The lift of the hydrogen injector is measured by a gap sensor (Ono-Sokki, VE231) installed in the back of the solenoid armature plate. The injection timing and injection duration of the injectors are varied by the electronically controlled injection system with 8255I/O detecting TDC and angle signals. For preventing the solenoid from overheating and improving its response, electric current with peak-hold wave form is supplied to the solenoid. The coil suppressor, consisting of a resistance and a diode, is installed in each end of the solenoid in parallel to remove the counterelectromotive force, which occurs when the solenoid is shut off.

The experiment is to measure whether backfire occurs or not and to determine the engine performance as a function of the injection timing, the injection pressure, the fuel-air equivalence ratio, and the ratio of the amount of fuel supplied into the intake pipe to the amount of total fuel supplied in the cycle R_{fe} . The pressures of the intake injection and direct-cylinder injection are varied from 3 to 5 bar, and from 20 to 30 bar, respectively. The fuel-air equivalence ratio is changed from 0.3 to 1.2 by 0.1. The R_{fe} is increased from 0% to its maximum value, where no backfire occurs. For each experiment, the coolant temperature, engine speed, intake throttle valve, and spark timing are fixed with values of 70 °C, 2000 rpm, WOT (Wide Open Throttle), and MBT (Minimum spark advance for Best Torque), respectively.

Suitable Operating Conditions of Dual Injection

Injection Timing and Injection Pressure

For the Intake Injection. Figure 8 shows the torque and the backfire limit (BFL) equivalence ratio for the case of the external mixture as a function of the intake injection pressure. The BFL equivalence ratio is defined as the upper limit of the fuel-air equivalence ratio where the hydrogen engine can be normally operated without backfire occurrence. The injection timing is set to intake TDC according to the above results. The torque is almost constant with all intake injection pressures. But the BFL equivalence ratio is decreased as the intake injection pressure is increased. This may be caused by the possibilities that any ignition source causing backfire occurrence and burning velocity are increased due to the difference of mixing rate and the increase of flow velocity of in-cylinder mixture according to variation of injection pressure. The thermal efficiency of the dual-injection hydrogen engine with external mixture is higher than direct-cylinder injection so that it is reasonable that the BFL equivalence ratio is expanded to increase the thermal efficiency of the dual injection

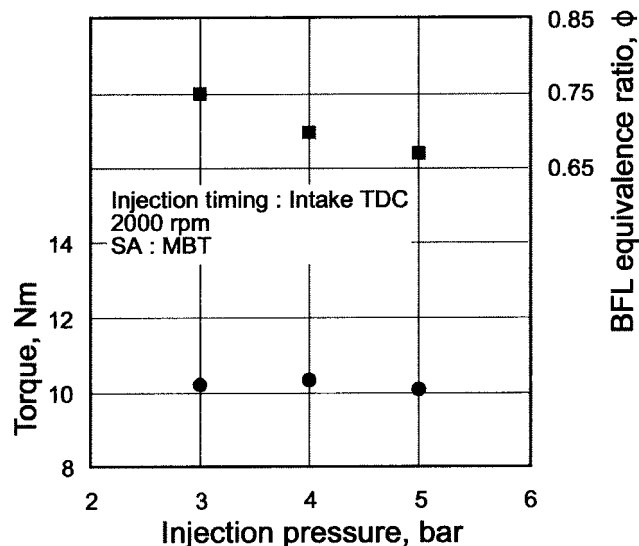


Fig. 8 The torque and the intake air flow of the dual-injection hydrogen engine with external mixture

as high as possible. From the above results, intake TDC for intake injection timing and the 3 bar for injection pressure are adopted, respectively.

Figure 9 illustrates the torque and the intake air flow rate in the dual-injection hydrogen engine using only the external mixture as a function of intake injection timing. The highest torque is shown at intake TDC injection, and the torque has decreasing tendency as the intake injection timing is advanced or retarded from intake TDC. But the intake air flow rate is gradually decreased with retarding the intake injection timing. It may be due to the decrease of entrainment duration entraining an air into hydrogen jet injected with high speed. With the advance of injection timing, the torque is decreased in spite of the increase of intake air flow, since a small portion of the induced hydrogen in cylinder is leaked out to the exhaust pipe during the valve overlap. The torque is decreased by the decrease of the amount of intake air flow with the retard of the injection timing from intake TDC.

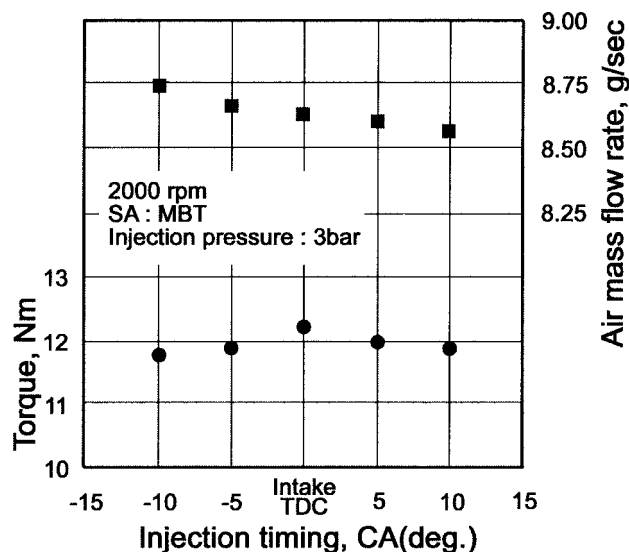


Fig. 9 The torque and the BFL equivalence ratio of the external mixture for each intake injection pressure

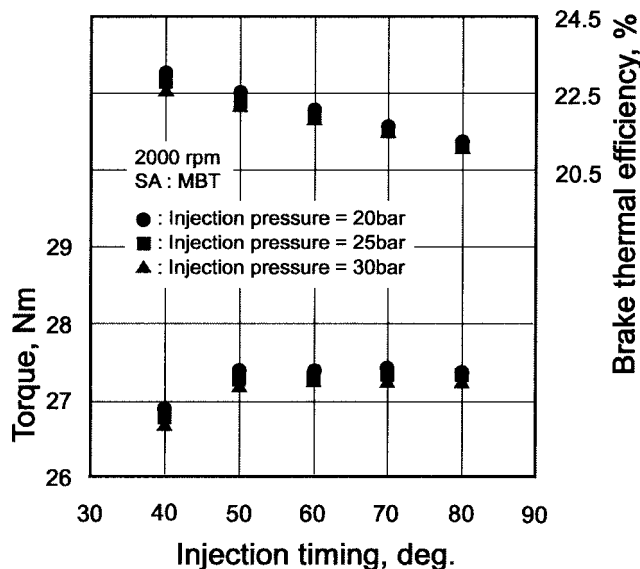


Fig. 10 The torque and the brake thermal efficiency of direct-cylinder injection for each injection pressure as a function of injection timing

For Direct Cylinder Injection. Figure 10 shows the torque and the thermal efficiency using only direct-cylinder injection as a function of injection timing for three injection pressure conditions. The torque shows a little increase until the injection timing is retarded to the intake valve close timing (55 deg aBDC), but then remains unchanged in spite of further retarding the injection timing. The decrease of the torque before intake valve close timing is caused by a restriction of the induction of intake air mass flow due to the increasing of in-cylinder pressure related to direct injection.

The thermal efficiency shows an increasing tendency with the advance of injection timing because the hydrogen-air mixing duration becomes relatively longer. As hydrogen is injected before intake valve close, a portion of the hydrogen flows back into intake pipe. This hydrogen-air mixture that flowed back into the intake pipe could cause a backfire occurrence. It is concluded that the proper direct-injection timing is, therefore, 120 deg bTDC (retarded by 5 deg from the intake valve close timing).

As shown in Fig. 10, the torque and the brake thermal efficiency are essentially unchanged in spite of increasing the direct-cylinder injection pressure, and higher injection pressures have the disadvantages of more difficult gas tightness and practical use. So, for direct injection pressure, 20 bar is confirmed as the proper condition.

Transient Injection Region (Changing Injection Method).

The injection regions of the dual-injection hydrogen-fueled engine can be divided according to the fuel supply method into (i) the region of external mixture preparation, (ii) the transient-injection region of changing injection method, and (iii) the region of direct-cylinder injection. The transient-injection region is defined as the shift region of injection method where the amount of external fuel mixture is decreased and that of direct-cylinder injection is increased, simultaneously.

The brake thermal efficiencies and the occurrence point of backfire with engine loads are shown for the hydrogen engine with external mixture and direct-cylinder injection in Fig. 11. Using external mixture injection has higher brake thermal efficiencies compared with direct-cylinder injection, but normal operation is restricted to under 62% of load because of backfire occurrence. The start point of transient injection region, therefore, has to be prior to 62% of load. Determining the end point of that, it is worth regarding how to increase the relative low-brake thermal effi-

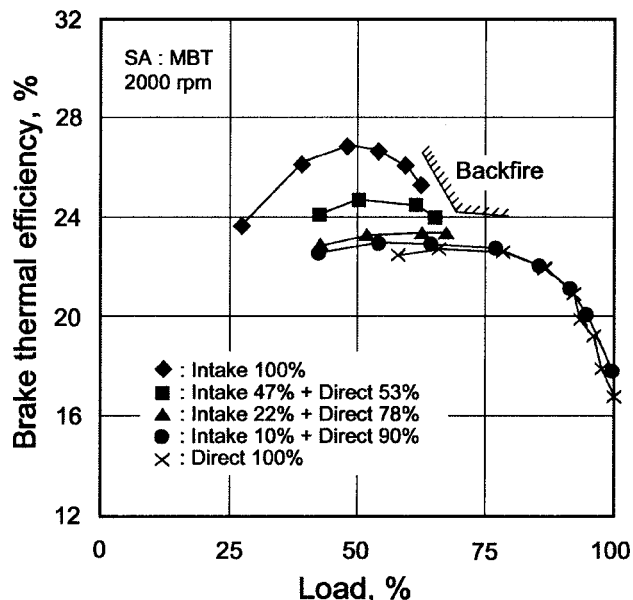


Fig. 11 The brake thermal efficiency and where backfire occurs for external mixture and direct-cylinder injection with the change of the amount of external mixture

ciency of direct injection as high as possible. The low thermal efficiency of direct injection is due to the shorter hydrogen-air mixing duration. As mentioned previously, supplying a portion of hydrogen into the intake pipe of the dual injection engine before direct-cylinder injection could enhance the mixture homogeneity and lead to higher brake thermal efficiency. To evaluate the effect of an auxiliary supply of external mixture on the brake thermal efficiency, the brake thermal efficiency of direct cylinder injection is investigated with the amount of hydrogen gas supplied into the intake pipe, and the results are also shown in Fig. 11. The direct-cylinder injection with some external mixture has a higher brake thermal efficiency than only direct injection as a whole. The brake thermal efficiency shows further increased tendency as the amount of the external mixture is increased. The more auxiliary external mixture is supplied with direct injection, the higher its brake thermal efficiency is increased. But the amount of external mixture supplied with direct-cylinder injection depends on backfire occurrence. The upper limited value of engine load operated without backfire occurrence is around 75% in 47% of R_{fe} , and 77% in 22% of R_{fe} . Under 10% of R_{fe} , nonbackfire appears and a little increment of brake thermal efficiency is shown. This means that the transient-injection region should start around 62% and end around 78% of load. Using 5% to the above range for a safe margin for maintaining reliable normal operation, the transient injection region ranged from 59 to 74% of load.

The brake thermal efficiency varied little for up to 10% supplement of hydrogen gas into intake pipe. Since the auxiliary supply of the external mixture in the direct-cylinder injection region contributes to the enhancement of the mixture homogeneity and the utilization of the low-pressure hydrogen gas, it seems to be better that about 10% of external mixture to total fuel amount is supplied in the region of direct-cylinder injection.

The heat release per cycle and the fuel-air equivalence ratio of the dual-injection hydrogen engine operated in the transient-injection region are shown in Fig. 12. The heat release continuously increased with the increase of load. The fuel-air equivalence ratio is increased until the end point of the region of external mixture, but adversely decreased from the transient-injection region and then increased again from that of direct-cylinder injection. Although the heat release is increased in the transient-injection region, the fuel-air equivalence ratio is decreased by the

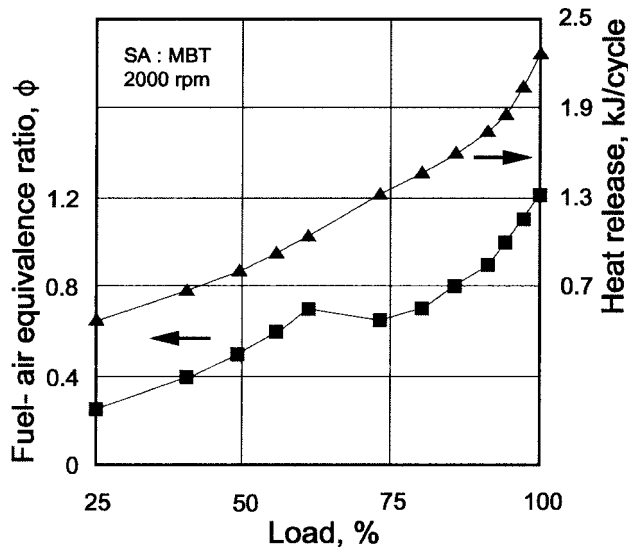


Fig. 12 The heat release per cycle and the fuel-air equivalence ratio of the dual-injection hydrogen engine

increase of intake air flow due to reducing of the amount of intake hydrogen injection. The fuel-air equivalence ratio for direct-cylinder injection begins to increase in accordance with the increase of the amount of fuel mass acquired because the amount of intake air mass flow is fixed. For these reasons, the transient-injection region from 59 to 74% of load is equivalent to be from $\phi=0.7$ in the region of external mixture to $\phi=0.65$ with 10% of R_{fe} in the region of direct-cylinder injection.

Injection Conditions in the Transient-Injection Region.

Figure 13 shows the torque and brake thermal efficiency in the transient-injection region as a function of the R_{fe} . Here, 0% in R_{fe} means only direct injection and 100% in R_{fe} means only external mixture. The brake thermal efficiency is highest for a fuel-air equivalence ratio of 0.6 and decreases slightly with the increase of the fuel-air equivalence ratio. As the R_{fe} is increased, the brake thermal efficiency is also increased by the tendency of the enhancement of mixture homogeneity, but the torque is decreased due to the decrease of the amount of intake air flow in

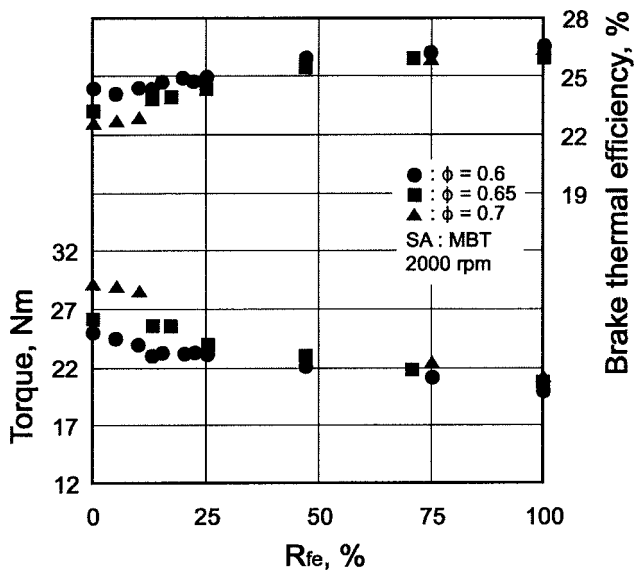


Fig. 13 The torque and the thermal efficiency in the transient region with the change of R_{fe}

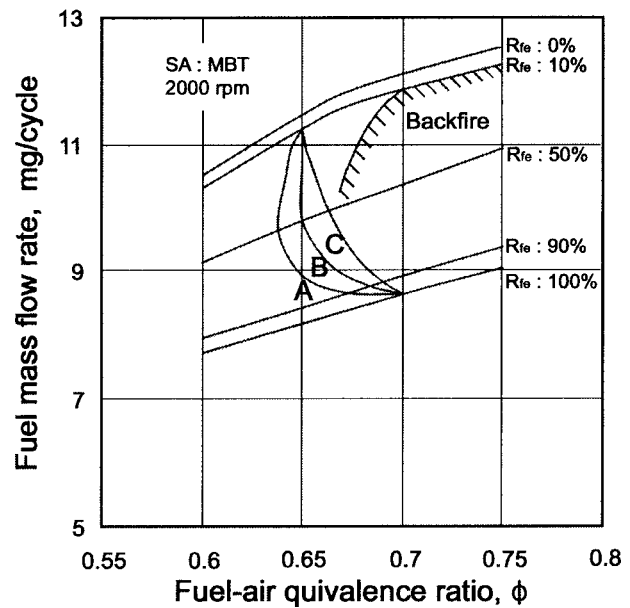


Fig. 14 Three types of processes how to change injection method in the transient region

spite of the increasing effect of the brake thermal efficiency. The reduction rate of torque is increased by the decrease of intake air flow mass. The torque reduction rate is about 6.2% at the fuel-air equivalence ratio of 0.65, and about 12% at an equivalence ratio of 0.7.

Three processes (A, B, and C in Fig. 14) of changing the fuel supply during the transient-injection period are examined. These three processes change the fuel-air equivalence ratio and the R_{fe} in the transient injection region as shown in Fig. 14. These three processes have to avoid the upper limited R_{fe} to avoid backfire occurrence in the beginning stage of the transient-injection region, hence the process of the transient-injection region has to start with the increase of $d\phi/dR_{fe}$.

The A-process begins to change injection method for condition of the largest $d\phi/dR_{fe}$ than any other process. It decreases both the fuel-air equivalence ratio and the R_{fe} up to the lower fuel-air equivalence ratio than that of the end point of the transient injection region, and then increases the fuel-air equivalence ratio and decreases the R_{fe} . The A-process can obtain higher thermal efficiency in the transient injection region because it passes near to $\phi=0.6$, where thermal efficiency is relatively higher. But if the $d\phi/dR_{fe}$ is increased so much, it is difficult to control the amount of fuel injection and could cause the fluctuation of torque.

For the case of the B-process, the fuel-air equivalence ratio and the R_{fe} are decreased until its fuel-air equivalence ratio is the same as that of the end point of the transient-injection region, and then the R_{fe} is decreased with the constant fuel-air equivalence ratio. As the R_{fe} is decreased under the constant fuel-air equivalence ratio, the amount of the direct-cylinder injection is increased by the increase of intake air mass flow due to the reduction of the amount of intake fuel injection. This may result in the torque fluctuation of the dual-injection hydrogen engine; hence, this process has a demerit in that the intake air flow is controlled by the throttle valve installed in the intake pipe.

The C-process is to decrease the fuel-air equivalence ratio and the R_{fe} gradually in the transient injection region. Comparing with the other processes, it is easy to control the amount of fuel and the engine output, and the unstable operation should rarely occur. The thermal efficiency of the C-process is lower than that of the A-process, but its difference is very slight and the C-process has a better controllability on the amount of fuel injection. Therefore,

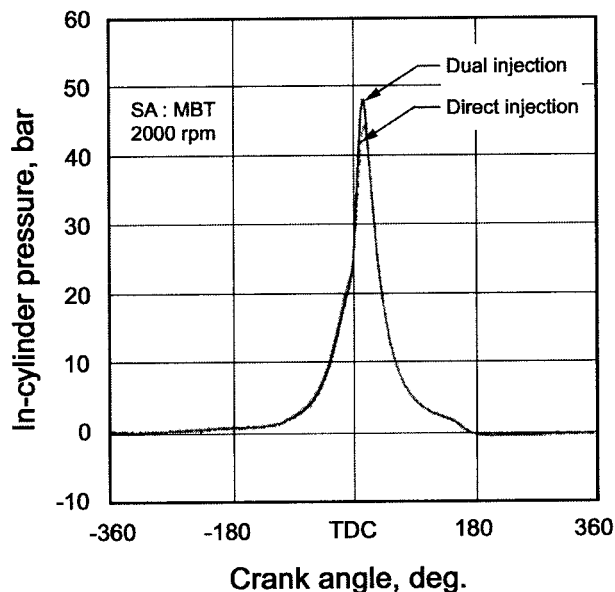


Fig. 15 The comparison of in-cylinder pressure of the dual injection with that of direct cylinder injection

the C-process is confirmed to be the suitable injection condition in the transient injection region from the above results.

Characteristics of Performance in the Dual Injection Hydrogen Engine

Combustion and Operation Characteristics. Figure 15 shows the comparison of the in-cylinder pressure of the dual-injection hydrogen engine with that of direct-cylinder injection hydrogen engine for the same fuel amount. The conditions for this test are that the R_{fe} of the dual injection is 30% and the spark timing is 10 deg bTDC. The maximum pressure of the dual injection is 48 bar, which is a little higher than the 45 bar of the direct-cylinder injection. The appearance point of maximum pressure is also advanced about 2 deg more than for the direct injection case. This seems to be caused by the fact that the combustion in the dual injection is promoted due to the enhancement of hydrogen-air mixing rate by the auxiliary hydrogen gas injection into the intake pipe during the intake process.

To clarify these tendencies, the combustion durations are investigated as a function of R_{fe} , and the results are shown in Fig. 16. Here, constant fuel mass is supplied into the cylinder though R_{fe} is changed. The combustion duration is obtained from an ensemble average of the in-cylinder pressure data from 100 cycles.

The combustion duration, which is the duration of 0–100% mass burned rate, has a decreasing tendency with the increase of the R_{fe} . This tendency may be explained by the fact that the combustion promotion depends on the increase of the fuel-air equivalence ratio by the decrease of the intake air mass flow and the enhancement of mixing rate. The duration of 0–10% mass burned rate shows almost the same 8 deg crank angle regardless of the change of the R_{fe} , the duration of 10–90% is decreased due to the enhancement of mixing state with the increase of the R_{fe} , and the duration of 90–100% shows a slight decreasing tendency.

In general, higher maximum in-cylinder pressures increases NOx emission so that a dual-injection hydrogen engine may be inclined to have increased NOx emissions. But a dual-injection method may have a stratifying effect on the hydrogen-air mixture. Potentially, this could lead to the decrease of the maximum temperature and, thus, NOx emission would be decreased with the retard of direct injection timing [20]. Lean burn, EGR, and ex-

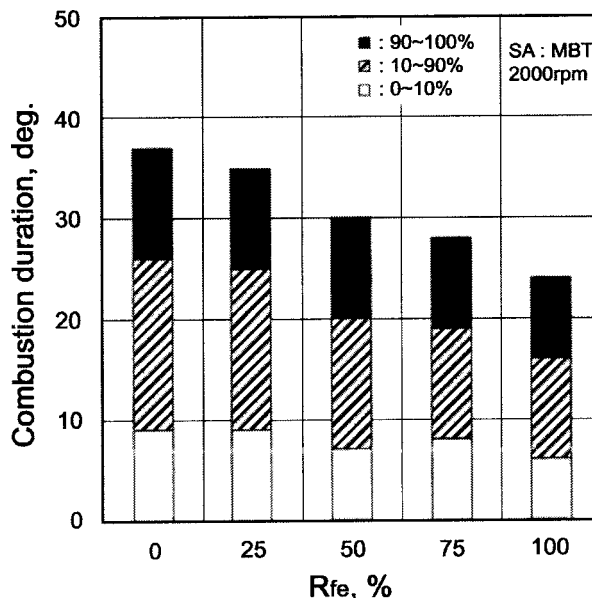


Fig. 16 The combustion duration of the dual-injection hydrogen engine at each R_{fe}

haust aftertreatment are considered the possible strategies to achieve a near-zero emission level for a dual-injection hydrogen engine as would be true for a conventional hydrogen engine. NOx emission is one of the important remaining problems that must be solved before the hydrogen engine may be put into production. Therefore, possible strategies for reducing NOx emission for the dual-injection hydrogen engine will have to be investigated in the next research step.

Figure 17 represents the minimum spark advance for the best torque (MBT) as a function of load. As the load of the dual-injection hydrogen engine is increased, the MBT is retarded in the region of external mixture, but advanced slightly in the transient-injection region and retarded adversely in the region of direct-cylinder injection. One of the most important parameters in deter-

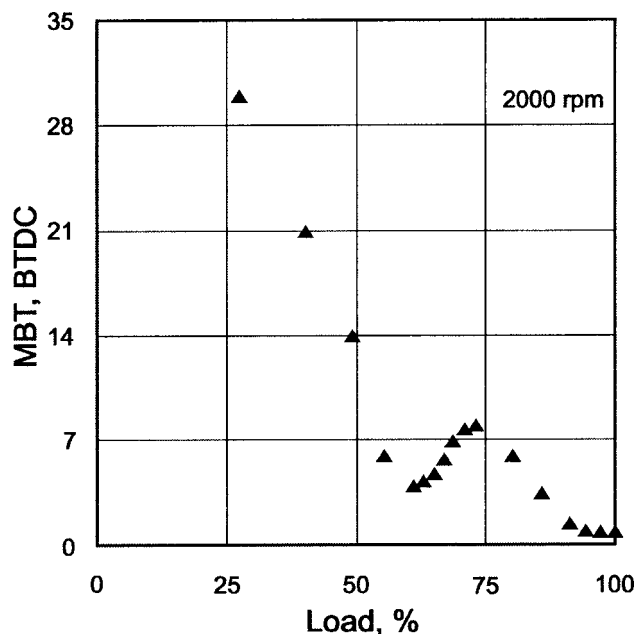


Fig. 17 The minimum spark advance for best torque of the dual-injection hydrogen engine as a function of load

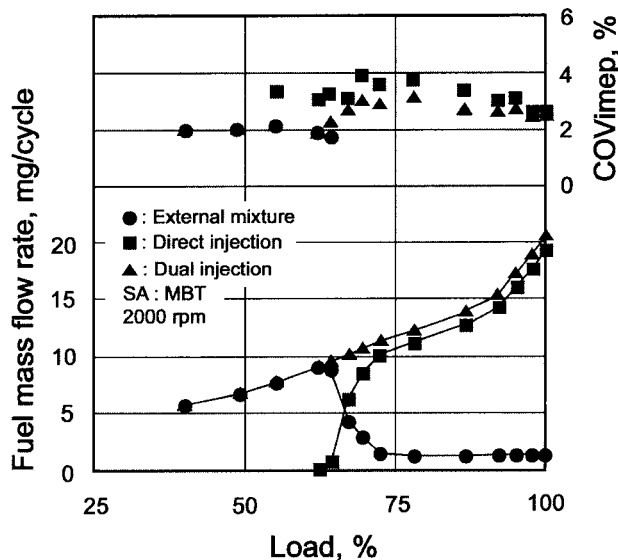


Fig. 18 The fuel mass flow rate and COV_{imep} of the dual-injection hydrogen engine as a function of load

mining the MBT is the combustion duration, which is essentially dependent on the fuel-air equivalence ratio. Since the fuel-air equivalence ratio is increased according to the increase of the engine load, the MBT is retarded as a whole. The fuel-air equivalence ratio is decreased by the reduction of intake air flow rate in the transient injection region so that the MBT is a little advanced. Although a point of inflection of the MBT exists in the transient-injection region, this may not be a problem to control spark ignition timing because the differences are negligible.

Figure 18 shows the fuel mass flow rate and the COV_{imep} with the increase of the load. The COV_{imep} is defined as the coefficient of variation of the indicated mean effective pressure. The numbers of consecutive sample cycles are 100. The figure shows the total fuel amount of the dual injection is nearly proportional to the load, and its gradient of increment has the increasing tendency from 90% of the load. For the transient injection region, the fuel amounts of intake injection and direct-cylinder injection are varied with a little higher deviation in the beginning stage and gradually in the later stage.

It can be also seen that the COV_{imep} of the dual-injection engine is a little higher than that of the external mixture, but lower than that of the direct-cylinder injection as a whole. The COV_{imep} of the transient-injection region is slightly increased by the decrease of the external mixture and the increase of the direct-cylinder injection. The COV_{imep} of the dual injection does not exceed about 5% that could cause unstable engine operation. This means that the dual-injection hydrogen engine can be operated with good stability for all load conditions. No combustion noise or vibration were observed in the transient-injection region where the injection methods are changed.

Effect of Dual Injection on Improving Performance. The torque and brake thermal efficiency of the dual-injection hydrogen engine as compared to external mixture and direct-cylinder injection are shown in Fig. 19. As the mass flow rate of injected fuel is increased, the torque of external mixture and the dual injection are increased. But the maximum value of external mixture is toward $\phi=0.75$ due to backfire occurrence, whereas that of the dual injection continues to be increased about up to $\phi=1.1$. The maximum torque of the dual injection is higher by 60% than that of the external mixture, and it is almost equal to that of the direct-cylinder injection. The torque of the dual injection in the transient-injection region is increased proportionally with the increase of the amount of supplied energy without its fluctuation.

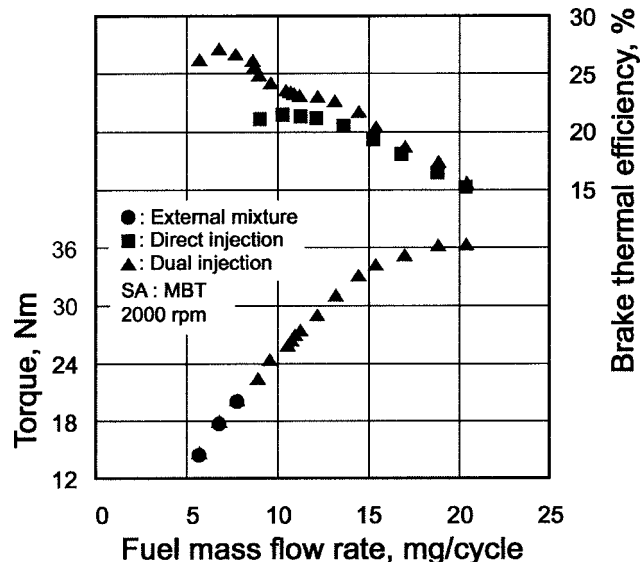


Fig. 19 The comparison of the torque and the thermal efficiency of the dual-injection engine with that of external mixture and that of direct injection

The brake thermal efficiency of the dual injection, as compared to direct-cylinder injection, is improved for all load conditions. The improvement in low load is remarkable. The incremental rate of the brake thermal efficiency by adopting the dual injection represents about 22% for low load and about 5.3% for high load conditions, compared to direct injection.

Considering the above results, it was verified that the dual-injection hydrogen-fueled engine can be operated with stability and achieve both maximum power of direct-cylinder injection hydrogen engine and the maximum efficiency of an external-mixture hydrogen engine.

Summary and Conclusions

Several tasks were completed to develop the dual-injection hydrogen-fueled engine with high power and high efficiency. First, a high-pressure hydrogen injector of ball-valve type actuated by a solenoid was developed. This high-pressure injector and an intake injector were installed on a modified single-cylinder dual-injection hydrogen engine. The systematic experimental studies on the proper direct-cylinder injection method, the suitable operating conditions, including the transient injection region, and the characteristics of combustion and power were investigated by using the above experimental engine. In addition, the feasibility of achieving high power and high efficiency were evaluated by comparing to typical hydrogen engines. In summary,

1. The gas tightness of the high-pressure hydrogen injector with a solenoid actuator was improved by the use of a poppet valve face with a spherical shape, the linkage of spherical pair structure between the valve stem end and the piston for generating differential pressure, and the rotation of the poppet valve.
2. Considering the theoretical cycle analyses and the facilities of practical use, the dual injection with early direct injection during compression process was more reasonable than that with late direct injection.
3. The transient injection region, in which the injection methods are quickly varied from external fuel injection to direct-cylinder fuel injection, ranged from 59 to 74% of load. The best fuel supply method to obtain stable operation in the transient injection region was determined to be when both the fuel-air equivalence ratio and the R_{fe} were decreased gradually.

4. The maximum torque of the dual-injection hydrogen engine was increased by about 60% compared to a hydrogen engine using external mixture preparation, and the brake thermal efficiency was higher by about 22% at low load compared with direct-cylinder injection hydrogen engine.
5. From the above results, it was shown that the dual-injection hydrogen engine is feasible. This engine can derive the advantage of both high efficiency from external mixture and high power from a direct-cylinder injection hydrogen engine, and has stable operation performance for all load conditions. Further studies on the dual-injection hydrogen engine will be needed for the continued refinement of this concept.

Acknowledgment

The authors would like to gratefully acknowledge generous support of The Korean Energy Management Corporation.

References

- [1] Furuhashi, S., 1991, "Trend of Social Requirements and Technical Development of Hydrogen-Fueled Automobiles," *JSME Rev.*, **13**, pp. 4–13.
- [2] Blarigan, P. V., Paradiso, N., and Goldsborough, S., 1998, "Homogeneous Charge Compression Ignition With a Free Piston: A New Approach to Ideal Otto Cycle Performance," SAE Technical Paper 982484.
- [3] Swabowski, S. J., Hashemi, S., Stockhausen, W. F., Natkin, R. J., Reams, L., Kabat, D. M., and Potts, C., 2002, "Ford Hydrogen Engine Powered P2000 Vehicle," SAE Technical Paper 2002-01-0243.
- [4] Nakajima, Y., Yamane, K., Shudo, T., Hiruma, M., and Takagi, Y., 2000, "Research and Development of a Hydrogen-Fueled Engine for Hybrid Electric Vehicles," SAE Technical Paper 2000-01-0993.
- [5] Lutz, A., and Keller, J., 2000, "Hydrogen Fueled Engine in Hybrid Vehicles," SAE Technical Paper 2000-01-0546.
- [6] Lynch, F. E., 1974, "Backfire Control Techniques for Hydrogen Fueled Internal Combustion Engines," *Hydrogen Energy, Part B, Proc. World Hydrogen Energy Conference*, Miami, International Association for Hydrogen Energy, pp. 686–696.
- [7] Lee, J. T., Kim, Y. Y., Lee, C. W., and Caton, J. A., 2001, "An Investigation of a Cause of Backfire and Its Control Due to Crevice Volumes in a Hydrogen Fueled Engine," *ASME J. Eng. Gas Turbines Power*, **123**, pp. 204–210.
- [8] Furuhashi, S., 1977, "Combustion Improvement in a Hydrogen Fueled Engine," *Int. J. Hydrogen Energy*, **2**, pp. 329–340.
- [9] Kim, J. M., Kim, Y. T., Lee, J. T., and Lee, S. Y., 1995, "Performance Characteristics of Hydrogen Fueled Engine With the Direct Injection and Spark Ignition System," SAE Technical Paper No. 952488, pp. 162–175.
- [10] Tsujimura, T., Mikami, S., Achiba, N., Tokunaga, Y., Senda, J., and Fujimoto, H., 2003, "A Study of Direct Injection Diesel Engine Fueled With Hydrogen," SAE Technical Paper 2003-01-1761.
- [11] Lee, J. T., 1996, "Current Status and Characteristics of Hydrogen Fueled Engine," *Trans. KSAE*, **18**, pp. 29–52.
- [12] Kim, Y. Y., Park, J. B., and Lee, J. T., 1997, "A Study on Development of Hydrogen Fueled Engine With High Power and High Efficiency," *Proc. 4th KHES-HESS Joint Symposium*, Yokohama, Aug., Hydrogen Energy Systems Society, pp. 62–71.
- [13] Choi, H. K., Ahn, J. Y., Kim, Y. Y., and Lee, J. T., 1999, "A Basic Study on the Hydrogen Fueled Engine With Dual Injection," *Proc. 5th KHES-HESS Joint Symposium*, Taejeon, Nov., Korea Hydrogen Energy Society, pp. 237–248.
- [14] Kwon, B. J., Lee, J. Y., Lee, J. T., and Lee, S. Y., 1993, "The Effect of Compression Ratio on Combustion and Performance Characteristics of Direct Injection Spark Ignition Hydrogen Fueled Engine," *Trans. KSAE*, **1**, pp. 17–26.
- [15] Lee, J. T., Lee, S. Y., Kim, Y. H., and Lee, J. C., 1988, "A Basic Study on the Development of Hydrogen Fueled Engine," *Proc. KSAE Spring Conference*, Korea Society of Automotive Engineering, pp. 59–63.
- [16] Nam, S. W., Park, J. B., Choi, K. H., and Lee, J. T., 1995, "Cooling Losses and Heat Flux of Hydrogen Fueled Spark Ignition Engine With Inner Injection," *Proc. of 3rd KHES-HESS Joint Symposium*, Sep., pp. 83–91.
- [17] Hong, H., Lee, J. T., and Lee, S. Y., 1992, "An Experimental Study on the Suitable Configuration of Injection Hole in Direct Injection Hydrogen Fueled Engine," *KSME-JSME 2nd Thermal Engineering Conference*, Vol. 2, Oct., pp. 1–10.
- [18] Kondo, T., Hiruma, M., and Furuhashi, S., 1996, "A Study on the Mechanism of Backfire in External Mixture Formation Hydrogen Engines," *Proc. WHEC*, Vol. III, Stuttgart, June, International Association for Hydrogen Energy, pp. 1547–1556.
- [19] Kim, Y. Y., Ryu, T. H., and Lee, J. T., 1998, "Backfire Occurrence by Abnormal Electric Discharge in Hydrogen Fueled Engine," *Proc. of KHES Autumn Annual Meeting*, Jinju, May, Korea Hydrogen Energy Society, pp. 105–115.
- [20] Eichseder, H., Wallner, T., Freymann, R., and Ringler, J., 2003, "The Potential of Hydrogen Internal Combustion Engines in a Future Mobility Scenario," SAE Technical Paper 2003-01-2267.

K. K. Srinivasan

S. R. Krishnan

S. Singh

K. C. Midkiff¹

e-mail: cmidkiff@coe.eng.ua.edu

Department of Mechanical Engineering,
The University of Alabama,
Tuscaloosa, AL 35487

S. R. Bell

School of Engineering,
The University of Kansas,
Lawrence, KS 66045

W. Gong

S. B. Fiveland

M. Willi

Caterpillar, Inc.,
Peoria, IL

The Advanced Injection Low Pilot Ignited Natural Gas Engine: A Combustion Analysis

The Advanced (injection) Low Pilot Ignited Natural Gas (ALPING) engine is proposed as an alternative to diesel and conventional dual fuel engines. Experimental results from full load operation at a constant speed of 1700 rev/min are presented in this paper. The potential of the ALPING engine is realized in reduced NO_x emissions (to less than 0.2 g/kWh) accompanied by fuel conversion efficiencies comparable to straight diesel operation. Some problems at advanced injection timings are recognized in high unburned hydrocarbon (HC) emissions (25 g/kWh) and poor engine stability reflected by high COV_{IMEP} (about 6%). This paper focuses on the combustion aspects of low pilot ignited natural gas engines with particular emphasis on advanced injection timings (45°–60° BTDC). Ignition phasing at advanced injection timings (~60° BTDC), and combustion phasing at retarded injection timings (~15° BTDC) are recognized as important combustion parameters that profoundly impact the combustion process, HC emissions, and the stability of engine operation. [DOI: 10.1115/1.1915428]

Introduction

The drive for “ultra” low emissions from combustion engines of the future has fueled widespread research in alternative combustion strategies [1–4]. Homogeneous charge compression ignition (HCCI) engines, lean burn spark-ignited (SI) natural gas engines, and pilot ignited natural gas engines have emerged as possible alternatives to the conventional diesel engine, whose future application may be limited due to objectionable levels of NO_x and particulate matter (PM) emissions. HCCI engines, while promising very low emissions, are still faced with challenges in ignition and combustion control at high brake mean effective pressures [5]. Pilot ignited natural gas engines have received considerable attention in recent years because the lean combustion of natural gas produces relatively insignificant amounts of PM and reduced NO_x compared to the burning of straight diesel fuel [6]. Low pilot ignited natural gas engines employ the compression ignition of small diesel pilots, which account for about 2%–3% of the total fuel energy input, to ignite a premixed mixture of natural gas and air. The motivation for smaller diesel pilots stems from the fact that in traditional dual fuel engines, where as much as 20% or more of the total fuel energy input is supplied from diesel and the remaining fuel energy from natural gas, the NO_x emissions increase with increasing pilot quantities [7]. Conventional NO_x reduction strategies in pilot ignited natural gas engines utilize retarded injection timings (15°–35° BTDC) [8,9]. However, this approach often results in reduced fuel conversion efficiencies. The ALPING engine is presented as a viable and more effective alternative to retarded injection strategies to reduce NO_x while maintaining satisfactory performance. In this engine, a small diesel pilot is injected into the cylinder at advanced injection timings

(45°–60° BTDC) and is subsequently compression ignited to achieve combustion in a premixed mixture of natural gas and air. It has been demonstrated that at these injection timings, a judicious choice of intake manifold temperature and pressure results in very low NO_x (less than 0.2 g/kWh) at all loads with diesel-like fuel conversion efficiencies [10,11]. However, the low NO_x emissions are accompanied by increased (~20 g/kWh) unburned hydrocarbons (HC), which are predominantly methane, increased CO emissions (~5 g/kWh), and increased combustion variability (COV_{IMEP} of about 6%) at advanced injection timings of 55°–60° BTDC. The reduction in NO_x is attributed to a fundamental difference in combustion at advanced injection timings (45°–60° BTDC) compared to retarded injection timings (15°–35° BTDC). This paper attempts to characterize the nature of cyclic variability in combustion and its effect on engine-out emissions at advanced and retarded injection timings.

Experiment

Figure 1 is a schematic of the experimental setup used to test the ALPING engine. The experiments were carried out in a single-cylinder Caterpillar 3401 engine. Table 1 lists the engine specifications. The engine was coupled to a dc dynamometer through a torque meter. Intake, exhaust, coolant, and oil temperatures were measured using type-K thermocouples. To simulate turbocharging, compressed inlet air was heated in a surge-tank and fed to the intake manifold while the exhaust back pressure was controlled by regulating the pressure in the exhaust tank. In all tests, city natural gas was used. Gas composition analysis, reported in Table 2, showed that the natural gas contained predominantly methane (approximately 98.3%).

The intake airflow rate (\dot{m}_a) and natural gas flow rate (\dot{m}_{ng}) were measured using a laminar flow element and a thermal mass flow meter, respectively. Pilot injection of diesel fuel was achieved using a customized accumulator-type common rail injection system. The system is capable of consistently metering a

¹To whom correspondence should be addressed.

Contributed by the Internal Combustion Engine Division of ASME for publication in the JOURNAL OF ENGINEERING FOR GAS TURBINES AND POWER. Manuscript received October 10, 2003; final manuscript received May 3, 2004. Assoc. Editor: D. Assanis.

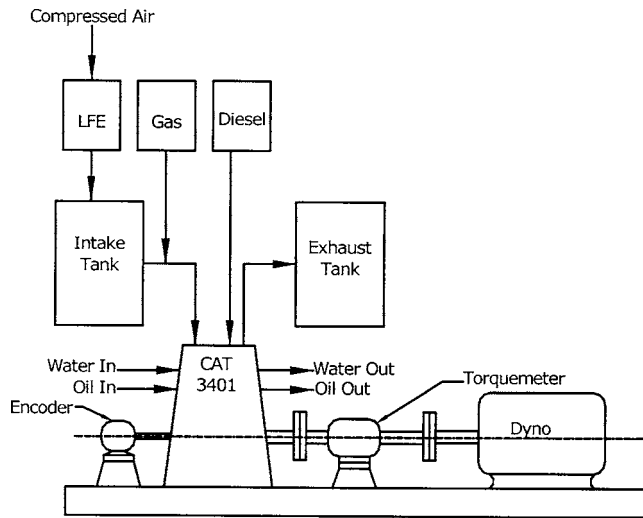


Fig. 1 Schematic of the experiment

minimum injected quantity of $4.6 \text{ mm}^3/\text{stroke}$ and a maximum injected quantity of $20 \text{ mm}^3/\text{stroke}$. Additional details of the pilot injection system, its design, and operating principles are provided elsewhere [3,12]. Crank resolved pressure data acquired over 150 engine cycles were used in a two-zone thermodynamic heat release analysis program [13] to obtain experimental heat release and mass burn rates and other combustion parameters.

The exhaust emissions were measured by an integrated emissions bench. The emissions were sampled near the exhaust port and directed to the emissions bench through a heated sample line. Total hydrocarbons (HC) and NO_x were measured in the hot, undried sample using a heated flame ionization detector (HFID) and

Table 1 Engine specifications

Parameter	Specification
Engine type	Four cycle, simulated turbocharging
Bore \times stroke, cm	13.7×16.5
Displacement, L	2.43
Compressions ratio	14.5:1
Primary fuel	Compressed natural gas
Gas supply	Intake port, 206 kPa
Ignition source	Diesel pilot
Fuel injection	Direct injection
Injection system	Electronically controlled common rail
Number of nozzles	4
Combustion chamber	Bowl in piston
Number of valves per cylinder	4
Rated power, kW	52 @ 2100 rpm

Table 2 Natural gas composition and properties

Component	Volumetric concentration (%)
Methane	98.33
Ethane	0.11
Carbon dioxide	0.21
Carbon monoxide	0.01
Nitrogen	1.28
Oxygen	0.05
Hexane	0.01
Propane	0.02
Iso-butane, <i>n</i> -butane,	0.01
Iso-pentane, <i>n</i> -pentane	
Higher heating value @ 60°F and 14.73 psia=54 MJ/kg	
Molecular weight=16.3 kg/kmol	
Specific gravity=0.5622	
Overall fuel composition= $\text{C}_{0.99}\text{H}_{3.95}\text{O}_{0.01}\text{N}_{0.03}$	

Table 3 Full load operating conditions

Parameter	Value
Load	Full load
Speed	1700 rev/min
Power	42 kW
Intake temperature (T_{in})	35°C
Intake pressure (P_{in})	202 kPa
Exhaust pressure (P_{ex})	191 kPa
Pilot injected quantity, \dot{m}_d	3.3 g/min
Natural gas flow rate, \dot{m}_{ng}	Varied between 117–135 g/min to maintain a constant power of 42 kW over the range of injection timings
Overall equivalence ratio range (ϕ_{ov})	0.49–0.57
Injection timing range (BOI)	$15^\circ\text{--}60^\circ$ BTDC

a chemiluminescent detector (CLD), respectively. The exhaust sample was cooled and dried prior to the measurement of O_2 , CO , and CO_2 . The species CO and CO_2 were measured using the nondispersive infrared method (NDIR) and O_2 was measured by the paramagnetic method in a separate analyzer.

The engine tests included the measurement of gaseous emissions (CO , CO_2 , O_2 , NO_x , and unburned hydrocarbons), engine speed and torque, and in-cylinder pressure over a wide range of injection timings ($15^\circ\text{--}60^\circ$ BTDC) at a constant speed of 1700 rev/min at suitable combinations of intake charge temperature (T_{in}), intake pressure (P_{in}), exhaust back pressure (P_{ex}), and total injected quantity of diesel pilot (\dot{m}_d). The results reported in this paper correspond to the operating conditions given in Table 3. The intake and exhaust manifold conditions were chosen by performing exhaust backpressure calculations based on an assumed total turbocharger efficiency of 55% and typical exhaust manifold temperatures at full load diesel operation, along with some base-line diesel operating conditions provided by the engine manufacturer. The overall equivalence ratio was defined as follows:

$$\phi_{ov} = \frac{(A/F)_s}{(A/F)_a} \quad (1)$$

$$(A/F)_a = \frac{\dot{m}_a}{(\dot{m}_d + \dot{m}_{ng})} \quad (2)$$

In Eqs. (1) and (2), $(A/F)_a$ is the actual air-fuel ratio and $(A/F)_s$ is the stoichiometric air-fuel ratio for the diesel-natural gas-air mixture, which is dependent on the relative proportions of diesel and natural gas present in the cylinder. The overall equivalence ratio was calculated using measured fuel and air flow rates and also backcalculated from emissions measurements. The overall equivalence ratio values mentioned in Table 3 were obtained from emissions calculations.

Alping Combustion Concept

Classical dual fuel combustion employs compression ignition of a diesel pilot to ignite a premixed mixture of air and NG. The energy release from conventional dual fuel combustion can be considered to occur in three distinct phases [14]. The first phase involves energy release from the combustion of the diesel pilot; the second consists of the combustion of NG in the vicinity of the diesel pilot; and the third phase is due to the combustion of the lean NG-air mixture by flame propagation. During the first and second phases, combustion occurs at richer equivalence ratios in the vicinity of the developing diesel spray, resulting in higher local temperatures that favor the formation of NO_x . Clearly, the size of the fuel rich zones is decided by the size of the initial diesel pilot. Therefore, increasing the pilot size favors the formation of NO_x . Recognition of this fact, led to the development of low pilot ignited natural gas engines that used smaller diesel pi-

lots. However, current low pilot ignited natural gas engines employ the conventional strategy of retarded injection timings, in the range of 5°–15° BTDC, which is often applied to diesel engines to achieve low NO_x emissions [3]. Unfortunately, retarded timings are accompanied by compromised fuel conversion efficiencies. The ALPING engine uses advanced injection (45°–60° BTDC) of pilot diesel to obtain very low NO_x (less than 0.2 g/kWh) with diesel-like fuel conversion efficiencies [10,11]. Early injection of diesel pilot provides increased residence time for the pilot fuel to mix with the surrounding NG–air mixture. This results in the availability of broadly distributed ignition centers at the time of ignition, which in turn is determined by local equivalence ratios, temperatures, and pressures. Due to the dispersion of the diesel fuel in the NG–air mixture, it is speculated that the ensuing pilot combustion occurs at locally lean equivalence ratios, resulting in lower local temperatures and reduced NO_x emissions. At the same time, the availability of these distributed ignition centers increases the burn rate of the NG–air mixture, resulting in better and more efficient combustion compared to retarded timings.

Combustion Parameters

The following combustion parameters are defined to facilitate the analysis of the combustion process for both advanced and retarded injection timings:

$$\Delta_{IGN} = \Theta_{IGN} - \Theta_{TDC} \quad (3)$$

$$\Delta_{COM} = \Theta_{COM} - \Theta_{TDC} \quad (4)$$

$$\Delta_{DUR} = \Delta_{COM} - \Delta_{IGN} \quad (5)$$

$$\Delta_{PHRR} = \Theta_{PHRR} - \Theta_{TDC} \quad (6)$$

$$COV_{IMEP} = \frac{std - dev(imep)}{mean(imep)} \quad (7)$$

$$COV_{DUR} = \frac{std - dev(\Delta_{DUR})}{mean(\Delta_{DUR})} \quad (8)$$

In Eqs. (3)–(8), Θ_{IGN} is the crank angle corresponding to ignition of the pilot diesel fuel. Throughout this paper, ignition is defined as the crank angle at which the measured cylinder pressure during combustion exceeds the measured cylinder pressure during engine motoring under similar intake manifold conditions by 1 bar. It must be noted that the overall combustion process is initiated by the ignition of diesel fuel since it has better compression ignition properties than natural gas. The ignition phasing (timing of ignition) relative to compression TDC is Δ_{IGN} . The crank angle corresponding to 50% mass burn is Θ_{COM} . The combustion phasing, Δ_{COM} is the 50% mass burn CAD relative to compression TDC. Here, the combustion phasing is determined from the mass burn rates computed using the two-zone heat release analysis [13] of crank-resolved cylinder pressure data. Therefore, this definition does not pertain exclusively to either diesel or natural gas combustion; rather, it should be construed as the instant at which 50% of the total in-cylinder mass has undergone combustion. Nevertheless, it is likely that most of the diesel fuel would have burned by this time; considering the fact that the amount of diesel fuel is only a small fraction of the total fuel mass (diesel+natural gas). The phasing terminology used in this paper, although unconventional, helps to effectively elicit details of the combustion process which are otherwise buried in the conventional heat release rate profiles. The duration of combustion defined as the difference between the combustion phasing and ignition phasing, respectively, is Δ_{DUR} . The crank angle corresponding to peak heat release rate (PHRR) is Θ_{PHRR} . The phasing of the PHRR relative to TDC is Δ_{PHRR} . The COV_{IMEP} [Eq. (7)], defined as the coefficient of variation of indicated mean effective pressure (IMEP), is a quantitative estimate of the cyclic

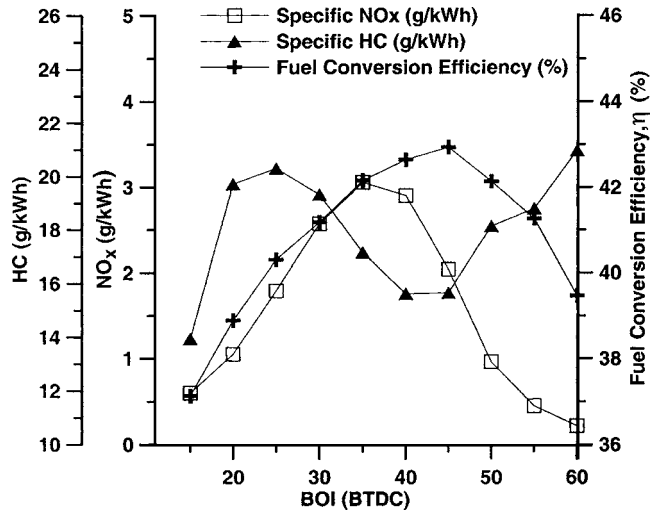


Fig. 2 Fuel conversion efficiency and brake specific NO_x and HC emissions vs injection timing

fluctuations of the in-cylinder work output. The coefficient of variation of duration, COV_{DUR} [Eq. (8)], is a measure of the cyclic variation in combustion duration, as defined in Eq. (5).

Results and Discussion

Figure 2 shows the measured brake specific emissions and fuel conversion efficiency, η , defined as the ratio of brake power to the fuel energy feed rate based on lower heating values of NG and diesel, as functions of injection timing. The fuel conversion efficiency and specific NO_x emissions curves exhibit an increasing trend from 15° to 35° BTDC. Between 40° and 60° BTDC, the NO_x emissions exhibit a decreasing trend. On advancing the injection timing from 35° to 45° BTDC, the NO_x emissions decrease sharply from 3 g/kWh to almost 2 g/kWh, approximately a 30% reduction. On the contrary, the fuel conversion efficiency continues to increase and attains a maximum value of about 43% at 45° BTDC. Further advancement in injection timing leads to decreased fuel conversion efficiencies. A comparison at the extremes of 15° and 60° BTDC of the injection timing sweep indicates that advanced BOI operation is beneficial both in terms of η and NO_x compared to retarded BOI operation. The reason for reduced NO_x emissions with ALPING operation (45°–60° BTDC) is the significant change in the combustion process described earlier in the ALPING combustion concept section of this paper.

The HC emissions exhibit an increasing trend between 15° and 25° BTDC, followed by a decrease between 30° and 45° BTDC, and finally a steady increase between 45° and 60° BTDC. The maximum HC of about 22 g/kWh and the minimum of about 14 g/kWh are obtained at 60° BTDC and 15° BTDC injection timings, respectively. The increase in HC at 60° BTDC is attributed to inconsistent ignition phasing, i.e., due to the early injection, some engine cycles may experience overleaning of the diesel pilot in the surrounding NG–air mixture that lead to partial or total misfire. On the other hand, at 15° BTDC, the fact that the measured exhaust manifold temperatures were high (about 560 °C) supports the view that the unburned fuel may still continue to burn in the exhaust manifold, leading to lower measured engine-out HC emissions.

The ignition and combustion processes in spark-ignited and pilot-ignited natural gas engines are affected by in-cylinder fluid motion. So, cyclic variations of in-cylinder fluid flow are responsible for cyclic ignition and combustion variations [15]. In pilot ignited natural gas engines, it is believed that these flow variations affect the preparation of the pilot diesel–air mixture prior to ignition. As a result, the extent of spatial dispersion of the pilot diesel

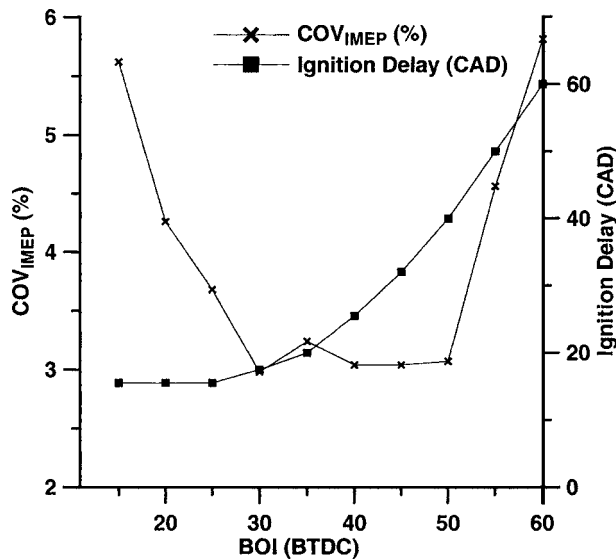


Fig. 3 COV_{IMEP} and ignition delay vs injection timing

fuel and its mixing with the surrounding natural gas-air mixture are subjected to variation from one engine cycle to another resulting in variations in the ignition and combustion processes. These cyclic ignition and combustion variations are reflected in the in-cylinder pressure history. Therefore, in this paper, measured cylinder pressure data are used to analyze the cyclic ignition and combustion variations.

Based on the analyses by Matekunas [16] and Heywood [17], cyclic variations can be broadly classified into cyclic variabilities related to the in-cylinder pressure history, such as magnitude and crank angle corresponding to peak pressures in the cylinder, maximum rate of pressure rise and the corresponding crank angle, COV_{IMEP} ; and cyclic variabilities related to combustion, such as magnitude and crank angle corresponding to PHRR, ignition and combustion phasing, and the combustion duration. Figure 3 shows the COV_{IMEP} and ignition delay versus injection timing. As previously discussed, COV_{IMEP} is a measure of cyclic variations in engine work output. From Fig. 3 it is seen that the COV_{IMEP} is similar in magnitude and highest at the two extreme injection timings of 15° and 60° BTDC, reaching values near 6%. However, the reasons for the high COV_{IMEP} at the two injection timings are quite different and will be discussed below. In this regard, it is helpful to remember that the IMEP is a function of the in-cylinder pressure history, energy release rates or burn rates, and the rate of change of volume due to expansion. Therefore, the variations in IMEP are sensitive to changes in magnitude of peak pressures, ignition phasing, combustion phasing, phasing of PHRR and combustion duration.

A simultaneous comparison of Figs. 4–6 helps in understanding the essential differences in combustion between injection timings of 15° and 60° BTDC. From Fig. 2 it is observed that the 40° BTDC injection timing is similar to a point of inflection for the specific set of engine operating conditions shown in Table 3. Advancing or retarding injection from this point results in the ALPING combustion regime (45°–60° BTDC) or conventional low pilot ignition engine operation (15°–35° BTDC), respectively. Further discussion of heat release schedules for different injection timings is provided in Refs. [10,11].

Figure 4 compares the measured peak in-cylinder pressures at 15°, 40°, and 60° BTDC injection timings over 150 engine cycles. It is seen that the cyclic variations in peak pressures are highest at 60° BTDC, and that for some of the cycles the peak pressure equals the motoring peak pressure, indicating partial and/or total misfire. However, the peak pressure variations for both 15° and 40° BTDC are small compared to variations at 60° BTDC. The

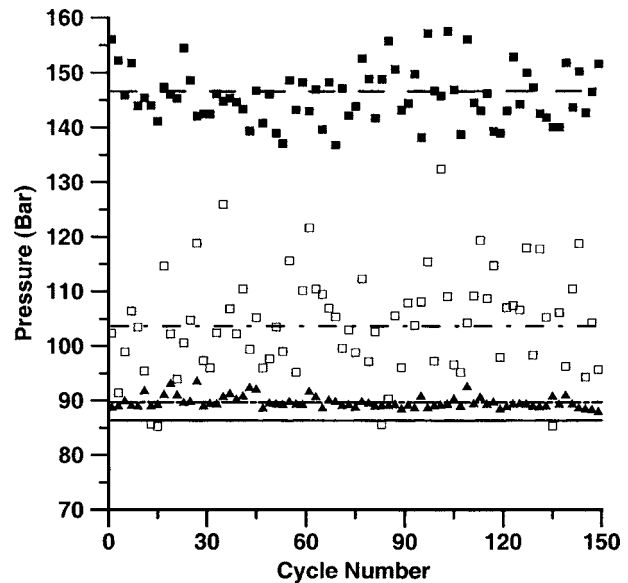


Fig. 4 Peak pressures vs cycle number at 15° (▲), 40° (■), and 60° BTDC (□). The continuous line is the peak motoring pressure and the dashed lines are the cycle averaged peak pressures at these injection timings

extreme variability in the magnitude of peak pressures at 60° BTDC can arise from either deteriorated combustion phasing or inconsistent ignition phasing (Δ_{IGN}) relative to TDC. Figures 5 and 6 show the ignition and combustion phasing, respectively, versus cycle number. It is clear from Fig. 5 that the onset of ignition is highly variable for 60° BTDC injection timing while the variation is smaller for both 15° and 40° BTDC injection timings. Considering Fig. 6, two observations are in order; first, the average combustion phasing for 15° BTDC injection occurs later in the expansion stroke compared to the 60° BTDC injection timing. Second, the variation in the combustion phasing appears to be of the same magnitude for these two injection timings. These observations coupled with the fact that the variations in ignition phasing at 15° BTDC are smaller compared to those at 60° BTDC leads to the belief that the variations in combustion phasing at 60° BTDC are linked to the variations in ignition phasing at this in-

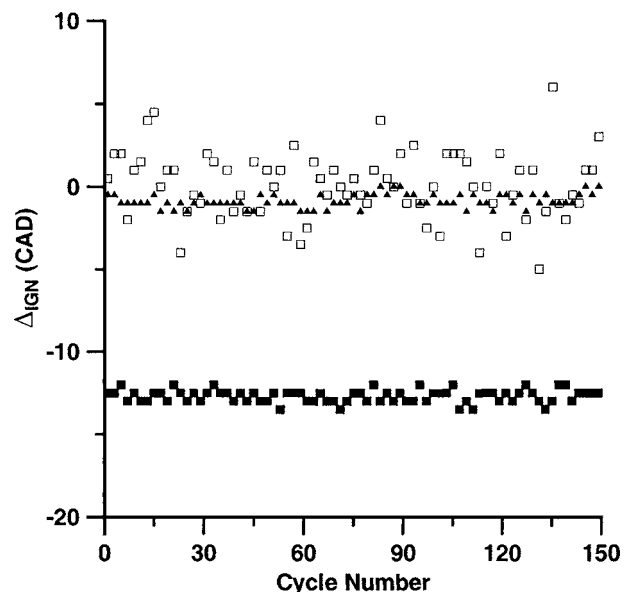


Fig. 5 Δ_{IGN} vs cycle number at 15° (▲), 40° (■), and 60° BTDC (□)

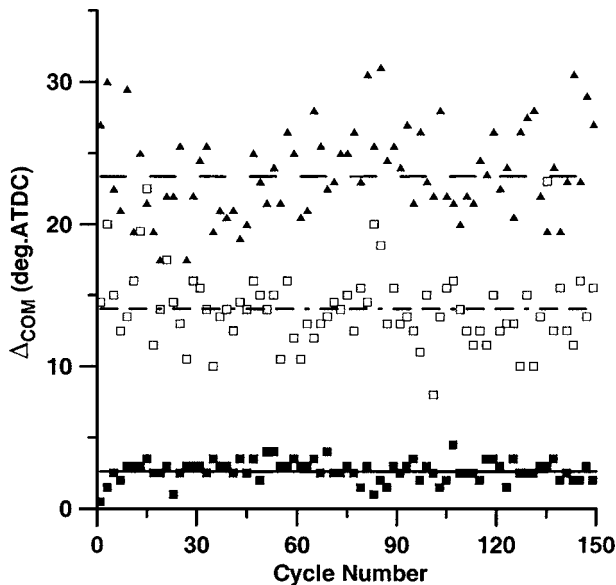


Fig. 6 Δ_{COM} vs cycle number at 15° (\blacktriangle), 40° (\blacksquare), and 60° BTDC (\circ). The lines are the cycle averaged durations at these injection timings.

jection timing. Therefore, it can be concluded that the reason for the high cyclic variability in the magnitude of peak pressure and high COV_{IMEP} at 60° BTDC is primarily due to inconsistency in the onset of ignition of the diesel pilot. The reason for this inconsistent ignition phasing at very advanced injection timings can be attributed to the nature of combustion. The long ignition delay at 60° BTDC (60 CAD, see Fig. 3) provides ample residence time for the diesel pilot to mix with the surrounding NG-air mixture. As a result, the local equivalence ratios may reach limiting values that result in partial misfire (Fig. 4). The partial misfire cycles would experience bulk quenching of the NG-air mixture, thereby increasing the engine-out HC emissions.

Since the variabilities in the magnitudes of the peak pressures and the onset of ignition as indicated by Figs. 4 and 5 are relatively small at 15° BTDC injection timing, the reason for high COV_{IMEP} at this injection timing can be attributed to a deteriorated combustion phasing. From Fig. 6 it can be seen that the average combustion phasing at 15° BTDC is poor ($\sim 25^\circ$ ATDC) and the combustion phasing is also highly variable from one cycle to another. These effects indicate cyclic variations in burn rate and work output that result in high IMEP variations manifested in Fig. 3.

Figure 7 shows the peak heat release rate, PHRR, versus the phasing of the PHRR relative to TDC at all injection timings from 15° to 60° BTDC. The error bars in Fig. 7 are standard error bars about the mean value of the PHRR at these timings. It can be seen that at 15° BTDC, the variation in the phasing of the PHRR is the highest, consistent with the observation of poor combustion phasing. As the injection timing is advanced beyond 15° BTDC, the magnitude of the PHRR increases and reaches a maximum at 45° BTDC, and the PHRR occurs closer to TDC. At 45° BTDC, there is considerable variation in both the magnitude of the PHRR and its occurrence relative to TDC. At 60° BTDC, the variability in the magnitude of PHRR is much higher than the variability in Δ_{PHRR} . These variabilities appear to be associated with inconsistent combustion phasing arising primarily from the inconsistencies in ignition phasing at advanced injection timings and from inconsistencies in combustion phasing arising from the delayed combustion process at retarded injection timings.

Figure 8 is a plot of COV_{DUR} and 50% mass burn duration (Δ_{DUR}) versus injection timing. The similarity in the COV_{DUR} and COV_{IMEP} curves shown in Figs. 8 and 3, respectively, indicate

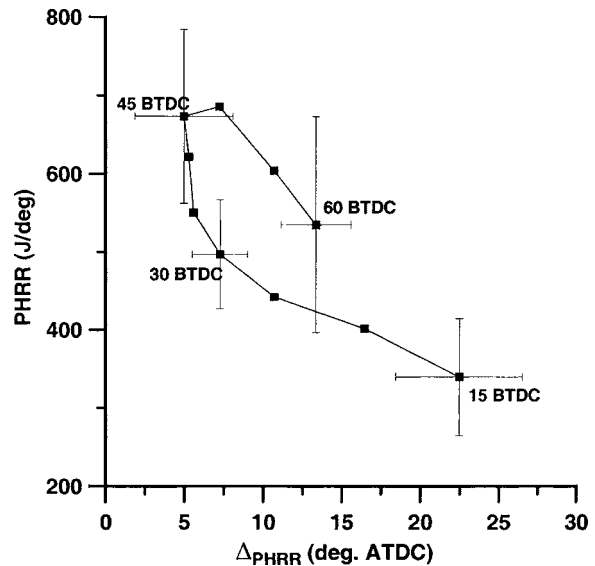


Fig. 7 PHRR vs Δ_{PHRR} for injection timings between 15° and 60° BTDC

that the indicated mean effective pressure depends on the 50% mass burn duration, and the variabilities in this duration lead to cyclic variabilities in the indicated mean effective pressures. The 50% mass burn duration (Δ_{DUR}) steadily decreases as the injection timing is advanced from 15° to 40° BTDC indicating that the combustion process becomes progressively rapid. Further advancement of injection timing (45°–60° BTDC) results in little variation in Δ_{DUR} indicating no further appreciable difference in the rapidity of the combustion process. This observation is very useful in accounting for the primary feature of ALPING operation, which is the achievement of very low NO_x with modest sacrifice in fuel conversion efficiency. Due to the almost invariant 50% burn duration (and burn rates) from 45° to 60° BTDC, the fuel conversion efficiencies and indicated mean effective pressures at these timings are affected only by ignition and combustion phasing, respectively. Again, at the advanced injection timings (45°–60° BTDC), as explained earlier, the more important variable affecting the fuel conversion efficiency and IMEP is ignition phasing. On the other hand, as mentioned before, from 40° BTDC to 15° BTDC the 50% burn durations exhibit an increasing trend,

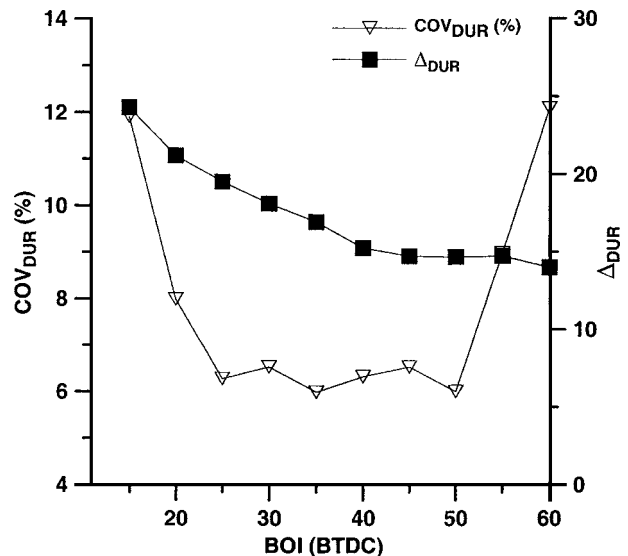


Fig. 8 COV_{DUR} and Δ_{DUR} vs injection timing

thereby resulting in progressively slower combustion. A comparison with the fuel conversion efficiencies for these injection timings in Fig. 2 suggests that the fuel conversion efficiency at 15° BTDC decreases by almost 6 percentage points from the value at 40° BTDC injection timing. However, for 60° BTDC injection timing, fuel conversion efficiency decreases by only about 3 percentage points from the value at 40° BTDC. The greater decrease in fuel conversion efficiencies in the retarded injection timing regime can be attributed to either poor ignition phasing or poor combustion phasing. Consistent with the earlier explanations and in view of the relatively invariant ignition phasing at 15° BTDC, the more important variable affecting the combustion duration and, hence, the fuel conversion efficiencies at 15° BTDC, appears to be combustion phasing rather than ignition phasing.

Conclusions

A single cylinder compression ignited engine was modified to operate successfully in the advanced injection, low-pilot ignited natural gas (ALPING) mode. The impact of several combustion parameters on engine performance, stability of operation, and emissions were analyzed. The results obtained lead to the following conclusions:

- (1) ALPING operation yielded reduced engine-out NO_x emissions (less than 0.2 g/kWh) with little sacrifice in fuel conversion efficiencies.
- (2) Ignition phasing, combustion phasing and the 50% mass burn duration are recognized as important parameters that influence the nature of combustion and HC emissions in the ALPING mode.
- (3) Inconsistency in ignition phasing is identified as the reason for high cyclic variabilities, about 6%, in the indicated mean effective pressure, COV_{IMEP}, and increased HC emissions, on the order of 25 g/kWh, associated with very advanced injection timing (60° BTDC).
- (4) The high COV_{IMEP} of about 6% associated with the very retarded injection timing of 15° BTDC is attributed more to delayed and inconsistent combustion phasing than to inconsistent ignition phasing.
- (5) The duration of 50% mass burn (Δ_{DUR}) at advanced injection timings is almost constant, while it exhibits an increasing trend as the injection timing is retarded beyond 40° BTDC. This fact, in conjunction with the variations in ignition phasing and combustion phasing (Figs. 5 and 6), suggests that the primary factor responsible for reduced fuel conversion efficiency down to about 39.5% at 60° BTDC injection timing is inconsistent ignition phasing, while that responsible for reduced fuel conversion efficiency down to about 36% at 15° BTDC injection timing is deteriorated combustion phasing.

Acknowledgment

The authors wish to acknowledge the financial support of Caterpillar, Inc., the Alabama Department of Economic and Community Affairs, and the Center for Advanced Vehicle Technologies at The University of Alabama, which receives partial funding from the U.S. Department of Transportation Federal Highway Administration under Grant No. DTFH61-99-X-00007.

Nomenclature

ALPING = advanced (injection) low pilot ignited natural gas
 ATDC = after top dead center
 $(A/F)_a$ = actual air–fuel ratio
 $(A/F)_s$ = stoichiometric air–fuel ratio
 BOI = beginning of (pilot fuel) injection
 BTDC = before top dead center

CAD = crank angle degrees
 COV_{IMEP} = coefficient of variation in IMEP (percent)
 COV_{DUR} = coefficient of variation of combustion duration (percent)
 IMEP = indicated mean effective pressure
 NG = natural gas
 PHRR = peak heat release rate (J/deg)
 TDC = top dead center (compression)
 \dot{m}_a = air flow rate (g/min)
 \dot{m}_d = pilot injected quantity (g/min)
 \dot{m}_{ng} = natural gas flow rate (g/min)
 ϕ_{ov} = overall equivalence ratio
 Θ_{IGN} = crank angle corresponding to ignition (CAD)
 Θ_{TDC} = compression TDC (CAD)
 Θ_{COM} = crank angle corresponding to 50% mass burn (CAD)
 Θ_{PHRR} = crank angle corresponding to the location of peak heat release rate (CAD)
 Δ_{IGN} = ignition phasing relative to TDC (CAD)
 Δ_{COM} = combustion phasing relative to TDC (CAD)
 Δ_{DUR} = duration of combustion (CAD)
 Δ_{PHRR} = phasing of the peak heat release rate relative to TDC (CAD)
 η = fuel conversion efficiency (percent)

References

- [1] Tanaka, S., Ayala, F., Keck, J. C., and Heywood, J. B., 2003, "Two-Stage Ignition in HCCI Combustion and HCCI Control by Fuels and Additives," *Combust. Flame*, **132**, pp. 219–239.
- [2] Flowers, D. L., Aceves, S. M., Smith, R., Torres, J., Girard, J., and Dibble, R., 2000, "HCCI in a CFR Engine: Experiments and Detailed Kinetic Modeling," SAE Paper No. 2000-01-0328.
- [3] Gebert, K., Beck, J., Barkhimer, R. L., and Wong, H. C., 1997, "Strategies To Improve Combustion and Emission Characteristics of Dual-Fuel Pilot Ignited Natural Gas Engines," SAE Paper No. 971712.
- [4] Zhang, D., and Frenkel, S. H., 1998, "A Numerical Study of Natural Gas Combustion in a Lean Burn Engine," *Fuel*, **77**, pp. 1339–1347.
- [5] Stanglmaier, R. H., and Roberts, C. E., 1999, "Homogeneous Charge Compression Ignition (HCCI): Benefits, Compromises, and Future Engine Applications," SAE Paper No. 1999-01-3682.
- [6] Papagiannakis, R. G., and Hountalas, D. T., 2003, "Experimental Investigation of Natural Gas Percentage on Performance and Emissions of a D.I. Dual Fuel Engine," *Appl. Therm. Eng.*, **23**, pp. 353–365.
- [7] Abd Alla, G. H., Soliman, H. A., Badr, O. A., and Abd Rabbo, M. F., 2000, "Effect of Pilot Fuel Quantity on the Performance of a Dual Fuel Engine," *Energy Convers. Manage.*, **41**, pp. 559–572.
- [8] Abd Alla, G. H., Soliman, H. A., Badr, O. A., and Abd Rabbo, M. F., 2002, "Effect of Injection Timing on the Performance of a Dual Fuel Engine," *Energy Convers. Manage.*, **43**, pp. 269.
- [9] Daisho, Y., Koseki, T., Saito, T., and Kihara, R., 1995, "Combustion and Exhaust Emissions in a Direct-Injection Diesel Engine Dual-Fueled with Natural Gas," SAE Paper No. 950465.
- [10] Krishnan, S. R., Srinivasan, K. K., Singh, S., Bell, S. R., Midkiff, K. C., Gong, W., Fiveland, S., and Willi, M., 2002, "Strategies for Reduced NO_x Emissions in Pilot Ignited Natural Gas Engines," ICEF2002-518, *Proc. of the 2002 Fall Technical Conference of the ASME IC Engines Division*, V. Wong, ed., ICE-Vol. 39, Sept. 8–11, New Orleans, LA, pp. 361–368.
- [11] Srinivasan, K. K., Krishnan, S. R., Singh, S., Midkiff, K. C., Bell, S. R., Gong, W., Fiveland, S., and Willi, M., 2003, "The Advanced Low Pilot Ignition Natural Gas Engine—A Low NO_x Alternative to the Diesel Engine," *Proceedings of The International Joint Power Generation Conference*, June 16–19, Atlanta, GA, IJPGC2003-40098.
- [12] Gebert, K., Beck, N. J., Barkhimer, R. L., Wong, H. C., and Wells, A. D., 1996, "Development of Pilot Fuel Injection System for CNG Engine," SAE Paper No. 961100.
- [13] Krishnan, S. R., 2001, "Heat Release Analysis of Dual Fuel Combustion in a Direct Injection Compression Ignition Engine," M.S. thesis, The University of Alabama, Tuscaloosa, AL.
- [14] Karim, G. A., 2000, "Combustion in Gas-Fuelled Compression Ignition Engines," 2000-ICE-299, the Soichiro Honda Lecture-2000, *Proc. of the 2000 Fall Technical Conference of the ASME IC Engines Division*, ICE-Vol. 35–1.
- [15] Reynolds, W. C., 1980, "Modeling of Fluid Motions in Engines—An Introductory Overview," in James N. Mattavi and Charles A. Amann, eds., *Combustion Modeling in Reciprocating Engines*, Plenum, New York, pp. 41–69.
- [16] Matekunas, F., 1983, "Modes and Measures of Cyclic Combustion Variability," SAE Paper No. 830337.
- [17] Heywood, J. B., 1988, *Internal Combustion Engine Fundamentals*, McGraw-Hill, New York, pp. 413–427, Chap. 9.

Heat Transfer in Reciprocating Planar Curved Tube With Piston Cooling Application

Shyy Woei Chang

Professor
Thermal Fluids Laboratory,
National Kaohsiung Marine University,
No. 142; Hai-Chuan Road,
Nan-Tzu District, Kaohsiung 811, Taiwan, ROC

Yao Zheng

Cheung Kong Chair Professor
Center for Engineering and Scientific
Computation and College of Computer Science,
Zhejiang University,
Hangzhou, Zhejiang 310027, P. R. China

This paper describes an experimental study of heat transfer in a reciprocating planar curved tube that simulates a cooling passage in piston. The coupled inertial, centrifugal, and reciprocating forces in the reciprocating curved tube interact with buoyancy to exhibit a synergistic effect on heat transfer. For the present experimental conditions, the local Nusselt numbers in the reciprocating curved tube are in the range of 0.6–1.15 times of static tube levels. Without buoyancy interaction, the coupled reciprocating and centrifugal force effect causes the heat transfer to be initially reduced from the static level but recovered when the reciprocating force is further increased. Heat transfer improvement and impediment could be superimposed by the location-dependent buoyancy effect. The empirical heat transfer correlation has been developed to permit the evaluation of the individual and interactive effects of inertial, centrifugal, and reciprocating forces with and without buoyancy interaction on local heat transfer in a reciprocating planar curved tube. [DOI: 10.1115/1.1995768]

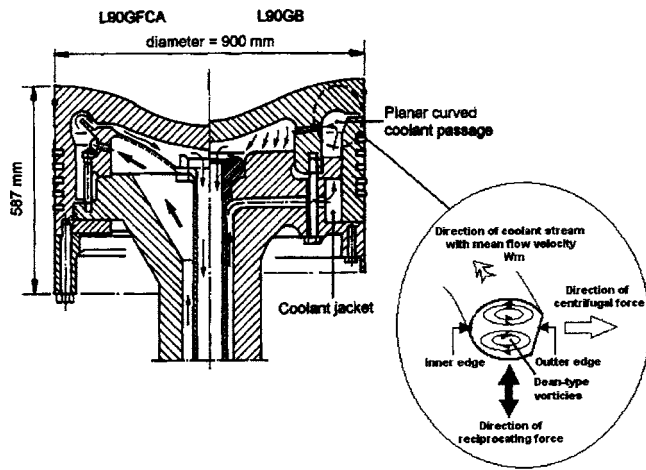
1 Introduction

1.1 Industrial Application. The marine propulsive diesel engines widely adopt the large stroke-to-bore ratio for low running speed in the range of 90–115 rpm. This obviates the use of reduction gear and matches the requirements for improving propeller efficiency. To increase the power-to-weight ratio and thermal efficiency of the engine, the maximum pressure and temperature in the thermodynamic cycle for this class of engines reach the current levels of about 150 bar and 1500°C. The piston that is in direct contact with the erosive hot gas requires the internal cooling system in order to maintain the material temperatures at the sustainable levels for structure integrity. As an illustrative example, Fig. 1 shows the internal cooling networks of pistons for B&W L90GFCA and L90GB heavy-duty marine diesel engines. The pressurized coolant, fed from the concentric passage in piston rod, flows into the “jacket” inside the piston skirt. This coolant stream is subsequently guided into a pair of planar curved channels arranged around the upper edge of the piston crown. Surrounding the upper edge of the piston crown is the high-momentum blow-by hot gas, which could cause considerable erosive damage when the material of piston is softened at high temperature. This pair of planar curved channels plays an important role for this type of piston-cooling system. As shown in Fig. 1, the centrifugal forces are generated in the planar curved channel when the coolant stream flows through this curved channel. The centrifugal forces in the curved channel drive the cooler fluids from the channel core toward the outer edge of channel. To preserve continuity, the return-flows along the periphery of channel wash the heated wall and are directed toward the inner edge. A pair of Dean-type vortices is generated over the cross-sectioned plane of the curved channel. The hot and cold spots are respectively developed at the inner and outer edges. Nevertheless, as the piston reciprocates in the direction orthogonal to the coolant stream, the flow structure developed in the planar curved channel inside the piston is further complicated by the reciprocating force. Because of the temporally varied nature of the reciprocating force, the flow inside the reciprocating planar curved channel becomes unsteady. Therefore the

inertial, centrifugal, and reciprocating forces could interact with buoyancy to affect the cooling performance of the planar curved channel. As indicated in Fig. 1, the flow parameters that control the cooling performance of reciprocating planar curved channel are Reynolds, Dean, pulsating, and reciprocating-Grashof numbers. After the coolant streams in the pair of curved channels merging at the opposite side of flow entrance, the bulk coolant flow is redirected into the plenum chamber underneath the crown and convected out of the piston from the central bore inside the piston rod.

1.2 Literature Survey. When the coolant flows through a static curved tube, the centrifugal force is induced to generate a pair of Dean-type cross-plane secondary flows. With the presence of Dean-type vortices, the spatially averaged heat transfer is enhanced, but the local heat transfer varies peripherally. When the Dean number increases, the degree of heat transfer augmentation along the outer edge of curved tube enhances, whereas the inner-edge heat transfer could be reduced from the straight tube level if the through flow momentum is relatively weak [1–5]. Also, the transition from laminar to turbulent flow in curved tubes requires the higher Reynolds numbers than those in a straight duct [6,7]. The relevant studies looked into the effects of externally imposed streamwise oscillation and pulsatile pressure waves on the flow and heat transfer in static coils [8–15]. It is worth mentioning that this type of research studied the flow and heat transfer in the static coils with the externally applied pulsating pressure waves from the flow entrance. These coils are static rather than reciprocating. When the coolant flows in a planar bend with a small curvature that is subject to high-frequency time-sinusoidal pressure oscillation, an additional pair of secondary circulations to the Dean vortices could develop in the inviscid core [8]. For low-frequency pure oscillatory flows in the planar curved pipe, Zalosh and Nelson [9] found the flow structure similar with the low Dean number steady flow. However, the growth or decline of secondary flow circulations in a curved pipe is often accompanied by the secondary flow reversals during each pulsation cycle. These time-varied secondary flows promote the temporally and periodically varied transverse mixing between the central and wall regions. This mechanism could trigger the Prandtl number effect on heat transfer [10]. At very small Prandtl numbers heat transfer was insensitive to the pulsation. The Dean number had to be considerably increased before the additional heat transportation associated with

Contributed by the Internal Combustion Engine Division of ASME for publication in the JOURNAL OF ENGINEERING FOR GAS TURBINES AND POWER. Manuscript received by the ICE Division October 20, 2003; final revision received March 1, 2005. Assoc. Editor: D. Assanis.



Controlling parameters for cooling performance in reciprocating planar curved tube

Flow parameters	Physical identities
Reynolds number (Re)	Relative strength of inertial force of coolant stream
Dean number (Dn)	Relative strength of centrifugal force in curved pipe
Pulsating number (Pu)	Relative strength of reciprocating force
Reciprocating Grashof number (Gr_p)	Relative reciprocating buoyancy force

Fig. 1 Piston-cooling networks of B&W L90G FCA and L90 GB diesel engines

the unsteady transverse mixing became the dominant mechanism. As a result, Simon et al. [10] and Rabadi et al. [11] showed that the time-averaged Nusselt number in a planar curved tube was most evidently increased for the flow conditions with high Prandtl number, high oscillating amplitudes, and low oscillating frequencies. In the static helical passage with pulsatile flows, Zabielski and Mestel [12] numerically unraveled the cross-pipe fluid motion that consists of three time-varied recirculating regions rotating around the center of the pipe. These unsteady flow cells change their sizes and orientations in time. The considerable increase of the pulsatile amplitude could result in the richer modes of vortical structures. Because of these dynamic vortical flow structures, the streamwise pulsation in a helical pipe could considerably increase the instant local and the circumferential time-averaged heat transfers [13]. The temporally varied flow field had the reverse phase angle with the instant heat transfer [13]. The minimum local heat transfers develop at the instants with maximum flow velocity in each pulsatile cycle. In the vicinity of the outer edge, the locally maximum heat transfer values opposite to the inner-edge counterpart with the minimum heat transfer rates were consistently detected even if the flow pulsated [13].

Also relevant with the present orthogonal-mode reciprocating flow in the planar curved tube are the studies of turbulent flows over a spanwisely oscillating wall. The logarithmic velocity profile in the channel with one sidewall to oscillate in the spanwise direction could be shifted upward from the oscillating wall. This phenomenon suggested that the viscous sublayer is thickened as a result of spanwise wall oscillation. The turbulence intensities in such a channel were also reduced across the boundary layer. As a result, the skin-friction drag of the turbulent boundary layer could be reduced by the spanwise wall oscillation [14–16]. In this respect, the experimental results of Choi and Clayton [17] reported that a net spanwise vorticity was generated by the periodic Stokes layer developed over the spanwisely oscillating wall. This effect resulted in the reduction of mean velocity gradient across the boundary layer near the wall. In addition, such spanwise vorticity could also hamper the longitudinal vortices in the viscous sublayer and to stretch in the streamwise direction. Therefore the streamwise vorticity was reduced and resulted in the weakened near-wall burst activity for turbulent channel flow [17]. These

results [14–17] demonstrate the influence of spanwise wall oscillation on boundary layer, vortical flow structure, and turbulence, which raise the possibility of heat transfer reduction in the planar curved tube that reciprocates orthogonally. Although the studies of oscillatory and pulsating flows in coils [6–13] or the ducted flows with spanwise wall oscillations [14–17] share partial degrees of similarity with the coolant flows in the reciprocating planar curved passages as depicted in Fig. 1, the subtle differences exist between these two types of flows. The lack of fundamental knowledge concerning the heat transfer performance of this particular cooling geometry, despite its apparent engineering applications for piston cooling, motivates the present study.

The relevant studies summarized in the literature survey have demonstrated that the oscillatory and pulsating flows could modify the vortical flow structures from the Dean-type vortices to the time-dependent dynamic vortical flow structures. This experimental study examines the effect of orthogonal-mode reciprocation on heat transfer in a planar curved tube for piston-cooling application. The streamwise and circumferential Nusselt number distributions with and without system reciprocation are presented over a range of buoyancy levels, Reynolds, Dean, and pulsating numbers. The impact of reciprocation on heat transfer is analyzed to assist the derivation of empirical heat transfer correlations for the present cooling configuration.

2 Experiments

2.1 Strategy. The primary tasks of the present study are to generate the heat transfer data in a planar curved tube and to examine the effect of orthogonal-mode reciprocation on heat transfer. The parametric analysis was adopted with the dimensionless flow parameters identified from the energy and momentum flow equations suitable for describing the conservation laws under the reciprocating environment. Equation (1) shows the dimensionless flow-momentum equation in the direction of reciprocation. This equation considers the effect of reciprocation-induced translating acceleration of the coordinate system on the fluid motion to describe the dynamic mechanism of the governing forces involved in a reciprocating system [18]

$$Pu \frac{\partial W}{\partial \tau} + \left(U \frac{\partial W}{\partial X} + V \frac{\partial W}{\partial Y} + W \frac{\partial W}{\partial Z} \right) = - \frac{\partial \chi}{\partial Z} + \frac{1}{Re} \nabla^2 W + \frac{Gr_p}{Re^2} \sin \tau \quad (1)$$

All the dimensionless groups appearing in Eq. (1) are defined in the Nomenclature. Two additional reciprocation related flow parameters, namely, the pulsating (Pu) and reciprocating Grashof (Gr_p) numbers are identified, respectively, to quantify the ratio of reciprocating to inertial forces and the relative strength of the reciprocating buoyancy effect [18]. It is worth noting that the reciprocating Grashof number features the physically different buoyancy interactions from the free-convection-like scenarios. The mechanism of free-convection effect normally develops in the steady flow, where the temperature gradients over the flow field are stable and the differences in volumetric gravity force promote the fluid motion. The reciprocating buoyancy effect, motivated by the reciprocating acceleration, typifies another mode of complex buoyancy interactions in the temporally periodical flow. The buoyancy interactions in a reciprocating system are likely to be induced from their effects on the instant fluid vorticity as the curl of reciprocating acceleration coupled with local density perturbation remains a finite physical quantity. Also, the gravitational buoyancy is unlikely to exert considerable effect on flow and heat transfer inside a reciprocating flow system, as the flow and temperature fields are never steady.

For a coolant under the condition that its temperature variation due to heat transfer did not make a considerable change of coolant's Prandtl number, the local Nusselt number (Nu) over the heating surface of a planar curved tube that reciprocates could be parametrically described by the following equation:

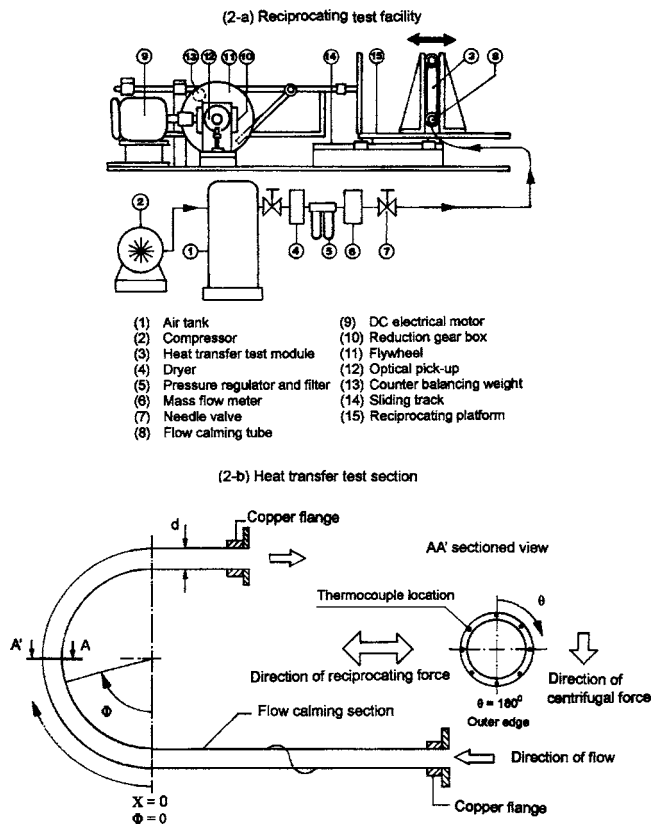


Fig. 2 Experimental apparatus

$$Nu(X, \theta) = \psi\{Re, Dn, Pu, Gr_p, \text{Boundary conditions}\} \quad (2)$$

The X and θ coordinates are in the streamwise and circumferential directions, respectively. The boundary conditions in Eq. (2) involve the geometrical, heating, and flow entry conditions simulated by the test apparatus. The effects of the constituent dimensionless groups of Eq. (2) on heat transfer are examined by systematically varying each of the flow parameters involved in Eq. (2). However, the experimental data with zero buoyancy interaction ($Gr_p=0, Pu \neq 0$) are not feasible to be directly generated by the heat transfer experiments because a real fluid has a finite value of thermal expansion coefficient. It is such a limiting case to have a vanishing small wall-to-fluid temperature difference, but the thermal fluids system reciprocates; the solution of Ψ function in Eq. (2) recasts the combined Re - Dn and Pu effects on heat transfer without any buoyancy interaction. These zero-buoyancy heat transfer data are inferred by extrapolating a family of heat transfer data taken at a specific Reynolds-Dean or pulsating number but with different wall-to-fluid temperature differences into the zero-buoyancy asymptote. The parametric study of the individual and combined effects of the nondimensional groups appearing in Eq. (2) with the attempt to devise a physically consistent empirical heat transfer correlation is the strategic aim.

2.2 Apparatus. The planar curved test tube was mounted on a reciprocating test facility, which has been previously described in [19]. A brief description of the reciprocating test facility and a detailed illustration of the heat transfer test module now follow. Figure 2(a) shows the reciprocating test facilities and the airflow loop, featuring the main components and instrumentation. The test coolant, dry air, was fed from tank (1). The coolant was pressurized by IWATA SC 175C screw-type compressor unit (2) after which the flow was dehumidified and cooled to the ambient temperature through a refrigerating system that was integrated with the compressor. The test coolant was channeled into the heat

transfer test module (3) through a dryer (4), a pressure regulator and filter (5), a pressure transducer and Tokyo Kesio TF-1120 mass flow meter (6), and a needle valve (7) for the control and measurement of mass flow rate. The nominal through-flow Reynolds number was controlled by adjusting the mass flow rate measured at 50 tube diameters upstream of the planar curved test tube (3). Because the coolant properties, such as viscosity and density, varied with the local fluid temperature the mass flow rate was adjusted to compensate the fluid-property variations in order to maintain the variations of Reynolds, Dean, and pulsating numbers at the flow entrance within $\pm 1\%$ of the nominal values. On entering the planar curved test section (3), the coolant flowed through a straight-tube flow-calming section (8) with an equivalent length of 9 tube diameters, in which the flow could be settled. System reciprocation is created by a crank-wheel mechanism driven by a 2500 W DC motor (9). Through a reduction gearbox (10), the flywheel (11) could be controlled to rotate at the required speed measured by the optical pickup (12). A counterbalancing weight (13) is fixed on the rotating wheel (11) to maintain the dynamic balance during reciprocation. A pair of slider tracks (14) is fitted underneath the platform (15) in order to support the heat transfer test module. As a result, the translating velocity of reciprocating test facility motivated by the rigid slider-crank mechanism is not a constant value but a skewed temporal sinusoidal function, which is attempted to simulate the dynamic motion of a reciprocating piston.

The constructional details of the heat transfer test module are illustrated in Fig. 2(b). The complete test channel was made of a 1 mm thick stainless tube with tube diameter d of 36 mm. Test fluid was channeled through a straight-tube flow-calming section of 324 mm into the planar curved section. The diameter of curvature for the planar curved test section D was 376 mm, which gives a dimensionless D/d ratio of 10.44. The system reciprocation involved the reciprocations of planar curved test section and the straight-tube flow-calming section that was arranged to be orthogonal with the streamwise flow direction. Both ends of test section were connected with an adjustable high-current-low-voltage electrical power through the copper joints. The electrically heating power was generated within the tube material so that a basically uniform heat flux heating condition was created. To minimize the external heat loss, fiberglass thermal insulation material was wrapped on the outside of the complete test tube.

Thirty-six thermocouples measuring the wall temperatures of the planar curved section were spark welded on the outer surface of the heating coil at locations illustrated in Fig. 2(b). The streamwise X , circumferential Φ , and angular θ coordinate systems are also defined in Fig. 2(b). As indicated in Fig. 2(b), the origin of the present coordinate system with $X=0$ and $\Phi=0$ deg is allocated after the straight flow-calming section. The angular coordinate system θ is in the clockwise direction with 180 deg at the outer edge of test tube. Because the direction of reciprocation is orthogonal to the streamwise flow direction, the reciprocating force is acting along the direction of $\theta=90$ deg and 270. The circumferential wall-temperatures along five cross-sectioned planes of $\Phi=0, 45, 90, 135,$ and 180 deg in the curvature of planar curved section were measured. At the 0 deg cross-sectioned plane of $\Phi=0$ deg, where it corresponded to the end of straight-tube calming section and the start of the planar curved section, there were four thermocouples installed at the angular locations of 0, 90, 180, and 270 deg along the outer circumference of heated tube. At the cross-sectioned planes of $\Phi=45, 90, 135,$ and 180 deg in the curvature of planar curved section, there were eight thermocouples installed along each circumference at the angular coordinates of $\theta=0, 45, 90, 135, 180, 225, 270,$ and 315 deg. The ceramic cement provided the essential adhesion to secure the thermocouple bead at the precise location. The variations in circumferential distributions of wall temperatures because of the combined effects of coil-curvature and orthogonal-mode reciprocation were recorded by these thermocouples. Two additional thermocouples penetrated

into the core of the flow path to measure the bulk-flow entry and exit temperatures. All these temperature measurements were monitored and stored on a PC through a Net-Daq Fluke Hydra 2640A data logger for the subsequent data processing. Prior to conducting the heat transfer test, all the thermocouples were calibrated in a constant temperature bath to ensure the measurement accuracy of ± 0.1 K. The local coolant properties, such as β_0 , Cp_0 , k_0 , and μ_0 (which were used to evaluate the controlling nondimensional parameters, such as Gr_0 , Gr_{p0} , Pu_0 , Dn_0 , and Re_0), were evaluated by means of standard polynomial functions with the reference flow entry temperature T_0 measured at the flow entry section as the determined variable. Having acquired the coolant temperatures at the entry and exit of the heated coil, a routine procedure was subsequently performed to evaluate the fluid temperature rise using the net amount of convective heat and the total coolant mass flow rate. The calculated fluid temperature rise between flow entrance and exit was compared to the actual measurement to check the accuracy of energy accountancy. The data batch was only collected when the difference between the calculated and measured fluid temperature rises was less than $\pm 10\%$. The local bulk flow temperatures T_f at the streamwise locations corresponding to the five cross-sectioned planes, where the circumferential wall-temperature measurements were made, were also acquired for the evaluation of local Nusselt number.

2.3 Program. The program involves three phases. The static flow conditions in the first phase are initially examined to generate the database against which the reciprocating results obtained at the second phase could be compared to unravel the reciprocating effects on heat transfer. The local heat transfer measurements along the X and θ axes with and without system reciprocation are illustrated. This is followed by a parametric study of the interactive and individual effects of reciprocating forces with and without buoyancy interaction on heat transfer. In the third phase, a methodology is proposed to devise the physically consistent heat transfer correlation. The Nusselt number was determined experimentally using

$$Nu = \frac{qd}{k_f(T_w - T_f)} \quad (3)$$

The local heat flux to the fluid q was determined from the heat flux generated in the tube material with a correction to account for external heat loss. The local external heat loss was found to be proportional to the locally prevailing wall-to-ambient temperature difference, with the various proportionality constants taken from the heat-loss calibration plots for different locations and reciprocating frequencies. Because the wall temperature distributions varied with the different flow conditions tested, the locally prevailing wall-to-ambient temperature differences changed with flow conditions, which effects produced different heat losses. Because of the thermal insulation for the test module, the experimentally processed heat flux distribution based on the wall-temperature measurements detected by the present allocations of thermocouples over the outer surface of test tube was controlled with the maximum variation range of $\pm 5.9\%$, which allowed the approximation of basic uniform heat flux boundary condition. The wall temperature T_w in Eq. (3) was corrected onto the inner surface of test tube from the actual thermocouple measurements based on the one-dimensional conduction law. The local bulk flow temperature T_f in Eq. (3) was determined using the enthalpy balance method. Having defined the streamwise bulk flow temperatures at locations corresponding to the measurement spots for wall temperatures, the fluid properties were accordingly evaluated to account for the influences of fluid temperature on the physical properties. The characteristic length selected to define the Nusselt, Reynolds, Dean, pulsating, and Grashof numbers was the hydraulic diameter of test tube d .

At each selected Reynolds, Dean, and pulsating number test, five different levels of heating power, which, respectively, heated

Table 1 Range of experimental nondimensional parameters

Nondimensional parameter	Range
Reynolds number (Re)	2500–14,500
Dean number (Dn)	780–4500
Pulsating number (Pu)	0–0.55
Gravitational Grashof number (Gr)	36,700–45,200
Pulsating Grashof number (Gr_p)	0–970,000

the wall temperature at the inner edge of exit plane to the levels of 323, 343, 363, 383, and 403 K. Each set of heat transfer data generated in this manner compared the influences of buoyancy on heat transfer when the heating power or the buoyancy level was systematically increased. The reciprocating tests at each Reynolds-Dean number with five buoyancy levels tested were performed at four different frequencies, namely, 0.83, 1.25, 1.67, and 2 Hz. Because of the reciprocating force effects, the flow structures, heat transfer rates, and local wall temperatures were temporal functions. For each individual set of tests, the flow and heating level were fixed for about 30 min in order to assure that the flow reached an equilibrium state. When the differences between the successive time-averaged wall-temperature measurements remained within ± 0.7 K, the temporal-repeated state was assumed and the on-line data acquisition system was activated to store the instantaneous data for a period of 10 s. These raw experimental data were subsequently processed to generate the appropriate Reynolds, Dean, pulsating, and Grashof numbers, and the individual effect of these parameters on the Nusselt number distribution was examined. The range of these nondimensional parameters is given in Table 1. An uncertainty approximation of the data reduction was conducted [20]. The temperature measurements were the major sources to attribute uncertainty. With the temperature difference between the wall and fluid varied from 25 to 102 K, the maximum uncertainty for the Nu, Re, Dn, Pu, Gr, and Gr_p were about 12.2%, 4.6%, 4.8%, 2.05%, 4.6%, and 4.9%, respectively.

3 Results and Discussion

3.1 Static Results. The typical circumferential Nusselt number distributions along five streamwise cross-sectioned planes of static planar curved tube at five Reynolds-Dean numbers tested are shown in Fig. 3. The variations in circumferential heat transfer profiles along the streamwise (X) direction unravel the downstream development of Dean vortices. At the immediate entrance where the planar curvature initiates, there is no circumferential heat transfer variation observed. Heat transfer levels along this cross-sectioned plane for all the Reynolds numbers tested are in close agreement with the Dittus-Boelter Nusselt number values Nu_x [21]. This agreement ensures the flow conditions on entering the planar curved section, after traveling the straight-pipe flow-calming section, remain fully developed turbulent flows. Further downstream, the circumferential heat transfer variations are generated with a tendency to develop the higher heat transfer rate at the outer edge relative to its inner counterpart. Along each circumference at the cross-sectioned planes of $\Phi=45, 90, 135,$ and 180 deg, the circumferential heat transfer distributions are symmetrical about the plane connecting the inner and outer edges. Heat transfers at the inner and outer edges are, respectively, impeded and enhanced from the Dittus-Boelter levels [21]. Because there is no repeated circumferential heat transfer profiles observed at the various cross-sectioned planes examined in Fig. 3, the developing nature of circumferential Nusselt number profiles is demonstrated so that the flow remains developing in the present planar curved tube.

The streamwise heat transfer distributions of developing Dean-type flows in the planar curved tube along the angular edges of $\theta=0, 45, 90, 135, 180, 225, 270,$ and 315 deg at Reynolds (Dean) numbers of 14,500(4470) are shown in Fig. 4. Nusselt numbers at

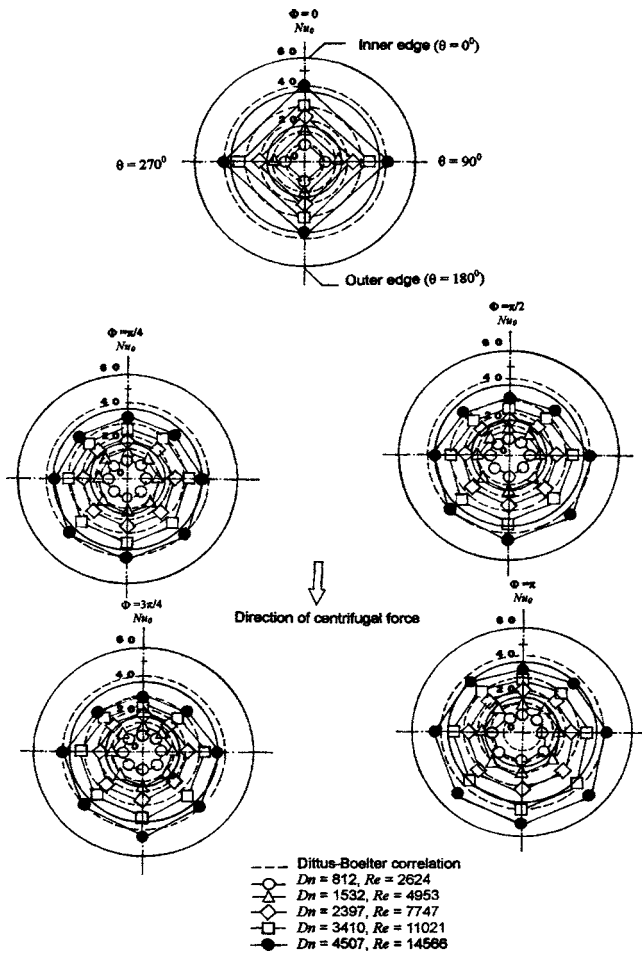


Fig. 3 Typical circumferential heat transfer distributions in static coil

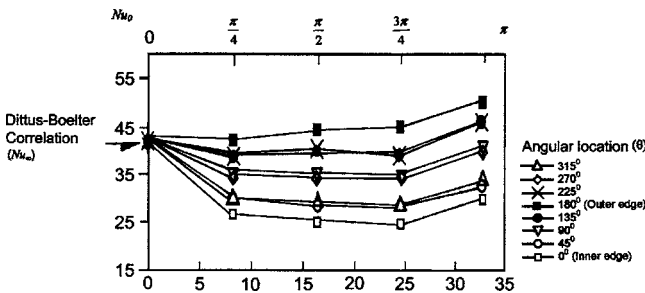


Fig. 4 Streamwise heat transfer variations along measured angular edges in static coil

Table 2 Coefficients A and B for heat transfer in static planar curved pipe

Streamwise location $X(x/d)$	Radian of curvature Φ (rad)	B	A				
			Angular location θ (deg)				
			$\theta=0$	$\theta=45/315$	$\theta=90/270$	$\theta=135/225$	$\theta=180$
0	0	0.8			0.051		
8.2	$\pi/4$	0.76	0.0516	0.0555	0.0646	0.0734	0.0762
16.4	$\pi/2$	0.742	0.0593	0.0652	0.0778	0.0902	0.0958
24.6	$3\pi/4$	0.72	0.0682	0.0754	0.0891	0.1044	0.1107
32.8	π	0.63	0.1711	0.184	0.2196	0.2410	0.2594

angular locations of $\theta=0, 90, 180,$ and 270 deg collapse into a tight data band with levels similar to the Dittus-Boelter value [21] at the immediate curvature of $X=\Phi=0$. Further downstream where the flow- and curvature-induced centrifugal forces gradually build up, the considerable data spreads driven by varying θ value are observed. In this respect, the heat transfers along three pairs of angular edges of $45\text{--}315, 90\text{--}270,$ and $135\text{--}225$ deg share almost identical values because of the symmetrical nature of Dean vortices. Along the outer edge of the coil ($\theta=180$ deg), heat transfer levels are consistently higher than the Dittus-Boelter value Nu_{∞} . The streamwise Nusselt number distributions along the various angular edges depicted in Fig. 4 reflect the influences of developing Dean vortices on heat transfer. The centrifugal force induced in the planar curved tube drives the cooler fluids toward the outer edge from the central core. A pair of cross-plane secondary flows washes the heated wall circumferentially and joins at the spot of inner edge. Therefore, the wall temperatures increase along the circumference from the outer edge toward the inner edge when the pipe wall is heated with uniform heat flux. The considerable heat transfer reductions from the Dittus-Boelter value Nu_{∞} are observed along the angular edges of $\theta=0, 45\text{--}315,$ and $90\text{--}270$ deg. Also depicted in Fig. 4 are the streamwise heat transfer increases along each angular edge. As the flow in present planar curved channel is driven upward from entrance of $\Phi=0$ deg to exit of $\Phi=180$ deg, the gravitation field decelerates the mainstream flow. In this respect, the streamwise heat transfer increase in a curved tube has also been reported by Guo et al. [13], for which the decelerating gravity effect in the upward flow region that moderated the radial velocity distribution was considered as the main cause for such heat transfer increments.

In the static planar curved pipe, heat transfer data acquired from five variable heat fluxes for any tested Reynolds-Dean number collapses into a tight data band at each streamwise and angular location. Therefore, the gravitation-driven buoyancy effect on heat transfer in the present parametric range remains negligible. As there is neither noticeable change in the coolant Prandtl number nor the considerable buoyancy interaction for the range of temperatures covered by the experimental program in the static planar curved pipe, the plots of all versions of static Nusselt number Nu_0 at any prescribed streamwise and angular location consistently increase with the increased Dean number. A limiting condition of zero Dean number could be incurred by zero coolant mass flow, which implies the vanished forced convective capability in static curved channel of $Nu_0=0$. Thus the local static Nusselt number is correlated in the form of

$$Nu_0(X, \theta) = A(X, \theta) \times Dn^{B(X, \theta)} \quad (4)$$

Coefficients A and B are functions of streamwise and angular locations. Table 2 summarizes the correlating coefficients A and B at various streamwise and angular locations.

The streamwise variations of coefficients A and B listed in Table 2 reflect the developing nature of Dean vortices and the inertial force effects on heat transfer, respectively. The variation of A value at a specific streamwise location depicts the influences of

Dean vortices on local heat transfer. The symmetry of Dean vortices thus generates very close values of A coefficients along three pairs of angular edges of 45–315, 90–270, and 135–225 deg. It is interesting to note that the correlating processes performed independently at various angular θ locations result in a similar B value for any streamwise cross-sectioned plane. The physical implication of the constant B value at any X or Φ location is the independency of convective inertial force effect on heat transfer with θ location. The reduction of B value from 0.8 to 0.63 from the plane of $\Phi=0$ to $\Phi=\pi$ indicates the gradually streamwise weakened forced convective inertial effect on heat transfer due to the development of Dean vortices. Over the entire range of Reynolds-Dean numbers and the heat flux levels studied, 93% of the present experimental Nusselt numbers are correlated by Eq. (4) within $\pm 11\%$. Nevertheless, since the Prandtl number effects are absorbed into the coefficients of correlations and are not included as a parameter in the correlations that are developed, the results of this study are essentially limited to dry air. Having established the nonreciprocating heat transfer datum of Eq. (4), the comparative difference of heat transfer in the static and reciprocating planar curved pipe can be examined as follows.

3.2 General Reciprocating Effects. When the planar curved pipe reciprocates, the periodically time-varied reciprocating forces arise to act on fluid flows along the direction orthogonal to the curvature-induced centrifugal force. As a result, the reciprocation could modify the turbulence structure, vorticity, and boundary layers [16] and is likely to trigger a dynamic process of timewise variations in secondary flow cells originated from Dean-type vortices in the curved pipe, similar to that found in the artery of human heart [12]. A combined effect of reciprocating and centrifugal forces on heat transfer is to produce the attendant temporal Nusselt number variations along the reciprocating surface. After taking the averaged value of the timewise local Nusselt number data for a period of 10 s, the time-averaged heat transfer results along the measured angular edges were obtained. Figure 5 shows the circumferential heat transfer variations in a reciprocating planar curved pipe at five cross-sectioned planes of $\Phi=0, \pi/4, \pi/2, 3\pi/4,$ and π . The Nusselt numbers were obtained with nominal Reynolds(Dean) numbers of 14,500(4400) at reciprocating frequencies of 0, 1.25, 1.67, and 2 Hz, which correspond to the pulsating numbers of 0, 0.086, 0.115, and 0.138, respectively. Although the reciprocating Grashof number Gr_p for all the data collected in Fig. 5 is selected with a nominal value of 86,400, the heat transfer results are generated with the finite wall-to-fluid temperature differences that involve certain degrees of buoyancy interactions. The data unraveled in Fig. 5 thus typify the combined pulsating and buoyancy effects on heat transfer. As shown in Fig. 5 for all the Φ planes detected, the increase of pulsating number at Reynolds(Dean) numbers of 14,500(4400) induces a systematic heat transfer reduction from the static level at each angular θ location. The amounts of heat transfer reduction from the static Nusselt number values also increase circumferentially from the inner edge toward the outer edge. Nevertheless, as the reciprocating forces are orthogonal to the centrifugal forces acting toward two side edges of $\theta=90$ and 270 deg, the circumferential heat transfer profiles still remain symmetrical with respect to the plane connecting the inner and outer edges for all the pulsating numbers examined. With regard to the combined $Pu-Gr_p$ effects, all the data batches reveal a consistent data trend that shows that heat transfer is initially impeded from the static level when the pulsating number gradually increases from zero. However, a subsequent heat transfer recovery that could convert the impeding effect into augmenting heat transfer by further increasing the pulsating number is found for several data batches with various $Re(Dn)$ numbers. The values of pulsating number beyond which the heat transfer recovery proceeds are $Re(Dn)$ dependent. This particular phenomenon is attributed to the Pu effect without buoyancy interaction, which will be further addressed when the isolated pulsat-

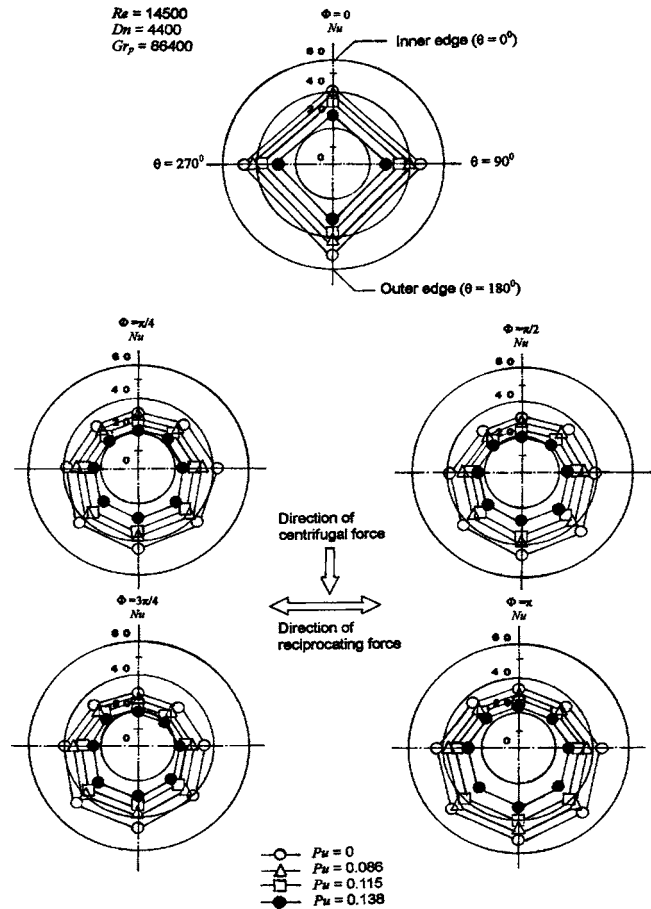


Fig. 5 Typical circumferential heat transfer distributions in a reciprocating coil

ing force effects are discussed parametrically. In order to highlight the reciprocating effect on heat transfer, the relative Nusselt number Nu/Nu_0 is defined by normalizing the reciprocating Nusselt number Nu with the equivalent static Nusselt number Nu_0 obtained at the same Reynolds-Dean number. The data collected in Fig. 5 is converted into the relative Nusselt number Nu/Nu_0 as depicted in Fig. 6. The relative Nusselt numbers at the angular locations of $\theta=0, 90, 180,$ and 270 deg are with similar values along the circumference of cross-sectioned plane of $\Phi=0$. Further downstream over the planes of $\Phi=\pi/4, \pi/2, 3\pi/4,$ and π , the relative Nusselt numbers are no longer identical at various angular θ locations, but circumferentially reduced from the inner edge toward the outer edge even if the symmetrical profiles are retained. In this respect, the most considerable heat transfer reductions at these particular $Re(Dn)$ numbers develop at the outer edge, at which the relative Nusselt number could be reduced to the value about 0.7 at a pulsating number of 0.138. The above observation demonstrates the dependency of $Pu-Gr_p$ coupling effect on the streamwise and angular locations due to the development of Dean vortices. Therefore, in order to identify the thermal physics, which control the heat transfer inside a reciprocating planar curved pipe, the parametric analysis attempted to unravel the isolated and interactive influences of $Re-Dn, Pu,$ and Gr_p on heat transfer are individually performed at each $X(\Phi)$ and θ location.

3.3 Parametric Analysis. The data generated by a heat-transfer experiment inevitably inherits a certain degree of buoyancy interaction as the finite wall-to-fluids temperature difference is required to facilitate heat transfer. As each series of Nusselt numbers for any predefined $Re(Dn)$ and Pu options are generated with five various Gr_p levels, an attempt to unravel the zero-

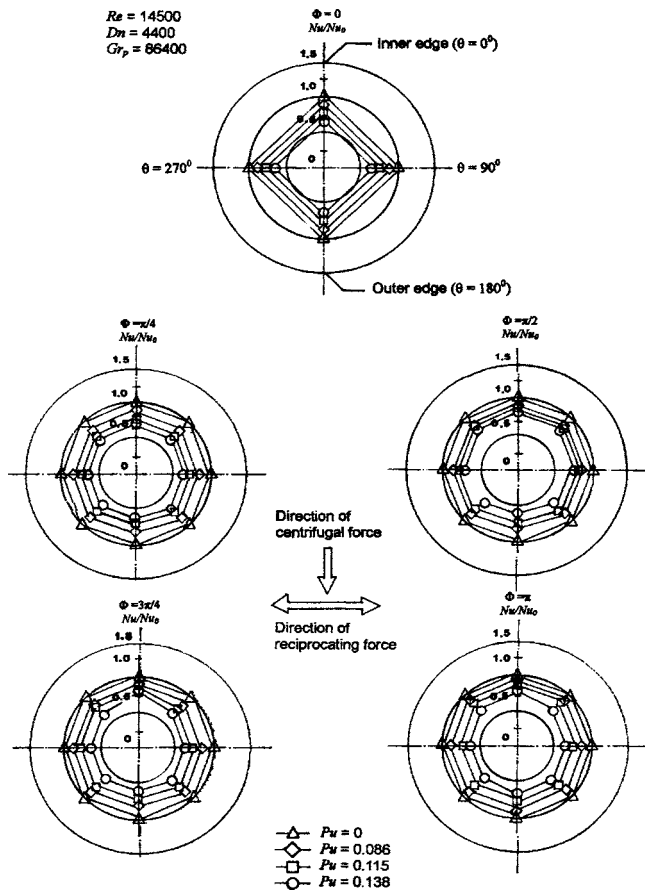


Fig. 6 Circumferential distributions of relative Nusselt number in reciprocating coil

buoyancy heat transfer data is performed by extrapolating these relative Nusselt numbers, Nu/Nu_0 , onto their asymptotic limit of zero Gr_p condition. Each five-point relative Nusselt number Nu/Nu_0 generated at a particular set of $Re(Dn)$ and Pu numbers are plotted against Gr_p . Figure 7 is an illustrative example to demonstrate this data extrapolating process. As shown in Fig. 7, each five-point data trend could be well approximated by a linear function. The relative Nusselt number at $Gr_p=0$ is treated as zero-buoyancy results for each set of $Re(Dn)$ and Pu numbers. In ad-

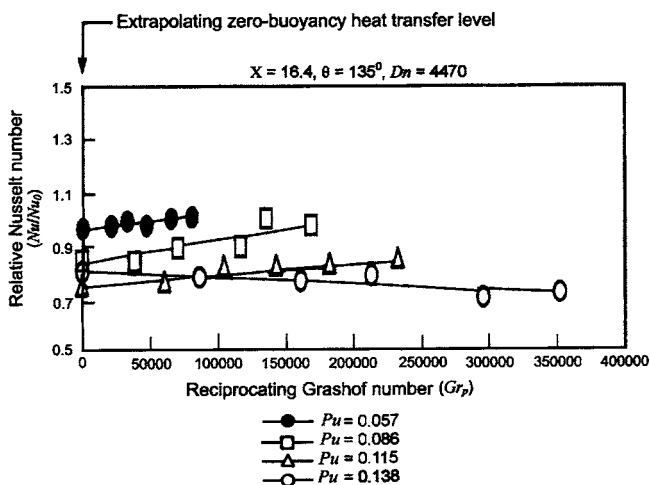


Fig. 7 Extrapolating heat transfer results into asymptotic zero-buoyancy levels

dition to the zero-buoyancy data unraveled by Fig. 7, the increase of Gr_p value permits systematic variation in relative Nusselt number Nu/Nu_0 which reflects the reciprocating buoyancy effect. A review of the entire data using the Nu/Nu_0-Gr_p plots reveals that there are about $\pm 20\%$ variations in relative Nusselt numbers due to the variations of Gr_p values in the parametric test range, although the typical reciprocating buoyancy effects featured in Fig. 7 are consistently followed. The slopes formulated by each five-point heat transfer data series, as demonstrated in Fig. 7, gradually reduce from positive to negative values when the pulsating numbers increase from 0.057 to 0.138. The buoyancy interaction could therefore improve heat transfer when the pulsating number is relatively low, which gradually weakens its improving impact and turns into an impeding effect when the pulsating number systematically increases. Such buoyancy reversal from improving to impeding heat transfer effects is also found at several other locations, but the Pu value above which the reverse buoyancy effect initiates vary with location and $Dn(Re)$ number.

In view of the zero-buoyancy heat transfer data as shown in Fig. 7 with $Dn=4470$, the zero-buoyancy heat transfer levels initially reduce from unity when the pulsating number increases from 0 to 0.115 at $\theta=135$ deg and $X=16.4$. Further increase of the pulsating number from 0.115 to 0.138 results in a subsequent heat transfer recovery for the zero-buoyancy scenario because of the isolated pulsating force effect at this particular spot. This zero-buoyancy heat transfer characteristic typifies all the reciprocating results. The detailed variation manner of zero-buoyancy heat transfer data with pulsating number appears to be functions of Dn and location. Figure 8 typifies the relative heat transfer changes caused by the pulsating force effect alone. At the limiting condition of zero pulsating number, the physical constraint forces the relative Nusselt number Nu/Nu_0 to be unity, which recovers the static forced convection solution correlated by Eq. (4). All the data trends formulated with a fixed Dn number at various locations indicate the initial heat transfer impediments that could lead the Nusselt numbers Nu/Nu_0 to the levels about 0.75. A subsequent heat transfer recovery is followed when the pulsating number further increases. In general, flow conditions with the higher Dean numbers require the higher pulsating numbers to initiate the subsequent heat transfer recovery. The impeding isolated Pu effect on heat transfer has to be particularly considered when the planar curved passage is adopted as a piston cooling measure. Justified by all the data trends typified as in Fig. 8, the heat transfer scenario of $Pu \neq 0$ and $Gr_p=0$, which features the isolated pulsating force effect, is defined as a ξ function having the structure of

$$\xi = 1 + f_a(X, \theta, Dn) \times Pu + f_b(X, \theta, Dn) \times Pu^2 \quad (5)$$

Using a series of cross plots based on Fig. 8, but applied to all the streamwise and angular locations examined, it interpolates a series of curves that correlate the values of f_a and f_b at all the Dean numbers tested. Figure 9 shows the typical example of the manner in which the functional values of f_a and f_b vary with the Dean number at a measurement location. The dependency of functional values f_a and f_b on Dn indicates the intercorrelative $Pu-Dn$ impact on local heat transfer. Justified by all the versions of Fig. 9 for different locations, the quadric function could well correlate the f_a and f_b values as function of Dn with the structure of

$$f_a = a_0(X, \theta) + a_1(X, \theta) \times Dn + a_2(X, \theta) \times Dn^2 \quad (6)$$

$$f_b = b_0(X, \theta) + b_1(X, \theta) \times Dn + b_2(X, \theta) \times Dn^2 \quad (7)$$

The numerically determined curve fits for the a_s and b_s coefficients involved in Eqs. (6) and (7) are summarized in Tables 3 and 4, respectively. It is worth noting that, for a specified curved tube, the Dean number is evaluated as $Re\sqrt{d/D}$ so that the interactive relationships of the $Pu-Dn$ coupling effect described by the a_s and b_s coefficients in Eqs. (6) and (7) implicitly involve the Reynolds number impact.

Having identified the interactive $Pu-Dn$ impact on heat transfer

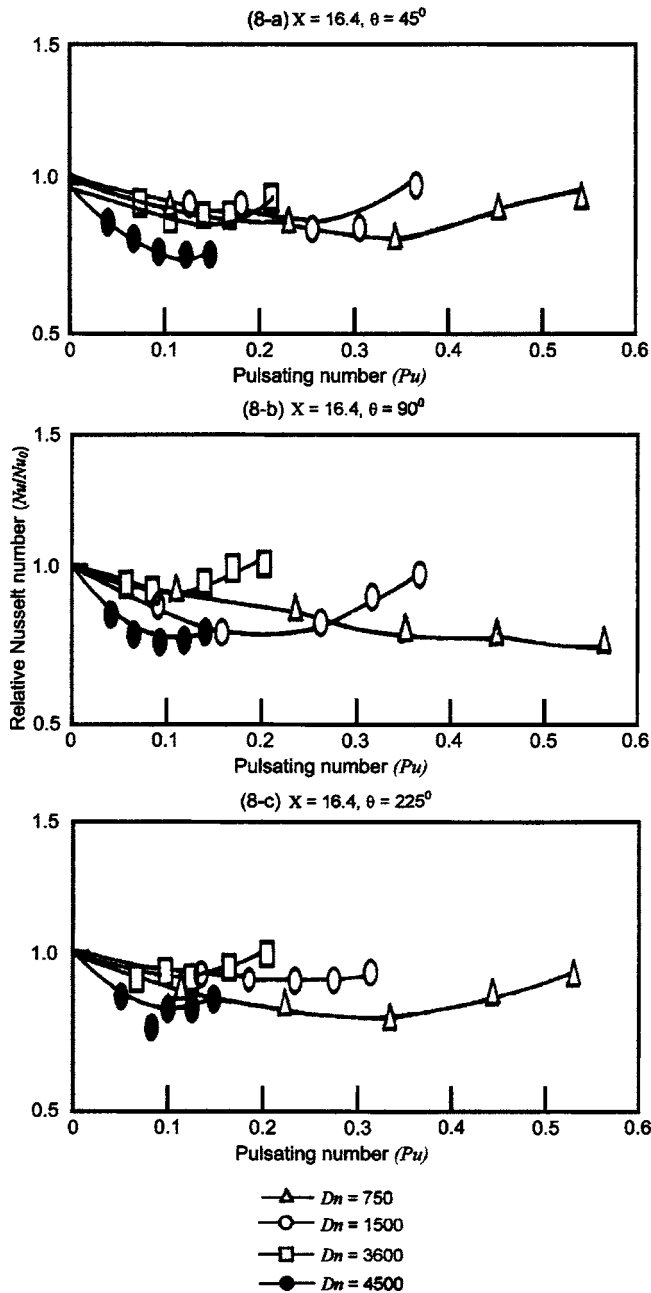


Fig. 8 Typical isolated Pu effect on heat transfer with various Dean numbers

and its correlating function for Eq. (1), the heat transfer modification in association with buoyancy interaction is obtained by subtracting the ξ value from each experimentally measured relative Nusselt number Nu/Nu_0 . This buoyancy-associated heat transfer variation is treated as a ζ value, which varies with Gr_p , $Dn(Re)$, and Pu . When all the ζ values generated at a measurement location for the entire range of $Dn(Re)$ and Pu numbers are plotted against Gr_p , the heat transfer modifications because of reciprocating-buoyancy interaction are controlled within the $\pm 20\%$ data spreads, as described previously. Figure 10 demonstrates the varying manner of ζ value with Gr_p in which all the data is converged into a band with data spreads of about $\pm 20\%$ Nu/Nu_0 . This data-collapsing tendency is consistently followed by all the versions of Fig. 10, but applied to different locations. Therefore, for the present test geometry, the reciprocating-buoyancy effect is considered as a secondary effect. Its influence

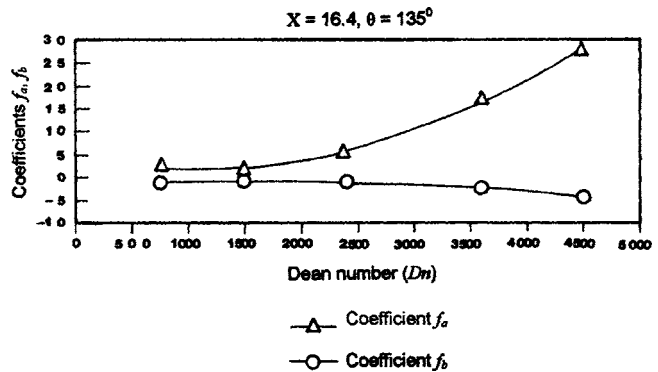


Fig. 9 Variations of f_a and f_b coefficients with Dean number at $X=16.4$ and $\theta=135$ deg

on heat transfer could be approximated by the reciprocating Grashof number alone. However, for conditions with zero Gr_p value, the buoyancy interaction vanishes and the functional value of ζ approaches zero. The data trends for all the location versions of Fig. 10 suggest that the values of ζ function could be reasonably correlated by

$$\zeta = f_c(X, \theta) \times Gr_p + f_d(X, \theta) \times Gr_p^2 \quad (8)$$

The numerically determined curve fits for the f_c and f_d coefficients involved in Eq. (8) are summarized in Table 5. Therefore, the heat transfer in the reciprocating planar curved tube in terms of relative Nusselt number Nu/Nu_0 is evaluated as

$$\frac{Nu}{Nu_0}(X, \theta) = \xi(X, \theta) + \zeta(X, \theta) \quad (9)$$

The attempts to reveal the heat transfer physics and uncouple the interactive Pu - Dn force effects from the buoyancy interaction in the reciprocating planar curved tube through the experimental program with a detailed data analysis have been illustrated. A net result is the empirical correlation of Eq. (9). The overall success of this proposal is indicated in Fig. 11 where all the experimental data are compared to the correlative predictions evaluated by Eq. (9). The maximum discrepancy of $\pm 30\%$ between the experimental and correlating results is achieved for 95% of all the data generated. The range of variation for the relative Nusselt number in the reciprocating planar curved tube because of the combined Pu - $Dn(Re)$ - Gr_p effects is 0.6–1.15, as shown in Fig. 11. The considerable heat transfer reduction as a result of system reciprocating requires particular attention in the design phase in order to avoid the overheating spot developed in a piston. Owing to the complex interactions between the Dean's vortices, the pulsating and buoyancy forces in the developing region of the reciprocating coiled tube, it becomes a formidable task to predict the local heat transfer. However, justified by the achieved accuracy, Eq. (9) could provide the reasonable heat transfer evaluation to assist the design initiative of the cooling networks featured in Fig. 1.

4 Conclusions

This experimental program investigates the heat transfer in a reciprocating planar curved tube along the circumferences of several streamwise locations. A detailed description of the data-correlating process, which complies with the heat transfer physics of the experimentally based observations, reveals the individual and interactive effects of centrifugal, pulsating, and buoyancy forces on heat transfer. In conclusion the following salient points emerge from this study.

- (1) In the static curved tube, the considerable centrifugal effect generates cross-stream Dean vortices that induce the symmetrically circumferential heat transfer variations with lo-

Table 3 Coefficients a_s at measured streamwise and angular locations

		Coefficient $f_a = a_0 + a_1 \times Dn + a_2 \times Dn^2$								
X	Φ		$\theta=0$ deg	$\theta=45$ deg	$\theta=90$ deg	$\theta=135$ deg	$\theta=180$ deg	$\theta=225$ deg	$\theta=270$ deg	$\theta=315$ deg
0	0	a_0	2.8		-0.878		3.77		2.61	
		a_1	2.26×10^{-6}		8.17×10^{-7}		2.54×10^{-6}		1.44×10^{-6}	
		a_2	-3.51×10^{-3}		-5.62×10^{-5}		-5.71×10^{-3}		-2.73×10^{-3}	
8.2	$\pi/4$	a_0	1.5	0.656	6.47	0.19	2.42	-0.978	-1.67	-0.947
		a_1	1.62×10^{-6}	3.00×10^{-6}	3.39×10^{-6}	2.10×10^{-6}	3.67×10^{-6}	2.15×10^{-6}	2.01×10^{-6}	8.85×10^{-7}
		a_2	-2.54×10^{-2}	-3.77×10^{-3}	-8.32×10^{-3}	-1.00×10^{-3}	-5.38×10^{-3}	-1.77×10^{-3}	-5.08×10^{-4}	7.44×10^{-4}
16.4	$\pi/2$	a_0	-3.16	1.78	-2.80	3.55	-1.07	-0.075	6.39	4.68
		a_1	1.04×10^{-7}	1.13×10^{-6}	2.88×10^{-9}	2.22×10^{-6}	2.58×10^{-8}	1.40×10^{-7}	2.42×10^{-6}	1.93×10^{-6}
		a_2	3.61×10^{-3}	6.24×10^{-5}	4.03×10^{-3}	-4.50×10^{-3}	2.61×10^{-3}	3.2×10^{-3}	-6.67×10^{-3}	-5.25×10^{-3}
24.6	$3\pi/4$	a_0	2.01	-1.47	-0.912	-0.92	2.01	8.49	2.33	8.96
		a_1	1.7×10^{-6}	1.99×10^{-6}	7.07×10^{-7}	5.39×10^{-7}	1.08×10^{-6}	3.33×10^{-6}	2.67×10^{-6}	3.67×10^{-6}
		a_2	-2.87×10^{-3}	-5.03×10^{-4}	1.99×10^{-3}	1.65×10^{-3}	-1.62×10^{-3}	-9.44×10^{-3}	-4.52×10^{-3}	-1.09×10^{-2}
32.8	π	a_0	3.8	-4.39	0.301	-0.662	-0.959	3.33	-1.98	-0.467
		a_1	2.84×10^{-6}	1.35×10^{-6}	1.20×10^{-6}	1.31×10^{-6}	1.15×10^{-6}	2.49×10^{-6}	1.22×10^{-6}	8.37×10^{-7}
		a_2	-6.18×10^{-3}	2.98×10^{-3}	-1.07×10^{-3}	-5.38×10^{-4}	1.27×10^{-3}	-1.59×10^{-3}	1.62×10^{-3}	3.55×10^{-3}

cal minimum and maximum values developed on the inner and outer edges at which the heat transfers are, respectively, impeded and enhanced from the Dittus-Boelter levels. Static heat transfer correlation is developed in Eq. (4) that permits the evaluation of local Nusselt number at the measurement locations.

- (2) The extrapolating zero-buoyancy results reveal the interactive Pu-Dn coupling impact, which has shown that the heat transfer is initially reduced from the static condition but recovered at the higher pulsating number. The reciprocating-buoyancy effect in isolation, which is treated as a secondary effect, could improve heat transfer when the pulsating number is relatively low, but gradually weakens its improving impact and turns into an impeding effect when the pulsating number systematically increases. The combined Pu-Dn(Re)- Gr_p effects on heat transfer have caused the relative Nusselt number Nu/Nu_0 falling to the

range of 0.6–1.15. Considerable heat transfer impediments from the static levels could result from the system reciprocation, which required particular attention in the design phase in order to avoid the development of over heating spots in a piston.

- (3) The proposed heat transfer correlation is physically consistent with the experimental observations, which permits the individual and interactive effects of forced convection (Re), centrifugal force (Dn), pulsating force (Pu), and reciprocating buoyancy (Gr_p) in the reciprocating planar curved tube to be taken into account.

Acknowledgment

This work was financially supported by National Science Council, Taiwan, Republic of China, under Grant No. NSC 91-2611-E-022-003. The efforts devoted by two of our research students,

Table 4 Coefficients b_s at measured streamwise and angular locations

		Coefficient $f_b = b_0 + b_1 \times Dn + b_2 \times Dn^2$								
X	Φ		$\theta=0$ deg	$\theta=45$ deg	$\theta=90$ deg	$\theta=135$ deg	$\theta=180$ deg	$\theta=225$ deg	$\theta=270$ deg	$\theta=315$ deg
0	0	b_0	-2.01		-1.07		-1.82		-2.14	
		b_1	-6.50×10^{-7}		-4.58×10^{-7}		-6.10×10^{-7}		-5.25×10^{-7}	
		b_2	2.08×10^{-3}		1.42×10^{-3}		2.14×10^{-3}		2.06×10^{-3}	
8.2	$\pi/4$	b_0	-1.65	-2.12	-2.07	-2.7	-2.39	-1.44	-1.59	-1.68
		b_1	-5.21×10^{-7}	-7.72×10^{-7}	-6.24×10^{-7}	-6.80×10^{-7}	-7.49×10^{-7}	-5.95×10^{-7}	-5.99×10^{-7}	-4.85×10^{-7}
		b_2	1.70×10^{-3}	2.47×10^{-3}	1.91×10^{-3}	2.35×10^{-3}	2.28×10^{-3}	1.77×10^{-3}	1.75×10^{-3}	1.62×10^{-3}
16.4	$\pi/2$	b_0	-0.931	-2.33	-1.93	-2.56	-1.50	-2.10	-2.50	-1.98
		b_1	-2.86×10^{-7}	-4.40×10^{-7}	-3.95×10^{-7}	-6.07×10^{-7}	-2.11×10^{-7}	-2.71×10^{-7}	-4.84×10^{-7}	-4.39×10^{-7}
		b_2	7.59×10^{-4}	1.45×10^{-3}	1.43×10^{-3}	2.16×10^{-3}	6.80×10^{-4}	8.60×10^{-4}	1.70×10^{-3}	1.54×10^{-3}
24.6	$3\pi/4$	b_0	-2.01	-1.13	-1.86	-1.76	-2.42	-2.90	-1.78	-2.98
		b_1	-5.20×10^{-7}	-4.18×10^{-7}	-3.59×10^{-7}	-3.34×10^{-7}	-4.58×10^{-7}	-6.55×10^{-7}	-5.99×10^{-7}	-7.37×10^{-7}
		b_2	1.72×10^{-3}	6.44×10^{-4}	8.55×10^{-4}	1.03×10^{-3}	1.74×10^{-3}	2.30×10^{-3}	1.80×10^{-3}	2.72×10^{-3}
32.8	π	b_0	-1.98	-0.801	-1.85	-2.20	-0.905	-2.58	-1.49	-1.66
		b_1	-6.05×10^{-7}	-3.85×10^{-7}	-4.37×10^{-7}	-5.55×10^{-7}	-2.38×10^{-7}	-4.85×10^{-7}	-4.48×10^{-7}	-2.85×10^{-7}
		b_2	1.98×10^{-3}	6.58×10^{-4}	1.60×10^{-3}	2.09×10^{-3}	3.16×10^{-4}	1.28×10^{-3}	1.17×10^{-3}	4.87×10^{-4}

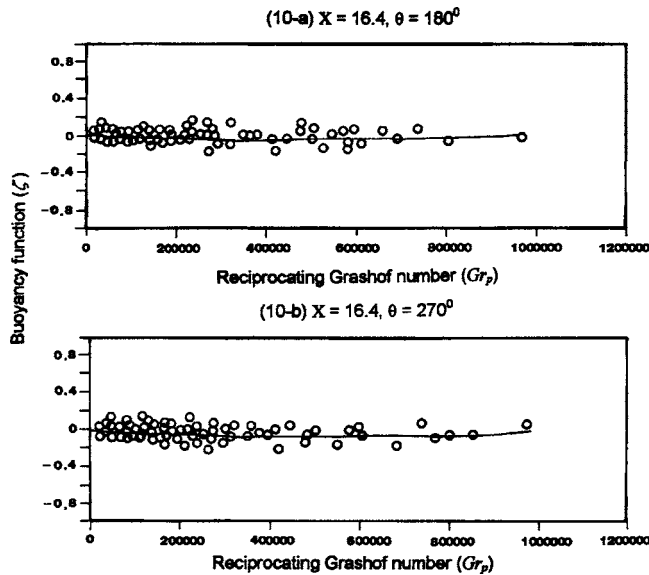


Fig. 10 Typical reciprocating-buoyancy effects on heat transfer

namely, Wen Hsiung Chang and Chih Che Lin toward the data collection and analysis are gratefully acknowledged.

Nomenclature

A, B, a_s, b_s, f_a, f_b = constant coefficients
 a = amplitude of reciprocating motion, m
 Cp_0 = specific heat of coolant at flow entrance, $\text{Jkg}^{-1} \text{K}^{-1}$
 D = diameter of curvature for planar curved tube, m
 d = hydraulic diameter of tube, m
 Dn = Dean number = $\text{Re} \sqrt{d/D}$
 g = gravitational acceleration, ms^{-2}
 Gr = gravitational Grashof number = $g\beta_0\Delta T d^3 / \nu_0^2$
 Gr_p = reciprocating Grashof number = $\omega^2 a \Delta T d^3 / \nu_0^2$
 k_0 = thermal conductivity of coolant at flow entrance, $\text{Wm}^{-1} \text{K}^{-1}$
 Nu = reciprocating Nusselt number = $qd / (T_w - T_f) k_f$
 Nu_0 = static Nusselt number

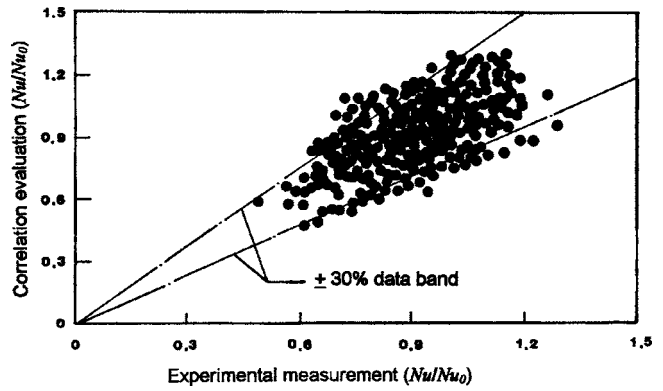


Fig. 11 Comparison of experimental measurements with correlation evaluations

Pu = pulsating number = $\omega d / W_m$
 q = convective heat flux, Wm^{-2}
 Re = Reynolds number = $\rho W_m d / \mu_0$
 T_0 = flow entry temperature, K
 T_f = streamwise flow bulk temperature, K
 T_w = wall temperature, K
 ΔT = wall to flow-bulk temperature difference, K
 U, V, W = dimensionless flow velocity vector with flow velocity normalized by W_m
 W_m = mean through flow velocity, ms^{-1}
 x = streamwise coordinate, m
 z = coordinate in the direction of reciprocation, m
 X, Z = dimensionless coordinates normalized by tube diameter $x/d, z/d$

Greek Symbols

β = thermal expansion coefficient of coolant, K^{-1}
 ρ = coolant density, kg m^{-3}
 τ = dimensionless time = ωt
 μ = dynamic viscosity of coolant, $\text{kg s}^{-1} \text{m}^{-1}$
 ν = kinematic viscosity of coolant, $\text{m}^2 \text{s}^{-1}$
 θ = angular coordinate along the circumference of tube, (deg)
 χ = dimensionless flow pressure = $p / (\rho W_m^2)$
 Φ = angular location along the curvature of planar curved section, rad

Table 5 Coefficients f_c and f_d at measured streamwise and angular locations

		$\xi = f_c(X, \theta) \times Gr_p + f_d(X, \theta) \times Gr_p^2$								
X	Φ		$\theta=0 \text{ deg}$	$\theta=45 \text{ deg}$	$\theta=90 \text{ deg}$	$\theta=135 \text{ deg}$	$\theta=180 \text{ deg}$	$\theta=225 \text{ deg}$	$\theta=270 \text{ deg}$	$\theta=315 \text{ deg}$
0	0	f_c	4.67×10^{-8}		1.61×10^{-7}		1.02×10^{-8}		-2.66×10^{-8}	
		f_d	1.24×10^{-13}		1.78×10^{-13}		1.36×10^{-13}		2.19×10^{-13}	
8.2	$\pi/4$	f_c	-7.81×10^{-7}	-2.98×10^{-7}	-4.73×10^{-8}	-3.75×10^{-7}	2.35×10^{-7}	-2.60×10^{-7}	-1.74×10^{-7}	-2.84×10^{-8}
		f_d	1.46×10^{-12}	8.61×10^{-13}	-7.24×10^{-14}	1.14×10^{-12}	6.96×10^{-13}	8.39×10^{-13}	7.77×10^{-13}	3.91×10^{-13}
16.4	$\pi/2$	f_c	-2.49×10^{-7}	-4.83×10^{-8}	-8.41×10^{-8}	-8.56×10^{-8}	-1.22×10^{-7}	-1.40×10^{-7}	-1.35×10^{-7}	-1.57×10^{-7}
		f_d	6.24×10^{-13}	8.05×10^{-15}	4.85×10^{-13}	2.36×10^{-13}	-1.31×10^{-14}	1.50×10^{-13}	4.26×10^{-14}	1.64×10^{-13}
24.6	$3\pi/4$	f_c	-5.86×10^{-8}	-2.92×10^{-7}	-6.44×10^{-8}	-1.48×10^{-7}	-1.33×10^{-7}	-1.53×10^{-7}	-5.28×10^{-8}	-2.10×10^{-7}
		f_d	2.99×10^{-13}	1.07×10^{-12}	3.62×10^{-13}	4.75×10^{-13}	3.40×10^{-13}	-1.17×10^{-13}	2.35×10^{-13}	2.10×10^{-14}
32.8	π	f_c	-2.19×10^{-7}	-2.61×10^{-7}	-2.75×10^{-7}	-2.88×10^{-7}	-1.67×10^{-7}	-3.47×10^{-7}	-2.85×10^{-7}	-2.36×10^{-7}
		f_d	4.10×10^{-13}	8.86×10^{-13}	6.80×10^{-13}	8.25×10^{-13}	3.07×10^{-13}	1.68×10^{-13}	6.36×10^{-13}	4.85×10^{-14}

ω = angular velocity of rotating disc creating reciprocating motion, rad s^{-1}
 Ψ, ξ, ζ = unknown functions

Subscripts

0 = flow entry condition
 f = local fluids condition

References

- [1] Dean, W. R., 1927, "Note on the Motion of Fluid in a Curved Pipe," *Philos. Mag.*, **4**, pp. 208–223.
- [2] Mori, Y., and Nakayama, W., 1965, "Study on Forced Convective Heat Transfer in Curved Pipes (1st Report, Laminar Region)," *Int. J. Heat Mass Transfer*, **8**, pp. 67–82.
- [3] Mori, Y., and Nakayama, W., 1967, "Study on Forced Convective Heat Transfer in Curved Pipes (2nd Report, Turbulent Region)," *Int. J. Heat Mass Transfer*, **10**, pp. 37–57.
- [4] Mori, Y., and Nakayama, W., 1967, "Study on Forced Convective Heat Transfer in Curved Pipes (3rd Report, Theoretical Analysis Under the Condition of Uniform Wall Temperature and Practical Formulae)," *Int. J. Heat Mass Transfer*, **10**, pp. 681–695.
- [5] Patankar, S. V., Prapat, V. S., and Spalding, D. B., 1974, "Prediction of Laminar Flow and Heat Transfer in Helical Coiled Pipes," *J. Fluid Mech.*, **62**, pp. 539–551.
- [6] Ito, H., 1959, "Friction Factors for Turbulent Flow in Curved Pipes," *ASME J. Basic Eng.*, **81**, pp. 123–124.
- [7] Kalb, C. E., and Seader, J. D., 1983, "Entrance Region Heat Transfer in a Uniform Wall-Temperature Helical Coil With Transition From Turbulent to Laminar Flow," *Int. J. Heat Mass Transfer*, **26**, pp. 23–32.
- [8] Lyne, W. H., 1971, "Unsteady Viscous Flow in Curved Pipe," *J. Fluid Mech.*, **45**, pp. 13–31.
- [9] Zalosh, R., and Nelson, W. G., 1973, "Pulsating Flow in a Curved Tube," *J. Fluid Mech.*, **59**, pp. 693–705.
- [10] Simon, H. A., Chang, M. H., and Chow, J. C. F., 1977, "Heat Transfer in Curved Tubes With Pulsatile Fully Developed Laminar Flow," *ASME J. Heat Transfer*, **99**, pp. 590–595.
- [11] Rabadi, N. J., Chow, J. C. F., and Simon, H. A., 1982, "Heat Transfer in Curved Tubes With Pulsating Flow," *Int. J. Heat Mass Transfer*, **25**, pp. 195–203.
- [12] Zabielski, L., and Mestel, A. J., 1998, "Unsteady Blood Flow in a Helically Symmetric Pipe," *J. Fluid Mech.*, **370**, pp. 321–345.
- [13] Guo, L., Chen, X., Feng, Z., and Bai, B., 1998, "Transient Convective Heat Transfer in a Helical Coiled Tube With Pulsatile Fully Developed Turbulent Flow," *Int. J. Heat Mass Transfer*, **41**, pp. 2867–2875.
- [14] Akhavan, R., Kamm, R. D., and Shapiro, A. H., 1991, "An Investigation of Transition to Turbulence in Bounded Oscillatory Flows, Part 1. Experiments," *J. Fluid Mech.*, **225**, pp. 395–422.
- [15] Jung, W. J., Mangiavacchi, N., and Akhavan, R., 1992, "Suppression of Turbulence in Wall-Bounded Flows by High Frequency Spanwise Oscillations," *Phys. Fluids A*, **4**(8), pp. 1605–1607.
- [16] Baron, A., and Quadrio, M., 1996, "Turbulent Drag Reduction by Spanwise Wall Oscillations," *Appl. Sci. Res.*, **55**, pp. 311–326.
- [17] Choi, K.-S., Clayton, B. R., 2001, "The Mechanism of Turbulent Drag Reduction With Wall Oscillation," *Int. J. Heat Mass Transfer*, **22**, pp. 1–9.
- [18] Chang, S. W., Su, L. M., Morris, W. D., and Liou, T. M., 2003, "Heat Transfer in a Smooth-Walled Reciprocating Anti-Gravity Open Thermosyphon," *Int. J. Therm. Sci.*, **42**, pp. 1089–1103.
- [19] Chang, S. W., 2001, "Forced Convective Heat Transfer of Parallel-Mode Reciprocating Tube Fitted With a Twisted Tape With Application to Piston Cooling," *ASME J. Eng. Gas Turbines Power*, **123**, pp. 146–156.
- [20] Editorial Board of ASME Journal of Heat Transfer, 1993, "Journal of Heat Transfer Policy on Reporting Uncertainties in Experimental Measurements and Results," *ASME J. Heat Transfer*, **115**, pp. 5–6.
- [21] Dittus, F. W., and Boelter, L. M. K., 1930, *University of California Berkeley, Univ. Calif. Publ. Eng.*, **2**, p. 443.

Hydrogen Fueled Spark-Ignition Engines Predictive and Experimental Performance

Hailin Li

Ghazi A. Karim¹

e-mail: karim@enme.ucalgary.ca

Department of Mechanical and Manufacturing
Engineering,
The University of Calgary,
Calgary T2N 1N4, Canada

Hydrogen is well recognized as a suitable fuel for spark-ignition engine applications that has many unique attractive features and limitations. It is a fuel that can continue potentially to meet the ever-increasingly stringent regulations for exhaust and greenhouse gas emissions. The application of hydrogen as an engine fuel has been tried over many decades by numerous investigators with varying degrees of success. However, the performance data reported often tend not to display consistent agreement between the various investigators, mainly because of the wide differences in engine type, size, operating conditions used, and the differing criteria employed to judge whether knock is taking place or not. With the ever-increasing interest in hydrogen as an engine fuel, there is a need to be able to model extensively various features of the performance of spark ignition (S.I.) hydrogen engines so as to investigate and compare reliably the performance of widely different engines under a wide variety of operating conditions. In the paper we employ a quasidimensional two-zone model for the operation of S.I. engines when fueled with hydrogen. In this approach, the engine combustion chamber at any instant of time during combustion is considered to be divided into two temporally varying zones: a burned zone and an unburned zone. The model incorporates a detailed chemical kinetic model scheme of 30 reaction steps and 12 species, to simulate the oxidation reactions of hydrogen in air. A knock prediction model, developed previously for S.I. methane-hydrogen fueled engine applications was extended to consider operation on hydrogen. The effects of changes in operating conditions, including a very wide range of variations in the equivalence ratio on the onset of knock and its intensity, combustion duration, power, efficiency, and operational limits were investigated. The results of this predictive approach were shown to validate well against the corresponding experimental results, obtained mostly in a variable compression ratio CFR engine. On this basis, the effects of changes in some of the key operational engine variables, such as compression ratio, intake temperature, and spark timing are presented and discussed. Some guidelines for superior knock-free operation of engines on hydrogen are also made.

[DOI: 10.1115/1.2055987]

Introduction

The ever-increasing need to improve air quality and the economy of fuel-consuming devices has led to a series of major changes in engine design, hardware, and fuel composition that are aimed at reducing exhaust emissions and improving the work production efficiency [1]. One of these improvements is the employment of nonconventional alternative fuels, such as natural gas or hydrogen. These can offer opportunities to achieve a cleaner exhaust gas and reductions in greenhouse gas emissions.

Hydrogen has long been recognized as a fuel having some unique and highly desirable combustion properties for applications in S.I. engines, such as a wide flammable mixture range, low ignition energy, and very fast flame propagation rates [2,3]. These attractive features made it possible to operate conventional S.I. engines on very lean mixtures so as to achieve high-power production efficiencies with low NO_x , negligible amounts of CO , CO_2 , and HC when the contribution of the oxidation of lubricating oil is considered [4]. However, to date hydrogen has tended not to live up to its full potential as an engine fuel. Apart from economic factors such as the high cost of the mass production of pure H_2 , there are still some lingering obstacles that limit the wide application of hydrogen in S.I. engines. For example, the operation of

H_2 as S.I. engine fuels tends to involve occasionally backfire, preignition [5,6] and the onset of knock [7]. The former is due mainly to the low ignition energy needed to ignite H_2 -air mixtures, the presence of hot residual gas, and hot spots including hot deposits on the surface of the combustion chamber while the onset of knock is associated with uncontrolled autoignition of the unburned end gas mixture resulting from high temperatures and the very fast flame propagation rates of H_2 in S.I. engine applications. Other limitations include the high NO_x emissions with mixtures around the stoichiometric and low-power output associated with lean operation, which is employed usually to avoid the onset of knock and provide also improved fuel economy and achieve low NO_x emissions. Among these lingering limitations, the onset of knock remains the most serious [7–9].

There are distinct operational limits beyond which satisfactory engine performance cannot be maintained due to irregular flame propagation leading to increased emissions, partial oxidation, and unacceptably high cyclic variations [10]. A successful approach we followed earlier to estimate the values of the operational mixture limits of the engine is based on the assumption that at the limit the combustion duration becomes exceedingly long.

The operation of S.I. engines on hydrogen was attempted over the decades only on a limited basis displaying varying degrees of success [3]. The engine performance data reported tend to display often inconsistencies among the various investigators mainly due to the widely different engine types and sizes, operating conditions, and the criteria employed to judge whether knock is taking place or not. Often, the tendency was to focus on the performance of single cylinder engines over narrow operating conditions. There

¹Author to whom correspondence should be addressed.

Contributed by the Internal Combustion Engine Division of ASME for publication in the JOURNAL OF ENGINEERING FOR GAS TURBINES AND POWER. Manuscript received by the ICE Division September 16, 2003; final revision received July 23, 2004. Associate Editor: D. Assanis.

is a need to obtain for any engine over a wide variety of operating conditions consistent data for the onset of knock, changes in the combustion duration, energy release rates, power production, efficiency, lean operational limits, and exhaust emissions. This cannot be accomplished solely by experiment; that requires much capital and time resources. Accordingly, reliable modeling approaches offer, in principle, the opportunity to produce comprehensively the results needed while requiring significantly less investment of time and money. However, attempts to model S.I. engine, performance with hydrogen, in comparison to other fuels, tend to remain quite limited [11–13].

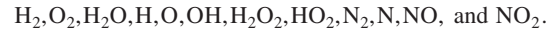
In this paper we employ a two-zone quasidimensional model developed for the prediction of the main features of the performance of a hydrogen fueled S.I. engine. The model was validated against some experimental results obtained earlier. The effects of changes in key operating variables such as the compression ratio, intake temperature, and spark timing on the knock limiting equivalence ratios were established. Some of the other parameters considered included the optimization of spark timing for the maximum indicated power output and efficiency and for the avoidance of the onset of knock while maintaining high thermal efficiency values.

Model Development for Hydrogen Fueled Engines

Modeling S.I. Engine Performance Including Knock (MEPIK). The MEPIK is a two-zone and quasidimensional model that predicts the performance of S.I. gas engines, including the onset of knock and establishing its intensity, whenever it occurs [12]. The homogeneous charge of the cylinder is assumed at any instant during turbulent flame propagation combustion to be divided into two zones of burned products and unburned reactants that include the end gas region. The intake stroke is simulated while accounting for the presence of residual gases. The simulation for the other strokes is based on the state of the mixture at the end of the intake stroke. Changes in the unburned reactants are evaluated up to the time of spark ignition while accounting for the heat transfer between the fuel mixture and surrounding walls. An appropriate combustion energy release pattern over the entire combustion period is employed to simulate the combustion and the corresponding energy release processes after ignition. Following the examination of a large number of experimental data for a variety of operating conditions, it was shown that a triangular function would be quite adequate for the present modeling approach [14]. The combustion duration and lag time model is validated against the experimental data. The composition of the burned products following flame propagation is calculated while accounting for thermodynamic dissociation. In the absence of specific information about heat transfer from the two combustion

zones to the outside walls with hydrogen combustion, a formulation [15] that was based on experimental observations made in hydrocarbon fueled engines was incorporated in the modeling.

In order to monitor at any instant during flame propagation the likelihood of the onset of knock due to autoignition of the unburned end gas, the reactivity of the temporally changing end gas region is evaluated employing a sufficiently detailed description of the chemical reaction kinetics of the unburned mixture. For hydrogen–air mixtures, this modeling involves 30 reactions, as shown in the Appendix, Table 1, selected from the reaction scheme of CH₄ reported earlier [12] and the following 12 species:



The net rates of formation and consumption of each species of the reactive end gas charge are calculated at every instant of time. The energy released by these oxidation reactions of the end gas ahead of the propagating flame is established and expressed as $[m_{u,t} * (h_{sp} - h_t)]$, where h_{sp} and h_t are the specific enthalpy of the unburnt end gas at the time of spark passage and at the instant time “ t ,” respectively. $m_{u,t}$ is the corresponding remaining instantaneous mass of the end gas at the time “ t .”

The model can predict engine performance parameters that include temporal variations in the value of a knock criterion, cylinder pressure, and mean temperatures of the two zones. This could be done for different mixture equivalence ratios, engine speeds, intake temperatures, intake pressures, and spark timings while accounting for the effects of changes in some design parameters such as compression ratio, engine size, and valve timing. Without the need to adjust some features of the kinetic scheme so as to provide good agreement with experiment, the model could predict satisfactorily the onset of knock due to the autoignition of the end gas and engine performance parameters, such as the indicated power production and thermal efficiency.

The Knock Prediction Model. In S.I. engine applications, the onset of knock is a prime limitation that needs to be avoided while maintaining superior performance. A knock prediction model was developed earlier based on establishing whether autoignition is to take place or not within the end gas region during the flame propagation period. The model with experimental verification showed that the onset of the borderline knock was encountered when the current value of the criterion “ K_n ” just exceeded a critical value. K_n is a function defined as the calculated, temporally varying, and accumulated energy released within the varying end gas mass, resulting from the preflame-front oxidation reactions per unit of the instantaneous cylinder volume, normalized relative to the corresponding total amount of energy to be released through normal flame propagation per unit of cylinder swept volume [12], i.e.:

$$\text{Knock Criterion } K_n = \frac{\frac{\text{total energy released by reactions of the current end gas at time “}t\text{”}}{\text{current cylinder volume}|_t}}{\frac{\text{total energy of the whole charge to be released by flame propagation}}{\text{initial cylinder volume}|_{t_0}}} \quad (1)$$

This function also represents the increase in cylinder pressure due to the prearrival of the flame-front oxidation reaction activity within the instantaneous size of the end gas relative to the mean effective combustion pressure reckoned with respect to the initial cylinder volume. Accordingly, the value of K_n is an integrated function of the normalized energetic consequences of any preflame-front oxidation energy release of the end gas.

Normally, for a S.I. engine when operated with most common fuels at moderate compression ratios, the earliest onset of knock,

if it is to take place, is usually associated with mixtures around the stoichiometric region. The knock criterion at any crank angle during flame propagation can be shown to approximate to the following equation [12,13]:

$$K_n = \frac{h_{sp} - h_t}{\Delta h_0} \times \frac{m_{u,t}}{m_0} \times (\text{CR} - 1) \quad (2)$$

Such a relatively simple modeling approach that incorporates detailed chemical kinetics calculations to evaluate “ h_t ,” was shown

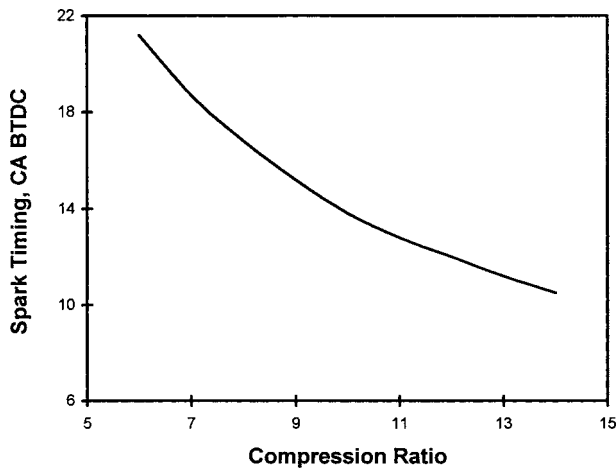


Fig. 1 The variation of spark timing with changes in compression ratio employed at 900 rev/min

to be capable of predicting successfully the onset of knock in CH_4 fueled S.I. engines while H_2 and C_3H_8 present as additives [12,13] when the critical value of K_n was just over unity (1.0–1.5). However, for engine operation with pure hydrogen, knock may be encountered over a wide range of equivalence ratio values on either side of the stoichiometric value and with very widely varying flame propagation rates. To account for these differences, the definition of K_n was extended so that the energy release is normalized also relative to that of the stoichiometric mixture while additionally the combustion duration is normalized relative to a typical constant value $\Delta\theta_{c,\text{ref}}$, such as that commonly observed for completing flame propagation with the common fuel methane (e.g., 50°C A), as shown in Eq. (3).

$$K_n = \frac{h_{\text{sp}} - h_t}{\Delta h_0} \times \frac{m_u}{m_0} \times (\text{CR} - 1) \times \frac{\Delta h_0}{(\Delta h_0)_{\text{stoich}}} \times \frac{\Delta\theta_{c,\text{ref}}}{\Delta\theta_{c,f.c.}} \quad (3)$$

This modified knock criterion approach is based on the examination of the autoignition process simulated by the chemical kinetic model stated earlier while considering the factors that would affect the intensity of knock once it occurs. These include the unburned mixture equivalence ratio, compression ratio, mixture energy density, and combustion duration. This model would be

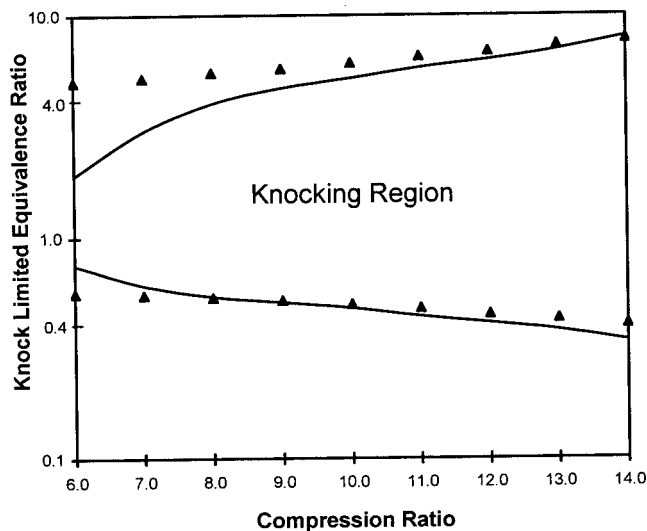


Fig. 2 A comparison of the predicted knock limited equivalence ratio with those determined experimentally (log scale). $T_{\text{in}}=311\text{ K}$. Triangle: Experimental data; solid line: prediction data.

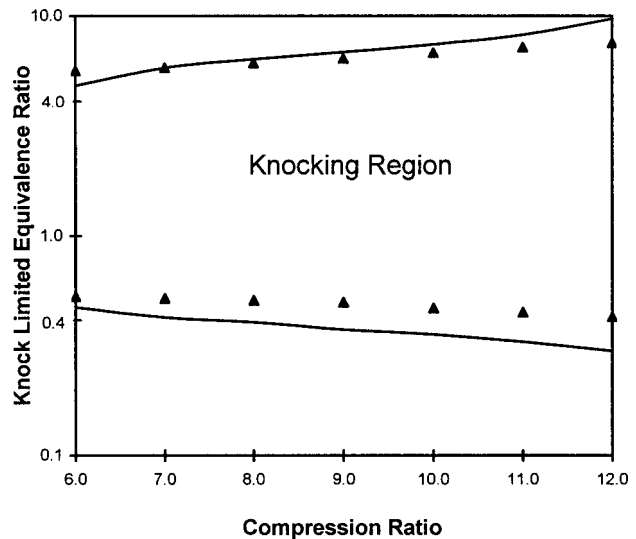


Fig. 3 A comparison of the predicted knock limited equivalence ratio with those determined experimentally (log scale). $T_{\text{in}}=345\text{ K}$. Triangle: experimental data; solid line: prediction data.

shown to be able to simulate the performance including the onset of knock of S.I. engines operated on hydrogen.

Validation and Results

The modification to the model was incorporated for simulating the performance, including the onset of knock, of a variable compression ratio, open throttle, single cylinder S.I., CFR engine of 82.6 mm bore, and 114 mm stroke operated on hydrogen. The prediction results were validated against the corresponding experimental results. In the experiments, the spark timing, which is a very important influencing variable, was made to change with the increase in compression ratio, as shown in Fig. 1. This is consistent with that employed earlier for the knock rating of a range of fuels, and it is similar to the ASTM recommendation [7]. Obviously, other forms of variations could have been employed. The experimental values of the limits were established from the observed changes in the pressure temporal development records over a large number of cycles and during light audible knocking noise

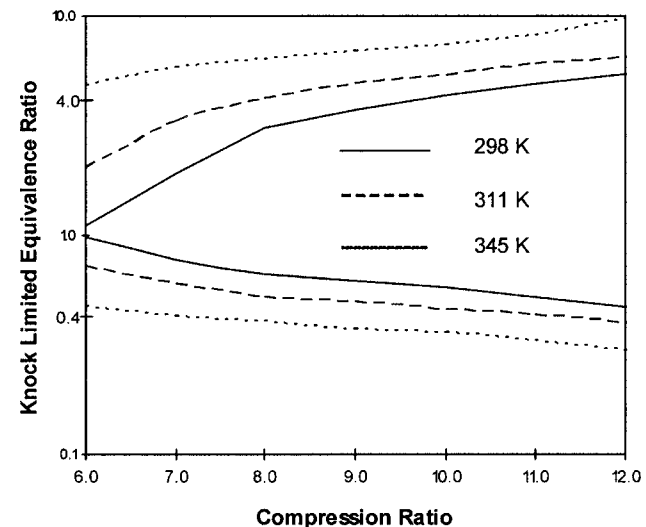


Fig. 4 Typical variation (log scale) of the predicted knock limited equivalence ratio with changes in the compression ratio for three intake temperatures. $P_{\text{in}}=100\text{ kPa}$.

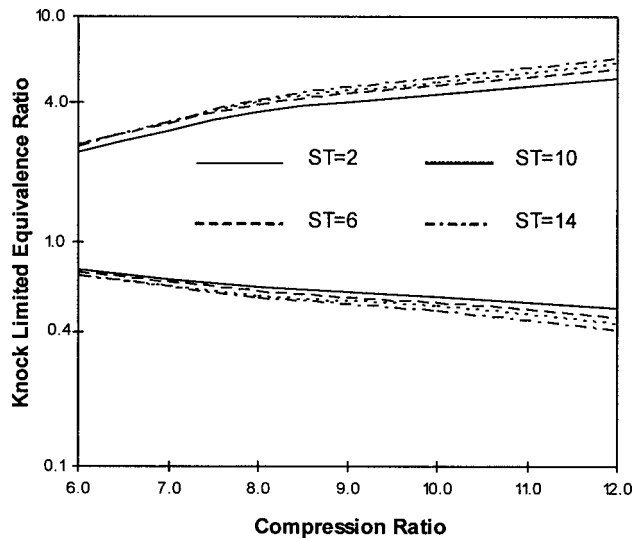


Fig. 5 Typical variation (log scale) of predicted knock-limited equivalence ratio with changes in the compression ratio for a range of spark timings (CA BTDC). $T_{in}=311$ K, $P_{in}=100$ kPa.

[7,9]. Also, during the knock rating of H_2 , the occurrence of pre-ignition was not encountered in this engine and the specific operating conditions employed. The knock observed was attributed to autoignition, which always occurred well after the initiation of the flame by the spark.

The predicted lean and rich knock limited equivalence ratios are shown plotted logarithmically with the corresponding experimental values in Fig. 2 and Fig. 3, displaying relatively good agreement. The less satisfactory agreement at the very low compression ratios and low intake temperature for the less practically important rich knock limit is probably the result of less adequate accounting for the increased effects of residuals and heat transfer on the onset of knock and the high rates of pressure rise resulting from the very fast flame propagation occurred mainly before top dead center when operated at advanced spark timing, as shown in Fig. 1.

The effects of changing some of the key operating variables on engine performance parameters were predicted. On this basis, it

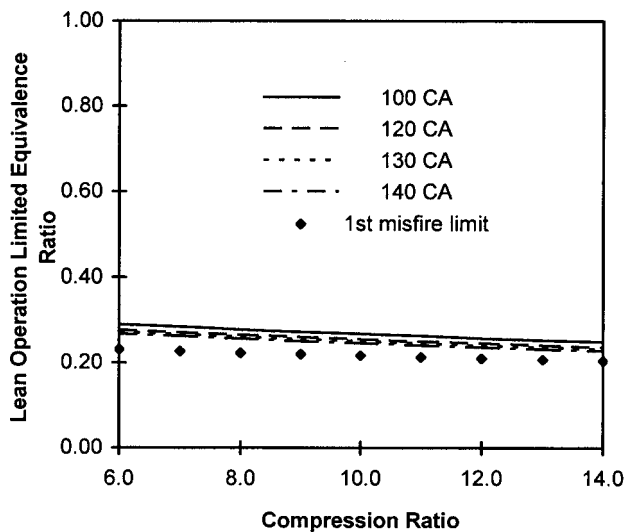
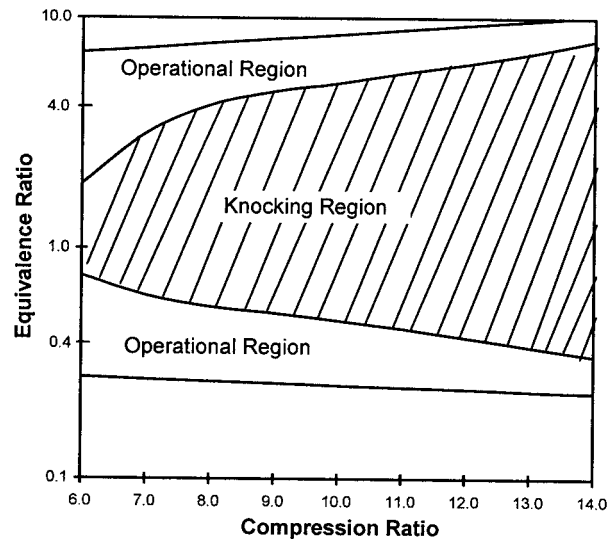
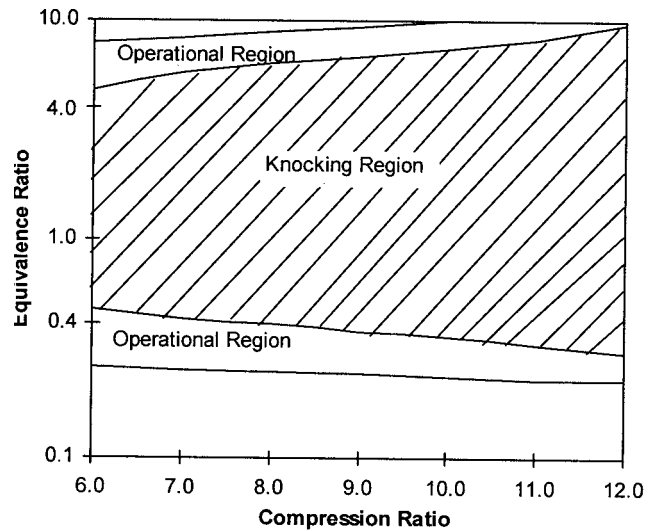


Fig. 6 Variation of the operation limited equivalence ratio predicted by using different values of the combustion duration, with changes in compression ratio, $T_{in}=311$ K, $P_{in}=100$ kPa. The experimentally determined first misfire limit values are also shown.



(a) $T_{in}=311$ K



(b) $T_{in}=345$ K

Fig. 7 The variation of the operational and knocking regions with compression ratio

was confirmed that the incidence of knock is the most important consideration in hydrogen engine operation. Figure 4 shows typically the effects of changing the compression ratio on the knock limits for different intake mixture temperatures, indicating that both the compression ratio and intake temperature are key variables that control the incidence of knock.

Retarded spark timing though lowers the fuel economy contributes to the suppression of the onset of knock. However, as shown in Fig. 5, the effects of retarding the spark timing additionally to what was employed and shown in Fig. 1, tended to produce in comparison a lesser effect than with changing the compression ratio or intake temperature.

The operation of the S.I. engine is normally limited by unacceptably slow flame propagation due to the excessively lean or rich equivalence ratio that would cause failure. Accordingly, apart from the knock limits, these operationally limiting equivalence ratios, known as operational limits, are also important parameters. In this research, the predicted combustion duration was used to estimate the operational limit on the basis that the limits are associated with combustion duration values in excess of 120° C A. Figure 6 shows a comparison among the operational limit values

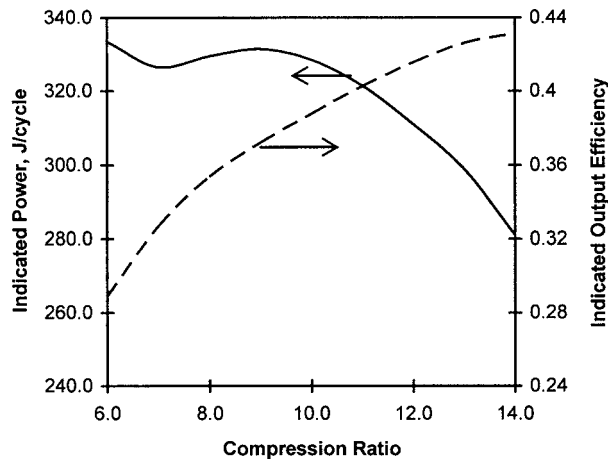


Fig. 8 Typical variations of the engine indicated power production and its efficiency at knock borderline operation with changes in compression ratios. $T_{in}=311$ K, $P_{in}=100$ kPa. Spark timing as shown in Fig. 1.

when predicted on this basis of different values of the combustion duration with those of the first misfire limits, as observed experimentally. It can be seen that the predicted values of the operational limits are very close for different limiting values of the combustion duration that were longer than 120°C A . This value of the limit would indicate, as expected, that flame propagation needs to be completed well before the instant of the exhaust valve opening.

For the satisfactory operation of a S.I. engine on pure hydrogen, a sufficiently wide operational mixture region is needed, especially for lean mixture operation when a high compression ratio is employed. This mixture region, which is bounded by the knock limit and the corresponding operational limit, narrows with increasing the compression ratio and/or intake temperature, as shown in Fig. 7. This would indicate that the S.I. engine, when operated on hydrogen, would not be run at very high compression ratios, even though the onset of knock could be avoided and high efficiency could be achieved with lean operation.

The main aim of H_2 engine control is to ensure high-power production efficiency and low NO_x emissions while producing superior power production. This would indicate that operation

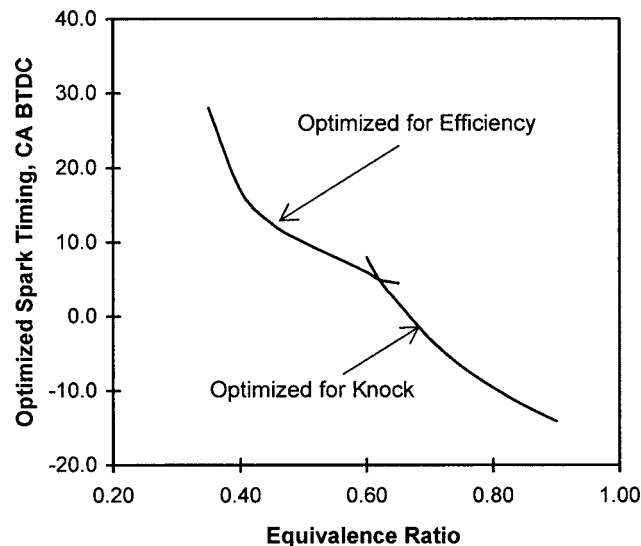


Fig. 9 Typical variation of optimized spark timing with changes in equivalence ratio at constant spark compression ratio. $\text{CR}=8$, $T_{in}=311$ K, $P_{in}=100$ kPa.

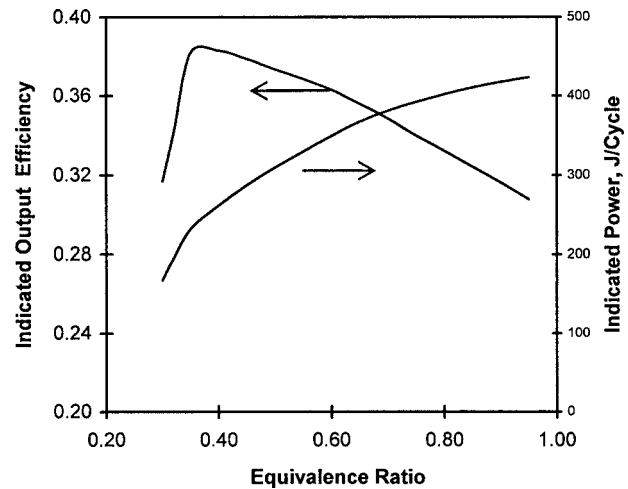


Fig. 10 Variation of engine performance with changes in equivalence ratios for optimized spark timing. $\text{CR}=8$, $T_{in}=311$ K, $P_{in}=100$ kPa.

close to borderline knock is desirable to obtain high-power output. Figure 8 shows typically the power output and efficiency values at a borderline knock operation for a range of values of compression ratio. It can be seen that the engine achieves a power production peak at a moderate value of compression ratio, but high efficiency values are achieved at high compression ratios. Generally, increasing the compression ratio tends to increase engine power production and efficiency. But the corresponding decrease in the equivalence ratio required to avoid the onset of the knock, tends to decrease the power output and increase the efficiency mainly due to the leaner operation. The necessary changes to the spark timing also contribute to this trend, since spark timing needs to be retarded at high compression ratios so that the combustion takes place near the top dead center.

Other than power production, to achieve a high value of efficiency is becoming increasingly important because of the need to reduce the relative hydrogen consumption. Spark timing control can be another effective approach to optimize engine performance. Such an optimization tends to be more complicated for hydrogen operation. This is because of the very wide variation possible in the flame propagation rates of the hydrogen-air mix-

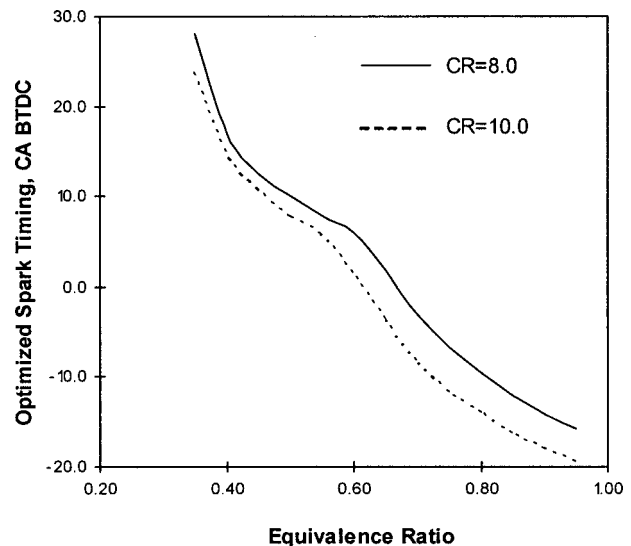


Fig. 11 A comparison of the typical variation of the optimized spark timing with changes in equivalence ratios and compression ratios. $T_{in}=311$ K, $P_{in}=100$ kPa.

tures and the need to avoid the onset of knock on the one hand and combustion failure on the other while aiming simultaneously at ensuring optimum engine performance [16]. Retarded spark timing is selected to avoid knock when the engine is running around the stoichiometric region where the onset of knock is the major concern, as shown in Fig. 9. However, the spark timing can be optimized on power production efficiency when knock-free operation was expected such as at a very lean operation. Figure 10 shows the indicated power output and efficiency variations with an equivalence ratio while using the optimized spark timing shown in Fig. 9. For example, the value of the peak power production efficiency for the single cylinder CFR engine being modeled is about 38%, achieved for a lean operation of $\Phi=0.36$ at a speed of 900 rev./min., open throttle and normally aspirated with ambient intake temperature.

The effect of changes in the compression ratio on the optimized spark timing is also analytically examined and shown typically in Fig. 11. It can be seen that for the values of the compression ratio considered, the spark timing must be retarded much more for operation around stoichiometric than for lean mixtures. This may be attributed to the more serious effect of the increase in compression ratio on autoignition reaction rates and the resulting knock intensity than that on the flame propagation rates.

Conclusion

A two-zone quasidimensional model developed earlier [12,13] for methane-hydrogen engine operation was modified and extended to consider hydrogen operation over a wide equivalence ratio range. The modified model was shown to be capable of predicting engine performance, including the onset of knock. Predicted results agreed well with the experimental values.

The avoidance of the incidence of knock is a most important consideration in H_2 engine operation. The compression ratio and

intake temperature are the main parameters that affect the knock-limited equivalence ratio while the effect of spark timing tends to be, in comparison, less effective. The knock-free operational mixture region tends to narrow significantly with increasing compression ratio and intake temperature. This represents a practical limitation to the improvement of power and efficiency of hydrogen engines.

It was shown that a combustion duration with an assumed length of 120°CA can be used for predicting the operational limit of the S.I. engines.

Acknowledgment

The contributions of Dr. S. R. Klat, Dr. J. Gao, Dr. A. A. Attar, and Dr. S. O. Bade Shrestha to this work are appreciated. The funding of the Canadian Natural Science and Engineering Research Council (NSERC) is also appreciated.

Nomenclature

- CR = compression ratio
- h_{sp} = enthalpy of the mixture at spark timing, kJ/kg
- h_t = enthalpy of the mixture at any instant "t," kJ/kg
- K_n = knock criterion
- m_u = mass of the end gas at any instant "t," kg
- m_0 = mass of the fresh charge, kg
- $\Delta\theta_c$ = Combustion duration, °CA
- $\Delta\theta_{c,f.c.}$ = combustion duration for fast flames, °CA
- $\Delta\theta_{c,ref}$ = reference combustion duration, °CA
- Δh_0 = effective heating value of the fresh charge, kJ/kg
- Φ = equivalence ratio
- Φ_{op} = operation limited equivalence ratio
- Φ_{kn} = knock limited equivalence ratio

Appendix

Table 1 The chemical kinetic scheme. Reaction rates units are in $m^3 \text{ mol s}^{-1}$.

No.	Reaction	Forward reaction constants			Backward reaction constants		
		A_f	B_f	E_f	A_b	B_b	E_b
1	$H_2+OH=H+H_2O$	2.20E+07	0	2.16E+04	9.30E+07	0	8.52E+04
2	$H_2+O=H+OH$	1.80E+04	1.00	3.71E+04	8.30E+03	1.00	2.90E+04
3	$H_2+O_2=HO_2+H$	5.00E+06	0.46	2.24E+05	6.60E+07	0	8.93E+03
4	$H_2+HO_2=H+H_2O_2$	7.24E+05	0	7.82E+04	1.70E+06	0	1.57E+04
5	$H+HO_2=OH+OH$	1.50E+08	0	4.19E+03	1.53E+04	0.84	1.42E+05
6	$H+H+M=H_2+M$	1.83E+06	-1.00	0.00E+00	6.28E+08	0	4.01E+05
7	$H+OH+M=H_2O+M$	3.60E+01	0	0.00E+00	8.30E+11	0	5.01E+05
8	$H+O_2+M=HO_2+M$	8.00E+05	-1	0.00E+00	2.40E+09	0	1.90E+05
9	$O+O+M=O_2+M$	4.70E+03	-0.28	0.00E+00	5.10E+09	0	4.80E+05
10	$OH+OH+M=H_2O_2+M$	3.20E+10	-2	0.00E+00	1.69E+18	-2	2.00E+05
11	$HO_2+OH=H_2O+O_2$	1.50E+07	0	0.00E+00	1.41E+10	-0.56	2.87E+05
12	$H_2O+O=OH+OH$	1.50E+04	1.14	7.21E+04	1.50E+03	1.14	0.00E+00
13	$H_2O_2+O_2=HO_2+HO_2$	1.00E+06	0	1.67E+05	2.50E+05	0	-5.20E+03
14	$H+H_2O_2=H_2O+OH$	1.00E+07	0	1.50E+04	3.34E+06	0	3.12E+05
15	$H+O_2=O+OH$	5.13E+10	-0.82	6.89E+04	1.30E+07	0	0.00E+00
16	$H_2O_2+OH=H_2O+HO_2$	1.00E+07	0	7.50E+03	2.80E+07	0	1.38E+05
17	$H+O+M=OH+M$	1.00E+04	0	0.00E+00	8.00E+13	-1.00	4.34E+05
18	$HO_2+O=O_2+OH$	2.00E+07	0	0.00E+00	2.81E+08	-0.33	2.14E+05
19	$H_2+O_2=OH+OH$	2.50E+06	0	1.63E+05	6.00E+04	0	8.54E+04
20	$H_2O_2+O=HO_2+OH$	2.80E+07	0	2.68E+04	9.51E+06	0	8.67E+04
21	$H+HO_2=O+H_2O$	3.00E+07	0	7.20E+03	2.95E+07	0	2.45E+05
22	$NO+N=O+N_2$	3.27E+06	0.30	0.00E+00	1.80E+06	0	3.17E+05
23	$N+O_2=O+NO$	1.10E+07	0	3.13E+04	2.10E+06	0	1.67E+05
24	$N+OH=H+NO$	3.80E+07	0	0.00E+00	1.20E+08	0	2.02E+05
25	$NO+HO_2=NO_2+OH$	8.70E+05	0	0.00E+00	6.00E+06	0	3.35E+04
26	$NO+O+M=NO_2+M$	5.80E-02	1	-3.58E+04	1.10E+10	0	2.72E+05
27	$NO_2+O=NO+O_2$	1.00E+07	0	2.51E+03	2.20E+06	0	1.93E+05
28	$NO_2+H=NO+OH$	2.90E+07	0	0.00E+00	3.50E+05	0	1.23E+05
29	$NO+NO=N_2+O_2$	1.41E+09	0	3.66E+05	2.85E+10	0	5.36E+05
30	$NO+NO+O_2=N_2+NO_2$	4.90E-06	1.00	2.51E+03	4.00E+06	0	1.13E+05

References

- [1] Nishizawa, K., Momoshima, S., Koga, M., and Tsuchida, H., 2000, "Development of New Technology Targeting Zero Emissions for Gasoline Engine," SAE Paper 2000-01-0890.
- [2] King, R. O., Hayes, S. V., Allan, A. B., Anderson, R. W. P., and Walker, E. J., 1958, "The Hydrogen Engine: Combustion Knock and the Related Flame Velocity," *Transaction of the Engg. Inst. of Canada (E.I.C.)*, **2**, pp. 143–148.
- [3] Karim, G. A., 2003, "Hydrogen as a Spark Ignition Engine Fuel," *Int. J. Hydrogen Energy*, **28**, pp. 569–577.
- [4] Furuhashi, S., and Hiruma, M., 1977, "Some Characteristics of Oil Consumption Measured by Hydrogen Fuelled Engine," *ASLE Trans.*, **34**, pp. 665–675.
- [5] Watson, H. C., and Milkens, E. E., 1978, "Some Problems and Benefits from the Hydrogen-Fuelled Spark Ignition Engine," *Proceedings of the 13th Inter-society Energy Conversion Engineering Conference*, Paper 789212, pp. 1170–1177.
- [6] Kondo, T., Lio, S., and Hiruma, M., 1997, "A Study on the Mechanism of Backfire in External Mixture Formation Hydrogen Engines-About Backfire Occurred by Cause of the Spark Plug," SAE Paper 971704.
- [7] Karim, G. A., and Klat, S. R., 1966, "The Knock and Autoignition Characteristics of Some Gaseous Fuels and Their Mixtures," *J. Inst. Fuel*, **39**, pp. 109–119.
- [8] Rosseel, E., and Sierens, R., 1997, "Knock Detection in a Hydrogen Engine," SAE Paper 970039.
- [9] Attar, A. A., and Karim, G. A., 2003, "Knock Rating of Gaseous Fuels," *Trans. ASME: J. Eng. Gas Turbines Power*, Vol. **125**, No. 2, pp. 41–47.
- [10] Bade Shrestha, S. O. B., and Karim, G. A., 2001b, "Considering the Effects of Cyclic Variations When Modeling the Performance of a S.I. Engine," SAE Paper 2001-01-3600.
- [11] Das, L. M., 1996, "Hydrogen-Oxygen Reaction Mechanism and Its Implication to Hydrogen Engine Combustion," *Int. J. Hydrogen Energy*, **21**, pp. 703–715.
- [12] Bade Shrestha, S. O. B., and Karim, G. A., 1999a, "A Predictive Model for Gas Fuelled Spark Ignition Engine Applications," SAE Paper 1999-01-3482.
- [13] Bade Shrestha, S. O. B., and Karim, G. A., 1999b, "Hydrogen as Additive to Methane for S.I. Engine Applications," *Int. J. Hydrogen Energy*, **24**, pp. 577–586.
- [14] Bade Shrestha, S. O. B., and Karim, G. A., 2001a, "An Experimental and Analytical Examination of the Combustion Period for Gas-Fuelled Spark Ignition Engine Applications," *Proc. Inst. Mech. Eng., IMechE Conf.*, **215**, pp. 1–12.
- [15] Woschni, G., 1967, "A Universally Applicable Equation for Instantaneously Heat Transfer Coefficient in the Internal Combustion Engines," *SAE Transaction 76(670931)*, pp. 3065–3083.
- [16] Nagalingam, B., Duebel, F., and Schmillen, K., 1983, "Performance Study Using Natural Gas, H₂-supplemented Natural Gas and Hydrogen in AVL Research Engine," *Int. J. Hydrogen Energy*, **8**, pp. 715–720.